

# HIGH-NUCLEARITY PARAMAGNETIC 3d-METAL COMPLEXES WITH OXYGEN- AND NITROGEN-DONOR LIGANDS

RICHARD E. P. WINPENNY

Department of Chemistry, The University of Manchester  
Manchester M13 9PL, United Kingdom

- I. Introduction
  - A. Single-Molecule Magnets
  - B. Strategies for Making Polynuclear Cages
- II. Serendipitous Assembly
- III. Survey of the 3d Metals
  - A. Vanadium
  - B. Chromium
  - C. Manganese
  - D. Iron
  - E. Cobalt
  - F. Nickel
  - G. Copper
- IV. Families of Cages
  - A. Wheels and Metallocrowns
  - B. Cubanes
  - C. Trigonal Prisms
- V. Conclusions
- References

## I. Introduction

It is probably fair to claim that we understand the magnetic and spectroscopic properties of mononuclear complexes of the 3d metals. Stretching a point, we could also claim we understand the preparative chemistry of mononuclear complexes—how to replace ligand A with ligand B and how to prepare complex X. Exploitation of known physical behavior, e.g., constructing devices based on spin-crossover complexes, remains a goal, but such studies build on a base of fundamental

understanding rather than extending it. One or two slightly esoteric questions remain to be answered, but for most purposes we can be confident we know which properties a specific combination of a single 3*d*-metal center and ligands is likely to display.

The work of Cotton, Chisholm, and others has created a huge body of knowledge concerning dinuclear species containing metal–metal bonds (1). Once species of higher nuclearity are considered, our knowledge falls off precipitately as the polymetallic complexes get larger. Fully characterized examples of 3*d*-metal cages become rare beyond hexanuclear species. The exceptions are studies of carbonyl cages by Dahl and others, and the chalcogenide cages reported by Fenske. The paucity of examples is illustrated in Table I, where the number of crystal structures on the Cambridge Structural Database is listed against nuclearity for the 3*d* metals. Here, efforts to address this gap in the chemical literature are reviewed.

#### A. SINGLE-MOLECULE MAGNETS

Initial investigations demonstrate that such cage complexes show physical phenomena of fundamental importance, many of which may have potential application. The magnetic behavior of 3*d*-metal cages has proved particularly exciting. The most important observation, made in 1993, was that a Mn<sub>12</sub> cage showed hysteresis in a magnetization against field plot, and that this hysteresis was of molecular origin (2, 3). The cage in question is the first example of a so-called single-molecule magnet (SMM), and although other examples have since been reported, this remains the most fully studied example.

The dodecanuclear manganese cages have the formula [Mn<sub>12</sub>O<sub>12</sub>(O<sub>2</sub>CR)<sub>16</sub>(H<sub>2</sub>O)<sub>4</sub>], which can be made with a variety of carboxylates, and have ground states of  $S = 9$  or  $10$  (2–4). These molecules show very slow relaxation of their magnetization below 10 K owing to a large anisotropy barrier caused by zero-field splitting of the  $S = 9$  or  $10$  ground state. This leads to a picture where the  $M = \pm 10$  components are the lowest

TABLE I  
NUMBER OF CRYSTAL STRUCTURES ON CSD PER NUCLEARITY FOR 3*d* METALS

Nuclearity	1	2	3	4	5	6	7	8	9	10	11	12
No. of cases	32015	12164	3724	2521	417	619	95	197	40	101	26	83
Nuclearity	13	14	15	16	17	18	19	20	21	22	23	24
No. of cases	7	15	10	18	3	22	4	3	1	3	1	6

in energy, with only these levels populated at low temperature in zero field. If the sample is magnetized, one of these two components—say the  $M = +10$  level—is lowered in energy, and this level is then preferentially populated. If the external magnetic field is then switched off, there is now a marked energy barrier for loss of the magnetization because the system has to pass from  $M = +10 \rightarrow M = +9, +9 \rightarrow +8$ , etc., over the  $M = 0$  level and then down again to occupy the  $M = -10$  level. The presence of this energy barrier explains the long relaxation times observed.

The size of the energy barrier can be measured by a.c. magnetic susceptibility if a low enough temperature can be reached. In an a.c. susceptibility experiment the direction of the external field is changed at a specific frequency. The magnetization of the sample should follow the field, i.e., remain *in phase*, if there is no energy barrier to reorientation of the magnetization. If there is an energy barrier, the magnetization will begin to become *out of phase* with the changing external field, and a signal will appear in the out-of-phase magnetic susceptibility,  $\chi''$ . The appearance of a peak in  $\chi''$  can therefore be an indication that a complex is a SMM; however, other phenomena can lead to such a peak. For a SMM the temperature at which the maximum of the peak in  $\chi''$  is seen is dependent on the frequency with which the external field alternates, and the relaxation rate at a specific temperature can easily be derived from this frequency. Therefore, by measuring  $\chi''$  at a range of frequencies, a range of relaxation rates at various temperatures can be measured, and an Arrhenius treatment then gives the energy barrier for reorientation of the magnetization.

This observation poses the question, “why these compounds and not the other high-spin cages?” The answer appears to be that the high-spin state is here combined with a high anisotropy of the spin caused by the presence of Jahn–Teller distorted Mn(III) ions in the structure. The size of the energy barrier is  $DS^2$ , where  $D$  is the zero-field splitting parameter of the  $S$  ground state of the molecule. The vital issue is the sign of  $D$ —it must be negative for an energy barrier to reorientation to exist. If  $D$  were positive, then  $M = 0$  would be at the bottom of a well, and no significant barrier to reorientation of magnetization exists. More recent studies indicate that these  $\text{Mn}_{12}$  cages are not unique, as other distinct systems have shown similar behavior: an  $\text{Fe}_8$  cage with an  $S = 10$  ground state (5),  $\text{Mn}_4$  cages with an  $S = \frac{9}{2}$  ground state (6), a  $\text{V}_4$  cage with an  $S = 3$  ground state (7), a  $\text{Mn}_{10}$  cage with an  $S = 12$  ground state (8), an  $\text{Fe}_4$  cage with an  $S = 5$  ground state (9), an  $\text{Fe}_{19}$  cage with an  $S = \frac{33}{2}$  ground state (10), and an  $\text{Fe}_{10}$  cage with an  $S = 11$  or  $\frac{23}{2}$  ground state (11).

These properties are more exciting than the simple high-spin molecules because these features are those of a single-molecule magnetic memory, albeit one functioning at less than 10 K. The cages have also allowed studies of quantum-tunneling to be performed, as the particle size and energy barrier seem ideal for seeing quantum effects within these macroscopic systems (12, 13). Hysteresis loops for these cages show distinct “steps,” where the external magnetic field brings energy levels within each well into alignment with energy levels in the other well. Therefore, for physicists these molecules present a wonderful opportunity to examine behavior at the quantum–classical interface.

Serendipity played a role in the discovery of single-molecule magnetism. The first example recognized was  $[\text{Mn}_{12}\text{O}_{12}(\text{O}_2\text{CR})_{16}(\text{H}_2\text{O})_4]$ , where  $\text{R} = \text{Ph}$ , which was originally made as part of a project studying tetranuclear manganese cages as models for the oxygen-evolving complex within Photosystem II (2). The identical cage with  $\text{R} = \text{Me}$  had been reported several years earlier, but without any studies of the magnetic behavior (14). The behavior of the  $\text{Mn}_{12}$  SMMs led to reexamination of other high-spin cages, and previously reported cages were found to show this phenomenon. It is possible that other unrecognized SMMs remain in the literature.

For SMMs to be used in devices, e.g., as a magnetic memory, two problems need to be solved. First, the energy barrier for reorientation of the magnetization needs to be raised to  $>300$  K so that information is retained at room temperature rather than liquid-helium temperatures. Second, a method for writing to and reading from individual molecules needs to be discovered. The latter is a materials-science problem while the former belongs in coordination chemistry.

## B. STRATEGIES FOR MAKING POLYNUCLEAR CAGES

Two broad synthetic strategies are being pursued to make new cages that, ideally, will satisfy the criteria for a room-temperature SMM. One route is dominated by cyanide as the bridging ligand. It has been used as a component for construction of molecular magnetic materials, with influential early work by Babel (16), and later by Verdager (17, 18) and Girolami (19), who realized that Prussian Blue and its analogs might show interesting magnetic behavior. This research has led to the observation of ferro- and ferrimagnetic phases, with some having Curie temperatures above 300 K (20). Hashimoto later showed that these extended phases can also show photomagnetic behavior, with light-induced electron transfer between  $\text{Co(III)}$  and  $\text{Fe(II)}$  centers within

a three-dimensional cyanide-bridged lattice converting a diamagnetic compound into a ferrimagnet (21).

Cage complexes that contain cyanide bridges can be made by blocking suitable coordination sites on the metal fragments. An early synthetic success for this approach was the formation of heptanuclear  $M\{(CN)M'L\}_6$  cages made by Verdaguer and Mallah (22); these cages can have ground states as high as  $S = \frac{27}{2}$ . The choice of the cyanide bridge, which in this chemistry always binds to two metals and is always close to linear, and the use of blocking ligands to restrict the dimensionality of the cage allow an element of design in this approach. French workers adopting this strategy frequently term this "rational" synthesis of polynuclear cages; however, "designed" synthesis is probably better, as there is little evidence that coordination chemists pursuing the alternative strategy are "irrational." This approach is, in many ways, related to the work of Lehn and Saalfrank, in which polydentate ligands that impose structure on the resulting cages are designed.

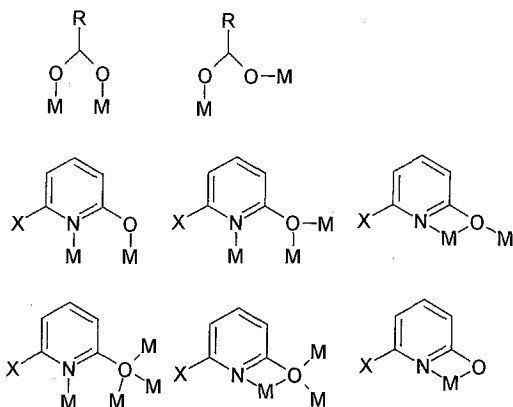
The metallocyanates work has made great progress, and use of different blocking ligands has generated a range of topologies, nuclearities, and spin states. Some of the more spectacular results have arisen, however, where greater freedom has been given to the system. Thus, Hashimoto (15), and later Decurtins (23), reported  $Mn_9Mo_6$  cages ( $M = W$  or  $Mo$ ) that contain a body-centered cube of  $Mn(II)$  centers face-capped by an octahedron of  $Mo(V)$  or  $W(V)$  sites. These cages display fascinating, and controversial, magnetic properties with very high-spin ground states for the molecules. Whether the  $Mn_9Mo_6$  cage reported by Decurtins undergoes a ferromagnetic phase transition, as initial evidence suggests (23), remains to be proved. Similarly, Long has shown that extraordinary cages form when some of the metal units used have a restricted number of coordination sites and others are completely free (24). These results suggest that, while designed assembly is in principle an elegant approach, there is, in fact, more serendipity in the outcome than is always acknowledged.

The second strategy, which is reviewed below, can be termed "serendipitous assembly," as it involves a much lower element of strict design. It is clear, however, that one cannot simply trust to luck in making such cages; considerable forethought must attend the choice of ligands, metals, and conditions used for any significant progress to be made. Before reviewing the range of complexes that have been reported, it is worth considering some of the thought processes behind this approach.

## II. Serendipitous Assembly

The first prerequisite for successful application of serendipitous assembly is humility; one must accept the impossibility of understanding the influence of all the factors involved in a reaction on the resulting product. The inevitable corollary of this understanding is that one must be prepared to try a wide range of conditions for any specific reaction. The metal salt, the substitution pattern of the ligand or ligands, the metal:ligand ratio, the crystallization solvent, the concentration of solution, and the crystallization temperature may all play a part in directing structure, which may not be easy to rationalize. A difficulty in this area is that the reliance on X-ray crystallography as the only dependable characterization tool means that only cages that crystallize well can be unambiguously identified. It is therefore of limited use to consider reaction mechanisms when product formation is controlled by solubility product.

Many of the approaches to serendipitous assembly rely on creating a mismatch between the number or type of coordination sites available on a single metal site, and the donor set supplied by the ligand. This is perhaps best illustrated with two examples. Carboxylates and pyridonates are frequently used as bridging ligands in this chemistry. They act as bridges because the alternative is for the two donor atoms present to chelate to one metal center, which creates a four-membered chelate ring. The four-membered chelate ring contains considerable ring strain, with unsatisfactory angles at the metal center. For carboxylate ligands the end result is normally for the ligand to become 1,3-bridging (Scheme 1). For pyridonate ligands the behavior is more



SCHEME 1

varied; while the 1,3-bridging mode is observed, other modes in which the two donor atoms bind to one metal and the oxygen binds to a second and sometimes a third metal are also seen (Scheme 1). The M—O bond involving the metal to which the N atom is also bound is normally the longest. The oxygen of the pyridonate ligand is not coordinatively saturated by binding to one metal, and therefore acts as a bridge, which leads to the buildup of larger cages.

The second example involves the reaction of oxo-centered manganese carboxylate triangles with bidentate ligands, e.g., 2,2'-bipyridyl (bpy). The oxo-centered triangles have the general formula  $[\text{Mn}_3\text{O}(\text{O}_2\text{CR})_6\text{L}_3]^{0/+1}$ , where L is a monodentate ligand, typically water or pyridine. Addition of a chelating ligand creates a mismatch, as there is only a monodentate site available for substitution *if* the triangular metal array is retained. Therefore, the structure is disrupted, and a larger  $\text{Mn}_4\text{O}_2$  butterfly is formed as the major product (25). In this case it is possible to predict that addition of a chelating ligand will disrupt the initial structure, but it is not possible to predict the product that will result. This is a frequent observation in serendipitous assembly: One can predict that there will be an effect, but not how that effect will be manifested.

The recognition that this synthetic approach generates unpredictable results should influence the choice of ligands. There is little point carrying out initial experiments with ligands that require considerable effort to make, as it cannot be foreseen whether they will have any utility. Moreover, minor variations in the ligands may influence structure and solubility; ideally, a series of related ligands should be explored. For example, our work has focused on the pyridonate ligands substituted in the 6 position, and we have found considerable difference in the behavior of the 6-chloro-2-pyridonate (chp) ligand from that of the 6-methyl equivalent (mhp). Both ligands are commercially available, and related derivatives, e.g., 6-fluoro-2-pyridonate, can be made very easily. Finally, a range of solvents will need to be used for crystallization of the cage compound; it is therefore useful if the ligand has solubility in as many solvents as possible. One frustrating result, which is regularly encountered, is the formation of perfect, colorless crystals of ligand grown from intensely colored solutions of complexes.

The use of mixtures of organic ligands can lead to higher nuclearities than result from the use of single ligands. The octanuclear copper(II) complexes  $[\text{Cu}_8\text{O}_2(\text{O}_2\text{CR})_4(\text{chp})_8]$ , which feature both carboxylates and pyridonates, are examples of this (26). Dinuclear complexes such as  $[\text{Cu}_2(\text{O}_2\text{CR})_4(\text{H}_2\text{O})_2]$  and  $[\text{Cu}_2(\text{chp})_4]$  form when either ligand is present solely; yet a much larger cage results when a mixture is used; indeed,

the dinuclear complexes react together to generate the larger cage. It is unclear why the larger cage results on this occasion. In other reactions use of two ligands can lead to soluble complexes, which can be crystallized, whereas one of the ligands alone would lead to an insoluble polymer. For example, reaction of cobalt or nickel salts with the dicarboxylate phthalate leads to intractable materials at conventional temperatures. Addition of pyridonate ligands leads to soluble materials that can be crystallized to give polynuclear cages (see below).

The choice of solvent for crystallization is important; but if a project is to make progress, it is vital that a range of solvents be tested for every crystallization. The coordination of solvent molecules is frequently observed in structures of crystals grown for solutions in MeOH or MeCN. Sometimes changing to a noncoordinating solvent will lead to much larger cages because the absence of solvent molecules to complete the coordination sphere of metal sites can lead to greater bridging by the ligand(s). A very specific example from our work is the formation of  $[\text{Ni}_3(\text{chp})_4(\text{O}_2\text{CMe})_2(\text{MeOH})_6]$  from  $\text{Ni}(\text{O}_2\text{CMe})$  and  $\text{Hchp}$ , crystallized from MeOH (27), whereas the identical reaction crystallized from THF gives  $[\text{Ni}_{12}(\text{chp})_{12}(\text{O}_2\text{CMe})_{12}(\text{THF})_6(\text{H}_2\text{O})_6]$  (28). The difference in the synthesis is that in the former cage six molecules of MeOH block coordination sites on the terminal Ni atoms, while in the latter cage the less strongly coordinating THF does not bind, thereby allowing growth of the wheel. More frequently, a change in solvent has a less easily rationalized influence.

### III. Survey of the 3d Metals

There are many ways for organizing this material; here, however, the review will proceed systematically across the 3d metals, beginning with vanadium and ending with copper. The other 3d metals are excluded because their polynuclear cages are normally diamagnetic. Discussion is restricted to N- and O-donor ligands for reasons of space—there is a huge body of work on sulfur-donor ligands that would be better reviewed by others. Finally, discussion will concentrate on cage compounds containing six or more metal centers with reference to smaller cages when relevant—in particular where they show the behavior of single-molecule magnets. Literature searching has predominantly used the Cambridge Structural Database. There is an attempt to include all high-nuclearity cages published prior to mid-2000; however, the richness of the field and the proliferation in the numbers of chemical journals make it likely that some examples will have been missed. For this,

I apologize. For some cages, such as the  $\{\text{Mn}_{12}\}$  and  $\{\text{Fe}_8\}$  SMMs, the number of papers published is enormous and not all these papers are referenced. For the latter cage a recent short review article (29) summarizes much of what is most exciting; however, a similar review has not yet been published for the  $\{\text{Mn}_{12}\}$  cage.

#### A. VANADIUM

Polynuclear vanadium chemistry is dominated by polyoxovanadates, and cages containing organic ligands are comparatively rare. Much of the chemistry of the ligated vanadium cages can be related to the polyoxovanadate cages; e.g., there are a number of cages that contain the  $[\text{V}_6\text{O}_{19}]^{8-}$  core where some of the external oxygen centers are now part of a ligand. Polyoxovanadates that contain organic ligands were reviewed in 1992 by Chen and Zubieta (30), and again by Khan and Zubieta in 1995 (31). These reviews are lengthy and authoritative accounts of this specific area. The following section is a summary, included here so that parallels between the vanadium chemistry and that of later 3d metals can be easily drawn.

The most interesting cage from a magnetic viewpoint is a tetranuclear V(III) cage,  $[\text{V}_4\text{O}_2(\text{O}_2\text{CEt})_7(\text{bpy})_2](\text{ClO}_4)$  (**1**) (bpy = 2,2'-bipyridyl), reported by Christou and co-workers (7). This cage has a “butterfly” structure, i.e., two  $\text{V}_3\text{O}$  triangles sharing a  $\text{V}\cdots\text{V}$  edge, and has an  $S = 3$  spin ground state and a zero-field splitting  $D = -1.5 \text{ cm}^{-1}$ , which makes the cage a SMM with an energy barrier of  $\sim 13.5 \text{ cm}^{-1}$  for reorientation of the magnetization. Other tetranuclear V(III) complexes have also been reported, but there are few examples of larger cages containing exclusively this oxidation state. One is a V(III) wheel,  $[\text{V}_8(\text{OH})_4(\text{OEt})_8(\text{O}_2\text{CMe})_{12}]$  (**2**), reported by Kumagai and Kitagawa in 1996 (32). The eight vanadium centers within the wheel are alternately bridged by two carboxylates and a hydroxide, or by one carboxylate and two ethoxides. Both these bridging motifs are found in rings of other metals. No further studies have been reported on this cage, which is surprising.

The vast array of polyoxovanadate cages, synthesized by the Müller group and others, is, in the main, beyond the scope of this review article as they do not involve organic ligands. Fully oxidized cages are clearly not paramagnetic; however, many cages are found that contain V(IV) in addition to V(V), and these cages can display cooperative magnetic behavior. For example,  $\{\text{V}_{18}\}$  cages containing 18, 16, and 10 V(IV) centers have been studied (33). In each of these cases the coupling observed is antiferromagnetic.

The hexametallic cages are, in the main, related to the  $[M_6O_{19}]^{8-}$  core found for  $M = Nb, Ta, Mo, W$ , containing a central  $\mu_6$ -oxygen surrounded by an octahedron of V atoms, with each edge of the octahedron bridged by a  $\mu_2$ -oxygen with a single terminal oxygen attached to each vanadium. The bridging oxide groups can be replaced by alkoxide ligands. The series  $[V_6O_{19-3n}\{(OCH_2)_3CR\}_n]^{x-}$  is known for  $n = 1-4$ , featuring tripodal alkoxides (34). Different protonation and oxidation states of the  $n = 2$  cage are known, i.e.,  $[V_6O_{13-x}(OH)_x\{(OCH_2)_3CR\}_2]^{2-}$  ( $R = Me, Et$ ), where  $x = 0, 2, 3, 4$ , or 6, and the cage contains between zero and six V(IV) centers. In each case the unpaired electrons couple antiferromagnetically. Replacement of the  $\mu_2$ -oxides by monodentate alkoxides has also been observed—completely in  $[V_6O_7(OEt)_{12}]$  (35) and partially in  $[V_6O_{12}(OMe)_7]^-$  (36). The former is presumably mixed-valent, but no magnetic studies are reported. One cage,  $[V_6O_{13}(OMe)_3\{(OCH_2)_3CEt\}]^{2-}$ , has been reported where both tris(alkoxide) and alkoxide ligands are present in place of bridging oxides (37).

Other cages that contain octahedral arrangements of V centers are known where the disposition of bridging and terminal ligands is different. For example, the cages  $[Cp_{6-x}V_6O_x(\mu_3-O)_8]_n$  ( $x = 0, n = 1$ ;  $x = 1, n = 1$  or 2) contain an octahedron of V centers with  $\mu_3$ -oxides on the faces of the octahedron and terminal cyclopentadienyl or oxide ligands (38). All these cages are mixed-valent, e.g.,  $[Cp_6V_6(\mu_3-O)_8]$  must contain four V(IV) and two V(III) centers, and all are reported to be paramagnetic at room temperature. Larger oligomers are known, and are related to other cyclopentadienyl metal oxides, an area that has been reviewed by Bottomley (38).

In  $[(VO)_6(^tBuPO_3)_8Cl]$  (**3**) the six vanadium centers are again arranged in an octahedron, with each organophosphonate group capping a triangular face of the octahedron (39). The chloride is encapsulated within the cage, which is mixed-valent with one V(IV) and five V(V) centers. A very similar cage can also be formed with the ligand  $Me_3SiOPO_3^-$  (40). The reaction that gave **3** gives a tetranuclear cage if  $PhPO_3H_2$  is used as the phosphonate (39). In this case a tetranuclear cage,  $[(VO)_4(PhO_2POPO_2Ph)_4Cl]^-$  (**4**), is found where the four V(IV) centers lie at the vertices of a tetrahedron and the condensed pyrophosphate ligands are disposed so the P atoms lie above the edges of the tetrahedron and the O atoms linking the P atoms lie above the centers of the faces of the tetrahedron. As is frequently the case, this subtle change in ligand has produced an unpredictable change in the resulting polynuclear complex.

In  $[\text{V}_6\text{O}_{10}(\text{O}_2\text{CPh})_9]$  (**5**) a cyclic array of five V(V) centers and one V(IV) center is found, bridged by carboxylate and oxide groups in an irregular manner (41). Three sequential edges are bridged by one oxide and one carboxylate, two edges are bridged by two carboxylates, and the final edge is bridged by one oxide and two carboxylates. This mixture of different bridges is reminiscent of **2**. The six vanadium centers in  $[\text{H}_2\{\text{V}_6\text{O}_{10}(\text{O}_3\text{AsPh})_6\}]^{2-}$  are also mixed-valent [four V(V) and two V(IV)] and arranged in a cyclic structure consisting of a twisted 24-membered ring  $\{\text{V}-\text{O}-\text{As}-\text{O}-\}_6$  with additional intraring V—O—V and As—O—V bridges (42).

An unusual hexanuclear cage is also formed on reaction of  $[(^t\text{Bupz})_4\text{VO}(\text{H}_2\text{O})_2]\text{Cl}_2$  with  $\text{Na}(\text{PhPO}_3)$  ( $^t\text{Bupz}$  = 3-*tert*-butylpyrazole) (43). The phosphonate displaces some of the pyrazole ligands, linking VO units together to give  $[(\text{VO})_6(\text{O}_3\text{PPh})_6(^t\text{Bupz})_6(\text{H}_2\text{O})_3]$ . This cage contains three pairs of vanadyl units, differing in the number of pyrazole ligands to which they are bound. While the polyhedron is described by the authors as “jug-like,” a more striking resemblance is to a bicapped pentagonal prism, with alternately P and V centers at the vertices. Thus, in the 1:5:5:1 polyhedron, the first cap would be a vanadium, the first pentagon would contain two V and three P centers, the second pentagon would contain three V and two P centers, and the final cap would also be a phosphorus.

Not all the hexanuclear cages containing  $\{(\text{OCH}_2)_3\text{CR}\}^{3-}$  ligands form octahedra.  $[\text{V}_6\text{O}_8\{(\text{OCH}_2)_3\text{CEt}\}_3\{(\text{OCH}_2)_2\text{C}(\text{CH}_2\text{OH})\text{R}\}_4]^{2-}$  contains a central  $\{\text{V}_4\text{O}_{16}\}$  core bound to two peripheral vanadium square pyramids via two  $\mu_2$ -O atoms from the doubly deprotonated tripodal ligands (37), as shown in Fig. 1. The cage is again mixed-valent, with a net four V(V) and two V(IV) sites; however, valence sum calculations suggest that the two *d*-electrons are delocalized over four of the vanadium centers. In  $[\text{H}_4\text{V}_6\text{O}_{10}\{(\text{OCH}_2)_3\text{CCH}_2\text{OH}\}_2\text{P}_4\text{O}_4]^{6-}$  (**6**), two  $\text{V}_3\text{O}_{10}\{(\text{OCH}_2)_3\text{CCH}_2\text{OH}\}$  units, each containing a triangle of V(IV) centers, are linked by four  $\{\text{PO}_4\}$  units (44). The magnetochemistry of **6** confirms the presence of exclusively V(IV) and demonstrates that at low temperature one unpaired electron remains on each triangle, and that there is no significant interaction between the two triangles.

A slight variation of this triangular motif is found in one of the two heptanuclear vanadium coordination clusters,  $[\{\text{V}_3\text{O}_9\text{F}\{(\text{OCH}_2)_3\text{CCH}_2\text{OH}\}(\text{V}_4\text{O}_7)\}]^{4-}$  (**7**) (44). Here, the triangular fragment (which contains a central fluoride rather than the central oxide in **6**) is linked by six corners to three  $\{\text{VO}_4\}$  tetrahedra, which are further linked through

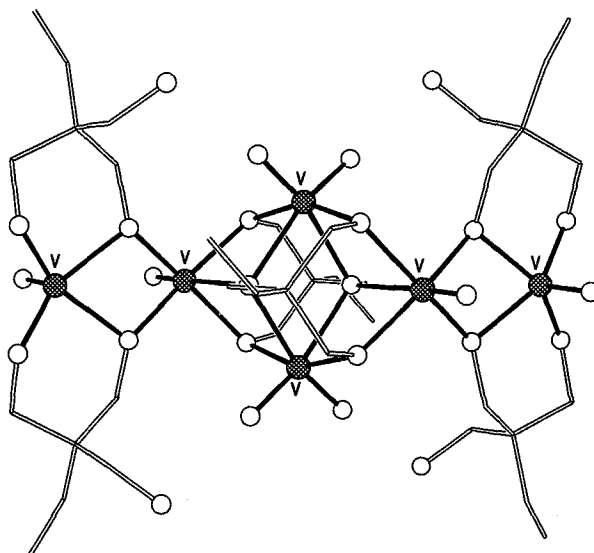


FIG. 1. The structure of  $[\text{V}_6\text{O}_8\{(\text{OCH}_2)_3\text{CEt}\}_3\{(\text{OCH}_2)_2\text{C}(\text{CH}_2\text{OH})\text{R}\}_4]^{2-}$  (based on data taken from Ref. 37). (Shading: V, hatched circles; O, open circles; C, lines.)

corners to a fourth  $\{\text{VO}_4\}$  tetrahedron, so that the entire anion has  $C_{3v}$  symmetry (discounting the terminal  $\text{CH}_2\text{OH}$  group on the ligand). The four tetrahedra contain V(V) centers.

The other heptanuclear cage,  $[(\text{VO})_7\text{O}_5(\text{O}_3\text{PPh})_6\text{Cl}]^{2-}$  (**8**), is spherical and contains an encapsulated chloride ion (45); it is therefore in many ways a larger version of the hexanuclear cage **3**. The reaction is similar to that which gave the tetranuclear cage **4**, but performed at room temperature rather than at  $100^\circ\text{C}$ , thus preventing the formation of the pyrophosphonate. Cage **8** has an irregular polyhedron of metals—perhaps best described as an edge-capped octahedron. Four of the phosphonate ligands sit on triangular faces of the octahedron, while the remaining two phosphonates bind to the “edge-capping” site. All the metals are present in the +5 oxidation state.

The octanuclear vanadium(IV) cage,  $[(\text{VO})_8(\text{OMe})_{16}(\text{C}_2\text{O}_4)]^{2-}$  (**9**), contains a  $\mu_8$ -oxalate within a cyclic  $\{(\text{VO})(\text{OMe})_2\}_8$  wheel (46). Each V...V edge is bridged by two methoxides, with every second edge further bridged by an O atom from the central oxalate. Cages **2** and **9** are therefore both octanuclear vanadium wheels, but in two different oxidation states. While cyclic structures have been reported for the later 3d metals (see below), vanadium appears to be unique in showing two different oxidation states for exclusively O donors.

A nonanuclear mixed-valent vanadium complex,  $[(VO_4)\{V_2O_3(bdta)\}_4]^{7+}$  ( $bdta$  = butanediarninetetraacetate), is known (47). The cage consists of a central  $\{V(V)O_4\}$  tetrahedron with each oxide bridging to a dinuclear  $\{V_2O_3(bdta)\}$  fragment. These dinuclear fragments are each mixed-valent with one V(IV) and one V(V) in each pair. Magnetic studies of this cage show antiferromagnetic exchange between the  $S = \frac{1}{2}$  centers. The X-band EPR spectrum contains a single broad line at all temperatures studied.

A further nonanuclear cage,  $[V_9O_{19}(O_2CMe)_5]^{3-}$ , forms on reaction of  $[VOCl_4]^{2-}$  with silver acetate (48). The cage is mixed-valent, with four V(V) and five V(IV) centers. The structure resembles a hemispherical bowl, with four acetates bridging along the edges of the bowl and one acetate within the bowl. The authors do not assign oxidation states to specific sites within the cage. Magnetization data show the cage to have an  $S = \frac{3}{2}$  ground state.

The majority of decanuclear cages have the decavanadate core, i.e.,  $\{V_{10}O_{28}\}$ , with bridging oxides displaced by oxygen atoms from tripodal tris(alkoxide) ligands. Where the cage contains four such ligands, as shown in Fig. 2, both the oxidation and protonation state can change to give a family of cages of formula  $[V_{10}O_{16-x}(OH)_x\{(OCH_2)_3CR\}_4]^{n-}$  ( $x = 0$ ,  $R = Et$ ,  $n = 4$ ;  $x = 0$ ,  $R = Me$  or  $Et$ ,  $n = 2$ ;  $x = 2$ ,  $R = CH_2OH$ ,  $n = 2$ ) (49, 50), while there is a unique cage,  $[V_{10}O_{13}\{(OCH_2)_3CET\}_5]^{-}$ , containing five tris(alkoxides) (50). Curiously, while electrochemical studies show that the mixed-valent species  $[V_{10}O_{16}\{(OCH_2)_3CMe\}_4]^{2-}$  undergoes two further single-electron oxidations, no reductions of this species could be observed without protonation of the cage with

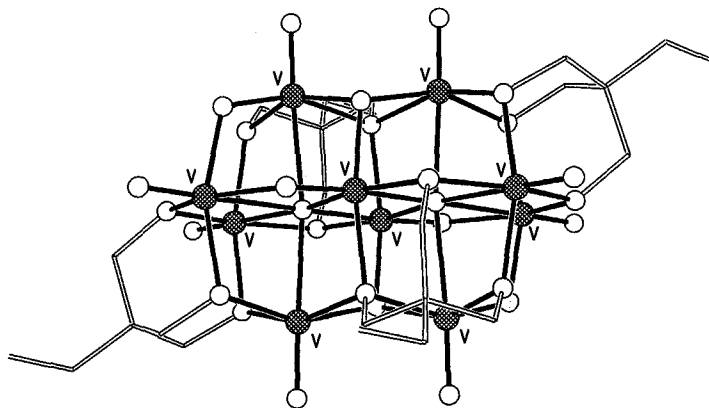


FIG. 2. The structure of  $[V_{10}O_{16-x}(OH)_x\{(OCH_2)_3CR\}_4]^{n-}$  (49). (Shading as in Fig. 1.)

HB $\text{F}_4$ . Magnetic studies of this family of cages reveal the normal antiferromagnetic exchange between spin centers. A tris(alkoxide) ligand also features in a further decanuclear cage, [ $\{\text{V}_3\text{O}_9\text{F}\{(\text{OCH}_2)_3\text{CCH}_2\text{OH}\}_2(\text{V}_4\text{O}_4)\}$ ] (**10**), in which two  $\{\text{V}_3\text{O}_9\text{F}\{(\text{OCH}_2)_3\text{CCH}_2\text{OH}\}$  triangles are linked by four  $\{\text{V(V)O}_5\}$  pyramids (44); the structure is therefore related to both **6** and **7**. The two V(IV) centers in this mixed-valence cage are in the triangular fragments and the interaction between them is negligible.

$[\text{V}_{10}\text{O}_{24}(\text{O}_3\text{AsC}_6\text{H}_4\text{NH}_2)_3]^{4-}$  has a quite distinct structure, and exclusively V(V) centers; however, it undergoes a reversible one-electron reduction to a paramagnetic compound (42). The structure may be described as a  $[\text{V}_9\text{O}_{21}(\text{O}_3\text{AsC}_6\text{H}_4\text{NH}_2)_3]^{3-}$  toroid encapsulating a  $\text{VO}_3^-$  fragment. The toroid consists of  $\{\text{V}_3\text{O}_{13}\}$  triangular units linked through the arsonato groups. A further decanuclear cage,  $[\text{H}_6\text{V}_{10}\text{O}_{22}(\text{O}_2\text{CMe})_6]^{2-}$ , is known which contains two sets of four edge-sharing  $\{\text{V(IV)O}_6\}$  octahedra, linked through two  $\{\text{V(V)O}_4\}$  tetrahedra to form a double-layer structure (51). The six carboxylates bridge some of the  $\text{V(IV)} \cdots \text{V(IV)}$  edges on the exterior of the cage. No magnetic studies are reported for this cage.

Several dodecanuclear vanadium cages containing organic ligands are known. The first,  $[\{\text{VO(OH)}\}_{12}(\text{O}_3\text{PPh})_8]^{4-}$ , is mixed-valent, containing four V(IV) and eight V(V) ions (52). The structure is best described as a pentagonal dodecahedron of V and P centers, with each  $\text{V} \cdots \text{P}$  edge bridged by one oxygen from a phosphonate, and each  $\text{V} \cdots \text{V}$  edge bridged by two hydroxides. The very limited magnetic data reported are described as showing antiferromagnetic exchange between the V(IV) centers.

Two further dodecanuclear cages containing phenylarsonate ligands have been reported. In  $[(\text{MeOH})_2 \subset \text{V}_{12}\text{O}_{14}(\text{OH})_4(\text{O}_3\text{AsPh})_{10}]^{4-}$  (**11**) two MeOH molecules are encapsulated within a cavity created by the cage (53). Two cages of very similar structure can also be isolated which contain 14 vanadium centers,  $[(\text{MeCN})_2 \subset \text{V}_{14}\text{O}_{22}(\text{O}_3\text{PPh})_8]^{6-}$  and  $[(\text{NH}_4)_2\text{Cl}_2 \subset \text{V}_{14}\text{O}_{22}(\text{OH})_4(\text{H}_2\text{O})_2(\text{O}_3\text{PPh})_8]^{6-}$ , with the phosphonate or arsonate ligands playing identical roles in all the cages (Fig. 3) and two of the AsPh units in **11** replaced by VO units in the larger cages (54). The structures are complex, involving edge- and corner-sharing vanadium-centered square pyramids and tetrahedral organoarsonate units. Increasing the ratio of phenylarsonic acid in the reaction that gave **11** produces another, structurally distinct dodecanuclear cage,  $[(\text{H}_2\text{O})_2 \subset \text{V}_{12}\text{O}_{12}(\text{OH})_2(\text{H}_2\text{O})_2(\text{O}_3\text{AsPh})_{10}(\text{HO}_3\text{AsPh})_4]^{2-}$  (53). This structure consists of vanadium-centered square pyramids and octahedra, and organoarsonate tetrahedra and square pyramids; the structure is virtually indescribable.

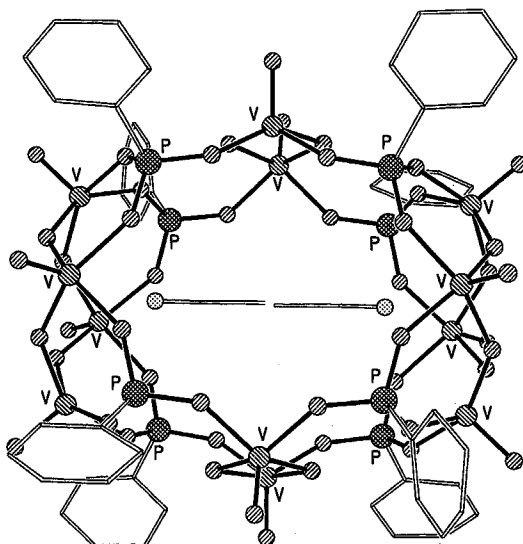


FIG. 3. The structure of  $[(\text{MeOH})_2\text{C} \cdot \text{V}_{12}\text{O}_{14}(\text{OH})_4(\text{O}_3\text{AsPh})_{10}]^{4-}$ . (Data taken from Ref. 53.)

The final dodecanuclear cage is a further example of  $\{\text{V}_3\text{O}_9\text{F}\{(\text{OCH}_2)_3\text{CCH}_2\text{OH}\}$  triangles linked by vanadium-containing fragments; in this case two triangles are linked by four  $\{\text{V(IV)O}_5\}$  and two  $\{\text{V(V)O}_5\}$  triangles, giving  $[\{\text{V}_3\text{O}_9\text{F}\{(\text{OCH}_2)_3\text{CCH}_2\text{OH}\}_2\text{V}_6\text{O}_6]^{6-}$  (44). No X-ray structure is reported but the connectivity is deduced from spectroscopic, analytical, and magnetic data, which confirms that the structure must be very closely related to the naked vanadate cage  $[\text{H}_6\text{V}_{12}\text{O}_{30}\text{F}_2]^{6-}$ . The magnetic behavior of both these cages shows strong antiferromagnetic exchange between the V(IV) centers, but a resulting ground state that contains two uncorrelated unpaired electrons.

Two hexadecanuclear cages are known: one with a phosphonate and one with a tripodal alkoxide ligand. The phosphonate cage,  $[\text{H}_6(\text{VO}_2)_{16}(\text{O}_3\text{PMe})_8]^{8-}$ , resembles a tire with four  $(\text{VO}_2)_4$  tetramers spanning the tread and linked together along each rim by four  $\text{O}_3\text{PMe}^-$  ligands (55). Redox titrations were used to confirm the presence of 14 V(IV) centers. This initial publication is intriguing, and frustrating in two ways. First, the authors thank a colleague for magnetic measurements, but report no magnetic data; and second, they state that further  $(\text{VO}_2)_{16}$  tires have been structurally characterized with ethyl- and phenylphosphonate, yet no additional papers have appeared. Given the beauty of the structure and the large central cavity of the tire, it is surprising that no further studies have appeared in the open literature.

The alkoxide cage  $[\text{V}_{16}\text{O}_{20}\{(\text{OCH}_2)_3\text{CCH}_2\text{OH}\}_8(\text{H}_2\text{O})_4]$  (**12**) (56) shown in Fig. 4 is related to the decavanadate structure; its construction can be considered to involve four corner-sharing interactions between two  $\{\text{V}_8\text{O}_{24}\}$  cores, which are derived from the decavanadate by removal of two adjacent  $\{\text{VO}_2\}$  caps. The synthesis is similar to that of  $[\text{V}_{10}\text{O}_{14}(\text{OH})_2\{(\text{OCH}_2)_3\text{CCH}_2\text{OH}\}_4]^{2-}$ , the major difference being that the solvothermal synthesis was performed at  $170^\circ\text{C}$  to give **12**, and  $150^\circ\text{C}$  to give the decanuclear cage. All the metal centers present are V(IV), and magnetic studies show antiferromagnetic exchange between these centers.

The octadecanuclear vanadium cage  $[\text{Cl}_4 \subset \text{V}_{18}\text{O}_{25}(\text{H}_2\text{O})_2(\text{O}_3\text{PPh})_{20}]^{4-}$  (**13**) (39) can be described as four  $[\text{V}_4\text{O}_6(\text{O}_3\text{PPh})_5]^{2-}$  clusters linked through P—O—V interactions to a central  $\{\text{V}_2\text{O}(\text{H}_2\text{O})_2\}^{8+}$  unit. It is made in MeCN; however, the same reaction in MeOH generates a pentanuclear cage,  $[\text{V}_5\text{O}_7(\text{OMe})_2(\text{O}_3\text{PPh})_5]^-$ . The structure of **13** can be related to that of the pentanuclear cage, but not simply and not in words. All the vanadium centers are V(V).

The largest vanadium coordination cage reported thus far is nonanuclear  $[\{\text{V}_3\text{O}_{10}\{(\text{OCH}_2)_3\text{CCH}_2\text{OH}\}\text{V}_{16}\text{O}_{37}\}]^{7-}$  (**14**) (44), which is closely

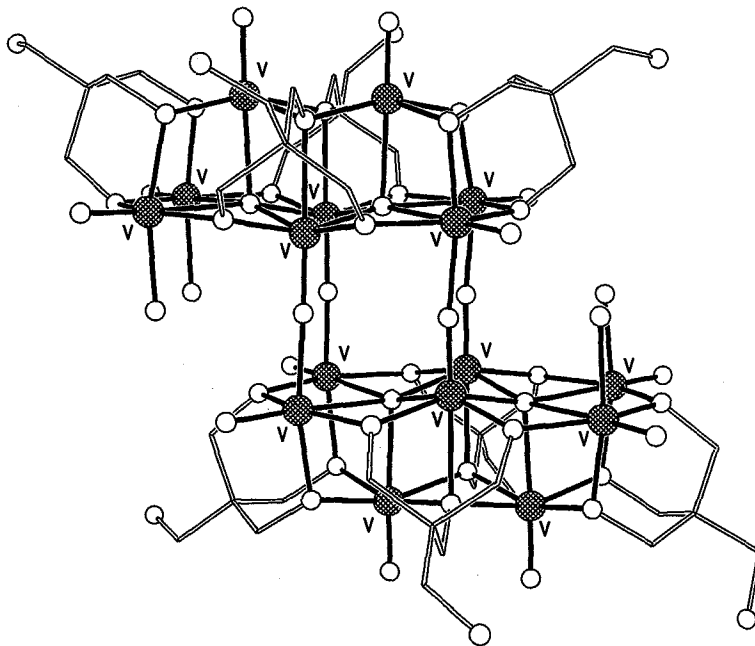


FIG. 4. The structure of  $[\text{V}_{16}\text{O}_{20}\{(\text{OCH}_2)_3\text{CCH}_2\text{OH}\}_8(\text{H}_2\text{O})_4]$  (56). (Shading as in Fig. 1.)

related to a naked vanadate cage,  $[\text{H}_{10}\text{V}_{19}\text{O}_{40}]^{7-}$ . Each contains two  $\{\text{V}_3\text{O}_{13}\}$  triangles, seven  $\{\text{V}(\text{V})\text{O}_4\}$  tetrahedra, and six  $\{\text{V}(\text{IV})\text{O}_6\}$  octahedra, with the tris(alkoxide) ligand attached to one of the triangles in **14**. There are 12 (net) V(IV) centers, and they couple antiferromagnetically. Larger vanadate cages that do not contain organic ligands are known.

The above cages involve organic ligands in linking between metal centers. In other vanadate cages, organic ligands are "guests" within vanadate "hosts." Two examples are known: the inclusion of MeCN in a  $[\text{V}_{12}\text{O}_{32}]^{4-}$  cage (57) and the inclusion of acetate in a  $[\text{H}_2\text{V}_{22}\text{O}_{54}]^{6-}$  host (51). Other guests such as thiocyanate, water, and nitrate can also be included in the latter cage.

The range and structural diversity of the vanadium cages are extraordinary—even when discussion is restricted, as here, to cages that contain organic ligands. The richness of the area, and the productivity of the Müller and Zubieta groups in particular, also means that the above list is unlikely to remain exhaustive for long. There are several points that will be reflected in the synthetic chemistry of the cages of the later 3d metals. First, reactions appear to be sensitive to a very wide range of variables—solvent, counteraction, temperature, substitution pattern of organic ligands—in an unpredictable manner. Sometimes the products of closely related reactions have similar structures, but this observation is not universal. Second, as structures become larger, they become, in general, more difficult to describe. This may seem a truism, but consider carbonyl clusters for example. In this case, the larger clusters clearly become fragments of the metallic elements that are coated with CO ligands. For the vanadium cages there is no straightforward relationship between all the larger clusters and any extended structure. Third, the range of organic ligands used is extremely small, with phosphonate/arsonate and tris(alkoxide) ligands dominant, and a limited number of cages with carboxylate ligands. The remainder of the 3d period shows a quite different use of ligands, with carboxylates extremely common and phosphonate/arsonate ligands very rare in cage complexes.

## B. CHROMIUM

Until recently, polynuclear chromium chemistry was largely restricted to the oxo-centered metal triangles that have been studied for a number of years. Cannon and White reviewed this chemistry in 1988 (58). The lack of larger clusters appeared to be due to the stability of the oxo-centered triangles and to the unreactive nature of the Cr(III) ion;

hence strategies that worked with more substitutionally labile metals [e.g., Mn(III) or Fe(II)] simply failed. A Moldovan research group, led by Professor N. V. G rb l u, made the breakthrough to larger chromium cages (59, 60). The necessary insight was that the inertness of the Cr(III) center could be useful, allowing reactions under more forcing conditions than are conventionally employed in coordination chemistry. Several groups have since followed up this work, employing very similar techniques. Most of this work has appeared since 1999.

The Moldovan work is somewhat older, with the two most relevant papers appearing in the early nineties. The first involves the reaction of chromium trifluoride with pivalic acid at around 130 C, followed by crystallization from acetone, which gives an octanuclear wheel  $[\text{CrF}(\text{O}_2\text{CCMe}_3)_2]_8$  (15) (59a), as shown in Fig. 5. This is the first of a series of chromium wheels that have been reported, all of which feature carboxylates and a second ligand which might be fluoride, hydroxide, or alkoxide. The analogous  $\text{Fe}_8$  wheel is also known (59b). The second paper involves a two-step reaction (60). Sodium pivalate is added to an aqueous solution of chromium nitrate in the first step, producing a blue-green precipitate. In the second step this precipitate is heated to 400 C under a stream of  $\text{N}_2$ , leading to a color change to dark green. This green solid has reasonable solubility

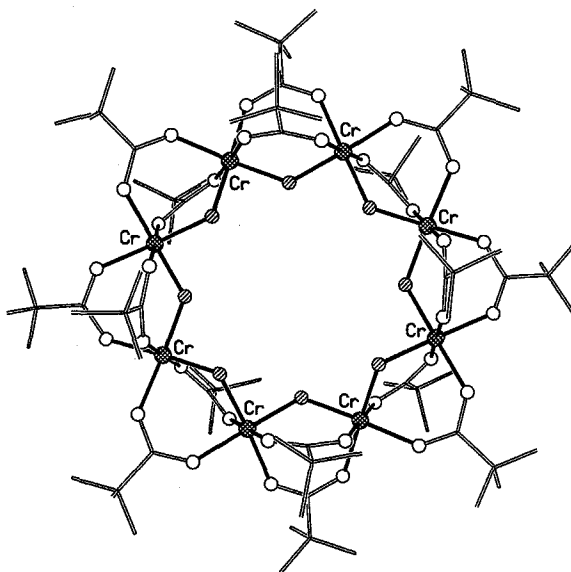


FIG. 5. The structure of  $[\text{CrF}(\text{O}_2\text{CCMe}_3)_2]_8$  (59). (Shading: Cr, hatched; F, striped; O and C as in Fig. 1.)

in organic solvents, and can be crystallized from isopropanol to give a complex initially reported as  $[\text{Cr}_{12}\text{O}_{12}(\text{O}_2\text{CCMe}_3)_{15}]$  (60), as shown in Fig. 6, which would be mixed-valent as written. The magnetic properties of this compound were not reported.

The compound crystallizes in a rhombohedral space group, and the molecular structure has crystallographic  $D_{3h}$  symmetry. The metal sites lie on the vertices of a centered pentacapped trigonal prism. There are four independent metal sites—at the center of the molecule (one Cr atom), at the vertices of the prism (six Cr atoms), capping the trigonal faces of the prism (two Cr atoms), and capping the rectangular faces of the prism (three Cr atoms). The central Cr atom is bound to six  $\mu_4$ -O atoms, each bridging to three further Cr centers, one vertex, and one of each type of cap. The pivalate ligands bridge in a 1,3-fashion on the outside of the metal cage. There are also six  $\mu_3$ -O atoms, each bridging between one vertex Cr, one trigonal cap, and one rectangular cap. Reexamination of this structure by neutron diffraction (61) revealed that half of a H atom was bound to each of these  $\mu_3$ -O atoms, making the correct formula  $[\text{Cr}_{12}\text{O}_9(\text{OH})_3(\text{O}_2\text{CCMe}_3)_{15}]$  (16). The compound is therefore homovalent.

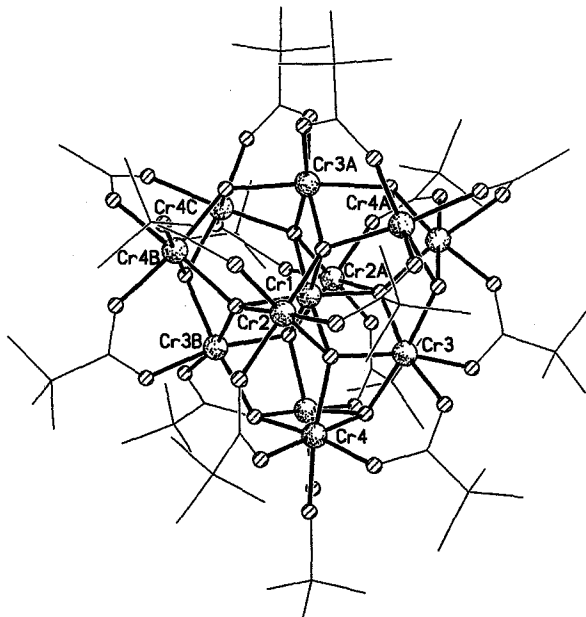
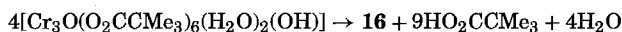


FIG. 6. The structure of  $[\text{Cr}_{12}\text{O}_9(\text{OH})_3(\text{O}_2\text{CCMe}_3)_{15}]$  (61). (Shading: Cr, random shaded; O, striped; C, lines.)

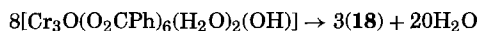
The magnetic properties of the cage are also interesting (61). Although the predominant exchange interaction appears to be antiferromagnetic, the ground spin state has  $S = 6$ . This can be shown by isothermal magnetization measurements, but also by EPR spectroscopy where the 12-line fine structure associated with this spin state can be observed at low temperature and frequencies of 34 GHz and higher. EPR spectroscopy also shows that the zero-field splitting parameter  $D = +0.085 \text{ cm}^{-1}$ , which makes the complex a high-spin cage but not a single-molecule magnet. Unfortunately, the size of the cage makes it impossible, at present, to model the variable temperature susceptibility behavior to quantify the exchange interactions. The  $S = 6$  ground state was, at the time, the equal highest for this metal, matching the ground state observed for  $[\text{Cr}_4\text{S}(\text{O}_2\text{CMe})_8(\text{H}_2\text{O})_4][\text{BF}_4]_2$  (**17**) by Bino and co-workers (62).

The reaction that gave **16** is capable of wide variation. The blue-green precipitate can be crystallized, and X-ray analysis shows that the crystals contain the oxo-centered chromium carboxylate triangles  $[\text{Cr}_3\text{O}(\text{O}_2\text{CCMe}_3)_6(\text{H}_2\text{O})_2(\text{OH})]$  and  $[\text{Cr}_3\text{O}(\text{O}_2\text{CCMe}_3)_6(\text{H}_2\text{O})_3][\text{NO}_3]$  (63). The reaction at  $400^\circ\text{C}$  is therefore a decarboxylation and dehydration of the triangle, and, given the good yield of the reaction, a balanced equation for the reaction is



Reaction of other triangles at temperatures between  $200$  and  $400^\circ\text{C}$  show similar color changes and other polynuclear cages can be crystallized. However, the carboxylate present influences the ratio of carboxylic acid to water lost on heating.

For benzoate at temperatures above  $300^\circ\text{C}$ , only water is lost in generating the cage  $[\text{Cr}_8\text{O}_4(\text{O}_2\text{CPh})_{16}]$  (**18**) (64) shown in Fig. 7. The structure contains a central  $\text{Cr}_4\text{O}_4$  heterocubane, each oxygen center of the cube bridging to an additional Cr cap. The O atoms are therefore  $\mu_4$ -bridging. The benzoate ligands adopt two coordination modes: either 1,3-bridging between Cr atoms within the heterocubane and capping Cr centers, or chelating to the capping chromiums. The balanced equation for this reaction is



At around  $200^\circ\text{C}$ , a second product,  $[\text{Cr}(\text{OH})(\text{O}_2\text{CPh})_2]_8$  (**19**), can be crystallized, in very low yield (64). At  $200^\circ\text{C}$ , the predominant species is the oxo-centered triangle starting material. The octanuclear cage has the

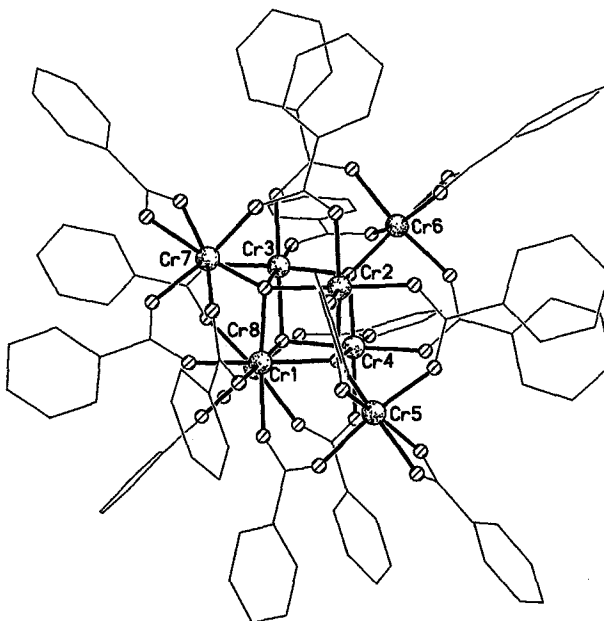
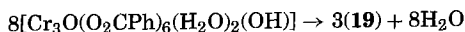


FIG. 7. The structure of  $[\text{Cr}_8\text{O}_4(\text{O}_2\text{CPh})_{16}]$  (64). (Shading as in Fig. 6.)

cyclic wheel structure found previously in **15**. A small quantity of this wheel can also be crystallized with *p*-chlorobenzoate as the carboxylate (65). While the reaction is very low-yielding, the balanced equation for the formation of the wheel is worth considering:



The system therefore appears to show a temperature-dependent dehydration. Unfortunately, it is difficult to produce exclusively the octanuclear wheel, as very little of the oxo-centered triangle appears to react at 200°C, and the reaction proceeds further at higher temperatures, giving the octanuclear capped heterocubane. It will also be interesting to examine whether the wheel and capped cubane can be interconverted by addition or removal of water. The structure of the octanuclear capped heterocubane is closely related to a mixed-valent cobalt cubane  $[\text{Co}_8\text{O}_4(\text{O}_2\text{CPh})_{12}(\text{sol})_4]$  reported by Christou and co-workers, who prepared it by oxidation of cobalt(II) benzoate in DMF or MeCN with  $\text{H}_2\text{O}_2$  (66). The same metal topology has also been observed by Raptis and co-workers for an iron pyrazolate cage (67) (see below).

With iso-butyrate as the carboxylate, a further structural type forms at 400°C. This has the stoichiometry  $[\text{Cr}_{12}(\mu_4\text{-O})_8(\text{OH})_4(\text{O}_2\text{CCHMe}_2)_{16}(\text{HO}_2\text{CCHMe}_2)_4]$  (**20**) (68), as illustrated in Fig. 8. The cage consists of three face-sharing  $\text{Cr}_4\text{O}_4$  heterocubanes, with the two terminal cubanes capped by further chromium centers attached to the external  $\mu_4$ -oxides. The central cubane is held together exclusively through four  $\mu_4$ -oxides with an unusual "sawhorse" geometry rather than tetrahedral, with one  $\text{Cr}-\text{O}-\text{Cr}$  angle of  $\sim 164^\circ$  and five further  $\text{Cr}-\text{O}-\text{Cr}$  angles between 90 and  $101^\circ$ . The  $\mu_4$ -oxides involved in the external heterocubanes have a geometry approximating tetrahedral.

The chromium sites fall into three groups. All are six-coordinate with regular octahedral geometries, but they vary in the groups attached to them. Each Cr site in the central cubane is bound to four  $\mu_4$ -oxides and two oxygen donors from carboxylate bridges. Each Cr site at the exterior of the triple cubane is bound to three  $\mu_4$ -oxides and three O atoms from carboxylates. Each Cr sites capping the tricubane is bound to one  $\mu_4$ -oxide, three oxygens from bridging carboxylates, and two terminal groups that can be described as a hydroxide and a  $\text{HO}_2\text{CCHMe}_2$  group or as a water molecule and a  $^-\text{O}_2\text{CCHMe}_2$  group. Given the strong H bond ( $\text{O}\cdots\text{O}$  2.47–2.53 Å) between these two groups, the exact description is perhaps unimportant.

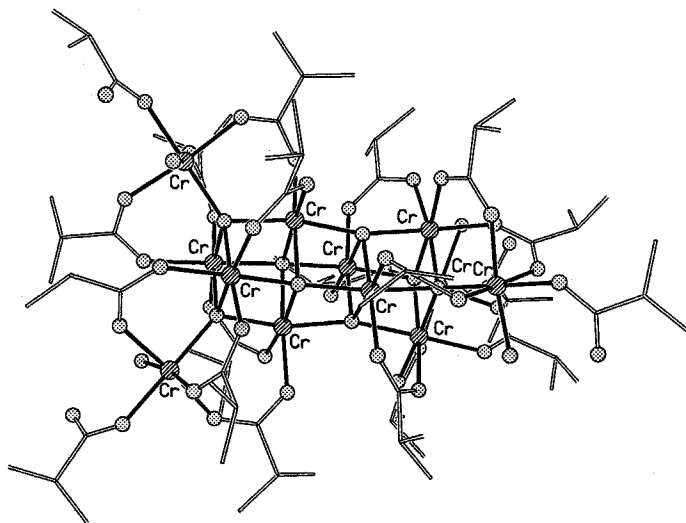
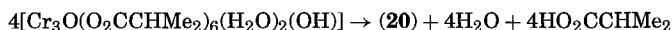


FIG. 8. The structure of  $[\text{Cr}_{12}(\mu_4\text{-O})_8(\text{OH})_4(\text{O}_2\text{CCHMe}_2)_{16}(\text{HO}_2\text{CCHMe}_2)_4]$  (68). (Shading: C, striped; O dotted; Cr, lines.)

The structure is related to both  $[\text{Cr}_8\text{O}_4(\text{O}_2\text{CPh})_{16}]$  and other cubane cages. The nearest relation is an octanuclear triple cubane containing mixed-valent cobalt(II)/(III), reported by Beattie and co-workers, which lacks the final four capping atoms (69). A double cubane of nickel (70) and a heptacubane of manganese (70) have also been reported, as has a “supercubane” of manganese featuring eight cubanes arranged in a cube (see below) (71).

The balanced equation for formation of **20** is



As for pivalate, this represents loss of water and carboxylic acid; however, the  $\text{H}_2\text{O}$  : acid ratio is 1 : 1 compared with 4 : 9; i.e., less acid is lost per molecule of **20** formed than was the case in the synthesis of **16**. This could be related to the relative  $\text{p}K_{\text{a}}$  values of the carboxylic acids formed. It is noticeable that for benzoate, which has the lowest  $\text{p}K_{\text{a}}$  (4.19) of the three carboxylates, water is lost and the carboxylate is retained, while for both pivalate ( $\text{p}K_{\text{a}}$  5.03) and iso-butyric acid ( $\text{p}K_{\text{a}}$  4.84) a mixture of acid and water is lost. Further evidence is needed before it is clear whether this is an example of structure controlled by the  $\text{p}K_{\text{a}}$  of the leaving group.

Including the carboxylate as the counterion of the oxo-centered triangle precursor can influence the amount of acid lost on heating. The reaction of  $[\text{Cr}_3\text{O}(\text{O}_2\text{CCMe}_3)_6(\text{H}_2\text{O})_3][\text{O}_2\text{CCMe}_3]$  at  $300^\circ\text{C}$  is very different from the reaction of  $[\text{Cr}_3\text{O}(\text{O}_2\text{CCMe}_3)_6(\text{H}_2\text{O})_3][\text{NO}_3]$  or  $[\text{Cr}_3\text{O}(\text{O}_2\text{CCMe}_3)_6(\text{H}_2\text{O})_2(\text{OH})]$ . Whereas the latter two complexes lose pivalate to give **16**,  $[\text{Cr}_3\text{O}(\text{O}_2\text{CCMe}_3)_6(\text{H}_2\text{O})_3][\text{O}_2\text{CCMe}_3]$  loses less pivalate to give a hexanuclear complex of apparent stoichiometry  $[\text{Cr}_6\text{O}_4(\text{O}_2\text{CCMe}_3)_{11}]$  (**21**) (65). This again contains a heterocubane, but now only doubly capped on two  $\mu_4$ -oxo sites. If the remaining two  $\mu_3$ -oxygen sites are either both protonated or both deprotonated, the cage would be mixed-valent. However, electrospray mass spectrometry reveals one multiplet centered at  $m/z$  1488 in the negative ion spectrum, while in the positive ion spectrum the multiplet is found at  $m/z$  1490. These peaks match well for  $[\text{Cr}_6\text{O}_4(\text{O}_2\text{CCMe}_3)_{11}]^-$  and  $[\text{Cr}_6\text{O}_2(\text{OH})_2(\text{O}_2\text{CCMe}_3)_{11}]^+$ , respectively. Therefore, it appears that the crystals contain both these species, and presumably also the monoprotanated neutral complex. It is perhaps noteworthy that **16**, **20**, and **21** present the possibility of isolation of different protonation states of the same metal core, a phenomenon that has been regularly observed for vanadium cages.

Preliminary magnetic studies of these cages reveal that, with the exception of **16**, the antiferromagnetic exchange between chromium(III) centers leads to low-spin ground states. For **18** and **19** it was possible to model the antiferromagnetic exchange interactions, giving Cr...Cr exchange parameters of  $2.1\text{ cm}^{-1}$  within the cubane in **18** and  $3.4\text{ cm}^{-1}$  between the cubane Cr centers and the capping Cr centers. In **19** an antiferromagnetic exchange interaction of  $12.0\text{ cm}^{-1}$  was used to model the interaction between nearest-neighbor Cr centers within the wheel.

Oligomerization of oxo-centered triangles can also occur on heating in protic solvents. Refluxing basic chromium acetate in water for two hours produces a wheel of stoichiometry  $[\text{Cr}_8(\text{OH})_{12}(\text{O}_2\text{CMe})_{12}]$  (**22**) (72). The structure is very similar to that of the V(III) wheel **2** (see above), with an octanuclear structure with Cr...Cr vectors alternately bridged by two  $\mu$ -OH and one 1,3-bridging carboxylate or two 1,3-carboxylates and one  $\mu$ -OH. Again, antiferromagnetic exchange is found between Cr centers. McInnes and co-workers have reported a more complicated magnetic picture for a pair of "chromic wheels" made by heating basic chromium acetate in MeOH or EtOH in an autoclave at  $200^\circ\text{C}$ —a piece of solvothermal chemistry reminiscent of the vanadium chemistry discussed above (73). These cages have the formula  $[\text{Cr}(\text{O}_2\text{CMe})(\text{OR})_2]_{10}$  [where R = Me (**23**) or Et (**24**)], and the wheel is symmetric in each case, with each Cr...Cr vector bridged by one 1,3-carboxylate and two  $\mu$ -alkoxides. Therefore, **23** and **24** contain the same metal topology as the older "ferric wheels" (see below). An oddity is that while the Cr...Cr exchange in **24** is very weak ( $0.9\text{ cm}^{-1}$ ) and antiferromagnetic, the exchange in **23** is weak ( $4.5\text{ cm}^{-1}$ ) but ferromagnetic with significant inter-wheel interactions. Each wheel in **23** should therefore have an  $S = 15$  ground state, which is among the highest known.

A final version of these chromium wheels can be made by addition of secondary amines to the reaction mixture that gave the fluoride-bridged wheel **15**. A hydrogen-bonded assembly of cages can be formed of stoichiometry  $[(\text{R}_2\text{NH}_2)_3\{\text{Cr}_6\text{F}_{11}(\text{O}_2\text{CCMe}_3)_{10}\}(\text{H}_2\text{O})_2]$  (R = *n*-propyl, **25**; R = *n*-pentyl, **26**). The supramolecule consists of two symmetry-related  $[\text{Cr}_6\text{F}_{11}(\text{O}_2\text{CCMe}_3)_{10}]^{3-}$  "horseshoes" held together by H bonds to protonated amines (74). Each  $[\text{Cr}_6\text{F}_{11}(\text{O}_2\text{CCMe}_3)_{10}]^{3-}$  horseshoe is derived from **15** by removal of two of the Cr sites. The Cr sites within the horseshoe are bridged by  $\mu_2$ -F and 1,3-bridging carboxylates in an analogous manner to that found in **15**. The two Cr sites at the tips of the horseshoe have three terminal fluoride ligands, and these terminal fluorides are involved in the H bonding that links the horseshoes. Two fluorides on each chromium H-bond to H atoms of  $[\text{R}_2\text{NH}_2]^+$  cations which lie between the tips of the horseshoes. These eight F...H—N bonds therefore

create a dodecanuclear pseudomacrocyclic. The third fluoride on each terminal Cr site is involved in an additional H-bonding interaction. These four fluorides accept H bonds from two further  $[R_2NH_2]^+$  cations and from two water molecules which are encapsulated within the pseudomacrocyclic. The result is a supramolecule consisting of two hexametallic trianions, six ammonium cations, and two water molecules. It is notable that the H bonding involves only the terminal F-ligands, and not those that bridge between Cr centers. Magnetic studies again indicate antiferromagnetic exchange between the Cr centers within the molecule.

Although the cage is diamagnetic, the linear heptanuclear cage  $[Cr_7(teptra)_4Cl_2]$  deserves a mention ( $teptraH_3$  = tetrapyridyltriamine) (75). This Cr(II) cage is made from reaction of  $CrCl_2$  with the deprotonated form of the heptadentate ligand, and the resulting "metal string" contains seven metal centers bridged by four ligands, with two terminal chloride ligands completing the structure. Calculations suggest that this compound is a metal since the Fermi level is located within the HOMO band, and there is therefore no band gap.

### C. MANGANESE

Work on manganese cages is dominated by the use of carboxylate ligands, and by synthetic work from the Christou/Hendrickson grouping (76). Much of this work originated in a study of the tetranuclear oxygen-evolving complex in Photosystem II; however, restricting the nuclearity of carboxylate cages is not straightforward, and many larger cages result from the synthetic methods adopted.

The earliest hexanuclear manganese cage was reported by Thornton and co-workers in 1986 (77).  $[Mn_6O_2(O_2CCMe_3)_{10}(HO_2CCMe_3)_4]$  consists of an edge-sharing bitetrahedral cage, with each tetrahedron centered by a  $\mu_4$ -oxo ion. The carboxylate ligands present bridge in 1,3- and 1,1,3-fashion. Four terminal protonated pivalates are attached to the exterior metal vertices of the bitetrahedron. The cage is mixed-valent, containing four Mn(II) and two Mn(III) centers, with the Mn(III) centers localized at the shared edge of the bitetrahedron. The cage was originally made by refluxing a toluene solution of  $MnCO_3$  and pivalic acid, and can also be made by reaction of manganese(II) nitrate and pivalic acid in dioxane (78). Several similar cages have been made (79–82); these cages differ in the terminal ligands (pyridine, MeCN, EtOH,  $H_2O$ , acetone, THF) and in the bridging carboxylate (pivalate, benzoate, or nitrobenzoate). The simplicity of the reaction and moderate yields make these cages suitable starting materials

for further synthesis. The magnetic properties have been studied for  $[\text{Mn}_6\text{O}_2(\text{O}_2\text{CPh})_{10}(\text{py})_2(\text{MeCN})_2]$ , and the cage has an  $S = 0$  ground state (79).

The second hexanuclear manganese cage reported is the first "high-spin cage" to be reported (83). It is a cyclic molecule with a formula  $[\text{Mn}(\text{hfac})_2(\text{NITPh})]_6$  (27), as shown in Fig. 9 (hfac = hexafluoroacetylacetonate, NITPh = 2-phenyl-4,4,5,5-tetramethyl-4,5-dihydro-1*H*-imidazol-1-oxyl-3-oxide—see Scheme 2), with each nitronyl-nitroxide ligand bound to two  $\{\text{Mn}(\text{hfac})_2\}$  fragments through the two oxygen atoms, giving a wheel that is homovalent (unlike the majority of manganese cages). Synthesis involves mixing the two components in heptane. Magnetic studies show a value for  $\chi_m T$  at low temperature consistent with an  $S = 12$  ground state, which arises from antiferromagnetic exchange between the  $S = \frac{1}{2}$  centers on the radicals, and the  $S = \frac{5}{2}$  metal centers.

Hexanuclear cages with carbamate ligands have been reported for manganese, iron, and cobalt. The manganese cage,  $[\text{Mn}_6(\text{O}_2\text{CNET}_2)_6]$ , is made by addition of  $[\text{Mn}(\text{Cp})_2]$  to a solution of  $\text{NHET}_2$  in toluene,

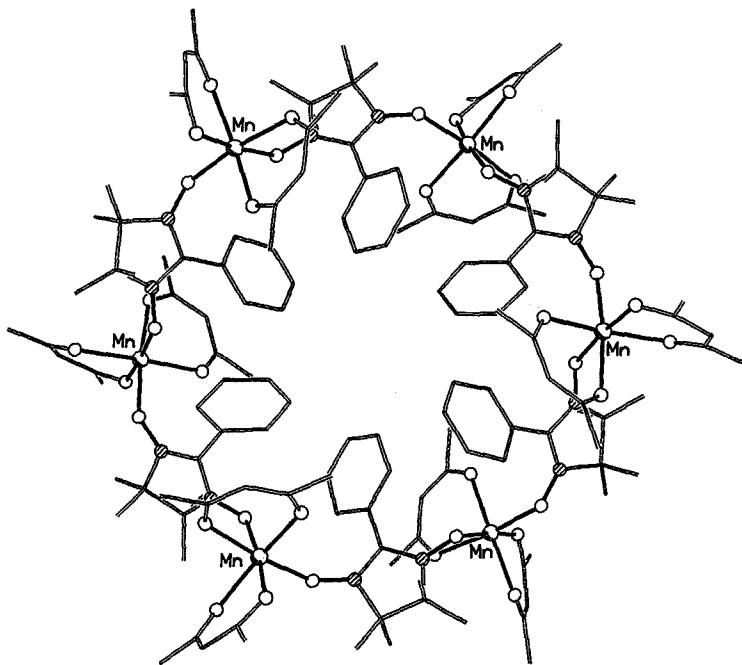


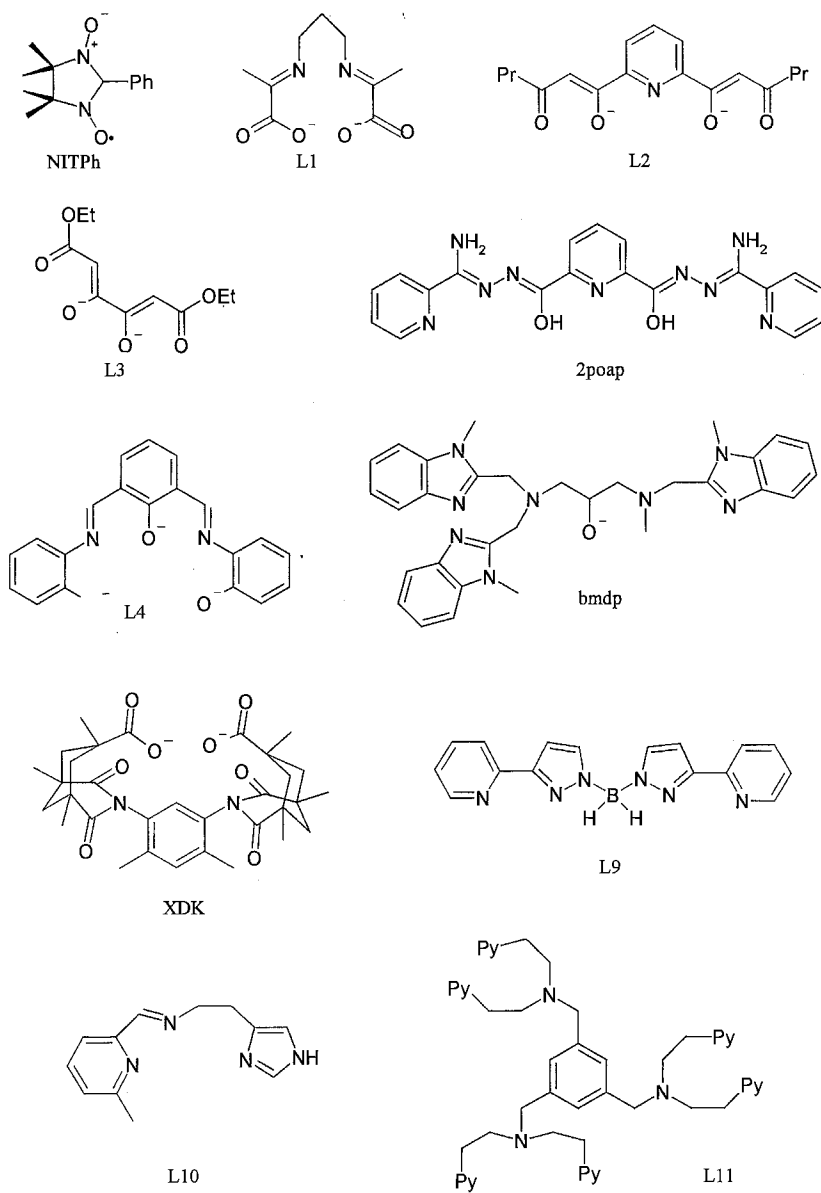
FIG. 9. The structure of  $[\text{Mn}(\text{hfac})_2(\text{NITPh})]_6$  (83). (Shading: Mn, shaded; O, open; C lines.)

followed by reaction with carbon dioxide (84). The structure consists of an edge-sharing bitetrahedron of manganese(II) centers. Both five- and six-coordinate Mn(II) sites are found, and the carbamate ligands show three different bridging modes: 1,1-, 1,1,3-, and 1,1,3,3-bridges are found.

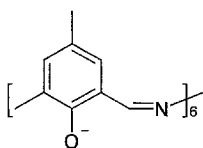
Further hexanuclear cages can be made with the pentadentate Schiff-base ligand, *N*-(*X*-substituted salicylidene)-*N,N'*-bis(2-hydroxyethyl)ethylenediamine (*X* = 5-MeO, 5-Cl, 5-Br) (85). These cages contain exclusively Mn(III) centers, which are arranged in a planar array, bridged by two  $\mu_3$ -oxides, two  $\mu_3$ -methoxides, four  $\mu_2$ -methoxides, two  $\mu_2$ -acetates, and two ligands. Magnetic studies of the cages indicate antiferromagnetic exchange between the Mn(III) centers.

A series of hexanuclear cages featuring the anions of derivatives of dibenzoyl methane (Hdbm) have been made, and show  $S = 12$  ground states (86). These cages have the general formula  $[\text{Mn}_6\text{O}_4\text{X}_4(\text{R}_2\text{dbm})_6]$  (*X* = Cl or Br, *R* = Me, Et). The structures consist of a Mn(III) octahedron with four nonadjacent faces bridged by  $\mu_3$ -oxides and the other four faces bridged by  $\mu_3$ -chlorides. A chelating  $\text{R}_2\text{dbm}$  group is attached to each manganese center, completing an approximately octahedral coordination geometry. As expected, each Mn(III) site displays Jahn–Teller distortion of the coordination sphere. The syntheses of these cages is via five-coordinate, mononuclear Mn(III) complexes  $[\text{MnX}(\text{R}_2\text{dbm})_2]$ . Slow evaporation of MeCN/ $\text{CH}_2\text{Cl}_2$  or MeCN solutions of these monomers generated the hexanuclear cages. Magnetic studies show ferromagnetic exchange of  $\sim 8.5 \text{ cm}^{-1}$  between neighboring Mn(III) centers, leading to an  $S = 12$  ground state. Magnetization data fit well with this ground state, and with  $D = 0$ , which is consistent with the virtual  $T_d$  of the cages. Therefore, the cages have a high spin; but if they are SMMs, they would have one of the smallest known energy barriers to reorientation of the magnetization.

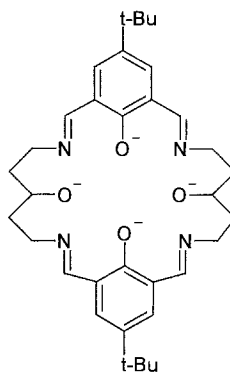
The hexanuclear cage,  $[\text{Mn}_6\{(\text{PhSiO}_2)_6\}_2\text{Cl}(\text{ROH})_6]^-$  (**28**) (*R* = *n*Bu) (87) contains a  $\{\text{Mn}_6\text{Cl}\}$  plane sandwiched between two cyclohexasiloxanolate ligands, as shown in Fig. 10. The manganese centers are at the corners of a regular hexagon, with each Mn···Mn edge bridged by two O atoms from the cyclohexasiloxanolate ligands, thus creating an approximately square plane of O atoms about the Mn centers. The coordination geometry of each site is then completed by a coordinated alcohol molecule and by a long contact to the central chloride. The cage could be described as a host–guest molecule, with the chloride ion trapped within the metallocryptand. The preparation of the cage is from dissolution of  $[\text{PhSiO}_{1.5}]_n$  in hot *n*BuOH in the presence of NaOH, followed by addition of manganese(II) chloride.



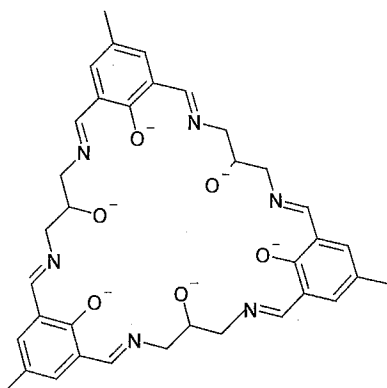
SCHEME 2



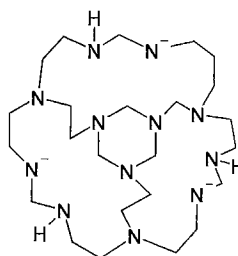
L12



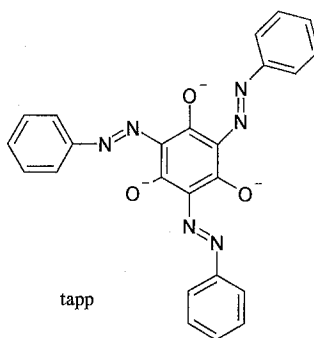
L13



L14



L15



tapp

SCHEME 2 (Continued)

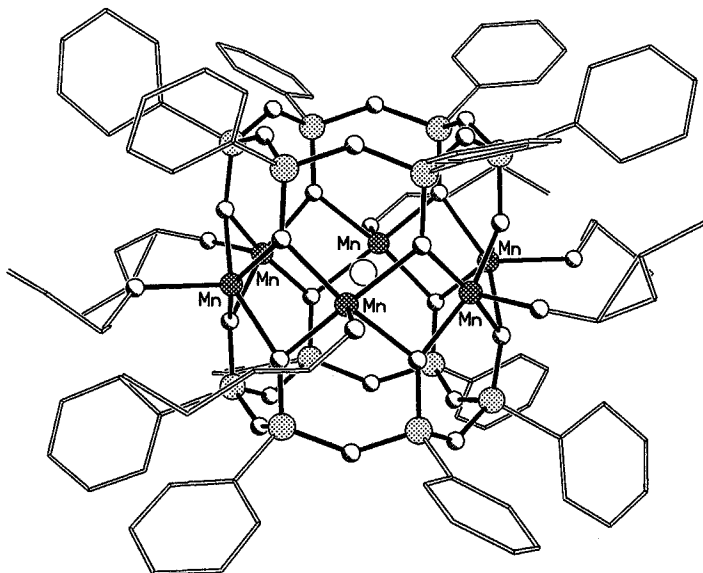


FIG. 10. The structure of  $[\text{Mn}_6\{(\text{PhSiO}_2)_6\}_2\text{Cl}(\text{ROH})_6]^-$  (87). (Shading: Mn, hatched; O, shaded; Si, dotted; Cl, open; C, lines.)

The compounds  $[\text{Mn}_6\text{O}_6(\text{O}_2\text{CR})_3(3,2,3\text{-tet})_4]^{5+}$  (3,2,3-tet = 1,5,8,12-tetraazadodecane; R = Me or Ph) were reported by Weatherburn and co-workers, and contain a planar mixed-valent cage (88). The structure consists of an approximately linear arrangement of four manganese ions, with each  $\text{Mn} \cdots \text{Mn}$  vector bridged by two oxides. The central two oxides also bind to the final two Mn centers in the structure. One of the three carboxylates spans the central  $\text{Mn} \cdots \text{Mn}$  contact, and the remaining two bridge from these Mn centers to the fifth and sixth Mn centers. The tetradentate amine ligands bind to the four external Mn sites. The two Mn(IV) sites in the structure are assigned as the external manganese of the central linear portion of the structure, the other four sites being Mn(III). No detailed magnetic measurements are reported for this compound.

This group also synthesized the first heptanuclear manganese cage,  $[\text{Mn}_7\text{O}_4(\text{trien})_2(\text{dien})_2(\text{O}_2\text{CMe})_8]^{4+}$  (29) (trien = triethylenetetramine, dien = diethylenetriamine), which also features both carboxylate and amine ligands (89), as shown in Fig. 11. The cage can be described as two mixed-valent  $\{\text{Mn}_4\text{O}_2\}$  butterflies, three Mn(III) and one Mn(II), sharing the Mn(II) center. The cage is held together by the four oxides, each of which is  $\mu_3$ -bridging, and the carboxylate ligands, which all

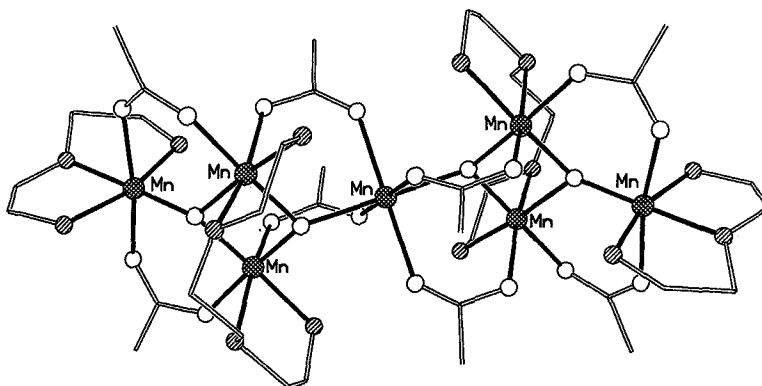


FIG. 11. The structure of  $[\text{Mn}_7\text{O}_4(\text{trien})_2(\text{dien})_2(\text{O}_2\text{CMe})_8]^{4+}$  (**89**). (Shading: Mn, hatched; O, open; C, lines.)

act as 1,3-bridges. The dien ligands act as chelating, terminal ligands while the trien ligands bind to both Mn(III) centers, which act as the body of the butterfly fragments. The synthetic procedure that gives **29** illustrates the redox activity of manganese; the cage can be made from reaction of either Mn(II) or Mn(III) acetate with trien in air, and the dien found must result from oxidation of trien ligands during the reaction.

A similar arrangement of six manganese centers is found in  $[\text{Mn}_7\text{O}_4(\text{O}_2\text{CMe})_{10}(\text{dbm})_4]^-$  (**30**) (dbm = the anion of dibenzoylmethane), which is homovalent (**90**). The chelating dien ligands in **29** are replaced by dbm ligands, and dbm ligands are also found chelating to two of the four Mn(III) centers that make up the butterfly bodies. Eight of the ten acetates adopt bonding modes similar to those in **29**, while the additional two acetates bridge in a 1,1,3-mode. The synthetic procedure is quite different, involving addition of  $\text{NEt}_4\text{Cl}$  to a tetranuclear manganese(III) butterfly,  $[\text{Mn}_4\text{O}_2(\text{O}_2\text{CMe})_6(\text{py})_2(\text{dbm})_2]$  in  $\text{CH}_2\text{Cl}_2$ . This transformation is both solvent-dependent and difficult to rationalize; in MeCN, the same reaction gives  $[\text{Mn}_4\text{O}_3\text{Cl}(\text{O}_2\text{CMe})_3(\text{dbm})_3]$  (**91**). Magnetic measurements indicate that **30** has a complicated spin structure, and it was not possible to conclude whether the ground state was  $S = 3$  or  $S = 4$  based on preliminary magnetization studies.

A heptanuclear manganese(II) cage,  $[\text{Mn}_7\text{O}_6(\text{OEt})_{18}(\text{HOEt})_2]$ , has also been crystallized from the reaction of anhydrous  $\text{MnCl}_2$  with  $\text{NaSb}(\text{OEt})_4$  by controlled hydrolysis in toluene-ethanol (**92**). The structure contains a central Mn(II) center surrounded by a trigonal prism of six further Mn(II) atoms, with the cage held together by  $\mu_5$ - and  $\mu_4$ -oxides, and  $\mu_3$ - and  $\mu_2$ -ethoxides.

The remaining heptanuclear manganese cages belong to the class of "metallocrowns." Six metal centers form part of a macrocyclic complex ligand that encapsulates the seventh metal. The earlier one is made from reaction of manganese(II) chloride, tetraethylammonium permanganate, and 2-hydroxymethylpyridine (Hhmp) in MeCN. The cationic species,  $[\text{Mn} \subset \text{Mn}_6(\text{OH})_3\text{Cl}_3(\text{hmp})_9]^{2+}$  (**31**), is mixed-valent, with the metal centers within the metallocrown alternating between Mn(II) and Mn(III), while the encapsulated metal is Mn(II) (93). This central Mn(II) is bound to oxygen donors derived from three hydroxides and three oxygens from hmp ligands. Each of these oxygens is shared with two further manganese centers from the wheel. The Mn(II) centers within the metallocrown are bound to one N and four O atoms, with a terminal chloride, while the Mn(III) centers are bound to two N and four O atoms. Magnetic studies indicate a high-spin ground state of either  $S = 10$  or  $S = 11$ . For either spin state, the fit of reduced magnetization plots requires a negative  $D$ -value of either  $-0.15$  or  $-0.18 \text{ cm}^{-1}$  respectively, which would indicate that **31** should be a SMM. However, no peak is observed in the out-of-phase a.c. susceptibility of this cage down to 2 K.

Similar cages can be formed by reacting  $\text{MnCl}_2$ ,  $\text{Na}(\text{OMe})$ , and Hdbm in MeOH, which gives  $[\text{Na} \subset \text{Mn}_6(\text{dbm})_6(\text{OMe})_{12}]^+$  (**32**) (94), as shown in Fig. 12, and  $[\text{Mn} \subset \text{Mn}_6(\text{dbm})_6(\text{OMe})_{12}]$  (**33**) (95); the only difference in

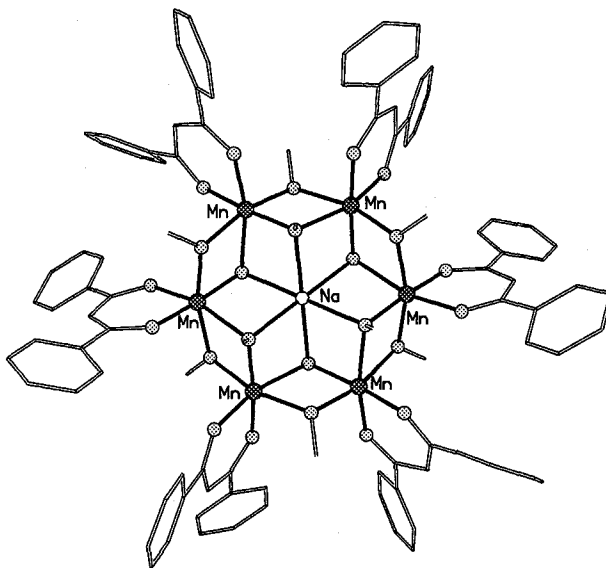


FIG. 12. The structure of  $[\text{Na} \subset \text{Mn}_6(\text{dbm})_6(\text{OMe})_{12}]^+$  (94). (Shading: Mn, hatched; O, dotted; Na, open; C, lines.)

the synthetic procedure is that Na(BPh<sub>4</sub>) was added to the reaction, which gave **32**. The structures consist of a metallocrown containing six Mn centers, each bound to one chelating dbm ligand, with each Mn···Mn vector bridged by two  $\mu$ -OMe ligands. Six of these methoxides provide a cavity where the seventh metal, either sodium or manganese, is encapsulated. The magnetic properties of both cages are interesting. Cage **32** is homovalent, containing only Mn(III) centers, and ferromagnetic exchange is observed between the metals, giving an  $S = 12$  ground state. Magnetization measurements indicate the presence of low-lying excited states with  $S < 12$ .

Cage **33** is mixed-valent, and probably contains a net three Mn(II) and four Mn(III) centers. The high, crystallographically imposed, symmetry of the cage ( $S_6$ ) requires that there be only two independent Mn sites—the encapsulated manganese, which appears to be Mn(II), and the manganese sites, which form part of the metallocrown. These sites are therefore required to be 1/3 Mn(II) and 2/3 Mn(III). It is extremely unusual to find electron-delocalized valence states of mixed-valence manganese cages; as this discussion illustrates, the majority belong to class I in the Robin–Day classification. This consideration, together with the UV–vis spectroscopy of **33**, suggests that static disorder effects are operating in the crystal lattice, creating the erroneous impression of electron delocalization. Interpretation of the magnetic data is difficult when assignment of specific oxidation states to specific sites is impossible. Magnetization data are consistent with three sets of parameters: (1) an  $S = \frac{15}{2}$  ground state with  $g = 2.36$  and  $D = -0.34$  cm<sup>-1</sup>; (2) an  $S = \frac{17}{2}$  ground state with  $g = 2.08$  and  $D = -0.27$  cm<sup>-1</sup>; (3) an  $S = \frac{19}{2}$  ground state with  $g = 1.86$  and  $D = -0.21$  cm<sup>-1</sup>. The authors prefer the  $S = \frac{17}{2}$  ground state; however, it is not even clear that an isolated ground state will be found in such a complicated spin-frustrated system.

It is perhaps worth commenting that the three metallocrowns, **31–33**, are also rare cases in which polynuclear manganese cages are formed without the use of carboxylate ligands. These structures are related to other heptanuclear metal cages formed with iron, cobalt, and copper (see below).

A final heptanuclear manganese cage, [Mn{Mn(L1)}<sub>6</sub>]<sup>2+</sup> (for L1 see Scheme 2), takes the metallocrown concept further toward metallocryptands, and contains a Mn(II) center within a twisted trigonal prism of six further Mn(II) centers (96). The cage is stabilized by a tetradentate iminocarboxylate ligand, which binds to the equatorial sites of the manganese centers comprising the prism, with the second carboxylate oxygens binding either to axial sites of neighboring Mn(II)

centers of the prism or to the encapsulated Mn(II). No magnetic data are reported for this cage.

The majority of octanuclear manganese cages are formed by dimerization of tetranuclear butterflies, and their formation is perhaps the closest this chemistry has come to “designed synthesis”: Not only was the type of reaction predicted, but the resulting structure is also clearly related to the tetranuclear “monomer.” For example,  $(\text{NBu}^n_4)[\text{Mn}_4\text{O}_2(\text{O}_2\text{CMe})_7(\text{pic})_2]$  (pic = picolate) reacts with one equivalent  $\text{Me}_3\text{SiCl}$ , with removal of one acetate per tetranuclear cage, followed by dimerization to give  $[\text{Mn}_8\text{O}_4(\text{O}_2\text{CMe})_{12}(\text{pic})_4]$  (97). The tetranuclear butterfly structures are maintained, and the major change is that picolate ligands, which are chelating via the ring N atom and one carboxylate oxygen in the tetranuclear cage, bridge to a second tetranuclear unit via the second carboxylate oxygen in the octanuclear cage. Alternatively, a bridging ligand can be added to replace the abstracted carboxylate; e.g.,  $(\text{NBu}^n_4)[\text{Mn}_4\text{O}_2(\text{O}_2\text{CMe})_7(\text{dbm})_2]$  reacts with  $\text{Me}_3\text{SiCl}$  to give  $[\text{Mn}_4\text{O}_2(\text{O}_2\text{CMe})_6(\text{dbm})_2]$ , which can be linked through *trans*-1,2-bis(4-pyridyl)ethane (bpe) to give  $[\text{Mn}_4\text{O}_2(\text{O}_2\text{CMe})_6(\text{dbm})_2(\text{bpe})]_2$  in which two butterflies are linked through the diimine ligand (98). A similar reaction with 4,4'-bipyridyl gives a polymer (98). Direct displacement of monocarboxylates by dicarboxylates can also lead to dimerization; however, here the reaction is not so straightforward. Addition of 2,2-diethylmalonate ( $\text{Et}_2\text{mal}^{2-}$ ) to  $(\text{NBu}^n_4)[\text{Mn}_4\text{O}_2(\text{O}_2\text{CMe})_9(\text{H}_2\text{O})]$  gives  $[\text{Mn}_8\text{O}_4(\text{O}_2\text{CMe})_{12}(\text{Et}_2\text{mal})_2(\text{H}_2\text{O})_2]^{2-}$  (**34**) (99), where the dicarboxylates link the cages by chelating to a manganese site in one tetranuclear fragment through O atoms in differing carboxylates, making a six-membered chelate ring, and to a manganese in the other fragment through both O atoms of a single carboxylate, making a four-membered chelate ring. A further bridging interaction is also provided by one of the oxide groups of the butterfly, which binds to a Mn body site in the other butterfly, hence becoming  $\mu_4$ -bridging. The octanuclear cage is mixed-valent, containing six Mn(III) and two Mn(II) centers, whereas the precursor contains exclusively Mn(III) ions. The two Mn(II) sites are assigned as wing tip sites based on bond length considerations and the absence of Jahn–Teller distortions at these sites.

No magnetic studies of the picolate-bridged cage were reported, and the interaction between the two tetranuclear cages bridged by bpe in  $[\text{Mn}_4\text{O}_2(\text{O}_2\text{CMe})_6(\text{dbm})_2(\text{bpe})]_2$  is too small to be noticeable. For **34** the magnetic moment could be fit from 2 to 300 K in a 10.0-kG field assuming only intra-butterfly interactions, which gave an  $S = \frac{5}{2}$  ground state for each butterfly and no inter-butterfly coupling. However, the authors fit the reduced magnetization from 2 to 4 K using an  $S = 3$

ground state with  $D = 4.92 \text{ cm}^{-1}$ . This value of  $D$  seems rather large, and it is unclear whether the magnetization data could have been fitted to a model of two noninteracting  $S = \frac{5}{2}$  centers with a smaller  $D$  value. It is also unclear why two subtly different, although not irreconcilable, models for the magnetic behavior are proposed in the same paper.

If  $(\text{NBu}^n_4)[\text{Mn}_4\text{O}_2(\text{O}_2\text{CPh})_9(\text{H}_2\text{O})]$  is treated with  $\text{Me}_3\text{SiCl}$ , a homovalent octanuclear Mn(III) cage is formed, but one which is not so clearly related to the tetranuclear precursor. The structure of  $(\text{NBu}^n_4)[\text{Mn}_8\text{O}_6\text{Cl}_6(\text{O}_2\text{CPh})_7(\text{H}_2\text{O})_2]$  (**35**) (100), shown in Fig. 13, contains an  $\{\text{Mn}_7\text{O}_6\text{Cl}_2\}$  core, related to two  $\{\text{Mn}_4\text{O}_3\text{Cl}\}$  cubes sharing an edge; however, there are two oxides in the shared edge rather than one. These two oxides bridge to the eighth manganese center in the cage. The benzoate ligands are all 1,3-bridging. The cage shows two reversible electrochemical processes: a one-electron oxidation at 0.91 V and a one-electron reduction at 0.12 V (vs. ferrocene). Magnetic studies indicate an  $S = 11$  ground state for **35**, with a very small negative  $D$  value of  $-0.04 \text{ cm}^{-1}$ . This small  $D$  value accounts for the absence of a peak in the out-of-phase a.c. magnetic susceptibility at the temperatures measured

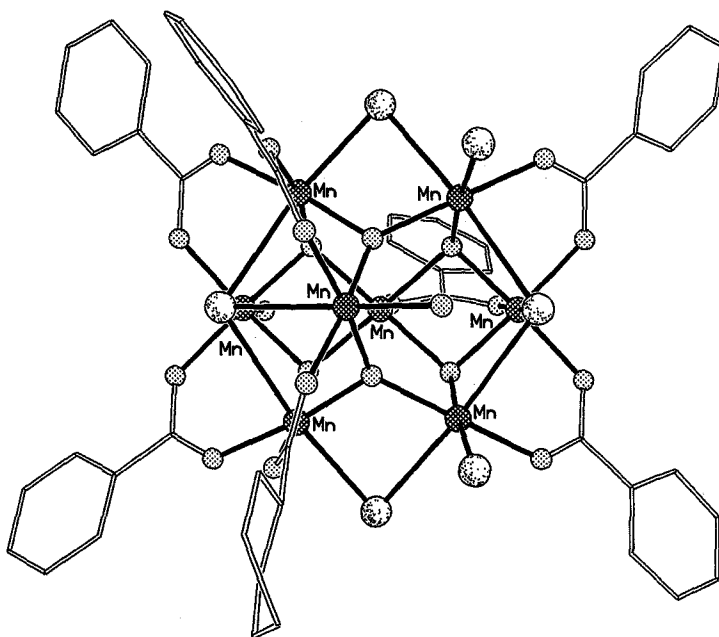


FIG. 13. The structure of  $[\text{Mn}_8\text{O}_6\text{Cl}_6(\text{O}_2\text{CPh})_7(\text{H}_2\text{O})_2]$  (100). (Shading as in Fig. 12, plus Cl, random shaded.)

(2.0–4.0 K). The formation of **35** should be compared with the quasi-designed synthesis that gave the other octanuclear manganese cages. It shows that disruption of the structure of a tetranuclear cage can be sufficient to generate a larger complex without addition of ligands designed to bridge the fragments. The element of design is lost, but the resulting cage, perhaps perversely, has more interesting magnetic and electrochemical behavior.

A quite different approach has been adopted by Saalfrank and co-workers, and has produced two octanuclear manganese cages. Use of polydentate ligands, L2 and L3 (see Scheme 2), has led to two strikingly beautiful compounds.  $[\text{Mn}_8\text{O}_2(\text{L2})_6]$  contains a trigonal prism of Mn(II) centers capped on the trigonal faces (101). Each of the six dianionic ligands binds to three manganese centers. The result is a bis(triple-helicate) arrangement of ligands about the metal core.  $[\text{Mn}_8(\text{L3})_8(\text{HOPr})_4]$ , shown in Fig. 14, contains two differently sized Mn(II) squares with the same center, the large square being turned  $45^\circ$  relative to the small one (102). The dianionic ligands again bridge three manganese centers. NMR studies of analogous, but diamagnetic, zinc and cadmium cages indicate that these structures are maintained in solution. No magnetic data are reported.

The other octanuclear manganese cage known forms part of a study of heterometallic alkoxides. (103).  $[\text{Mn}_8\text{Sb}_4\text{O}_4(\text{OEt})_{20}]$  is made from

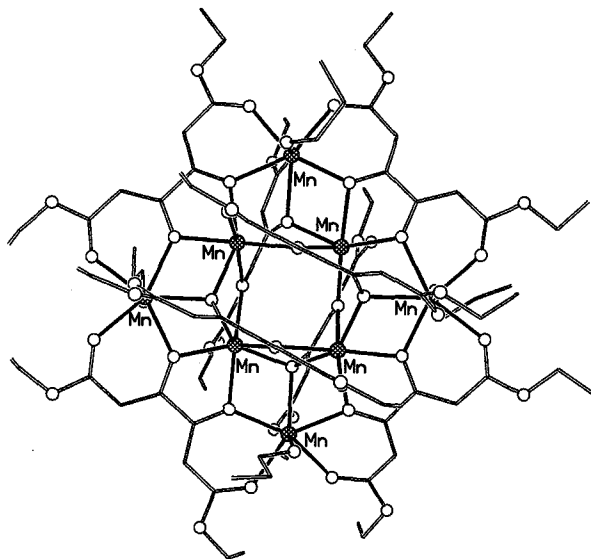


FIG. 14. The structure of  $[\text{Mn}_8(\text{L3})_8(\text{HOPr})_4]$  (102). (Shading as Fig. 9.)

reaction of  $\text{Na(OEt)}$ ,  $\text{Sb(OEt)}_3$ , and  $\text{MnCl}_2$  in toluene. The oxides are all  $\mu_5$ -bridging, while both  $\mu_3$ - and  $\mu_2$ -ethoxides are present. Three Mn(II) sites are six-coordinate with distorted octahedral geometries, and two are five-coordinate with square-pyramidal geometries. The overall structure is perhaps best described as two  $\{\text{Mn}_6\text{Sb}_2\}$  square antiprisms sharing a square face.

The nonanuclear cage  $[\text{Mn}_9\text{O}_4(\text{O}_2\text{CPh})_8(\text{sal})_4(\text{salH})_2(\text{py})_4]$  (**36**) ( $\text{salH}_2 = \text{salicylic acid}$ ) (104) contains fragments that can be recognized as tetranuclear butterflies; however, the synthesis is from the reaction of the oxo-centered triangle  $[\text{Mn}_3\text{O}(\text{O}_2\text{CPh})_6(\text{py})_2(\text{H}_2\text{O})]$  with salicylic acid in MeCN. Cage **36** contains a central  $\{\text{Mn}(\text{sal})_4\}^{6-}$  fragment, with an eight-coordinate Mn(II) center bound to the oxygen centers of four chelating carboxylates. Each of these carboxylate oxygens then bridges to Mn centers of the tetranuclear  $\{\text{Mn}_4\text{O}_2(\text{O}_2\text{CPh})_4(\text{salH})(\text{py})\}^{3+}$  units that sandwich this central fragment. The tetranuclear units contain exclusively Mn(III) sites. The hydroxyl oxygens of the  $\text{sal}^{2-}$  ligands also bind to metals within the tetranuclear units. The benzoate ligands act as 1,3-bridges within the butterflies. Cage **36** is therefore an early example of a “complex ligand,” in this case  $\{\text{Mn}(\text{sal})_4\}^{6-}$ , bridging polynuclear cages. Very elegant modeling of the magnetic data for **36** gave an  $S = \frac{3}{2}$  ground state, with five excited states within  $6 \text{ cm}^{-1}$ . This in turn results in several states being thermally populated even at 4 K.

The tetranuclear cage  $(\text{NBu}^n_4)[\text{Mn}_4\text{O}_2(\text{O}_2\text{CPh})_9(\text{H}_2\text{O})]$  reacts with dibenzoyl peroxide to give a second nonanuclear cage,  $[\text{Mn}_9\text{Na}_2\text{O}_7(\text{O}_2\text{CPh})_{15}(\text{MeCN})_2]$  (**37**) (100). Although the reagent is an oxidizing agent, no oxidation state change is observed, as **37** contains only Mn(III). Similarly,  $[\text{Mn}_3\text{O}(\text{O}_2\text{CPh})_6(\text{py})_2(\text{H}_2\text{O})]$  reacts with PhIO to give  $[\text{Mn}_9\text{O}_7(\text{O}_2\text{CPh})_{13}(\text{py})_2]$  (**38**) (105), which contains the same manganese core as **37**—again with no oxidation state change on reaction of a Mn(III) cage with an oxidizing agent. Finally,  $[\text{Mn}_9\text{K}_2\text{O}_7(\text{O}_2\text{CCMe}_3)_{15}(\text{HO}_2\text{CCMe}_3)_2]$  (**39**), shown in Fig. 15, can be made from reaction of  $[\text{Mn}_6\text{O}_2(\text{O}_2\text{CCMe}_3)_{10}(\text{THF})_4]$  with permanganate (82); however, here there is an oxidation state change from mixed-valent Mn(II)/Mn(III) in the hexanuclear cage to Mn(III) in the nonanuclear product. Compounds **37–39** have very similar arrays of manganese sites. If the alkali-metal cations present in **37** and **39** are included in the description, the polyhedron found in each case is very close to a centered icosahedron missing two vertices. No reversible redox processes were found in electrochemical studies of either **37** or **38**. Magnetic studies of **37** conclude that the cage has an  $S = 4$  ground state (99), with  $D = -0.25 \text{ cm}^{-1}$ , with several low-lying excited states which complicate magnetization studies in high fields.

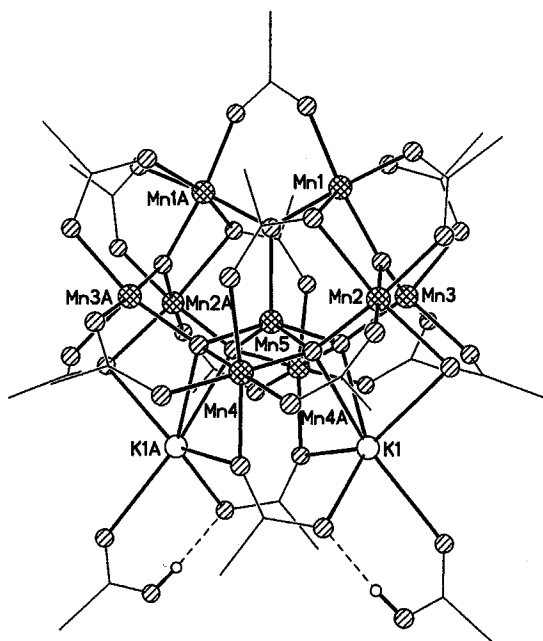


FIG. 15. The structure of  $[\text{Mn}_9\text{K}_2\text{O}_7(\text{O}_2\text{CPh})_{15}(\text{MeCN})_2]$  (82). (Shading: Mn, hatched; O, striped; K, open; C, lines.)

A nonanuclear manganese(II)  $3 \times 3$  grid has also been reported.  $[\text{Mn}_9(2\text{poap})_6]$  (for 2poap, see Scheme 2) contains a polydentate N,O donor with three “pockets” designed to bind to metal sites (106). Six such ligands bridge to create the planar metal array. The magnetic ground state of the cage is  $S = \frac{5}{2}$  owing to antiferromagnetic exchange between the Mn(II) centers.  $[\text{Mn}_9(2\text{poap})_6]$  has an extremely rich electrochemistry, with five reversible redox waves found between +0.72 and +1.58 V (vs. SCE). The first wave is a four-electron oxidation, while each of the following waves corresponds to a one-electron oxidation. The most oxidized cage therefore corresponds to one Mn(II) and eight Mn(III) centers; if this cage could be isolated, the magnetic properties might prove more interesting.

The first decanuclear manganese cage reported was formed by aerial oxidation of a solution of  $\text{Mn}(\text{CF}_3\text{SO}_3)_2$  and  $\text{N}(\text{CH}_2\text{CH}_2\text{NH}_2)_3$  (tren) in MeCN to give  $[\text{Mn}_{10}\text{O}_{14}(\text{tren})_6]^{8+}$  (40) (107), shown in Fig. 16, which is mixed-valent containing four Mn(III) and six Mn(IV) centers. The cage consists of a planar core containing six octahedral Mn centers, with each octahedron sharing an edge with a neighbor. The 14 oxide ligands are

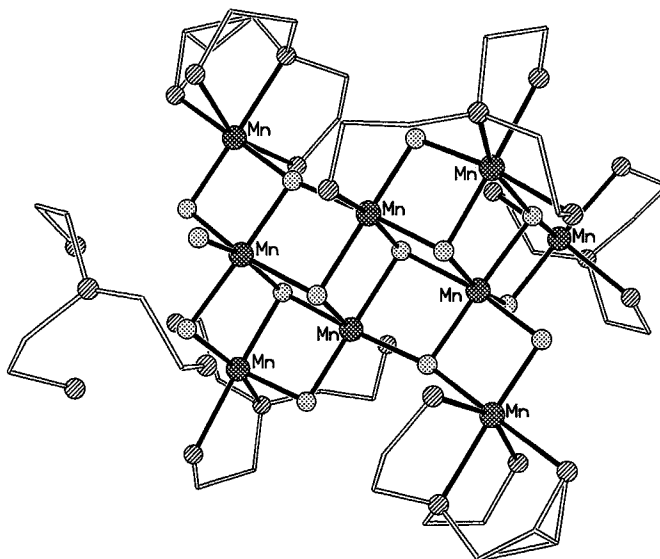


FIG. 16. The structure of  $[\text{Mn}_{10}\text{O}_{14}(\text{tren})_6]^{8+}$  (107). (Shading: Mn, hatched; O, dotted; N, striped; C, lines.)

found within this central raft. The four additional manganese centers are attached above and below the raft, and are bound to four of the six tren ligands, with the final two tren ligands bound to the terminal Mn atoms of the raft. The cage displays no reversible redox behavior in the range 1.5 to  $-1.5$  V (vs.  $\text{Ag}/\text{Ag}^+$ ), and no detailed magnetic studies have been reported.

The decanuclear cage  $[\text{Mn}_{10}\text{O}_2\text{Cl}_8\{\text{OCH}_2\}_3\text{CMe}\}_6]^{2-}$  (**41**) (108), reported by Zubietta and co-workers, is a direct analog of the equivalent cages made with vanadium and has the  $\{\text{M}_{10}\text{O}_{28}\}$  decametallate core with 18 of the bridging oxide sites replaced by alkoxides from the tripodal ligand and the eight terminal oxides replaced by chlorides (see Fig. 2). The cluster is mixed-valence, containing two Mn(II) and eight Mn(III) sites; the eight Mn(III) sites are those attached to the terminal chloride ligands. The synthesis of the cage appears remarkably straightforward—reaction of  $(\text{NEt}_4)_2[\text{MnCl}_4]$  with  $\text{MeC}(\text{CH}_2\text{OH})_3$  in MeCN, followed by addition of MeOH, produces **41** in 50% yield. The magnetic properties have not been reported in detail, only a room-temperature moment that indicates antiferromagnetic exchange between the metal centers.

Two decanuclear cages have been reported using 2,2'-biphenoxide (biphen) as a ligand (Fig. 17).  $[\text{Mn}_{10}\text{O}_4(\text{biphen})_4\text{X}_{12}]^{4-}$  ( $\text{X} = \text{Cl}$ , **42**;

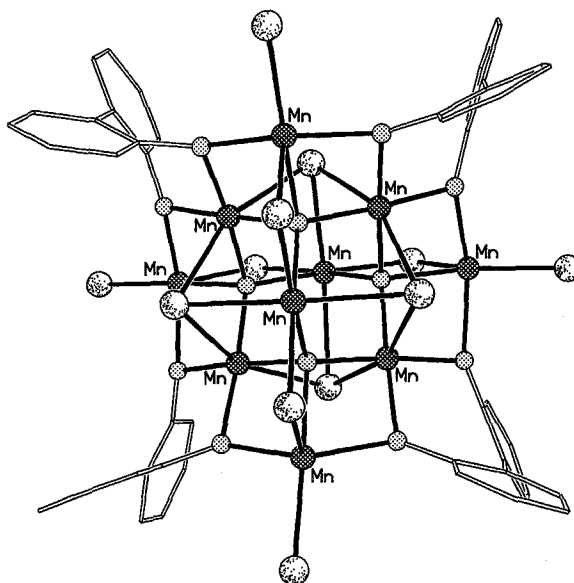


FIG. 17. The structure of  $[\text{Mn}_{10}\text{O}_4(\text{biphen})_4\text{X}_{12}]^{4-}$  (109). (Shading as in Fig. 16, plus Cl, random shading.)

X = Br, **43**) (109) can be made from reaction of appropriate manganese(II) halide with 2,2'-biphenol in the presence of a base (either triethylamine or tetramethylammonium hydroxide); the bromide analog has been crystallized with four tetramethylammonium counterions (**43a**) and with two  $[\text{Et}_3\text{NH}]^+$  and one  $[\text{Mn}(\text{MeCN})_4(\text{H}_2\text{O})_2]^{2+}$  counterions (**43b**). In each case the structure of the cage consists of a central  $\{\text{Mn}_6\text{O}_4\}$  adamantane, i.e., a tetrahedron of oxide ions with each edge containing a Mn center. Each oxide therefore binds to three Mn centers within the adamantane, and also binds to a fourth Mn center, which creates a larger  $\text{Mn}_4$  tetrahedron outside this central adamantane core. The 12 halide ions have three distinct structural roles: Four are bound terminally to the Mn centers of the external tetrahedron; four are  $\mu_2$ -bridging between a Mn atom of the adamantane and a Mn of the tetrahedron; and the final four are  $\mu_3$ -bridging between Mn centers within the adamantane. Each of the four biphen ligands chelates to one Mn center of the adamantane, then each O atom bridges in a  $\mu_2$  fashion to an external Mn. The molecular structure therefore has  $D_{2d}$  symmetry, which is crystallographically imposed for **43b**. As is usual for Mn cages, both **42** and **43** are mixed-valent. The four Mn(III) sites are the four metal centers within the adamantane

that do not lie on the principal rotation axis; the remaining sites are Mn(II).

The magnetic properties of **42** and **43** have proved difficult to interpret (109). Susceptibility data alone do not differentiate between  $S = 12$ , 13, or 14 ground states; however, EPR measurements at 245 GHz support an assignment of an  $S = 12$  ground state with  $D = -0.037 \text{ cm}^{-1}$  (8) for **43b** and  $-0.047 \text{ cm}^{-1}$  for **42** (109). A single-crystal polarized neutron diffraction study shows that the spins of the four Mn(III) sites are aligned parallel, with the spins of four of the Mn(II) centers also aligned in this direction and the spins of two Mn(II) centers on the principal rotation axis aligned opposed to this direction (111). This would give  $S = 13$ , but in the presence of spin frustration lower values of  $S$  are allowed, so  $S = 12$  is not unreasonable. The negative  $D$  value means that these cages are SMMs, albeit with very low energy barriers to re-orientation of the magnetization. This has been confirmed by a.c. susceptibility, which gives  $E_a/k = 7.0 \text{ K}$ , which is very close to the value calculated for  $DS^2$  using the parameters measured by high-frequency EPR (8).

Two more recently reported decanuclear cages,  $[\text{Mn}_{10}\text{O}_8(\text{O}_2\text{CPh})_6(\text{pic})_8]$  (**44**) and  $[\text{Mn}_{10}\text{O}_8(\text{O}_2\text{CPh})_6(\text{pic})_6(\text{dbm})_2]$  (**45**) (112), can be made by dissolving the tetranuclear cage  $[\text{Mn}_4\text{O}_2(\text{O}_2\text{CMe})_6(\text{pic})_2(\text{MeCN})_2]$  in  $N,N'$ -dimethylacetamide, followed by dilution with  $\text{CH}_2\text{Cl}_2$ ; the difference in the two syntheses is that the latter compound requires addition of Hdbm to the reaction mixture. It is unclear why  $N,N'$ -dimethylacetamide should induce precisely this change in structure; the authors consider the good donor properties of the solvent important in destabilizing the tetranuclear butterfly precursor. It is worth contrasting this synthesis with the formation of the octanuclear cage  $[\text{Mn}_8\text{O}_4(\text{O}_2\text{CMe})_{12}(\text{pic})_4]$ ; this required disruption of the structure of a butterfly cage by addition of a carboxylate-abstracting agent; however, the resulting structure is clearly a dimer of the precursor. Here the structural transformation is more dramatic. The metal cores of the two structures are identical, with an  $\{\text{Mn}_{10}\text{O}_8\}^{4+}$  core surrounded by the carboxylate ligands. The core can be described as two  $\{\text{Mn}_6\text{O}_4\}$  adamantanes sharing a  $\text{Mn} \cdots \text{Mn}$  edge. The presence of the adamantane fragment relates **44** and **45** to the other decanuclear cages, **42** and **43**. The magnetic properties of **44** and **45** are less interesting, however, with susceptibility studies indicating a diamagnetic ground state. All the metal centers are Mn(III) in **44** and **45**.

The Christou group reported the only  $\{\text{Mn}_{11}\}$  cage in 1991 (113). It was formed by disrupting the structure of a tetranuclear butterfly cage,  $[\text{Mn}_4\text{O}_2(\text{O}_2\text{CMe})_7(\text{bpy})_2]^+$ , by addition of  $\text{Me}_3\text{SiCl}$ . The

structure of  $[\text{Mn}_{11}\text{O}_{10}\text{Cl}_2(\text{O}_2\text{CMe})_{11}(\text{bpy})_2(\text{MeCN})_2(\text{H}_2\text{O})_2]^{2+}$  **46** (bpy = 2,2'-bipyridyl) has considerable aesthetic appeal. A linear trinuclear manganese core lies on a mirror plane and bridges between two  $\{\text{Mn}_4\text{O}_3\text{Cl}\}$  heterocubanes. The bridges are provided by four  $\mu_3$ -oxides, each of which binds to two Mn centers of the trinuclear block and to one Mn from a cubane, and four carboxylates which bridge between the terminal Mn centers of the central fragment and Mn centers of the cubanes. The bpy ligands chelate to Mn centers within the cubanes. No properties were reported for **46**.

A dodecanuclear manganese(II) cage,  $[\text{Mn}_{12}(\text{OH})_4(\text{L4})_6(\text{O}_2\text{CMe})_2]$ , was reported by Tuchagues and co-workers in 1988 (114), using a binucleating Schiff-base ligand (L4, see Scheme 2) formed by condensation of 2,6-diformyl-4-methylphenol with two equivalents of 2-aminophenol. Each pentadentate L4 ligand binds to two Mn(II) centers, with the phenol oxygens bridging to further Mn(II) centers, generating a cyclic belt-like structure. Magnetic susceptibilities studies indicate antiferromagnetic coupling between the metal centers, giving a diamagnetic ground state for the cage.

This very beautiful structure has been largely overlooked because of the fascinating magnetic behavior of the other structural type found for dodecanuclear manganese cages. Lis first reported this structure in 1980 (14), but significant work on these cages dates from a report in 1988 by Christou, Hendrickson, and co-workers (115). In a recent paper, Yoo *et al.* list forty-six papers describing studies of these  $\{\text{Mn}_{12}\}$  cages (116); this list is unlikely to be exhaustive. Given this level of interest, it is impossible to review all this work within a more general review; the following merely summarizes the major points of interest to chemists, without attempting to explain the controversial aspects of the quantum phenomena displayed by these extraordinary molecules. Given the level of excitement, it is reasonable to describe these  $\{\text{Mn}_{12}\}$  cages as the coordination chemists' fullerenes.

The cages have the general formula  $[\text{Mn}_{12}\text{O}_{12}(\text{O}_2\text{CR})_{16}(\text{H}_2\text{O})_4]$ , shown in Fig. 18, with cages known for a wide range of carboxylates (2, 14, 117). The Christou and Hendrickson groups have also prepared, isolated, and studied the cages in three different oxidation states—neutral, mononegative (118), and dinegative (119)—and a heterometallic  $[\text{Fe}_4\text{Mn}_8\text{O}_{12}(\text{O}_2\text{CMe})_{16}(\text{H}_2\text{O})_4]$  cage (120). While the majority of physical studies have concentrated on the neutral  $[\text{Mn}_{12}\text{O}_{12}(\text{O}_2\text{CMe})_{16}(\text{H}_2\text{O})_4]$  (**47**) cage, the availability of other derivatives of this cage has given much insight into why this specific family of cages displays such unusual magnetic behavior.

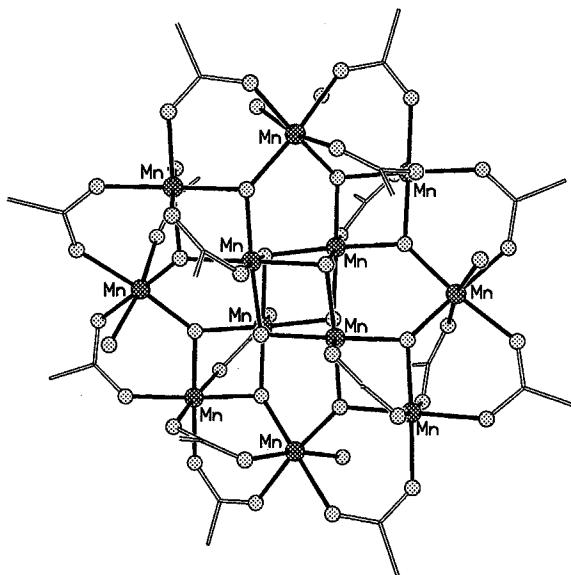


FIG. 18. The structure of  $[\text{Mn}_{12}\text{O}_{12}(\text{O}_2\text{CR})_{16}(\text{H}_2\text{O})_4]$  (**14**). (Shading as in Fig. 16.)

The common structure for this family of cages consists of a  $\{\text{Mn}_4\text{O}_4\}$  heterocubane surrounded by an octanuclear manganese wheel, bridged by carboxylates and oxide ligands. The central heterocubane contains exclusively Mn(IV) sites, while the octanuclear wheel contains eight Mn(III) sites. Where the cages are redox-active, the reduction sites are the external Mn(III) centers (*117*), which means that the mono- and dinegative cages contain three oxidation states—Mn(II), Mn(III), and Mn(IV). Neither the  $\{\text{Mn}_4\text{O}_4\}$  cubane nor the octanuclear manganese wheel can be found in isolation for this metal, although close structural analogs to each fragment are known for other elements; e.g., the octanuclear vanadium and chromium wheels (**2** and **19**) resemble the wheel in these  $\{\text{Mn}_{12}\}$  cages.

The compounds are remarkably straightforward to make. Cage **47** can be made in  $\sim 80\%$  yield by reaction of manganese(II) acetate with potassium permanganate in acetic acid (*2*). While other cages can be made directly by use of other manganese carboxylates in this comproportionation reaction, they are more easily made by simple ligand exchange of the carboxylates of **47**. Thus, reaction of **47** with a 100% excess of benzoic acid substitutes most (but not all) of the acetates, while repeating the reaction a second time leads to the completely exchanged

product  $[\text{Mn}_{12}\text{O}_{12}(\text{O}_2\text{CPh})_{16}(\text{H}_2\text{O})_4]$  (**48**) (2). The cages with other carboxylates can be made in a similar manner.

Cage **47** has an  $S = 10$  ground state, which arises because the antiferromagnetic exchange between the Mn(III) and Mn(IV) centers is stronger than the antiferromagnetic exchange between either Mn(III)–Mn(III) or Mn(IV)–Mn(IV). This leads to the spins on the metals of the central cubane being aligned parallel with each other but antiparallel to the spins on the metals of the wheel. However, in such a complex system other ground states can be found; for example, **48** has an  $S = 9$  ground state in zero-field, but  $S = 10$  in field. The  $S = 10$  ground state is highly anisotropic, with  $D$  values of around  $-0.5 \text{ cm}^{-1}$ . This leads to the  $M_s = \pm 10$  being lowest in energy in zero-field. When cooled in a magnetic field, only one of these levels will be occupied and there will be a significant energy barrier to reorientation of the magnetization. Therefore, the cage behaves as a single molecule magnet, with very slow relaxation of magnetization in the absence of a field at sufficiently low temperatures.

These cages were the first of the SMMs to be discovered, and remain the most heavily studied. The observations of steps on hysteresis loops of magnetization vs. field indicate the occurrence of quantum tunneling between  $M_s$  levels as an alternative to thermal relaxation of magnetization (12, 13). This has allowed physicists to study the mechanism of the quantum tunneling of magnetization, offering an opportunity of testing theory against experiment that has proved difficult in other systems.

The ability to vary the carboxylate in the  $\{\text{Mn}_{12}\}$  cages creates many possibilities for systematic study of these materials. The large anisotropy of the spin in the cages results, in the main, because the Jahn–Teller axes for all the Mn(III) centers in the cage are aligned parallel. The Christou/Hendrickson groups have demonstrated that variation of carboxylate and even lattice solvation can change the relative orientations of these Jahn–Teller axes, producing cages with a lower energy barrier to reorientation of the magnetization (117). Unfortunately, it appears that the original systems were optimized, and no increase in the energy barrier has yet been found, either in these cages or in the other SMMs. The ability to replace acetate in **47** with other carboxylates also allows introduction of long-chain carboxylates, which allows processing of SMMs into Langmuir–Blodgett films.

The monoreduced cages have been less intensively studied, but are also SMMs (118). They have been made with a more limited range of carboxylates, only benzoate and propionate. The ground states are  $S = \frac{19}{2}$ , with  $D$  values of around  $-0.43 \text{ cm}^{-1}$ , and the energy barrier to reorientation of the spin is slightly lower than that for the neutral

species, with  $E_a/k$  of  $\sim 57$  K. Quantum tunneling has again been observed, which was unexpected in the absence of an external field in a system with an odd number of unpaired electrons. However, the nuclear spins on the Mn centers generate a considerable internal magnetic field, which may make tunneling allowed. The heterometallic cage  $[\text{Fe}_4\text{Mn}_8\text{O}_{12}(\text{O}_2\text{CMe})_{16}(\text{H}_2\text{O})_4]$  has much less interesting magnetic properties, with Fe(III) ions replacing Mn(III) ions in the octanuclear wheel (120). The ground state appears to be  $S = 2$ , which is probably too low for phenomena associated with SMMs to be observed at measurable temperatures. The dianionic members of the family reported,  $[\text{Mn}_{12}\text{O}_{12}(\text{O}_2\text{CCR})_{16}(\text{H}_2\text{O})_4]^{2-}$  [ $\text{R} = \text{CHCl}_2, \text{C}_6\text{F}_5, \text{C}_6\text{H}_3(\text{NO}_2)_2$ ], require electron-withdrawing carboxylate groups to stabilize the lower oxidation states. The spin ground state of  $[\text{Mn}_{12}\text{O}_{12}(\text{O}_2\text{CCCHCl}_2)_{16}(\text{H}_2\text{O})_4]^{2-}$  is  $S = 10$ , and the axial zero-field splitting was found to be  $-0.27 \text{ cm}^{-1}$ . Therefore, comparing the three oxidation states, the ground state spins are  $\{\text{Mn}_{12}\}$ ,  $S = 10$ ;  $\{\text{Mn}_{12}\}^-$ ,  $S = \frac{19}{2}$ ;  $\{\text{Mn}_{12}\}^{2-}$ ,  $S = 10$ . The  $D$  value declines as the cage is reduced, from about  $-0.5 \text{ cm}^{-1}$  for the neutral species to about  $-0.3 \text{ cm}^{-1}$  for the dianion; this may reflect the replacement of Mn(III) centers by Mn(II) centers in the reduced compounds.

Several larger manganese cages are known. A tridecanuclear cage,  $[\text{Mn}_{13}\text{O}_8(\text{OEt})_6(\text{O}_2\text{CPh})_{12}]$  (49), has perhaps the most appealing structure (121), which is shown in Fig. 19. It is a supercubane, containing

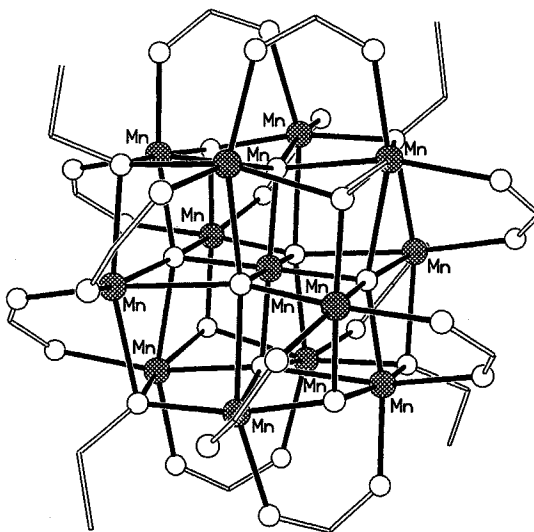


FIG. 19. The structure of  $[\text{Mn}_{13}\text{O}_8(\text{OEt})_6(\text{O}_2\text{CPh})_{12}]$  (121), with phenyl groups excluded for clarity. (Shading: Mn, hatched; O, open; C, lines.)

eight cubanes arranged in a cube. The central manganese site is a Mn(IV) center, and is shared by all eight cubanes. The 12 surrounding Mn centers are half Mn(III) and half Mn(II), and can be assigned because the Mn(III) sites show a Jahn–Teller elongated coordination geometry. Six oxides are found at the centers of the faces of the cube, and are  $\mu_5$ -bridging, while two oxides and six ethoxide oxygens are  $\mu_3$ -bridging at the corners of the supercubane. The 12 benzoates are all 1,3-bridging between pairs of Mn sites on the faces of the supercubane, with two carboxylates per face. The magnetic properties of this cage can be interpreted as due to an  $S = \frac{15}{2}$  ground state with  $D = 0.33 \text{ cm}^{-1}$ . The synthesis of this cage involves two distinct steps: (1) addition of tetramethylammonium hydroxide to a mixture of  $\text{Mn}(\text{O}_2\text{CPh})_2 \cdot 2\text{H}_2\text{O}$  and biphen in MeOH/THF followed by evaporation to dryness; (2) crystallization of the resulting red-brown material from THF/EtOH/ $\text{CH}_2\text{Cl}_2$ . The presence of ethoxide in the structure suggests that **49** forms during the crystallization step as that is the only stage where ethoxide is present.

A hexadecanuclear manganese cage,  $[\text{Mn}_{16}\text{Ba}_8\text{Na}_2\text{ClO}_4(\text{OH})_4(\text{CO}_3)_4(\text{H}_2\text{O})_{22}(\text{L5})_8]$  (where L5 = 1,3-diamino-2-hydroxypropane- $N,N',N',N'$ -tetraacetic acid), has been the subject of a U.S. patent (122), but no structure or magnetic properties have appeared in the open literature. Two octadecanuclear cages have been reported. The earlier involves reaction of the butterfly cage  $(\text{N}^n\text{Bu}_4)[\text{Mn}_4\text{O}_2(\text{O}_2\text{CPh})_9(\text{H}_2\text{O})]$  with the monopotassium salt of phthalic acid in MeCN. Phthalate (phth) displaces benzoate, and slow concentration of the solution gives  $[\text{Mn}_{18}\text{O}_{16}(\text{O}_2\text{CPh})_{22}(\text{phth})_2(\text{H}_2\text{O})_4]^{4-}$  (**50**) (123), as shown in Fig. 20. The structure is complicated, and can be described as a central region containing three  $\{\text{Mn}_4\text{O}_2\}$  butterflies sharing body vertices, which gives an  $\{\text{Mn}_{10}\text{O}_6\}$  “raft.” This section links together two  $\{\text{Mn}_4\text{O}_3\}$  fragments where the Mn centers describe tetrahedra that are bridged on two faces by  $\mu_3$ -oxides and on the opposite edge by one further oxide. This oxide binds to the wingtip Mn site of the central  $\{\text{Mn}_4\text{O}_2\}$  butterfly of the raft, and is therefore also  $\mu_3$ -bridging. The benzoates all act as 1,3-bridging ligands and the two phthalates are  $\mu_4$ -bridging. All 16 oxides are  $\mu_3$ -bridging. The magnetic properties of **50** show a diamagnetic ground state, indicating that antiferromagnetic exchange between the 18 Mn(III) centers dominates.

The other octadecanuclear cage,  $[\text{Mn}_{18}\text{O}_{14}(\text{OMe})_{14}(\text{O}_2\text{CCMe}_3)_8(\text{MeOH})_6]$  (**51**), is mixed-valent, with a net fourteen Mn(III) and four Mn(II) sites (124); the core is shown in Fig. 21. The cage is made by mixing manganese(II) chloride, sodium pivalate, and Na(mhp) (mhp = the anion of 6-methyl-2-hydroxypyridine) in MeOH, which gives a brown precipitate. Extraction of this precipitate with hot MeOH gives

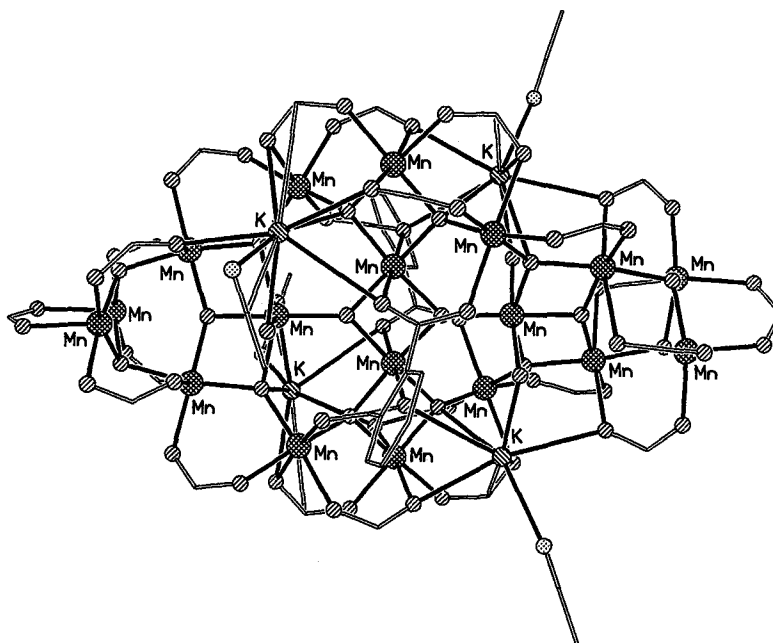


FIG. 20. The structure of  $[\text{Mn}_{18}\text{O}_{16}(\text{O}_2\text{CPh})_{22}(\text{phth})_2(\text{H}_2\text{O})_4]^{4-}$  (123), with phenyl groups of benzoate ligands excluded for clarity. (Shading: Mn, hatched; O, striped; K, lines.)

a very pale solution from which crystals of **51** grow after two weeks. The structure consists of a central cubane capped on each face by a further cubane, generating a heptacubane  $\{\text{Mn}_{16}\text{O}_{14}(\text{OMe})_2\}$  core. Of the fourteen oxides, four are  $\mu_6$ -, two are  $\mu_4$ - and eight are  $\mu_3$ -bridges, while both methoxides are  $\mu_3$ -bridges. Twelve of the metal sites show some form of Jahn-Teller distortion typical of Mn(III), while the remaining four sites need to be mixed-valent owing to charge-balance considerations. However, structural parameters do not distinguish between the sites and it appears they are a mixture of two Mn(II) and two Mn(III) sites. Whether this reflects genuine electron delocalization or static disorder in the crystal lattice is debatable. The two additional metal sites, which are attached to the heptacubane by  $\mu_4$ -bridging oxides, are clearly Mn(II). The pivalate ligands all act as 1,3-bridges.

#### D. IRON

The studies of high-nuclearity iron cages were originally motivated by a desire to understand biomineralization processes and the form of iron found in the iron-storage protein ferritin. Therefore, many of the

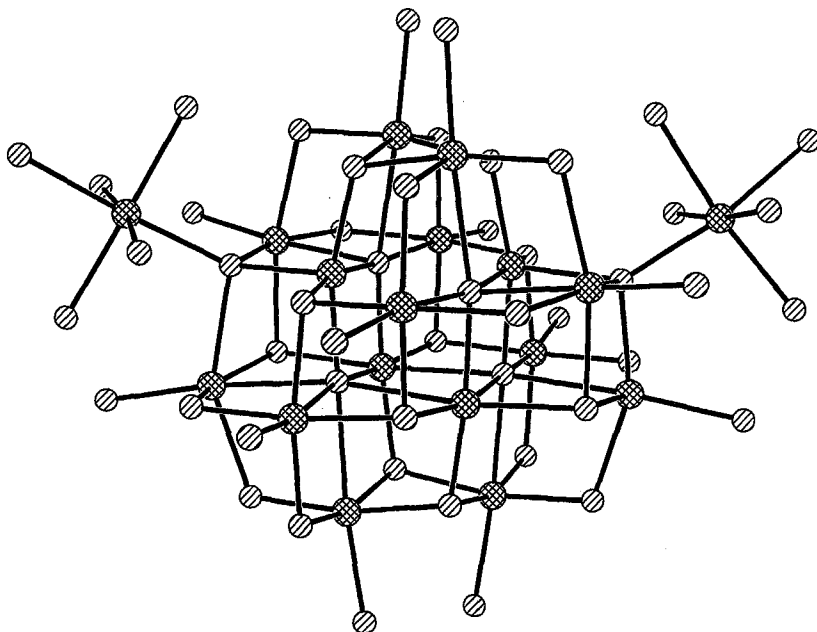


FIG. 21. The Mn—O core of  $[\text{Mn}_{18}\text{O}_{14}(\text{OMe})_{14}(\text{O}_2\text{CCMe}_3)_8(\text{MeOH}_6)]$  (124). (Shading as in Fig. 20.)

most important early papers were published by bioinorganic groups, especially that of Lippard. As with manganese, a very broad range of structures has been found. In contrast to manganese, diamagnetic ground states are much more common for iron cages, especially those with even numbers of metals, and homovalent cages tend to be the rule with Fe(III), the predominant oxidation state.

The earliest hexanuclear iron complexes reported contain two  $\{\text{Fe}_3\text{O}\}$  carboxylate-bridged triangles linked by two  $\mu_2$ -hydroxide to form a planar  $\{\text{Fe}_6\text{O}_2(\text{OH})_2\}$  unit. G rb l u and co-workers reported the derivative with pivalate ligands (125), followed closely by a report by Micklitz and Lippard of the benzoate analog (126). Magnetic studies of the benzoate analog show a diamagnetic ground state. Lippard and co-workers also demonstrated that oxo-centered iron triangles could be linked by a  $\mu_4$ -peroxide, to give a planar cage,  $[\text{Fe}_6(\text{O}_2)\text{O}_2(\text{O}_2\text{CPh})_{12}(\text{H}_2\text{O})_2]$  (127). Very recently, pivalate and trifluoroacetate analogs of the peroxide-bridged cage have been prepared with a variety of monodentate ligands attached to the terminal Fe sites of the triangles (128). These cages have been studied as mediators in the Gif-like oxygenation of organic

substrates by  $O_2/Zn$ . Much more extraordinary is the trigonal-prismatic cage,  $[Fe_6(O_2)_3O_2(O_2CMe)_9]^-$ , shown in Fig. 22, made by reaction of hydrogen peroxide with basic iron acetate (129). The cage contains two oxo-centered iron triangles arranged in a face-to-face fashion, forming a trigonal prism, with three  $\eta^2-\mu_4$ -peroxides placed within each rectangular face of the prism. Each of the nine edges of the trigonal prism is bridged by a  $\mu_2$ -acetate. The magnetic data on this cage indicate an  $S = 1$  ground state for the cage.

Further hexanuclear cages have been reported by Hendrickson and co-workers, using polydentate ligands featuring N-heterocycles. Reaction of 1,1-bis(N-methylimidazol-2-yl)-1-hydroxyethane (bimOH) with  $[Fe_3O(O_2CMe)_6(py)_3](ClO_4)$  in MeCN, followed by crystallization from  $CH_2Cl_2$ , gives  $[Fe_6O_2(OH)_2(O_2CMe)_{10}(bimO)_2]$  (52) (130), where the hydroxy diimidazole ligand has displaced a terminal pyridine and a bridging carboxylate group from the original oxo-centered triangle, while two  $\mu_2$ -hydroxides and four 1,3-bridging carboxylates now bridge two triangles into a hexanuclear cage. A very similar cage,  $[Fe_6O_2(OH)_2(O_2CMe)_{10}(mimO)_2]$  (53) (131), results if 2-(N-methylimidazol-2-yl)-2-hydroxypropane (mimOH) is used in this reaction. Reaction of 2-hydroxymethylpyridine (Hhmp) with hydrated

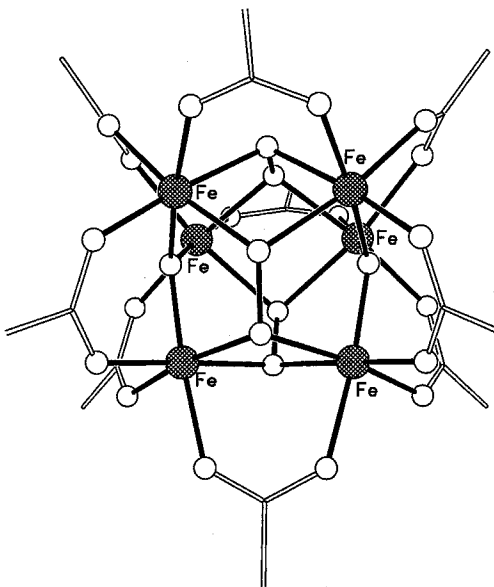


FIG. 22. The structure of  $[Fe_6(O_2)_3O_2(O_2CMe)_9]^-$  (129). (Shading: Fe, hatched; O, open; C, lines.)

iron(III) chloride in MeCN gives a further hexanuclear cage,  $[\text{Fe}_6\text{O}_2(\text{hmp})_8\text{Cl}_4]$  (**54**) (131). This cage also has a core involving two bridged  $\{\text{Fe}_3\text{O}\}$  triangles. Magnetic studies of these cages illustrate the complexity that can result in such compounds. Whereas the earlier hexanuclear cages studied have diamagnetic ground states, **52** and **53** have  $S = 5$  ground states while **54** has an  $S = 3$  ground state. Spin frustration in these complexes means that although antiferromagnetic exchange is found between every pair of Fe(III) centers, the resulting spin ground states can still vary dramatically.

Hegetschweiler and co-workers have made a series of octahedral iron(III) cages based on the  $\{\text{M}_6\text{O}_{19}\}$  hexametallate core.  $[\text{Fe}_6\text{O}(\text{OMe})_{18}]^{2-}$  (**132**) can be made by addition of sodium methoxide to a solution of anhydrous  $\text{FeCl}_3$  dissolved in MeOH, while two cages are known with tripodal tris(alkoxide) ligands,  $[\text{Fe}_6\text{O}\{(\text{OCH}_2)_3\text{Et}\}_6]^{2-}$  (**133**) and  $[\text{Fe}_6\text{O}\{(\text{OCH}_2)_3\text{Et}\}_3(\text{OMe})_3\text{Cl}_6]^{2-}$  (**134**). The yield of the homoleptic cage is rather low (one crystal!); however, the mixed-ligand cage could be made in 20% yield by reaction of anhydrous  $\text{FeCl}_3$  with  $(\text{HOCH}_2)_3\text{Et}$  in MeOH in the presence of  $[\text{NMe}_4](\text{OH})$  as a base. These cages are very similar to the hexavanadium cages reported by Zubieta (see above), with a central  $\mu_6$ -oxide surrounded by an octahedron of iron(III) centers, while the remaining oxygen atoms of the hexametallate structure are provided by the alkoxide or chloride ligands. Magnetic studies show antiferromagnetic exchange between the Fe(III) centers, leading to diamagnetic ground states for these cages (**134**).

Further octahedral iron cages result from reaction of oxo-centered iron(III) triangles with Hhmp in MeCN.  $[\text{Fe}_6\text{O}_2(\text{O}_2\text{CR})_6(\text{hmp})_6]^{2+}$  cages result for  $\text{R} = \text{Ph}$  and  $\text{CMe}_3$  (**135**). Here, two  $\{\text{Fe}_3\text{O}(\text{O}_2\text{CR})_3\}$  triangles are linked by hmp ligands, with an oxygen of each hmp ligand  $\mu_2$ -bridging each  $\text{Fe} \cdots \text{Fe}$  vector of the triangle while the pyridine nitrogen binds to an Fe atom in the second triangle. The cages therefore have noncrystallographic  $S_6$  symmetry. Magnetic studies of these octahedral Fe cages indicate that they have  $S = 0$  ground states owing to antiferromagnetic exchange between the metal centers.

A rare example of a high-nuclearity Fe(II) cage is formed when anhydrous iron(II) chloride is reacted with  $\text{NH}_4\text{Et}_2$  and  $\text{CO}_2$  in toluene (**136**).  $[\text{Fe}(\text{O}_2\text{CNEt}_2)_2]_6$  forms in good yield with a structure having the six Fe(II) centers arranged in an edge-sharing bitetrahedron. Six of the carbamate ligands are 1,3-bridging, four are 1,1,3-bridging, and two are 1,1,3,3-bridging. The iron sites are a mixture of five- and six-coordinate. Similar manganese and cobalt cages have been reported. Hydrolysis of the isopropyl derivative has led to an octanuclear Fe(II) cage,  $[\text{Fe}_8\text{O}_2(\text{O}_2\text{CN}^i\text{Pr}_2)_{12}]$  (**136**). This cage contains two oxo-centered

$\{\text{Fe}_4\}$  tetrahedra, bridged by carbamate ligands. The iron sites are either four- or five-coordinate, and the carbamate ligands show both the 1,3- and 1,1,3-bridging modes.

The hexanuclear cage  $[\text{NaFe}_6(\text{OMe})_{12}(\text{dbm})_6]^+$  (**55**) (137) is closely related to **32**; however, the iron analog of **33**, where the transition metal is also found at the center of the metallocrown, has not been reported. Cage **55** is made from anhydrous  $\text{FeCl}_3$  reacted with Hdbm and  $\text{Na}(\text{OMe})$  in MeOH. The ground state is diamagnetic. Larger wheels involving  $\{\text{Fe}(\text{dbm})\}$  bridged by methoxide have also been reported when sodium is replaced by potassium or cesium.  $[\text{Fe}(\text{OMe})_2(\text{dbm})]_{12}$  (138) contains a twisted cyclic structure, which appears to be a compromise between the requirements of a regular dodecagon (where each  $\text{Fe}\cdots\text{Fe}\cdots\text{Fe}$  angle would be  $150^\circ$ ) and the preferred angle in edge-sharing octahedra ( $120^\circ$ ). The ribbon structure is unprecedented. Magnetic studies reveal an  $S = 0$  ground state for both these cages. The dodecanuclear wheel reacts readily with sodium and lithium ions to form **55** (139).

Control of the size of metallocrowns has also been reported for cages made with the ligands triethanolamine and *N*-methyldiethanolamine. Reaction of the former ligand with  $\text{FeCl}_3$  in THF in the presence of either NaH or LiH gave  $[\text{MFe}_6\{\text{OCH}_2\text{CH}_2\}_3\text{N}\}_6]\text{Cl}$  (**56**) ( $\text{M} = \text{Li}$  or  $\text{Na}$ ) (140). The cage contains six iron centers at the corners of a regular hexagon, bridged by alkoxide oxygens from the tripodal ligand. Six of these oxygens line the inside of the cage, creating a cavity for incorporation of the alkali-metal ion. Use of  $\text{Cs}_2\text{CO}_3$  leads to an octanuclear cage,  $[\text{CsFe}_8\{\text{OCH}_2\text{CH}_2\}_3\text{N}\}_8]\text{Cl}$  (**57**) (140), which has an octagon of  $\text{Fe}(\text{III})$  centers in the metallocrown, encapsulating the larger Cs cation. Clearly the alkali metal is templating the formation of one cage rather than the other. With *N*-methyldiethanolamine, reaction with  $\text{FeCl}_3$  in THF in the presence of  $\text{Cs}_2\text{CO}_3$  leads to an empty cage,  $[\text{Fe}_6\text{Cl}_6\{\text{OCH}_2\text{CH}_2\}_2\text{NMe}\}_6]$  (140), with bridging between Fe centers similar to that in **56**, but with six terminal chloride ligands attached to the six Fe sites.

Use of a bis(bipyridine) ligand has also generated a hexanuclear iron(III) cage,  $[\text{Fe}_6\text{O}_4\text{Cl}_4(\text{O}_2\text{CPh})_4(\text{L6})_2]^{2+}$  (141), where  $\text{L6} = 1,2\text{-bis}(2,2'\text{-bipyridyl-6-yl})\text{ethane}$ . This cage contains an  $\{\text{Fe}_4\text{O}_4\}$  ladder at its core, with two further  $\text{Fe}(\text{III})$  centers attached to the external oxides of the ladder. These final iron sites are tetrahedrally coordinated to two terminal chlorides, the bridging oxide, and an oxygen from a 1,3-bridging carboxylate. Each of the bis(bipyridine) ligands binds to two iron centers of the ladder. The ground state for this cage is diamagnetic.

A further hexanuclear cage has been reported simultaneously by two different groups (142, 143), using *N*-(2-hydroxypropyl)iminodiacetic

acid (hpida), which is a ligand very similar to those used previously by Heath and Powell to make much larger iron cages (see below). The six Fe(III) sites in  $[\text{NaFe}_6(\text{hpida})_6\text{O}_3]^+$  lie at the corners of a distorted trigonal-prism. A carboxylate group bridges each edge of the triangles of the prism, while oxides bridge the edges linking the triangles. Carboxylate oxygen atoms also form a trigonal-prismatic cavity where the sodium ion is encapsulated. The cage therefore acts as a metal-locryptand. Magnetic studies indicate that the cage has a diamagnetic ground state owing to strong antiferromagnetic coupling between the iron sites bridged by oxides.

A mixed-valent heptanuclear iron complex has recently been reported using the the anion of bis(2-pyridylcarbonyl)amine (bpca) as the chief ligand (144). A mononuclear complex of this ligand,  $[\text{Fe}(\text{bpca})\text{Cl}_2(\text{EtOH})]$ , is reacted with NaOH to give a trinuclear anionic Fe(III) cluster,  $[\text{Fe}_3\text{O}(\text{bpca})_2\text{Cl}_4(\text{EtO})_2]^-$ , in which a T-shaped iron array is bridged by a  $\mu_3$ -oxide and two  $\mu_2$ -ethoxides. Reaction of this cage with  $[\text{Fe}(\text{H}_2\text{O})_6]^{2+}$  gives a heptanuclear cage,  $[\text{Fe}\{\text{Fe}_3\text{O}(\text{bpca})_2\text{Cl}_4(\text{EtO})_2\}_2(\text{EtOH})_2]$ . Magnetization studies suggest an  $S = 6$  ground state.

The oldest octanuclear Fe(III) cage is also the iron cage with the most heavily studied magnetic properties.  $[\text{Fe}_8(\text{O})_2(\text{OH})_{12}(\text{tacn})_6]^{8+}$  (58) (tacn = 1, 4, 7-triazacyclononane), shown in Fig. 23, was first reported

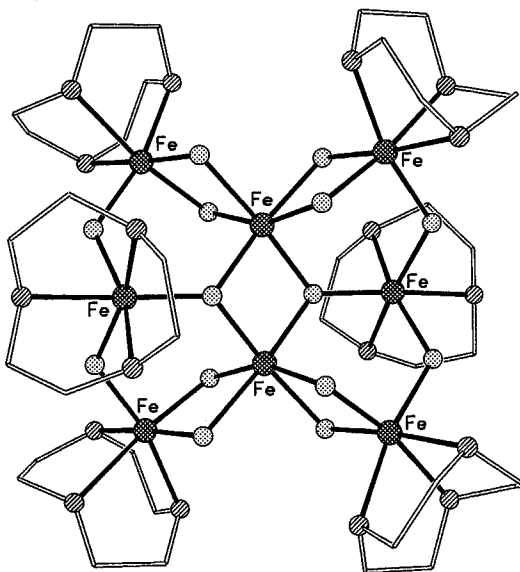


FIG. 23. The structure of  $[\text{Fe}_8(\text{O})_2(\text{OH})_{12}(\text{tacn})_6]^{8+}$  (145). (Shading: Fe, hatched; O, dotted; N, striped; C, lines.)

by Wieghardt and co-workers in 1984 (145). The cage was made by hydrolysis of  $[\text{FeCl}_3(\text{tacn})]$  at pH 9 in the presence of bromide. The structure consists of a planar octanuclear iron core, bridged by two  $\mu_3$ -oxides and twelve  $\mu_2$ -hydroxides. The iron atoms can be considered to be a central  $\{\text{Fe}_4\text{O}_2\}$  butterfly capped on each edge by a further Fe(III) center. The six tacn ligands bind in a tridentate fashion to all the iron atoms except the two Fe(III) atoms at the body of the butterfly.

Later magnetic studies indicated an  $S = 10$  ground state (146) with slow relaxation of the magnetization at low temperature (5); **57** is a SMM (29). The  $S = 10$  state arises because the spin on the two Fe(III) sites at the wingtips of the central butterfly are aligned antiparallel to the spins at the other six Fe(III) centers. Polarized neutron diffraction experiments are in agreement with this picture. High-field EPR (147) and inelastic neutron scattering experiments (148) have allowed derivation of all the zero-field splitting parameters, including the conventionally considered quadrupolar terms  $D$  and  $E$ , as well as hexadecupolar terms  $B_4^0$ ,  $B_4^2$  and  $B_4^4$ .  $E$  is nonzero in **57**, which leads to mixing of  $M_s$  states that differ in  $M_s$  by  $\pm 2$ . This leads to a more complicated manifold of spin states than in the  $\{\text{Mn}_{12}\}$  SMMs. Hysteresis in magnetization vs. field plots are observed below 1 K (5), and steps indicative of quantum tunneling are observed on these plots. The contribution of nuclear hyperfine fields to quantum tunneling can be demonstrated for **58** by substitution of natural-abundance Fe in the cage with  $^{57}\text{Fe}$  ( $I = \frac{5}{2}$ ) (149); this increases the rate of relaxation of the magnetization by quantum tunneling by increasing the intrinsic width of the tunnel splitting. Deuteration of the hydroxide sites of **58** reduces the hyperfine field, thereby reducing the width of the tunnel splitting and slowing the relaxation rate. Therefore, **58** is an excellent subject for studying these fundamental physical phenomena.

Replacement of the macrocyclic tridentate amine ligand tacn by the tripodal amine ligand tren leads to another octanuclear cage,  $[\text{Fe}_8\text{O}_5(\text{O}_2\text{CMe})_8(\text{tren})_4]^{6+}$  (**59**) (150). Cage **59** can be made by passing oxygen through a colorless slurry containing  $[\text{Fe}(\text{tren})(\text{O}_2\text{CMe}_2)]$  and  $\text{Fe}(\text{CF}_3\text{SO}_3)_2 \cdot 2\text{MeCN}$  in butyronitrile. The structure has noncrystallographic  $S_4$  symmetry. There is a central  $\{\text{Fe}_4\text{O}\}$  square, with each edge of the square bridged by an acetate ligand and an oxide, which alternate in being either above or below the plane of the square. The oxides bridge to the four further Fe(III) centers, which are bound to the tridentate tren ligands. Each of the final four acetates bridges between one Fe(III) of the square and an external Fe(III) site. Preliminary magnetic studies indicate that antiferromagnetic exchange dominates, but that either the ground state or a low-lying excited state is paramagnetic. NMR studies reveal that the structure is maintained in solution.

A further cage with  $S_4$  symmetry, this time crystallographically imposed, is  $[\text{Fe}_8\text{O}_4(\text{bmdp})_4(\text{OH})_4(\text{O}_2\text{CMe})_4]$  (**151**) ( $\text{Hbmdp} = N,N,N'$ -tris((*N*-methyl)-2-benzimidazolymethyl)-*N'*-methyl-1,3-diamino-2-propanol; see Scheme 2). This cage was made by reaction of hydrated iron(III) nitrate with the polydentate ligand in water/acetone followed by addition of sodium acetate. This gives a tetranuclear tetracation. Metathesis of the anion with tetrafluoroborate leads to formation of the octanuclear cage. The Fe(III) centers lie on a square, with four centers at the corners and four at the midpoints of the edges. The Fe...Fe vectors are bridged alternately around the square by either a 1,3-bridging acetate and an alkoxide oxygen from bmdp, or by a  $\mu_2$ -oxide. No magnetic data are reported for this cage.

A cage of still higher symmetry is formed from reaction of anhydrous  $\text{FeCl}_3$  with pyrazolate.  $[\text{Fe}_8\text{O}_4(\text{pz})_{12}\text{Cl}_4]$  (**60**) (**67**) ( $\text{Hpz} = \text{pyrazole}$ ) has a central  $\{\text{Fe}_4\text{O}_4\}$  heterocubane, with each oxide binding to an additional Fe(III) center; the oxides are therefore  $\mu_4$ -bridging and the additional Fe centers form a second Fe tetrahedron around the first. Each contact between an Fe within the cubane and an external iron is bridged by a pyrazolate ligand, and each external iron has a terminal chloride attached. The cage therefore has noncrystallographic  $T$  symmetry. There is considerable resemblance to the octanuclear chromium benzoate cage **18**. The magnetic properties of **60** are not reported; however, the electrochemical behavior is extremely interesting. Three reversible reductions are observed between  $-0.43$  and  $-1.07$  V (vs. ferrocene/ferrocenium). A fourth reduction is irreversible at 285 K, but becomes quasireversible at lower temperatures. Coulometry is not reported, so it is not clear whether these are one- or two-electron reductions.

An octanuclear Fe(III) compound,  $[\text{Fe}_8\text{O}_4(\text{OCH}_2\text{CCMe}_3)_2(\text{O}_2\text{CPh})_{14}(\text{HOCH}_2\text{CCMe}_3)_2]$  (**152**) with an iron-oxo core based on an edge-sharing bitetrahedron, has recently been reported, bridged by oxide, alkoxide, and carboxylate ligands. The cage was made by reaction of the oxo-centered iron benzoate triangle with neopentanol in toluene. At the center of the cage six Fe(III) centers are arranged in a bitetrahedron, with a  $\mu_4$ -oxide at the center of each tetrahedron. The two centers in each tetrahedron that are not in the shared edge are bridged by further oxides, which also bridge to the final iron centers in the polyhedron; these are therefore  $\mu_3$ -oxides. The carboxylates bridged in a typical 1,3-fashion, while the alkoxides are either  $\mu_2$ -bridging or terminal. Magnetic studies reveal antiferromagnetic exchange, leading to an  $S = 0$  ground state.

Reaction of  $\text{FeCl}_3$  with  $\text{Na}(\text{O}_2\text{CR})$  ( $\text{R} = \text{Ph}$  or  $\text{Me}$ ) and  $\text{Na}(\text{hmp})$  in  $\text{MeOH}$  gave further octanuclear cages,  $[\text{Fe}_8\text{O}_4(\text{O}_2\text{CPh})_{11}(\text{hmp})_5]$  (**61**)

and  $[\text{Fe}_8\text{O}_4(\text{O}_2\text{CMe})_{12}(\text{hmp})_4]$  (**62**) (135). The two structures are clearly related, involving four  $\{\text{Fe}_3\text{O}\}$  triangles linked either through a single Fe atom or through a shared  $\text{Fe}_2$  edge. The shared edge is at the center of the cage, creating an  $\{\text{Fe}_4\text{O}_2\}$  butterfly. In **61** the two terminal triangles are *anti* about the central butterfly, while in **62** they are *syn*. The carboxylates adopt their usual 1,3-bridging mode, except for one benzoate in **61**, which is present as a terminal ligand. The hmp groups all chelate to one Fe center, and bridge to a second via the O atom. Cage **61** has an  $S = 0$  ground state, while magnetic studies for **62** were not reported.

A nonanuclear iron cage,  $[\text{Fe}_9\text{O}(\text{cit})_8(\text{H}_2\text{O})_3]^{7-}$  (**63**) (cit = citrate), has been reported (153) by Bino *et al.* from reaction of iron(III) nitrate, sodium citrate, and 2,9-dimethyl-1,10-phenanthroline (neocuproine) in water; the neocuproine is protonated during the reaction and acts as the counterion on crystallization. The pH of the solution is 2.2–2.3. The structure consists of three parallel  $\{\text{Fe}_3\}$  units that form a slightly distorted trigonal prism. Each exterior plane is connected to the central fragment by three tetradentate  $\text{cit}^{4-}$  ligands, and is also capped by a further citrate. The central plane has a typical oxo-centered triangle structure, with a central  $\mu_3$ -oxo group surrounded by three Fe(III) atoms, with each Fe··Fe edge bridged by two carboxylates from citrate groups. The external planes have  $\{\text{Fe}_3\text{O}_4\}$  cores, with the O atoms supplied by the alkoxide groups of the deprotonated citrates. The remaining coordination sites on the Fe atoms are occupied by terminal carboxylates. No magnetic data are reported; however, Mössbauer spectroscopy supports stronger magnetic exchange within the central plane than within the exterior planes.

The first decanuclear iron(III) cage reported was the “ferric wheel,” reported by the Lippard group and shown in Fig. 24. This cage has the formula  $[\text{Fe}(\text{OMe})_2(\text{O}_2\text{CCH}_2\text{Cl})]_{10}$  (**64**) (154). Similar cages have since been reported with other carboxylates: acetate (155) and 3-(4-methylbenzoyl)propionate (156). The original preparation involves reaction of the oxo-centered triangle of chloroacetate and hydrated iron(III) nitrate in MeOH; however, later reports suggest that direct reaction of iron(III) nitrate with the sodium salt of the carboxylate and sodium methoxide in MeOH can also be used. The structure consists of a decanuclear wheel, with each Fe··Fe edge bridged by one 1,3-bridging carboxylate and two  $\mu_2$ -methoxides. Magnetic studies of these wheels all show antiferromagnetic exchange, leading to an  $S = 0$  ground state in zero-field (154). However detailed studies of **64** at 0.6 K have shown that states of higher spin multiplicity become the ground state as the external field is increased. Thus at 4.6 T, a component of an

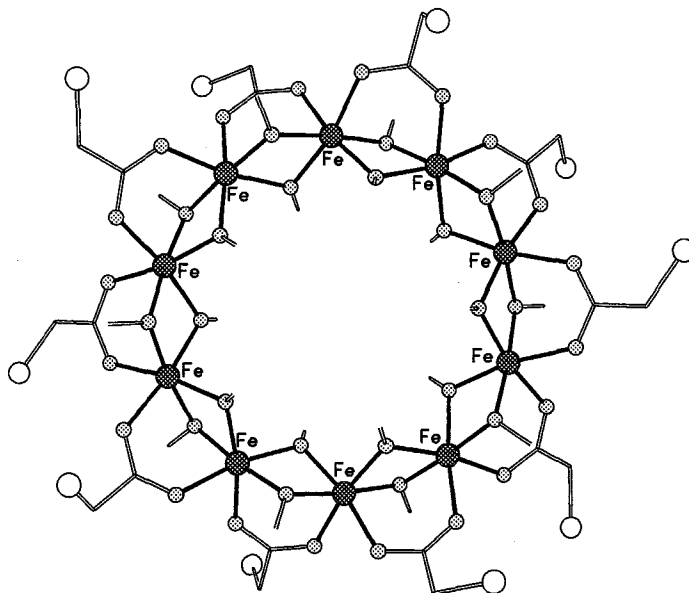


FIG. 24. The structure of  $[\text{Fe}(\text{OMe})_2(\text{O}_2\text{CCH}_2\text{Cl})]_{10}$  (**154**). (Shading as in Fig. 23, plus Cl, open.)

$S = 1$  state becomes the ground state; then at higher field sequentially  $S = 2, 3, 4, 5, 6, 7, 8$ , and  $9$  states could be made lowest in energy. The highest field reported was  $50 \text{ T}$ .

$[\text{Fe}_{10}\text{O}_4(\text{OMe})_{16}(\text{dbm})_6]$  (**65**) (**157a**) can be made from a process very similar to that which gives the metallocrown **52**: reaction of  $\text{FeCl}_3$  with Hdbm and  $\text{Na}(\text{OMe})$  in  $\text{MeOH}$ . The yield of **65** is poor. The structure consists of three layers of a cubic-close-packed array of oxygen atoms, with five  $\text{Fe}(\text{III})$  ions occupying octahedral holes between each of the layers. The five  $\text{Fe}(\text{III})$  sites in each case describe a trapezium. The magnetic behavior of **65** indicates a low spin, probably  $S = 0$  ground state, which results from antiferromagnetic exchange between the iron centers. The same core has also been reported coated in methoxide and chloride (**157b**).

In  $[\text{Fe}_{10}\text{Na}_2\text{O}_6(\text{OH})_4(\text{O}_2\text{CPh})_{10}(\text{chp})_6(\text{H}_2\text{O})_2(\text{Me}_2\text{CO})_2]$  (**66**) ( $\text{chp} = 6\text{-chloro-2-pyridonate}$ ) (**155**), shown in Fig. 25, antiferromagnetic exchange is also dominant, but a very high spin ground state of around  $S = 11$  or  $\frac{23}{2}$  results. Cage **66** can be made by reaction of  $[\text{Fe}_2\text{OCl}_6]^{2-}$  with  $\text{Na}(\text{chp})$  and  $\text{Na}(\text{O}_2\text{CPh})$  in  $\text{MeCN}$ , followed by crystallization from acetone/ether. The  $\{\text{Fe}_{10}\text{O}_{10}\}$  core is perhaps best described as two  $\{\text{Fe}_6\text{O}_6\}$  hexagonal prisms sharing a square face. The complicated structure and mixture of bridging groups present make modeling the

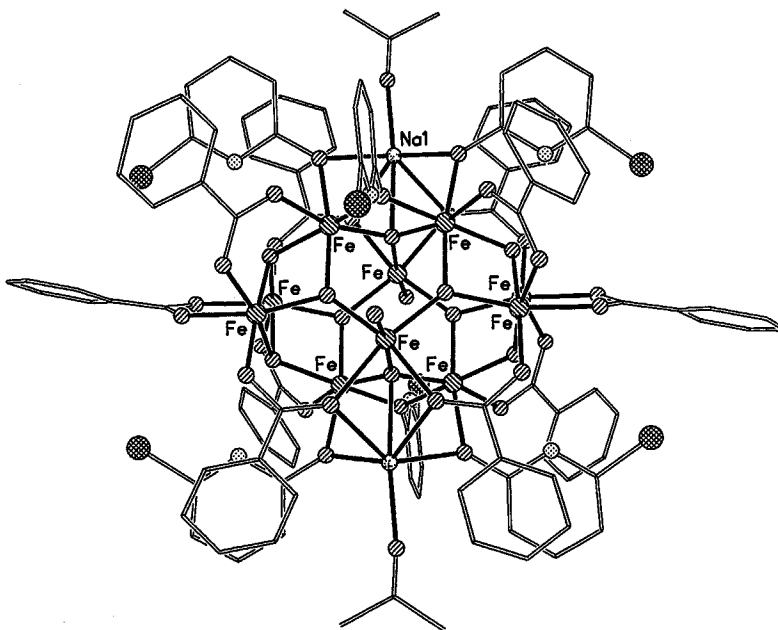


FIG. 25. The structure of  $[\text{Fe}_{10}\text{Na}_2\text{O}_6(\text{OH})_4(\text{O}_2\text{CPh})_{10}(\text{chp})_6(\text{H}_2\text{O})_2(\text{Me}_2\text{CO})_2]$  (**155**). (Shading: Fe, striped top-left/bottom-right; O, striped top-right/bottom-left; N, dotted; Cl, hatched; C, lines; Na, shaded.)

variable temperature magnetic data difficult; however, Cano *et al.* have recently reported Monte Carlo studies that allow exchange parameters to be calculated (11). A.c. susceptibility studies also reveal that **66** is a SMM, with an energy barrier of 5.3 K to reorientation of the magnetization (11).

The first undecanuclear iron cage,  $[\text{Fe}_{11}\text{O}_6(\text{OH})_6(\text{O}_2\text{CPh})_{15}]$  (**67**), shown in Fig. 26, was also reported by the Lippard group (158). It is formed by controlled slow hydrolysis of a solution containing  $[\text{Fe}_2\text{OCl}_6]^{2-}$  and  $\text{Na}(\text{O}_2\text{CPh})$  in MeCN. The structure consists of a pentacapped trigonal prism of Fe(III) centers, with six  $\mu_3$ -oxides inside the prism, each bridging between one iron at the vertex of the trigonal prism, one cap on a triangular face, and one cap on a rectangular face. The six  $\mu_3$ -hydroxides are on the exterior of the prism, and each bridges between two Fe centers that make an edge of the prism and a cap on a rectangular face. The carboxylates bridged in a 1,3-fashion. Magnetic studies show a low-spin ground state, probably  $S = \frac{1}{2}$ ; however, there are clearly low-lying excited states of higher spin multiplicity. The presence of exterior hydroxides on this cage makes **67** a good model for iron

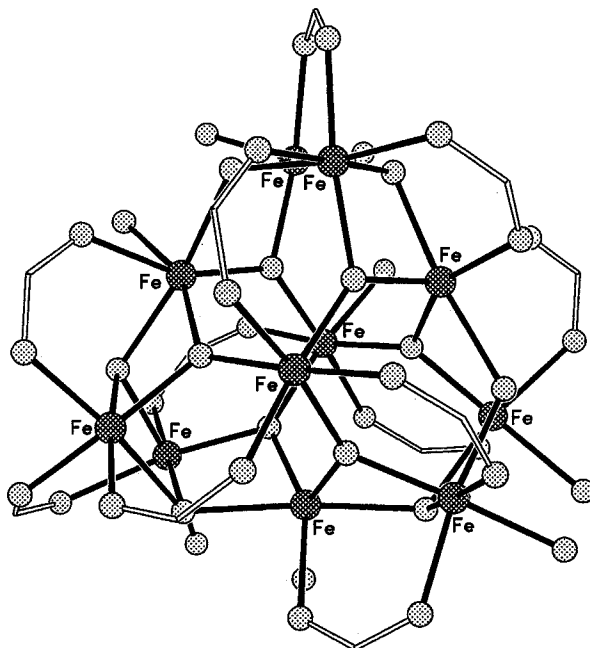


FIG. 26. The structure of  $[\text{Fe}_{11}\text{O}_6(\text{OH})_6(\text{O}_2\text{CPh})_{15}]$  (158). (Shading: Fe, hatched; O, dotted; C, lines.)

oxyhydroxide surfaces, and a derivative of **67** has been made with the corrosion inhibitor for mild steel, 3-(4-methylbenzoyl)propionate (156). This keto-carboxylate shows the same carboxylate binding mode as the benzoate in **67**; however, the ketone groups form hydrogen bonds to the  $\mu_3$ -hydroxides. It has been suggested that this H bond plays an important part in the utility of 3-(4-methylbenzoyl)propionate as a surface-modifying agent; not only because it increases the binding strength of the ligand to a metal surface, but also because it imposes a specific orientation of the organic backbone with respect to the surface, creating a hydrophobic layer.

A mixed-valent dodecanuclear iron cage can be made from reaction of iron(II) acetate with lithium methoxide in MeOH, followed by careful addition of dry dioxygen.  $[\text{Fe}_{12}\text{O}_2(\text{OMe})_{18}(\text{O}_2\text{CMe})_6(\text{HOMe})_{4,67}]$  (**68**) (159) contains four Fe(III) and eight Fe(II) centers arranged in a core which is related to the decametallates  $\{\text{M}_{10}\text{O}_{28}\}$  found for vanadium and manganese (see 41), with two additional octahedral Fe sites attached to the decametallate core. The terminal groups are methoxides or acetates, without the naked oxygen centers typical of the vanadium

cages. The four Fe(III) sites are assigned as the four metal sites *trans* to the shared edge of a decametallate core. Magnetic studies show that **68** has a diamagnetic ground state.

A mixed-valent heptadecanuclear iron cage has also been reported by this group, as part of a series of general formula  $[\text{Fe}_{16}\text{MO}_{10}(\text{OH})_{10}(\text{O}_2\text{CPh})_{20}]$  ( $M = \text{Fe}, \text{Mn}$  or  $\text{Co}$ ) (**160**); the cage with  $M = \text{Fe(II)}$  is shown in Fig. 27. These cages are formed in low yield from reactions of the mixed-valent triangle  $[\text{Fe}_3\text{O}(\text{O}_2\text{CPh})_6(\text{H}_2\text{O})_2(\text{MeCN})]$ ; the  $\{\text{Fe}_{17}\}$  cage results from hydrolysis of a solution of the triangle in MeCN (with some **67** also found), while the cages containing Mn or Co involved reaction with suitable metal salts prior to crystallization. The structures of all three cages are virtually identical, and complicated. A core is, in each case, an  $\{[\text{Fe}_3\text{O}_3(\text{OH})]\text{M}\}$  double cubane sharing a corner, with the divalent ion  $[\text{Mn(II)}, \text{Co(II)}$  or  $\text{Fe(II)}]$  at the shared corner. This double cubane is surrounded by an  $\{\text{Fe}_{10}\text{O}_4(\text{OH})_4\}$  ring, with the surface coated with benzoate ligands. The authors also note structural similarities between these cages and **67**. Magnetic studies show antiferromagnetic exchange between the metal centers, giving low-spin ground states.

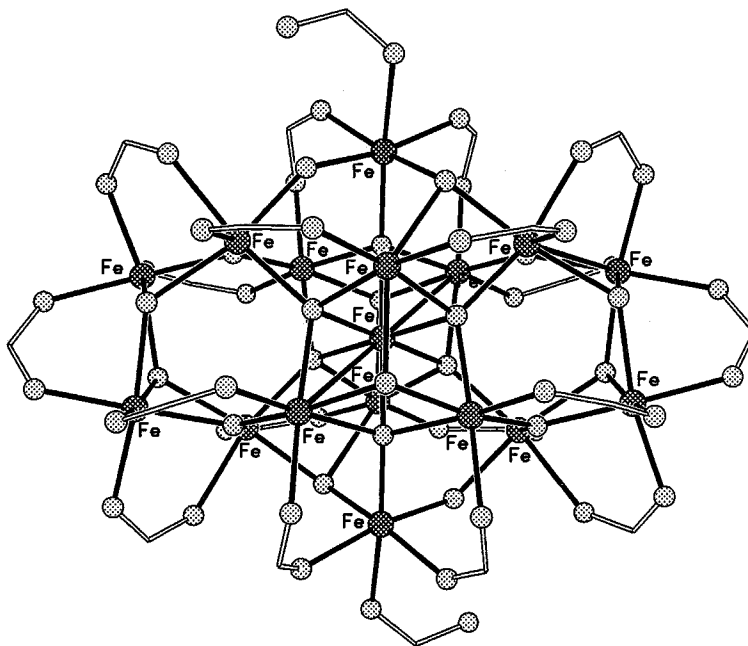


FIG. 27. The structure of  $[\text{Fe}_{16}\text{MO}_{10}(\text{OH})_{10}(\text{O}_2\text{CPh})_{20}]$  (**160**). (Shading as in Fig. 26.)

Another heptadecanuclear cage,  $[\text{Fe}_{17}\text{O}_{15}(\text{OH})_6(\text{chp})_{12}(\text{phen})_8(\text{OMe})_3]$  (161) can be formed by reaction of  $[\text{Fe}_2\text{OCl}_6]^{2-}$  with  $\text{Na}(\text{chp})$  and phen in MeCN, followed by crystallization from EtOAc—again with a poor yield. The structure is extremely irregular, perhaps due to packing of the chelating phen ligands, which leads to “ridges” along the cage. The central portion of the cage has some similarities to the core of **66**, which also features a pyridonate ligand.

Heath and Powell (162) report a further heptadecanuclear cage which is cocrystallized with a nonadecanuclear cage; this heptadecanuclear cage is shown in Fig. 28. More recently, Goodwin *et al.* (163) have isolated the pure nonadecanuclear cage by variation of the polydentate ligand used. In the original work, the ligand heidi  $[\text{H}_3\text{heidi} = \text{N}(\text{CH}_2\text{COOH})_2(\text{CH}_2\text{CH}_2\text{OH})]$  was reacted with hydrated iron nitrate in water, with the pH controlled by addition of pyridine. The more recent work uses methyl- or ethyl-substituted derivatives,  $\text{N}(\text{CH}_2\text{COOH})_2(\text{CHRCH}_2\text{OH})$  ( $\text{R} = \text{Me}$ , metheidi;  $\text{R} = \text{Et}$ , etheidi), which exclusively trap the larger cluster. The structures contain a core that resembles a fragment of an  $\{\text{Fe}(\text{OH})_2\}$  lattice, which is surrounded

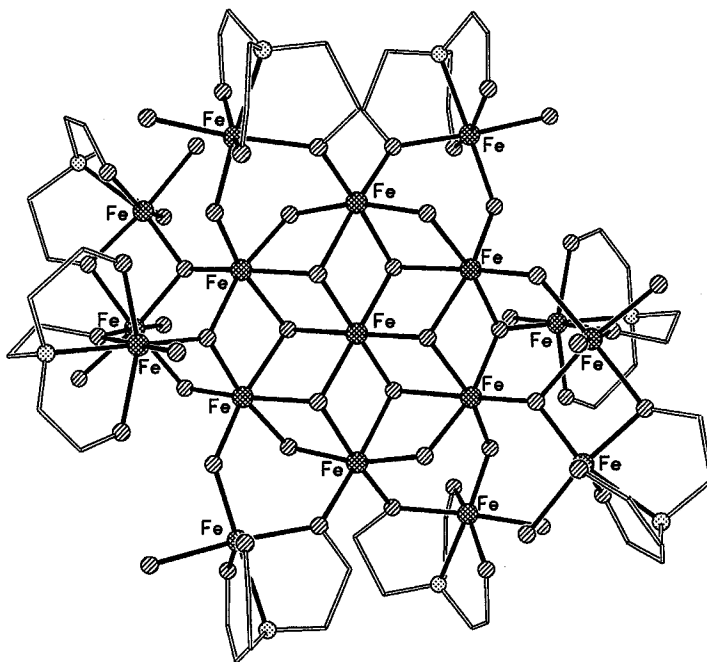


FIG. 28. The structure of  $[\text{Fe}_{19}(\text{metheidi})_{10}(\text{OH})_{14}\text{O}_6(\text{H}_2\text{O})_{12}]$  (163). (Shading: Fe, hatched; O, striped; C, lines.)

by tripodal ligands that prevent formation of an insoluble "rust." Original magnetic studies indicated that the two cages had very high-spin ground states, but the presence of both cages in one lattice restricted discussion. The more recent work demonstrates that the spin ground state for the cage  $[\text{Fe}_{19}(\text{metheidi})_{10}(\text{OH})_{14}\text{O}_6(\text{H}_2\text{O})_{12}](\text{NO}_3)$  (**69**) is  $S = \frac{33}{2}$ , and that a small negative zero-field splitting is present. Therefore, **69** is a SMM with one of the highest spin ground states known. However, the small magnetic anisotropy leads to a very low energy barrier for reorientation of the magnetization. Subtle variation of the ligand produces a pure material; it is possible that further variation may allow inclusion of more anisotropic ions, hence leading to SMMs with higher blocking temperatures.

The final iron cage discussed is the largest known ferric wheel. The octadecanuclear wheel,  $[\text{Fe}(\text{OH})(\text{XDK})\text{Fe}_2(\text{OMe})_4(\text{O}_2\text{CMe})_2]_6$  (**70**) [XDK = the dianion of *m*-xylylenediamine bis(Kemp's triacid imide); see Scheme 2] (164), shown in Fig. 29, is made from reaction of the dinuclear iron complex of XDK with  $[\text{NEt}_4](\text{O}_2\text{CMe})$  in methanol, followed

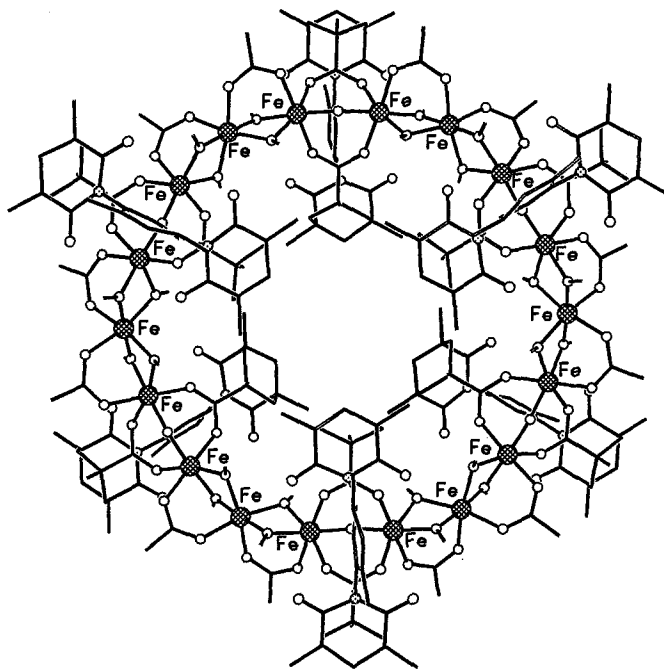


FIG. 29. The structure of  $[\text{Fe}(\text{OH})(\text{XDK})\text{Fe}_2(\text{OMe})_4(\text{O}_2\text{CMe})_2]_6$  (164). (Shading: Fe, hatched; O, open; C, lines.)

by addition of 1-methylimidazole. Cage **70** retains the dinuclear units of the precursor, but these are linked by additional Fe(III) centers which are bridged to the dinuclear units through two  $\mu_2$ -OMe bridges and one acetate bridge—the same links that appear in the decanuclear wheel **64**. Magnetic studies reveal the usual antiferromagnetic exchange between Fe(III) centers, resulting in a diamagnetic ground state. The existence of cyclic  $\{\text{Fe}_6\}$ ,  $\{\text{Fe}_{10}\}$ ,  $\{\text{Fe}_{12}\}$ , and  $\{\text{Fe}_{18}\}$  wheels is of great value for physicists interested in finite size effects in antiferromagnetically coupled systems.

The polynuclear iron chemistry, therefore, has produced a very large number of cages, which show a range of fascinating magnetic properties. The contribution to understanding iron storage in ferritin is perhaps more debatable. The majority of large iron cages can be related to close-packed arrays of oxides with iron centers occupying octahedral sites between the layers; however, there are many exceptions. Finally, the diversity of structures is clearly very dependent on the ligands present; thus, extrapolating from these clusters with simple bridging ligands to ferritin, which contains  $\sim 4500$  iron centers and polypeptide ligands, is difficult.

#### E. COBALT

Many fewer high-nuclearity cages are known for cobalt than for manganese or iron, and their magnetic properties have not been well studied. Unless otherwise stated, magnetic data have not been reported for the following complexes.

The first hexanuclear cobalt(II) cage reported was a  $[\text{Co}_6(\text{O}_2\text{CNEt}_2)_{12}]$  (*165*), which has a structure similar to that of Mn(II) and Fe(II) complexes of the same ligand (see above). The cage was prepared by addition of anhydrous cobalt(II) chloride to a toluene solution of diethylamine, which had previously been treated with  $\text{CO}_2$ . The cage consists of an edge-sharing bitetrahedron of cobalt centers. Both five- and six-coordinate cobalt sites are found, and the carbamate ligands show three different bridging modes: 1,1-, 1,1,3-, and 1,1,3,3-bridges are found.

A hexanuclear cobalt(II) metallocrown has been reported by Thornton and co-workers (*166*). Reaction of  $\text{Na}(\text{OMe})$  with cobalt(II) acetate and Hmhp in MeOH apparently gives  $[\text{Co}_6\text{Na}(\text{mhp})_{12}]^+$ , and anion was not located in a highly disordered crystal structure. A yield is not reported, and crystallization required a period of months. The structure contains six tetrahedral Co(II) centers, each bound to two N and two O donors from pyridonate ligands. Six of these oxygen atoms lie within the metallocycle, and form an ideal cavity for coordination of sodium.

This cage is closely related to the previously reported hexanuclear copper metallocrown  $[\text{Cu}_6\text{Na}(\text{mhp})_{12}]^+$  (see below) (167).

A better characterized cobalt wheel is made from the solvothermal reaction of hydrated cobalt nitrate with the tripodal ligand  $\text{N}(\text{CH}_2\text{PO}_3\text{H}_2)(\text{CH}_2\text{CO}_2\text{H})_2$  in the presence of KOH in MeOH (168). Within  $\text{K}_2[\text{Co}\{\text{N}(\text{CH}_2\text{PO}_3)(\text{CH}_2\text{CO}_2)_2\}]_6$  each cobalt(II) center is five-coordinate, with a trigonal-bipyramidal geometry. One apical site is occupied by the N donor of the tripodal ligand, while the three equatorial sites are occupied by O atoms from carboxylate or phosphonate groups. The final apical site is occupied by an O atom from a phosphonate attached to a neighboring cobalt, producing a cyclic structure. This compound shows a room-temperature magnetic moment consistent with noninteracting cobalt(II) centers, but at 14 K there is a magnetic phase transition to a canted antiferromagnetic state (167). This appears to be the first observation of canting in a molecular inorganic compound.

A planar hexanuclear cobalt cage,  $[\text{Co}_6\{(\text{PhSiO}_2)_6\}_2\text{Cl}(\text{solvent})_6]^-$ , which has the same metal core as the manganese(II) cage **28**, has been reported (87). The experimental details are so limited that it is difficult to identify the molecules attached in the axial positions of the six cobalt centers.

A very recent report of a further hexanuclear cobalt cage involves 6-(diethylamino)-2-hydroxy-4-sulfanyl-1,3,5-triazine ( $\text{H}_2\text{OSta}$ ) and a condensation product of this ligand (169). The cage was formed in very poor yield by reaction of  $\text{Na}(\text{OSta})$  with cobalt(II) chloride and  $\text{Na}(\text{O}_2\text{CPh})$ . The complex has the formula  $[\text{Co}_6\text{NaO}(\text{OSta})_7(\text{L7})_2(\text{O}_2\text{CPh})_2(\text{H}_2\text{O})_2]$ , and a complicated array of two Co(III) and four Co(II) sites. The structure is virtually indescribable.

Six cobalt centers are also found in the mixed-metal cage  $[\text{Co}_6\text{Cu}_2(\text{OH})_4(\text{mhp})_2(\text{O}_2\text{CPh})_{10}(\text{mhp})_2(\text{Hmhp})_4(\text{H}_2\text{O})_2]$  (**71**) (170), which is formed by reaction of a mixture of copper and cobalt benzoates with Hmhp, followed by crystallization from EtOAc. The structure is dominated by oxo-centered metal triangles. At the core of the cage is a  $\{\text{Co}_4\text{O}_2\}$  butterfly. Each wingtip cobalt site is then part of a further  $\{\text{Co}_2\text{CuO}\}$  triangle. All Co(II) sites have octahedral coordination geometry, while the two Cu(II) sites are five-coordinate. The benzoate ligands show three different binding modes: Two are bound through a single oxygen to a cobalt; two are 1,1,3-bridging; and the remainder bridge in the conventional 1,3-fashion. The mhp ligands chelate to the copper sites, and bridge to a cobalt atom through the oxygen donor.

The equivalent reaction involving copper and cobalt acetates reacted with Hchp gives a nonanuclear cage,  $[\text{Co}_7\text{Cu}_2(\text{OH})_2(\text{chp})_{10}(\text{O}_2\text{CMe})_6]$  (**72**) (170). Here the copper sites are both five-coordinate, while the

cobalt atoms are found with either five or six ligands bound to them. The polyhedron defined by the metal sites is extremely irregular. The seven Co(II) sites can be described as belonging to two  $\{\text{Co}_4\text{O}_2\}$  butterflies that share a body vertex. The two Cu(II) atoms then cap opposite edges of this central  $\{\text{Co}_7\text{O}_4\}$  fragment. Magnetic studies indicate anti-ferromagnetic exchange between the metal centers, which gives a spin ground state of  $S = \frac{3}{2}$  at most.

A series of heptanuclear cobalt cages have been reported of general formula  $[\text{Co}_7(\text{OH})_2(\text{O}_2\text{CR})_4(\text{chp})_8(\text{solv})]$  (**73**) (171), where R = Ph or  $\text{CMe}_3$  and solv = MeCN or 0.69 Hchp : 0.31 MeCN or 0.75 Hchp : 0.25  $\text{H}_2\text{O}$ . The structure, illustrated in Fig. 30, consists of a square-based pyramid of Co(II) centers, capped on one triangular face and on the adjacent edge of the square base by two further cobalt atoms. One of the  $\mu_3$ -hydroxides bridges between the capping atom on the edge and the two atoms within the edge, while the second  $\mu_3$ -hydroxide bridges the three Co centers in the triangular face opposite. The four carboxylates are all 1,3-bridging; however, the eight pyridonates show four different bonding modes. These are best described using Harris notation (169), where the binding mode is referred to as  $[\text{X} \cdot \text{Y}_1\text{Y}_2\text{Y}_3, \dots, \text{Y}_n]$ , where X is the overall number of metals bound by the whole ligand, and each value of Y represents the number of metal atoms attached to the different donor

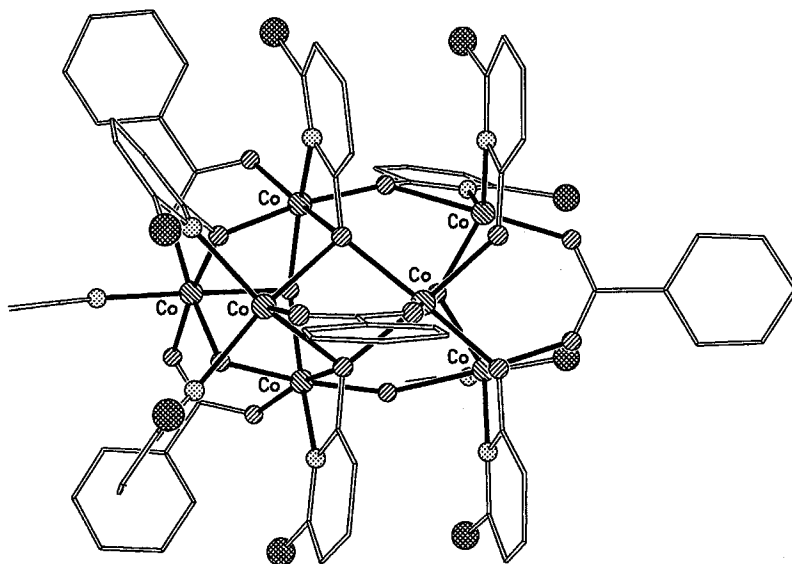


FIG. 30. The structure of  $[\text{Co}_7(\text{OH})_2(\text{O}_2\text{CR})_4(\text{chp})_8(\text{solv})]$  (171). (Shading: Shading: Co, striped top-left/bottom-right; O, striped top-right/bottom-left; N, dotted; Cl, hatched; C, lines.)

atoms. Therefore for chp, there will be two values for Y. The ordering of Y is listed by the Cahn–Ingold–Prelog priority rules; hence O precedes N here. The four binding modes observed in these cages are therefore the 2.21, 2.20, 3.31, and 3.21. For consistency, the binding mode found for the carboxylates would be described as 2.11. A polymeric structure involving similar heptanuclear cobalt cages linked through carboxylate bridges has also been reported (171).

The other heptanuclear cobalt(II) cage in the literature involves *o*-mercaptophenolate ligands.  $[\text{Co}_7\text{Na}_2(1,2\text{-OSC}_6\text{H}_4)_8(\text{DMF})_{12}]$  (172) is formed from reaction of  $\text{CoBr}(\text{PPh}_3)_3$  with sodium mercaptophenolate in DMF. The structure consists of an almost linear chain of five tetrahedrally coordinated Co(II) and two sodium centers, with two further Co centers attached at the end of the chain. Four of the cobalt centers are bound to two S and two O donors from mercaptophenolate ligands, two are bound to four DMF molecules (one of which bridges in a  $\mu_2$ -fashion via the oxygen in each case), and one cobalt center is bound to two DMF molecules and two O donors from mercaptophenolate ligands. The room-temperature magnetic moment is a little lower than would be expected for seven cobalt(II) centers.

The octanuclear cobalt cages fall into two categories. A number of mixed-valence clusters based on cubane cores have been reported, and two cyclic structures are known. The cubane cages have two distinct structures. The earlier structure, found in  $[\text{Co}_8\text{O}_4(\text{O}_2\text{CPh})_{12}(\text{solv})_3(\text{H}_2\text{O})]$  (74) (66) ( $\text{solv} = \text{MeCN}$  or  $\text{DMF}$ ), contains a central  $\{\text{Co}_4\text{O}_4\}$  heterocubane, with each oxide also bridging to a further cobalt site and thus acting as a  $\mu_4$ -bridge. These structures are therefore directly analogous to the octanuclear chromium cage **18**. These cobalt cubanes are made from addition of hydrogen peroxide to cobalt(II) benzoate dissolved in either DMF or MeCN. Charge balance requires four Co(III) and four Co(II) sites in the structure. Structural parameters indicate that the molecule is trapped-valence, the cobalt sites within the heterocubane being Co(III) while the external sites are Co(II). Each  $\text{Co(III)} \cdots \text{Co(II)}$  contact is bridged by a 1,3-bound benzoate. The external Co(II) sites have trigonal-bipyramidal coordinate geometries, with the fifth coordination site occupied by a solvent molecule. Magnetic studies show a decline in magnetic moment with temperature; however, this decline is probably due to single-ion effects of the five-coordinate Co(II) sites rather than an antiferromagnetic exchange between them. These cages also show interpretable  $^1\text{H}$  NMR spectra, suggesting that the structures are maintained in solution.

The second cubane-related structure, originally found in  $[\text{Co}_8\text{O}_4(\text{OH})_4(\text{O}_2\text{CMe})_6(\text{L8})_2]^{2+}$  (75) (173) ( $\text{L8} = 1,2\text{-bis}(2,2'\text{-bipyridyl-6-yl})\text{ethane}$ ), is shown in Fig. 31. The cage forms from treatment of an ethanol solution

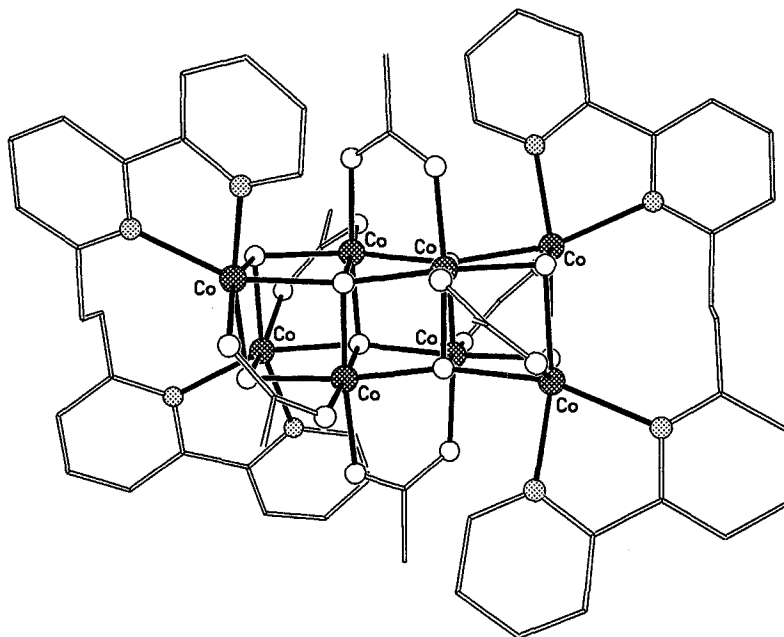


FIG. 31. The structure of  $[\text{Co}_8\text{O}_4(\text{OH})_4(\text{O}_2\text{CMe})_6(\text{L8})_2]^{2+}$  (**173**). (Shading: Co, hatched; O, open; N, dotted; C, lines.)

of cobalt(II) acetate and L8 with hydrogen peroxide. The structure consists of a triple-cubane structure, with the central  $\{\text{Co}_4\text{O}_4\}$  hetero-cubane containing four Co(III) centers and the four Co(II) centers in the exterior sites of the cage. In **74** the four  $\mu_4$ -oxides have almost tetrahedral geometries, but in **75** they have a sawhorse arrangement. There are also four  $\mu_3$ -hydroxides which bridge within the exterior cubanes. Each  $\text{Co(II)} \cdots \text{Co(II)}$  edge is bridged by a bis(bipyridyl) ligand while the carboxylate ligands bridge in a 1,3-fashion across six of the faces of the triple cubane. Magnetic studies again show a decline in magnetic moment with temperature.

A very similar structure is found for  $[\text{Co}_8\text{O}_4(\text{O}_2\text{CMe})_6(\text{OMe})_4\text{Cl}_4(\text{OH}_n)_4]$  (**76**) ( $n = 1$  or  $2$ ) (**69**), which is formed by passing ozone through a solution of cobalt(II) acetate in acetic acid. The triple cubane and the bridging modes adopted by carboxylate and  $\mu_4$ -oxide ligands are identical to those in **75**. The role of the  $\mu_3$ -hydroxides is taken by  $\mu_3$ -methoxides. The four terminal sites, occupied by the bis(bipyridyl) ligand in **75**, are occupied by chloride and hydroxide/water ligands in **76**. As written, the formula suggests that at least six Co(III) centers are

present; however, the room-temperature magnetic moment reported is too high for this proposition to be correct.

The two octanuclear cobalt(II) wheels contain very different ligands. In  $[\text{Co}_8(\text{L9})_{12}(\text{ClO}_4)]^{3+}$  (**77**) [ $\text{L9} = \text{bis}\{3-(2\text{-pyridyl})\text{pyrazol-1-yl}\}$  dihydroborate; see Scheme 2] (**174**), each of the eight Co(II) centers is bound to three ligands which act as bidentate ligands to individual centers, then bridge to a second. Either one or two L9 units bridge the Co...Co edges of the octagon. A perchlorate anion is found at the center of the ring. Electrospray mass spectrometry indicates that the structure is maintained in solution, including the encapsulated anion. Evidence for a similar nickel wheel is presented, but no crystal structure is reported.

$[\text{Co}_8(\text{O}_2\text{CMe})_8(\text{OMe})_{16}]$  (**175**) is a much more typical wheel, clearly related to the ferric and chromium wheels described above. The cage is formed by dissolution of cobalt(III) acetate in MeOH in the presence of  $\text{NH}_4\text{PF}_6$ . Each Co...Co edge is bridged by two methoxides and one carboxylate. An ammonium cation is found at the center of the cage. As the cage contains exclusively Co(III) centers, it is diamagnetic.

The nonanuclear cobalt(II) cage  $[\text{Co}_9(\text{chp})_{18}]$  (**78**) (**176**), shown in Fig. 32, is a rare example of a homoleptic paramagnetic cage. It is formed by reaction of freshly prepared cobalt hydroxide with Hchp at  $130^\circ\text{C}$ , followed by crystallization from EtOAc. The structure has crystallographic  $D_{3d}$  symmetry and contains four  $\{\text{Co}_4\text{O}_6\}$  adamantanes, sharing either  $\{\text{Co}_3\text{O}_3\}$  faces or a single cobalt vertex. Each chp ligand binds in a 2.21 fashion (Harris notation), i.e., chelating to one cobalt center through both N and O donors and bridging to a second cobalt through the oxygen.

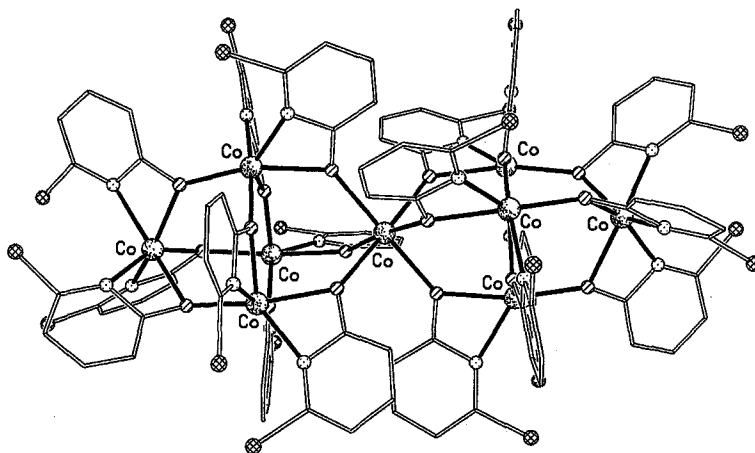


FIG. 32. The structure of  $[\text{Co}_9(\text{chp})_{18}]$  (**176**). (Shading: Co, random shading; O, striped, N, dotted; C, lines.)

The nonanuclear cobalt(II) cage,  $[\text{Co}_9\{(\text{py})_2\text{CO}_2\}_4(\text{O}_2\text{CMe})_8(\text{OH})_2]$  (**79**) (177), shown in Fig. 33, is formed by reaction of cobalt(II) acetate and di-2-pyridylketone,  $(\text{py})_2\text{CO}$ , in MeCN. This structure contains two  $\{\text{Co}_5\}$  square-based pyramids sharing a cobalt vertex. The two hydroxides bridge the four cobalt centers within the square bases while each of the eight acetates bridges an edge of the base. The two pyramids are bridged by the  $\{(\text{py})_2\text{CO}_2\}$  dianions, which act as 5.3311 ligands (Harris notation); i.e., each oxygen is  $\mu_3$ -bridging while each pyridyl-nitrogen binds to one of the metal centers to which an oxygen binds. The central Co atom is bound to all eight oxygens from the four  $\{(\text{py})_2\text{CO}_2\}$  dianions. Magnetic studies reveal a fall in magnetic moment with temperature.

The four known decanuclear cobalt cages all come from similar chemistry, which was originally said to give a dodecanuclear cage,  $[\text{Co}_{12}(\text{OH})_6(\text{mhp})_{12}(\text{O}_2\text{CMe})_6]$  (**80**) (178). This complex, reported by Garner and co-workers in 1983, formed from reaction of cobalt acetate with Hmhp. The structure, shown in Fig. 34, contains a centered-pentacapped trigonal prism; however, although the dodecanuclear nickel analog has since been reported, no further studies of **80** have been possible. Two decanuclear cages,  $[\text{Co}_{10}(\text{OH})_6(\text{mhp})_6(\text{O}_2\text{CPh})_7(\text{Hmhp})_3\text{Cl}(\text{MeCN})]$

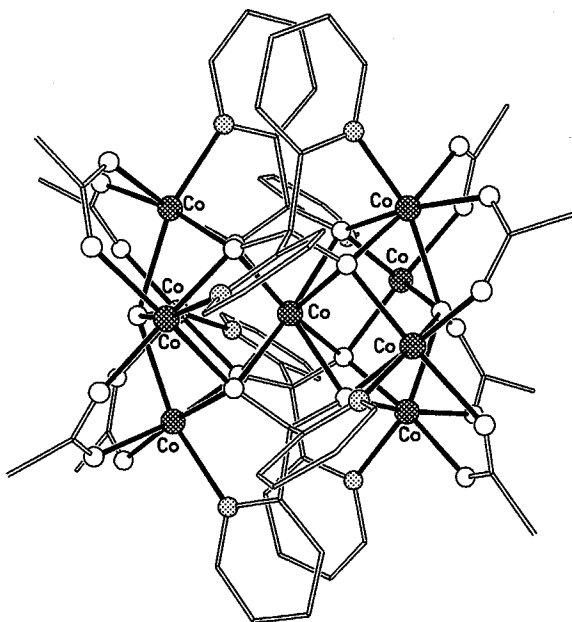


FIG. 33. The structure of  $[\text{Co}_9\{(\text{py})_2\text{CO}_2\}_4(\text{O}_2\text{CMe})_8(\text{OH})_2]$  (177). (Shading: Co, hatched; O, open; N, dotted; C, lines.)

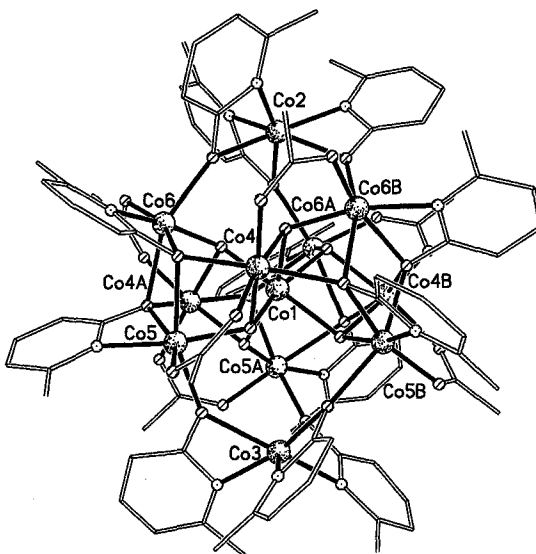


FIG. 34. The structure of  $[\text{Co}_{12}(\text{OH})_6(\text{mhp})_{12}(\text{O}_2\text{CMe})_6]$  (**178**). (Shading: Co, random shading; O, striped; N, dotted; C, lines.)

(**81**) and  $[\text{Co}_{10}(\text{OH})_6(\text{mhp})_6(\text{O}_2\text{CCMe}_3)_7(\text{Hmhp})\text{Cl}(\text{MeCN})_3]$  (**82**) contain a similar core, but it is now a centered tricapped-trigonal prism (ttp) missing the two caps on trigonal faces found in **80** (**179**).

The central cobalt site in **80–82** is bound to six  $\mu_3$ -hydroxides that bridge to the nine further metals forming the ttp. The metal atoms at the vertices of the prism share one  $\mu_3$ -OH with the central cobalt, while the metal atoms capping the rectangular faces of the prism share two  $\mu_3$ -hydroxides with Co(1), forming three  $\text{M}_2\text{O}_2$  rings. The exterior of this central ttp is bridged by six mhp and six acetate ligands. Each mhp ligand adopts the 3.31 bonding mode, chelating to one of the cobalt atoms at the vertices of the prism and bridging to two further Co sites through the exocyclic O atom. The six  $\mu_3$ -O donors from the pyridonates occupy the six triangular faces around the “waist” of the ttp; e.g., they center the faces bounded by one-cap- and two-vertex-metal sites. The carboxylates bridge in a 2.11 fashion between cap and vertex sites, with each cap attached to two acetate ligands. The result of these various bridges is to create a central  $[\text{M}_{10}(\mu_3\text{-OH})_6(\eta^2, \mu_3\text{-xhp})_6(\eta^2, \mu_2\text{-O}_2\text{CR})_6]^{2+}$  fragment, and this fragment recurs in nickel trigonal prisms (see below), differing only in the carboxylate present.

The metal sites are all six-coordinate, with the central metal bonded exclusively to  $\mu_3$ -hydroxides. The capping sites are bonded to two

$\mu_3$ -hydroxides, two  $\mu_3$ -O atoms from mhp, and two oxygens derived from carboxylates. The vertex sites are bound to just five donors from within this central fragment: one  $\mu_3$ -hydroxide, two  $\mu_3$ -O atoms from mhp, one oxygen from a carboxylate, and one N donor from an mhp ligand. The final coordination site for these vertex metals is where the structural variation in these cages takes place. In **80**, each of the six  $\mu_2$ -O atoms from mhp ligands occupies one of these sites, these ligands being part of two  $[\text{Co}(\text{mhp})_3]^-$  fragments that occupy both the upper and lower triangular faces of the trigonal prism. In **81** and **82** these faces are occupied by disordered arrays of solvent molecules, chlorides, and Hmhp ligands.

Two further decanuclear cages have been crystallized.  $[\text{Co}_{10}(\text{OH})_4(\text{chp})_{10}(\text{O}_2\text{CCMe}_3)_6(\text{EtOH})_2]$  (**83**) (179) was made from reaction of cobalt chloride with Na(chp) and  $\text{Na}(\text{O}_2\text{CCMe}_3)$  in MeOH, followed by crystallization from EtOH. The core of **83** appears to be quite different from the ttp structures; however, it is related to the pentacapped centered-trigonal prism in **80**, but is missing two metal centers from one edge of the prism. Complex **83** is held together by four  $\mu_3$ -OH ligands, six 1,3-bridging carboxylates, and ten pyridonate ligands. The pyridonates adopt four different bridging modes, described as 1.11, 2.21, 3.31, and 3.21 using Harris notation.

$[\text{Co}_{10}(\text{OH})_6(\text{mhp})_6(\text{O}_2\text{CCPh}_3)_6(\text{Hmhp})_3(\text{HCO}_3)_3]$  (**84**) (180) is formed in very low yield from reaction of cobalt chloride with Na(mhp) and  $\text{Na}(\text{O}_2\text{CCPh}_3)$  in MeOH, followed by crystallization from EtOAc. The structure contains a centered-trigonal prism; however, this prism is capped on the midpoint of the edges of the prism rather than on the rectangular faces (as in **80–82**). The central cobalt site is Co(III) rather than Co(II), and it is surrounded by six  $\mu_3$ -hydroxides, each of which bridges to a cobalt at a vertex of the prism and a capping cobalt site. The triphenylacetate ligands bind in the 2.11 mode, while each mhp ligand adopts the 2.21 mode. A curiosity of the structure is the apparent presence of coordinated hydrogen carbonate.

No undecanuclear paramagnetic cobalt cage has been reported. A second dodecanuclear cage,  $[\text{Co}_{12}(\text{chp})_{18}(\text{OH})_4\text{Cl}_2(\text{Hchp})_2(\text{MeOH})_2]$  (**85**), shown in Fig. 35, can be made in a three-step procedure (181). Cobalt chloride is reacted with Na(chp) in MeOH, followed by evaporation to dryness. The resulting paste is heated under vacuum for several days, and the resulting powder is then dissolved in  $\text{CH}_2\text{Cl}_2$  and crystallized by diffusion of ether vapor into the solution. Cage **85** is centrosymmetric and contains two  $\{\text{Co}_4\text{O}_3\text{Cl}\}$  cubanes linked by a central eight-membered ring involving four Co(II) centers and four O atoms from pyridonate ligands. The final cobalt sites are at the periphery of

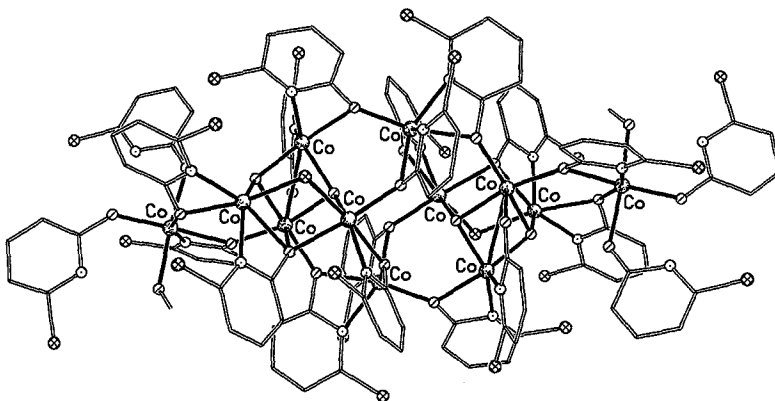


FIG. 35. The structure of  $[\text{Co}_{12}(\text{chp})_{18}(\text{OH})_4\text{Cl}_2(\text{Hchp})_2(\text{MeOH})_2]$  (181). (Shading as in Fig. 34, plus Cl, hatched.)

the cage and are attached to the cubanes through  $\mu_2$ -oxygen atoms from chp ligands. The chp ligands show four different bonding modes in **85**.

A tridecanuclear cobalt cage,  $[\text{Co}_{13}(\text{chp})_{20}(\text{phth})_2(\text{OH})_2]$  (**86**) (171), shown in Fig. 36, can be made by the procedure that gives the heptanuclear cages **73**, but replacing the monocarboxylate ligand benzoate with the dicarboxylate ligand, phthalate. An irregular, centrosymmetric

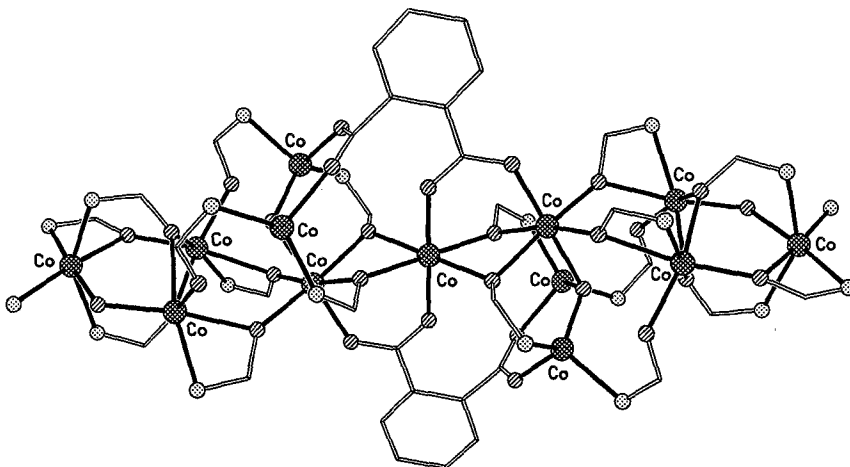


FIG. 36. The structure of  $[\text{Co}_{13}(\text{chp})_{20}(\text{phth})_2(\text{OH})_2]$  (171) with all C-atoms of pyridonate ligands except C2 removed for clarity. (Shading: Co, hatched; O, striped; N, dotted; C, lines.)

cage, **86** can be considered to contain two square-based pyramids of Co(II) centers arranged about a central cobalt, which lies on the crystallographic inversion center. Two further Co(II) sites cap edges of the square bases of the pyramids. The two phthalate ligands are both bound to four metal centers, with a 4.1111 mode in Harris notation, while the twenty pyridonate ligands adopt three binding modes: 3.21, 2.21, and 3.31. The cage can be related to the structure of **73**, with the square-based pyramid common to both.

The largest cobalt cage reported is  $[\text{Co}_{24}(\text{OH})_{18}(\text{OMe})_2\text{Cl}_6(\text{mhp})_{22}]$  (**87**) (182). This complex is formed by reaction of partially hydrated cobalt chloride with Na(mhp) in MeOH, followed by evaporation to dryness and crystallization from EtOAc. The structure is based on the structure of cobalt hydroxide, with a central raft of  $\{\text{Co}_3(\text{OH})_4\}$  incomplete cubanes sharing edges, surrounded by mhp ligands. Ten of the cobalt(II) sites at the center of the cage have regular octahedral geometries, while the cobalt sites at the periphery have very distorted geometries. The mhp ligands adopt three binding modes: 2.11, 2.21, and 3.21. It is clear that the immense coordinative flexibility of the pyridonate ligands is of vital importance in stabilizing these large cobalt cages. The structure of **87** is clearly related to that of the  $\{\text{Fe}_{17}\}$  and  $\{\text{Fe}_{19}\}$  cages reported by Heath and Powell (162, 163).

#### F. NICKEL

High-nuclearity cage complexes of nickel(II) with O- or N-donor ligands are rather rare; this is surprising, as ferromagnetic exchange is frequently found for this metal in smaller cages, and hence high-spin ground states could be expected. Some of the chemistry is very similar to that discussed above for cobalt.

A heterometallic cage,  $[\text{Ni}_6\text{Zn}_2\text{O}_2(\text{O}_2\text{CN}^i\text{Pr}_2)_{12}]$ , was made by addition of  $[\text{Ni}(\text{MeCN})_6][\text{ZiCl}_4]$  to a toluene solution of  $\text{HN}^i\text{Pr}_2$  which had been previously saturated with  $\text{CO}_2$  (183). The structure is very similar to that of  $[\text{Fe}_8\text{O}_2(\text{O}_2\text{CN}^i\text{Pr}_2)_{12}]$  (136) and contains two oxo-centered  $\{\text{Ni}_3\text{Zn}\}$  tetrahedra, bridged by carbamate ligands. The nickel sites have trigonal-bipyramidal geometries and the zinc sites are tetrahedral. The carbamate ligands show both the 1,3- and 1,1,3-bridging modes, with the former mode used to bridge between Zn and Ni centers and the latter used to bridge Ni centers exclusively. No magnetic data were reported.

The hexanuclear cage  $[\text{Ni}_6\{(\text{PhSiO}_2)_6\}_2\text{Cl}(\text{ROH})_6]$  (**88**) ( $\text{R} = \text{Et}$  or  $n\text{Bu}$ ) (184) is very similar to the manganese cage **28**. Magnetic studies show antiferromagnetic exchange between the nickel centers, leading

to an  $S = 0$  ground state (184). A related octanuclear nickel cage has also been reported (185).

Three further heterometallic cages containing six nickel centers have been reported. The first,  $[\text{Ni}_6\text{Cu}_2(\text{OH})_4(\text{mhp})_2(\text{O}_2\text{CPh})_{10}(\text{mhp})_2(\text{Hmhp})_4(\text{H}_2\text{O})_2]$ , is isostructural with the cobalt cage (71) and is made by an analogous procedure (170). The other two contain central 4f ions surrounded by nickel-containing "complex ligands." Yukawa and co-workers reported  $[\text{Sm}\{\text{Ni}(\text{pro})_2\}_6]^{3+}$ , which is shown in Fig. 37, in 1997 (pro = L-proline) (186), and the Schröder group reported  $[\text{La}\{\text{Ni}(\text{L1})\}_6]^{3+}$  in 1999 (96). Very similar principles apply to both structures. A nickel(II) center is coordinated by two N and two O donors from the ligands, either two prolinates or one L1 ligand, with a square geometry. Six of these units then coordinate to a lanthanoid ion, which has an icosahedral coordination geometry. Carboxylate oxygens from neighboring units bind to the apical positions of the nickel centers, making the nickel sites octahedral and hence paramagnetic. No magnetic data are reported for any of these complexes. The complex ligand  $\{\text{Ni}(\text{L1})\}$  can also be used to construct a nonanuclear cage,  $[\text{Na}_4\{\text{Ni}(\text{L1})\}_9(\text{H}_2\text{O})(\text{MeOH})(\text{ClO}_4)]^{3+}$  (96), in which the Ni centers are arranged in a tricapped trigonal prism encapsulating the four sodium ions. This surprising change in nuclearity may be related to the size of the cavity of

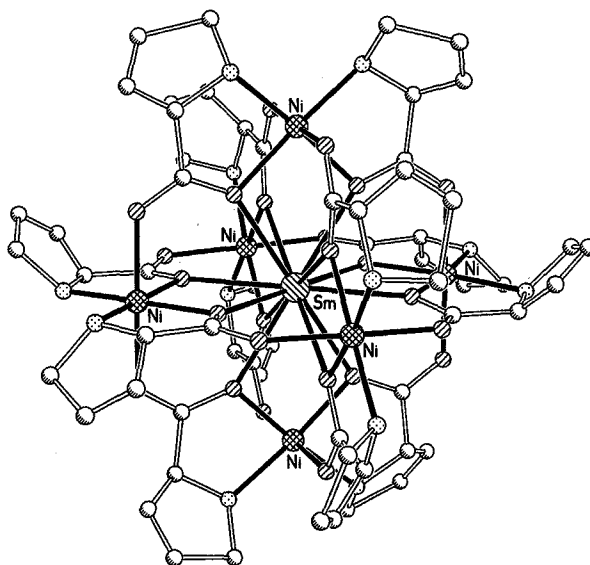


FIG. 37. The structure of  $[\text{Sm}\{\text{Ni}(\text{pro})_2\}_6]^{3+}$  (186). (Shading: Ni, hatched; Sm, striped top-left/bottom-right; O, striped top-right/bottom-left; N, dotted; C, shaded.)

the metallocryptand; the icosahedral cavity formed in  $[\text{La}\{\text{Ni}(\text{L}1)\}_6]^{3+}$  is probably too large for a single sodium center but too small for two.

Several heptanuclear nickel(II) cages are known.  $[\text{Ni}_7(\text{OH})_4(\text{NO}_2)_8(\text{OHpn})_2(\text{Opn})_2]$  (**89**) ( $\text{OHpn} = 1, 3\text{-diamino-2-propanol}$ ) was reported in 1996 (187), but without any description of the preparation. The structure consists of a distorted hexagon of Ni(II) centers, with a seventh nickel at the center. This central nickel site is coordinated to four hydroxides, two  $\mu_2$ - and two  $\mu_3$ -bridging, and the two oxygen atoms from nitrite groups. The nickel atoms of the hexagon fall into three groups: Two are bound to two nitrite nitrogens, two  $\mu_2$ -alkoxides, and two N atoms from amines; two are bound to two nitrite N atoms, an O atom from a third nitrite, one  $\mu_3$ -hydroxide, and one amine nitrogen; and two are bound to two nitrites, one  $\mu_2$ -alkoxide, two hydroxides, and one amine nitrogen. Magnetic studies reveal antiferromagnetic exchange between the spin centers, giving a low-spin ground state, presumably  $S = 1$ .

Two heptanuclear cages related to **78** have been reported (176).  $[\text{Ni}_7(\text{chp})_{12}\text{Cl}_2(\text{MeOH})_6]$  (**90**) and  $[\text{Ni}_7(\text{chp})_{12}(\text{OH})_2(\text{MeOH})_6]$  (**91**) are formed from reaction of freshly prepared nickel hydroxide or methoxide with Hchp at  $130^\circ\text{C}$ , followed by crystallization from MeCN/MeOH. Both cages contain  $\{\text{Ni}_4\text{O}_6\}$  adamantanes sharing a nickel vertex. The oxygen atoms on the  $\text{Ni}\cdots\text{Ni}$  edges are from chp ligands, all adopting the 2.21 bonding mode. In **90** the adamantane cages are regular, and the vacant sites on the exterior triangular nickel faces are occupied by six MeOH ligands, which then H-bond to two chloride counterions. In **91** this regularity is lost, as a  $\mu_3$ -hydroxide is found at the center of each of these faces. A closely related nonanuclear cage,  $[\text{Ni}_9(\text{chp})_{16}(\text{OH})_2(\text{MeCN})_2]$  (**92**), has also been prepared. This is an extension of **91**, but with two of the coordination sites on each triangular face occupied by O donors from  $\{\text{Ni}(\text{chp})_3\}$  "complex ligands"; the third O atom of this unit H-bonds to the  $\mu_3$ -hydroxide group. Magnetic studies are not reported.

The final heptanuclear nickel cage is equivalent to the chromium(II) cage  $[\text{Cr}_7(\text{teptra})_4\text{Cl}_2]$  ( $\text{teptraH}_3 = \text{tetrapyridyltriamine}$ ).  $[\text{Ni}_7(\text{teptra})_4\text{Cl}_2]$  is made by reaction of nickel chloride with the ligand in refluxing naphthalene in the presence of *t*-butoxide as a base (188). The structure has approximately  $D_4$  symmetry, with the linear  $\{\text{Ni}_7\}$  wire surrounded by four polydentate ligands. The inner five Ni centers have square-planar geometries, disregarding  $\text{Ni}\cdots\text{Ni}$  contacts, and are therefore diamagnetic, while the outer two Ni centers are square-pyramidal. Antiferromagnetic exchange is found between these two paramagnetic centers.

An octanuclear nickel(II) cage,  $[\text{Ni}_4(\text{cit})_3(\text{OH})(\text{H}_2\text{O})]_2^{5-}$ , is formed from the reaction of nickel hydroxide and citric acid in water at pH 9.20 (189). The structure consists of two highly distorted tetrahedra of Ni(II) centers whose coordination sites are occupied, in the main, by oxygen donors from the citrate ligands. The two tetrahedra are related by an inversion center, and are bridged by a carboxyl oxygen from each of two citrate units. Six of the nickel centers have octahedral geometries, the other two centers having square-pyramidal geometries. No magnetic data are reported.

An allegedly mixed-valent nonanuclear nickel cage has been reported with trimethylacetate ligands (190).  $[\text{Ni}_9\text{O}_3(\text{OH})_3(\text{O}_2\text{CCMe}_3)_{12}(\text{HO}_2\text{CCMe}_3)_4]$  (**93**), shown in Fig. 38, can be made by reaction of nickel chloride with potassium pivalate in water, followed by extraction of the precipitate in  $\text{CH}_2\text{Cl}_2$ , benzene, or hexane. A mirror plane passes through the center of the molecule. Six of the Ni centers form a trigonal prism, the three further nickel centers forming a  $\{\text{Ni}_3\text{O}\}$  oxo-centered triangle. A  $\mu_4$ -oxygen links the two Ni atoms in one edge of the prism to two Ni atoms comprising one edge of the triangle. The exterior of the cage is then coated with carboxylate ligands, which show a range of binding modes, including 1,3- and 1,1,3-bridging and terminally bound through one O donor. The authors suggest that Ni(III) is present in addition to Ni(II); however, neither the synthesis nor the structural

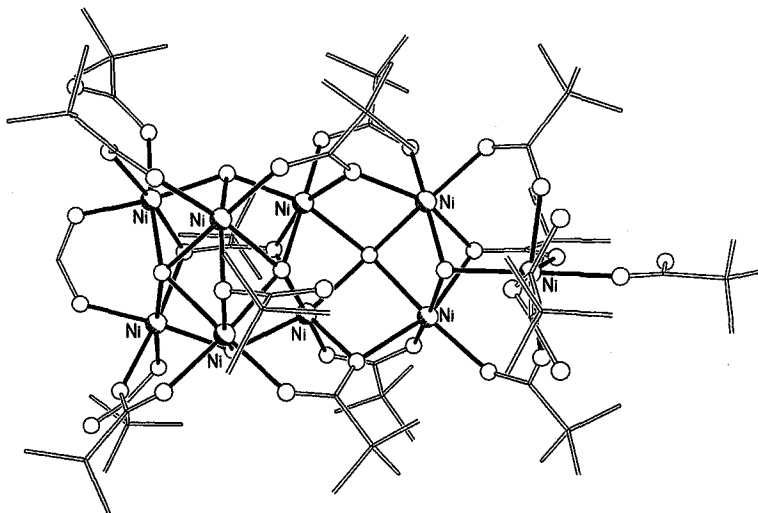


FIG. 38. The structure of  $[\text{Ni}_9\text{O}_3(\text{OH})_3(\text{O}_2\text{CCMe}_3)_{12}(\text{HO}_2\text{CCMe}_3)_4]$  (190). (Shading: Ni, shaded; O, open; C, lines.)

parameters for each Ni center support this proposition. It is a good deal more likely that additional protons are present, possibly attached to the "oxide" ligands. Such problems have also been found from chromium cages, e.g., **16**. Magnetic data are reported down to 83 K, which suggests weak antiferromagnetic exchange between metal centers.

A further nonanuclear cage,  $[\text{Ni}_9(\text{CO}_3)(\text{OH})_6(\text{chp})_3(\text{Hchp})_3(\text{O}_2\text{CCH}_2\text{NMe}_3)_9\text{Cl}]^{6+}$  (**94**) (180), is formed from the reaction of hydrated nickel chloride,  $\text{Na}(\text{chp})$ , and  $\text{O}_2\text{CCH}_2\text{NMe}_3$  in  $\text{MeOH}$ , followed by evaporation to dryness, and extraction of the green powder with  $\text{EtOAc}$ . The yield is extremely poor. Two features dominate the structure: first, a central carbonate ion which is  $\mu_6$ -bridging, leading to a planar hexagon of Ni centers [Ni(1), Ni(2), and s.e.]; second, the preference of the tertiary ammonium groups of the nine betaine ligands to lie as far apart as possible, leading to a very open structure. Three of the betaines bridge alternate Ni...Ni vectors of the hexagon in a 1,3-fashion. Three further betaines attach three additional Ni atoms below the hexagon, while the final three betaines bridge in a 1,1,3-manner, using one O donor as a  $\mu_2$ -bridge between Ni atoms within the hexagon, and the second O donor to bind to one of the Ni atoms below the hexagon. There are also six hydroxide anions in the cage. Three are  $\mu_3$ -bridging and are arranged so that the H atoms point toward the trigonal axis of the cage where a chloride anion is held by H bonds. The remaining three OH groups are  $\mu_2$ -bridging and lie above the hexagon, with the H atoms now involved in an interaction with a  $[\text{Ni}(\text{chp})_3]^-$  anion.

Decanuclear, undecanuclear, and dodecanuclear nickel cages related to **80–82** can be made by chemistry similar to that employed for the cobalt cages (179). The decanuclear cages  $[\text{Ni}_{10}(\text{OH})_6(\text{mhp})_{6.5}(\text{O}_2\text{CCHMe}_2)_{6.5}(\text{Hmhp})_3\text{Cl}(\text{H}_2\text{O})]$  (**95**) and  $[\text{Ni}_{10}(\text{OH})_6(\text{chp})_6(\text{O}_2\text{CCHPh}_2)_6(\text{Cl})_2(\text{Hchp})(\text{H}_2\text{O})_2(\text{MeOH})]$  (**96**) both involve carboxylates with two substituents at the  $\alpha$ -carbon, while the undecanuclear cages  $[\text{Ni}_{11}(\text{OH})_6(\text{mhp})_9(\text{O}_2\text{CMe})_6(\text{H}_2\text{O})_3]^+$  (**97**) and  $[\text{Ni}_{11}(\text{OH})_6(\text{mhp})_9(\text{O}_2\text{CMe})_7(\text{Hmhp})_2]$  (**98**) both involve acetate. The dodecanuclear cage  $[\text{Ni}_{12}(\text{OH})_6(\text{mhp})_{12}(\text{O}_2\text{CCH}_2\text{Cl})_6]$  (**99**) contains the same core as **80**, and involves chloroacetate as the carboxylate. These subtle variations in carboxylate must in some way cause the differences in the nuclearity observed for the cages, but it is far from clear how. In the undecanuclear cages, one of the Ni centers capping the trigonal face of the prism is missing when compared with **80** or **99**; in the decanuclear cages, both trigonal caps are absent.

Magnetic studies of these cages reveal a very complicated picture (179). Considering only the trigonal-prismatic core, the presence of six

$\mu_3$ -hydroxides around the central Ni(II) site creates a position where six distorted  $\{\text{Ni}_3(\text{OH})\}$  triangles intersect at this point. The relative magnitudes of the exchange interactions along the edges of these triangles determine the spin ground states for the cages. It appears that the ttp core of **99** has an  $S = 8$  ground state, that of **97** has an  $S = 4$  ground state, and that of **96** has an  $S = 2$  ground state.

Decanuclear nickel equivalents of **83** have also been made (179).  $[\text{Ni}_{10}(\text{OH})_4(\text{mhp})_{10}(\text{O}_2\text{CCMe}_3)_6(\text{MeOH})_2]$  and  $[\text{Ni}_{10}(\text{OH})_4(\text{mhp})_{10}(\text{O}_2\text{CCMe}_3)_6(\text{H}_2\text{O})_2]$  contain the same polyhedral core, which can be described as a pentacapped centered trigonal prism missing an edge of the prism. No magnetic studies of these cages have been reported.

A further decanuclear nickel cage contains two fused pentanuclear nickel(II) metallocrowns (191). The cage has the rather long-winded formula  $[\text{Ni}_2(\text{mcpa})_2][\text{Ni}_4(\text{shi})_2(\text{pko})_2(\text{MeOH})_2][\text{Ni}_4(\text{shi})_3(\text{pko})(\text{MeOH})(\text{H}_2\text{O})][\text{Hmcpa} = 2\text{-methyl-4-chlorophenoxyacetic acid, Hpko} = \text{di-(2-pyridyl)ketone oxime, H}_3\text{shi} = \text{salicylhydroxamic acid}]$ . The cage was made in good yield by reaction of nickel chloride with  $\text{H}_3\text{shi}$  and  $\text{Hpko}$  and  $\text{NaOH}$  in  $\text{MeOH}$ , followed by addition of  $\text{Na}(\text{mcpa})$ . While other groups have frequently introduced two potential bridging ligands, this use of three different bridging ligands in one pot is unusual. The structure consists of two  $\{\text{Ni}_5\}$  planes joined by  $\text{Ni}-\text{O}$  and  $\text{Ni}-\text{N}$  bonds between the two planes. The  $\{\text{Ni}_5\}$  fragments contain a Ni square, with a fifth nickel at the center. Magnetic studies show antiferromagnetic exchange between the nickel centers.

The undecanuclear cage  $[\{\text{Ni}_6(\text{OH})_6\}\{\text{Ni}(\text{mhp})_3\}_5(\text{Hmhp})\text{Cl}(\text{H}_2\text{O})_2]$  (**100**) can be made by reaction of nickel hydroxide with  $\text{Hmhp}$  at  $160^\circ\text{C}$ , followed by crystallization from  $\text{MeCN}$  (124). Complex **100** has a  $\{\text{Ni}_6(\text{OH})_6\}$  double-cubane core, with five  $\{\text{Ni}(\text{mhp})_3\}$  complex ligands that bind to faces of the cubane, using either three or two of the O atoms of the pyridones. All the nickel sites are six-coordinate, with terminal water, chloride, or  $\text{Hmhp}$  ligands completing the coordination environment of four of the nickel centers within the cubane. Magnetic studies show antiferromagnetic exchange between the metal centers.

$[\text{Ni}_{12}(\text{chp})_{12}(\text{O}_2\text{CMe})_{12}(\text{THF})_6(\text{H}_2\text{O})_6]$  (**101**) (28), shown in Fig. 39, is a cyclic molecule made from reaction of nickel acetate with  $\text{Hchp}$ , followed by crystallization from  $\text{THF}$ . Each of the  $\text{Ni} \cdots \text{Ni}$  contacts within the dodecanuclear wheel is bridged by two  $\mu_2$ -oxygen, derived from a  $\text{chp}$  ligand, a water, or an acetate, and a 1,3-bridging carboxylate. Ferromagnetic exchange between the nickel(II) centers leads to an  $S = 12$  ground spin state; however, the exchange is weak and lower spin levels are still

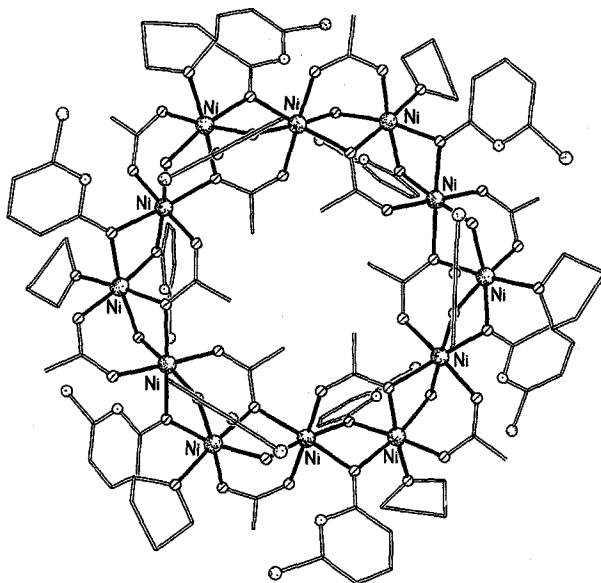


FIG. 39. The structure of  $[\text{Ni}_{12}(\text{chp})_{12}(\text{O}_2\text{CMe})_{12}(\text{THF})_6(\text{H}_2\text{O})_6]$  (28). (Shading: Ni, random shading; O, striped; N, dotted; Cl, light shading; C, lines.)

occupied at 1.8 K. The equivalent cage with 6-bromo-2-pyridonate can also be made (192).

$[\text{Ni}_{16}\text{Na}_6(\text{chp})_4(\text{phth})_{10}(\text{Hphth})_2(\text{MeO})_{10}(\text{OH})_2(\text{MeOH})_{20}]$  (**102**) (193), shown in Fig. 40, is made from reaction of nickel chloride with  $\text{Na}(\text{chp})$  and  $\text{Na}_2(\text{phth})$  in  $\text{MeOH}$ . The structure consists of four nickel cubanes arrayed about a central sodium octahedron. The  $\{\text{Na}_6\}$  octahedron provides the anchor point for the structure; a phthalate ligand bridges from each face of this octahedron to one of the nickel cubanes. There are therefore two phthalate bridges between each cubane and the central octahedron. The cubanes are imperfect, with three vertices occupied by  $\mu_3\text{-O}$  atoms from methoxides or hydroxides while the fourth vertex is occupied by a  $\mu_2\text{-O}$  atom from a phthalate ligand. This leaves one  $\text{Ni}\cdots\text{O}$  edge of the cubane unmade. The Ni sites are all octahedral, with the remaining coordination sites occupied by one chelating chp and five  $\text{MeOH}$  ligands per cubane. Magnetic studies are consistent with an  $S = 2$  ground state for each cubane, with immeasurably weak coupling between the cubanes.

The largest nickel(II) cage known is  $[\text{Ni}_{24}(\text{OH})_8(\text{mpo})_{16}(\text{O}_2\text{CMe})_{24}(\text{Hmpo})_{16}]$  ( $\text{Hmpo} = 3\text{-methyl-3-pyrazolin-5-one}$ ) (194), shown in Fig. 41, which can be made from reaction of nickel acetate with  $\text{Hmpo}$  in  $\text{MeOH}$ ,

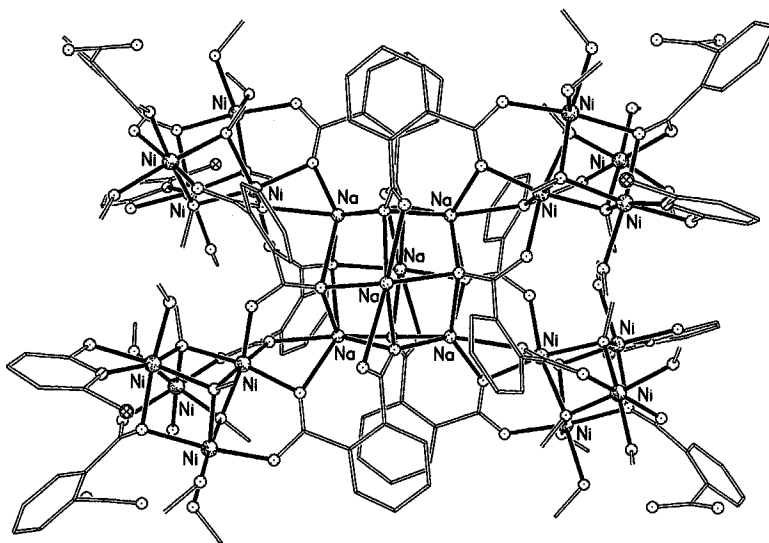


FIG. 40. The structure of  $[\text{Ni}_{16}\text{Na}_6(\text{chp})_4(\text{phth})_{10}(\text{Hphth})_2(\text{MeO})_{10}(\text{OH})_2(\text{MeOH})_{20}]$  (193). (Shading: Ni, random shading; O, dotted; N, striped; Na, light shading; Cl, hatched; C, lines.)

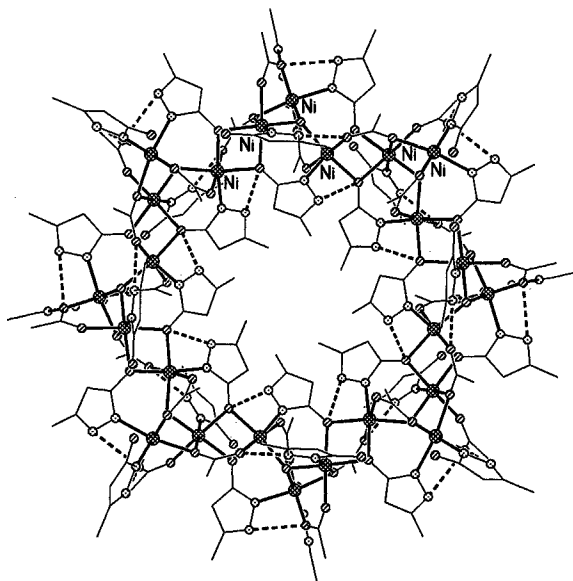


FIG. 41. The structure of  $[\text{Ni}_{24}(\text{OH})_8(\text{mpo})_{16}(\text{O}_2\text{CMe})_{24}(\text{Hmpo})_{16}]$  (194). (Shading: Ni, hatched; O, striped; N, dotted; C, lines.)

followed by crystallization of the green precipitate from MeCN. The structure consists of an octamer of chemically equivalent trinuclear building blocks  $\{\text{Ni}_3(\text{OH})(\text{mpo})_2(\text{O}_2\text{CMe})_3(\text{Hmpo})_2\}$ . Each Ni···Ni contact is bridged by a 1,3-carboxylate and two  $\mu_2$ -oxygen, with the latter groups derived from mpo, acetate, and hydroxide groups. The  $\text{Ni}_{24}$  structure is much less circular than other cyclic structures. The trinuclear fragments are so disposed that they point approximately at the center of the neighboring unit rather than at the end, with a  $51^\circ$  angle between the line described by one trinuclear unit and its neighbor. In addition to the metal–ligand bonding, the structure is stabilized by a large quantity of H bonding. The majority of these interactions arise from the proton on the second N atom within the pyrazolinone ligands. All the metal centers are six-coordinate, with approximately octahedral symmetry. Four of the crystallographically independent sites are bound to one N and five O donors, while the remaining two sites have two N and four O donors. Magnetic measurements indicate that while the magnetic behavior is dominated by antiferromagnetic exchange, this is rather weak and many magnetic states remain populated even at very low temperatures.

#### G. COPPER

The high-nuclearity cages reported for copper(II) contain a greater variety of ligands than for other 3*d*-metal cages. Cages of earlier 3*d*-metals tend to be stabilized by simple O-donor ligands (e.g., carboxylates, alkoxides), but for copper a number of polydentate and macrocyclic N-donor ligands have been used, with a relatively small number of O donors.

With carboxylates the “lantern” structure of copper(II) acetate is most commonly found, i.e., two copper centers bridged by four ligands. An exception is the hexanuclear cage formed by phenoxyacetate (195).  $[\text{Cu}(\text{O}_2\text{CCH}_2\text{OPh})_2]_6$  contains a compressed trigonal antiprism of copper centers bridged by phenoxyacetate ligands, which adopt one of two binding modes. Six bridge in the conventional 1,3-fashion common for carboxylate ligands, while the remaining six use the ether oxygen to bond in addition to the carboxylate group, which binds in a 1,1,3-fashion. The ether oxygen bonds to one of the three Cu(II) centers to which the carboxylate is bound, forming a five-membered chelate ring. The compound is prepared from reaction of copper carbonate with the acid in water. No magnetic data are reported for this compound.

Addition of alcohols to dimeric copper carboxylates can also produce hexanuclear complexes. Dissolving copper(II) acetate in 2-diethylaminoethanol, followed by addition of ether, produces

$[\text{Cu}_6(\text{O}_2\text{CMe})_6(\text{OH})_2(\text{OCH}_2\text{CH}_2\text{NEt}_2)_4(\text{H}_2\text{O})]$  (196). The structure is described as two distorted copper–oxygen heterocubanes sharing a common face. The oxygen vertices within the shared face come from aminoalkoxide ligands, while two hydroxides and two aminoalkoxide oxygens occupy the four external O sites of the dicubane. Two of the acetate groups are 1,3-bridging, with the remainder bound unidentately. A very similar cage,  $[\text{Cu}_6(\text{O}_2\text{CCH}_2\text{Cl})_6(\text{OH})_2(\text{OCH}_2\text{CH}_2\text{NEt}_2)_4(\text{H}_2\text{O})]$ , is found for chloropropionate (197). No magnetic data are reported for either compound.

A hexanuclear complex is also known where aminoalkoxide ligands are present without carboxylates.  $[\text{Cu}_6(\text{amp})_8](\text{ClO}_4)_4$  (amp = 2-amino-2-methyl-1-propanolato) is formed from reaction of copper(II) perchlorate with Hamp in MeOH (198). The structure consists of a bicapped  $\text{Cu}_4\text{O}_4$  heterocubane, with the four O atoms within the cubane derived from  $\mu_3$ -O atoms from amp ligands and the remaining coordination sites of the copper centers occupied either by amino groups or by  $\mu_2$ -bridging oxygens from further amp ligands that attach the two capping Cu centers to the central cubane. The magnetic behavior of the cage shows a diamagnetic ground state. The variable-temperature susceptibility behavior can be modeled with three exchange interactions; two of which are strongly antiferromagnetic and one ferromagnetic.

With 1,3-bis(dimethylamino)-2-propanolato (bdmap), a hexanuclear copper cage,  $[\text{Cu}_6(\text{bdmap})_3\text{Cl}_6(\text{O}_2\text{H})]$ , with an elongated trigonal antiprismatic structure is found (199). Each of the three bdmap ligands chelates to two copper centers, with the alkoxide oxygen shared between the two coppers. This creates the edges of the trigonal antiprism. The trigonal faces have a central oxygen atom, these lying below the face of the  $\{\text{Cu}_3\}$  triangle with an  $\text{O} \cdots \text{O}$  separation of 2.45 Å; a H atom lies between these two O atoms, forming a very strong H bond. Each of the six chlorides is terminally bound to a copper site. Magnetic studies show antiferromagnetic exchange, leading to a diamagnetic ground state.

Reaction of copper(II) pivalate with sodium methoxide in ethanol (presumably a source of ethoxide not methoxide) produces a cyclic hexanuclear structure  $[\text{Cu}(\text{O}_2\text{CCMe}_3)(\text{OEt})]_6$  (**103**) (200). The  $\text{Cu} \cdots \text{Cu}$  vectors are alternately bridged by two 1,3-carboxylates or two  $\mu_2$ -ethoxide oxygens. The bridging motifs are therefore similar to those found for metal wheels discussed above, e.g., the octanuclear chromium wheel **22**. Magnetic studies of **103** show strong antiferromagnetic exchange to between the Cu(II) centers.

Two hexanuclear cages with oxime ligands have been reported:  $[\text{Cu}_3\text{O}(\text{dpmieo})_3(\text{ClO}_4)]_2$  (**104**) [dpmieo = 1,2-diphenyl-2-(methylimino)ethanone 1-oxime] (201) and  $[\text{Cu}_3\text{O}(\text{bibo})_3(\text{ClO}_4)]_2$  (**105**) [bibo = 3-(benzylimino)butanone 2-oxime] (202). In both cases two

triangular  $\{\text{Cu}_3\text{O}\}$  fragments are linked through Cu–O bonds to form the hexanuclear unit. The oxime ligands bridge the edges of the triangle. The cages are formed from reaction of copper(II) perchlorate and the ligand in MeOH containing triethylorthoformate for **104** and MeOH–EtOH–MeNO<sub>2</sub> for **105**. Magnetic studies of **104** indicate a diamagnetic ground state, while electrochemical studies of **105** indicate a reversible one-electron oxidation *per triangle* to a mixed-valent species.

Linked copper triangles are also found in  $[\text{Cu}_6(\text{OH})_2(\text{pz})_6(\text{NO}_3)_4(\text{Hpz})_6]$  (Hpz = pyrazole) (203). Each triangle has a central hydroxide group, with each edge of the triangle bridged by a pyrazolate ligand. The triangles are linked by two nitrate groups, which bridge in a 1,3-fashion. One further nitrate binds to the upper face of each triangle in a  $\mu_3, \eta^4$ -fashion. The Hpz ligands bind through one N atom to a copper site.

$[\text{Cu}_2(\text{OMe})_2(\text{tftbd})_2]_3$  [tftbd = 4,4,4-trifluoro-1-(2-thienyl)-butane-1,3-dionate] (204) consists of three planar methoxo-bridged copper dimers, joined by out-of-plane copper–oxygen bonds involving either the methoxide or  $\beta$ -diketonate ligands. The former ligands are therefore present as both  $\mu_2$ - and  $\mu_3$ -bridges, and the latter ligands are either chelating or chelating and bridging within the structure. The magnetic properties of the cage can be fitted to a model where exchange within the dimeric units is important, being different between the “inner” dimer and the two “outer” dimers, but inter-dimer interaction can be neglected. This generates a Hamiltonian containing two exchange interactions, both of which are strongly antiferromagnetic.

Linked  $\beta$ -diketonates are found in  $[\text{K} \subset \{\text{Cu}_3(\text{L}3)_3\}_2(\text{OMe})]$  (205), which contains triangles of copper(II) centers, with each edge of the triangle bridged by a bis( $\beta$ -diketonate). The O atoms of six L9 ligands then form a cavity in which a single potassium ion is found. This cage is prepared by adding potassium hydroxide to a solution containing copper(II) chloride and H<sub>2</sub>L9 in MeOH. The analogous reaction with sodium generates  $[\text{Na} \subset \{\text{Cu}_3(\text{L}3)_3\}(\text{X})_2]$  (X = CuCl<sub>2</sub> or BF<sub>4</sub>) in which the Na centers sit within the copper triangles. The  $[\text{CuCl}_2]^-$  anions contain copper(I). A triple-decker cage,  $[\text{Na} \subset \{\text{Cu}_3(\text{L}3)_3\}(\text{BF}_4)_3]$ , can also be made (102). No magnetic data are reported for these cages.

A hexanuclear copper(II) cage,  $[\text{Cu}_6\{(\text{PhSiO}_2)_6\}_2(\text{EtOH})_6]^-$ , related to manganese (**28**), nickel (**88**), and cobalt cages, has been reported (87) (see Fig. 10); it differs from the cages of the other metals in lacking the central  $\mu_6$ -chloride. The cage has also been reported with terminal DMF ligands on the copper sites (206). The beauty of these structures, and the ability to make the same cage with at least four different transition

metals, makes them an intriguing class of compounds for study. It is unfortunate that the experimental details concerning the synthesis of these cages are so sparse.

$[\text{Cu}_3(\text{OH})(\text{CO}_3)(\text{bipy})_5]^{6+}_2$  is a centrosymmetric hexanuclear copper(II) cage (207), shown in Fig. 42. The center of the cage is a  $\{\text{Cu}_2(\text{OH})_2\}$  ring, with each five-coordinate Cu atom of this ring bound to one chelating bipy ligand. The apical site of the square-pyramidal copper sites is occupied by an O atom from carbonate. These carbonate groups are  $\mu_3$ -bridging, attaching the remaining copper sites to this central core. Each of the external copper sites is bound to two chelating bipy ligands. The cage is made from reaction of bipy with copper hydroxide in air, followed by addition of sodium perchlorate or hexafluorophosphate. The carbonate ions therefore come from fixing of atmospheric carbon dioxide. Magnetic studies of the cage show ferromagnetic exchange between the metal sites, and a resulting  $S = 3$  ground state. The magnetic behavior was modeled with four exchange parameters, which vary from  $+2.75$  to  $+24.5 \text{ cm}^{-1}$  in the best fit.

$[\text{Cu}_6(\text{ox})_3(\text{N}_3)_2(\text{tmen})_6(\text{H}_2\text{O})_2]^{4+}$  also contains simple dimine ligands, in this case  $N,N,N',N'$ -tetramethylethane-1,2-diamine (tmen) (208). Six copper centers, to each of which is coordinated a chelating tmen ligand,

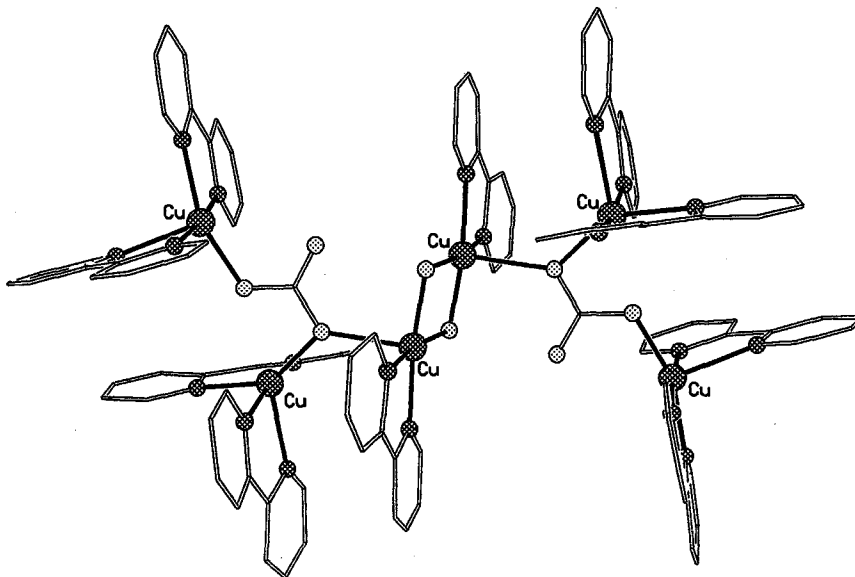


FIG. 42. The structure of  $[\text{Cu}_3(\text{OH})(\text{CO}_3)(\text{bipy})_5]^{6+}_2$  (207). (Shading: Cu, hatched; O, dotted; N, small hatched circles; C, lines.)

are alternately bridged by oxalate or azide groups. The azide ligands bridge in a 1,3-fashion. The cage is made by mixing copper(II) perchlorate, tmen, sodium oxalate, and sodium azide in water. Magnetic studies indicate antiferromagnetic exchange between the metal centers, leading to a diamagnetic ground state. The variable-temperature susceptibility data could be modeled with the Bleaney–Bowers equation, i.e., as noninteracting dimers, which indicates that the predominant exchange interaction is via the oxalate ligands.

The ligand 2-(4-imidazolyl)-ethylimino-6-methylpyridine (HL10; see Scheme 2) contains four N donors, and can form a cyclic hexameric structure depending on the pH of the solution (209). Reacting HL10 with copper(II) chloride in MeOH at pH 7–8 gives a monomeric complex,  $[\text{Cu}(\text{HL10})\text{Cl}_2]$ , in which the five-coordinate metal is bound to one imidazole N atom and the pyridine and imine N donors, as well as two chlorides. At higher pH values a cyclic hexamer,  $[\text{Cu}(\text{L10})_6](\text{ClO}_4)_6$ , shown in Fig. 43, could be crystallized, where the second imidazole N atom has been deprotonated. Within the hexamer each copper site is four-coordinate, bound to the pyridine and imine N atoms and one

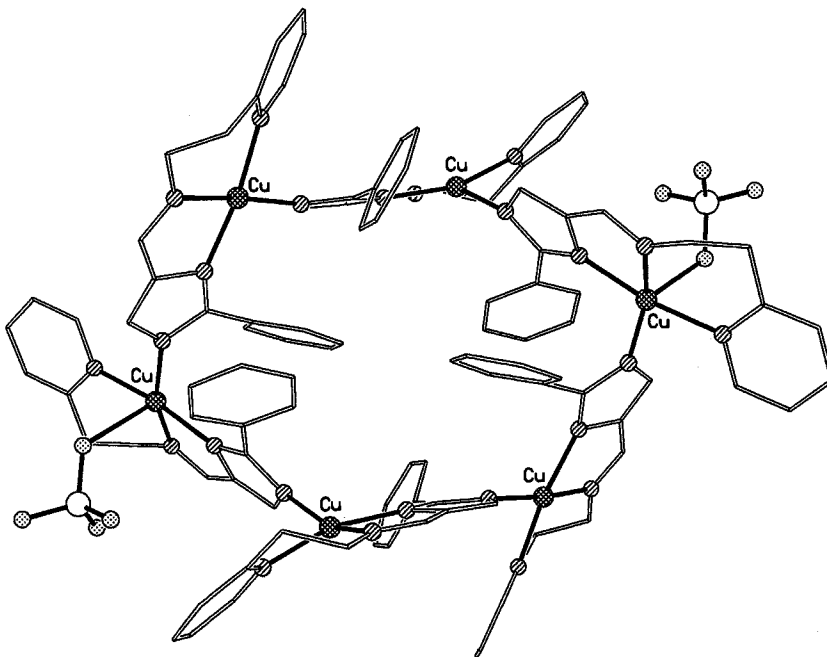


FIG. 43. The structure of  $[\text{Cu}(\text{L10})_6](\text{ClO}_4)_2$  (209). (Shading: Cu, hatched; O, dotted; N, striped; Cl, open; C, lines.)

imidazole N atom from one ligand, and the second imidazole N atom from the neighboring atom.

Several hexanuclear copper cages are known with more complicated ligands. With the tris-tridentate ligand L11 (see Scheme 2), a hexanuclear copper(II) complex is formed from the reaction of the trinuclear copper(I) complex with air in the presence of sodium azide (210).  $[\text{Cu}_3(\text{OH})_2(\text{N}_3)(\text{L11})]^{6+}$  contains a central  $\{\text{Cu}_2(\text{OH})_2\}$  ring, with the remaining coordination sites on the central copper sites occupied by one tridentate unit from L11. The remaining tridentate binding sites bond to the four further copper(II) atoms. These are arranged in two pairs, with the  $\text{Cu} \cdots \text{Cu}$  vector bridged by  $\mu_2$ -azides and hydroxides. No magnetic data are reported; however, EPR spectroscopy suggests that strong antiferromagnetic exchange is present within each dinuclear unit.

A hexanuclear complex also results from reaction of 1,1,6,6-tetrakis(imidazol-2-yl)-2,5-diazahehexane (Htidah) with copper chloride in ethanol (211).  $[\text{Cu}_6(\text{tidah})_2\text{Cl}_{10}(\text{H}_2\text{O})_4]$  contains an irregular centrosymmetric array of copper(II) centers, bridged by imidazole groups from tidah and four  $\mu_2$ -chlorides; the remaining chlorides are terminally bound to copper sites. The structure can be described as a central copper rectangle, with opposite edges bridged by chloride or imidazolate groups. The additional two copper sites are attached to the rectangle by bridging chlorides which are approximately collinear with the  $\text{Cu} \cdots \text{Cu}$  vector bridged by the imidazolate. Magnetic studies show antiferromagnetic exchange between the copper(II) centers, giving a low-spin ground state.

Reaction of 2,6-bis(aminomethyl)-4-methylphenol monohydrochloride, 2,6-diformyl-4-methylphenol, copper(II) acetate, and  $(\text{NBu}_4)(\text{BF}_4)$  in boiling MeOH gives a cyclic hexanuclear cage bound to a hexa-Schiff base macrocyclic ligand (L12; see Scheme 2) (212). The cage  $[\text{Cu}_6(\text{L12})(\text{O}_2\text{CMe})_2(\text{OH})_2(\text{MeOH})_2(\text{H}_2\text{O})_2]^{2+}$  contains the six copper centers having a cyclohexane-like boat configuration, with each  $\text{Cu} \cdots \text{Cu}$  vector bridged by a phenolate O atom from L12 and one further bridge. This is provided either by a  $\mu_2$ -hydroxide or by a 1,1,3-bridging acetate ligand. The yield of the complex is moderate (30%). No magnetic data are reported.

A similar reaction of 2,6-diformyl-4-methylphenol or 4-*tert*-butyl-2,6-diformylphenol with 1,5-diamino-3-hydroxypropane in MeOH in the presence of copper salts generates a series of tetranuclear cages (213). Slow recrystallization of these tetranuclear cages from DMF–MeOH, or from dry MeOH in presence of a base, generates octanuclear cages.  $[\text{Cu}_4\text{O}(\text{L13})(\text{ClO}_4)]^{2+}_2$  has been structurally characterized (L13 is shown in Scheme 2), and shows that a planar tetranuclear copper cage is

encapsulated within the Schiff base macrocycle, with the four copper centers bound to a central oxide. This oxide bridges to a copper of the second tetranuclear fragment within the cage. The magnetic behavior of the cage indicates antiferromagnetic exchange between the Cu(II) centers.

A similar reaction involving 2,6-diformyl-4-methylphenol with 1,3-diamino-2-hydroxypropane in the presence of copper nitrate gives a second hexanuclear cage encapsulated within a macrocyclic ligand, L14 (see Scheme 2) (214). A difference is that in  $[\text{Cu}_6(\text{L14})(\text{OH})_3]_2(\text{NO}_3)_6$  the planar hexanuclear cages “dimerize” via out-of-plane Cu—O bonds to create a dodecanuclear array, as shown in Fig. 44. Within the hexanuclear cage, Cu··Cu contacts are alternately bridged by a single phenolate oxygen or by a phenolate oxygen and an exogenous hydroxide. Two of the hydroxides also bridge to Cu centers in the second hexanuclear cage in the dimer. Magnetic properties show strong antiferromagnetic exchange between the Cu centers within the hexanuclear cages, and could be modeled with a single exchange constant, despite the presence of two nonequivalent bridging motifs.

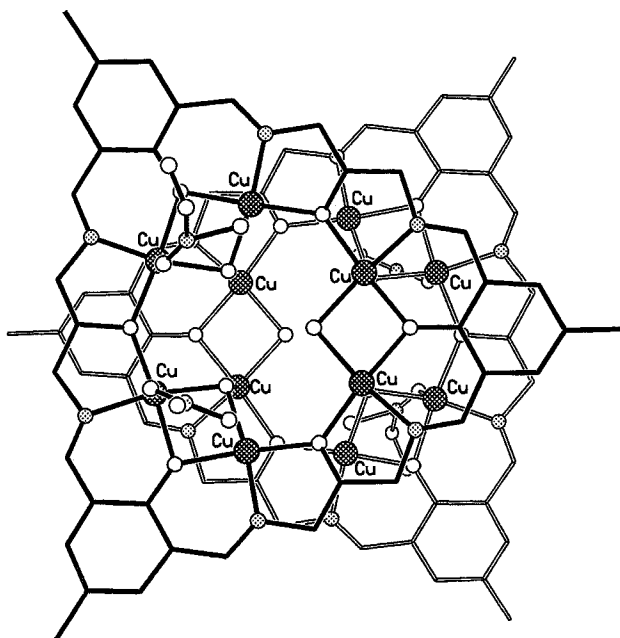


FIG. 44. The structure of  $[\text{Cu}_6(\text{L14})(\text{OH})_3]_2$  (214), with the upper hexanuclear unit shown in heavy lines, and the lower as open lines. (Shading: Cu, hatched; O, open; N, dotted; C, lines.)

Two hexanuclear copper “metallocrowns” have been reported, formed from the solid-state reaction of copper(II) nitrate with Na(mhp), followed by crystallization from  $\text{CH}_2\text{Cl}_2$  (215).  $[\text{Na} \subset \text{Cu}_6(\text{mhp})_{12}](\text{NO}_3)$  (**106**) is related to earlier metallocrowns, with six four-coordinate copper sites bridged by pyridonate ligands, which are 1,3-bridging with regard to Cu sites alone. Six of the mhp O atoms form a central cavity, in which the sodium ion is found. The analogous cage,  $[\text{Cu} \subset \text{Cu}_6(\text{mhp})_{12}]^{2+}$  with copper at the center, has been reported (216). No magnetic data have been reported for either of these metallocrowns.

A heptanuclear complex results from the reaction of  $\text{Na}(\text{O}_2\text{N}_2\text{NEt}_2)$  with copper(II) chloride and  $\text{Na}(\text{OMe})$  in MeOH (217). The structure contains a central linear trinuclear copper unit,  $[\text{Cu}_3(\text{OMe})_4(\text{O}_2\text{N}_2\text{NEt}_2)_2]$ , in which each of the  $\text{Cu} \cdots \text{Cu}$  contacts is bridged by two methoxides, with  $\text{O}_2\text{N}_2\text{NEt}_2$  ligands chelating to the external copper sites. This trinuclear unit is bound through  $\text{Cu} \cdots \text{O}(\text{methoxide})$  contacts to two dinuclear  $[\text{Cu}_2(\text{OMe})_2(\text{O}_2\text{N}_2\text{NEt}_2)_2]$  fragments. Preliminary magnetic measurements suggest strong antiferromagnetic exchange between the copper centers.

Crystals of a vertex-sharing double cubane,  $[\text{Cu}_7(\text{OH})_8(\text{bpym})_6(\text{H}_2\text{O})_2]^{6+}$  (**107**) (bpym = 2,2'-bipyrimidine), can be grown from slow evaporation of an aqueous solution of copper(II) nitrate, bpym, and sodium carbonate (218). The structure is shown in Fig. 45. The central  $\{\text{Cu}_7(\text{OH})_8\}$  double cubane is somewhat distorted, the two *trans* Cu—O bonds involving the shared copper vertex being longer than other Cu—O bonds within the cubane. The bpym ligands chelate to the six copper vertices that are not shared. Magnetic studies show weak ferromagnetic exchange between the copper(II) centers, with an  $S = \frac{7}{2}$  ground state. A fit of the magnetic data allowed four exchange constants to be derived, which vary from +0.4 to +5.4  $\text{cm}^{-1}$  (218).

Work from the Perlepes group has produced a series of copper cages using ligands derived from di-2-pyridyl ketone,  $(\text{py})_2\text{CO}$ . A heptanuclear cage,  $[\text{Cu}_7\{(\text{py})_2\text{CO}_2\}_3(\text{O}_2\text{CMe})_6(\text{OH})_2]$  (**108**), and a dodecanuclear cage,  $[\text{Cu}_{12}\{(\text{py})_2\text{CO}_2\}_6(\text{O}_2\text{CMe})_{12}]$  (**109**), result from reaction of copper(II) acetate with  $(\text{py})_2\text{CO}$  in hot MeCN, followed by layering the reaction solution with ether/hexane (219). The smaller cage forms green crystals, while the latter gives violet-blue crystals. With cobalt(II) acetate a nonanuclear cage, **79** results (177) (see above). Complex **108** contains a highly distorted vertex-sharing copper dicubane core. The  $(\text{py})_2\text{CO}_2^{2-}$  *gem*-diolate ligands adopt two bridging modes, 3:2211 and 4.3211 (Harris notation), and lie at the center of the cage. This contrasts with the 5.3311 mode adopted in **79**. The acetate groups bridged the external edges of the cage in the classic 1,3-mode (2.11 by Harris

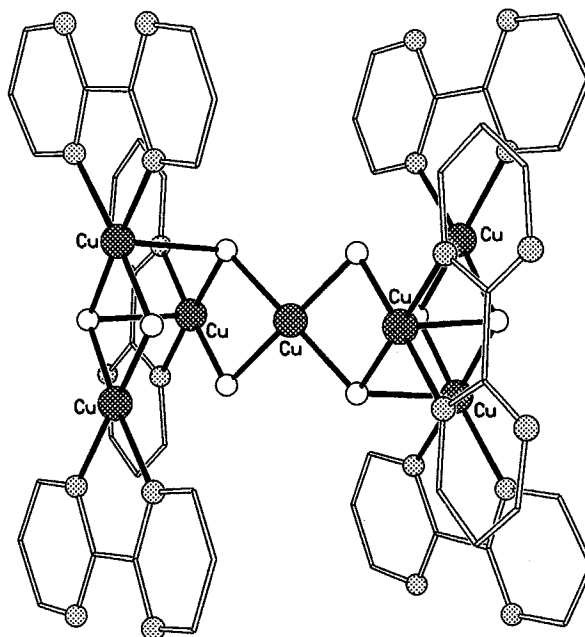


FIG. 45. The structure of  $[\text{Cu}_7(\text{OH})_8(\text{bpym})_6(\text{H}_2\text{O})_2]^{6+}$  (218). (Shading as in Fig. 44.)

notation). Magnetic studies demonstrate that **108** has an  $S = \frac{1}{2}$  ground state.

Complex **109** is the minor product of the reaction; it has a beautiful "flywheel" structure (219), as shown in Fig. 46. Six internal Cu centers form a chair-shaped cluster, which lies within a second, larger chair-shaped cluster consisting of the outer copper(II) sites. All the  $(\text{py})_2\text{CO}_2^{2-}$  ligands adopt the 4.3211 bonding mode, bridging one outer and three inner copper sites. Six acetate ligands bridge between copper centers of the inner and outer chair in a 2.11 fashion, while the final six acetate ligands bind monodentately to exterior copper sites. No magnetic data are reported for this unique cluster.

When copper(II) acetate and  $(\text{py})_2\text{CO}$  are mixed in water, followed by addition of sodium perchlorate and slow evaporation of the solution, an octanuclear copper cage,  $[\text{Cu}_8\{(\text{py})_2\text{CO}(\text{OH})\}_8(\text{O}_2\text{CMe})_4]^{4+}$  (**110**), can be isolated (220). This features two  $\{\text{Cu}_4\text{O}_4\}$  heterocubanes bridged by acetate ligands, with the oxoatom of the  $(\text{py})_2\text{CO}(\text{OH})^-$  ligands occupying the O-atom vertices. The bonding mode of the ligand is therefore 3 : 3011, with the hydroxyl oxygen not bound to any metals. Magnetic studies of **110** show that antiferromagnetic exchange within

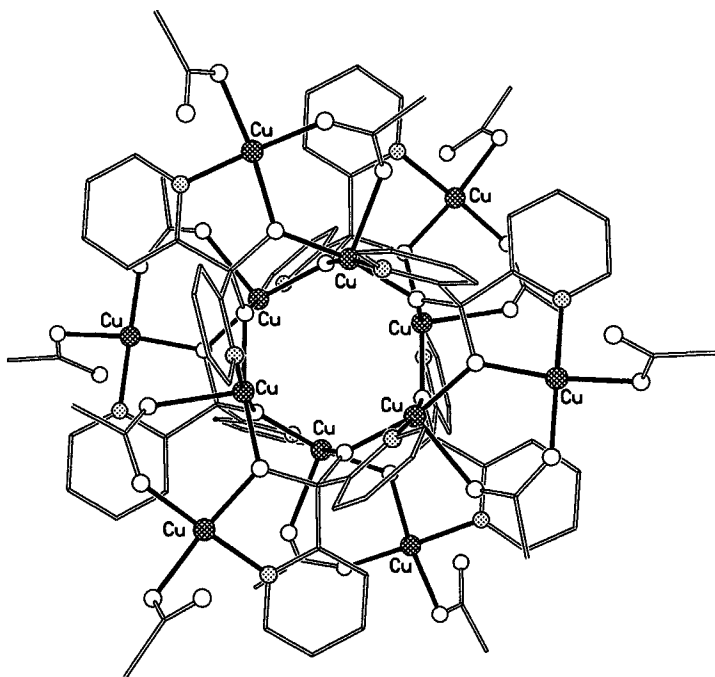


FIG. 46. The structure of  $[\text{Cu}_{12}\{(\text{py})_2\text{CO}_2\}_6(\text{O}_2\text{CMe})_{12}]$  (219). (Shading as in Fig. 44.)

the cubanes dominates the behavior, leading to a low-spin ground state. EPR studies suggest that a spin triplet may be the ground state, but this is a tentative assignment.

A further octanuclear cage featuring  $(\text{py})_2\text{CO}_2^{2-}$  has recently been reported (221).  $[\text{Cu}_8\{(\text{py})_2\text{CO}_2\}_4(\text{O}_2\text{CMe})_4(\text{Hhp})_4]^{4+}$  ( $\text{Hhp} = 2$ -hydroxypyridine) (**111**) is formed from reaction of copper acetate with  $(\text{py})_2\text{CO}$  in  $\text{MeCN}/\text{H}_2\text{O}$ , followed by addition of Hhp, sodium acetate, and sodium perchlorate. The structure is in some ways reminiscent of **109**, containing an inner and outer portion. In **111**, the inner copper structure is a tetrahedron while the outer structure is a distinctly flattened tetrahedron. The  $(\text{py})_2\text{CO}_2^{2-}$  ligands adopt a new 4:2211 mode, while an acetate ligand bridged in a 2.11 fashion and the Hhp ligands are attached through the exocyclic oxygen atom. Magnetic studies show that antiferromagnetic exchange is dominant, giving a low-spin ground state. The cage also shows two quasireversible reduction processes.

The copper cage  $[\{\text{Cu}_3\text{O}(\text{L15})\}_2\text{Cu}]$  is mixed-valent, containing two oxo-centered copper(II) triangles, bridged by a single copper(I) center, bound to the two oxo groups (222). The triangles are encapsulated in a

polydentate N-donor ligand L15 (see Scheme 2). It is prepared in two steps. First, tris(2-aminoethyl)amine and formaldehyde are reacted together in the presence of Cu(II) ions, to give the trinuclear unit. This is then dissolved in DMSO in the presence of KOH, and the solution gradually changes color from green to brown. The heptanuclear cage crystallizes after addition of acetone. Magnetic studies show antiferromagnetic exchange between the Cu(II) centers, giving a diamagnetic ground state.

An octanuclear copper complex containing uridine (urid) as a ligand has been reported (223). The cage  $[\text{Cu}_8(\text{urid})_8\text{Na}(\text{H}_2\text{O})_6]^{7-}$  contains copper centers bound to a pyrimidine nitrogen atom from one uridine, and ribose oxygen atoms from two different uridines. The resulting cage has a square antiprismatic array of copper centers, with the eight bridging uridine ligands forming a torus. A  $\{\text{Na}(\text{H}_2\text{O})_6\}^+$  cation is found at the center of the cage. No magnetic data are reported for this cage.

Reaction of polymeric copper(I)-3,5-dimethylpyrazolate (dmpz) suspended in wet  $\text{CH}_2\text{Cl}_2$  with dioxygen gives  $[\text{Cu}(\text{dmpz})(\text{OH})]_8$  (**112**) (224). Complex **112** contains a planar ring of copper(II) centers, with each  $\text{Cu} \cdots \text{Cu}$  vector bridged by a dmpz and hydroxide. No magnetic data are reported for the compound. Complex **112** oxidizes a number of organic species, including triphenylphosphine.

Two series of octanuclear copper complexes have been reported using pyridonate ligands. Wang and co-workers have reported heterometallic  $\{\text{Y}_2\text{Cu}_8\}$  and  $\{\text{Nd}_2\text{Cu}_8\}$  cages (225), and discussed their use as precursors for synthesis of high-temperature superconductors, while Blake *et al.* have made a series of homometallic cages (26).

$[\text{Y}_2\text{Cu}_8\text{O}_2(\text{hp})_{12}\text{Cl}_2(\text{NO}_3)_4(\text{H}_2\text{O})_2]$  and  $[\text{Nd}_2\text{Cu}_8\text{O}_2(\text{hp})_{12}\text{Cl}_2(\text{OMe})_4(\text{H}_2\text{O})_4]$  (hp = 2-pyridonate) are made from reaction of copper methoxide with Hhp in MeOH, followed by addition of either yttrium nitrate or neodymium chloride (225). The metal core is similar in both compounds, with a central  $\{\text{M}_2\text{Cu}_4\}$  octahedron (M = Y or Nd), with the heterometallic centers *trans* to one another. The final four copper(II) centers are then arranged in two pairs parallel to the  $\text{M} \cdots \text{M}$  axis. Two  $\mu_4$ -oxides are found within the  $\{\text{M}_2\text{Cu}_4\}$  octahedra, while all the hp ligands adopt the 3.21 bridging mode. Antiferromagnetic exchange is found between the copper centers.

The homometallic cages  $[\text{Cu}_8\text{O}_2(\text{O}_2\text{CR})_4(\text{xhp})_8]$  (26) (R = Me, Ph or  $\text{CF}_3$ ; xhp = 6-chloro-, 6-bromo- or 6-methyl-2-pyridonate), shown in Fig. 47, can be prepared either from reaction of the copper carboxylate with the neutral ligands, or by reaction of the copper carboxylate with copper complexes of pyridonate ligands,  $[\text{Cu}_2(\text{chp})_4]$  (226) or **106** (215). The structures consist of a central edge-sharing oxygen-centered

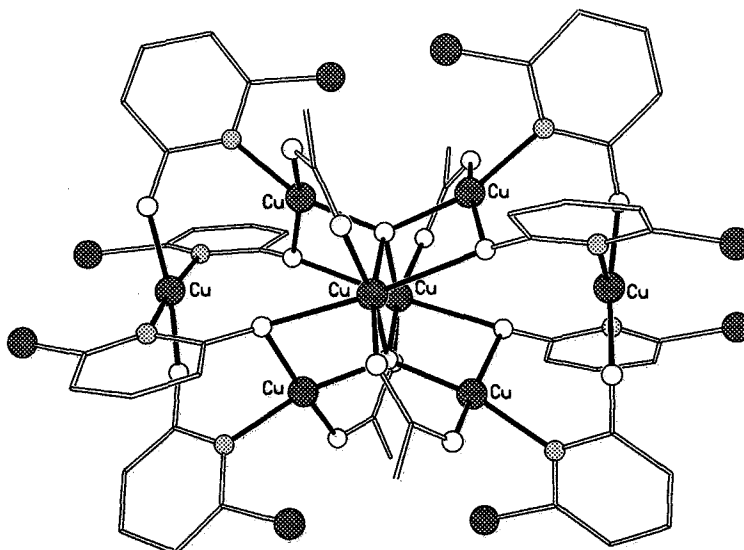


FIG. 47. The structure of  $[\text{Cu}_8\text{O}_2(\text{O}_2\text{CR})_4(\text{xhp})_8]$  (26). (Shading as in Fig. 44.)

bitetrahedron  $\{\text{Cu}_6\text{O}_2\}$ , surrounded by two  $\{\text{Cu}(\text{xhp})_4\}^{2-}$  “complex ligands.” Each carboxylate ligand bridges in a 2.11 fashion, while the pyridonate ligands adopt both the 2.11 and 3.21 binding modes. Magnetic studies of the cages show a decline in magnetic moment at low temperature. The exchange within the bitetrahedron can be modeled using three exchange interactions, two of which are antiferromagnetic and one ferromagnetic. The ground state is sensitive to the relative sizes of the two antiferromagnetic terms, and can be either  $S = 0$  or  $S = 1$  (26); both cases are found for different cages.

A further octanuclear cage has been crystallized using 6,6'-oxybis[1,4-bis(2'-pyridylamino)phthalazine] (obpp), which binds to four copper centers, with the resulting cage linked through a nitrate group to give  $[\{\text{Cu}_4(\text{obpp})(\text{OH})_2(\text{NO}_3)_2(\text{H}_2\text{O})_7\}_2(\text{NO}_3)]^{7+}$  (227). The ligand obpp contains two distinct cavities, in each of which is bound a  $\{\text{Cu}_2(\text{OH})\}$  fragment. In one cavity of the pair a nitrate ion bridges between the two copper centers, while in the second cavity the nitrate present bridges to a neighboring tetranuclear fragment, generating the complete octanuclear cation. The magnetic behavior of the compound could be modeled with the Bleaney-Bowers equation, using a large antiferromagnetic exchange constant.

The trianion of a pentadentate Schiff base, 2-hydroxy-1,3-propanediylbis (acetylacetonimine) (hpbaa), reacts with copper(II)

perchlorate in MeOH to give the octanuclear cage  $[\text{Cu}_8(\text{hpbaa})_4(\text{OH})_3]^+$  (228). The cage has an unusual structure containing four dinuclear  $\{\text{Cu}_2(\text{hpbaa})\}$  units linked through hydroxides. No magnetic data are reported for the cage.

An octanuclear copper complex has been reported featuring the immunosuppressant drug azathioprine (aza) as a coligand with the  $\beta$ -diketonate 2,2,6,6-tetramethylheptane-3,5-dione (thd) (229).  $[\text{Cu}_4(\text{aza})_2(\text{thd})_5(\text{OH})]_2$  was made by reaction of  $[\text{Cu}(\text{thd})_2]$  with aza in MeCN. The cage contains  $\{\text{Cu}_3(\text{OH})\}$  fragments, with two edges of the triangles bridged in a 1,3-fashion by aza ligands. The second N atom of the imidazole ring binds to further copper atoms, in one case binding a fourth copper center to the triangle and in the second case bridging to the second triangle within the octanuclear cage. Magnetic measurements indicate antiferromagnetic exchange between the copper centers within the triangle.

A nonanuclear cage,  $[\text{Cu}_9(\text{O}_2\text{CCHCl}_2)_{10}\{\text{OCH}_2\text{C}(\text{NH}_2)\text{Me}_2\}_6(\text{OH})_2]$ , can be made from reaction of copper(II) dichloroacetate with 2-dimethylaminoethanol in ethanol (230). The structure consists of two distorted copper heterocubanes bridged, via carboxylate and hydroxide ligands, through a central ninth copper center. The carboxylates adopt both the conventional 2.11 bonding mode and the less frequently found 3.21 mode. The aminoalkoxide ligands triply bridge through the O atom, with the N donor bound to one of the three copper centers to which the O atom is bound—the 3.31 bonding mode in Harris notation. The magnetic behavior of the cage is complicated and suggests antiferromagnetic exchange between the copper centers, leading to a doublet ground state.

The nonanuclear cage  $[\text{Cu}_9(2\text{poap})_6]^{12+}$  can be crystallized with nitrate or sulfate counterions (231). The structure is closely related to the equivalent manganese cage  $[\text{Mn}_9(2\text{poap})_6]$  (106), containing a  $3 \times 3$  grid of copper(II) centers bridged by the linear polydentate ligand. Magnetic studies support an assignment of an  $S = \frac{7}{2}$  ground state cage owing to predominant ferromagnetic exchange between the copper(II) centers. These two cages resemble the ladders and grids reported by Lehn and co-workers (232), but differ in the use of paramagnetic metal centers, which leads to interesting magnetic behavior as well as unusual architectures.

The majority of cages containing twelve copper(II) centers are heterometallic. The first to be reported was  $[\text{Cu}_{12}\text{La}_8(\text{OH})_{24}(\text{NO}_3)_{21.2}(\text{Hmhp})_{13}(\text{H}_2\text{O})_{5.5}][\text{NO}_3]_{2.8}$ , which contains a cuboctahedron of copper(II) centers within a cube of eight lanthanums, with a  $\mu_3$ -hydroxide at the center of each  $\text{Cu}_2\text{La}$  triangle (215). The remaining ligands are

bound to the lanthanum sites, except for a central nitrate anion, which is encapsulated within the cage. The cage is formed in very low yield from hydrolysis of **106** by lanthanum nitrate in  $\text{CH}_2\text{Cl}_2$ . No magnetic data have been reported for this cage.

A curious observation is that the same copper and hydroxide arrays are found in several other heterometallic cages formed with betaine and carboxylate ligands. Thus,  $[\text{Cu}_{12}\text{M}_6(\text{OH})_{24}(\text{O}_2\text{CCH}_2\text{NC}_5\text{H}_5)_{12}(\text{H}_2\text{O})_{18}(\text{ClO}_4)](\text{ClO}_4)_{17}$  ( $\text{M} = \text{Y}, \text{Nd}$  or  $\text{Gd}$ ) (233),  $[\text{Cu}_{12}\text{M}_6(\text{OH})_{24}(\text{O}_2\text{CCH}_2\text{CH}_2\text{NC}_5\text{H}_5)_{12}(\text{H}_2\text{O})_{16}(\text{ClO}_4)](\text{ClO}_4)_{17}$  ( $\text{M} = \text{Sm}$  or  $\text{Gd}$ ) (234), and  $[\text{Cu}_{12}\text{M}_6(\text{OH})_{24}(\text{O}_2\text{CR})_{12}(\text{H}_2\text{O})_{18}(\text{ClO}_4)](\text{NO}_3)_4(\text{OH})$  ( $\text{R} = \text{CH}_2\text{Cl}$  or  $\text{CCl}_3$ ;  $\text{M} = \text{La}$  or  $\text{Nd}$ ) (235) all contain a copper cuboctahedron, but in these cages the second metal forms an octahedron, as shown in Fig. 48. The encapsulated perchlorate ions found in all these cages are  $\mu_{12}$ -bridging. Magnetic studies (233, 235) reveal antiferromagnetic exchange between copper(II) centers to be the dominant magnetic interaction in most cases. However, for  $[\text{Cu}_{12}\text{Gd}_6(\text{OH})_{24}(\text{O}_2\text{CCH}_2\text{NC}_5\text{H}_5)_{12}(\text{H}_2\text{O})_{18}(\text{ClO}_4)](\text{ClO}_4)_{17}$ ,

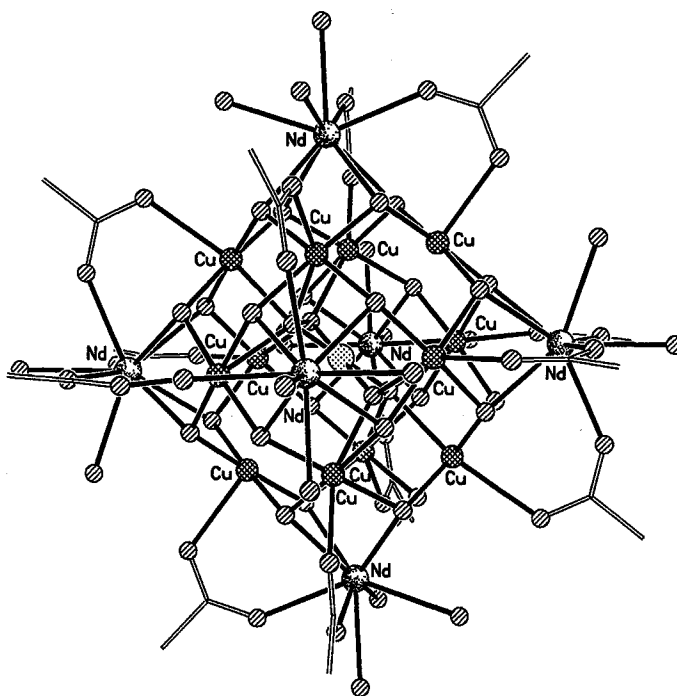


FIG. 48. The structure of  $[\text{Cu}_{12}\text{M}_6(\text{OH})_{24}(\text{O}_2\text{CCCl}_3)_{12}(\text{H}_2\text{O})_{18}(\text{ClO}_4)]$  (235) with chlorine atoms of the carboxylate groups excluded for clarity. (Shading: Cu, hatched; Nd, random shading; O, striped; C, lines.)

this coupling appears to be less overwhelmingly important (233) and the decline in moment as temperature decreases is much slower. This suggests that either the  $\text{Cu} \cdots \text{Cu}$  coupling is weaker or a second exchange interaction, possibly  $\text{Cu} \cdots \text{Gd}$ , is important here.

A further dodecanuclear copper(II) cage also contains a cuboctahedron of copper centers. The ligand is the trianion of 2,4,6-triazophenyl-1,3,5-trihydroxybenzene (tapp; see Scheme 2), which acts as a tri-bidentate chelator (236). The centroids of these ligands in  $[\text{Cu}_{12}(\text{tapp})_8]$ , illustrated in Fig. 49, are at the corners of a cube, placing the copper centers at the midpoint of the edges of this cube—thus creating a cuboctahedron. The cage is made from reaction of  $\text{H}_3\text{tapp}$  in DMF with  $[\text{NMe}_4](\text{OH})$  in MeOH, followed by addition of copper nitrate dissolved in DMF. No magnetic data are reported for this extraordinary complex, which contains an approximately  $816 \text{ \AA}^3$  cavity.

Recently a mixed-ligand cage has been reported, which also contains a dodecanuclear copper core (237).  $[\text{Cu}_{12}\text{Cl}_6(\text{dmpz})_{10}(\text{O}_3\text{P}^t\text{Bu})_6(\text{HO}_3\text{P}^t\text{Bu})_2]$ , shown in Fig. 50, contains an elaborate array of metal centers held together by  $\mu_3$ - and  $\mu_4$ -chlorides,  $\mu_2$ -pyrazolates,  $\mu_3$ - and

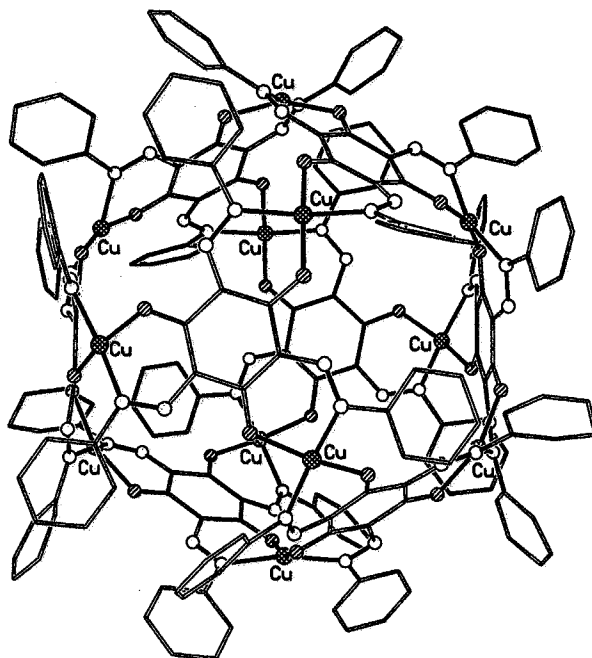


FIG. 49. The structure of  $[\text{Cu}_{12}(\text{tapp})_8]$  (236). (Shading: Cu, hatched; N, open; O, striped; C, lines.)

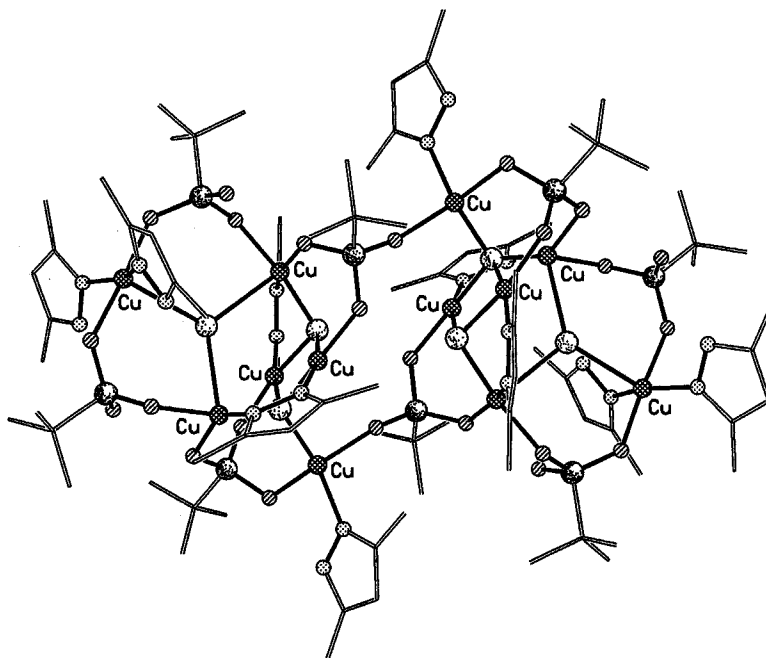


FIG. 50. The structure of  $[\text{Cu}_{12}\text{Cl}_6(\text{dmpz})_{10}(\text{O}_3\text{P}^t\text{Bu})_6(\text{HO}_3\text{P}^t\text{Bu})_2]$  (237). (Shading: Cu, hatched; O, striped; N, dotted; P, random shading; C, lines.)

$\mu_2$ -phosphonates, and  $\mu_2$ -hydrogenphosphonates. The cage consists of two linked hexanuclear units. Within each unit there is a  $\{\text{Cu}_4\text{Cl}_2\}$  butterfly, the two wingtip copper sites being linked by a third chloride. This chloride bridges to the fifth copper of the hexanuclear block, with one of the chlorides within the butterfly binding to the sixth copper. The compound was made by mixing copper(II) chloride and dmpz in  $\text{CH}_2\text{Cl}_2$ , followed by addition of *tert*-butylphosphonic acid and  $\text{NEt}_3$  also dissolved in  $\text{CH}_2\text{Cl}_2$ . This green solution was evaporated to dryness and extracted with benzene. Magnetic measurements show weak antiferromagnetic exchange between copper centers (237).

Two mixed-valent tetradecanuclear cages,  $[\text{Cu}(\text{II})_6\text{Cu}(\text{I})_8\{\text{SC}(\text{Me})_2\text{CH}_2\text{NH}_2\}_{12}]^{7+}$  (238) and  $[\text{Cu}(\text{II})_6\text{Cu}(\text{I})_8(\text{pen})_{12}\text{Cl}]^{5-}$  [ $\text{H}_2\text{pen} = \text{D-penicillamine}$ ,  $\text{HSC}(\text{Me})_2\text{CH}(\text{CO}_2\text{NH}_3)$ ] (239), also contain a mixture of high-symmetry polyhedra. The latter cage is made by mixing D-penicillamine and copper chloride in water, followed by layering with a solution containing a suitable cation— $[\text{Co}(\text{NH}_3)_6]^{3+}$ ,  $[\text{Ru}(\text{NH}_3)_6]^{3+}$ , or  $\text{Tl}^+$  can be used. The purple crystals contain a central chloride anion, surrounded by the S atoms from twelve pen ligands, which form an

icosahedron. The eight Cu(I) centers are at the centers of eight of the triangular faces of the icosahedron, and hence bound to three S atoms. No two Cu(I) atoms are in adjacent triangles. These Cu(I) centers therefore lie at the corners of a cube. The six Cu(II) atoms bond to pairs of S atoms which define edges of the icosahedron, and are also bound to amino nitrogen atoms from the pen ligands. These six Cu(II) atoms lie at the corners of an octahedron. No magnetic data are reported, beyond a statement that the room-temperature value for the magnetic moment of these compounds is consistent with  $\sim 40\%$  of the copper being present as copper(II).

#### IV. Families of Cages

The structures discussed above show an enormous range of structural types, and a frustration in this area is the inability to recognize any central organizing principle to describe and rationalize these structures. Several "families of cages" exist, however, in which cages can be grouped by the metal polyhedron displayed. Three of these families of cages are discussed briefly below.

##### A. WHEELS AND METALLOCROWNS

Cyclic structures have an enormous aesthetic appeal. For cages ranging upward from hexanuclear, wheels (Table II), which contain no central metal, are more common than the metallocrowns (Table III), which contain a further metal encapsulated within the cyclic array. Pecoraro and co-workers have made many smaller metallocrowns, and have recently reviewed the area (240).

An obvious observation concerning these larger cyclic structures is that they always contain an even number of metal centers within the backbone of the wheel or crown. There is no straightforward explanation for the absence of hepta- and nonanuclear wheels, especially as metallocrown analogs of 15-crown-5 are well known (240). Hexa- and octanuclear wheels are known for most of the  $3d$  metals—chromium is absent from hexanuclear wheels, while no octanuclear nickel wheels are known. An octanuclear titanium(IV) wheel has been included for completeness (241). These cages involve a range of ligands that bridge the  $M \cdots M$  edges of the wheel in a variety of ways. For octanuclear cages, bridging by two 1,3-carboxylates and one further  $\mu_2$ -bridge (fluoride, hydroxide, methoxide, or oxide) is the most common motif, but many other variants are known. For decanuclear wheels, only one bridging

TABLE II  
 METAL WHEELS

Cage	Reference
<i>Hexanuclear</i>	
$[\text{V}_6\text{O}_{10}(\text{O}_2\text{CPh})_9]$	41
$[\text{Mn}(\text{hfac})_2(\text{NITPh})]_6$	83
$[\text{Mn}_6\{(\text{PhSiO}_2)_6\}_2\text{Cl}(\text{EtOH})_6]^-$	87
$[\text{Fe}_6\text{Cl}_6\{\text{OCH}_2\text{CH}_2)_2\text{NMe}\}_6]$	140
$[\text{Co}\{\text{N}(\text{CH}_2\text{PO}_3)(\text{CH}_2\text{CO}_2)_2\}_6]^{2-}$	168
$[\text{Co}_6\{(\text{PhSiO}_2)_6\}_2\text{Cl}(\text{solvent})_6]^-$	87
$[\text{Ni}_6\{(\text{PhSiO}_2)_6\}_2\text{Cl}(\text{EtOH})_6]$	184
$[\text{Cu}(\text{O}_2\text{CCMe}_3)(\text{OEt})]_6$	200
$[\text{Cu}_6\{(\text{PhSiO}_2)_6\}_2(\text{EtOH})_6]^-$	87
$[\text{Cu}(\text{L}10)]_6$	209
<i>Octanuclear</i>	
$[\text{TiO}(\text{O}_2\text{CC}_6\text{F}_5)_2]_8$	241
$[\text{V}_8(\text{OH})_4(\text{OEt})_8(\text{O}_2\text{CMe})_{12}]$	32
$[(\text{VO})_8(\text{OMe})_{16}(\text{C}_2\text{O}_4)]^{2-}$	46
$[\text{CrF}(\text{O}_2\text{CCMe}_3)_2]_8$	59a
$[\text{Cr}(\text{OH})(\text{O}_2\text{CPh})_2]_8$	64
$[\text{Fe}_8\text{O}_4(\text{bmdp})_4(\text{OH})_4(\text{O}_2\text{CMe})_4]$	151
$[\text{Fe}(\text{O}_2\text{CCMe}_3)_2]_8$	59b
$[\text{Co}_8(\text{L}9)_{12}(\text{ClO}_4)]^{3+}$	174
$[\text{Co}_8(\text{O}_2\text{CMe})_8(\text{OMe})_{16}]$	175
$[\text{Cu}(\text{dmpz})(\text{OH})]_8$	224
<i>Decanuclear</i>	
$[\text{Cr}(\text{O}_2\text{CMe})(\text{OMe})_2]_{10}$	73
$[\text{Cr}(\text{O}_2\text{CMe})(\text{OEt})_2]_{10}$	73
$[\text{Fe}(\text{OMe})_2(\text{O}_2\text{CCH}_2\text{Cl})]_{10}$	154
$[\text{Fe}(\text{OMe})_2(\text{O}_2\text{CMe})]_{10}$	155
$[\text{Fe}(\text{OMe})_2(\text{O}_2\text{CCH}_2\text{CH}_2\text{C}(\text{O})-\text{C}_6\text{H}_4\text{Me})]_{10}$	156
<i>Dodecanuclear</i>	
$[(\text{R}_2\text{NH}_2)_3\{\text{Cr}_6\text{F}_{11}(\text{O}_2\text{CCMe}_3)_{10}\}(\text{H}_2\text{O})]_2$	74
$[\text{Fe}(\text{OMe})_2(\text{dbm})]_{12}$	138
$[\text{Ni}_{12}(\text{chp})_{12}(\text{O}_2\text{CMe})_{12}(\text{THF})_6(\text{H}_2\text{O})_6]$	28
$[\text{Ni}_{12}(\text{bhp})_{12}(\text{O}_2\text{CMe})_{12}(\text{THF})_6(\text{H}_2\text{O})_6]$	192
<i>Higher nuclearities</i>	
$[\text{Fe}(\text{OH})(\text{XDK})\text{Fe}_2(\text{OMe})_4(\text{O}_2\text{CMe})_2]_6$	164
$[\text{Ni}_{24}(\text{OH})_8(\text{mpo})_{16}(\text{O}_2\text{CMe})_{24}(\text{Hmpo})_{16}]$	194

type is seen, the bis- $\mu_2$ -alkoxide and single 1,3-carboxylate bridge originally seen for the ferric wheel (154). This nuclearity is also seen only for the metal centers in the +3 oxidation state. The two cages with higher nuclearity both consist of repeating trinuclear units; the

TABLE III

## METALLOCROWNS

Cage	Reference
<i>Hexanuclear</i>	
$[\text{Mn} \subset \text{Mn}_6(\text{OH})_3\text{Cl}_3(\text{hmp})_9]^{2+}$	93
$[\text{Na} \subset \text{Mn}_6(\text{dbm})_6(\text{OMe})_{12}]^+$	94
$[\text{Mn} \subset \text{Mn}_6(\text{dbm})_6(\text{OMe})_{12}]$	95
$[\text{Na} \subset \text{Fe}_6(\text{OMe})_{12}(\text{dbm})_6]^+$	137
$[\text{Li} \subset \text{Fe}_6\{\text{OCH}_2\text{CH}_2)_3\text{N}\}_6]^+$	140
$[\text{Na} \subset (\text{Co}_6(\text{mhp}))_{12}]^+$	166
$[\text{Na} \subset \text{Cu}_6(\text{mhp})_{12}]^+$	215
$[\text{Cu} \subset \text{Cu}_6(\text{mhp})_{12}]^{2+}$	216
<i>Octanuclear</i>	
$[\text{Cs} \subset \text{Fe}_8\{\text{OCH}_2\text{CH}_2)_3\text{N}\}_8]$	140

octadecanuclear Fe(III) cage is a hexamer of trinuclear fragments (164), while the tetraicosanuclear Ni(II) cage is an octamer of trinuclear blocks (194). Therefore, if still larger wheels are to be constructed, a design principle might be to look for either larger oligomers of trinuclear fragments or oligomers of higher-nuclearity building blocks.

Only one metallocrown containing more than six metals in the cyclic backbone has been reported (140). This may be due to problems with templating larger metallocrowns. Where larger cations or more than one cation are encapsulated, spherical cages or "metallocryptands" tend to result, for example, in the nonanuclear cage  $[\text{Na}_4\{\text{Ni}(\text{L}1)_9(\text{H}_2\text{O})(\text{MeOH})(\text{ClO}_4)\}]^{3+}$  reported by Doble *et al.* (96) where four sodium ions lie within a tricapped trigonal prism of Ni(II) centers.

## B. CUBANES

These are very common building blocks in larger cages (Table IV). Inclusion of incomplete  $\{\text{M}_3\text{O}_4\}$  cubanes would increase the members of the family to include most of the planar structures described above. The structures listed in Table III contain only those with at least one complete  $\{\text{M}_4\text{X}_4\}$  cubane core.

There are several points worth noting. Face-sharing cubanes exist for dicubanes, tricubanes, heptacubanes, and octacubanes, with additional capping metal centers found for di-, tri-, and heptacubanes. The decavanadate core is described here as a "face-sharing dicubane,

TABLE IV

## CUBANES

Cage	Description	Reference
<i>Hexanuclear</i>		
$[\text{Cr}_6\text{O}_4(\text{O}_2\text{CCMe}_3)_{11}]^-$	Cubane, capped by two Cr centers	65
$[\text{Cr}_6\text{O}_2(\text{OH})_2(\text{O}_2\text{CCMe}_3)_{11}]^+$	Cubane, capped by two Cr centers	65
$[\text{Cu}_6(\text{O}_2\text{CMe})_6(\text{OH})_2(\text{OCH}_2\text{CH}_2\text{NEt}_2)_4(\text{H}_2\text{O})]$	Face-sharing dicubane	196
$[\text{Cu}_6(\text{O}_2\text{CCH}_2\text{Cl})_6(\text{OH})_2(\text{OCH}_2\text{CH}_2\text{NEt}_2)_4(\text{H}_2\text{O})]$	Face-sharing dicubane	197
$[\text{Cu}_7(\text{OH})_8(\text{bpym})_6(\text{H}_2\text{O})_2]^{6+}$	Vertex-sharing dicubane	218
$[\text{Cu}_7\{(\text{py})_2\text{CO}_2\}_3(\text{O}_2\text{CMe})_6(\text{OH})_2]$	Vertex-sharing dicubane	219
<i>Octanuclear</i>		
$[\text{Cr}_8\text{O}_4(\text{O}_2\text{CPh})_{16}]$	Cubane, capped by four Cr centers	64
$[\text{Mn}_8\text{O}_6\text{Cl}_6(\text{O}_2\text{CPh})_7(\text{H}_2\text{O})_2]^-$	Dicubane, sharing an edge	100
$[\text{Fe}_8\text{O}_4(\text{pz})_{12}\text{Cl}_4]$	Cubane, capped by four Fe centers	67
$[\text{Co}_8\text{O}_4(\text{O}_2\text{CPh})_{12}(\text{solv})_3(\text{H}_2\text{O})]$	Cubane, capped by four Co centers	66
$[\text{Co}_8\text{O}_4(\text{OH})_4(\text{O}_2\text{CMe})_6(\text{L}_8)_2]^{2+}$	Triple cubane, sharing two faces	173
$[\text{Co}_8\text{O}_4(\text{O}_2\text{CMe})_6(\text{OMe})_4\text{Cl}_4(\text{OH})_4]$	Triple cubane, sharing two faces	69
$[\text{Cu}_8\{(\text{py})_2\text{CO}(\text{OH})\}_8(\text{O}_2\text{CMe})_4]^{4+}$	Two linked cubanes	220
<i>Nonanuclear</i>		
$[\text{Cu}_9(\text{O}_2\text{CCHCl}_2)_{10}\{\text{OCH}_2\text{C}(\text{NH}_2)\text{Me}_2\}_6(\text{OH})_2]$	Two cubanes linked via a Cu center	230
<i>Decanuclear</i>		
$[\text{V}_{10}\text{O}_{16-x}(\text{OH})_x\{(\text{OCH}_2)_3\text{CR}\}_4]^{n-}$	Face-sharing dicubane, capped by four V centers	49, 50
$[\text{Mn}_{10}\text{O}_2\text{Cl}_8\{\text{OCH}_2)_3\text{CMe}\}_6]^{2-}$	Face-sharing dicubane, capped by four Mn centers	108
<i>Undecanuclear</i>		
$[\{\text{Ni}_6(\text{OH})_6\}\{\text{Ni}(\text{mhp})_3\}_5(\text{Hmhp})\text{Cl}(\text{H}_2\text{O})_2]$	Face-sharing dicubane, capped by five further Ni centers	124
<i>Dodecanuclear</i>		
$[\text{Cr}_{12}\text{O}_8(\text{OH})_4(\text{O}_2\text{CCHMe}_2)_{16}(\text{HO}_2\text{CCHMe}_2)_4]$	Face-sharing tricubane, capped by four Cr centers	68
$[\text{Mn}_{12}\text{O}_{12}(\text{O}_2\text{CR})_{16}(\text{H}_2\text{O})_4]$	Cubane surrounded by ring of eight Mn centers	2, 14
$[\text{Fe}_{12}\text{O}_2(\text{OMe})_{18}(\text{O}_2\text{CMe})_6(\text{HOMe})_{4.67}]$	Four cubanes, sharing one face and two edges	159
$[\text{Co}_{12}(\text{chp})_{18}(\text{OH})_4\text{Cl}_2(\text{Hchp})_2(\text{MeOH})_2]$	Two linked cubanes	181
<i>Higher nuclearities</i>		
$[\text{Mn}_{13}\text{O}_8(\text{OEt})_6(\text{O}_2\text{CPh})_{12}]$	Eight cubanes sharing faces, arranged in a cube	121
$[\text{V}_{16}\text{O}_{20}\{(\text{OCH}_2)_3\text{CCH}_2\text{OH}\}_8(\text{H}_2\text{O})_4]$	Two linked cubanes, each capped by four V centers	56
$[\text{Ni}_{16}\text{Na}_6(\text{chp})_4(\text{phth})_{10}(\text{Hphth})_2(\text{MeO})_{10}(\text{OH})_2(\text{MeOH})_{20}]$	Four linked cubanes	193
$[\text{Fe}_{16}\text{MO}_{10}(\text{OH})_{10}(\text{O}_2\text{CPh})_{20}]$	Double cubane sharing a vertex surrounded by ring of ten Fe centers	160
$[\text{Mn}_{18}\text{O}_{14}(\text{OMe})_{14}(\text{O}_2\text{CCMe}_3)_8(\text{MeOH})_6]$	Six cubanes arranged on the faces of a seventh cubane capped by two Mn centers	124

capped by four V centers"; each of these capping V centers is part of an incomplete cubane that shares edges with the central dicubane. In the dodecanuclear iron cage  $[\text{Fe}_{12}\text{O}_2(\text{OMe})_{18}(\text{O}_2\text{CMe})_6(\text{HOMe})_{4.67}]$  (159), the presence of two additional iron centers completes these additional cubanes. Similarly, in the hexanuclear vanadium cage  $[\text{V}_6\text{O}_{20}\{(\text{OCH}_2)_3\text{CCH}_2\text{OH}\}_8(\text{H}_2\text{O})_4]$  (56), the additional centers are part of incomplete cubanes.

The capping atoms in the hexa-, octa-, dodeca-, and octadecanuclear structures listed in Table III all have the same disposition; i.e., they are attached to a  $\mu_4$ -oxo group of the central cubane(s) to complete a tetrahedral coordination geometry about this site. This contrasts with the additional metal sites in the decanuclear cages, where they are attached to  $\mu_6$ -oxo groups which have octahedral geometries.

### C. TRIGONAL PRISMS

Whereas examples of this polyhedron are formed for chromium, manganese, and iron, the majority of structures containing this core are formed for cobalt and nickel (Table V). All nuclearities between hexa- and dodecanuclear are observed, differing in the presence of additional metal centers. Thus, simple hexanuclear trigonal prisms have been found for iron(III), as well as two centered heptanuclear trigonal prisms for manganese(II). If only the trigonal faces of the prism are capped, an octanuclear manganese(II) cage is observed, while capping exclusively on the edges of the rectangular faces or on these faces themselves generates nonanuclear cages.

Decanuclear cages can be formed in three ways, but all require the presence of a central atom. They are found with caps on the edges of the rectangular faces, on the rectangular faces, and with caps on all faces of the prism but with one edge of the prism missing. Undecanuclear cages form two related polyhedra: capped on both trigonal and all three rectangular faces, but without the central metal site; and centered, but lacking one cap on a trigonal face. The three dodecanuclear cages are all centered and capped on all five faces of the trigonal prism. No clearcut examples of linked trigonal prisms have been reported, although the heptanuclear  $[\text{Fe}_{16}\text{MO}_{10}(\text{OH})_{10}(\text{O}_2\text{CPh})_{20}]$  cages can be related to the undecanuclear iron(III) cages.

Although the regular occurrence of cages based on cubane units can be easily rationalized as related to the sodium chloride structure, it is considerably more difficult to rationalize the regular occurrence of trigonal prisms. An attempt has been made to relate the cobalt and

TABLE V  
TRIGONAL PRISMS

Cage	Description	Reference
<i>Hexanuclear</i>		
$[\text{Fe}_6(\text{O}_2)_3\text{O}_2(\text{O}_2\text{CMe})_9]^{--}$		129
$[\text{NaFe}_6(\text{hpida})_6\text{O}_3]^+$		142, 143
<i>Heptanuclear</i>		
$[\text{Mn}_7\text{O}_6(\text{OEt})_{18}(\text{HOEt})_2]$	Centered	92
$[\text{Mn}\{\text{Mn}(\text{L}1)\}_6]^{2+}$	Centered	96
<i>Octanuclear</i>		
$[\text{Mn}_8\text{O}_2(\text{L}2)_6]$	Capped on trigonal faces	101
<i>Nonanuclear</i>		
$[\text{Fe}_9\text{O}(\text{cit})_8(\text{H}_2\text{O})_3]^{7-}$	Capped on edges linking triangles	153
$[\text{Na}_4\{\text{Ni}(\text{L}1)_9(\text{H}_2\text{O})(\text{MeOH})(\text{ClO}_4)\}_3]^{3+}$	Capped on rectangular faces	96
<i>Decanuclear</i>		
$[\text{Co}_{10}(\text{OH})_6(\text{mhp})_6(\text{O}_2\text{CPh})_7(\text{Hmhp})_3\text{Cl}(\text{MeCN})]$	Capped on rectangular faces and centered	179
$[\text{Co}_{10}(\text{OH})_6(\text{mhp})_6(\text{O}_2\text{CCMe}_3)_7(\text{Hmhp})\text{Cl}(\text{MeCN})_3]$	Capped on rectangular faces and centered	179
$[\text{Co}_{10}(\text{OH})_4(\text{chp})_{10}(\text{O}_2\text{CCMe}_3)_6(\text{EtOH})_2]$	Pentacapped, centered, missing one edge	179
$[\text{Co}_{10}(\text{OH})_6(\text{mhp})_6(\text{O}_2\text{CCHPh}_3)_6(\text{Hmhp})_3(\text{HCO}_3)_3]$	Capped on edges linking triangles and centered	180
$[\text{Ni}_{10}(\text{OH})_6(\text{mhp})_{6.5}(\text{O}_2\text{CCHMe}_2)_{6.5}(\text{Hmhp})_3\text{Cl}(\text{H}_2\text{O})]$	Capped on rectangular faces and centered	179
$[\text{Ni}_{10}(\text{OH})_6(\text{chp})_6(\text{O}_2\text{CCHPh}_2)_6(\text{Cl})_2(\text{Hchp})(\text{H}_2\text{O})_2(\text{MeOH})]$	Capped on rectangular faces and centered	179
$[\text{Ni}_{10}(\text{OH})_4(\text{mhp})_{10}(\text{O}_2\text{CCMe}_3)_6(\text{MeOH})_2]$	Pentacapped, centered, missing one edge	179
$[\text{Ni}_{10}(\text{OH})_4(\text{mhp})_{10}(\text{O}_2\text{CCMe}_3)_6(\text{H}_2\text{O})_2]$	Pentacapped, centered, missing one edge	179
<i>Undecanuclear</i>		
$[\text{Fe}_{11}\text{O}_6(\text{OH})_6(\text{O}_2\text{CPh})_{15}]$	Pentacapped	158
$[\text{Fe}_{11}\text{O}_6(\text{OH})_6(\text{O}_2\text{CCH}_2\text{CH}_2\text{C}(\text{O})\text{C}_6\text{H}_4\text{Me})_{15}]$	Pentacapped	156
$[\text{Ni}_{11}(\text{OH})_6(\text{mhp})_9(\text{O}_2\text{CMe})_6(\text{H}_2\text{O})_3]^+$	Capped on rectangular faces and one trigonal face, centered	179
$[\text{Ni}_{11}(\text{OH})_6(\text{mhp})_9(\text{O}_2\text{CMe})_7(\text{Hmhp})_2]$	Capped on rectangular faces one trigonal face, centered	179
<i>Dodecanuclear</i>		
$[\text{Cr}_{12}\text{O}_9(\text{OH})_3(\text{O}_2\text{CCMe}_3)_{15}]$	Pentacapped and centered	61
$[\text{Co}_{12}(\text{OH})_6(\text{mhp})_{12}(\text{O}_2\text{CMe})_6]$	Pentacapped and centered	178
$[\text{Ni}_{12}(\text{OH})_6(\text{mhp})_{12}(\text{O}_2\text{CCH}_2\text{Cl})_6]$	Pentacapped and centered	179

nickel structures to the structure of the  $M(OH)_2$  hydroxide (171), but whether this relationship is meaningful remains to be proved.

## V. Conclusions

There are now a large number of high-nuclearity paramagnetic cages known, and the rate at which the number of cages increases is accelerating. The diversity of structures is remarkable, and has prevented any guiding structural principles from being proposed. It is already clear that the cages do not correspond in a straightforward manner to fragments of common minerals or to polyhedral archetypes, but rather, display a richness of topology and nuclearity that is unpredictable but intriguing.

Many gaps remain in this field. Ligands that are regularly applied to one metal may not feature at all in the cage chemistry of another metal. The tendency in the area is for O-donor ligands to be used with early 3d metals, with nitrogen donors becoming more common as the transition series is traversed. Although this obeys the "hard-soft" principle, it is not clear whether the absence of alkoxide cages of nickel or pyrazolate cages of chromium is because these cages cannot be made or because no one has yet looked. The recent paper by Chandrasekar and Kingsley (237) is a very rare example of a phosphonate ligand used with a 3d metal other than vanadium.

Heterometallic cages are rather rare, and, in the context of magnetic behavior, could be very interesting. The few examples known are rather disappointing, in contrast to the heterometallic cyanate cages known (18–24). Application of rigid, polydentate ligands is rare, except for the work of Saalfrank (101, 102) and Thompson (106, 231), in contrast to the many diamagnetic cages produced by Lehn and co-workers (232). This approach could generate many exciting cages, with the advantage of control of structure.

The reactivity of these cages is clearly something of a mystery. The paramagnetism makes NMR a technique of limited applicability, especially in cases where some ligands are weakly bound, creating additional problems of fluxionality. Vibrational and electronic spectra of such cages contain too many and too few spectroscopic handles, respectively, to be useful. Therefore, solution studies have been limited. The growing use of electrospray mass spectrometry suggests more will be known in the future. There are several systems in which several cages can be crystallized from very similar reaction mixtures, and an examination of which of these cages is present in solution would be a step toward understanding how, and when, cages form.

## NOTE ADDED IN PROOF

There are doubtless many omissions in this account. One must be corrected: There is no reference to the beautiful polyol work of Klüfers and co-workers. This is unusual and exciting chemistry, and the Fe<sub>14</sub> (242) and C<sub>M16</sub> (243) clusters made by this method are important molecules.

## ACKNOWLEDGMENTS

Our work in this area has been supported by the EPSRC(UK), The Leverhulme Trust, The European Union (HPRN-CT-1999-00012), The British Council, and The Royal Societies of London and Edinburgh. I am also grateful for free access to the Cambridge Structural Database, which has been invaluable in compiling this review. Finally, I have to thank Dr. Steve Harris (Edinburgh) for assistance in preparation of the figures.

## REFERENCES

1. Cotton, F. A.; Walton, R. "Multiple Bonds between Metal Atoms"; 2nd ed.
2. Sessoli, R.; Tsai, H.-L.; Schake, A. R.; Wang, S.; Vincent, J. B.; Folting, K.; Gatteschi, D.; Christou, G.; Hendrickson, D. N. *J. Am. Chem. Soc.* **1993**, *115*, 1804–1816.
3. Sessoli, R.; Gatteschi, D.; Caneschi, A.; Novak, M. A. *Nature* **1993**, *365*, 141–142.
4. Sun, Z.; Ruiz, D.; Rumberger, E.; Incarvito, C. D.; Folting, K.; Rheingold, A. L.; Christou, G.; Hendrickson, D. N. *Inorg. Chem.* **1998**, *37*, 4758–4759.
5. Sangregorio, C.; Ohm, T.; Paulsen, C.; Sessoli, R.; Gatteschi, D. *Phys. Rev. Lett.* **1997**, *78*, 4645–4648.
6. Wemple, M. W.; Adams, D. M.; Hagen, K. S.; Folting, K.; Hendrickson, D. N.; Christou, G. *J. Chem. Soc., Chem. Commun.* **1995**, 1591–1593.
7. Castro, S. L.; Sun, Z.; Grant, C. M.; Bollinger, J. C.; Hendrickson, D. N.; Christou, G. *J. Am. Chem. Soc.* **1998**, *120*, 2365–2375.
8. Barra, A. L.; Caneschi, A.; Gatteschi, D.; Goldberg, D. P.; Sessoli, R. *J. Sol. State Chem.* **1999**, *145*, 484–487.
9. Barra, A. L.; Caneschi, A.; Cornia, A.; deBiani, F. F.; Gatteschi, D.; Sangregorio, C.; Sessoli, R.; Sorace, L. *J. Am. Chem. Soc.* **1999**, *121*, 5302–5310.
10. Goodwin, J. C.; Sessoli, R.; Gatteschi, D.; Wernsdorfer, W.; Powell, A. K.; Heath, S. L. *J. Chem. Soc., Dalton Trans.* **2000**, 1835–1840.
11. Benelli, C.; Cano, J.; Journaux, Y.; Sessoli, R.; Solan, G. A.; Winpenny, R. E. P. *Inorg. Chem.* **2001**, *40*, 188–189.
12. Friedman, J.; Sarachik, M.; Tejada, J.; Ziolo, R. *Phys. Rev. Lett.* **1996**, *76*, 3830–3833.
13. Thomas, L.; Lioni, F.; Ballou, R.; Gatteschi, D.; Sessoli, R.; Barbara, B. *Nature* **1999**, *393*, 145–147.
14. Lis, T. *Acta Crystallogr., Sect. B* **1980**, *36*, 2042–2045.
15. Zhong, Z. J.; Seino, H.; Mizobe, Y.; Hidai, M.; Fujishima, A.; Ohkoshi, S.; Hashimoto, K. *J. Am. Chem. Soc.* **2000**, *122*, 2952–2953.
16. Babel, D. *Comm. Inorg. Chem.* **1986**, *5*, 285.
17. Mallah, T.; Thiébaud, S.; Verdager, M.; Veillet, P. *Science* **1993**, *262*, 1554–1557.
18. Verdager, M.; Bleuzen, A.; Train, C.; Garde, R.; Fabrizi de Biani, F.; Desplanches, C. *Phil. Trans. R. Soc. Lond. (A)* **1999**, *357*, 2959–2976.
19. Entley, W. R.; Girolami, G. S. *Science* **1995**, *268*, 397–400.

20. Ferlay, S.; Mallah, T.; Quahes, R.; Veillet, P.; Verdaguer, M. *Nature* **1995**, 378, 701–703.
21. Hashimoto, K.; Ohkoshi, S. *Phil. Trans. R. Soc. Lond. (A)* **1999**, 357, 2977–3003.
22. Mallah, T.; Auburger, C.; Verdaguer, M.; Veillet, P. *J. Chem. Soc., Chem. Commun.* **1995**, 61–62.
23. Larionova, J.; Gross, M.; Pilkington, M.; Andres, H.; Stoeckli-Evans, H.; Güdel, H. U.; Decurtins, S. *Angew. Chem. Int. Ed. Engl.* **2000**, 39, 1605–1609.
24. Berseth, P. A.; Sokol, J. J.; Shores, M. P.; Heinrich, J. L.; Long, J. R. *J. Am. Chem. Soc.* **2000**, 122, 9655–9662.
25. Christou, G. *Acc. Chem. Res.* **1989**, 22, 328–335.
26. Blake, A. J.; Grant, C. M.; Gregory, C. I.; Parsons, S.; Rawson, J. M.; Reed, D.; Winpenny, R. E. P. *J. Chem. Soc., Dalton Trans.* **1995**, 163–175.
27. Blake, A. J.; Brechin, E. K.; Codron, A.; Gould, R. O.; Grant, C. M.; Parsons, S.; Rawson, J. M.; Winpenny, R. E. P. *J. Chem. Soc., Chem. Commun.* **1995**, 1983–1986.
28. Blake, A. J.; Grant, C. M.; Parsons, S.; Rawson, J. M.; Winpenny, R. E. P. *J. Chem. Soc., Chem. Commun.* **1994**, 2363–2364.
29. Gatteschi, D.; Sessoli, R.; Cornia, A. *Chem. Commun.* **2000**, 725–732.
30. Chen, Q.; Zubieta, J. *Coord. Chem. Rev.* **1992**, 114, 107–167.
31. Khan, M. I.; Zubieta, J. *Prog. Inorg. Chem.* **1995**, 43, 1–149.
32. Kumagai, H.; Kitagawa, S. *Chem. Lett.* **1996**, 471–472.
33. Müller, A.; Sessoli, R.; Krickemeyer, E.; Bögge, H.; Meyer, J.; Gatteschi, D.; Pardi, L.; Westphal, J.; Hovemeier, K.; Rohlffing, R.; Döring, J.; Hellweg, F.; Beugholt, C.; Schmidtman, M. *Inorg. Chem.* **1997**, 36, 5239–5250.
34. Khan, M. I.; Chen, Q.; Höpe, H.; Parkin, S.; O'Connor, C. J.; Zubieta, J. *Inorg. Chem.* **1993**, 32, 2929–2937.
35. Kessler, V. G.; Seisenbaeva, G. A. *Inorg. Chem. Comm.* **2000**, 3, 203–204.
36. Hou, D.; Kim, G.-S.; Hagen, K. S.; Hill, C. L. *Inorg. Chim. Acta* **1993**, 211, 127–130.
37. Chen, Q.; Zubieta, J. *J. Chem. Soc., Chem. Commun.* **1993**, 1180–1182.
38. Bottomley, F. *Polyhedron* **1992**, 11, 1707–1731.
39. Salta, J.; Chen, Q.; Chang, Y.-D.; Zubieta, J. *Angew. Chem., Int. Ed. Engl.* **1994**, 33, 757–760.
40. Thorn, D. L.; Harlow, R. L.; Herron, N. *Inorg. Chem.* **1995**, 34, 2629–2638.
41. Rehder, D.; Prietsch, W.; von Oeynhausen, M. *Angew. Chem., Int. Ed. Engl.* **1989**, 28, 1221–1222.
42. Khan, M. I.; Chang, Y.; Chen, Q.; Hope, H.; Parkin, S.; Goshorn, D. P.; Zubieta, J. *Angew. Chem., Int. Ed. Engl.* **1992**, 31, 1197–1199.
43. Mokry, L. M.; Thompson, J.; Bond, M. R.; Otieno, T.; Mohan, M.; Carrano, C. J. *Inorg. Chem.* **1994**, 33, 2705–2706.
44. Müller, A.; Meyer, J.; Bögge, H.; Stämmler, A.; Botar, A. *Chem. Eur. J.* **1998**, 4, 1388–1397.
45. Chang, Y.-D.; Salta, J.; Zubieta, J. *Angew. Chem., Int. Ed. Engl.* **1994**, 33, 325–326.
46. Chen, Q.; Liu, S.; Zubieta, J. *Inorg. Chem.* **1989**, 28, 4433–4434.
47. Launay, J.-P.; Jeannin, Y.; Daoudi, M. *Inorg. Chem.* **1985**, 24, 1052–1059.
48. Karet, G. B.; Sun, Z.; Streib, W. E.; Bollinger, J. C.; Hendrickson, D. N.; Christou, G. *Chem. Commun.* **1999**, 2249–2250.
49. Khan, M. I.; Chen, Q.; Goshorn, D. P.; Hope, H.; Parkin, S.; Zubieta, J. *J. Am. Chem. Soc.* **1992**, 114, 3341–3346.
50. Khan, M. I.; Chen, Q.; Goshorn, D. P.; Zubieta, J. *Inorg. Chem.* **1993**, 32, 672–680.
51. Müller, A.; Rohlffing, R.; Krickemeyer, E.; Bögge, H. *Angew. Chem., Int. Ed. Engl.* **1993**, 32, 909–912.

52. Huan, G.; Day, V. W.; Jacobson, A. J.; Goshorn, D. P. *J. Am. Chem. Soc.* **1991**, *113*, 3188–3189.
53. Khan, M. I.; Zubieta, J. *Angew. Chem., Int. Ed. Engl.* **1994**, *33*, 760–762.
54. Müller, A.; Hovemeier, K.; Rohlfing, R. *Angew. Chem., Int. Ed. Engl.* **1992**, *31*, 1192–1195.
55. Huan, G.; Jacobson, A. J.; Day, V. W. *Angew. Chem., Int. Ed. Engl.* **1991**, *30*, 422–423.
56. Khan, M. I.; Lee, Y.-S.; O'Connor, C. J.; Zubieta, J. *J. Am. Chem. Soc.* **1994**, *116*, 5001–5002.
57. Day, V. W.; Klemperer, W. G.; Yaghi, O. M. *J. Am. Chem. Soc.* **1989**, *111*, 5959–5961.
58. Cannon, R. D.; White, R. P. *Prog. Inorg. Chem.* **1988**, *36*, 195–298.
- 59a. Gérébéléu, N. V.; Struchkov, Y. T.; Timco, G. A.; Batsanov, A. S.; Indrichan, K. M.; Popovich, G. A. *Dokl. Akad. Nauk SSSR.* **1990**, *313*, 1459–1462.
- 59b. Gérébéléu, N. V.; Struchkov, Y. T.; Timco, G. A.; Marole, O. S.; Batsanov, A. S. *Dokl. Akad. Nauk SSSR.* **1993**, *331*, 184–186.
60. Batsanov, A. S.; Timco, G. A.; Struchkov, Y. T.; Gérébéléu, N. V.; Indrichan, K. M. *Koord. Khim.* **1991**, *17*, 662–669.
61. Mabbs, F. E.; McInnes, E. J. L.; Murrie, M.; Parsons, S.; Smith, G. M.; Wilson, C. C.; Winpenny, R. E. *P. Chem. Commun.* **1999**, 643–644.
62. Bino, A.; Johnston, D. C.; Goshorn, D. P.; Halbert, T. R.; Stiefel, E. I. *Science* **1988**, *241*, 1479–1481.
63. Murrie, M.; Parsons, S.; Smith, A. A.; Winpenny, R. E. P. Unpublished results.
64. Atkinson, I. M.; Benelli, C.; Murrie, M.; Parsons, S.; Winpenny, R. E. P. *Chem. Commun.* **1999**, 285–286.
65. Coxall, R. A.; Parkin, A.; Parsons, S.; Smith, A. A.; Timco, G. A.; Winpenny, R. E. P. *J. Sol. State Chem.* **2001**, manuscript accepted for publication.
66. Dimitrou, K.; Sun, J.-S.; Folting, K.; Christou, G. *Inorg. Chem.* **1995**, *34*, 4160–4166.
67. Raptis, R. G.; Georgakaki, I. P.; Hockless, D. C. R. *Angew. Chem., Int. Ed. Engl.* **1999**, *38*, 1632–1634.
68. Parsons, S.; Smith, A. A.; Winpenny, R. E. P. *Chem. Commun.* **2000**, 579–580.
69. Beattie, J. K.; Hambley, T. W.; Kleptko, J. A.; Masters, A. F.; Turner, P. *Polyhedron* **1997**, *16*, 2109–2112.
70. Brechin, E. K.; Clegg, W.; Murrie, M.; Parsons, S.; Teat, S. J.; Winpenny, R. E. P. *J. Am. Chem. Soc.* **1998**, *120*, 7365–7366.
71. Sun, Z.; Gantzel, P. K.; Hendrickson, D. N. *Inorg. Chem.* **1996**, *35*, 6640–6641.
72. Eshel, M.; Bino, A.; Felner, I.; Johnston, D. C.; Luban, M.; Miller, L. L. *Inorg. Chem.* **2000**, *39*, 1376–1380.
73. McInnes, E. J. L.; Anson, C.; Powell, A. K.; Thomson, A. J.; Poussereau, S.; Sessoli, R. *Chem. Commun.* **2001**, 89–90.
74. Gérébéléu, N. V.; Parsons, S.; Smith, A. A.; Timco, G. A.; Winpenny, R. E. P. Unpublished results.
75. Chen, Y.-H.; Lee, C.-C.; Wang, C.-C.; Lee, G.-H.; Lai, S.-Y.; Li, F.-Y.; Mou, C.-Y.; Peng, S.-M. *Chem. Commun.* **1999**, 1667–1668.
76. Aromi, G.; Aubin, S. M. J.; Bolcar, M. A.; Christou, G.; Eppley, H. J.; Folting, K.; Hendrickson, D. N.; Huffman, J. C.; Squire, R. C.; Tsai, H.-L.; Wang, S.; Wemple, M. W. *Polyhedron* **1998**, *17*, 3005–3020.
77. Baikie, A. R. E.; Howes, A. J.; Hursthouse, M. B.; Quick, A. B.; Thornton, P. *J. Chem. Soc., Chem. Commun.* **1986**, 1587–1588.
78. Batsanov, A. S.; Struchkov, Y. T.; Timco, G. A.; Gérébéléu, N. V.; Manole, O. S.; Grebenko, S. V. *Koord. Khim.* **1994**, *20*, 604–606.

79. Schake, A. R.; Vincent, J. B.; Li, Q.; Boyd, P. D. W.; Folting, K.; Huffman, J. C.; Hendrickson, D. N.; Christou, G. *Inorg. Chem.* **1989**, *28*, 1915–1923.
80. Blackman, A. G.; Huffman, J. C.; Lobkovsky, E. B.; Christou, G. *Polyhedron* **1992**, *11*, 251–255.
81. Halcrow, M. A.; Streib, W. E.; Folting, K.; Christou, G. *Acta Crystallogr., Sect. C* **1995**, *51*, 1263–1267.
82. Murrie, M.; Parsons, S.; Winpenny, R. E. P. *J. Chem. Soc., Dalton Trans.* **1998**, 1423–1424.
83. Caneschi, A.; Gatteschi, D.; Laugier, J.; Rey, P.; Sessoli, R.; Zanchini, C. *J. Am. Chem. Soc.* **1988**, *110*, 2795–2799.
84. Belforte, A.; Calderazzo, F.; Zanazzi, P. F. *J. Chem. Soc., Dalton Trans.* **1988**, 2921–2926.
85. Xia, X. P.; Verelst, M.; Daran, J. C.; Tuchagues, J. P. *J. Chem. Soc., Chem. Commun.* **1995**, 2155–2157.
86. Aromi, G.; Knapp, M. J.; Claude, J.-P.; Huffman, J. C.; Hendrickson, D. N.; Christou, G. *J. Am. Chem. Soc.* **1999**, *121*, 5489–5499.
87. Igonin, V. A.; Shchegolikhina, O. I.; Lindeman, S. V.; Levitsky, M. M.; Struchkov, Yu. T.; Zhdanov, A. A. *J. Organomet. Chem.* **1992**, *423*, 351–360.
88. Bhula, R.; Collier, S.; Robinson, W. T.; Weatherburn, D. C. *Inorg. Chem.* **1990**, *29*, 4027–4032.
89. Bhula, R.; Weatherburn, D. C. *Angew. Chem., Int. Ed. Engl.* **1991**, *30*, 688–689.
90. Wang, S.; Tsai, H.-L.; Streib, W. E.; Christou, G.; Hendrickson, D. N. *J. Chem. Soc., Chem. Commun.* **1992**, 677–679.
91. Wang, S.; Folting, K.; Streib, W. E.; Schmitt, E. A.; McCusker, J. K.; Hendrickson, D. N.; Christou, G. *Angew. Chem., Int. Ed. Engl.* **1991**, *30*, 305–306.
92. Bemm, U.; Norrestam, R.; Nygren, M.; Westin, G. *J. Sol. State Chem.* **1997**, *134*, 312–318.
93. Bolcar, M. A.; Aubin, S. M. J.; Folting, K.; Hendrickson, D. N.; Christou, G. *Chem. Commun.* **1997**, 1485–1486.
94. Abbati, G. L.; Cornia, A.; Fabretti, A. C.; Caneschi, A.; Gatteschi, D. *Inorg. Chem.* **1998**, *37*, 1430–1431.
95. Abbati, G. L.; Cornia, A.; Fabretti, A. C.; Caneschi, A.; Gatteschi, D. *Inorg. Chem.* **1998**, *37*, 3759–3766.
96. Doble, D. M. J.; Benison, C. H.; Blake, A. J.; Fenske, D.; Jackson, M. S.; Kay, R. D.; Li, W.-S.; Schröder, M. *Angew. Chem., Int. Ed. Engl.* **1999**, *38*, 1915–1918.
97. Libby, E.; Folting, K.; Huffman, J. C.; Christou, G. *J. Am. Chem. Soc.* **1990**, *112*, 5354–5356.
98. Wang, S.; Tsai, H.-L.; Folting, K.; Martin, J. D.; Hendrickson, D. N.; Christou, G. *J. Chem. Soc., Chem. Commun.* **1994**, 671–672.
99. Wemple, M. W.; Tsai, H.-L.; Streib, W. E.; Hendrickson, D. N.; Christou, G. *J. Chem. Soc., Chem. Commun.* **1994**, 1031–1033.
100. Tsai, H.-L.; Wang, S.; Folting, K.; Streib, W. E.; Hendrickson, D. N.; Christou, G. *J. Am. Chem. Soc.* **1995**, *117*, 2503–2514.
101. Saalfrank, R. W.; Löw, N.; Trummer, S.; Sheldrick, G. M.; Teichert, M.; Stalke, D. *Eur. J. Inorg. Chem.* **1998**, 559–563.
102. Saalfrank, R. W.; Löw, N.; Demleitner, B.; Stalke, D.; Teichert, M. *Chem. Eur. J.* **1998**, *4*, 1305–1311.
103. Bemm, U.; Norrestam, R.; Nygren, M.; Westin, G. *Inorg. Chem.* **1995**, *34*, 2367–2370.
104. Christmas, C.; Vincent, J. B.; Chang, H.-R.; Huffman, J. C.; Christou, G.; Hendrickson, D. N. *J. Am. Chem. Soc.* **1988**, *110*, 823–830.

105. Low, D. W.; Eichhorn, D. M.; Draganescu, A.; Armstrong, W. H. *Inorg. Chem.* **1991**, *30*, 878–880.
106. Zhao, L.; Matthews, C. J.; Thompson, L. K.; Heath, S. L. *Chem. Commun.* **2000**, 265–266.
107. Hagen, K. S.; Armstrong, W. H.; Olmstead, M. M. *J. Am. Chem. Soc.* **1989**, *111*, 774–775.
108. Cavaluzzo, M.; Chen, Q.; Zubieta, J. *J. Chem. Soc., Chem. Commun.* **1993**, 131–133.
109. Goldberg, D. P.; Caneschi, A.; Delfs, C. D.; Sessoli, R.; Lippard, S. J. *J. Am. Chem. Soc.* **1995**, *117*, 5789–5800.
110. Barra, A. L.; Caneschi, A.; Gatteschi, D.; Sessoli, R. *J. Am. Chem. Soc.* **1995**, *117*, 8855–8856.
111. Caneschi, A.; Gatteschi, D.; Sessoli, R.; Schweizer, J. *Physica (B)* **1998**, *241–243*, 600–602.
112. Eppley, E. J.; Aubin, S. M. J.; Streib, W. E.; Bollinger, J. C.; Hendrickson, D. N.; Christou, G. *Inorg. Chem.* **1997**, *36*, 109–115.
113. Perlepes, S. P.; Huffman, J. C.; Christou, G. *J. Chem. Soc., Chem. Commun.* **1991**, 1657–1659.
114. Luneau, D.; Savariault, J.-M.; Tuchagues, J.-P. *Inorg. Chem.* **1988**, *27*, 3912–3918.
115. Boyd, P. D. W.; Li, Q.; Vincent, J. B.; Folting, K.; Chang, H.-R.; Streib, W. E.; Huffman, J. C.; Christou, G.; Hendrickson, D. N. *J. Am. Chem. Soc.* **1988**, *110*, 8537–8538.
116. Yoo, J.; Brechin, E. K.; Yamaguchi, A.; Nakano, M.; Huffman, J. C.; Maniero, A. L.; Brunel, L.-C.; Awaga, K.; Ishimoto, H.; Christou, G.; Hendrickson, D. N. *Inorg. Chem.* **2000**, *39*, 3615–3623.
117. Sun, Z.; Ruiz, D.; Rumberger, E.; Incarvito, C. D.; Folting, K.; Rheingold, A. L.; Christou, G.; Hendrickson, D. N. *Inorg. Chem.* **1998**, *37*, 4758–4759.
118. Aubin, S. M. J.; Sun, Z.; Pardi, L.; Krzystek, J.; Folting, K.; Brunel, L.-C.; Rheingold, A. L.; Christou, G.; Hendrickson, D. N. *Inorg. Chem.* **1999**, *38*, 5329–5340.
119. Soler, M.; Chandra, S. K.; Ruiz, D.; Davidson, E. R.; Hendrickson, D. N.; Christou, G. *Chem. Commun.* **2000**, 2417–2418.
120. Schake, A. R.; Tsai, H.-L.; De Vries, N.; Webb, R. J.; Folting, K.; Hendrickson, D. N.; Christou, G. *J. Chem. Soc., Chem. Commun.* **1992**, 181–183.
121. Sun, Z.; Gantzel, P. K.; Hendrickson, D. N. *Inorg. Chem.* **1996**, *35*, 6640–6641.
122. Gorun, S. M.; Stibrany, R. T. U.S. Patent 5,041,575, 1991.
123. Squire, R. C.; Aubin, S. M. J.; Folting, K.; Streib, W. E.; Hendrickson, D. N.; Christou, G. *Angew. Chem., Int. Ed. Engl.* **1995**, *34*, 887–889.
124. Brechin, E. K.; Clegg, W.; Murrie, M.; Parsons, S.; Teat, S. J.; Winpenny, R. E. P. *J. Am. Chem. Soc.* **1998**, *120*, 7365–7366.
125. G  rb  l  u, N. V.; Batsanov, A. S.; Timco, G. A.; Struchkov, Y. T.; Indrichan, K. M.; Popovich, G. A. *Dokl. Akad. Nauk SSSR* **1987**, *293*, 364–367.
126. Micklitz, W.; Lippard, S. J. *Inorg. Chem.* **1988**, *27*, 3067–3069.
127. Micklitz, W.; Bott, S. G.; Bentsen, J. G.; Lippard, S. J. *J. Am. Chem. Soc.* **1989**, *111*, 372–374.
128.   elenligil-  etin, R.; Staples, R. J.; Stavropoulos, P. *Inorg. Chem.* **2000**, *39*, 5838–5846.
129. Shweky, I.; Pence, L. E.; Papaefthymiou, G. C.; Sessoli, R.; Yun, J. W.; Bino, A.; Lippard, S. J. *J. Am. Chem. Soc.* **1997**, *119*, 1037–1042.
130. McCusker, J. K.; Christmas, C. A.; Hagen, P. M.; Chadhu, R. K.; Harvey, D. F.; Hendrickson, D. N. *J. Am. Chem. Soc.* **1991**, *113*, 6114–6124.

131. Christmas, C. A.; Tsai, H.-L.; Pardi, L.; Kesselman, J. M.; Gantzel, P. K.; Chadhu, R. K.; Gatteschi, D.; Harvey, D. F.; Hendrickson, D. N. *J. Am. Chem. Soc.* **1993**, *115*, 12483–12490.
132. Hegetschweiler, K.; Schmalte, H. W.; Streit, H. M.; Gramlich, V.; Hund, H.-U.; Erni, I. *Inorg. Chem.* **1992**, *31*, 1299–1302.
133. Hegetschweiler, K.; Schmalte, H. W.; Streit, H. M.; Schneider, W. *Inorg. Chem.* **1990**, *29*, 3625–3627.
134. Cornia, A.; Gatteschi, D.; Hegetschweiler, K.; Hausherr-Primo, L.; Gramlich, V. *Inorg. Chem.* **1996**, *35*, 4414–4419.
135. Brechin, E. K.; Knapp, M. J.; Huffman, J. C.; Hendrickson, D. N.; Christou, G. *Inorg. Chim. Acta* **2000**, *297*, 389–399.
136. Belli Dell'Amico, D.; Calderazzo, F.; Labella, L.; Maichle-Mössmer, C.; Strähle, J. *J. Chem. Soc., Chem. Commun.* **1994**, 1555–1556.
137. Caneschi, A.; Cornia, A.; Lippard, S. J. *Angew. Chem., Int. Ed. Engl.* **1995**, *34*, 467–469.
138. Caneschi, A.; Cornia, A.; Fabretti, A. C.; Gatteschi, D. *Angew. Chem., Int. Ed. Engl.* **1999**, *38*, 1295–1297.
139. Abbatti, G. L.; Caneschi, A.; Cornia, A.; Fabretti, A. C.; Gatteschi, D. *Inorg. Chim. Acta* **2000**, *297*, 291–300.
140. Saalfrank, R. W.; Bernt, I.; Uller, E.; Hampel, F. *Angew. Chem., Int. Ed. Engl.* **1997**, *36*, 2482–2484.
141. Grant, C. M.; Knapp, M. J.; Streib, W. E.; Huffman, J. C.; Hendrickson, D. N.; Christou, G. *Inorg. Chem.* **1998**, *37*, 6065–6070.
142. Goodwin, J. C.; Price, D. J.; Powell, A. K.; Heath, S. L. *Eur. J. Inorg. Chem.* **2000**, 1407–1410.
143. Scheppensieper, T.; Liehr, G.; van Eldik, R.; Ensling, J.; Gütllich, P. *Inorg. Chem.* **2000**, *39*, 5565–5568.
144. Kajiwar, T.; Ito, T. *Angew. Chem., Int. Ed. Engl.* **2000**, *39*, 230–233.
145. Wieghardt, K.; Pohl, K.; Jibril, I.; Huttner, G. *Angew. Chem., Int. Ed. Engl.* **1984**, *23*, 77–78.
146. Delfs, C.; Gatteschi, D.; Pardi, L.; Sessoli, R.; Wieghardt, K. *Inorg. Chem.* **1993**, *32*, 3099–3103.
147. Barra, A. L.; Debrunner, P.; Gatteschi, D.; Schulz, Ch. E.; Sessoli, R. *Europhys. Lett.* **1996**, *35*, 133–138.
148. Caciuffo, R.; Amoretti, G.; Murani, A.; Sessoli, R.; Caneschi, A.; Gatteschi, D. *Phys. Rev. Lett.* **1998**, *81*, 4744–4747.
149. Wernsdorfer, W.; Ohm, T.; Sangregorio, C.; Sessoli, R.; Mailly, D.; Paulsen, C. *Phys. Rev. Lett.* **1999**, *82*, 3903–3906.
150. Nair, V. S.; Hagen, K. S. *Inorg. Chem.* **1994**, *33*, 185–186.
151. Satcher, Jr., J. H.; Olmstead, M. M.; Droegge, M. W.; Parkin, S. R.; Noll, B. C.; May, L.; Balch, A. L. *Inorg. Chem.* **1998**, *37*, 6751–6758.
152. Ammala, P.; Cashion, J. D.; Kepert, C. M.; Moubaraki, B.; Murray, K. S.; Spiccia, L.; West, B. O. *Angew. Chem., Int. Ed. Engl.* **2000**, *39*, 1688–1690.
153. Bino, A.; Shweky, I.; Cohen, S.; Bauminger, E. R.; Lippard, S. J. *Inorg. Chem.* **1998**, *37*, 5168–5172.
154. Taft, K. L.; Delfs, C. D.; Papaefthymiou, G. C.; Foner, S.; Gatteschi, D.; Lippard, S. J. *J. Am. Chem. Soc.* **1994**, *116*, 823–832.
155. Benelli, C.; Parsons, S.; Solan, G. A.; Winpenny, R. E. P. *Angew. Chem., Int. Ed. Engl.* **1996**, *35*, 1825–1828.
156. Frey, M.; Harris, S. G.; Holmes, J. M.; Nation, D. A.; Parsons, S.; Tasker, P. A.; Winpenny, R. E. P. *Chem. Eur. J.* **2000**, *6*, 1407–1415.

- 157a. Caneschi, A.; Cornia, A.; Fabretti, A. C.; Gatteschi, D. *Angew. Chem., Int. Ed. Engl.* **1995**, *34*, 2716–2718.
- 157b. Asirvatham, S.; Khan, M. A.; Nicholas, K. M. *Inorg. Chem.* **2000**, *39*, 2006–2007.
158. Gorun, S. M.; Papaefthymiou, G. C.; Frankel, R. B.; Lippard, S. J. *J. Am. Chem. Soc.* **1987**, *109*, 3337–3348.
159. Taft, K. L.; Papaefthymiou, G. C.; Lippard, S. J. *Inorg. Chem.* **1994**, *33*, 1510–1520.
160. Micklitz, W.; McKee, V.; Rardin, R. L.; Pence, L. E.; Papaefthymiou, G. C.; Bott, S. G.; Lippard, S. J. *J. Am. Chem. Soc.* **1994**, *116*, 8061–8069.
161. Parson, S.; Solan, G. A.; Winpenny, R. E. P. *J. Chem. Soc., Chem. Commun.* **1995**, 1987–1988.
162. Powell, A. K.; Heath, S. L.; Gatteschi, D.; Pardi, L.; Sessoli, R.; Spina, G.; Del Giallo, F.; Pieralli, F. *J. Am. Chem. Soc.* **1995**, *117*, 2491–2502.
163. Goodwin, J. C.; Sessoli, R.; Gatteschi, D.; Wernsdorfer, W.; Powell, A. K.; Heath, S. L. *J. Chem. Soc., Dalton Trans.* **2000**, 1835–1840.
164. Watton, S. P.; Fuhrmann, P.; Pence, L. E.; Caneschi, A.; Cornia, A.; Abbati, G. L.; Lippard, S. L. *Angew. Chem., Int. Ed. Engl.* **1997**, *36*, 2774–2776.
165. Belli Dell'Amico, D.; Calderazzo, F.; Giovannitti, B.; Pelizzi, G. *J. Chem. Soc., Dalton Trans.* **1984**, 647–652.
166. McConnell, S.; Motevalli, M.; Thornton, P. *Polyhedron* **1995**, *14*, 459–462.
167. Blake, A. J.; Gould, R. O.; Milne, P. E. Y.; Winpenny, R. E. P. *J. Chem. Soc., Chem. Commun.* **1991**, 1453–1456.
168. Gutschke, S. O. H.; Price, D. J.; Powell, A. K.; Wood, P. T. *Angew. Chem., Int. Ed. Engl.* **1999**, *38*, 1088–1090.
169. Coxall, R. A.; Harris, S. G.; Henderson, D. K.; Parsons, S.; Tasker, P. A.; Winpenny, R. E. P. *J. Chem. Soc., Dalton Trans.* **2000**, 2349–2356.
170. Brechin, E. K.; Harris, S. G.; Parsons, S.; Winpenny, R. E. P. *J. Chem. Soc., Dalton Trans.* **1997**, 3403–3404.
171. Brechin, E. K.; Graham, A.; Parkin, A.; Parsons, S.; Seddon, A. M.; Winpenny, R. E. P. *J. Chem. Soc., Dalton Trans.* **2000**, 3243–3252.
172. Hong, M.; Jiang, F.; Huang, X.; Su, W.; Li, W.; Cao, R.; Liu, H. *Inorg. Chim. Acta* **1997**, *256*, 137–141.
173. Grillo, V. A.; Sun, Z.; Folting, K.; Hendrickson, D. N.; Christou, G. *Chem. Commun.* **1996**, 2233–2234.
174. Jones, P. L.; Byrom, K. J.; Jeffrey, J. C.; McCleverty, J. A.; Ward, M. D. *Chem. Commun.* **1997**, 1361–1362.
175. Beattie, J. K.; Hambley, T. W.; Klepetko, J. A.; Master, A. F.; Turner, P. *Chem. Commun.* **1998**, 45–46.
176. Brechin, E. K.; Harris, S. G.; Parsons, S.; Winpenny, R. E. P. *Angew. Chem., Int. Ed. Engl.* **1997**, *36*, 1967–1969.
177. Tsohos, A.; Dionyssopoloulou, S.; Raptopoulou, C. P.; Terzis, A.; Bakalbassis, E. G.; Perlepes, S. P. *Angew. Chem., Int. Ed. Engl.* **1999**, *38*, 983–985.
178. Clegg, W.; Garner, C. D.; Al-Samman, M. H. *Inorg. Chem.* **1983**, *22*, 1534–1538.
179. Benelli, C.; Blake, A. J.; Brechin, E. K.; Coles, S. J.; Graham, A.; Harris, S. G.; Meier, S.; Parkin, A.; Parsons, S.; Seddon, A. M.; Winpenny, R. E. P. *Chem. Eur. J.* **2000**, *6*, 883–896.
180. Graham, A.; Meier, S.; Parsons, S.; Winpenny, R. E. P. *Chem. Commun.* **2000**, 811–812.
181. Brechin, E. K.; Harris, S. G.; Parsons, S.; Winpenny, R. E. P. *Chem. Commun.* **1996**, 1439–1440.
182. Brechin, E. K.; Harris, S. G.; Harrison, A.; Parsons, S.; Whittaker, A. G.; Winpenny, R. E. P. *Chem. Commun.* **1997**, 653–654.

183. Bacchi, A.; Belli Dell'Amico, D.; Calderazzo, F.; Giurlani, U.; Pelizzi, G.; Rocchi, L. *Gazz. Chim. Ital.* **1992**, *122*, 429–435.
184. Cornia, A.; Fabretti, A. C.; Gatteschi, D.; Pályi, G.; Rentschler, E.; Shchegolikhina, O. I.; Zhdanov, A. A. *Inorg. Chem.* **1995**, *34*, 5383–5387.
185. Levitsky, M. M.; Shchegolikhina, O. I.; Zhdanov, A. A.; Igonin, V. A.; Ovchinniko, Yu. E.; Shklover, V. E.; Struchkov, Yu. T.; *J. Organomet. Chem.* **1991**, *401*, 199–210.
186. Yukawa, Y.; Igarashi, S.; Yamano, A.; Sato, S. *Chem. Commun.* **1997**, 711–712.
187. El Fallah, M. S.; Rentschler, E.; Caneschi, A.; Sessoli, R.; Gatteschi, D. *Inorg. Chem.* **1996**, *35*, 3723–3724.
188. Lai, S.-Y.; Lin, T.-W.; Chen, Y.-H.; Wang, C.-C.; Lee, G.-H.; Yang, M.-H.; Leung, M.-K.; Peng, S.-M. *J. Am. Chem. Soc.* **1999**, *121*, 250–251.
189. Strouse, J.; Layten, S. W.; Strouse, C. E. *J. Am. Chem. Soc.* **1977**, *99*, 562–571.
190. Eremenko, I. L.; Golubnichaya, M. A.; Nefedov, S. E.; Sidorov, A. A.; Golovanova, I. F.; Burkov, V. I.; Ellert, O. G.; Novotortsev, V. M.; Eremenko, L. T.; Sousa, A.; Bermejo, M. R. *Russ. Chem. Bull.* **1998**, *47*, 704–718.
191. Psomas, G.; Dendrinou-Samara, C.; Alexiou, M.; Tsohos, A.; Raptopoulou, C. P.; Terzis, A.; Kessissoglou, D. P. *Inorg. Chem.* **1998**, *37*, 6556–6557.
192. Grant, C. M. PhD Thesis, The University of Edinburgh, **1995**.
193. Brechin, E. K.; Gould, R. O.; Harris, S. G.; Parsons, S.; Winpenny, R. E. P. *J. Am. Chem. Soc.* **1996**, *118*, 11293–11294.
194. Dearden, A. L.; Parsons, S.; Winpenny, R. E. P. *Angew. Chem., Int. Ed. Engl.* **2001**, *40*, 151–154.
195. Carruthers, J. R.; Prout, K.; Rossotti, F. J. C. *Acta Cryst., Sect. B* **1975**, *31*, 2044–2046.
196. Ahlgrén, M.; Turpeinen, U.; Smolander, K. *Acta Cryst., Sect. B* **1980**, *36*, 1091–1095.
197. Smolander, K. *Acta Chem. Scand., Ser. A* **1983**, *37*, 5–13.
198. Muhonen, H.; Hatfield, W. E.; Helms, J. H. *Inorg. Chem.* **1986**, *25*, 800–805.
199. Wang, S.; Pang, Z.; Zheng, J.-C.; Wagner, M. J. *Inorg. Chem.* **1993**, *32*, 5975–5980.
200. Mikuriya, M.; Azuma, H.; Nukada, R.; Handa, M. *Chem. Lett.* **1999**, 57–58.
201. Butcher, R. J.; O'Connor, C. J.; Sinn, E. *Inorg. Chem.* **1981**, *20*, 537–545.
202. Agnus, Y.; Louis, R.; Metz, B.; Boudon, C.; Gisselbrecht, J. P.; Gross, M. *Inorg. Chem.* **1991**, *30*, 3155–3161.
203. Sakai, K.; Yamada, Y.; Tsubomura, T.; Yabuki, M.; Yamaguchi, M. *Inorg. Chem.* **1996**, *35*, 542–544.
204. Olejnik, Z.; Jezowska-Trzebiatowska, B.; Lis, T. *J. Chem. Soc., Dalton Trans.* **1986**, 97–101.
205. Saalfrank, R. W.; Löw, N.; Kareth, S.; Seitz, V.; Hampel, F.; Stalke, D.; Teichert, M. *Angew. Chem., Int. Ed. Engl.* **1998**, *37*, 172–175.
206. Lindeman, S. V.; Shchegolikhina, O. I.; Molodtsova, Y. A.; Zhdanov, A. A. *Acta Cryst., Sect. C* **1997**, *53*, 305–309.
207. Kruger, P. E.; Fallon, G. D.; Moubaraki, B.; Berry, K. J.; Murray, K. S. *Inorg. Chem.* **1995**, *34*, 4808–4814.
208. Vicente, R.; Escuer, A.; Solans, X.; Font-Bardia, M. *J. Chem. Soc., Dalton Trans.* **1996**, 1835–1838.
209. Matsumoto, N.; Mizuguchi, Y.; Mago, G.; Eguchi, S.; Miyasaka, H.; Nakashima, T.; Tuchagues, J.-P. *Angew. Chem., Int. Ed. Engl.* **1997**, *36*, 1860–1862.
210. Karlin, K. D.; Gan, Q.-F.; Farooq, A.; Liu, S.; Zubieta, J. *Inorg. Chem.* **1990**, *29*, 2549–2551.
211. Koolhaas, G. J. A. A.; Driessen, W. L.; van Koningsbruggen, P. J.; Reedijk, J.; Spek, A. L. *J. Chem. Soc., Dalton Trans.* **1993**, 3803–3807.
212. Hoskins, B. F.; Robson, R.; Smith, P. *J. Chem. Soc., Chem. Commun.* **1990**, 488–489.

213. McKee, V.; Tandon, S. S. *J. Chem. Soc., Dalton Trans.* **1991**, 221–229.
214. Tandon, S. S.; Thompson, L. K.; Bridson, J. N.; Benelli, C. *Inorg. Chem.* **1995**, *34*, 5507–5515.
215. Blake, A. J.; Gould, R. O.; Milne, P. E. Y.; Winpenny, R. E. P. *J. Chem. Soc., Chem. Commun.* **1991**, 1453–1455.
216. Blake, A. J.; Gould, R. O.; Grant, C. M.; Milne, P. E. Y.; Reed, D.; Winpenny, R. E. P. *Angew. Chem., Int. Ed. Engl.* **1994**, *33*, 195–197.
217. Christodoulou, D.; George, C.; Keefer, L. K. *J. Chem. Soc., Chem. Commun.* **1993**, 937–939.
218. Real, J. A.; De Munno, G.; Chiappeta, R.; Julve, M.; Lloret, F.; Journaux, Y.; Colin, J.-C.; Blondin, G. *Angew. Chem., Int. Ed. Engl.* **1994**, *33*, 1184–1186.
219. Tangoulis, V.; Raptopoulou, C. P.; Paschalidou, S.; Bakalbassis, E. G.; Perlepes, S. P.; Terzis, A. *Angew. Chem., Int. Ed. Engl.* **1997**, *36*, 1083–1085.
220. Tangoulis, V.; Raptopoulou, C. P.; Terzis, A.; Paschalidou, S.; Perlepes, S. P.; Bakalbassis, E. G. *Inorg. Chem.* **1997**, *36*, 3996–4006.
221. Tong, M.-L.; Lee, K. H.; Tong, Y.-X.; Chen, X.-M.; Mak, T. C. W. *Inorg. Chem.* **2000**, *39*, 4666–4669.
222. Han, M. Y.; Min, K. S.; Suh, M. P. *Inorg. Chem.* **1999**, *38*, 4374–4375.
223. Galy, J.; Mosset, A.; Grenthe, I.; Puigdomènech, I.; Sjöberg, B.; Hultén, F. *J. Am. Chem. Soc.* **1987**, *109*, 380–386.
224. Ardizzoia, G. A.; Angaroni, M. A.; La Monica, G.; Cariati, F.; Moret, M.; Masciocchi, N. *J. Chem. Soc., Chem. Commun.* **1990**, 1021–1023.
225. Wang, S.; Pang, Z.; Wagner, M. J. *Inorg. Chem.* **1992**, *31*, 5381–5388.
226. Blake, A. J.; Gould, R. O.; Milne, P. E. Y.; Winpenny, R. E. P. *J. Chem. Soc., Chem. Commun.* **1992**, 522–524.
227. Zhang, Y.; Thompson, L. K.; Bridson, J. N.; Bubenik, M. *Inorg. Chem.* **1995**, *34*, 5870–5877.
228. Geetha, K.; Nethaji, M.; Chakravarty, A. R. *Inorg. Chem.* **1997**, *36*, 6134–6137.
229. Zhu, F.-C.; Schmalke, H. W.; Fischer, B.; Dubler, E. *Inorg. Chem.* **1998**, *37*, 1161–1168.
230. Turpeinen, U.; Hämäläinen, R.; Reedijk, J. *Inorg. Chim. Acta* **1987**, *134*, 87–93.
231. Zhao, L.; Xu, Z.; Thompson, L. K.; Heath, S. L.; Miller, D. O.; Ohba, M. *Angew. Chem., Int. Ed. Engl.* **2000**, *39*, 3114–3117.
232. Baxter, P. N. W.; Lehn, J.-M.; Fischer, J.; Youinou, M.-T. *Angew. Chem., Int. Ed. Engl.* **1994**, *33*, 2284–2287.
233. Chen, X.-M.; Aubin, S. M. J.; Wu, Y.-L.; Yang, Y.-S.; Mak, T. C. W.; Hendrickson, D. N. *J. Am. Chem. Soc.* **1995**, *117*, 9600–9601.
234. Chen, X.-M.; Wu, Y.-L.; Tong, Y.-X.; Huang, X.-Y. *J. Chem. Soc., Dalton Trans.* **1996**, 2443–2448.
235. Cui, Y.; Chen, J.-T.; Huang, J.-S. *Inorg. Chim. Acta* **1999**, *293*, 129–139.
236. Abrahams, B. F.; Egan, S. J.; Robson, R. *J. Am. Chem. Soc.* **1999**, *121*, 3535–3536.
237. Chandrasekhar, V.; Kingsley, S. *Angew. Chem., Int. Ed. Engl.* **2000**, *39*, 2320–2322.
238. Schugar, H.; Ou, C.; Thich, G. A.; Potenza, J. A.; Lalancette, R. A.; Furey, Jr., W. *J. Am. Chem. Soc.* **1976**, *98*, 7357–7359.
239. Birker, P. J. M. W. L.; Freeman, H. C. *J. Am. Chem. Soc.* **1977**, *99*, 6890–6899.
240. Pecoraro, V. L.; Stemmler, A. J.; Gibney, B. R.; Bodwin, J. J.; Wang, H.; Kampf, J. W.; Barwinski, A. *Prog. Inorg. Chem.* **1997**, *45*, 83–117.
241. Burrow, H.; Brown, D. A.; Alcock, N. W.; Clase, H. J.; Wallbridge, M. G. H. *J. Chem. Soc., Chem. Commun.* **1995**, 1231–1232.
242. Burger, J.; Klüfers, P. *Angew. Chem., Int. Ed. Engl.* **1997**, *36*, 776–779.
243. Klüfers, P.; Schuhmacher, J. *Angew. Chem., Int. Ed. Engl.* **1995**, *34*, 2119–2121.

## TRANSITION METAL–NOBLE GAS COMPLEXES

D. C. GRILLS and M. W. GEORGE

School of Chemistry, University of Nottingham, University Park, Nottingham, NG7 2RD,  
United Kingdom

- I. Introduction
- II. The History of Transition Metal–Noble Gas Complexes
  - A. Matrix-Isolation Studies
  - B. Liquefied Noble Gas Studies
  - C. Gas-Phase Studies
  - D. Supercritical-Fluid Studies
- III. The Nature of the Transition Metal–Noble Gas Bond
- IV. Conclusions: Future Perspectives in Transition Metal–Noble Gas Bonding
- References

## I. Introduction

The first stable complex with transition metal–noble gas bonds has recently been reported by Seppelt and co-workers (1), thereby marking a key development in nearly 30 years of research worldwide. The reduction of  $\text{AuF}_3$  with elemental xenon in  $\text{HF/SbF}_5$  solution resulted in the formation of  $[\text{AuXe}_4^{2+}][\text{Sb}_2\text{F}_{11}^-]_2$ . Crystallization at  $-78^\circ\text{C}$  produced dark red crystals of  $[\text{AuXe}_4^{2+}][\text{Sb}_2\text{F}_{11}^-]_2$ , which were stable up to  $-40^\circ\text{C}$ . Indeed, under a xenon pressure of 10 bar this novel complex remained stable in solution up to room temperature. The X-ray crystal structure of  $[\text{AuXe}_4^{2+}][\text{Sb}_2\text{F}_{11}^-]_2$  is shown in Fig. 1. It consists of the square-planar cation  $\text{AuXe}_4^{2+}$  with four covalent Au–Xe bonds ranging in length from 272.8 to 275.0 pm. Three weak contacts between the Au center and the anion complete the coordination sphere. The complex was also characterized by Raman spectroscopy. A strong band was observed at  $129\text{ cm}^{-1}$ , which was assigned to the totally symmetric stretching vibration of  $\text{AuXe}_4^{2+}$  on the basis of the prediction of this band at  $\sim 100\text{ cm}^{-1}$  by a series of *ab initio* and density functional theory calculations. From these calculations the mean Au–Xe bond dissociation energy (BDE) was estimated to be  $199 \pm 49\text{ kJ mol}^{-1}$ , with the xenon

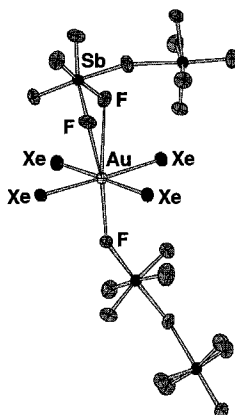


FIG. 1. The X-ray crystal structure of  $[\text{AuXe}_4]^{2+}[\text{Sb}_2\text{F}_{11}]^{2-}$  recently isolated by Seppelt and co-workers (1). Coordinates were obtained from the ICSD.

atoms functioning as simple  $\sigma$  donors toward  $\text{Au}^{2+}$ . The isolation of this molecule therefore represents a major breakthrough in the study of transition metal  $\sigma$  complexes.

The noble gases are extremely stable, chemically unreactive elements with closed electron shells and high ionization energies. Their chemistry is very limited, indeed, of the six noble gases, only krypton, xenon, and radon have so far been found to form stable compounds with other atoms at room temperature, most of which involve the most electronegative elements fluorine and oxygen. This can be attributed to the decrease in ionization energy and increase in polarizability on going down the group (see Table I).

Despite predictions of possible compounds containing bonds to helium and neon (2, 3), these elements retain the "noble gas" status and such

TABLE I

SOME PROPERTIES OF THE NOBLE GASES

Element	Symbol	First ionization energy ( $\text{kJ mol}^{-1}$ )	Polarizability ( $\times 10^{-30} \text{ m}^3$ )	Melting point at 1 atm (K)	Boiling point at 1 atm (K)	Critical temp. (K)	Critical pressure (atm)
Helium	He	2372	0.21	1.0	4.2	5.3	2.3
Neon	Ne	2080	0.40	24.6	27.1	44.4	26.2
Argon	Ar	1520	1.64	83.3	87.3	150.9	48.3
Krypton	Kr	1351	2.48	115.8	119.8	209.4	54.3
Xenon	Xe	1169	4.04	161.4	165.0	289.7	57.6
Radon	Rn	1037	5.30	202.0	211.3	378.2	62.0

molecules are yet to be observed. The technique of low-temperature matrix isolation spectroscopy has facilitated the generation of highly reactive argon compounds. However, only a few of these compounds have been produced. UV photolysis of Be atoms and molecular oxygen in an argon matrix at 10 K resulted in the formation of  $\text{ArBeO}$  (4), which was identified in the infrared by its  $\nu(\text{Ar–Be})$  stretch ( $1526\text{ cm}^{-1}$ ). The extremely high charge density of the  $\text{Be}^{2+}$  cation of BeO was capable of polarizing the Ar atoms, resulting in an induced dipole (i.e., van der Waals) interaction with the metal center. Theoretical calculations at the MP4 level, performed by Veldkamp and Frenking (5), predicted that the Ar–Be bond energy in this species would be  $28.0\text{ kJ mol}^{-1}$ . This should be contrasted with a recent very elegant study by Khriachtchev and co-workers (6), who succeeded in producing the first direct evidence<sup>1</sup> for a neutral species possessing a covalent bond to an argon atom. UV photolysis (127–160 nm) of HF in an Ar matrix at 7.5 K resulted in the appearance of three new bands in the infrared spectrum at about 1969.5, 687.0, and  $435.7\text{ cm}^{-1}$ , which were completely absent from the spectrum obtained with a pure Ar matrix. Identification of these bands was achieved through a series of isotopic substitution experiments. Changing the matrix from  $^{40}\text{Ar}$  to  $^{36}\text{Ar}$  and replacing HF with DF resulted in precise shifts in the positions of the IR bands (see Fig. 2). These shifts enabled them to assign the three bands to  $\nu(\text{H–Ar})$ ,  $\delta(\text{H–Ar–F})$  and  $\nu(\text{Ar–F})$  vibrations of  $\text{HArF}$ , isolated in solid Ar. The molecular properties of  $\text{HArF}$  were investigated using perturbation theory (MP2) and coupled cluster [CCSD(T)] molecular orbital calculations. These indicated that the molecule is linear with a strong degree of  $(\text{HAr})^+\text{F}^-$  charge transfer in the  $\text{HArF}$  electronic structure. Pyykkö has recently discussed the nature of the Ar–H bond through an analysis of the calculated bond lengths (7). The H–Ar bond length was calculated to be 133 pm, which corresponds to an argon radius of 103 pm. This is extremely close to the covalent radius of Ar (98 pm), which can be deduced from the bond lengths of the two gas-phase ions  $\text{ArH}^+$  (8) and  $\text{ArF}^+$  (9), suggesting that the Ar–H interaction in  $\text{HArF}$  is highly covalent in nature. In contrast, the effective Ar radius in  $\text{ArBeO}$  (obtained from the calculated Ar–Be bond length of 205 pm) is 126 pm, and although this is much lower than the van der Waals radius of Ar (188 pm), it demonstrates that the bonding in Ar–BeO is only weakly covalent.

<sup>1</sup>It should be noted that although Turner and co-workers originally discovered a covalent Ar interaction in  $\text{Cr}(\text{CO})_5\text{Ar}$  in 1975, the evidence they obtained for this bond was indirect.

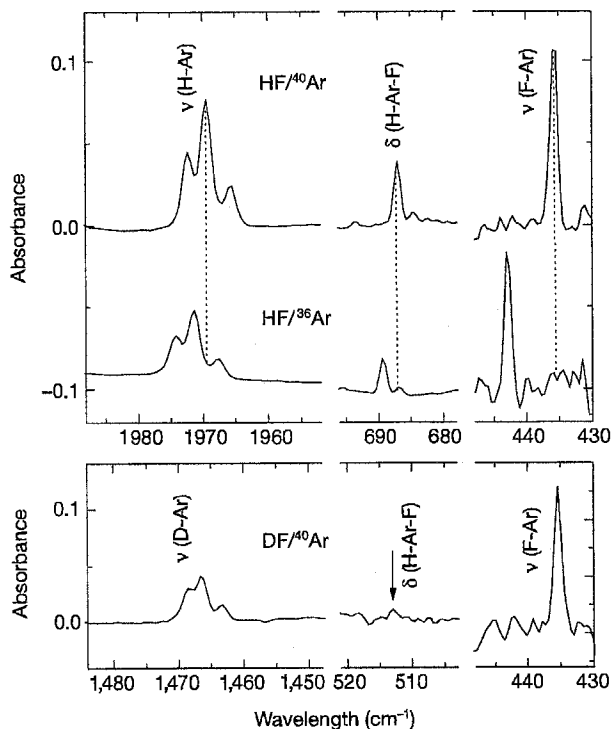


FIG. 2. The infrared absorptions of HArF in an argon matrix at 7.5 K, showing how  $^{40}\text{Ar}/^{36}\text{Ar}$  and H/D isotopic substitutions allowed the identification of these bands. Reproduced with permission from Fig. 1 in Ref. (6).

The chemistry of krypton is considerably more extensive than that of argon; nevertheless, it is still rather restricted. A series of krypton species containing Kr—H, Kr—C, and Kr—Cl bonds were recently formed in low-temperature matrix isolation experiments by Räsänen and co-workers (10). The only bulk compounds of krypton that have been isolated are  $\text{KrF}_2$  (a very powerful fluorinating agent) and a series of cationic species derived from it, e.g.,  $[\text{KrF}]^+[\text{SbF}_6]^-$  (11). All of these compounds contain krypton in the +2 oxidation state.

Xenon is much more reactive, forming a number of different fluorides, fluorocations, fluoroanions, oxides, and oxofluorides. The first noble gas compound to be discovered contained xenon—the orange/yellow solid  $\text{Xe}^+[\text{PtF}_6]^-$  discovered by Bartlett (12) in 1962.<sup>2</sup> The oxidation

<sup>2</sup>The original formulation of  $\text{Xe}^+[\text{PtF}_6]^-$  is now known to be incorrect. The material is actually thought to contain both  $[\text{XeF}]^+[\text{PtF}_6]^-$  and  $[\text{XeF}]^+[\text{Pt}_2\text{F}_{11}]^-$ .

states of Xe, which have been found since, range from +2 to +8 and its compounds exhibit a rich variety of stereochemistries. The fluorides ( $\text{XeF}_2$ ,  $\text{XeF}_4$ , and  $\text{XeF}_6$ ) are prepared by the direct reaction of xenon with fluorine. Most of the other compounds of xenon, e.g., the oxides and oxofluorides, are prepared from these binary fluorides. Reaction of fluoride-ion donors and acceptors with the binary fluorides and oxofluorides gives a variety of cationic and anionic derivatives. However, xenon has been found to form chemical bonds with elements other than fluorine and oxygen. For example, a stable Xe–C-bonded molecule,  $[\text{C}_6\text{F}_5\text{Xe}]^+[\text{B}(\text{C}_6\text{F}_5)_3\text{F}]^-$  was isolated in 1989 (13, 14). In condensed phases (15, 16), xenon readily forms the dixonon cation,  $\text{Xe}_2^+$ . A series of neutral compounds possessing Xe–H, Xe–I, Xe–Br, and Xe–S bonds have also recently been formed in low-temperature matrices (10).

In principle, radon should be even more reactive than xenon. In practice, the fact that it is intensely radioactive, with the longest-lived isotope ( $^{222}\text{Rn}$ ) having a half-life of only 3.8 days, means that it is very difficult to study. The  $\alpha$ -particles resulting from its decay destroy both the reagents and products; however, radiochemical tracer techniques have permitted the observation of a small number of species, e.g.,  $\text{RnF}_2$  and  $[\text{RnF}]^+[\text{TaF}_6]^-$ . For more details on recent advances in the main-group chemistry of the noble gases, see the excellent review by Holloway and Hope (17).

## II. The History of Transition Metal–Noble Gas Complexes

### A. MATRIX-ISOLATION STUDIES

Despite the fact that a transition metal–noble gas complex has been isolated only very recently, the study of noble gas coordination of transition metals actually has a long history. Early experiments used the technique of matrix isolation (18). Under the cryogenic conditions of frozen inert matrices, highly reactive photoproducts become sufficiently long-lived to allow their detection at leisure by conventional spectroscopic techniques such as UV/visible, IR, and EPR spectroscopy.

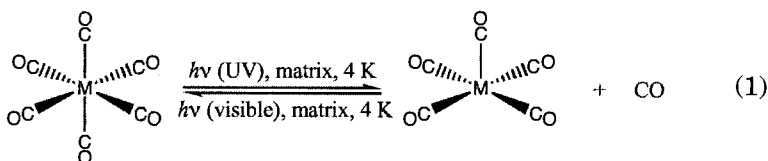
Following the discovery in 1972 by Turner and co-workers (18) that  $\text{Cr}(\text{CO})_5$  could form complexes with  $\text{CH}_4$ , Poliakoff and Turner used matrix isolation and infrared spectroscopy (19) to study the photolysis of  $\text{Fe}(\text{CO})_5$ . Photolysis of  $\text{Fe}(\text{CO})_5$  in a neon or argon matrix produced  $\text{Fe}(\text{CO})_4$ , which was found to have a relatively unusual structure with  $C_{2v}$  symmetry. The energy-factored (or Cotton–Kraihanzel) force field (EFFF) is a powerful method used in the analysis of the

$\nu(\text{C}-\text{O})$  vibrations of metal carbonyls (20). The structure of  $\text{Fe}(\text{CO})_4$  was established by performing a series of experiments using partial  $^{13}\text{C}$  enrichment and comparing the observed IR spectra with those predicted for different geometries using EFFF calculations. The best fit was obtained for a  $C_{2v}$  structure with angles between equivalent pairs of CO groups of about  $120^\circ$  and  $145^\circ$ . The angles are compatible only with a paramagnetic  $^3\text{B}_2$  electronic ground state expected on the basis of angular overlap (21), extended Hückel (22), and *ab initio* calculations (23) as well as more recent calculations. The paramagnetism of  $\text{Fe}(\text{CO})_4$  was subsequently confirmed using magnetic circular dichroism (MCD) spectroscopy (24). Triplet  $\text{Fe}(\text{CO})_4$  was also generated in Xe and  $\text{CH}_4$  matrices. However, in these matrices irradiation with near-IR light from the Nernst glower of an IR spectrometer or with IR radiation ( $\sim 2000\text{ cm}^{-1}$ ) from a CO laser (25) led to interesting changes in the IR spectrum. These spectroscopic changes were interpreted in terms of a geometry change in which the angle between one pair of CO groups increased from  $150^\circ$  to  $173.5^\circ$ . It was proposed that the new species were singlet  $\text{Fe}(\text{CO})_4\text{Q}$  ( $\text{Q} = \text{Xe}$  or  $\text{CH}_4$ ), with the Q species coordinated in an equatorial position. A series of experiments using Ar matrices doped with Xe or  $\text{CH}_4$  supported this explanation. Therefore  $\text{Fe}(\text{CO})_4\text{Xe}$  could reasonably be called one of the first transition metal-noble gas complexes.<sup>3</sup> At the time it was recognized that  $\text{Fe}(\text{CO})_4\text{Xe}$  was isoelectronic with  $[\text{Fe}(\text{CO})_4\text{I}]^-$ , a completely stable anion, so the existence of  $\text{Fe}(\text{CO})_4\text{Xe}$  did not seem totally unexpected. The authors also presented tentative evidence for the formation of  $\text{Fe}(\text{CO})_4\text{Kr}$ . (For a detailed discussion of the matrix isolation studies of  $\text{Fe}(\text{CO})_4$ , see Refs. 26 and 27.)

In 1975, Perutz and Turner reported the first detailed and systematic matrix-isolation study (28) of noble gas coordination to transition metal centers in an investigation that followed the UV/visible photochemistry of  $\text{M}(\text{CO})_6$  ( $\text{M} = \text{Cr}, \text{Mo},$  and  $\text{W}$ ) in noble gas, methane, and other matrices at 4 and 20 K. By comparing the IR spectra obtained with  $^{13}\text{C}$ -enriched metal hexacarbonyls with the results of EFFF calculations (29), it was demonstrated that, upon short-wavelength UV photolysis of  $\text{M}(\text{CO})_6$  in the matrix, a molecule of CO was ejected and a  $\text{M}(\text{CO})_5$  fragment with square-pyramidal ( $C_{4v}$ ) geometry was produced. The

<sup>3</sup> $\text{Cr}(\text{CO})_5\text{Ar}$  had already been observed in early matrix experiments (18), but the significance of the noble gas coordination was not considered in the literature until 1975 (28).

$M(CO)_5$  fragments exhibited long-wavelength visible absorption bands, and irradiation into these caused regeneration of  $M(CO)_6$  [Eq. (1)].



Although the IR spectra hardly changed in frequency between matrices, the visible absorption band of  $\text{Cr(CO)}_5$  was very sensitive to the matrix material (624 nm in Ne, 560 nm in  $\text{SF}_6$ , 547 nm in  $\text{CF}_4$ , 533 nm in Ar, 518 nm in Kr, 492 nm in Xe, and 489 nm in  $\text{CH}_4$ ) (Fig. 3). These shifts were very large when compared with those of related 18-electron complexes, e.g.,  $\text{Cr(CO)}_5\text{NH}_3$ , which were only of the order of 5 nm. In mixed matrices, such as Ne + 2% Xe,  $\text{Cr(CO)}_5$  showed two visible absorption bands in positions similar to those seen in the respective pure matrices and displayed substitutional photochemistry. Selective photolysis into one of these absorption bands caused a decrease in the intensity of that band, with a corresponding increase in the intensity of the other band. Furthermore, despite the small proportion of Xe in the mixed matrix, the band associated with the Xe matrix was much more intense than the one associated with the Ne matrix. These results demonstrated conclusively that the shift in visible absorption maximum was not due to

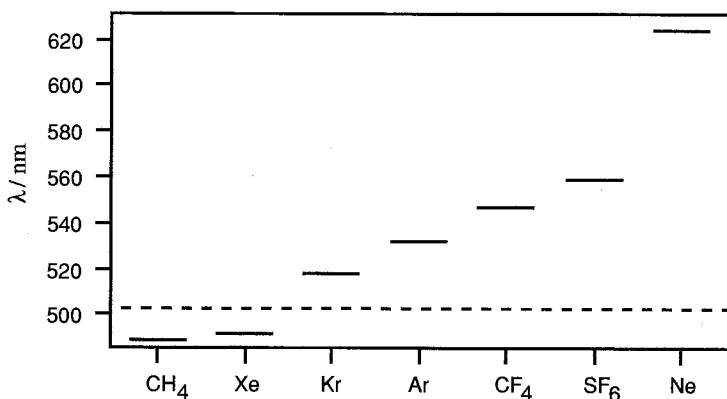


FIG. 3. Diagram representing the visible absorption maximum of  $\text{Cr(CO)}_5$  in different low-temperature matrices [adapted from Fig. 3 in Ref. (28).] The broken line is the value obtained from flash photolysis of  $\text{Cr(CO)}_6$  in cyclohexane solution (Kelly, J. M.; Hermann, H.; Koerner von Gustorf, E. *J. Chem. Soc., Chem. Commun.* **1973**, 105).

TABLE II

 IR AND VISIBLE ABSORPTION BANDS OF  $\text{Cr}(\text{CO})_5\text{L}$  ( $\text{L}$  = MATRIX SPECIES) IN LOW-TEMPERATURE MIXED MATRICES<sup>a</sup>

Matrix	IR band positions ( $\text{cm}^{-1}$ )			Visible band (nm)	Assignment
	<i>e</i>	Low-frequency $a_1$	High-frequency $a_1$		
Ne-2%Xe	1971 } 1966 }	1933 } 1943 }		628 487	$\text{Cr}(\text{CO})_5\text{Ne}$ $\text{Cr}(\text{CO})_5\text{Xe}$
	1972	1941		630 sh	$\text{Cr}(\text{CO})_5\text{Ne}$
Ar-2%Xe	1964.5 } 1962.9 }	1936.3 1939.1	2092.4 2088.6	533 525	$\text{Cr}(\text{CO})_5\text{Ar}$ $\text{Cr}(\text{CO})_5\text{Xe}$
	1964.9	1934.8		490	$\text{Cr}(\text{CO})_5\text{Ar}$
Ar-2%CH <sub>4</sub>	1964.3	1937.7		490	$\text{Cr}(\text{CO})_5\text{CH}_4$
	1961	1933		491	$\text{Cr}(\text{CO})_5\text{CH}_4$

<sup>a</sup> The data have been taken from Ref (28). Pairs of bands bracketed together were poorly resolved.

a generalized solvent effect and hence were interpreted as evidence for a stereospecific interaction between  $\text{Cr}(\text{CO})_5$  and the matrix material, which occupied the sixth coordination site as a weak ligand. From other mixed-matrix experiments, Perutz and Turner found that the strength of the  $\text{Cr}(\text{CO})_5\text{—L}$  interaction increased in the order  $\text{L} = \text{Ne} < \text{SF}_6 < \text{CF}_4 < \text{Ar} < \text{Kr} < \text{Xe} < \text{CH}_4$ ,<sup>4</sup> and only in a Ne matrix could the  $\text{M}(\text{CO})_5$  species be considered as essentially “naked.”

High-resolution IR spectra were recorded in the  $\nu(\text{C—O})$  region in the mixed-matrix experiments. This enabled small shifts in the IR band positions to be detected, and the assignment of these  $\nu(\text{C—O})$  bands to the  $a_1$  and  $e$  stretches of the two  $\text{Cr}(\text{CO})_5$ -matrix complexes (Table II). By analyzing the intensities of the IR bands in pure and mixed (Ar + 2% Xe) matrices and calculating CO-factored force constants for the two species, the axial-equatorial C—M—C bond angle,  $\alpha$ , was estimated. The calculated angle decreased from  $95.5 \pm 1^\circ$  in  $\text{Cr}(\text{CO})_5\text{Ar}$  to  $91.3 \pm 1^\circ$  in  $\text{Cr}(\text{CO})_5\text{Xe}$ . This change in bond angle was interpreted as being the main reason the visible absorption band of  $\text{Cr}(\text{CO})_5$  shifted with coordination of the different noble gas and alkane ligands. These findings were in agreement with those of Guenzburger *et al.* (30) and Burdett (21), who had previously shown that a small increase in  $\alpha$  can generate a large decrease in the energy of the  $e \rightarrow a_1$  transition (the visible absorption band) (see Fig. 4).

<sup>4</sup>Similar, but slightly less dramatic, shifts in  $\lambda_{\text{max}}$  were observed for  $\text{Mo}(\text{CO})_5$  and  $\text{W}(\text{CO})_5$ .

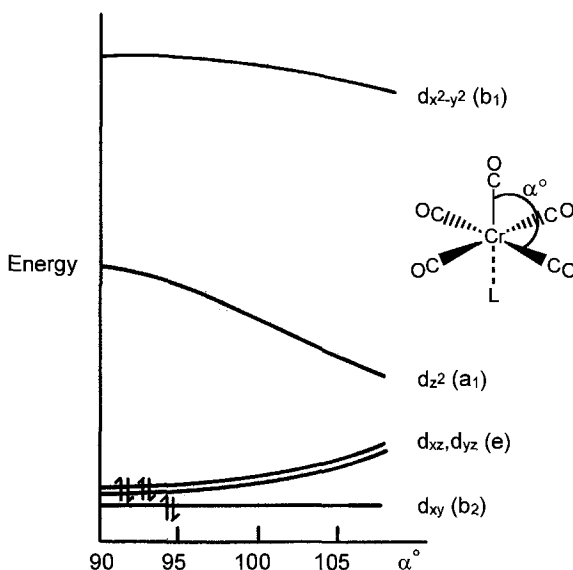


FIG. 4. The orbital energies of the  $d^6$   $\text{Cr}(\text{CO})_5$   $C_{4v}$  fragment as a function of the axial-equatorial C—M—C bond angle,  $\alpha$ . The energy of the  $e \rightarrow a_1$  transition is very sensitive to  $\alpha$ . Adapted from Fig. 4 in Turner, J. J.; Burdett, J. K.; Perutz, R. N.; Poliakoff, M. *Pure Appl. Chem.* **1977**, *49*, 271.

Following the original discovery (28) of an interaction between noble gas atoms and transition metal centers by Turner and Perutz, many more transition metal–noble gas complexes have been observed using matrix isolation. Numerous experimental and theoretical investigations have demonstrated that these elements coordinate to unsaturated transition metal centers via  $\sigma$  donation. The bonding in these  $\sigma$  complexes is fairly weak by conventional standards, and at room temperature they generally live, at most, on the microsecond timescale. In the majority of cases, the noble gas complex is formed by the UV photodissociation of a ligand (usually CO) from a precursor complex, followed by reaction of the photogenerated unsaturated intermediate with the noble gas (which is generally acting as both a reactant and matrix/solvent). Perutz and Turner's elegant mixed-matrix experiments confirmed that the large shifts in  $\lambda_{\text{max}}$  for the visible absorption bands of unsaturated transition metal complexes in different noble gas matrices were caused by coordination of the noble gases to the metal. Therefore, subsequent matrix-isolation studies have used the shift in the matrix visible spectrum between argon and xenon matrices as evidence for transition metal–noble gas bonding.

The UV photochemistry of  $\text{HMn(CO)}_5$  and  $\text{CH}_3\text{Mn(CO)}_5$  has been investigated (31, 32) in Ar and  $\text{CH}_4$  matrices at 20 K. It was demonstrated by  $^{13}\text{CO}$  isotopic labeling that photolysis of  $\text{HMn(CO)}_5$  in the matrix (31) produced the coordinatively unsaturated species  $\text{HMn(CO)}_4$  in a square-pyramidal configuration. Shifts in the visible absorption maximum between the Ar matrix (445 nm) and the  $\text{CH}_4$  matrix (400 nm) prompted the suggestion that the  $\text{CH}_4$  matrix was interacting with the Mn center as a weak sixth ligand. However, in light of the body of evidence (28) concerning noble gas coordination of transition metals, it is likely that the Ar matrix also coordinated to this unsaturated intermediate. Analogous experiments with  $\text{CH}_3\text{Mn(CO)}_5$  showed that UV photolysis in the matrix resulted in the formation of two isomers of  $\text{CH}_3\text{Mn(CO)}_4$  ( $C_{4v}$  and  $C_s$ ), each having a square-pyramidal structure. Again, shifts in the visible absorption maxima of both isomers between the Ar and  $\text{CH}_4$  matrices suggest that the matrices coordinate to the unsaturated Mn center (32).

In other studies,  $(\eta^2\text{-dfepe})\text{Cr(CO)}_4$  [ $\text{dfepe} = (\text{C}_2\text{F}_5)_2\text{PCH}_2\text{CH}_2\text{P}(\text{C}_2\text{F}_5)_2$ ] was photolyzed (33) in an Ar matrix at 12 K and a Xe matrix at 30 K. The UV/visible spectra of  $(\eta^2\text{-dfepe})\text{Cr(CO)}_4$  were essentially identical in both matrices. Upon photolysis, changes in the  $\nu(\text{C-O})$  IR bands demonstrated that a *cis*-carbonyl ligand was ejected, resulting in a 16-electron unsaturated photoproduct. This product exhibited a strong visible absorption band at 554 nm in the Ar matrix and at 490 nm in Xe. The large shift in visible absorption maximum proved that the species generated by photolysis were actually *fac*-( $\eta^2\text{-dfepe})\text{Cr(CO)}_3\text{L}$  ( $\text{L} = \text{Ar}$  or  $\text{Xe}$ ).

Transition metal-noble gas complexes containing a  $d^8$ -metal center have also been characterized using matrix-isolation spectroscopy. In addition to  $\text{Fe(CO)}_4\text{Xe}$  (19), discussed above, a series of ruthenium complexes have been reported. Photolysis of  $\text{Ru(CO)}_2(\text{PMe}_3)_2\text{H}_2$  and  $\text{Ru(CO)}_3(\text{PMe}_3)_2$  (34) in Ar and Xe matrices resulted in the photoejection of a molecule of hydrogen and CO, respectively, and formation of  $\text{Ru(CO)}_2(\text{PMe}_3)_2\text{L}$  ( $\text{L} = \text{Ar}$  or  $\text{Xe}$ ). The related complexes,  $\text{Ru(CO)}_2(\text{dmpe})\text{L}$  ( $\text{dmpe} = \text{Me}_2\text{PCH}_2\text{CH}_2\text{PMe}_2$ ;  $\text{L} = \text{Ar}$  or  $\text{Xe}$ ) were also generated following photolysis of  $\text{Ru(CO)}_3(\text{dmpe})$  in Ar and Xe matrices (35). Confirmation of noble gas coordination in these complexes was again obtained from shifts in the visible spectra between the Ar and Xe matrices. The shifts in the energy of the visible absorption bands for the  $d^6$  Cr, Mo, W, and Mn complexes were on the order of  $2000\text{ cm}^{-1}$ , whereas the shifts observed for the  $d^8$  complexes were much greater, being on the order of  $4800\text{ cm}^{-1}$ . Another complex for which an interaction with an Ar matrix has been postulated is the unsaturated intermediate,

$\text{Rh}_2(\mu\text{-Cl})_2(\text{CO})_3$  (36). This was generated by UV photolysis of  $\{\text{Rh}(\mu\text{-Cl})(\text{CO})_2\}_2$  in Ar,  $\text{CH}_4$ , and  $\text{N}_2$  matrices at 12 K. Evidence from IR and UV/visible spectra suggested that the primary photoproduct,  $\text{Rh}_2(\mu\text{-Cl})_2(\text{CO})_3$ , results from ejection of a terminal CO group and that the molecule retains the bridging Cl ligands. On the basis of the visible absorption spectrum, it was suggested that the unsaturated complex has a weak interaction with the Ar and  $\text{CH}_4$  matrices.

Seventeen-electron species have also been found to form complexes with noble gases. For example, the two paramagnetic radicals  $\text{KrMn}(\text{CO})_5$  and  $[\text{KrFe}(\text{CO})_5]^+$  have been detected by EPR spectroscopy by Morton, Perutz, and co-workers following the  $\gamma$ -radiolysis of  $\text{HMn}(\text{CO})_5$  and  $\text{Fe}(\text{CO})_5$  in krypton matrices at 77 and 20 K, respectively (37). Evidence for the interaction of Kr with the unpaired electron on the metal center came from the observation of hyperfine coupling with a single  $^{83}\text{Kr}$  nucleus in the EPR spectra of these species. As an example, the EPR spectrum obtained from  $\gamma$ -radiolysis of  $\text{HMn}(\text{CO})_5$  in a matrix of krypton enriched to 42% in the isotope  $^{83}\text{Kr}$  ( $I = \frac{9}{2}$ ) is shown in Fig. 5. The spectrum shows the resonances of the  $\text{Mn}(\text{CO})_5$  radical with characteristic decets of satellites due to hyperfine interaction between the unpaired spin on Mn and a  $^{83}\text{Kr}$  nucleus.

Matrix isolation spectroscopy has proved an invaluable technique for the isolation and characterization of transition metal–noble gas complexes (see Table III). However, this technique has obvious limitations. Although photoproducts in low-temperature matrices can be made to react with added dopants, it is impossible to accurately predict their reactivity and mechanisms in solution at room temperature. Therefore, in the years following the original discovery of transition metal–noble gas interactions in matrices, new techniques have been used to probe these species in solution, gas phase, and supercritical fluids.

## B. LIQUEFIED NOBLE GAS STUDIES

The liquid ranges of the individual noble gases are extremely short at atmospheric pressure (e.g., 161.4–165.0 K for Xe; see Table I). If the pressure over the liquid is allowed to rise, however, a substantial liquid temperature range becomes available (e.g., 160–248 K for Xe at 22 atm; see Fig. 6). The solubilities of organometallic complexes in liquefied noble gases, particularly xenon, are generally comparable to those in organic hydrocarbon solvents such as heptane at the same temperature. Furthermore, the noble gases are completely transparent throughout the IR, visible, and UV regions, providing a clear spectroscopic window and permitting very long cell path lengths to be used, thus overcoming

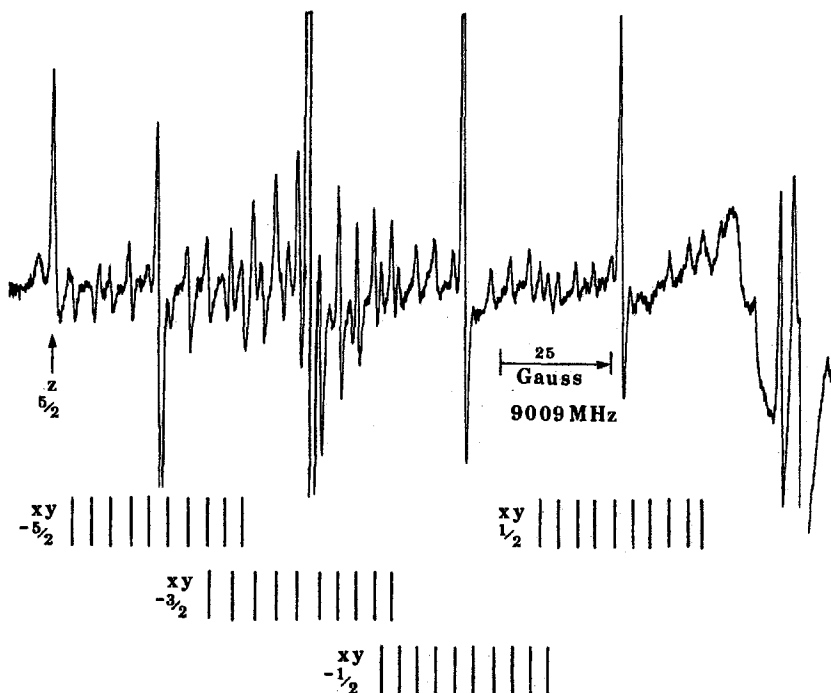


FIG. 5. Part of the EPR spectrum of  $\text{KrMn(CO)}_5$ , obtained following  $\gamma$ -radiolysis of  $\text{HMn(CO)}_5$  in a matrix of krypton enriched to 42% in the isotope  $^{83}\text{Kr}$  ( $I = \frac{9}{2}$ ). Coupling between the unpaired spin and the  $^{83}\text{Kr}$  nucleus is demonstrated by the decets of satellites. Reproduced with permission from Fig. 2 in Ref. (37).

TABLE III

SPECTROSCOPIC DATA USED TO CONFIRM THE FORMATION OF TRANSITION METAL–NOBLE GAS COMPLEXES IN MATRIX-ISOLATION EXPERIMENTS

Complex	$\nu(\text{C—O})$ ( $\text{cm}^{-1}$ )	$\lambda_{\text{max}}$ (nm)	Reference
$\text{Fe(CO)}_4$ in an Ar matrix	1995, 1989, 1973		
$\text{Fe(CO)}_4\text{Xe}$	2085, 1990, 1983, 1950	—	19
$\text{Mn(CO)}_5\text{Kr}$ and $[\text{Fe(CO)}_5\text{Kr}]^+$	—	—	37
<i>fac</i> -( $\eta^2$ -dfepe) $\text{Cr(CO)}_3\text{Ar}$	2020, 1965, 1922	545	
<i>fac</i> -( $\eta^2$ -dfepe) $\text{Cr(CO)}_3\text{Xe}$	2013, 1957, 1924	490	33
<i>mer</i> -( $\eta^2$ -dfepe) $\text{Cr(CO)}_3\text{Xe}$	2034, 1949 sh		
$\text{Ru(CO)}_2(\text{PMe}_3)_2\text{Ar}$	1850	423	34
$\text{Ru(CO)}_2(\text{PMe}_3)_2\text{Xe}$	1844	352	
$\text{Ru(CO)}_2(\text{dmpe})\text{Ar}$	1966, 1904	410, 600	35
$\text{Ru(CO)}_2(\text{dmpe})\text{Xe}$	1960, 1896	345, 457	

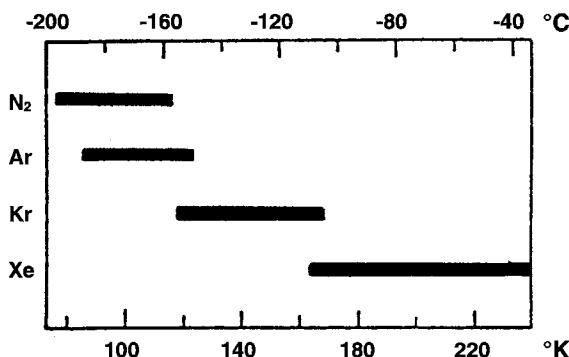
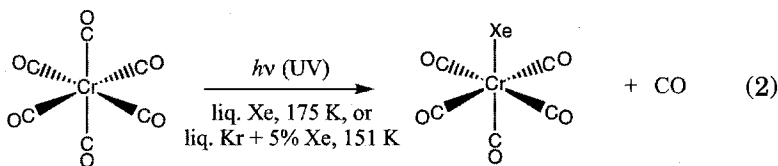


FIG. 6. Diagram showing the liquid range of the noble gases from 1 to 15 atm. Reproduced from Fig. 1 in Poliakoff, M.; Gadd, G. E.; Simpson, M. B.; Turner, J. J.; Upmacis, R. K. *Proc. 4th Int. Symp. Hom. Catal.* 1985, Leningrad, 873.

any problems of low solubility. The use of liquefied noble gases as solvents therefore permits the formation and detection of unstable species in solution.

The first transition metal–noble gas complex to be observed in liquefied noble gas solution was  $\text{Cr}(\text{CO})_5\text{Xe}$  (38). Continuous UV photolysis of  $\text{Cr}(\text{CO})_6$  dissolved in liquid Xe at 175 K or liquid Kr doped with 5% Xe at 151 K produced a new species. This new species had  $\nu(\text{C}-\text{O})$  IR bands (Fig. 7) which could be assigned to  $\text{Cr}(\text{CO})_5\text{Xe}$  by comparison with those of  $\text{Cr}(\text{CO})_5\text{Xe}$  in a Xe matrix [Eq. (2)]. When the photolysis was halted,  $\text{Cr}(\text{CO})_5\text{Xe}$  decayed with a lifetime of  $\sim 2$  s. The activation energy for the thermal decay of  $\text{Cr}(\text{CO})_5\text{Xe}$  in liquid Kr + 5% Xe was determined to be  $E_a = 15 \pm 2 \text{ kJ mol}^{-1}$ . The surprisingly long lifetime of  $\text{Cr}(\text{CO})_5\text{Xe}$  in solution at this temperature was attributed to the high concentration of Xe and the extremely low concentration of the other reactants.



More recently, Weiller (39) has extended this work by performing a detailed rapid-scan FTIR study of  $\text{M}(\text{CO})_6$  ( $\text{M} = \text{Cr}$  or  $\text{W}$ ) in liquid Xe and liquid Kr. A pulsed UV laser source, synchronized to the moving mirror of the FTIR interferometer, was used to photolyze the hexacarbonyls.  $\text{M}(\text{CO})_5\text{Kr}$  was characterized in liquid Kr,  $\text{Cr}(\text{CO})_5\text{Xe}$  in liquid Xe, and  $\text{W}(\text{CO})_5\text{Xe}$  in liquid Xe and liquid Kr doped with 5% Xe.  $\text{M}(\text{CO})_5\text{Kr}$  has

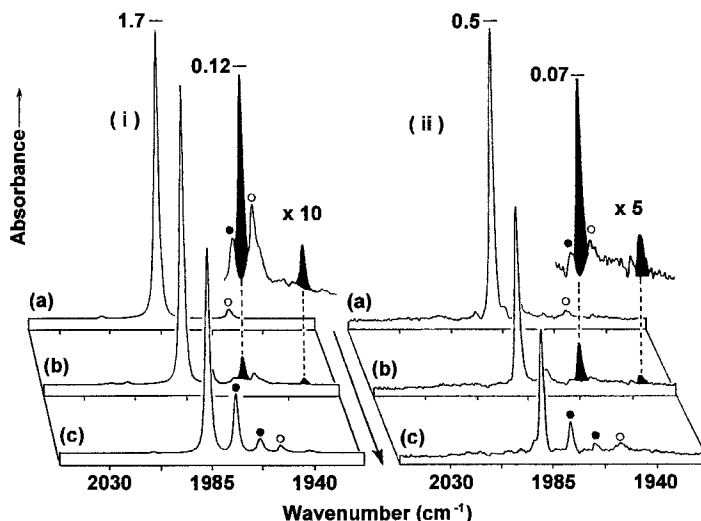
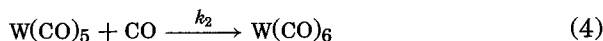
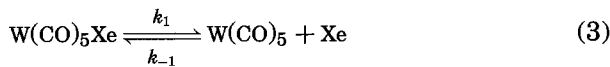


FIG. 7. FTIR spectra of  $\text{Cr(CO)}_6$  dissolved in (1) pure liquid Xe at 175 K and (2) liquid Kr doped with 5% Xe at 151 K. (a) Spectra before photolysis; (b) spectra during UV photolysis; (c) spectra after photolysis. The total time of the experiment is  $\sim 1$  min. In each spectrum, the strongest band is due to  $\text{Cr(CO)}_6$  and other bands are assigned as follows: black,  $\text{Cr(CO)}_5\text{Xe}$ ;  $\circ$ ,  $\text{Cr(CO)}_5(^{13}\text{CO})$  (natural abundance);  $\bullet$ ,  $\text{Cr(CO)}_5\text{N}_2$  formed from a small amount of  $\text{N}_2$  impurity. Reproduced with permission from Fig. 1 in Ref. (38).

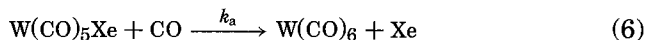
a lifetime of  $\sim 0.1$  s at 150 K in liquid Kr, while  $\text{W(CO)}_5\text{Xe}$  has a lifetime of  $\sim 1.5$  min at 170 K in liquid Xe. In order to elucidate the mechanism of the substitution of  $\text{W(CO)}_5\text{Xe}$  by CO to regenerate  $\text{W(CO)}_6$ , the observed rate of decay ( $k_{\text{obs}}$ ) of  $\text{W(CO)}_5\text{Xe}$  was measured as a function of CO concentration at six temperatures from 173 to 198 K. Applying the steady-state approximation to equations (3)–(4) for a dissociative substitution gives an expression (5) for  $k_{\text{obs}}$  that predicts a linear relationship of  $k_{\text{obs}}$  with  $[\text{CO}]$ .



$$k_{\text{obs}} = \frac{k_1 k_2 [\text{CO}]}{k_{-1} [\text{Xe}] + k_2 [\text{CO}]} \approx \frac{K_1 k_2 [\text{CO}]}{[\text{Xe}]} \quad \text{where } K_1 = \frac{k_1}{k_{-1}} \quad (5)$$

However, it was noted that, under the conditions of the experiment (i.e., when CO is in excess and the intermediate reacts via pseudo-first-

order kinetics), an associative mechanism could also predict a linear relationship of  $k_{\text{obs}}$  with  $[\text{CO}]$  [Eqs. (6)–(7)].



$$k_{\text{obs}} = k_a[\text{CO}] \quad (7)$$

Ideally, the measurement of  $k_{\text{obs}}$  as a function of Xe concentration would have provided strong evidence for the type of mechanism, since for a dissociative mechanism,  $k_{\text{obs}} \propto 1/[\text{Xe}]$ , whereas an associative mechanism would have no dependence on  $[\text{Xe}]$ . However, it is not possible to vary the concentration of Xe in liquid Xe, and so pre-exponential factors  $A$  obtained from Arrhenius plots were used to differentiate the two mechanisms. The value of  $\log A$  was found to lie within the expected range for a unimolecular dissociation reaction, and it was concluded that this reaction occurs by a dissociative substitution mechanism in liquid Xe. The Arrhenius plot therefore gave an estimate of the W–Xe BDE,  $\Delta H_{\text{W-Xe}} = 35.1 \pm 0.8 \text{ kJ mol}^{-1}$ .

Time-resolved infrared (TRIR) spectroscopy, a combination of UV/visible flash photolysis and fast infrared detection, is a powerful tool for probing highly unstable organometallic complexes in solution (40). Fast TRIR spectra may be obtained using a cw IR source (global or tunable IR CO or diode laser) to monitor the change in absorbance at one IR frequency following UV/visible flash photolysis (see Fig. 8). IR spectra are built up using the *point-by-point* approach by repeating this measurement at different frequencies and plotting the changes in absorbance versus wavenumber. An alternative approach to TRIR spectroscopy on the nanosecond timescale is time-resolved step-scan FTIR ( $s^2$ -FTIR) (41).  $s^2$ -FTIR is a technique that exploits spectral multiplexing, increased IR throughput, and fast data acquisition. The  $s^2$ -FTIR technique involves the movable mirror of the interferometer being displaced in a stepwise manner (see Fig. 8). At each mirror position, the time-dependent change in IR intensity is measured following excitation, producing a series of time-dependent interferograms. Fourier transformation of an interferogram corresponding to a particular time delay following excitation yields the spectral intensity changes at that particular time slice, and this can easily be converted to the corresponding IR absorption spectrum. Repeating this process at a variety of time delays following excitation results in a series of time-resolved spectra.

Bergman and co-workers used IR laser-based TRIR spectroscopy to investigate alkane C–H activation with  $(\eta^5\text{-C}_5\text{Me}_5)\text{Rh}(\text{CO})_2$  in liquid Kr and liquid Xe in the presence of cyclohexane (42–44) and neopentane (45). This permitted the detection of the noble gas intermediates,

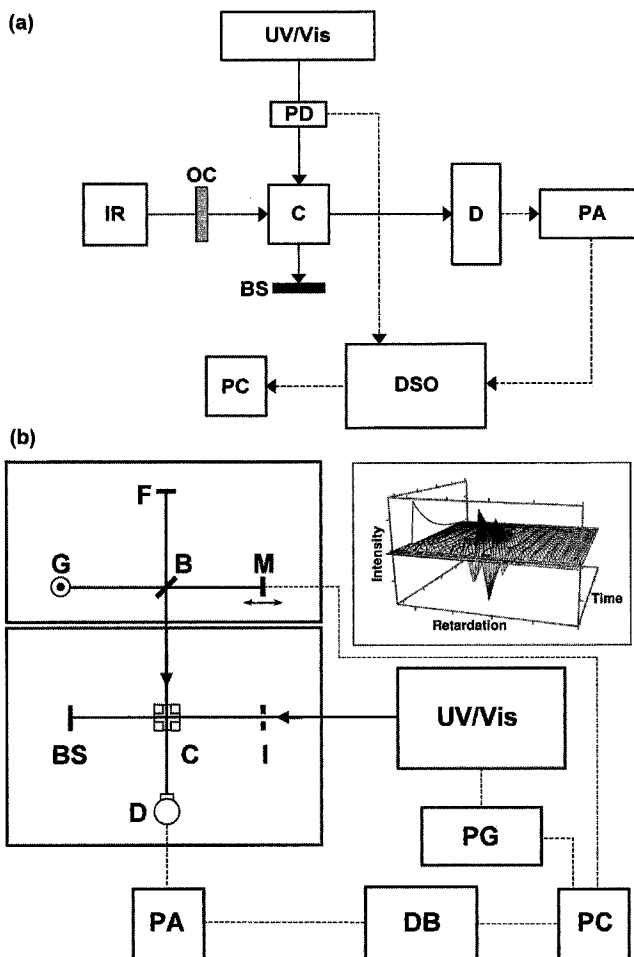
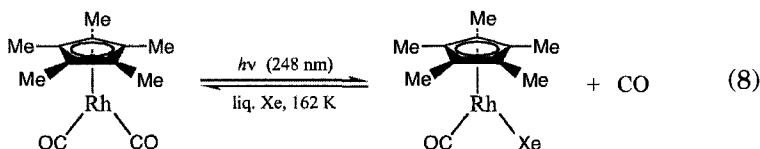


FIG. 8. (a) Schematic diagram of the point-by-point TRIR apparatus at Nottingham. Solid lines represent laser beams while broken lines indicate electrical connections. Components are labeled as follows: BS, beam stop; C, IR cell; D, IR detector; DSO, digital storage oscilloscope; IR, cw IR laser; OC, optical chopper; PA, preamplifier; PC, personal computer; PD, photodiode; UV/Vis, pulsed UV/visible laser. (b) Schematic diagram of the step-scan FTIR apparatus at Nottingham which is based around a Nicolet Magna 860 interferometer. Solid lines represent beams and dashed lines indicate electrical connections. Components are labeled as follows: B, beamsplitter; BS, beam stop; C, IR cell; D, IR detector; DB, digitizing board; F, fixed mirror; G, global IR source; I, iris; M, moving mirror; PA, preamplifier; PC, personal computer; PG, pulse generator; UV/Vis, pulsed UV/visible laser. The inset shows an example of the series of time-dependent interferograms that are generated during the experiment.

$(\eta^5\text{-C}_5\text{Me}_5)\text{Rh}(\text{CO})\text{L}$  ( $\text{L} = \text{Kr}$  and  $\text{Xe}$ ), and the observation that the Kr complex decays much more rapidly than the Xe complex, owing to the stronger metal–noble gas bond in the latter.



In an effort to calculate the Rh–Xe bond energy, Bergman and colleagues measured the CO substitution kinetics of  $(\eta^5\text{-C}_5\text{Me}_5)\text{Rh}(\text{CO})\text{Xe}$  in liquid Xe with TRIR spectroscopy (46). In liquid Xe at 162 K, photolysis of  $(\eta^5\text{-C}_5\text{Me}_5)\text{Rh}(\text{CO})_2$  [Eq. (8)] resulted in a new  $\nu(\text{C}-\text{O})$  IR band, which was consistent with  $(\eta^5\text{-C}_5\text{Me}_5)\text{Rh}(\text{CO})$  previously observed (47) in low-temperature matrices. The reaction of  $(\eta^5\text{-C}_5\text{Me}_5)\text{Rh}(\text{CO})\text{Xe}$  with dissolved CO was found to be very fast, with a rate constant  $k_{\text{CO}} = 5.7 (\pm 0.6) \times 10^5$  to  $1.9 (\pm 0.2) \times 10^6 \text{ dm}^3 \text{ mol}^{-1} \text{ s}^{-1}$  over the temperature range 202–242 K. Bergman used a similar approach to that used previously by Weiller, calculating the Arrhenius pre-exponential factor to identify the mechanism of CO substitution in liquid Xe. The kinetics for the reaction of  $(\eta^5\text{-C}_5\text{Me}_5)\text{Rh}(\text{CO})\text{Xe}$  with CO were consistent with an associative substitution mechanism, with the following activation parameters for the bimolecular rate constant:  $\log(A) = 8.8 \pm 0.3$  ( $\Delta S^\ddagger = -83.7 \pm 4.2 \text{ J mol}^{-1} \text{ K}^{-1}$ ) and  $E_a = 11.7 \pm 1.3 \text{ kJ mol}^{-1}$  ( $\Delta H^\ddagger = 10.0 \pm 1.3 \text{ kJ mol}^{-1}$ ). Therefore, only a lower estimate for the Rh–Xe bond energy could be calculated:  $\Delta H_{\text{Rh-Xe}} \geq 11.7 \pm 1.3 \text{ kJ mol}^{-1}$ .

Similar TRIR experiments were performed with  $\text{Tp}^*\text{Rh}(\text{CO})_2$  and  $\text{Bp}^*\text{Rh}(\text{CO})_2$  [ $\text{Tp}^* = \text{hydridotris}(3,5\text{-dimethylpyrazolyl})\text{borate}$ ;  $\text{Bp}^* = \text{dihydridobis}(3,5\text{-dimethylpyrazolyl})\text{borate}$ ] in liquid Xe solution at 223 K (48). From the positions of the observed transient infrared bands, it was found that the  $\text{Tp}^*$  species forms two xenon complexes upon photolysis,  $(\eta^3\text{-Tp}^*)\text{Rh}(\text{CO})\text{Xe}$  and  $(\eta^2\text{-Tp}^*)\text{Rh}(\text{CO})\text{Xe}$ , and that  $\text{Bp}^*\text{Rh}(\text{CO})\text{Xe}$  is produced from  $\text{Bp}^*\text{Rh}(\text{CO})_2$ .

The group VII complex  $\text{CpRe}(\text{CO})_2\text{Xe}$  was characterized in liquid Xe at 170 K and proved to be remarkably stable at this temperature (49). Continuous UV photolysis of  $\text{CpRe}(\text{CO})_3$  dissolved in liquid Xe resulted in the formation of two new  $\nu(\text{C}-\text{O})$  IR bands, which were readily assigned to  $\text{CpRe}(\text{CO})_2\text{Xe}$  by comparison with previous matrix-isolation and TRIR studies (see below). By monitoring the decay of the  $\nu(\text{C}-\text{O})$  bands, it was shown that  $\text{CpRe}(\text{CO})_2\text{Xe}$  has a lifetime of 3.5 min at 170 K in liquid Xe. This is very similar to the lifetime of the analogous

alkane complex  $\text{CpRe}(\text{CO})_2(n\text{-heptane})$ , which has a lifetime of 2.5 min in *n*-heptane at 190 K. The significance of these lifetimes is discussed further in Section II,D, when we examine photochemistry in supercritical noble gas solution.

### C. GAS-PHASE STUDIES

The advantage of the gas phase for studying reactive organometallic intermediates is that it is solvent-free, permitting naked 16-electron fragments to be produced more easily than in solution. Therefore, the effect of coordination of noble gas atoms is more easily detected than in the liquid phase owing to changes in both the spectrum and kinetics upon addition of the noble gas. However, photogenerated intermediates are often observed in vibrationally excited states and can undergo multiple ligand dissociations, whereas in studies in solution and solid matrices, collisional deactivation produces the ground vibrational state on the picosecond time scale. Since gas-phase studies are performed at room temperature, the resulting noble gas complexes will be extremely short-lived, although the lifetimes are sometimes lengthened by the reduced rates of intermolecular collisions in the gas phase. Therefore, a pulsed UV source is used to initiate the reaction, which is probed in real time in the UV/visible or infrared with flash lamps or IR lasers, respectively. In 1981, Breckenridge and co-workers performed laser flash photolysis experiments on  $\text{Cr}(\text{CO})_6$  vapor in the presence of other gases (50). After 355-nm photolysis of pure  $\text{Cr}(\text{CO})_6$  vapor or  $\text{Cr}(\text{CO})_6$  with 20 torr of He buffer gas, a transient absorption was observed at 485 nm, having a lifetime of hundreds of microseconds. With Ar present at  $\sim 150$  torr, a much shorter-lived species was also observed (lifetime  $\leq 50 \mu\text{s}$ ), displaying an absorption maximum at 500–530 nm. This shift in the transient visible absorption spectrum prompted these investigators to assign the short-lived species to the argon complex  $\text{Cr}(\text{CO})_5\text{Ar}$ . However, a subsequent flash photolysis study in the same laboratory (51) appeared to contradict this conclusion. This time, photolysis of  $\text{Cr}(\text{CO})_6$  in the presence of Ar,  $\text{CH}_4$ , or  $\text{C}_3\text{H}_8$  buffer gases produced transient absorption spectra that did not differ from those obtained with He buffer gas. Therefore, it appeared that, in the gas phase, the interaction of Ar with transition metal centers was too weak to permit the spectroscopic observation of such complexes.

More recently, Weitz and co-workers studied the bonding of Xe and Kr atoms to  $\text{M}(\text{CO})_5$  fragments [ $\text{M} = \text{Cr}$  and  $\text{Mo}$  (Xe only) and  $\text{W}$ ] in the gas phase using TRIR spectroscopy (52). The IR  $\nu(\text{C}-\text{O})$  bands of metal carbonyls in the gas phase are much broader than those in solution or

in a matrix because of rotation. This can lead to more substantial overlap of the bands, but nevertheless can provide excellent kinetic data. The TRIR characterization of  $\text{W}(\text{CO})_5\text{Xe}$  in the gas phase is shown in Fig. 9. The solid line spectrum was recorded  $1\ \mu\text{s}$  after 355-nm photolysis of 10 mtorr of  $\text{W}(\text{CO})_6$  and 80 torr of He. The parent absorption at  $2000\ \text{cm}^{-1}$  was bleached and a new band at lower wavenumber was observed. This was assigned to the  $e$  mode  $\nu(\text{C}-\text{O})$  band of “naked”  $\text{W}(\text{CO})_5$ , which possesses  $C_{4v}$  symmetry. Replacing the He with Xe caused the positive band to shift even lower in frequency to  $1975\ \text{cm}^{-1}$ . This absorption was assigned to the  $e$  band of  $\text{W}(\text{CO})_5\text{Xe}$ . A similar spectrum, corresponding to  $\text{W}(\text{CO})_5\text{Kr}$ , was obtained with 500 torr of Kr buffer gas; in this case, however, the positive band was overlapped with that of  $\text{W}(\text{CO})_5$ . With 500 torr of Ar buffer gas, the TRIR spectrum was essentially identical to that obtained with He, further confirming that  $\text{M}(\text{CO})_5\text{Ar}$  species cannot be spectroscopically distinguished from naked  $\text{M}(\text{CO})_5$  on this time scale. By investigating the CO substitution kinetics, Weitz and co-workers were able to calculate that the  $\text{M}-\text{Xe}$  ( $\text{M} = \text{Cr}, \text{Mo}, \text{or W}$ ) BDE has an average value of  $35.1\ \text{kJ mol}^{-1}$ . Owing to the overlap of the  $\text{W}(\text{CO})_5\text{Kr}$  band with that of  $\text{W}(\text{CO})_5$ , only an upper limit for the  $\text{W}-\text{Kr}$  BDE could be estimated ( $25.1\ \text{kJ mol}^{-1}$ ). An upper limit for the  $\text{W}-\text{Ar}$  BDE was tentatively estimated to be  $\sim 12.6\ \text{kJ mol}^{-1}$ . Ishikawa and co-workers (53) also recorded the TRIR spectra of  $\text{W}(\text{CO})_5\text{Xe}$  at five time intervals between  $0.4$  and  $2\ \mu\text{s}$  following 355-nm

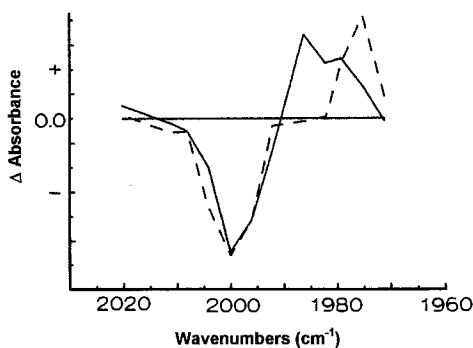
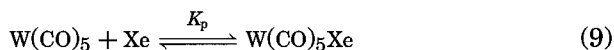


Fig. 9. TRIR spectra obtained  $1\ \mu\text{s}$  following 355-nm photolysis of  $\text{W}(\text{CO})_6$  in the gas phase. The solid line is the spectrum obtained with  $\sim 10$  mtorr of  $\text{W}(\text{CO})_6$  and 80 torr of He. The dashed line is that obtained when the He was replaced by 80 torr of Xe. The negative bands are due to depletion of  $\text{W}(\text{CO})_6$  and the positive bands represent the production of “naked”  $\text{W}(\text{CO})_5$  (solid line) and  $\text{W}(\text{CO})_5\text{Xe}$  (dashed line). The apparent production of two positive bands for naked  $\text{W}(\text{CO})_5$  is a result of the low spectral resolution of the IR CO laser used in these experiments. Reproduced with permission from Fig. 1 in Ref. (52).

photolysis of  $\text{W(CO)}_6$  ( $\sim 10$  mtorr) in the presence of Xe ( $\sim 6.0$  torr) at a total pressure of 10 torr with balance Ar. Their spectra were similar to those obtained by Weitz. However, Ishikawa probed to lower wavenumber and was therefore able to observe the lower intensity  $a_1$  mode  $\nu(\text{C-O})$  band of  $\text{W(CO)}_5\text{Xe}$  at  $1952\text{ cm}^{-1}$  in addition to the  $e$  band at  $1973\text{ cm}^{-1}$ . The position of the  $a_1$   $\nu(\text{C-O})$  band is more sensitive than that of the  $e$  band to interaction with the noble gas. By measuring the rates of decay of the  $\nu(\text{C-O})$  bands at various Xe pressures, they were able to calculate the equilibrium constant  $K_p$  for the reaction of  $\text{W(CO)}_5$  with Xe [Eq. (9)].



The W–Xe BDE was then evaluated by statistical mechanics from  $K_p$ , measured at a single temperature. Depending on the assumed rigidity of the xenon complex, these calculations predicted a W–Xe BDE ranging from  $29.3$  to  $41.0\text{ kJ mol}^{-1}$ , which is consistent with the W–Xe BDE of  $34.3\text{ kJ mol}^{-1}$  measured by Weitz (52). Their results suggested that Xe was acting as a weak  $\sigma$  donor toward the metal center. This led them to propose the schematic molecular orbital energy level diagram shown in Fig. 10 for the interaction of Xe with  $\text{W(CO)}_5$ . In this diagram, a net electron flow from Xe to the  $a_1$  orbital of  $\text{W(CO)}_5$  involves

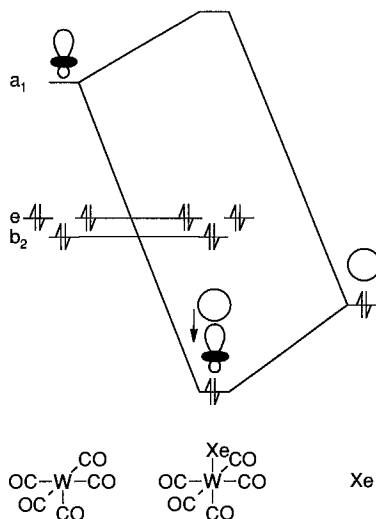


FIG. 10. The orbital interactions involved in the coordination of Xe onto  $\text{W(CO)}_5$ , proposed by Ishikawa and co-workers. The arrow indicates the direction of electron flow. Adapted from Fig. 10 in Ref. (53).

$\pi^*$  orbitals of the equatorial CO groups (see below). It is interesting that this molecular orbital energy level diagram is very similar to that proposed earlier by Burdett (21), apart from the additional interaction of the Xe orbital with the equatorial CO groups.

Gas-phase studies have not been restricted to the group VI hexacarbonyls. Fu and co-workers (54) have used TRIR to study the coordinatively unsaturated species  $\text{CpMn(CO)}_x$  ( $x = 1$  and 2) generated by 266- and 355-nm laser photolysis of  $\text{CpMn(CO)}_3$  in the gas phase. In the presence of noble gas L (L = He, Ar, or Xe), they were able to measure the rate constant for reaction of the noble gas complex  $\text{CpMn(CO)}_2\text{L}$  with CO. Interestingly, they found that only Ar significantly perturbed the rate from that observed in the absence of noble gas. This was thought to be because He has too high an ionization potential and Xe is too bulky to interact with the Mn center. In light of recent TRIR experiments conducted in supercritical fluid solution, the conclusion that Xe is unable to coordinate is incorrect.

In addition to UV/visible flash photolysis and TRIR spectroscopy, other techniques have been used for the detection of transition metal–noble gas interactions in the gas phase. The interaction of noble gases with transition metal ions has been studied in detail. A series of cationic dimeric species,  $\text{ML}^+$  (M = V, Cr, Fe, Co, Ni; L = Ar, Kr, or Xe), have been detected by mass-spectroscopic methods (55–58). It should be noted that noble gas cations  $\text{L}^+$  are isoelectronic with halogen atoms, therefore, this series of complexes is not entirely unexpected. The bond dissociation energies of these unstable complexes (Table IV) were determined either from the observed diabatic dissociation thresholds obtained from their visible photodissociation spectra or from the threshold energy for collision-induced dissociation. The bond energies are found to increase linearly with the polarizability of the noble gas.

TABLE IV

BOND DISSOCIATION ENERGIES ( $\text{kJ mol}^{-1}$ )  
OF  $\text{ML}^+$  SPECIES DETERMINED BY MASS  
SPECTROMETRIC METHODS<sup>a</sup>

M	L = Ar	Kr	Xe
V	37	47	$81 \pm 16$
Nb	37		
Cr	$28 \pm 4$		$68 \pm 10$
Fe			$38 \pm 9$
Co	49	65	$82 \pm 7$
Ni	53		

<sup>a</sup> The data are from Refs. (55–58).

Fourier-transform microwave spectroscopy of supersonic jets (59–62) has recently permitted the characterization of a series of neutral three-atom species,  $\text{ArAgX}$ ,  $\text{ArCuX}$  ( $X = \text{F}$ ,  $\text{Cl}$ , or  $\text{Br}$ ),  $\text{ArAuX}$  ( $X = \text{Br}$ ,  $\text{Cl}$ , or  $\text{F}$ ), and  $\text{KrAuCl}$ . These complexes were formed by laser ablation of the desired metal near the orifice of a pulsed nozzle using the second harmonic (532 nm) of a Nd:YAG laser and reaction of the resulting plasma, with the precursor gases ( $\text{SF}_6$ ,  $\text{Cl}_2$ , or  $\text{Br}_2$ ) contained in the Ar or Kr backing gas of the jet. All of these species were found to be linear and fairly rigid in their ground vibrational states. Theoretical calculations at the MP2 level allowed the noble gas–metal bond dissociation energies to be predicted. These ranged from  $23.2 \text{ kJ mol}^{-1}$  for the Ar–Ag bond in  $\text{ArAgF}$  to  $71 \text{ kJ mol}^{-1}$  for the Kr–Au bond in  $\text{KrAuCl}$ . Large changes in nuclear quadrupole coupling constants on complex formation suggested extensive charge rearrangement on formation of these complexes. The noble gas–transition metal bond lengths in these systems were found to be considerably shorter than those in typical van der Waals complexes, indicating a certain amount of noble gas–metal covalent bonding.

#### D. SUPERCRITICAL-FLUID STUDIES

In the study of transition metal–noble gas bonding, the use of supercritical noble gases as solvents is a natural extension of the use of liquefied noble gases. Supercritical fluids are a curious hybrid of gases and liquids, having physical properties intermediate between the two (see Table V). These properties can be explained with the use of a phase diagram (Fig. 11). At the end of the vapor–liquid phase boundary lies the critical point, marked by the critical temperature  $T_c$  and the critical pressure  $p_c$ . Any substance whose temperature and pressure exceed  $T_c$  and  $p_c$  is said to be a supercritical fluid (63). Thus, as can be seen from Table I, if operating at room temperature, only a modest pressure, on the order of 60 atm, is required to make argon, krypton, or xenon

TABLE V  
A COMPARISON OF SOME PHYSICAL PROPERTIES OF SUPERCRITICAL  
FLUIDS, LIQUIDS, AND GASES

Property	Liquid	Supercritical fluid	Gas
Density ( $\text{g cm}^{-3}$ )	1	0.1–0.5	$10^{-3}$
Viscosity ( $\text{Pa s}$ )	$10^{-3}$	$10^{-4}$ – $10^{-5}$	$10^{-5}$
Diffusivity ( $\text{cm}^2 \text{ s}^{-1}$ )	$10^{-5}$	$10^{-3}$	$10^{-1}$

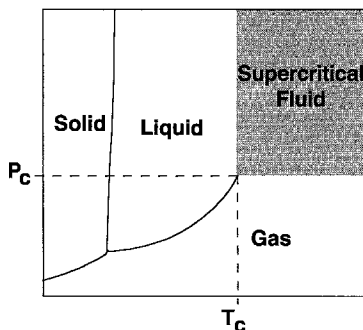


FIG. 11. A typical pressure–temperature phase diagram for a single-component system, e.g., xenon, showing the supercritical region, which can be accessed from either the liquid or gas phase without crossing a phase boundary.

supercritical, although a much higher pressure is needed to reach the critical densities of argon and krypton. Supercritical fluids are unique in that they have the liquid-like ability to act as good solvents, but, like gases, they are also highly compressible and are completely miscible with other gases. This in itself makes them ideal solvents for studying the reactions of transition metal complexes in solution with dissolved gases. More importantly, unlike any other solvent, supercritical fluids have physical properties such as density (or concentration), viscosity, and diffusivity, that can be “tuned” by simple changes of pressure and temperature. Thus, elaborate kinetic investigations become possible in these unique solvents.

Using TRIR spectroscopy, it has been possible to obtain the IR spectra of transition–metal noble gas complexes in solution at room temperature. Thus,  $W(CO)_5Ar$ ,  $M(CO)_5Kr$ , and  $M(CO)_5Xe$  ( $M = Cr, Mo, \text{ or } W$ ) have been characterized and their reactivity toward added CO has been measured at ambient temperature in supercritical Ar (scAr), scKr, and scXe, respectively (64). Figure 12 shows a typical  $s^2$ -FTIR spectrum obtained 1  $\mu s$  after irradiation (355 nm) of  $W(CO)_6$  in scXe. The positive bands were assigned to the formation of  $W(CO)_5Xe$ . In scKr, the  $\nu(C-O)$  bands assigned to  $W(CO)_5Kr$  shifted to a higher wavenumber relative to those assigned to  $W(CO)_5Xe$  in scXe and had a lifetime which was 12 times shorter than that of  $W(CO)_5Xe$ . However, this shift did not prove, in itself, that Xe or Kr coordinates to the metal center since the  $\nu(C-O)$  band of  $W(CO)_6$  is also shifted relative to scXe. Further evidence was obtained by repeating the experiment in scKr doped with 7% Xe using the approach pioneered by Perutz and Turner (28). The  $\nu(C-O)$  band of  $W(CO)_6$  was not moved by the doping, but the wavenumbers of

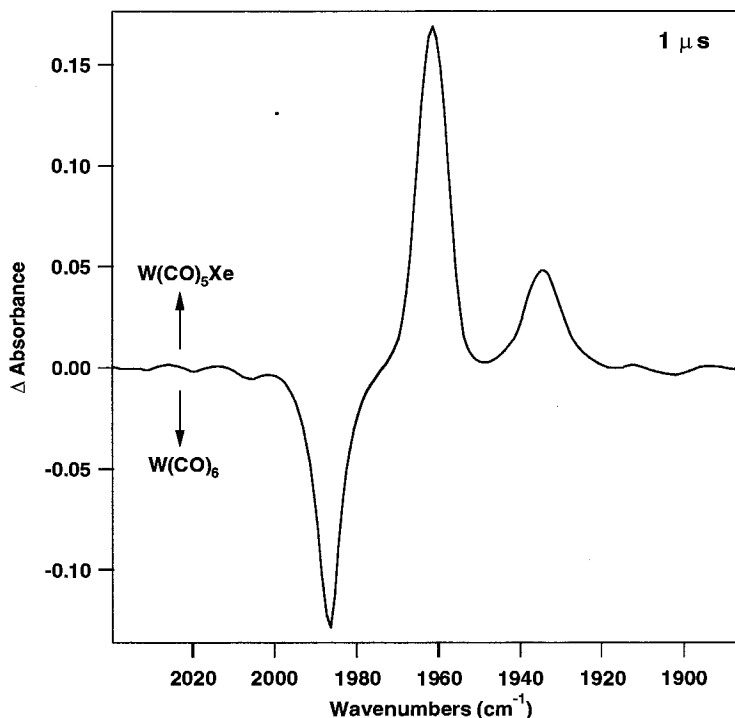
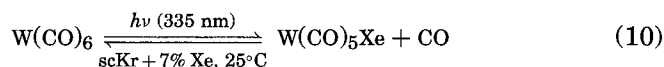


FIG. 12.  $s^2$ -FTIR spectrum obtained at Nottingham 1  $\mu$ s after 355-nm photolysis of  $W(CO)_6$  dissolved in scXe (1500 psi, 298 K) in the presence of 50 psi of CO. The negative band indicates depletion of the parent and the two positive bands are assigned to the  $e$  and low-frequency  $a_1$  mode  $\nu(C-O)$  vibrations of  $W(CO)_5Xe$ . Note that the high-frequency  $a_1$  vibration, expected for a molecule with  $C_{4v}$  symmetry, was not observed owing to its extremely low intensity. The spectral resolution used in this experiment was 8  $cm^{-1}$ .

the transients were identical to those of  $W(CO)_5Xe$  in scXe, and were assigned to  $W(CO)_5Xe$  in scKr [Eq. (10)]. Further evidence for coordination of Xe was obtained from the kinetic decay traces of the transient. The lifetime of the transient was increased by almost one order of magnitude in the presence of a modest quantity of Xe (see Fig. 13). Thus, Xe preferentially coordinates to the  $W(CO)_5$  moiety within the risetime of the TRIR apparatus (50 ns).



To confirm that Kr was actually coordinating to the metal center, a similar experiment was performed in scAr doped with Kr. As in the

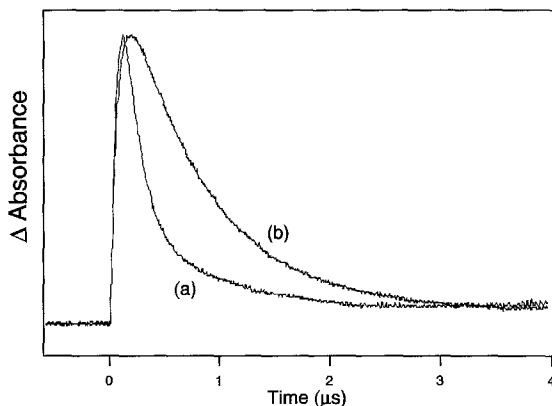


FIG. 13. TRIR kinetic decay traces recorded after 355-nm photolysis of  $\text{W}(\text{CO})_6$  in (a) scKr and (b) scKr + 7% Xe, both in the presence of CO (9 psi). Trace (a) corresponds to  $\text{W}(\text{CO})_5\text{Kr}$  and trace (b) corresponds to  $\text{W}(\text{CO})_5\text{Xe}$ . Adapted from Fig. 5 in Ref. (64).

Kr/Xe experiment, absorptions assigned to  $\text{W}(\text{CO})_5\text{Ar}$  in pure scAr were not seen, and preferential coordination of Kr was occurring, with an increase in the lifetime of the transient over the pure scAr experiment. From the observed rate constants for the reaction of  $\text{W}(\text{CO})_5\text{L}$  with CO in pure scL (L = Ar, Kr, or Xe), the reactivity of these complexes was found to decrease in the following order:  $\text{W}(\text{CO})_5\text{Ar} > \text{W}(\text{CO})_5\text{Kr} > \text{W}(\text{CO})_5\text{Xe}$ .

Further TRIR experiments with the analogous Cr and Mo complexes revealed that, for each complex  $\text{M}(\text{CO})_5\text{Kr}$  or  $\text{M}(\text{CO})_5\text{Xe}$ , the order of reactivity toward CO is  $\text{Cr} \approx \text{Mo} > \text{W}$ . For each metal, the reactivity of  $\text{M}(\text{CO})_5\text{L}$  complexes follows the order  $\text{Kr} > \text{Xe}$  (see Fig. 14). An investigation of the UV/visible absorption maxima of  $\text{Cr}(\text{CO})_5\text{L}$  in supercritical solution was carried out by visible flash photolysis. It was found that the  $\lambda_{\text{max}}$  of  $\text{Cr}(\text{CO})_5\text{Kr}$  in scKr is red-shifted by  $\sim 30$  nm relative to that of  $\text{Cr}(\text{CO})_5\text{Xe}$  in scXe. This result was consistent with previous matrix-isolation studies, which had shown that the stronger the Cr–L interaction, the higher the energy of the visible absorption band (28). The temperature dependence of the rate of decay of  $\text{W}(\text{CO})_5\text{Xe}$  at one CO concentration was measured, and an Arrhenius plot gave a value of the activation energy for the reaction of  $\text{W}(\text{CO})_5\text{Xe}$  with CO,  $E_a = 34.3 \pm 0.8 \text{ kJ mol}^{-1}$ . This value is very similar to the W–Xe bond strength in  $\text{W}(\text{CO})_5\text{Xe}$  obtained by Weitz in the gas phase (52) and by Weiller in liquid Xe (39), thus implying that the reaction between  $\text{W}(\text{CO})_5\text{Xe}$  and CO in scXe occurs mainly via a dissociative mechanism. One surprising result was that the reactivity of  $\text{W}(\text{CO})_5\text{Xe}$  toward CO

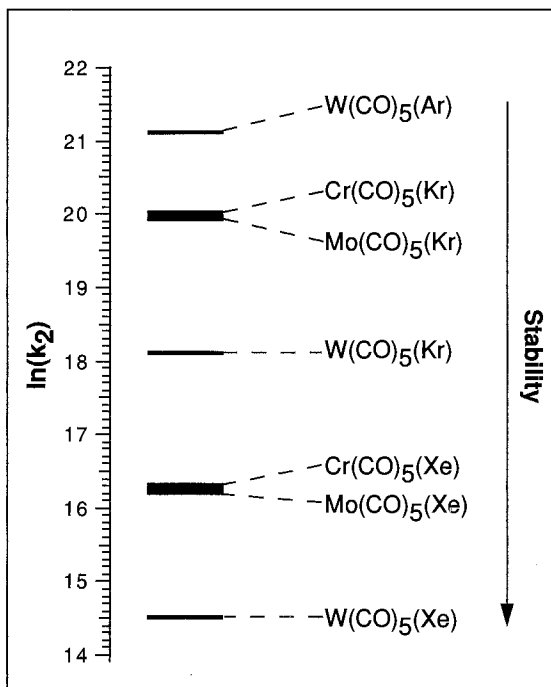


FIG. 14. Values of  $\ln(k_2)$  ( $k_2$  = bimolecular rate constant) for the reaction of a series of group VI noble gas complexes with CO in supercritical noble gas solution at 298 K, representing their relative stabilities. The data were taken from Ref. (64).

in scXe is just over twice that of  $\text{W(CO)}_5(n\text{-heptane})$  toward CO in *n*-heptane (65). By contrast, the W–Xe BDE ( $34.3 \text{ kJ mol}^{-1}$ ) (64) is nearly  $30 \text{ kJ mol}^{-1}$  lower than that of the W–heptane BDE ( $63 \text{ kJ mol}^{-1}$ ) (66). Organometallic alkane complexes are similar to noble gas complexes in that they involve  $\sigma$  donation to the metal center and as yet have been observed only as transient species (67). The comparable reactivity of organometallic alkane and noble gas complexes is important in the quest for isolating xenon complexes. Of the reported organometallic alkane complexes  $\text{CpRe(CO)}_2(\text{alkane})$  is the least reactive (68), and the only alkane complex to be characterized so far in solution by NMR spectroscopy (69). The products  $\text{CpRe(CO)}_2\text{Xe}$  and  $\text{CpRe(CO)}_2\text{Kr}$  are significantly less reactive toward CO than the corresponding  $\text{W(CO)}_5\text{Xe}$  and  $\text{W(CO)}_5\text{Kr}$  complexes. Furthermore, experiments conducted in scKr doped with Xe showed that the formation of the Re–Xe complex was slow enough to be followed in real time, presumably a result of a significant Re–Kr interaction in scKr (see Fig. 15). By conducting experiments

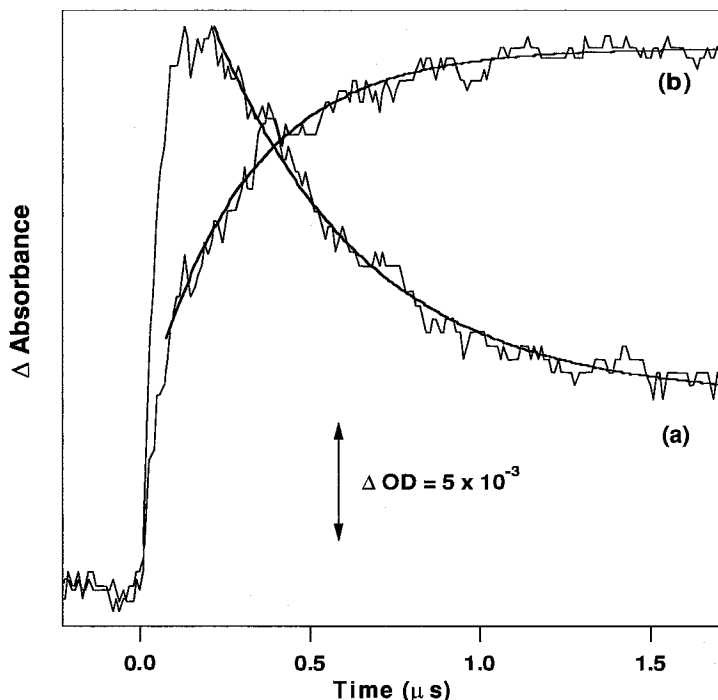


FIG. 15. TRIR decay traces recorded after 266-nm photolysis of  $\text{CpRe}(\text{CO})_3$  in scKr (3414 psi, 298 K) in the presence of CO (30 psi) and Xe (50 psi). (a) At  $1967\text{ cm}^{-1}$  and (b) at  $1962\text{ cm}^{-1}$ . The traces have been normalized in intensity. Adapted from Fig. 7 in Ref. (68).

over a range of temperatures above room temperature (70), it was possible to calculate the activation parameters for these reactions. This permitted estimates of the transition metal–noble gas BDEs to be made, and the Re–Xe BDE in  $\text{CpRe}(\text{CO})_2\text{Xe}$  was found to be  $\geq 47\text{ kJ mol}^{-1}$ . Indeed, the lifetime (49) of  $\text{CpRe}(\text{CO})_2\text{Xe}$  in liquid Xe at low temperature (see above) is very long, and this opens up the possibility of probing these reactive organometallic Xe complexes by  $^{129}\text{Xe}$  NMR spectroscopy.

The effect of cyclopentadienyl-ring substituents on the reactivity of the group VII half-sandwich complexes  $(\eta^5\text{-C}_5\text{R}_5)\text{M}(\text{CO})_2\text{L}$  [ $\text{M} = \text{Mn}$  and  $\text{Re}$ ;  $\text{R} = \text{H}$ ,  $\text{Me}$ , and  $\text{Et}$  ( $\text{Mn}$  only);  $\text{L} = \text{Kr}$  and  $\text{Xe}$ ] toward CO in supercritical fluid solution at room temperature has been investigated (70). The reactivity of the corresponding alkane complexes  $(\eta^5\text{-C}_5\text{R}_5)\text{Mn}(\text{CO})_2(n\text{-heptane})$  ( $\text{R} = \text{H}$ ,  $\text{Me}$ , and  $\text{Et}$ ) toward small molecules such as CO,  $\text{N}_2$ , and  $\text{H}_2$  in  $n$ -heptane solution steadily increased in the order  $\text{H} < \text{Me} < \text{Et}$  (71). These results indicated that steric rather

than electronic factors govern the reactivity of these alkane complexes. The steric bulk of the three types of ring substituent increases steadily in the order  $H < Me < Et$ , and the Me and Et substituents have almost identical electron-directing effects. This has allowed both the electronic and steric effects of the ring substituents on reactivity to be investigated.

Room-temperature CO substitution kinetics showed that for both noble gases, the H- and Me-substituted complexes,  $(\eta^5\text{-C}_5\text{R}'_5)\text{Mn}(\text{CO})_2\text{Xe}$  ( $\text{R}' = \text{H}$  and  $\text{Me}$ ) and  $(\eta^5\text{-C}_5\text{R}'_5)\text{Mn}(\text{CO})_2\text{Kr}$ , have very similar reactivity toward CO, whereas  $(\eta^5\text{-C}_5\text{Et}_5)\text{Mn}(\text{CO})_2\text{L}$  ( $\text{L} = \text{Xe}$  and  $\text{Kr}$ ) are approximately twice as reactive. Experiments were conducted with the manganese–xenon complexes in which the observed rate of decay was measured as a function of  $[\text{CO}]$  at a constant  $[\text{CO}]/[\text{Xe}]$  ratio. These suggested that the noble gas complexes react with CO in supercritical solution via a dissociative mechanism. Further evidence for the reaction mechanism was obtained from temperature-dependence studies (70) in which the enthalpies of activation were calculated for these noble gas complexes and the analogous alkane complexes  $(\eta^5\text{-C}_5\text{H}_5)\text{M}(\text{CO})_2(n\text{-heptane})$  ( $\text{M} = \text{Mn}$  and  $\text{Re}$ ). The value of  $\Delta H^\ddagger$  for the reaction of  $(\eta^5\text{-C}_5\text{H}_5)\text{M}(\text{CO})_2\text{Xe}$  ( $\text{M} = \text{Mn}$  or  $\text{Re}$ ) with CO in scXe was found to be very similar to that measured for the analogous reaction of  $(\eta^5\text{-C}_5\text{H}_5)\text{M}(\text{CO})_2(n\text{-heptane})$  with CO in *n*-heptane solution. For a given metal/ligand system the BDE for a metal–Xe bond is expected to be significantly less than that of the corresponding metal–alkane bond. The mean values of  $\Delta H^\ddagger$  for  $(\eta^5\text{-C}_5\text{R}'_5)\text{Mn}(\text{CO})_2\text{Xe}$  ( $\sim 31 \text{ kJ mol}^{-1}$ ) and  $(\eta^5\text{-C}_5\text{R}'_5)\text{Re}(\text{CO})_2\text{Xe}$  ( $\sim 46 \text{ kJ mol}^{-1}$ ) represent a lower limit for the M–Xe BDEs.

The characterization of  $\text{CpM}(\text{CO})_3\text{Xe}$  ( $\text{M} = \text{Nb}$  or  $\text{Ta}$ ) in scXe has recently been performed (72); and by combining the results of all our supercritical fluid studies, a trend in the reactivity of the group V, VI, and VII transition metal–noble gas complexes in solution appears. Their reactivity toward CO decreases on going down the groups and on moving across the periodic table from left to right (see Table VI). The complex  $\text{CpNb}(\text{CO})_2\text{Xe}$  is  $\sim 1000$  times more reactive than  $\text{CpRe}(\text{CO})_2\text{Xe}$ . It is tempting to predict that this trend would continue across the remaining groups into the late transition metals. However, a number of studies suggest that this is not the case and that rhenium is unique in producing extremely stable noble gas complexes. For example, the photogenerated 16-electron intermediates  $\text{CpCo}(\text{CO})$  and  $\text{Cp}^*\text{Co}(\text{CO})$  were found by Bergman and co-workers (73) to have no detectable interaction with cyclohexane or noble gas atoms. Furthermore, it has been shown (74) that the group IX complexes  $\text{Cp}'\text{Rh}(\text{CO})\text{Xe}$  ( $\text{Cp}' = \text{Cp}$  or  $\text{Cp}^*$ ) are

TABLE VI

THE BIMOLECULAR RATE CONSTANTS  $k_2$  FOR THE REACTION OF A SERIES  
OF TRANSITION METAL–NOBLE GAS COMPLEXES WITH CO IN  
SUPERCRITICAL NOBLE GAS SOLUTION AT 298 K

Noble gas complex	$k_2$ (dm <sup>3</sup> mol <sup>-1</sup> s <sup>-1</sup> )	Reference
( $\eta^5$ -C <sub>5</sub> H <sub>5</sub> )Nb(CO) <sub>5</sub> Xe	$5.7 \times 10^6$	72
( $\eta^5$ -C <sub>5</sub> H <sub>5</sub> )Ta(CO) <sub>3</sub> Xe	$4.9 \times 10^6$	72
Cr(CO) <sub>5</sub> Xe	$8.4 \times 10^6$	64
Mo(CO) <sub>5</sub> Xe	$1.1 \times 10^7$	64
W(CO) <sub>5</sub> Xe	$2.0 \times 10^6$	64
( $\eta^5$ -C <sub>5</sub> H <sub>5</sub> )Mn(CO) <sub>2</sub> Xe	$1.6 \times 10^6$	70
( $\eta^5$ -C <sub>5</sub> Me <sub>5</sub> )Mn(CO) <sub>2</sub> Xe	$1.8 \times 10^6$	70
( $\eta^5$ -C <sub>5</sub> Et <sub>5</sub> )Mn(CO) <sub>2</sub> Xe	$2.9 \times 10^6$	70
( $\eta^5$ -C <sub>5</sub> H <sub>5</sub> )Re(CO) <sub>2</sub> Xe	$4.8 \times 10^3$	68
( $\eta^5$ -C <sub>5</sub> Me <sub>5</sub> )Re(CO) <sub>2</sub> Xe	$6.0 \times 10^3$	70
Cr(CO) <sub>5</sub> Kr	$4.7 \times 10^8$	64
Mo(CO) <sub>5</sub> Kr	$4.3 \times 10^8$	64
W(CO) <sub>5</sub> Kr	$7.5 \times 10^7$	64
( $\eta^5$ -C <sub>5</sub> H <sub>5</sub> )Mn(CO) <sub>2</sub> Kr	$7.2 \times 10^7$	70
( $\eta^5$ -C <sub>5</sub> Me <sub>5</sub> )Mn(CO) <sub>2</sub> Kr	$7.5 \times 10^7$	70
( $\eta^5$ -C <sub>5</sub> Et <sub>5</sub> )Mn(CO) <sub>2</sub> Kr	$1.6 \times 10^8$	70
( $\eta^5$ -C <sub>5</sub> H <sub>5</sub> )Re(CO) <sub>2</sub> Kr	$8.1 \times 10^6$	68
( $\eta^5$ -C <sub>5</sub> Me <sub>5</sub> )Re(CO) <sub>2</sub> Kr	$7.8 \times 10^6$	70
W(CO) <sub>5</sub> Ar	$1.4 \times 10^9$	64

far more reactive than CpRe(CO)<sub>2</sub>Xe toward CO in scXe solution. The activation energies for the reaction of Cp’Rh(CO)Xe with CO in scXe are significantly lower than those measured (70) for the earlier transition metal Xe complexes. Furthermore, the activation entropy ( $\Delta S^\ddagger$ ) was large and negative (ca.  $-100$  J K<sup>-1</sup> mol<sup>-1</sup>), which implies an associative reaction mechanism.

### III. The Nature of the Transition Metal–Noble Gas Bond

Experimental research into transition metal–noble gas complexes has provided a plethora of spectroscopic information, allowing their characterization and their reactivities to be determined. Table VII collates all of the transition metal–noble gas BDEs that have been determined experimentally by spectroscopic methods. However, these studies give no insight into the nature of the metal–noble gas bonds, e.g., bond lengths, degree of covalency, molecular orbital interactions. Apart

TABLE VII

TRANSITION METAL–NOBLE GAS BDEs THAT HAVE BEEN DETERMINED EXPERIMENTALLY

Complex	Conditions	Detection method	M–NG BDE (kJ mol <sup>-1</sup> )	Reference
Cr(CO) <sub>5</sub> Xe	Liquid Xe at 175 K	FTIR	$E_a = 15 \pm 2$	38
W(CO) <sub>5</sub> Xe	Liquid Xe at 173–198 K	Rapid-scan FTIR	$35.1 \pm 0.8$	39
( $\eta^5$ -C <sub>5</sub> Me <sub>5</sub> )Rh(CO) <sub>2</sub> Xe	Liquid Xe at 202–242 K	TRIR	$\geq 11.7 \pm 1.3$	46
M(CO) <sub>5</sub> L	Gas phase at 298–340 K	TRIR	Cr–Xe = $37.7 \pm 3.8$	52
[M = Cr, Mo, or W;			Mo–Xe = $33.5 \pm 4.2$	
L = Ar, Kr (W only)			W–Xe = $34.3 \pm 4.2$	
or Xe]			W–Kr $\leq 25.1$	
			W–Ar $\leq 12.6$	
W(CO) <sub>5</sub> Xe	Gas phase at 298 K	TRIR	$35.0 \pm 6.0$	53
W(CO) <sub>5</sub> Xe	scXe at 298–343 K	TRIR	$34.3 \pm 0.8$	64
( $\eta^5$ -C <sub>5</sub> H <sub>5</sub> )Mn(CO) <sub>2</sub> Xe	scXe at 298–343 K	TRIR	$\geq 30.0 \pm 2.0$	70
( $\eta^5$ -C <sub>5</sub> Me <sub>5</sub> )Mn(CO) <sub>2</sub> Xe	scXe at 298–343 K	TRIR	$\geq 34.0 \pm 2.0$	70
( $\eta^5$ -C <sub>5</sub> Et <sub>5</sub> )Mn(CO) <sub>2</sub> Xe	scXe at 298–343 K	TRIR	$\geq 28.0 \pm 2.0$	70
( $\eta^5$ -C <sub>5</sub> H <sub>5</sub> )Re(CO) <sub>2</sub> Xe	scXe at 298–343 K	TRIR	$\geq 47.0 \pm 2.0$	70
( $\eta^5$ -C <sub>5</sub> Me <sub>5</sub> )Re(CO) <sub>2</sub> Xe	scXe at 298–343 K	TRIR	$\geq 44.0 \pm 2.0$	70
( $\eta^5$ -C <sub>5</sub> Me <sub>5</sub> )Re(CO) <sub>2</sub> Kr	scKr at 298–343 K	TRIR	$\geq 31.0 \pm 2.0$	70

from the recent X-ray crystal structure of [AuXe<sub>4</sub><sup>2+</sup>][Sb<sub>2</sub>F<sub>11</sub><sup>-</sup>]<sub>2</sub> (1), this information has been obtained only from theoretical calculations.

The first theoretical investigation into the bonding of transition metals with noble gases was by Demuyne and co-workers in 1979 (75). It concerned the interaction of the pentacarbonyls M(CO)<sub>5</sub> (M = Cr and Mo) with noble gas atoms L (L = Ar, Kr, Xe). *Ab initio* calculations were performed both at the SCF level and at the level of the dispersion energy. The dispersion energy is responsible for most of the stabilization of van der Waals molecules and can also be important in the stabilization of electron donor–acceptor complexes. At the SCF level the interaction was found to be repulsive. The reason postulated was that the noble gas atom is too bulky, leading to steric interactions with the other ligands. The dispersion energy in Mo(CO)<sub>5</sub>Kr was estimated to be at least 10.5 kJ mol<sup>-1</sup>. However, owing to the extremely limited computational power available at that time, this study can only be considered to be qualitative.

In 1997, Ehlers and co-workers (76) extended these early studies by making use of vastly improved modern computational power. Quantum-mechanical *ab initio* calculations at the MP2 and CCSD(T) level of theory using effective core potentials for the heavy atoms as well as density functional calculations using various gradient corrections were

TABLE VIII

TRANSITION METAL–NOBLE GAS BDES THAT HAVE BEEN CALCULATED USING  
THEORETICAL METHODS

Complex	Theoretical method	M–NG BDE (kJ mol <sup>−1</sup> )	Reference
ArAgF, ArCuF, ArAuCl, ArAuF, and KrAuCl	MP2	Ar–AgF = 23.2 Ar–CuF = 47.3 Ar–AuCl = 46.9 Ar–AuF = 59.0 Kr–AuCl = 71.3	59–62
MXe (M = Pd or Pt)	MP2, CCSD(T), CIS, and CISD	Pd–Xe = 41.6 Pt–Xe = 67.9 Cr–Ar = 12.6 Cr–Kr = 16.7 Cr–Xe = 26.8 Mo–Ar = 15.1	79
M(CO) <sub>5</sub> L (M = Cr, Mo, or W; L = Ar, Kr, or Xe) <sup>a</sup>	MP2 and CCSD(T)	Mo–Kr = 19.7 Mo–Xe = 33.1 W–Ar = 19.2 W–Kr = 25.1 W–Xe = 36.8	76
AuXe <sup>+b</sup>	CCSD(T)	87.8	77
XeAuXe <sup>+b</sup>	CCSD(T)	108.5	77
AuXe <sup>+</sup>	CCSD(T)	126.8	78
[AuXe <sub>4</sub> <sup>2+</sup> ][Sb <sub>2</sub> F <sub>11</sub> ] <sub>2</sub>	HF	150.6	
	DFT Becke3	238.5	1
	MP2	208.2	

<sup>a</sup> Only one set of the MP2 level calculations is shown. <sup>b</sup> Several other gold–noble gas cations were calculated in this study.

reported for the complexes M(CO)<sub>5</sub>L (M = Cr, Mo, W; L = Ar, Kr, Xe). They found an increasing metal–noble gas distance in the order Ar < Kr < Xe and Cr < W < Mo. In addition, their predicted M–L bond dissociation energies (see Table VIII) were very close to previous experimental values.

Through a consideration of decomposition characteristics, Ehler and colleagues were able to identify the different contributions to the bond energy and determine which orbital interactions occurred. These interactions are shown in the molecular orbital energy level diagram in Fig. 16. They found a relatively large Pauli repulsion ( $\Delta E_{\text{Pauli}}$ ) between M(CO)<sub>5</sub> and the noble gas, in the range 42–84 kJ mol<sup>−1</sup>. However, this is compensated by an electrostatic attraction ( $\Delta E_{\text{Elstat}}$ ) and the orbital interactions ( $\Delta E_{\text{oi}}$ ). The transition metal *d* orbitals were found to

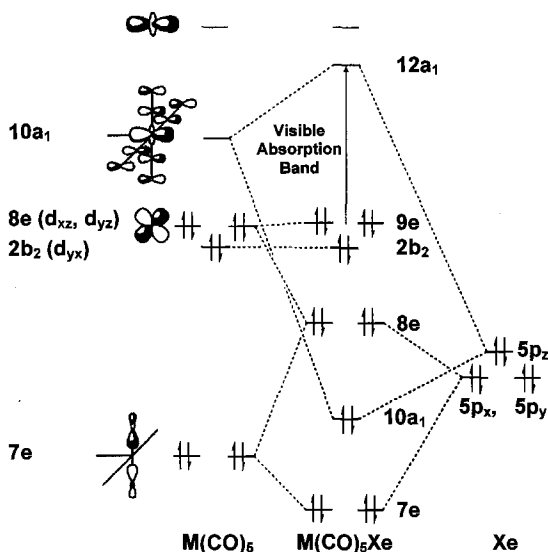


FIG. 16. The molecular orbital energy level diagram for  $M(CO)_5Xe$  ( $M = Cr, Mo, \text{ or } W$ ) calculated by Ehlers and co-workers. Adapted from Fig. 4 in Ref. (76).

be unaffected, with the noble gas  $np$  orbitals interacting mainly with energetically low-lying fragment orbitals of the pentacarbonyl complexes.

The Pauli repulsion is mainly a result of a four-electron destabilizing interaction of the  $np_{x,y}$  orbitals with low-lying pentacarbonyl fragment orbitals of  $e$  symmetry. The stabilizing orbital interaction results from mixing of the  $np_z$  orbital of the noble gas with the carbonyl-based  $10a_1$  LUMO of  $M(CO)_5$ ; in addition, a small stabilizing interaction comes from the polarization of the  $e$ -type orbitals. It should be noted that in 1993 Ishikawa and co-workers (53) postulated a qualitative orbital interaction diagram for  $W(CO)_5Xe$  as a result of their gas-phase studies (see earlier). Although much less detailed, it was very similar to that calculated by Ehlers and co-workers in that it involved net electron flow from xenon to the  $a_1$  orbital of  $W(CO)_5$ , which involves  $\pi^*$  orbitals of the equatorial CO groups.

Finally, Ehlers found that the axial-equatorial C–M–C bond angle remains constant for the three noble gases studied. This is in contrast to the matrix-isolation study of Perutz and Turner (28), who calculated, from the intensities of the  $\nu(C-O)$  IR bands, that the bond angle decreases on changing the noble gas matrix from Ar to Xe. It was proposed that the change in bond angle is the principal cause of the shift in visible absorption band energy with noble gas. However, the approximate

nature of the intensity measurements, caused by matrix splitting of the IR bands, may have introduced errors in the estimated bond angles. Ehler's result suggests that the shift of the visible absorption band ( $e \rightarrow a_1$  transition; see Fig. 16) is a result of the different interaction energies of the noble gases with the metal center and is not merely a structural phenomenon in which the noble gas is not necessarily bonded to the metal center.

Ehlers and co-workers conclude that "the interaction of the noble gas with  $M(CO)_5$  is dominated by the orbital interactions between the noble gas  $p$  orbitals and the orbitals of the equatorial carbonyl groups. The resulting stabilization of the noble gas  $p_z$  orbital *and* the dipole-induced dipole interaction are responsible for the bond between the pentacarbonyl fragments and the noble gases."

The field has now reached a breakthrough point. The recent isolation of  $[AuXe_4^{2+}][Sb_2F_{11}^-]_2$  by Seppelt and co-workers (1) has allowed, for the first time, the chemical bonds between transition metals and noble gas atoms to be identified by crystallography. Their theoretical calculations showed that the xenon atoms were functioning as simple  $\sigma$  donors toward  $Au^{2+}$ , with the main part of the positive charge residing on the xenon atoms. However, it is important to understand why this complex in particular proved isolable and why all other noble gas complexes are highly reactive transient intermediates.

In 1995, Pyykkö performed a theoretical study (77) of the gold(I) cation complexes  $AuL^+$  and  $LAuL^+$  ( $L = He, Ne, Ar, Kr, \text{ and } Xe$ ). In this study he found that the  $Au-Xe$  BDE in  $AuXe^+$  is  $87.8 \text{ kJ mol}^{-1}$  and that for the dimeric species,  $XeAuXe^+$ , it is slightly larger at  $108.5 \text{ kJ mol}^{-1}$ . Substantial charge transfer from  $Xe$  to  $Au^+$  occurs, with the bonds having considerable covalent character. In fact, for  $AuXe^+$  the bond energy at the equilibrium bond length is about 2 times greater than the electrostatic charge-polarizability interaction calculated from the  $R^{-4}$  law,  $V(R) = -(\alpha Z^2/2R^4)$ . More than half of the  $Au-Xe$  bond energy was found to come from relativistic effects. In 1998, Schröder and Pyykkö performed a combined experimental and high-level theoretical investigation of cationic gold(I) complexes of xenon and other ligands (78). The improved theoretical methods increased the predicted  $Au-Xe$  bond energy in  $AuXe^+$  to  $126.8 \text{ kJ mol}^{-1}$ . Once again, relativity plays a large part in making these bonds strong.

The strong relativistic effect, caused by the high nuclear charge of gold accelerating the  $6s$  valence electrons to high speeds as they approach the nucleus, makes the covalent bonds to gold anomalously strong and short. Approximately half of the  $Au-Xe$  bond energy in  $[AuXe_4^{2+}][Sb_2F_{11}^-]_2$  is due to relativity (7). These effects are not so

prevalent in the earlier transition metal–noble gas complexes, which have been observed, thus far, only as short-lived transients.

Burda and co-workers recently performed one other theoretical study of the noble gas coordination of transition metals (79). In this study, the lowest potential-energy curves were calculated for the species  $\text{MXe}$  ( $\text{M} = \text{Ni}, \text{Pd}, \text{or Pt}$ ). No bound states were found for  $\text{NiXe}$ . However, the  $\text{PdXe}$  species was calculated to have a BDE of  $41.6 \text{ kJ mol}^{-1}$  and  $\text{PtXe}$  was found to dissociate to an excited state but remain bound by  $67.9 \text{ kJ mol}^{-1}$ . It was therefore suggested that the Pd and Pt complexes could potentially be observed in the gas phase or in low-temperature matrices.

#### IV. Conclusions: Future Perspectives in Transition Metal–Noble Gas Bonding

Although a transition metal–noble gas complex has now been isolated, the quest to understand the bonding and interactions in these unique molecules is fundamental to allow the continued development of the area. The isolation of an early/mid-transition metal–noble gas complex remains an unfulfilled goal. However, the majority of studies on early/mid-transition metal–noble gas complexes in solution have been performed on neutral complexes. Making the metal center as electron-deficient as possible would increase the strength of the transition metal–noble gas bond in such species. This would lower the energy of the metal fragment's molecular orbitals (decreasing their ability to  $\pi$ -backbond and increasing their overlap with the noble gas  $p$  orbitals) and also increase the induced dipole moment and hence the electrostatic attraction between the metal center and noble gas. Electron deficiency at the metal center could be achieved in one of two ways: either by using highly electron-withdrawing ancillary ligands in order to reduce the electron density at the metal center or by making the complex cationic, i.e., extremely electron-deficient. Cationic transition metal complexes offer the most extreme form of electron withdrawal and, apart from potential solubility problems, may be more effective at stabilizing noble gas complexes than simply using strongly electron-withdrawing ancillary ligands in neutral complexes. This is because the positive charge strongly contracts the metal  $d$  orbitals, and greatly enhances the electrostatic charge–polarizability attraction between the metal center and noble gas atom.

In the absence of a reactant gas (e.g., CO), all the noble gas complexes we have studied in supercritical noble gas solution at room temperature have been kinetically unstable with respect to decomposition pathways

such as dimerization reactions. Steric bulk is the conventional method of thwarting such dimerization. For example,  $[(\eta^5\text{-C}_5\text{Ph}_5)\text{Fe}(\text{CO})_2]_2$  exists in solution as an equilibrium mixture of  $[(\eta^5\text{-C}_5\text{Ph}_5)\text{Fe}(\text{CO})_2]_2$  and the 17-electron radical,  $(\eta^5\text{-C}_5\text{Ph}_5)\text{Fe}(\text{CO})_2^\bullet$  (80), while  $\text{CpFe}(\text{CO})_2^\bullet$  lives in solution for only a few microseconds (81). Similarly,  $[\text{Cp}^*\text{Cr}(\text{CO})_3]_2$  exists as a mixture of radical and dimer in solution, even though only the dimer is found in the solid state (82). However, replacing  $\text{Cp}^*$  by  $(\eta^5\text{-C}_5\text{Ph}_5)$  allowed the isolation of the radical  $(\eta^5\text{-C}_5\text{Ph}_5)\text{Cr}(\text{CO})_3^\bullet$  (83). New synthetic methodologies may also aid the isolation of new noble gas complexes. For example, Poliakoff and co-workers have recently had considerable success with the synthesis of  $\text{Cr}(\text{CO})_5(\eta^2\text{-C}_2\text{H}_4)$  and  $\text{CpMn}(\text{CO})_2(\eta^2\text{-H}_2)$  in supercritical fluid solution (84). These compounds had previously proved impossible to isolate using conventional synthetic methods. Using a continuous photochemical flow reactor, they photolyzed the precursor complex  $\text{Cr}(\text{CO})_6$  or  $\text{CpMn}(\text{CO})_3$  dissolved in  $\text{scC}_2\text{H}_4$  or  $\text{scCO}_2/\text{H}_2$ , respectively. As had previously been observed in static cell steady-state photolysis studies (85, 86), this caused photoejection of a molecule of CO and coordination of  $\text{C}_2\text{H}_4$  or  $\text{H}_2$  (confirmed by online FTIR detection). The product was then isolated using the RESS process (rapid expansion of supercritical solution). RESS involves a sudden reduction to atmospheric pressure at the end of the high-pressure flow system, causing the supercritical fluid to turn into gas and the solid product to precipitate extremely rapidly out of solution, thus minimizing the chances of losing the labile ligand. In addition, the rapid expansion causes cooling of the solid to below ambient temperature. Therefore, an attractive medium in which to perform the synthesis of a transition metal–noble gas complex is  $\text{scXe}$  itself. We would like to think that the isolation and X-ray structure of an organometallic noble gas complex will be an early 21st-century achievement in this area.

#### ACKNOWLEDGMENTS

Both authors are deeply grateful to Professor J. J. Turner for guidance and inspiration in the early stages of their careers. We thank Professors R. N. Perutz and M. Poliakoff for helpful comments.

#### REFERENCES

1. Seidel, S.; Seppelt, K. *Science* **2000**, *290*, 117.
2. Frenking, G.; Koch, W.; Reichel, F.; Cremer, D. *J. Am. Chem. Soc.* **1990**, *112*, 4240.
3. Wong, M. W. *J. Am. Chem. Soc.* **2000**, *122*, 6289.

4. Thompson, C. A.; Andrews, L. *J. Am. Chem. Soc.* **1994**, *116*, 423.
5. Veldkamp, A.; Frenking, G. *Chem. Phys. Lett.* **1994**, *226*, 11.
6. Khriachtchev, L.; Pettersson, M.; Runeberg, N.; Lundell, J.; Räsänen, M. *Nature* **2000**, *406*, 874.
7. Pyykkö, P. *Science* **2000**, *290*, 64.
8. Laughlin, K. B.; Blake, G. A.; Cohen, R. C.; Hovde, D. C.; Saykally, R. *J. Phys. Rev. Lett.* **1987**, *58*, 996.
9. Bogey, M.; Cordonnier, M.; Demuyne, C.; Destombes, J. L. *J. Mol. Spectrosc.* **1992**, *155*, 217.
10. Pettersson, M.; Lundell, J.; Räsänen, M. *Eur. J. Inorg. Chem.* **1999**, 729.
11. Christe, K. O.; Wilson, W. W.; Wilson, R. D. *Inorg. Chem.* **1984**, *23*, 2058.
12. Bartlett, N. *Proc. Chem. Soc.* **1962**, 218.
13. Naumann, D.; Tyrre, W. *J. Chem. Soc., Chem. Commun.* **1989**, 47.
14. Frohn, H. J.; Jacobs, S. *J. Chem. Soc., Chem. Commun.* **1989**, 625.
15. Brown, D. R.; Clegg, M. J.; Downs, A. J.; Fowler, R. C.; Minihan, A. R.; Norris, J. R.; Stein, L. *Inorg. Chem.* **1992**, *31*, 5041.
16. Drews, T.; Seppelt, K. *Angew. Chem., Int. Ed. Eng.* **1997**, *36*, 273.
17. Holloway, J. H.; Hope, E. G. *Adv. Inorg. Chem.* **1999**, *46*, 51.
18. Graham, M. A.; Perutz, R. N.; Poliakoff, M.; Turner, J. J. *J. Organomet. Chem.* **1972**, *34*, C34.
19. Poliakoff, M.; Turner, J. J. *J. Chem. Soc., Dalton Trans.* **1974**, 2276.
20. Braterman, P. S. "Metal Carbonyl Spectra." Academic Press, London, 1975.
21. Burdett, J. K. *J. Chem. Soc., Faraday Trans. 2*, **1974**, *70*, 1599.
22. Elian, M.; Hoffmann, R. *Inorg. Chem.* **1975**, *14*, 1058.
23. Daniel, C.; Bernard, M.; Dedieu, A.; Wiest, R.; Veillard, A. *J. Phys. Chem.* **1984**, *88*, 4805.
24. Barton, T. J.; Grinter, R.; Thomson, A. J.; Davies, B.; Poliakoff, M. *J. Chem. Soc., Chem. Commun.* **1977**, 841.
25. McNeish, A.; Poliakoff, M.; Smith, K. P.; Turner, J. J. *J. Chem. Soc., Chem. Commun.* **1976**, 859.
26. Poliakoff, M. *Chem. Soc. Rev.* **1978**, *7*, 527.
27. Poliakoff, M.; Weitz, E. *Acc. Chem. Res.* **1987**, *20*, 408.
28. Perutz, R. N.; Turner, J. J. *J. Am. Chem. Soc.* **1975**, *97*, 4791.
29. Perutz, R. N.; Turner, J. J. *Inorg. Chem.* **1975**, *14*, 262.
30. Guenzburger, D.; Caride, A. O.; Zuleta, E. *Chem. Phys. Lett.* **1972**, *14*, 239.
31. Church, S. P.; Poliakoff, M.; Timney, J. A.; Turner, J. J. *Inorg. Chem.* **1983**, *22*, 3259.
32. Horton-Mastin, A.; Poliakoff, M.; Turner, J. J. *Organometallics* **1986**, *5*, 405.
33. Brookhart, M.; Chandler, W.; Kessler, R. J.; Liu, Y.; Pienta, N. J.; Santini, C. C.; Hall, C.; Perutz, R. N.; Timney, J. A. *J. Am. Chem. Soc.* **1992**, *114*, 3802.
34. Mawby, R. J.; Perutz, R. N.; Whittlesey, M. K. *Organometallics* **1995**, *14*, 3268.
35. Whittlesey, M. K.; Perutz, R. N.; Virrels, I. G.; George, M. W. *Organometallics* **1997**, *16*, 268.
36. Bays, J. T.; Bitterwolf, T. E.; Lott, K. A.; Ollino, M. A.; Rest, A. J.; Smith, L. A. *J. Organomet. Chem.* **1998**, *554*, 75.
37. Fairhurst, S. A.; Morton, J. R.; Perutz, R. N.; Preston, K. F. *Organometallics* **1984**, *3*, 1389.
38. Simpson, M. B.; Poliakoff, M.; Turner, J. J.; Maier, W. B., II.; McLaughlin, J. G. *J. Chem. Soc., Chem. Commun.* **1983**, 1355.
39. Weiller, B. H. *J. Am. Chem. Soc.* **1992**, *114*, 10910.
40. George, M. W.; Poliakoff, M.; Turner, J. J. *Analyst* **1994**, *119*, 551.

41. Sun, X. Z.; Nikiforov, S. M.; Yang, J.; Colley, C. S.; George, M. W. *Appl. Spectrosc.* submitted.
42. Weiller, B. H.; Wasserman, E. P.; Bergman, R. G.; Moore, C. B.; Pimentel, G. C. *J. Am. Chem. Soc.* **1989**, *111*, 8288.
43. Schultz, R. H.; Bengali, A. A.; Tauber, M. J.; Weiller, B. H.; Wasserman, E. P.; Kyle, K. R.; Moore, C. B.; Bergman, R. G. *J. Am. Chem. Soc.* **1994**, *116*, 7369.
44. Bengali, A. A.; Arndtsen, B. A.; Burger, P. M.; Schultz, R. H.; Weiller, B. H.; Kyle, K. R.; Moore, C. B.; Bergman, R. G. *Pure Appl. Chem.* **1995**, *67*, 281.
45. Bengali, A. A.; Schultz, R. H.; Moore, C. B.; Bergman, R. G. *J. Am. Chem. Soc.* **1994**, *116*, 9585.
46. Weiller, B. H.; Wasserman, E. P.; Moore, C. B.; Bergman, R. G. *J. Am. Chem. Soc.* **1993**, *115*, 4326.
47. Rest, A. J.; Whitwell, I.; Graham, W. A. G.; Hoyano, J. K.; McMaster, A. D. *J. Chem. Soc., Dalton Trans.* **1987**, 1181.
48. Yeston, J. S.; McNamara, B. K.; Bergman, R. G.; Moore, C. B. *Organometallics* **2000**, *19*, 3442.
49. Childs, G. I.; Colley, C. S.; Dyer, J.; Grills, D. C.; Sun, X. Z.; Yang, J.; George, M. W. *J. Chem. Soc., Dalton Trans.* **2000**, 1901.
50. Breckenridge, W. H.; Sinai, N. *J. Phys. Chem.* **1981**, *85*, 3557.
51. Breckenridge, W. H.; Stewart, G. M. *J. Am. Chem. Soc.* **1986**, *108*, 364.
52. Wells, J. R.; Weitz, E. *J. Am. Chem. Soc.* **1992**, *114*, 2783.
53. Jyo-O, M.; Takeda, H.; Omiya, K.; Ishikawa, Y.; Arai, S. *Bull. Chem. Soc. Jpn.* **1993**, *66*, 3618.
54. Zheng, Y.; Wang, W.; Lin, J.; She, Y.; Fu, K.-J. *J. Phys. Chem.* **1992**, *96*, 7650.
55. Lessen, D. E.; Asher, R. L.; Brucat, P. J. *Chem. Phys. Lett.* **1991**, *177*, 380.
56. Khan, F. A.; Clemmer, D. E.; Schultz, R. H.; Armentrout, P. B. *J. Phys. Chem.* **1993**, *97*, 7978.
57. Haynes, C. L.; Armentrout, P. B.; Perry, J. K.; Goddard, W. A. *J. Phys. Chem.* **1995**, *99*, 6340.
58. Buthelezi, T.; Bellert, D.; Hayes, T.; Brucat, P. *J. Chem. Phys. Lett.* **1996**, *262*, 303.
59. Evans, C. J.; Gerry, M. C. L. *J. Chem. Phys.* **2000**, *112*, 1321.
60. Evans, C. J.; Gerry, M. C. L. *J. Chem. Phys.* **2000**, *112*, 9363.
61. Evans, C. J.; Lesarri, A.; Gerry, M. C. L. *J. Am. Chem. Soc.* **2000**, *122*, 6100.
62. Evans, C. J.; Rubinoff, D. S.; Gerry, M. C. L. *Phys. Chem. Chem. Phys.* **2000**, *2*, 3943.
63. McHugh, M. A.; Krukonis, V. J. "Supercritical Fluid Extraction: Principles and Practice," 2nd ed. Butterworth-Heinemann, Boston, 1994.
64. Sun, X. Z.; George, M. W.; Kazarian, S. G.; Nikiforov, S. M.; Poliakov, M. *J. Am. Chem. Soc.* **1996**, *118*, 10525.
65. Hodges, P. M.; Jackson, S. A.; Jacke, J.; Poliakov, M.; Turner, J. J.; Grevels, F. W. *J. Am. Chem. Soc.* **1990**, *112*, 1234.
66. Burney, D. P.; Burkey, T. J. *Abs. Pap. ACS* **1994**, *207*, 19-INOR.
67. Hall, C.; Perutz, R. N. *Chem. Rev.* **1996**, *96*, 3125.
68. Sun, X. Z.; Grills, D. C.; Nikiforov, S. M.; Poliakov, M.; George, M. W. *J. Am. Chem. Soc.* **1997**, *119*, 7521.
69. Geftakis, S.; Ball, G. E. *J. Am. Chem. Soc.* **1998**, *120*, 9953.
70. Grills, D. C.; Sun, X. Z.; Childs, G. I.; George, M. W. *J. Phys. Chem. A*, **2000**, *104*, 4300.
71. Johnson, F. P. A.; George, M. W.; Bagratashvili, V. N.; Vereshchagina, L. N.; Poliakov, M. *Mendeleev Commun.* **1991**, 26.
72. Grills, D. C.; Childs, G. I.; George, M. W. *Chem. Commun.* **2000**, 1841.
73. Bengali, A. A.; Bergman, R. G.; Moore, C. B. *J. Am. Chem. Soc.* **1995**, *117*, 3879.

- 74. Jina, O. S.; Sun, X. Z.; George, M. W. *Bull. Chem. Soc. Jpn.* to be submitted.
- 75. Demuynck, J.; Kochanski, E.; Veillard, A. *J. Am. Chem. Soc.* **1979**, *101*, 3467.
- 76. Ehlers, A. W.; Frenking, G.; Baerends, E. J. *Organometallics* **1997**, *16*, 4896.
- 77. Pykkö, P. *J. Am. Chem. Soc.* **1995**, *117*, 2067.
- 78. Schröder, D.; Schwarz, H.; Hrušák, J.; Pykkö, P. *Inorg. Chem.* **1998**, *37*, 624.
- 79. Burda, J. V.; Runeberg, N.; Pykkö, P. *Chem. Phys. Lett.* **1998**, *288*, 635.
- 80. Kuksis, I.; Baird, M. C. *Organometallics* **1996**, *15*, 4755.
- 81. Moore, B. D.; Simpson, M. B.; Poliakoff, M.; Turner, J. J. *J. Chem. Soc., Chem. Commun.* **1984**, 972.
- 82. Watkins, W. C.; Jaeger, T.; Kidd, C. E.; Fortier, S.; Baird, M. C.; Kiss, G.; Roper, G. C.; Hoff, C. D. *J. Am. Chem. Soc.* **1992**, *114*, 907.
- 83. Hoobler, R. J.; Hutton, M. A.; Dillard, M. M.; Castellani, M. P.; Rheingold, A. L.; Rieger, A. L.; Rieger, P. H.; Richards, T. C.; Geiger, W. E. *Organometallics* **1993**, *12*, 116.
- 84. Banister, J. A.; Lee, P. D.; Poliakoff, M. *Organometallics* **1995**, *14*, 3876.
- 85. Gregory, M. F.; Jackson, J. A.; Poliakoff, M.; Turner, J. J. *J. Chem. Soc., Chem. Commun.* **1986**, 1175.
- 86. Howdle, S. M.; Poliakoff, M. *J. Chem. Soc., Chem. Commun.* **1989**, 1099.

# THE MATERIALS CHEMISTRY OF ALKOXYSTILBAZOLES AND THEIR METAL COMPLEXES

DUNCAN W. BRUCE

School of Chemistry, University of Exeter, Stocker Road, Exeter EX4 4QD, United Kingdom

- I. Introduction
- II. Background
- III. Synthesis and Characterization
  - A. Stilbazole Ligands
  - B. Metal Complexes
- IV. Nonlinear Optics
  - A. A Brief Introduction to Nonlinear Optics
  - B. NLO Properties of the Stilbazole Derivatives
- V. Langmuir–Blodgett Films
  - A. A Brief Introduction to Langmuir–Blodgett Films
  - B. Langmuir–Blodgett Films of Metal Stilbazole Complexes
- VI. Liquid Crystals
  - A. A Brief Introduction to Liquid Crystals
- VII. Liquid-Crystalline Metal Complexes of Alkoxy stilbazoles
  - A. Introduction
  - B. Mesomorphic Complexes of Group 8 Metals
  - C. Mesomorphic Stilbazole Complexes of Groups 10 and 11 Metals
- VIII. Hydrogen-Bonded Stilbazole Mesogens
- IX. Concluding Remarks
- References

## I. Introduction

This review concentrates on work carried out in Sheffield and then Exeter over a 15-year period. It centers on the alkoxy stilbazole molecule and its derivatives, covering its synthesis, liquid-crystalline properties, and behavior in the general area of materials chemistry, both as a moiety in its own right and in combination with various different metals. It is not intended that the review be comprehensive; the aim is to

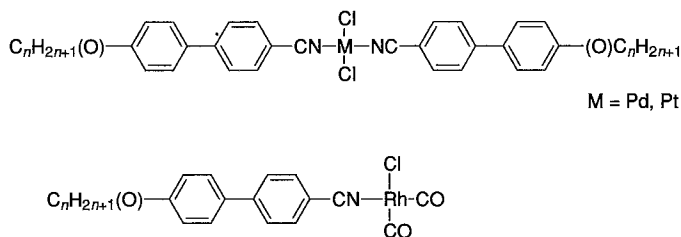


FIG. 1. Cyanobiphenyl complexes of Pd(II), Pt(II), and Rh(I).

concentrate primarily on work performed the author's laboratory and in collaboration with others. The review highlights the properties of stilbazoles in liquid crystals, nonlinear optics, and Langmuir-Blodgett films, and in each area, a brief introduction is offered to enable the reader to gain a working understanding of the key ideas.

## II. Background

Our work with alkoxy stilbazoles originated from previous work with metal complexes of cyanobiphenyls in which liquid-crystalline "ligands" were complexed to Rh(I), Pd(II), and Pt(II) (Fig. 1) (1). With the first two, evidence was obtained that the complexes were rather labile, which we attributed to the rather weak donor ability of the organonitriles. We therefore sought a ligand motif that would bind more strongly to a variety of metals and could be readily elaborated. From this point of view, 4-alkoxy-4'-stilbazoles seemed good candidates and we first synthesized them in our laboratory in Sheffield during the summer of 1985 (2).

## III. Synthesis and Characterization

### A. STILBAZOLE LIGANDS

The stilbazoles have been synthesized using three different routes, and these are now described briefly (Figs. 2 and 3). The first attempts involved reacting 4-alkoxybenzaldehyde with 4-picoline in acetic anhydride, which led to extremely poor yields of the stilbazoles after a week's work (2). This route was subsequently superseded by a Heck coupling method in which 4-vinylpyridine was reacted with 4-alkoxyiodobenzene in the presence of a palladium catalyst (2). The reaction worked very

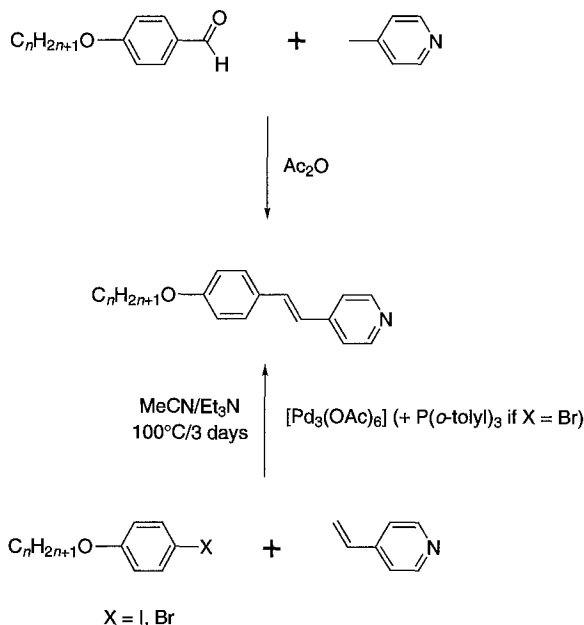


FIG. 2. Synthesis of 4-alkoxy-4'-stilbazoles using acetic anhydride or via a Heck methodology.

well and, when iodides were not readily accessible, could be modified to work with bromides using tri(*o*-tolyl)phosphine as a cocatalyst. However, as more elaborate stilbazoles were synthesized, it became more difficult to access suitable aryl halides, thus, it was necessary to return a procedure using benzaldehydes and picoline, only this time in a more controlled manner, as described in Fig. 3 (3). Picoline was deprotonated with lithium diisopropylamide, then reacted with the benzaldehyde to give the intermediate alcohol which was dehydrated under acidic conditions. This last method was particularly useful with di- and trialkoxy-stilbazoles where the parent di- and trihydroxybenzaldehydes, or their synthetic equivalents, were readily available.

The stilbazoles themselves are creamy, slightly off-white materials which are normally solid at room temperature. The  $^1\text{H}$  NMR spectrum offers some useful features: The methylene group next to the phenolic oxygen gives a triplet at about  $\delta$  4; the AB system of the vinyl group has a coupling constant of  $^3J_{\text{HH}} \approx 16$  Hz, confirming the *E* nature of the substitution; and the aromatic protons *ortho* to the pyridine nitrogen are seen as the broadened half of an AA'XX' spin system at about  $\delta$  8.5, shifting to higher frequency on either complexation or protonation of

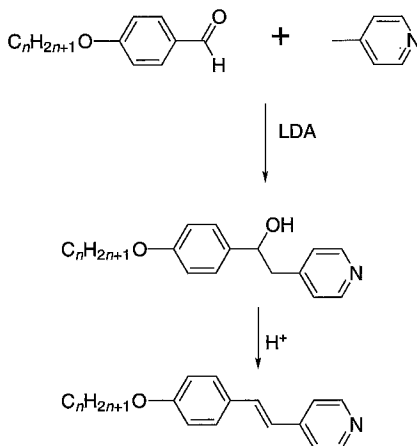


FIG. 3. Synthesis of alkoxy-4'-stilbazoles from benzaldehydes and 4-picoline using LDA.

the ring nitrogen (Fig. 4). In solution in THF, 4-alkoxystilbazoles have a strong absorption at 326 nm which red-shifts to around 368 nm on protonation (the protonated stilbazoles are strongly yellow).

The X-ray single-crystal structure of stilbazole ligands has been determined on three occasions; these are shown in Fig. 5A–C. The structure of 3,4-diethoxy-4'-stilbazole (Fig. 5A) (*4*) showed that the two aromatic rings are planar (r.m.s. deviations 0.0022 Å for the pyridine and 0.0050 Å for the benzene ring), and are twisted with respect to the plane of the alkenic moiety by 6.3° (pyridine) and 18.3° (benzene ring) and mutually twisted by 25.3°. The conformation of the ethoxy chains is antiperiplanar (torsion angles of 179.2° and 179.1° for the chains in the 4- and 3-positions, respectively). A similar arrangement is shown in the structures of 4-undecyloxy-3-fluoro-4'-stilbazole (Fig. 5B) (*5*) and *N*-(4'-methylbenzyl)-4-methoxy-4'-stilbazolium bromide (Fig. 5C) (*6*). For example, the former shows only one of the two possible geometric isomers based on the trans configuration. The two aromatic rings are planar (r.m.s. deviations 0.002 and 0.006 Å) and are twisted with respect to the plane of the olefinic fragment (r.m.s. deviation 0.007 Å) by 4 and 1°, and mutually twisted by 4°; the conformation of the undecyloxy chain is antiperiplanar throughout.

## B. METAL COMPLEXES

The work reported here concentrates on three series of metal complexes whose synthesis is now described. Complexes of Rh(I) and Ir(I)

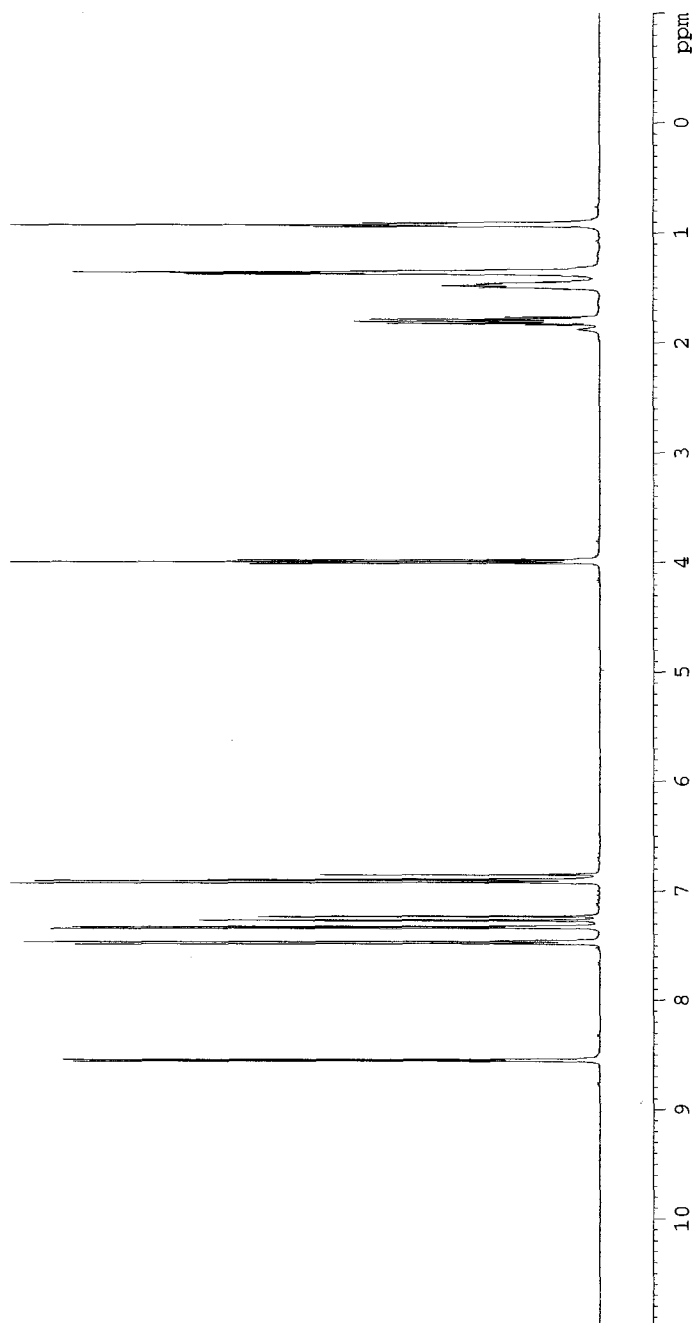


FIG. 4.  $^1\text{H}$  NMR spectrum of 4-hexyloxy-4'-stilbazole.

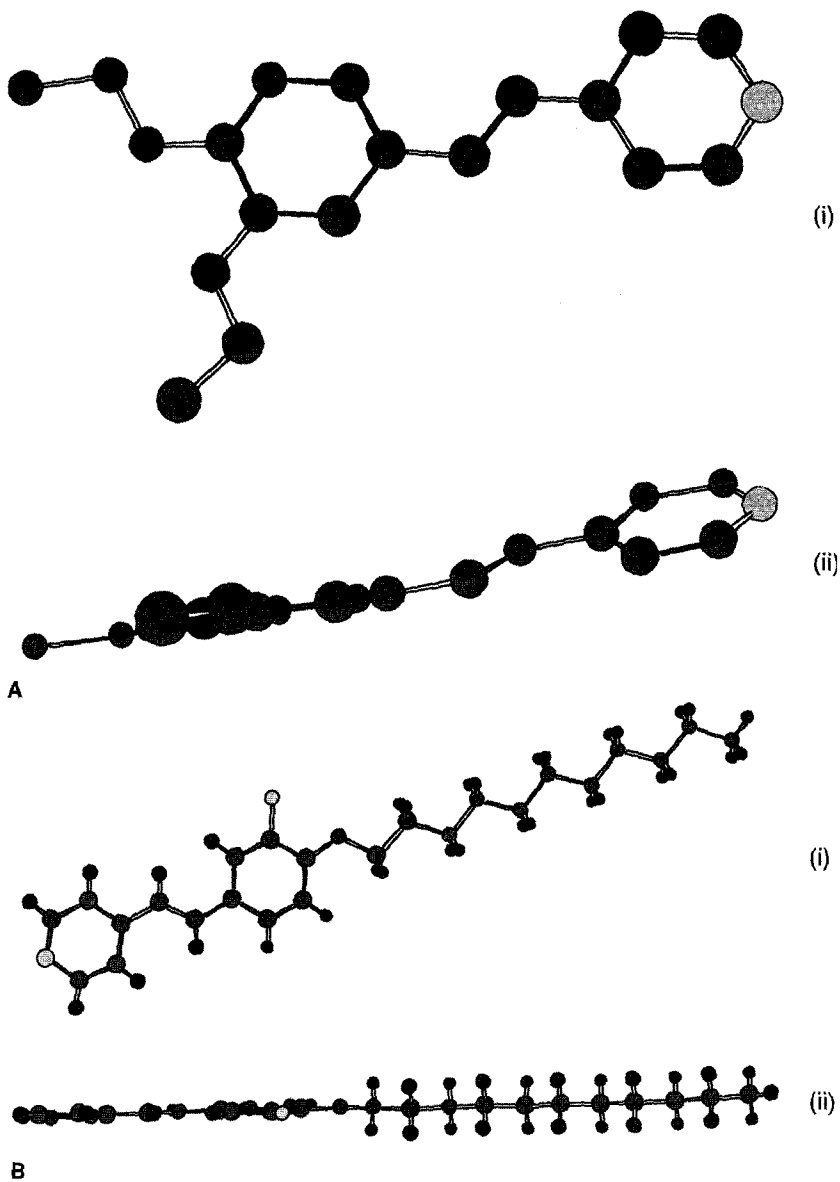


FIG. 5. (A) Two views of 3,4-diethoxy-4'-stilbazole. (B) Two views of the molecular structure of 4-undecyloxy-3-fluoro-4'-stilbazole. (C) Two views of the molecular structure of the *N*-(4''-methylbenzyl)-4-methoxy-4'-stilbazole cation.

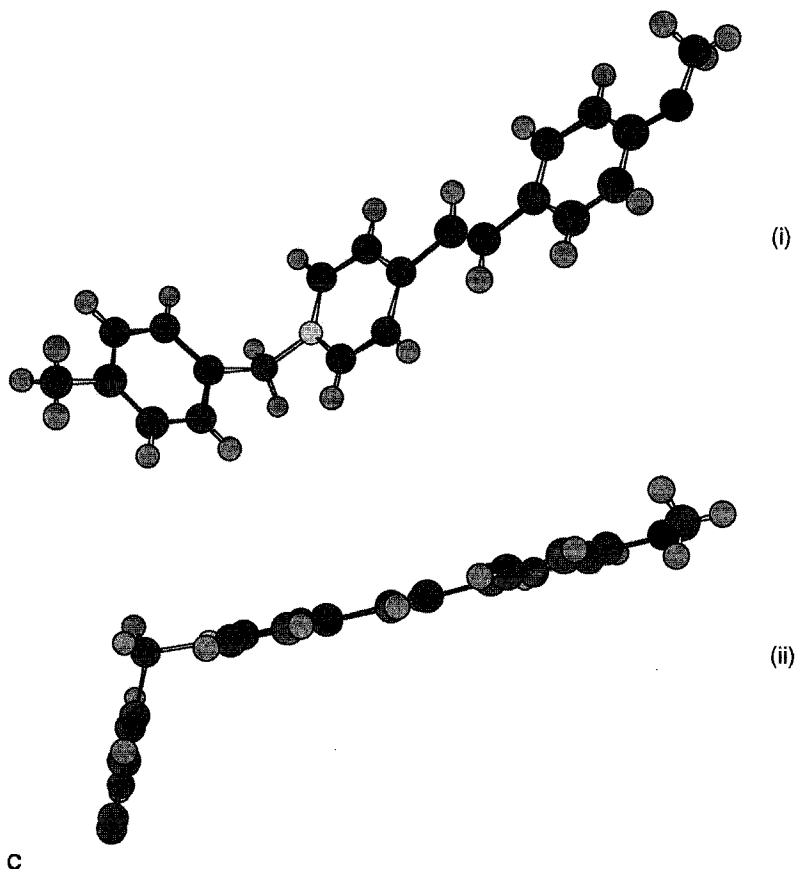


FIG. 5. (Continued)

were obtained starting from the free ligand and, in each case, the chloro-bridged 1,5-cyclooctadiene complex (Fig. 6) (7). Thus, the metal complex and the stilbazole were dissolved in dichloromethane under nitrogen and, after stirring for a few minutes, CO was bubbled through the solution for 10–15 min. The complexes precipitated on addition of hexane to give yields of around 50–80%. Complexes of palladium(II) chloride were most readily accessed by reaction of  $[\text{PdCl}_2(\text{PhCN})_2]$  with just over 2 equivalents of the stilbazole in acetone from which the product precipitated (1). After crystallization, isolated yields were of the order of 85%. The related complexes of platinum(II) were synthesized by adding  $\text{PtCl}_2$  to 2–3 equivalents of the molten ligand at temperatures of 120–140°C (8). The reaction was complete after about 30 min

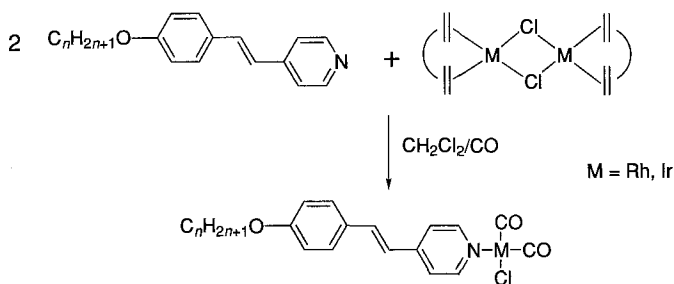


FIG. 6. Synthesis of Rh(I) and Ir(I) complexes of alkoxy stilbazoles.

and, following work-up and crystallization, the products were obtained in yields of about 60%. The Pd(II) complexes can be made in this way, but are better made by the method described above. Complexes of palladium(II) carboxylates were obtained in two steps (Fig. 7). First, the palladium(II) carboxylate was synthesized by reaction of  $[\text{Pd}_3(\text{OAc})_6]$  with the relevant carboxylic acid in benzene, with the acetic acid product being removed in a Dean–Stark trap (9). The isolated carboxylate complexes could then be reacted with the desired stilbazole in acetone to give the target complex (10). These syntheses were carried out using a wide range of palladium carboxylates and stilbazoles, and yields were very variable. Finally, stilbazole complexes of silver(I) were obtained by reacting the parent silver salt with 2 equivalents of the stilbazole in an organic solvent. The exact solvent used is a function of the silver salt and the stilbazole; yields are in the range of 40–85%.

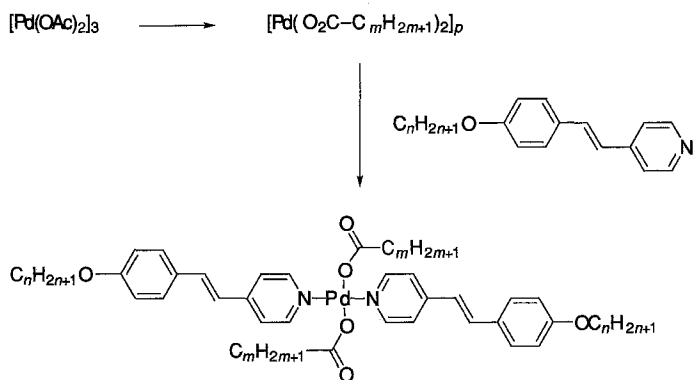


FIG. 7. Synthesis of palladium(II) carboxylates and their complexes with alkoxy stilbazoles.

## IV. Nonlinear Optics

A. A BRIEF INTRODUCTION TO NONLINEAR OPTICS<sup>1</sup>

All molecules exhibit a linear optical response when subjected to an external field; that is to say, the dipole moment induced by that field ( $\mu_i$ ) is linearly proportional to the field [ $E$ : Eq. (1), where  $\alpha$  is the dipole polarizability, a complex number whose real part is related to the refractive index of the material and whose imaginary part relates to the extinction coefficient for photon absorption].

$$\mu_i = \alpha E \quad (1)$$

This recognizes that the external field results in a redistribution of the electrons in the test material. However, this expression is only an approximation to an infinite series expanded on powers of the field, as shown in Eq. (2), where  $\beta$  and  $\gamma$  are the first and second hyperpolarizabilities, respectively:

$$\mu_i = \alpha E + \beta E^2 + \gamma E^3 + \dots \quad (2)$$

Because the coefficients  $\alpha$ – $\gamma$  decrease as  $\alpha \gg \beta \gg \gamma$ , the effects arising from the higher terms are observed only at very high fields, typically those found in laser light. Let us concentrate here on materials giving rise to second-order nonlinear optical effects, i.e., those in which the  $\beta$  term is important.

Nonzero second-order effects are found only in noncentric molecules,<sup>2</sup> and this is readily seen in the following argument. Assuming that only the first two terms of Eq. (2) are relevant, the induced dipole moment of some centrosymmetric molecule, on application of a field  $E$ , is given by Eq. (3):

$$\mu_i = \alpha E + \beta E^2 \quad (3)$$

If, however, a field  $-E$  is applied, the same expression gives Eq. (4):

$$\mu_i = -\alpha E + \beta E^2 \quad (4)$$

<sup>1</sup>For a much more detailed account, see Ref. (11).

<sup>2</sup>This has always been held to be true. However, in a limited number of examples, centric molecules *do* give rise to second-order nonlinear optical effects in the bulk. This is attributed to solid-state effects. See, for example, Ref. (12).

However, the molecule is centrosymmetric; hence the induced dipole moment cannot depend on the polarity of the applied field. Therefore, the only way that the two expressions can be equated is if  $\beta = 0$ . But life is not quite that simple. The equations used above all refer to events at the molecular level, and, of course, the effects we wish to observe occur in the bulk. Thus, there is a macroscopic equivalent of Eq. (2) which applies to the bulk; this is given as Eq. (5):

$$P_i = \chi^{(1)} E + \chi^{(2)} E^2 + \chi^{(3)} E^3 + \dots \quad (5)$$

Here  $P_i$  is the macroscopic induced polarization; and for molecular materials,  $\alpha$ ,  $\beta$ , and  $\gamma$  are related to their macroscopic counterparts  $\chi^{(1)}$ ,  $\chi^{(2)}$  and  $\chi^{(3)}$ , where polarization is dipole moment/unit volume.

The consequences of this are that the noncentric molecules are also required to pack in a noncentric space group. Thus, the best nonlinear optical molecule in the world will show no bulk effect if it packs in a centric space group. Without going into details, it also follows that different noncentric space groups give different NLO responses. Furthermore, for a given space group the orientation of the chromophore within the crystal system can also have a dramatic effect on the NLO response. Quite a tall order to control!

Once these conditions are met, a range of optical effects is possible. There is not the space to go into these in this review, but one example is that of parametric amplification, where a probe beam ( $\nu_2$ ) may be detected in the presence of a pump beam ( $\nu_1$ ) (Fig. 8). Assuming that  $\nu_2$  is of weak intensity (so that  $2\nu_2$  does not arise), the nonlinear optical medium gives rise to two output beams, namely  $2\nu_1$  (this effect is known as frequency doubling or second harmonic generation, SHG) and  $\nu_1 + \nu_2$  (parametric amplification), whereupon  $\nu_2$  is detected. Note that for SHG, doubling the frequency halves the wavelength, so that the fundamental of a Nd-YAG laser at 1064 nm (infrared) ends up as a beam at 532 nm (visible—green). Note also that the material must be transparent at the wavelength of the fundamental and the resultant beams; otherwise, absorption and hence damage can occur.

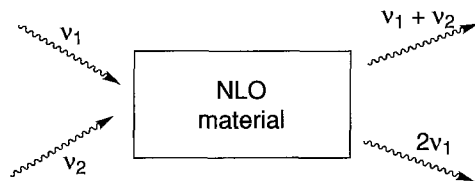


FIG. 8. Schematic diagram of a parametric amplifier.

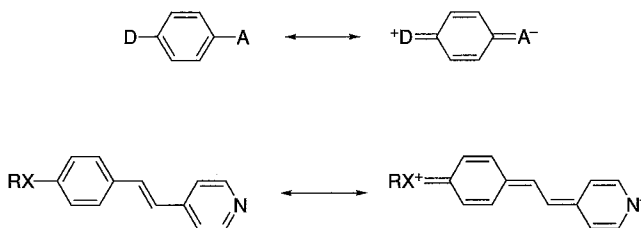


FIG. 9. Charge-transfer excited states in a schematic donor-acceptor molecule and in a stilbazole.

## B. NLO PROPERTIES OF THE STILBAZOLE DERIVATIVES

Given that both linear and nonlinear optical (NLO) effects have their origins in the redistribution of electrons, it is not surprising that large effects are seen in materials with extended  $\pi$  systems and where there are donor and acceptor groups in conjugation (see Fig. 9). Thus, as a molecular species, the stilbazole fragment is a good NLO candidate. Indeed, Meredith (13) reported that in the solid state, 4-(*N,N*-dimethylamino)-*N'*-methylstilbazolium methylsulfate (Fig. 10;  $X = \text{MeSO}_4$ ) gave a second-order NLO response 250 times greater than that of urea (taken as an arbitrary standard and evaluated by the Kurtz powder technique, which simply measures the intensity of the frequency-doubled radiation). This work was followed much later by studies from Marder, who showed that in related derivatives (Fig. 10;  $X = \text{OTf}$ ,  $\text{OTs}$ ,  $\text{Cl}$ ,  $\text{BF}_4$ ,  $\text{I}$ ), NLO responses of up to  $10^3$  times that of urea were possible (14). This work was also interesting in showing how important solid-state effects were in determining the SHG response. For

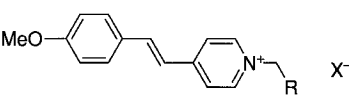
	X	$\chi^{(2)}/\text{urea}$
	$\text{MeSO}_4$	250
	$\text{OTf}$	0
	$\text{OTs}$	1,000
	$\text{Cl}$	0
	$\text{I}$	80
	$\text{BF}_4$	75

$X^-$

FIG. 10. SHG efficiencies of some 4-(*N,N*-dimethylamino)-*N'*-methylstilbazolium salts.

example, much higher SHG values were found in stilbazolium derivatives where there was a hydrated chloride counteranion, compared to the situation where the anion was not hydrated. This serves to emphasize the point made above about the importance of chromophore orientation in the crystal.

Three approaches were adopted. First, instead of using *N*-methylstilbazolium cations, *N*-benzyl derivatives were examined. These are stable moieties; moreover, other substitution of the benzyl group is possible, which could aid noncentric packing. Thus, the compounds shown in Fig. 11 were synthesized, but the NLO response at 1064 nm was poor, with one derivative crystallizing centrosymmetrically, giving  $\chi^{(2)} = 0$  (15). Next, an alternative donor function was examined, employing the jullolidine ring rather than a 4-(*N,N*-dimethylamino)phenyl group, as the nitrogen ought to be a good donor to the phenyl ring (Fig. 12). However, the results were disappointing, with all SHG efficiencies at 1907 nm being less than that of urea itself (16). Thus, the two fused rings had adversely affected the packing of the NLO chromophores in the solid state.



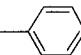
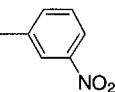
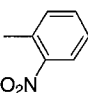
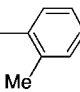
X	R	$\chi^{(2)}/\text{urea}$
Br		0
OTf		21.8
OTf		0.3
OTf		2.7

FIG. 11. SHG efficiencies of some *N*-benzylstilbazolium salts.

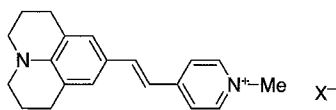
	X	$\chi^{(2)}/\text{urea}$
	MeSO <sub>4</sub>	0.02
	OTf	0.03
	OTs	0.1
	NO <sub>3</sub>	0.5

FIG. 12. SHG efficiency of some salts of a jullolidine-based chromophore.

It was then decided to look at metal complex derivatives, with a view to evaluating the effect of complexation on the molecular hyperpolarizability, i.e.,  $\beta$ . In this case, the stilbazole used was a chiral derivative bearing a resolved 2-methylbutyloxy chain, in the hope that this might have a positive effect on the crystal packing (recall that chiral compounds crystallize noncentrally). First the uncomplexed ligand was examined and then its complexes with Rh(I), Ir(I), and Pt(II), as shown in Fig. 13. The molecular hyperpolarizability,  $\beta$ , was measured using the EFISH technique with a fundamental wavelength of 1.9  $\mu\text{m}$

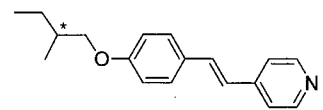
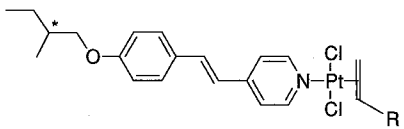
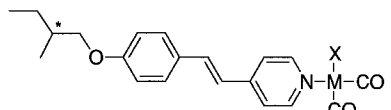
		$\beta \cdot 10^{30}/\text{esu}$ (1.9 $\mu\text{m}$ in $\text{CHCl}_3$ )
		15.8
	R = H	27.0
	R = Ph	31.0
	M = Rh, X = Cl	24.4
	M = Rh, X = Br	23.9
	M = Ir, X = Cl	24.4
	M = Ir, X = Br	56.0 (In acetone)

FIG. 13. Molecular hyperpolarizabilities of 4'-(2-methylbutyloxy)-4''-stilbazole and some of its metal complexes.

(generated from a Nd-YAG fundamental using a pressurized-hydrogen Raman shifter). EFISH (electric-field-induced second harmonic generation) is carried out in solution, and the noncentrosymmetric environment required for SHG observation is obtained by the application of a large electric field across the sample, which creates polar order of the solute molecules, allowing a frequency-doubled signal to be observed and measured.

The results showed a 1.5- to 3-fold enhancement of  $\beta$  on complexation. It is interesting to consider the origin of this enhancement (17). Figure 14A shows an idealized situation where an NLO chromophore contains a  $\pi$  donor and a  $\pi$  acceptor in conjugation, in which case a charge-transfer contribution to  $\beta$  ( $\beta_{CT}$ ) can be considered. However, one can also consider the situation in which donors or acceptors act independently, individually perturbing the electronic distribution of the molecule, as illustrated in Fig. 14B. These effects, which are not restricted to situations in which the donor/acceptor is in  $\pi$  conjugation with the aromatic system, are termed additive effects ( $\beta_{add}$ ); thus,  $\beta$  can be thought of as the sum of these two terms [Eq. (6)], with  $\beta_{CT}$  normally being the greater of the two.

$$\beta = \beta_{CT} + \beta_{add} \quad (6)$$

If in these complexes the dicarbonylhalometal(I) fragment is acting as a  $\pi$  acceptor and enhancing the conjugation of the stilbazole ligand (Fig. 14C), then the complex might be expected to be quite strongly colored, and the carbonyl stretching frequencies in the infrared spectrum to be much lower than in, for example, the analogous complex with a pyridine ligand. However, the complexes were found to be yellow or slightly orange (Rh) (for Ir-Cl species,  $\lambda_{max} = 364$  nm,  $\epsilon = 30,304$  dm<sup>3</sup> mol<sup>-1</sup> cm<sup>-1</sup>) (7); moreover, there is no hint of a charge-transfer absorption, and the carbonyl stretching frequencies of the

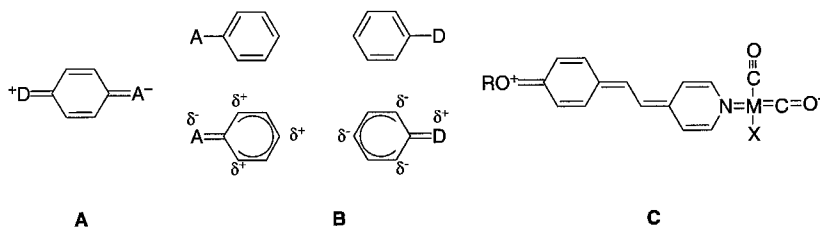


FIG. 14. Diagram to show (A) the first excited state of a conjugated donor/acceptor aromatic, (B) inductive charge redistribution caused by isolated donor and acceptor atoms, and (C) a hypothetical charge delocalization in a group 8 metal stilbazole complex.

stilbazole complexes ( $\nu_{\text{CO}} = 2074$  and  $1993 \text{ cm}^{-1}$ ) are almost identical to those of *cis*-[IrCl(CO)<sub>2</sub>(py)] ( $\nu_{\text{CO}} = 2075$  and  $1981 \text{ cm}^{-1}$ ) (18). Thus, the enhancement of the NLO response must be due purely to  $\sigma$ -effects, which is consistent with related work where the stilbazoles were complexes with boron(III) species and a two-fold enhancement of NLO response was found (19).

## V. Langmuir–Blodgett Films

### A. A BRIEF INTRODUCTION TO LANGMUIR–BLODGETT FILMS<sup>3</sup>

If a water-insoluble, amphiphilic material is deposited at the water/air interface (e.g., by layering a solution of the amphiphile in an organic solvent on the water and letting the organic solvent evaporate), the polar part of the amphiphile will associate with the water while the nonpolar part will stand proud of the surface (Fig. 15). The isotropic arrangement of amphiphiles adsorbed at the interface (sometimes referred to as a two-dimensional gas) may be compressed mechanically to give thin films with differing degrees of order (two-dimensional liquids or solids). This process can be monitored via a pressure ( $\Pi$ )/area (A) isotherm (Fig. 16). The isotherm shows features that are attributable to the formation of the “liquid” and “solid” states, it also shows a feature

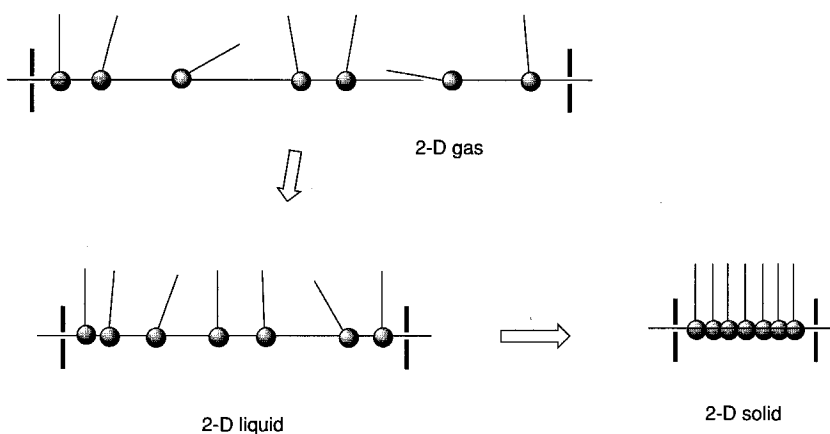
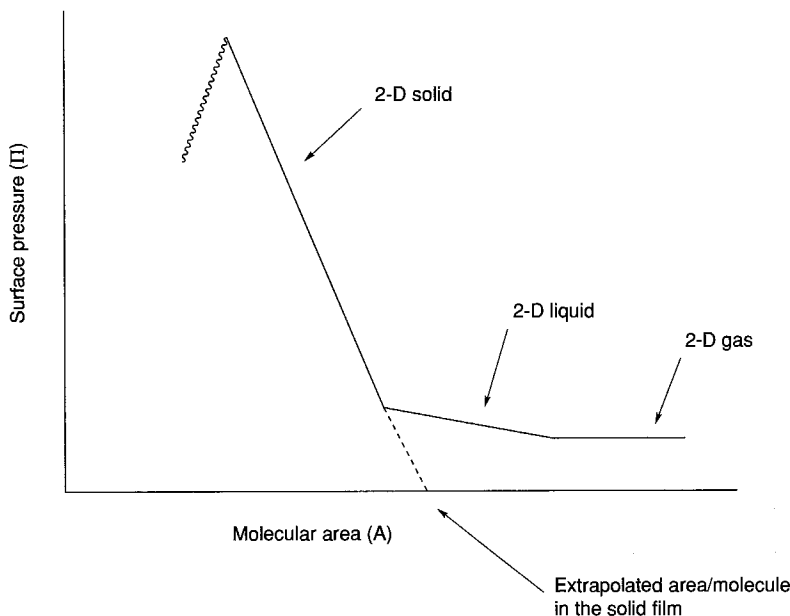


FIG. 15. Diagrammatic representation of a Langmuir monolayer as a 2-D gas, liquid, and solid.

<sup>3</sup> For a much more detailed account, see Ref. (20).

FIG. 16. Schematic  $\Pi/A$  isotherm.

corresponding to the collapse of the film when the pressure exceeds the critical value for that film. The isotherm also allows the molecular area at the surface to be evaluated by extrapolation. "Solid" films prepared in this way are known as Langmuir films.

Such films may be transferred from the water/air interface to a solid substrate by dipping the substrate into the water and removing it (Fig. 17). This process may be repeated, permitting multilayer (Langmuir–Blodgett) films to be built up. Four main types of film may be identified: namely, X-, Y-, and Z-type films, as well as alternate-layer films (Fig. 17). Normally, Y-type films are the easiest to form, and the most robust, mainly because like parts of the molecules are kept with like. For the same reasons, X- and Z-type films tend to be less robust, as do alternate-layer films. However, the last three film types have the potential advantage that they are noncentrosymmetric and hence are potentially amenable to a range of useful physical effects.

Archetypal species that have been studied in Langmuir–Blodgett (L-B) deposition include conventional amphiphilic species such as long-chain carboxylic acids and some of their metal salts; a feature of many systems that have been deposited is that stable films appear to require quite long alkyl chains (typically  $>C_{14}$ ).

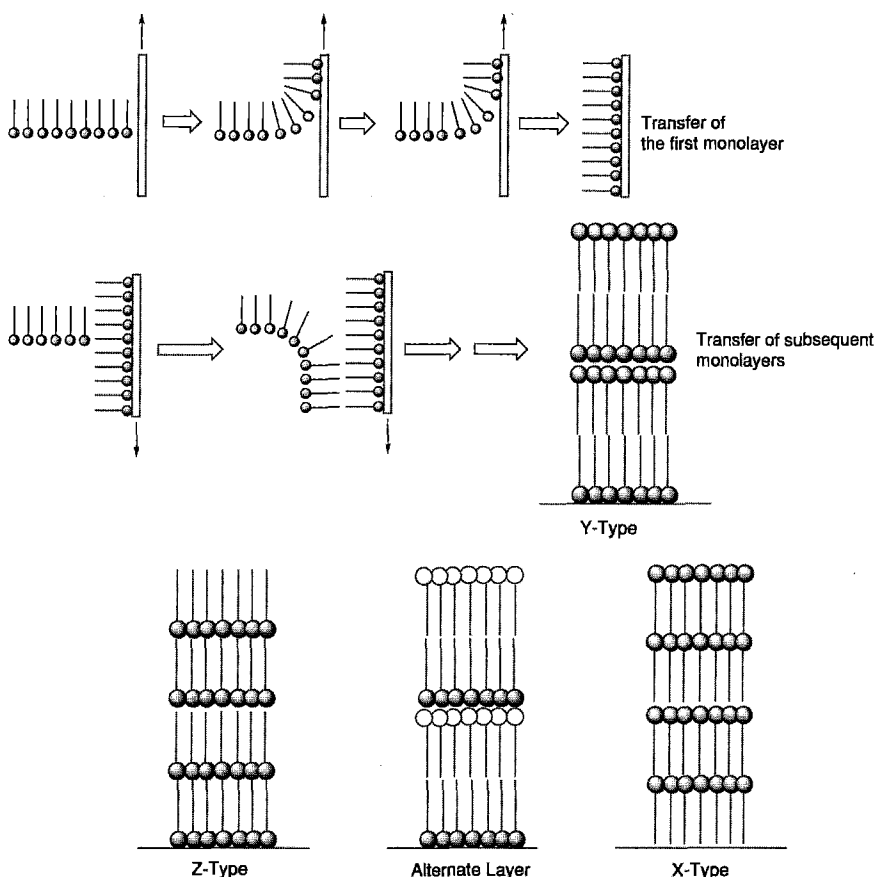


FIG. 17. Diagram to show the deposition of a Y-type L-B film and the structure of X- and Z-type films.

## B. LANGMUIR-BLODGETT FILMS OF METAL STILBAZOLE COMPLEXES

Our work with L-B films was carried out in collaboration with Dr. Tim Richardson of the Department of Physics at Sheffield University and started as a "look-see" experiment. The complexes studied were the Rh(I) and Ir(I) complexes of the simple alkoxy stilbazoles illustrated in Fig. 6. Surprisingly, with these materials it was possible to form films of the materials with alkoxy chain lengths as short as pentyloxy, with very stable films being accessed with octyloxy chains (21). All of these depositions were Y-type, and linear increases in absorption were seen with successive depositions. As implied above, these are short chain

lengths relative to most Langmuir-film-forming materials, but the fact that the complexes are liquid-crystalline is significant, as the complexes are clearly predisposed to forming ordered structures. It is also relevant to note that parallels have been drawn between the structures formed in Langmuir monolayers and those seen in liquid-crystal smectic phases.

While Y-type deposition was successful, the effects of potential interest to us are not found in centrosymmetric structures; thus, it was necessary to look at methods for forming noncentric multilayer fabrications. This was achieved by using docosanoic acid so that the multilayer was composed of a layer of stilbazole complex, then a layer of the acid, then the complex and so on. Using this method, films of up to 23 layers were fabricated. One effect sought was a nonlinear optical response, given the good chromophoric properties of the stilbazole described above. Various factors militated against a detailed study, but suffice it to say that, mysteriously, it was not possible to observe any SHG from noncentric, alternate-layer systems of this type.

However, it was possible to look at pyroelectric response, that is, the change in polarization as a function of temperature. This is expressed mathematically in Eq. (7):

$$\Delta P_i = p_i \Delta T \quad (7)$$

Here  $P_i$  is the change in spontaneous polarization,  $p_i$  is the pyroelectric coefficient, and  $\Delta T$  is the temperature change. A graphical representation of a typical response profile is shown in Fig. 18. Clearly, devices that produce a current when the temperature changes can be applied in a variety of heat-sensing applications; thus, there was some interest in seeing how these thin-film samples performed. Here the response was found to be very good indeed, and values for  $p_i$  as high as  $3.2 \mu\text{C m}^{-2} \text{K}^{-1}$  were measured (22); at the time, this was the largest value reported, although these values have since been exceeded in certain calixarenes and poly(siloxanes) measured by Richardson (23). However, an interesting

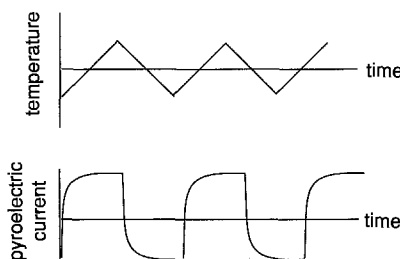


FIG. 18. Graphical representation of a theoretical pyroelectric response profile.

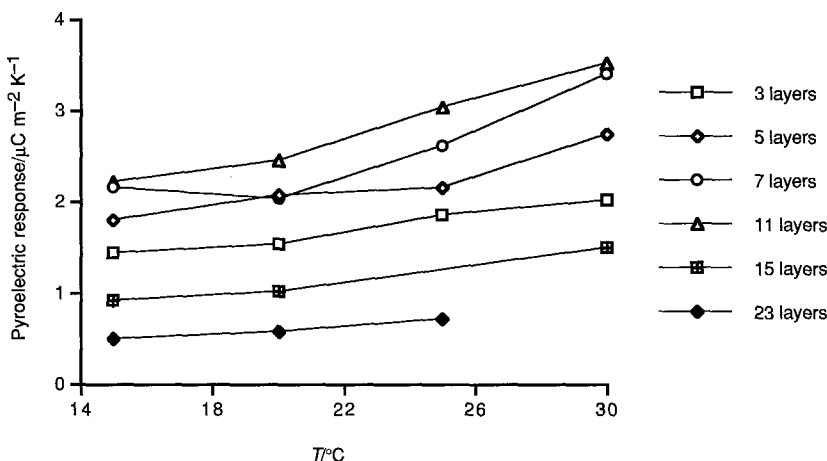


FIG. 19. Graph showing the pyroelectric response of the stilbazole L-B films as a function of both temperature and number of layers.

aspect of this study was that while  $p_i$  increased with the number of layers (as would be expected), this lasted only for fabrications with up to nine layers, after which the response collapsed (Fig. 19). The reason for this may be that, with so many layers, the multilayer structure was somehow unstable and that the nice, regular arrangement of complex and acid collapsed, thus limiting the extent to which the response in these systems could be maximized.

## VI. Liquid Crystals

The greatest amount of work we have carried out with alkoxy stilbazoles is in the field of liquid crystals; indeed, this is where our interest in stilbazoles started. After a brief and rather general introduction to liquid crystals, we will consider various types of complex that form liquid-crystal mesophases when complexed to stilbazoles, emphasizing patterns of behavior without delving into the subtleties. A more detailed discussion of the silver systems may be found elsewhere (24). Finally, although this article appears in a series that concentrates on inorganic chemistry, we offer an overview of some of our work with stilbazoles in hydrogen-bonded liquid crystals.

### A. A BRIEF INTRODUCTION TO LIQUID CRYSTALS

The liquid crystal state represents a fourth state of matter. Located between the solid and liquid states, it is bounded by these states,

possessing properties reminiscent of both. As in the solid state, there is order; as in the liquid state, there is fluidity. Moreover, transitions from the solid to the liquid crystal state are strongly thermodynamically first-order, while transitions from the liquid-crystal to the liquid state [the latter termed *isotropic* liquid (I) to distinguish it from the liquid crystal] are weakly first-order. Transitions between liquid-crystal mesophases are usually weakly first-order or second-order. The result is an ordered liquid in which the physical properties are anisotropic; indeed, this anisotropy in the physical properties has led to their widespread application. Clearly, the liquid-crystal state is not found for all molecules. What, then, are the criteria necessary for liquid-crystal phase (mesophase) formation? There are several, but uppermost is the requirement that molecules be structurally anisotropic. This leads to intermolecular anisotropic dispersion forces that are strong enough to stabilize the mesophases. The two most common anisotropic forms are rods and disks; liquid crystals derived from the former shape are termed *calamitic* liquid crystals (mesogens), while those derived from the latter are *discotic* mesogens.

### 1. Calamitic Mesogens and the Phases They Form

Design guidelines for calamitic materials suggest that the molecules may be built up of two or more rings, linked by a variety of functional groups and terminated by either one or two alkyl chains. The rings are most frequently phenyl rings, but heteroaromatic, alicyclic, and even bicyclic rings have been used [indeed, it may be of interest to readers that boron clusters have been employed by Kaszynski (25)]. The linking groups act to preserve the overall linearity of the molecule, although the preservation of conjugation is not important; typical examples are shown in Fig. 20. Finally, it is worth noting that, almost without exception, calamitic mesogens possess at least one terminal chain and most possess two. The chains contribute to the structural anisotropy and, because they do not pack easily into a crystalline form, act to reduce the melting point. Where there is only one terminal chain, it is common to

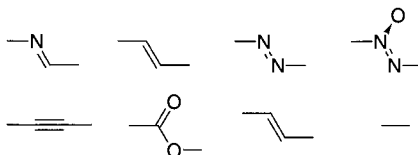


FIG. 20. Examples of linking groups used in the construction of calamitic liquid crystal molecules.

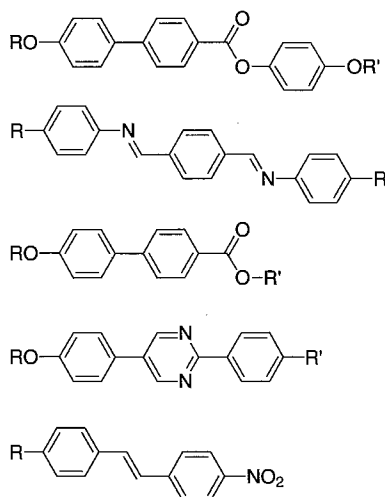


FIG. 21. Examples of calamitic mesogens.

find a small, polar group at the other end of the molecule, e.g., a nitrile or nitro group. Because the number of liquid crystals is huge, it is not possible to give representative examples of all calamitic mesogens. The reader is therefore referred to the website of the Hamburg Liquid Crystal Group (<http://liqcryst.chemie.uni-hamburg.de/>), where a wealth of information can be found, including the *LiqCryst* Database (26), which contains details of all published mesophase materials. However, to give a flavor of what might constitute a calamitic mesogen, a few examples are presented in Fig. 21.

Calamitic mesogens in general form two main types of mesophase: the nematic phase (N) and the smectic (S) phases. The nematic phase is the most disordered of the mesophase types; in it, the molecules possess one-dimensional orientational order and no positional order (Fig. 22).

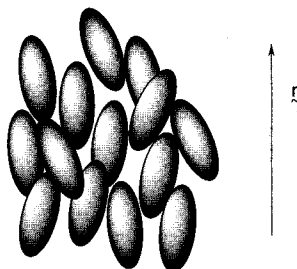


FIG. 22. Schematic molecular arrangement in the nematic phase of rod-like molecules.

The average orientational direction of the molecules is denoted by the director,  $\underline{n}$ , with the degree of orientational correlation evaluated by the order parameter,  $S$ , expressed as in Eq. (8), where  $\theta$  is the angle between a molecule and the director. It is the nematic phase of calamitic molecules that is used in liquid crystal displays.

$$S = 1/2 \langle 3 \cos^2 \theta - 1 \rangle \quad (8)$$

Smectic phases differ from the nematic phase in that the molecules within them, possess some partial positional order, resulting in a sort of layering of the mesogens; consequently, they are more ordered and occur to lower temperature of the nematic phase. There are two subclasses of smectic phase: those without any in-plane order ( $S_A$  and  $S_C$ ) and those with some in-plane order ( $S_B$ ,  $S_F$ , and  $S_I$ ). (Note that the subscripts are simply identifiers and carry no other information.) Thus, in the  $S_A$  phase (Fig. 23), which is very fluid, the molecules are on average orthogonal to the layer direction, and there is a high probability for molecules to move between layers. The  $S_C$  phase (Fig. 23) is similar except that the average orientation of the molecules is at some angle,  $\theta$ , to the layer direction, giving a lower-symmetry situation. The  $S_B$ ,  $S_F$ , and  $S_I$  phases (Fig. 23) all possess hexagonal symmetry within the layers; in the  $S_B$  phase the molecules are orthogonal to the layers, while in the other two phases they are tilted—toward the edge of the hexagon in the case of  $S_F$  and toward a vertex of the hexagon for  $S_I$ . A fuller account of the structure of these phases is found elsewhere (27).

## 2. Discotic Mesogens and the Phases They Form

To some extent, the design criteria for discotic mesogens are somewhat simpler than those for their calamitic counterparts. In many cases, it is possible to choose a favorite disk-like molecule, then add 6–8 peripheral alkyl chains to generate a mesomorphic (i.e., liquid-crystalline) material. Thus, phthalocyanines, triphenylenes, truxenes, and many other systems will generate mesogenic (i.e., liquid-crystal-like) materials with appropriate substitution; these examples are shown in Fig. 24. Note that it is not necessary for the mesogen to have a planar core.

In calamitic systems it is the long axis of the molecules that is correlated in the mesophases; but in discotic systems it is the short axis and different types of organization are seen, although disk-like molecules also form a nematic phase in which a unique axis is orientationally correlated (Fig. 25). However, below the nematic phase is a series of columnar phases (Col) in which the disks are stacked up into columns, which are themselves arranged according to some symmetric pattern. Typical

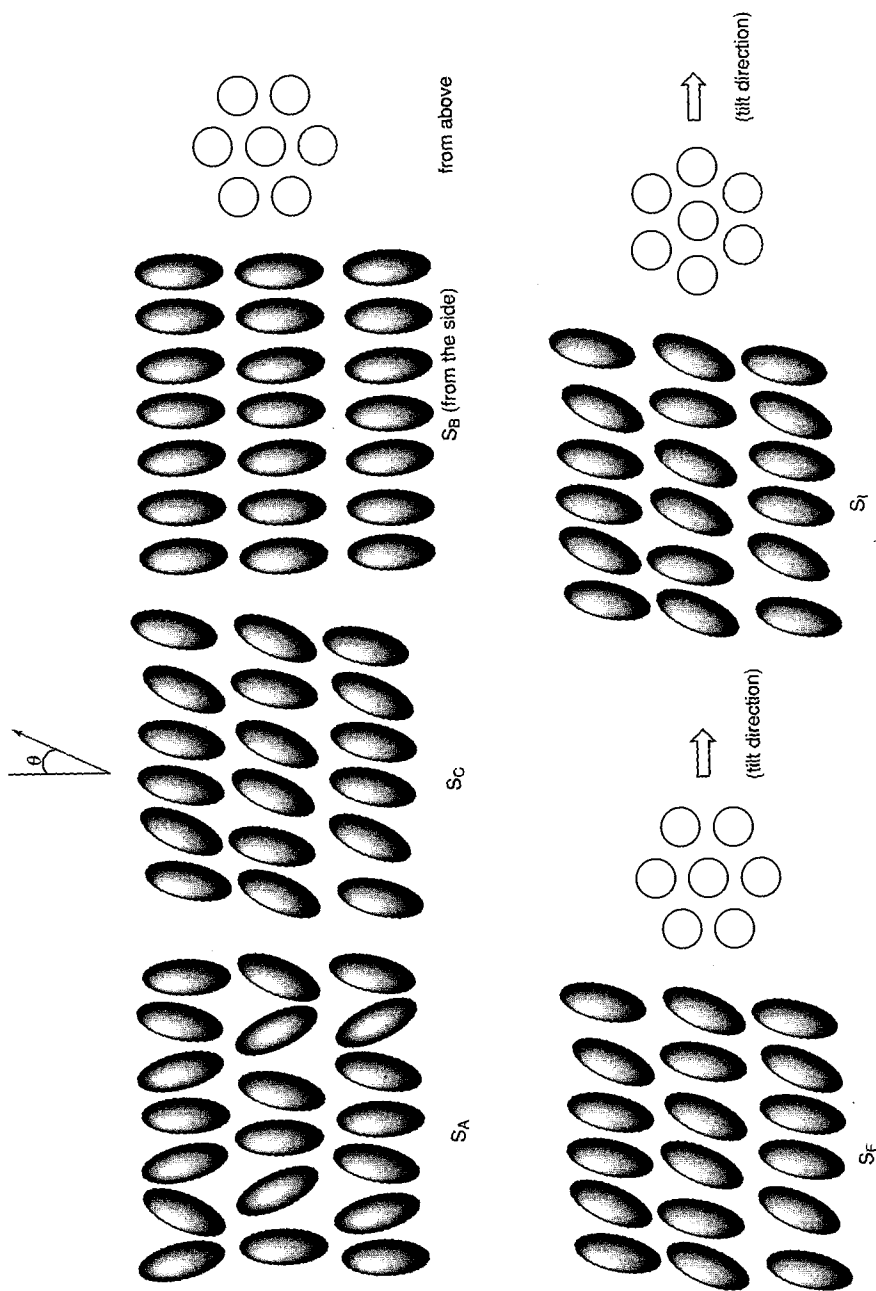


FIG. 23. Molecular arrangement in the  $S_A$ ,  $S_B$ ,  $S_C$ ,  $S_F$ , and  $S_I$  phases.

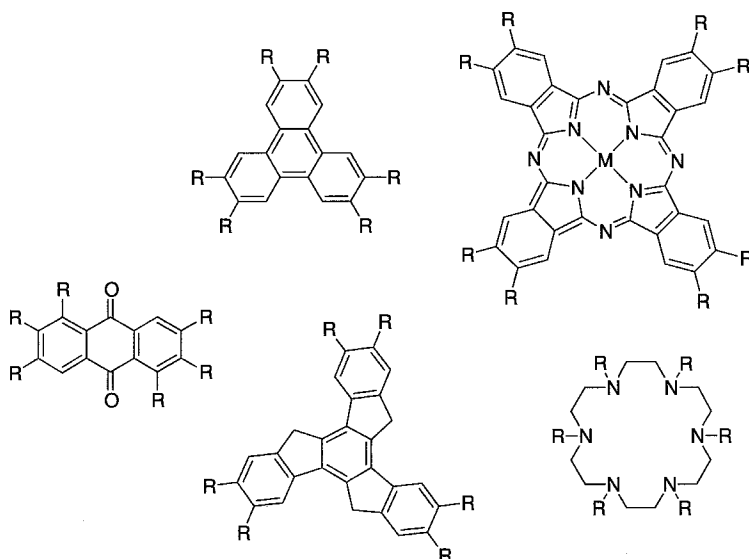


FIG. 24. Examples of some discotic mesogens.

examples are the hexagonal columnar ( $\text{Col}_h$ ), rectangular columnar ( $\text{Col}_r$ ), and the oblique ( $\text{Col}_{ob}$ ) phases, as illustrated in Fig. 26.

A few words of clarification about the nomenclature are relevant here. Columnar phases have been known for many years; they were evident, for example, in the work of Spegt and Skoulios (28) on metal soaps, although these are not classical disk-shaped molecules. In 1977, however, a hexasubstituted benzene derivative was reported (29), this derivative was the first example of a properly disk-like mesogen, and the term *discotic* was coined to describe the mesophases it formed. Thus, for example, the discotic hexagonal phase was labeled  $\text{D}_h$ . The introduction of this nomenclature has actually caused confusion as disk-like molecules are not alone in their capacity to form columnar phases (indeed, some

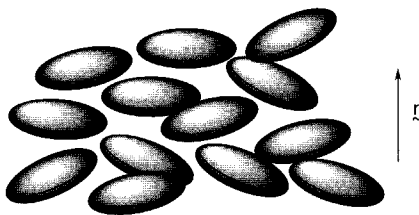


FIG. 25. Schematic molecular arrangement in the nematic phase of disklike molecules.

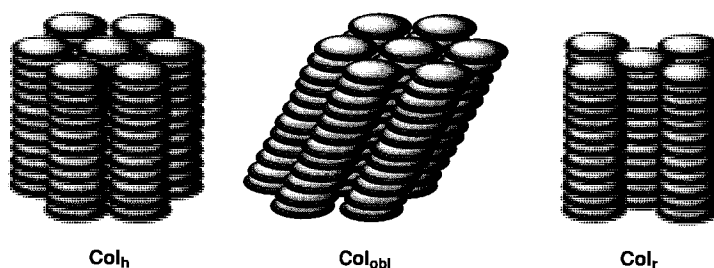


FIG. 26. The molecular organization in some columnar mesophases.

other classes will be discussed below). Thus, it is wrong to categorize a phase by the shape of the molecule of which it is constituted; rather, the description must reflect the organization and the symmetry. Another aspect of the nomenclature relates to the presence or absence of order within the columns: i.e., How well correlated are the molecules within each column? The nomenclature adopted required that the term *ordered* be applied to the phase if the correlation was high. Hence high correlation is indicated by  $\text{Col}_{ho}$ , while low correlation, which gives a *disordered* phase, is indicated by  $\text{Col}_{hd}$ . Evidence for the presence or absence of disorder came from X-ray diffraction studies (*vide infra*). In some cases, it was possible to see the 3.4-Å stacking repeat (typical in columnar phases of planar aromatic systems) and therefore to assign the phase as ordered or disordered. But questions remain. At what point does an ordered phase become disordered? What correlation length is the boundary between one and the other? And, how does one cope in systems whose 3.4-Å repeat is not seen for some reason? Faced with these problems, many workers, particularly those engaged in structural studies, prefer to drop the designations “ordered” and “disordered”—a preference this author supports fully.

### 3. Polycatenar Mesogens

While rods and disks represent extremes of shape anisotropy that give rise to mesophases, one class of compounds appears to bridge the gap between these extremes. These materials are termed *polycatenar liquid crystals* (30), where *polycatenar* simply means “many tails.” The mesogens are characterized by their rod-like shape, with a rather extended core, and by possession of three to six terminal chains. There are several isomeric possibilities for such systems, two of which are considered in this review.

The first, and arguably the most interesting, are tetracatenar mesogens whose terminal chains are attached to the 3 and 4 positions of the

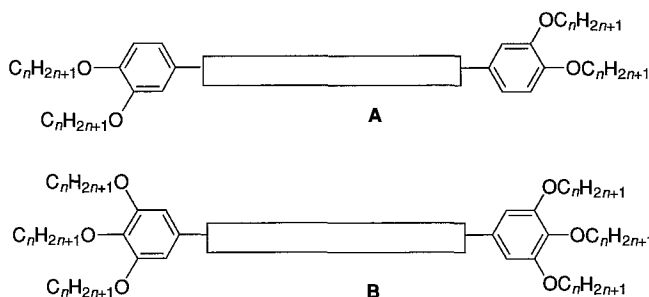


FIG. 27. Schematic diagram to show (A) a 3,4-substituted tetracatenar mesogen and (B) a 3,4,5-substituted hexacatenar mesogen.

end phenyl groups (schematized in Fig. 27A). At short chain lengths, these materials show either the nematic or smectic C phase or both, while at longer chain length, columnar phases are found. Understanding the formation of the nematic and smectic phases, is straightforward. But how do we understand the formation of the columnar phase? To do this, it is necessary to introduce the idea of *surface curvature*.

At short chain lengths, the volume of the mesogen core is greater than or similar to that of the terminal chains, and so it is easy for a lamellar phase to result. However, as the chains get longer, they take up more volume (this can also be achieved by raising the temperature), eventually culminating in a mismatch between the volume required by the core and that required by the chains. In this circumstance, one can postulate a curvature that can lead to undulations in the smectic layers. When this curvature is sufficiently developed, the lamellar arrangement is disrupted, and columns form in which the columnar repeat "unit" consists of three or four molecules. The effect is illustrated in Fig. 28 (31). While lamellar and columnar phases represent the extremes of behavior, it is often the case that cubic phases form at intermediate chain lengths. These are discussed in the next section. Thus, tetracatenar mesogens

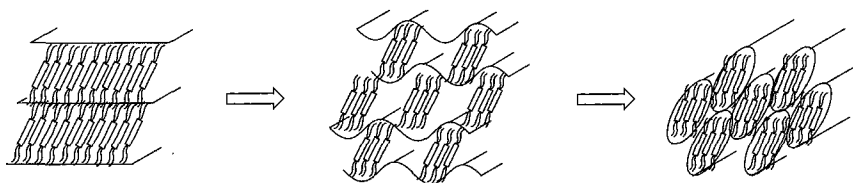


FIG. 28. Schematic diagram to show how interfacial curvature in a smectic phase can lead to the formation of a columnar phase.

with this substitution pattern appear to bridge the gap between the mesomorphism exhibited by rod- and disk-like molecules.

The second example is that of hexacatenar mesogens whose terminal chains are in the 3, 4, and 5 positions of the end phenyl rings (Fig. 27B). Here, the presence of three terminal chains ensures the presence of surface curvature, and so the mesomorphism is dominated by the formation of columnar phases.

Note that, for some time, the columnar phase of these polycatenar mesogens was given the symbol  $\phi$ . However, following the arguments presented above, the use of Col is more appropriate and is now widely accepted.

#### 4. The Cubic Phase

The cubic phase is a real curiosity in the study of thermotropic liquid crystals, although much has been done to unravel issues concerning its formation. Interested readers are directed to other sources for a detailed discussion (32); however, the phase does crop up rather a lot in systems we have studied, so a brief introduction is in order.

In thermotropic mesogens, the phase was first identified in 1957 by Gray (33) in some alkoxy-nitrobiphenyl carboxylic acids (Fig. 29A;  $Y = \text{NO}_2$ ) and was found to exist above the  $S_C$  phase and below the  $S_A$  phase (where the  $S_A$  was present). Except for reports of cubic phases in related nitrile compounds (34) (Fig. 29A;  $Y = \text{CN}$ ) and some hydrazines (Fig. 29B) (35), the cubic phase (or  $S_D$  as it was long known) remained for many years a rare intellectual curiosity. The phase is found to exist in two major space groups,  $\text{Im}\bar{3}\text{m}$  and  $\text{Ia}\bar{3}\text{d}$ , and a brief consideration of these serves to exemplify the two models used to understand their structure and hence the way in which the molecules are arranged within the phase.

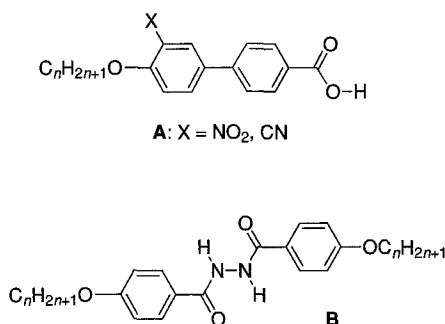


FIG. 29. The first two calamitic materials known to show the cubic phase.

The first model to be advanced was the *interconnecting rod model*, in which the phase symmetry was described by a series of interconnecting rods arranged in three dimensions, the rods being composed of the molecules that form the mesophase (36). This model was originally developed to explain the formation of cubic phases in surfactant mesophases, but is equally applicable here. The rod model for  $\text{Im}\bar{3}\text{m}$  is shown in Fig. 30A and that for  $\text{Ia}\bar{3}\text{d}$  in Fig. 30B. Note that in both cases there are two independent rod networks. In the latter, each independent rod network is chiral (threefold screw axis), but the two are of opposite chirality. The other model is the *infinite periodic minimal surface model* (37). Here, the arrangement of the rods is related to the minimal surfaces, as the minimal surfaces divide space up into parts. Thus, for example, Fig. 30C shows the minimal surface for the  $\text{Im}\bar{3}\text{m}$  space group which gives rise to two noninterconnected rod networks (Fig. 30A). Therefore, one can consider that the molecular cores form the rods and that the chains extend out to describe the minimal surfaces, illustrating the role of curvature in the structure of these phases.

Although the cubic phase is interesting in several regards, it is particularly worth noting that while liquid crystal mesophases are fluid, cubic phases are very viscous. Furthermore, because of their high symmetry, cubic phases possess isotropic physical properties, setting them apart from other liquid-crystal mesophases. Transitions into, and out of, cubic phases tend to be rather slow. Exactly why cubic phases form in calamitic systems is unclear at the present time.

### 5. Transitions between Mesophases

In the present article, the focus is on transitions between solid, isotropic, and liquid-crystal phases that are effected by the action of

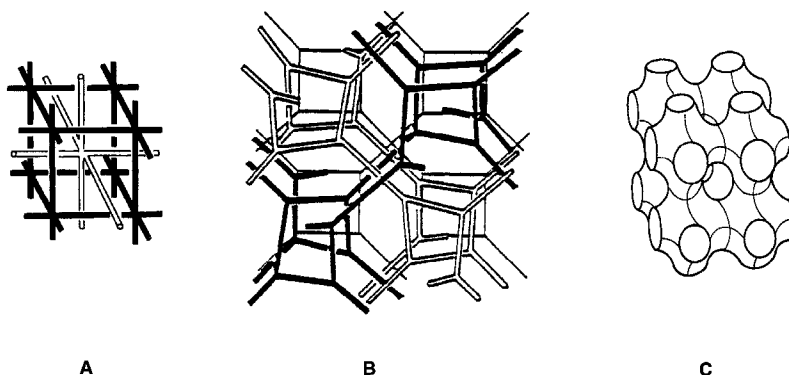


FIG. 30. Interlocking rod model for the  $\text{Im}\bar{3}\text{m}$  (A) and  $\text{Ia}\bar{3}\text{d}$  (B) cubic phases and the infinite periodic minimum surface model for  $\text{Im}\bar{3}\text{m}$  (C).

temperature; in such studies, *thermotropic* liquid crystals are considered. Although one can make predictions about the type of mesophase that might form based on molecular composition and previous experience, only experiments can actually determine which mesophases are formed and at what temperature. A given mesogen may possess only one mesophase or several, and one of those phases may or may not be nematic. What is known is that, except in special circumstances, smectic phases occur at lower temperatures than those obtaining in the nematic phase; moreover, within the smectic phases, there is a general order of formation that reflects the degree of order within the phases: with increasing temperature,

$$S_B < S_F < S_I < S_C < S_A < N < I$$

An interesting "variable" in all this is the position of the melting point in the sequence (here, the term *melting point* indicates the temperature at which the solid melts to form a disordered phase, while *clearing point* indicates the temperature at which the isotropic liquid forms from a mesophase), for there is no real reason for the solid to be less stable than the mesophase(s). Thus, Fig. 31 shows three possible examples of situations that could occur. In the first (A), the sample melts to the mesophase (LC), which then clears to give the isotropic liquid, and on cooling, the whole thing reverses. This mesophase is termed *enantiotropic*. In the second example (B), the solid melts directly to the isotropic liquid and then supercools into the mesophase (LC), which then crystallizes. here, the mesophase is termed *monotropic*. In the

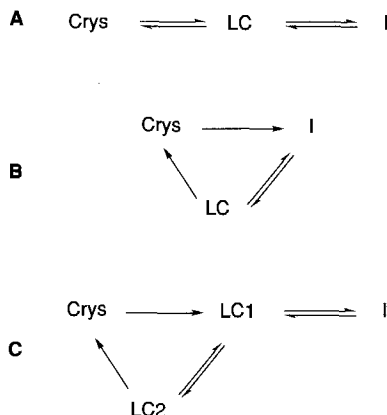


FIG. 31. Illustration of some possible thermodynamic relationships between crystal, isotropic, and liquid-crystal phases.

third example (C), the solid melts to give mesophase LC1, which then clears. On cooling, LC1 re-forms and then supercools into LC2 before crystallizing; here, LC1 is enantiotropic, while LC2 is monotropic. All of this must be determined experimentally.

#### 6. *The Characterization of Liquid Crystal Mesophases*

While it is not proposed to look at this topic in any real detail, it is appropriate to explain briefly the ways in which one can distinguish between the different phases and the techniques used to do so.

The primary technique is polarized optical microscopy [for the definitive text to date, see Ref. (38)]. This technique makes use of the fact that the mesophases, being anisotropic, possess two refractive indices. In this experiment, a small (<1 mg) sample is placed between two microscope coverslips and placed on a hotstage, which is itself positioned between two polarizers set at 90° to each other. When in the mesophase, the plane polarized light that impinges on the sample is split into two beams (or, more formally, the light become elliptically polarized) which interfere to give a pattern that depends on the symmetry of the phase. In the hands of an experienced experimentalist, this characteristic *optical texture* can identify a mesophase. This is always the first method used to determine mesomorphism. Some examples of textures can be found at: [http://www.tu-berlin.de/~insi/ag\\_heppke/fotos-e.htm](http://www.tu-berlin.de/~insi/ag_heppke/fotos-e.htm)). Complementary to microscopy is *differential scanning calorimetry* (DSC), which is used to measure the enthalpy change during a transition. It is important that DSC data be obtained along with that from microscopy so that every optical transition can be matched with a change in enthalpy (or heat capacity) and vice versa. Furthermore, the system is at equilibrium at a transition between phases, hence  $\Delta G = 0$  and it follows that  $\Delta S = \Delta H/T$ . Thus, the entropy of transition can be calculated. Note that DSC alone cannot identify a material as mesomorphic, nor can it characterize any mesophase formed.

However, the most unequivocal method for determining the identity of a mesophase is X-ray diffraction. Small samples (~10 mg) are heated into the mesophase and X-rays are passed through, the experiment being carried out in transmission geometry with data being collected either on film or electronically. Because the samples are fluid, the information content is rather low; but in an  $S_B$  phase, for example, it would be possible to observe the layer spacing at low angles, the molten alkyl chains at 4.5 Å, and the hexagonal symmetry of the layer. Similarly, for a columnar hexagonal phase of a discotic molecule, one would expect to see repeat distances of 3.4 and 4.5 Å at high angle (the stacking repeat and molten alkyl chains, respectively) as well as, for example, the (10), (11), and (20) reflections of the hexagonal lattice. A higher data content

is obtained if the sample can be obtained in an aligned monodomain; normally, however, this is readily achieved only with nematic samples aligned by an applied magnetic field.

### 7. *Why Put Metals into Liquid Crystals?*

Why, indeed? The main reason has to be in response to scientific curiosity—to know what will happen. Although this article does not concentrate entirely on mesomorphic metal complexes, some properties are predictable, and it is appropriate to mention these briefly here. [This area is; however, well reviewed; see Ref. (39).]

First, the coordination possibilities around a metal are considerable, and coordination numbers from 1 to 9 and more are known. Metals can be stable radicals, making it possible to exploit paramagnetic effects that are greater than those of their diamagnetic analog. Metal complexes are often colored and this color can be redox-dependent; thus, they have potential as liquid-crystal dyes (40). Metals are centers of highly polarizable electron density, which affects the linear (41) and nonlinear polarizability (17) and hence the refractive indices (42) and dielectric response. The possibilities are manifold. Thus, the prize is to combine the best of what inorganic chemists know with the best the liquid-crystal world can provide—an exciting prospect, indeed.

## VII. Liquid-Crystalline Metal Complexes of Alkoxy stilbazoles

### A. INTRODUCTION

The first metallomesogens we made were Pd(II) and Pt(II) complexes of cyanobiphenyl mesogens with the structure shown in Fig. 1. However, nitrile ligands can be rather labile (there is evidence of their lability on Pd centers), and so we looked for a generic ligand type that might bind to metal centers a little more strongly. This is where we encountered stilbazoles. Since this time, the summer of 1985 when Elena Lalinde carried out the first synthesis, we have examined the liquid-crystal behavior of stilbazoles in combination with metals from groups 8, 10, and 11 as well as in hydrogen-bonded systems. This work is now described.

### B. MESOMORPHIC COMPLEXES OF GROUP 8 METALS

As has already been seen these complexes have interesting properties in the fields of nonlinear optics and thin films. Indeed, it was the fact that such complexes were available from liquid-crystal projects that prompted our studies. The work with Rh(I) and Ir(I) complexes was

inspired by related materials described by the Zaragoza group, who had used an iminopyridine ligand (Fig. 32). It was found that the use of a nonmesomorphic ligand could lead to liquid-crystalline materials on complexation (43, 44).

In our case, the ligands exhibited some liquid-crystal properties; X-ray diffraction gave evidence of a crystal smectic E phase<sup>4</sup> and optical microscopy gave evidence for an S<sub>B</sub> phase. On complexation, however, S<sub>A</sub> and N phases were found at temperatures higher than those of the stilbazoles themselves. The phase diagram for the Ir(I) complexes (Fig. 33) shows behavior that is quite typical for a simple dipolar mesogen—namely, the formation of a nematic phase at short chain lengths, giving way to an S<sub>A</sub> phase as the alkyl chain lengthens. The mesomorphism of the Rh(I) congeners was similar, except that the complexes decomposed on clearing to the isotropic phase.

The ability of the *cis*-[MX(CO)<sub>2</sub>] fragment to promote mesomorphism in pyridine-based ligands is quite remarkable, prompting an examination of how good the results are in stilbazole systems. In the literature of organic liquid crystals, terminal groups are rated according to their ability to stabilize the nematic phase and, of these, the cyano group is in the premier league. Details of the comparisons we made are in the original paper; but here suffice it to say that our estimates were that the *cis*-[MX(CO)<sub>2</sub>] fragment was *at least* as effective as the cyano group in promoting the nematic phase. Why this should be? In fact, the reasons are tied up with the ability of the terminal group to enhance both the polarizability of the mesogen and the polarizability anisotropy of the mesophase. Suitable measurements were carried out and the results are collected in Table I. Thus, it can be seen that complexation of the metal fragment to the stilbazole nearly doubles the linear polarizability, while the ratio of the polarizability anisotropy,  $\Delta\alpha$  ( $\Delta\alpha = \alpha_{\parallel} - \alpha_{\perp}$ , where  $\alpha_{\parallel}$  and  $\alpha_{\perp}$  are, respectively, the polarizability parallel and perpendicular to the nematic director; see Fig. 34) to the mean linear polarizability ( $\bar{\alpha}$ ) has increased almost to unity. The large value of  $\Delta\alpha$  is predicted by theory to give rise to stable nematic phases.

### C. MESOMORPHIC STILBAZOLE COMPLEXES OF GROUPS 10 AND 11 METALS

The stilbazole complexes of these metals, Pd(II), Pt(II), Ag(I), and Au(I), are considered together because a good deal can be learned by looking at them in this way, particularly as we begin to look at more highly substituted stilbazoles. The liquid-crystal aspects of the silver

<sup>4</sup>The crystal smectic phases differ from those already discussed in that the layers are rather well correlated. The crystal smectic E phase is an orthogonal, orthorhombic phase.

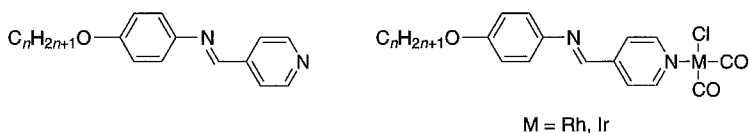


FIG. 32. Iminopyridines and their complexes as synthesized in Zaragoza.

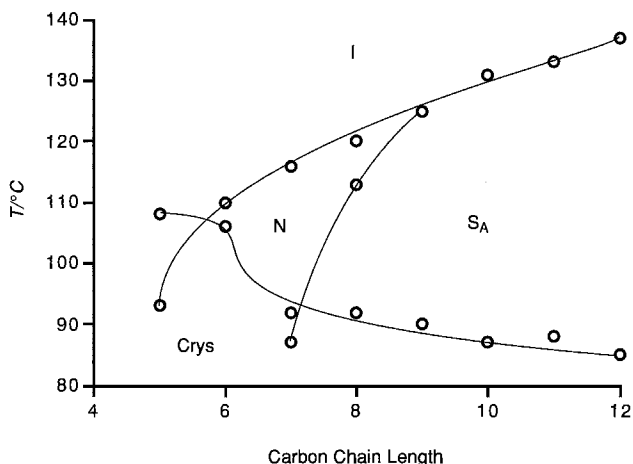


FIG. 33. Phase diagram for iridium stilbazole complexes.

TABLE I

MEAN LINEAR POLARIZABILITIES ( $\bar{\alpha}$ ) AND POLARIZABILITY ANISOTROPHIES ( $\Delta\alpha$ ) FOR A STILBAZOLE LIGAND AND ITS IRIIDIUM (I) COMPLEX

Compound	$\bar{\alpha}/10^{-40} \text{ C}^2\text{m}^2\text{J}^{-1}$	$\Delta\alpha/10^{-40} \text{ C}^2\text{m}^2\text{J}^{-1}$	$\Delta\alpha/\alpha$
<chem>C_8H_{17}O-c1ccc(cc1)/C=C/c2ccncc2</chem>	$31 \pm 4$	$22 \pm 6$	0.7
<chem>C_8H_{17}O-c1ccc(cc1)/C=C/c2ccncc2N[M](Cl)(C(=O)O)C(=O)O</chem>	$59 \pm 6$	$54 \pm 10$	0.92

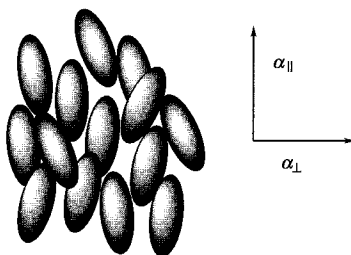


FIG. 34. Diagram to show the origins of the polarizability anisotropy.

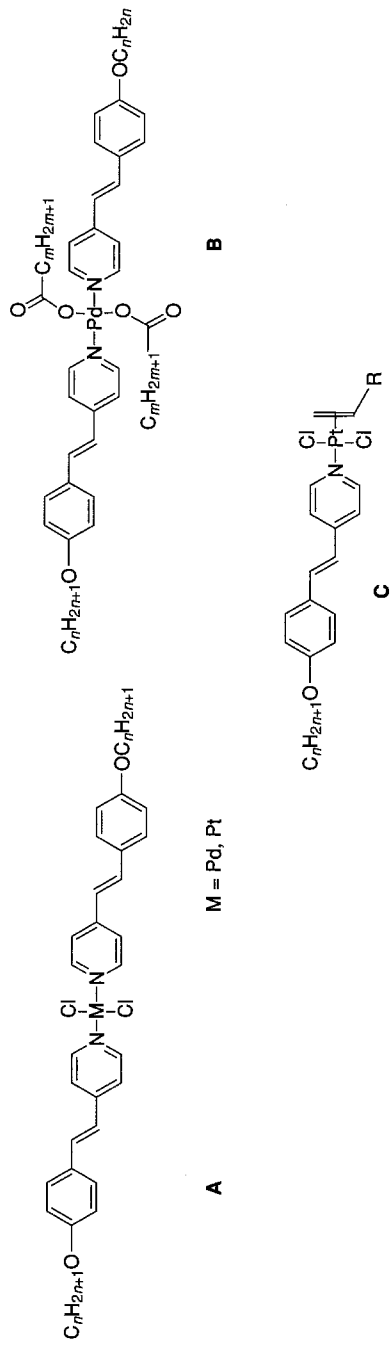


Fig. 35. Structure of the group 10 complexes of alkoxystilbazoles.

complexes are particularly complex and involved, and the reader is referred to a more detailed review of these materials for an extended discussion (24).

### 1. Complexes of Monoalkoxystilbazoles

Liquid-crystalline complexes of silver(I) were among the first complexes we studied; and even now, some sixteen years later, we continue to find aspects that fascinate us. The silver complexes are different from the other complexes we have considered in that they are formally ionic, and the anion is an additional variable to take into account. As will be seen, this proves to be a most subtle structural parameter.

Before looking at the silver complexes, it is worth considering the palladium and platinum complexes. These complexes (Fig. 35A) were readily made but proved rather frustrating. The platinum materials were nonmesomorphic, and while some of the longer-chain palladium derivatives showed  $S_C$  phases, this was at rather elevated temperatures (45). However, Maitlis and co-workers showed that if the chloride ligands were replaced by long-chain alkanoates (Fig. 35B), transition temperatures were reduced and a nematic phase was observed (46). These results later proved to be more important than was realized at the time, as discussed later.

It is also interesting to note the complexes described by Maitlis in which a stilbazole was bound to a *trans*-[PtCl<sub>2</sub>(olefin)] moiety (Fig. 35C). Almost all of these materials showed an  $S_A$  phase whose existence turned out to be a function of the chain length on the olefin as well as on the stilbazole (46, 47).

With silver, we initially made complexes of AgBF<sub>4</sub> (Fig. 36; X = BF<sub>4</sub>). These, like most silver complexes, are synthesized by direct reaction of the ligand with the salt. The mesomorphism of the tetrafluoroborate complexes was not investigated extensively, as they were highly moisture-sensitive and showed very high transition temperatures (clearing point around 300°C) and accompanying decomposition (48). In some freshly prepared samples with longer alkoxy chains,  $S_C$  and  $S_A$  phases were identified, consistent with observations by the Zaragoza group on related complexes of 4'-alkoxy-*N*-(4-pyridylbenzylidene)anilines and 4'-(4-alkoxyphenyl)pyridine

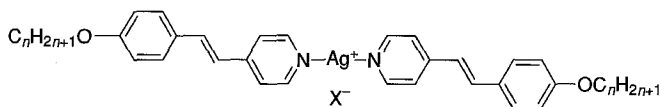


FIG. 36. General structure of the silver stilbazole complexes.

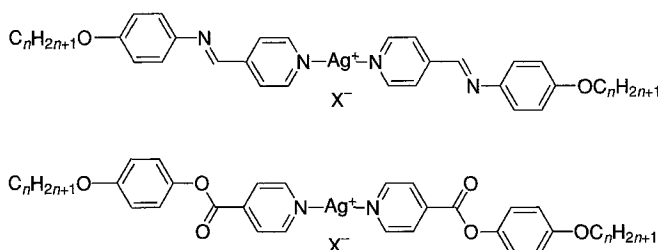


FIG. 37. Structure of some silver stilbazole analogs made in Zaragoza.

carboxylates (Fig. 37) (49). Because of the high transition temperatures in these complexes, it was necessary to see whether materials with lower transition temperatures could be obtained. Thus, in a naïve attempt to realize this the anion was changed to dodecylsulfate (DOS) in the hope that this rather “floppy” anion might just do the trick (Fig. 36;  $X = C_{12}H_{25}OSO_3$ ) (48).

Inasmuch as the transition temperatures of the DOS salts were lower than those of the  $BF_4$  analogs (e.g., clearing points around  $170^\circ C$ ), the strategy was successful. But in the event, these apparently simple systems became a real “group favorite” for many years. To begin with, consider the phase diagram of the DOS salts, which shows areas of phase stability plotted as a function of ligand chain length and temperature (Fig. 38). Note that at short chain lengths, there is a nematic phase,

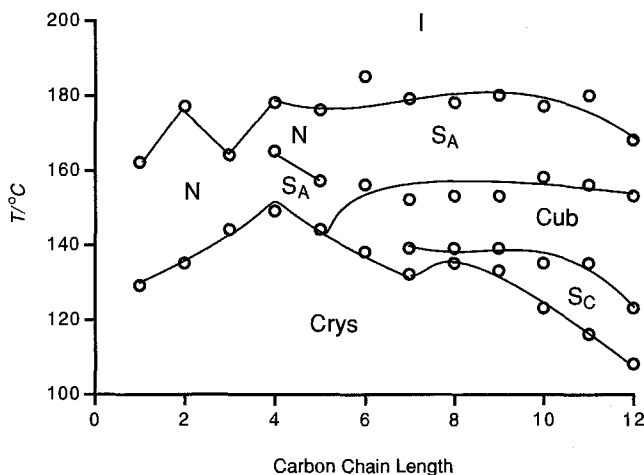


FIG. 38. Phase diagram for the stilbazole complexes of AgDOS. Reprinted with permission from *Acc. Chem. Res.* 2000, 33, 831. Copyright 2000 American Chemical Society.

while at longer chain lengths  $S_C$  and  $S_A$  phases become evident, as well as one marked Cub (a cubic phase), which has  $Ia\bar{3}d$  symmetry (50). The observation of each of these phases is remarkable for reasons to be described, as follows.

The complexes are formally ionic, making the observation of a nematic phase remarkable because one would expect the rather weak anisotropic dispersion forces stabilizing this phase to be incompatible with the strong isotropic coulombic forces normally associated with ionic materials (51). However, this turns out not to be the case inasmuch as conductivity measurements showed no conductivity (48)—that is, the cation and anion are closely associated, as suggested by the crystal structure shown in Fig. 42. Once this is known, the nematic phase becomes expected, because rod-like mesogens with lateral chains exclusively form this phase as the lateral chain suppresses the formation of the smectic layers (52). Again, the crystal structure in Fig. 42 suggests that regarding these materials as calamitic materials with lateral chains is appropriate. However, having classified the silver complexes in this way, how do we explain the formation of two smectic phases and the cubic phase? This will be considered later.

Having found that silver complexes of this type were mesomorphic, it was of interest to look at gold congeners, particularly complexes with the DOS anion (53). For gold, it was not possible to start from AuDOS and react directly with the stilbazole; thus we took an alternative approach (Fig. 39) that led us to the gold triflate salts *en route* to the DOS analogs. The approach was successful and the target gold complexes were realized. But on the way, we checked the thermal behavior of the gold triflates and found that they, too, were liquid crystals. Unfortunately, it was not possible to investigate any of these gold complexes in great detail as gold(I) is not stable in these circumstances and the complexes tend to decompose on heating. Nevertheless, we did ascertain that both the triflate and DOS salts showed both an  $S_C$  and an N phase.

Having found that gold triflates were mesomorphic, we returned to silver and decided to look at other anions. In so doing, we made complexes of silver triflate and nitrate, each of which exhibited similar patterns of liquid-crystal behavior: namely, the formation of  $S_C$  and  $S_A$  phases at rather elevated temperatures (the phase diagram for the nitrates is reproduced in Fig. 40) (54). While neither of these systems showed a cubic phase, we did find a nematic phase in the triflates.

Next we addressed another variable in these systems—the length of the chain attached to the alkylsulfate headgroup. The only series we

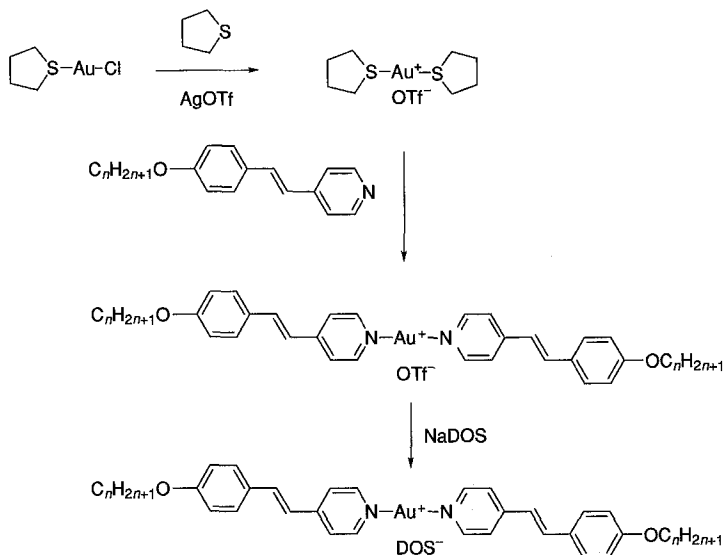
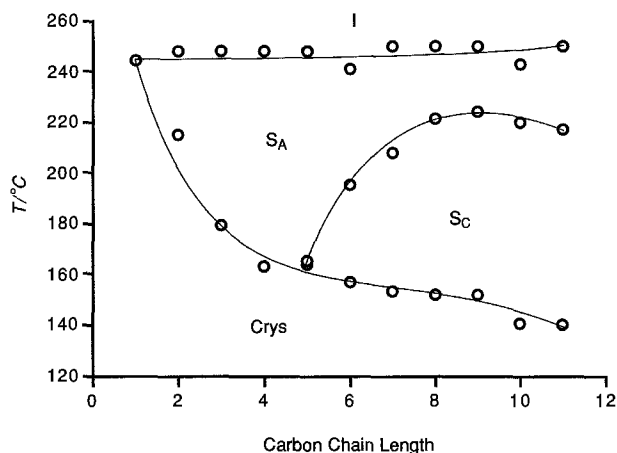


FIG. 39. Synthesis of the gold stilbazole complexes.

investigated extensively was that based on octylsulfate (OS). Here it was found that the phase diagram was very similar to that found for the DOS, *except* that the cubic phase had disappeared, its place in the phase diagram being taken by the  $S_A$  phase (Fig. 41) (55). An important aspect of this study was that it was possible to grow single crystals of

FIG. 40. Phase diagram for stilbazole complexes of  $\text{AgNO}_3$ .

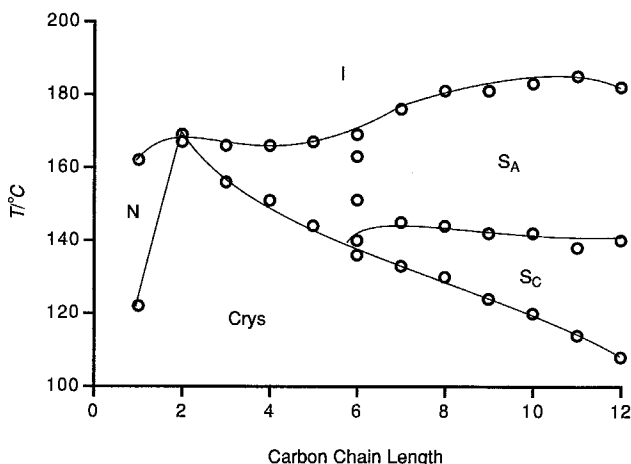


FIG. 41. Phase diagram for stilbazole complexes of AgOS.

one of the complexes, the methoxystilbazole derivative (Fig. 42). In the solid state, the molecules exist as dimers held together by the sulfate group of the anion, which acts in a bridging, bidentate mode; the structure is centrosymmetric about the midpoint of the Ag...Ag vector. The essential features are that the covalent Ag—N distances are as expected for materials of this type, while the Ag—O distances are of the order of 2.7–2.9 Å, suggesting a noncovalent interaction. Moreover, the structure crystallizes as a hemihydrate, giving rise to a kind of polymeric

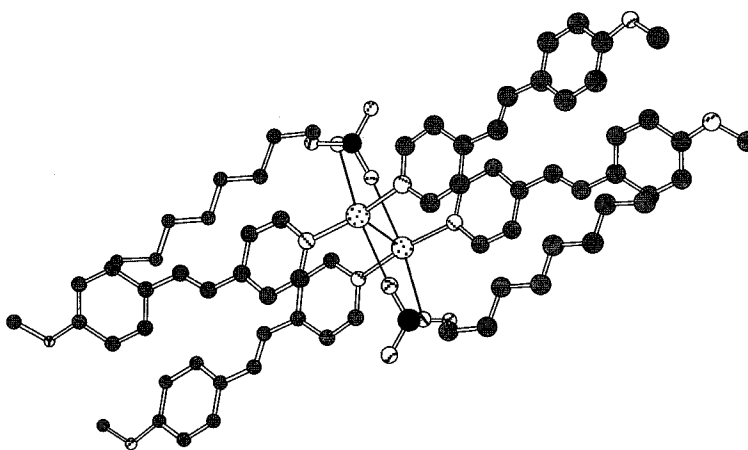


FIG. 42. Molecular structure of the methoxystilbazole complexes of silver octylsulfate.

structure in which one dimer is linked to two others through the sulfate anion and a water of crystallization. Another important factor is that the anion chain does not extend beyond the rigid core of the molecule.

Other studies looked at decyl- and tetradecylsulfate and showed that the cubic phase was absent in the former case, while it reappeared in the latter. Note that consideration of the crystal structure of the OS salt shows that anion chains shorter than DOS will not extend past the rigid core.

With this information in hand, we began to piece together an explanation for the formation of the smectic phases and a rationalization for the formation of the cubic phase. In the former case, the argument is straightforward: Intermolecular ionic (electrostatic) interactions act to stabilize the smectic phases, overcoming the disruptive effect of the lateral (anion) chain. It is clear that these forces are not too strong because and there is no evidence of a smectic phase at the shortest ligand chain lengths. In liquid crystals in general, it is found that as the terminal chain length increases, nematic phases tend to be replaced by smectic phases. This is accounted for by the phenomenon of *microphase separation*—that is, the molecules tend to associate via core–core and chain–chain interactions, which are preferred over core–chain interactions. The result is layering. At short chain lengths, chain–chain interactions are inconsequential, so the effect is not observed. Thus, in silver complexes it is the *combined* effect of the electrostatic interactions and the microphase separation that stabilizes the smectic phase.

So what about the cubic phase? In polycatenar systems, it is possible to rationalize the formation of cubic phases on the basis of surface curvature alone, which will be considered in subsequent sections. However, it can be argued that, for calamitic systems, these arguments do not hold—at least on their own—and that other factors are important. For example, if cubic-phase formation is due to surface curvature, it is not possible to explain why an  $S_A$  phase (lamellar and with no surface curvature) is seen at higher temperatures. An important factor is the presence of specific intermolecular interactions; and in the case of the silver systems, these are the intermolecular electrostatic interactions resulting from the presence of formally ionic groups. This is consistent with the observation of cubic phases in the biphenylcarboxylic acids and hydrazines (Fig. 29), as well as with other materials. However, it is also evident that this is not the only factor, as no cubic phase is seen with anion chains shorter than DOS, while other studies with fluorinated alkoxy stilbazoles showed that the position of fluorine substitution could determine the presence or absence of the mesophase observed in the unsubstituted derivatives (56). Thus, structural factors are clearly not negligible.

## 2. Complexes of Poly(alkoxy)stilbazoles

Having synthesized a number of complexes of monoalkoxystilbazoles, we explored the effect of using various poly(alkoxy)stilbazoles, given the interesting mesomorphism found in polycatenar mesogens (Section VI,A,3). This work is discussed in detail elsewhere (24). Here, we give an overview of the work to enable the reader to see the overall pattern of liquid-crystal behavior and the issues that arise.

The first series to be examined was that of the 3,4-dialkoxystilbazole complexes of silver dodecylsulfate, whose phase diagram is shown in Fig. 43 (3). As can readily be seen, the phase diagram is dominated by the formation of a cubic and a columnar hexagonal phase, both of which are expected in polycatenar systems. However, the  $S_C$  phase characteristic of shorter chain lengths is absent, which can be attributed to the presence of the lateral chain. An interesting feature (one not shown on the phase diagram) is that a nematic phase for the methyloxy and ethyloxy derivatives is seen. However, this is not a nematic phase of a complex that contains two stilbazole ligands bound to AgDOS; rather it is formed from a complex with the stoichiometry  $[Ag(\text{ligand})][DOS]$ . Thus, it seems that the complex  $[Ag(\text{ligand})_2][DOS]$  thermally dissociates on heating, expelling a stilbazole ligand, and that the  $[Ag(\text{ligand})][DOS]$  thus formed shows a monotropic nematic phase.

The silver complexes of 3,4-dialkoxystilbazoles were further examined by looking at their complexes with alkylsulfates of varying chain

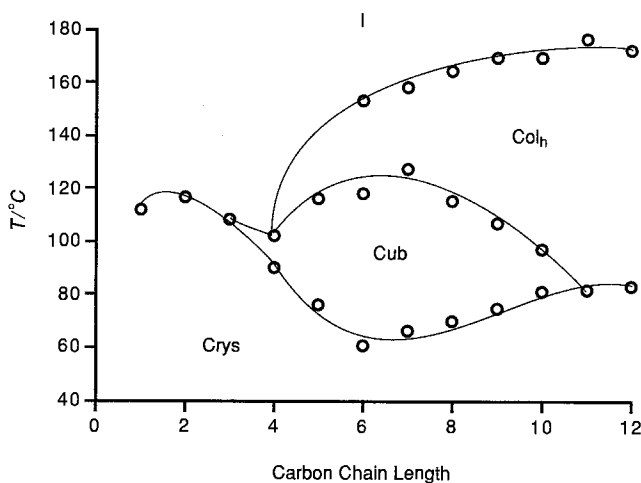


FIG. 43. Phase diagram for the 3,4-dialkoxystilbazole complexes of AgDOS.

length (57). The results, which are plotted in Fig. 44, show an interesting pattern which serves to confirm the premises used to interpret the mesomorphism of these systems. That is, we assume that the alkylsulfate chain contributes to the volume of the core as long as it does not extend past the end of the core, after which it contributes to the surface curvature. Thus, the greater the surface curvature, the more likely a columnar phase is to result, with a cubic phase being seen at lower curvatures. The data in Fig. 44 are consistent with this conclusion.

Finally, in our discussion of these silver systems, we note that the hexacatenar systems based on 3,4,5-trialkoxystilbazoles all showed a columnar phase just above ambient temperature (Fig. 45), as might have been expected (58).

Now let us turn our attention to the related palladium and platinum complexes (59). The first point to note is that for the hexacatenar complexes derived from 3,4,5-trialkoxystilbazoles, the mesomorphism is dominated by the columnar phase, although very recent X-ray studies, yet to be published (60), show that there are in fact two columnar phases in the phase diagram.

The behavior of the tetracatenar palladium complexes based on 3,4-dialkoxystilbazoles differs markedly from that observed in the silver complexes, the phase diagram now breaking into halves, with an  $S_C$

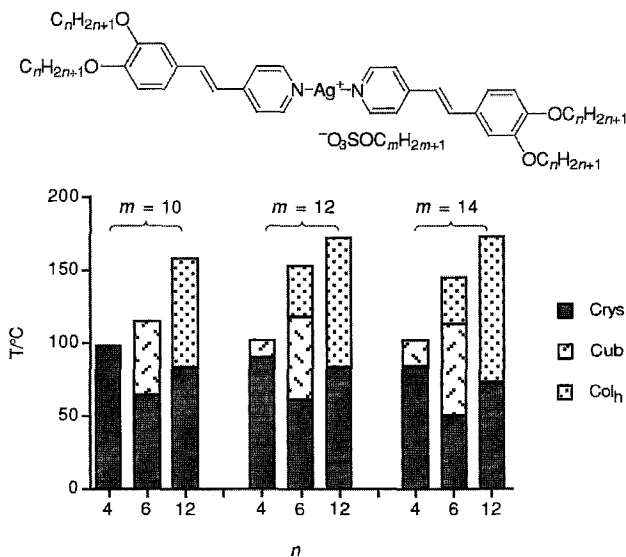


FIG. 44. Graphical representation of the phase behavior of some 3,4-dialkoxystilbazole complexes of some silver alkylsulfates. Reprinted with permission from *Acc. Chem. Res.* 2000, 33, 831. Copyright 2000 American Chemical Society.

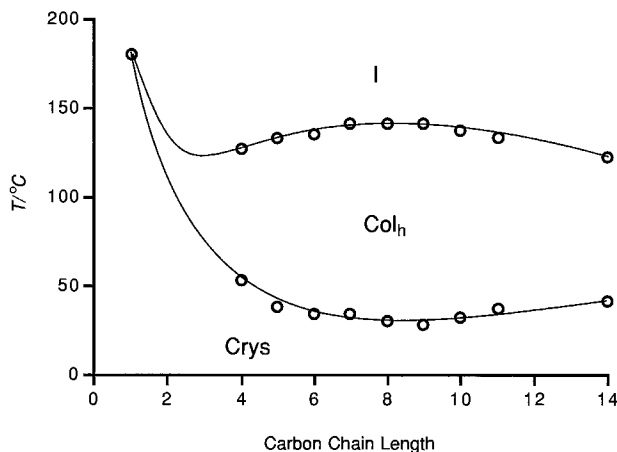


FIG. 45. Phase diagram for the 3,4,5-trialkoxystilbazole complexes of AgDOS. Reprinted with permission from *Acc. Chem. Res.* 2000, 33, 831. Copyright 2000 American Chemical Society.

phase found at shorter chain lengths and another phase that appears to be columnar when the terminal chains are longer (Fig. 46). However, there are no complexes having both phases with no cubic phase in the middle. For platinum, the picture is very similar except that the chain length where the S<sub>C</sub> phase ends is slightly longer.

Comparison of the silver and palladium systems shows that the major difference is the presence in the former of the lateral chain. Thus we reasoned that if we could make the palladium systems more like the

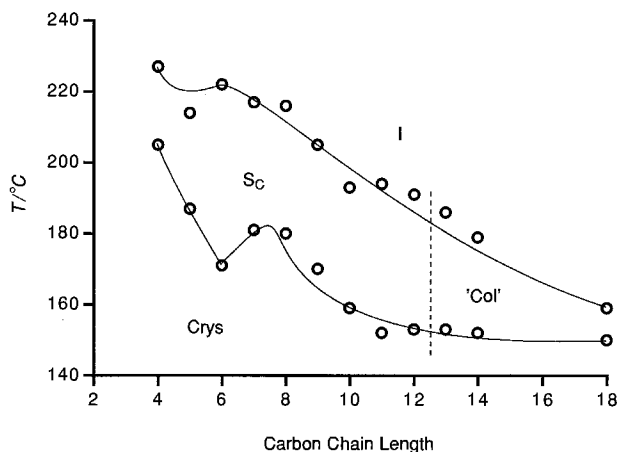


FIG. 46. Phase diagram for the 3,4-dialkoxystilbazole complexes of palladium(II).

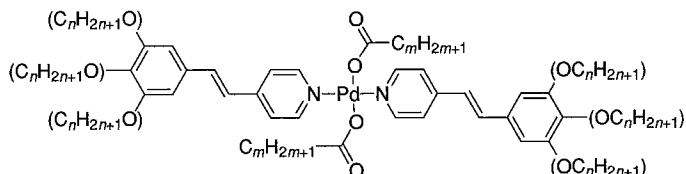


FIG. 47. Polycatenar palladium complexes with lateral alkanolates. The parentheses around the alkoxy groups on the stilbazole indicate that a variety of isomers were studied.

silver materials, we might be able to mimic their phase behavior more closely. The approach we took was to replace the chloride ligands by alkanolates and see whether the change in the effective volume of the core would have the desired effect. In fact, we made a whole series of complexes of differing alkanolate chain length and with different numbers of alkoxy chains on the stilbazoles and in different positions (Fig. 47). The result was rather unexpected in that *every* example we examined showed only a nematic phase—even those with six ligand chains and two lateral chains, which one might argue for consideration as discotic materials (10)! Clearly, the nature of the comparison between these palladium systems and the silver complexes is not precise, as the latter has only one lateral chain while the former has two. So, it is necessary to carry out further studies in order to understand fully the factors governing the mesomorphism in these fascinating systems.

Thus, we have seen how simply changing the central metal changes the mesomorphism by virtue of the other groups that are bound to the metal and the way in which they are bound (e.g., covalent versus ionic). This is interesting in its own right, but also serves to show that the extra structural possibilities offered by the presence of the metal allow a systematic investigation of factors that control mesophase formation.

### VIII. Hydrogen-Bonded Stilbazole Mesogens

Hydrogen bonding is a concept as old as science itself; in recent years, however, it has undergone something of a renaissance in synthetic chemistry, with the fashion for supramolecular chemistry. The classical definition supposes that hydrogen bonds can exist when a

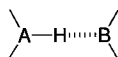


FIG. 48. Diagram to show the hydrogen bond between two electronegative elements, A and B.

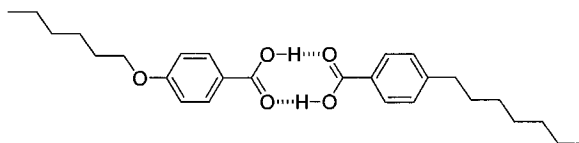


FIG. 49. The hydrogen-bonded alkoxybenzoic acid dimers.

hydrogen atom bound to an electronegative element, A, can interact with another electronegative element, B (Fig. 48). This definition is certainly true, although there are now many examples where, for example, A is not a particularly electronegative element (61).

Hydrogen bonding in thermotropic liquid crystals is also a well-established concept (62); for instance, the liquid crystallinity of the 4-alkoxybenzoic acids derives from the formation of hydrogen-bonded dimers (Fig. 49). More recently, there has been interest in the creation of new liquid-crystalline species via hydrogen bonding—an idea that originated in studies initiated by Kato and Fréchet (63). This work, and other studies in the area, are well reviewed (61) and we propose to concentrate on our own studies here. However, before these results are discussed, it is worth noting how the complexes are generally prepared. In many cases, it is possible simply to dissolve the two components in the same solvent, then remove that solvent, leaving the new species. Stilbazoles usually offer good visual evidence that this has happened, as pure stilbazoles are effectively colorless while their protonated equivalents are bright yellow. The formation of a yellow tinge of variable intensity is thus a good indication that the complex has formed. Occasionally however, complex formation is not so straightforward. Here it is necessary to heat the mixture recovered from solution to above the melting point of at least one, if not both, of the components, to ensure complex formation.

Kato and Fréchet showed that a 1:1 mixture of a stilbazole and a benzoic acid can lead to a hydrogen-bonded species whose phase behavior is largely independent of the two species from which it is formed (Fig. 50) (63). This work, which was later pursued independently by Kato, concentrated for some time on interactions between benzoic acids of one sort or another and various stilbazoles, producing a number of interesting results. We collaborated with Kato on a small part of this

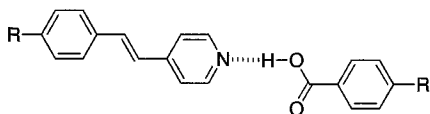


FIG. 50. General interaction between a stilbazole and a benzoic acid.

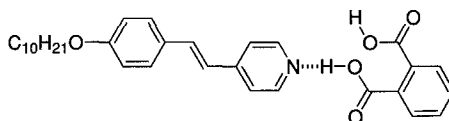


FIG. 51. Indicative 1 : 1 complex between decyloxystilbazole and phthalic acid.

work, and in one study, we worked with him to reinterpret initial observations on the mesomorphism derived from complexes between phthalic acid and 4-alkoxystilbazoles. Initial observations (64) suggested that, consistent with two carboxylate groups bonded to the phenyl ring, a 2 : 1 complex was formed which possessed a nematic phase. However, a careful study, which involved the construction of a binary phase diagram, showed that in fact the stable species was a 1 : 1 complex which formed an  $S_A$  phase (Fig. 51) (65). Other work carried out later showed that the reported complex formation between stilbazoles and both terephthalic and isophthalic acids also required reinterpretation (66).

To form discrete hydrogen-bonded species, there must be a balance between the basicity of the Lewis base and the acidity of the proton. Clearly, stilbazoles and benzoic acids are almost perfect bedfellows in this regard. From this point of view, one might not expect phenols to be ideal hydrogen donors; occasionally, however, research students go and do things without asking advice, often leading to extremely interesting consequences. So it was that alkoxy stilbazoles were combined with 4-cyanophenol; and, lo and behold, mesophases were observed, albeit of the monotropic variety (67). That the mesophases were not so stable is easy to understand, given that the phenolic oxygen acts as an angular unit in the complex to destroy the overall molecular linearity normally associated with mesophase formation. This is illustrated by a single-crystal structure of the complex between 4-cyanophenol and octyloxystilbazole (Fig. 52) (68). We therefore rationalized the formation of the phase on the basis of known antiparallel correlations in certain cyano compounds to give an associated unit like that shown in Fig. 53.

A similar approach with 4-nitrophenol also generated mesomorphic systems. This time, the mesophases were slightly more stable and some phases appeared to be enantiotropic (i.e., they became more stable than their crystal phase) (69). However, the beauty of the hydrogen-bonding approach to liquid crystals is that it is not always necessary to synthesize complete molecules. Thus, it was realized that if the 4-substituted phenols lowered the anisotropy as indicated in Fig. 53, the anisotropy ought to recover to give much more stable systems if the 3-substituted systems were used (Fig. 54) (69). That this approach was viable was

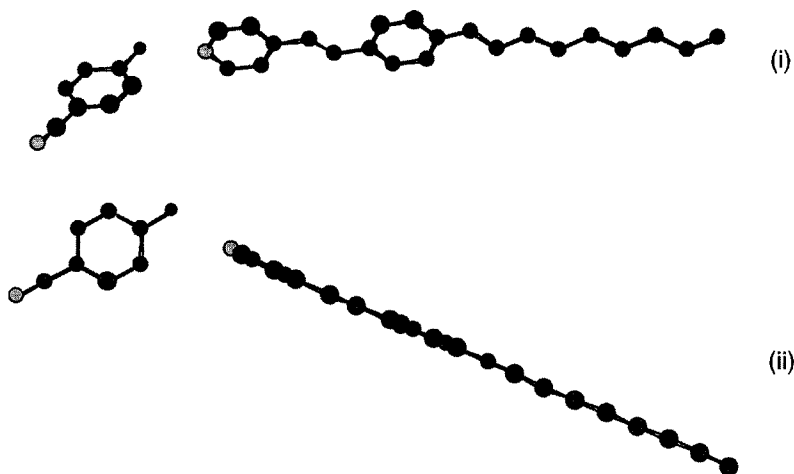


FIG. 52. Two views of the molecular structure of a complex between 4-cyanophenol and octyloxystilbazole.

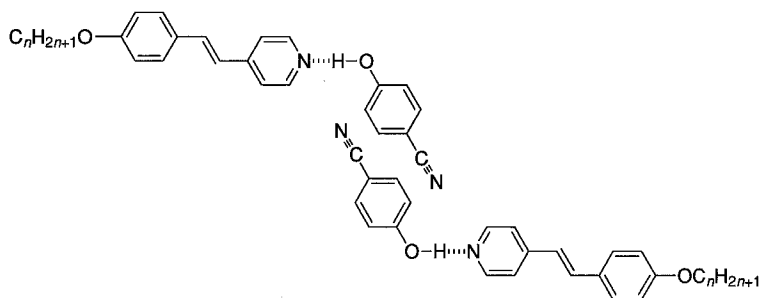


FIG. 53. Diagram to show the proposed antiparallel correlations that stabilize the mesophase in 4-cyanophenol complexes.

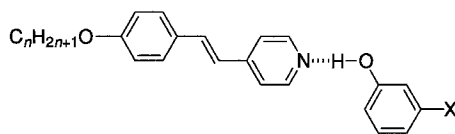


FIG. 54. Enhanced anisotropy in complexes of 3-substituted phenols.

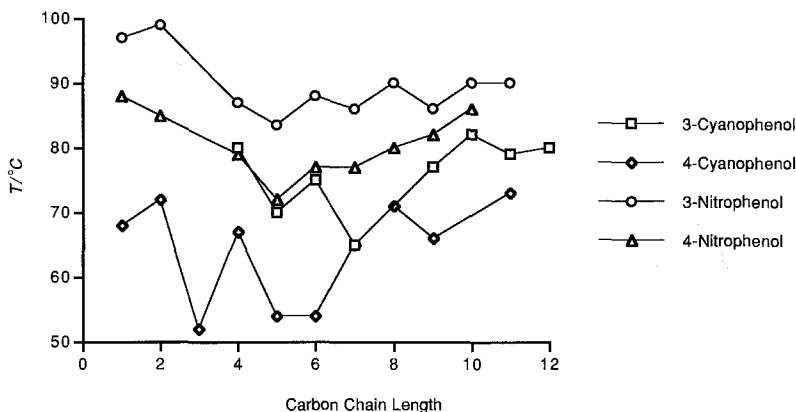


FIG. 55. Comparison of the nematic-to-isotropic temperatures for a series of 3- and 4-substituted phenols with different 4-alkoxystilbazoles.

supported by the fact that each series of 3-substituted materials gave more stable mesophases than its 4-substituted isomer, as illustrated by the comparative diagram in Fig. 55. A nice feature of this study was the binary phase diagram constructed for mixtures of 3-nitrophenol and 4-octyloxystilbazole (Fig. 56). This diagram clearly shows that it is the

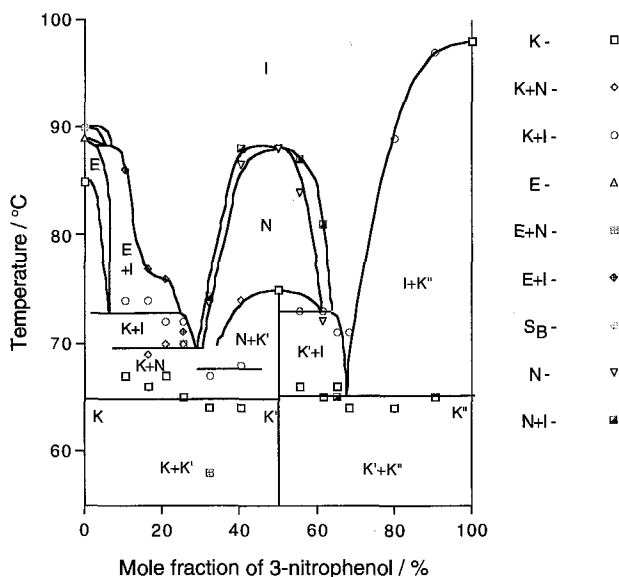


FIG. 56. Binary phase diagram formed between 3-nitrophenol and 4-octyloxystilbazole. Here, K represents the crystal phase. Reprinted with permission from *J. Chem. Soc., Chem. Commun.* **1995**, 1911. Copyright 1995 Royal Society of Chemistry.

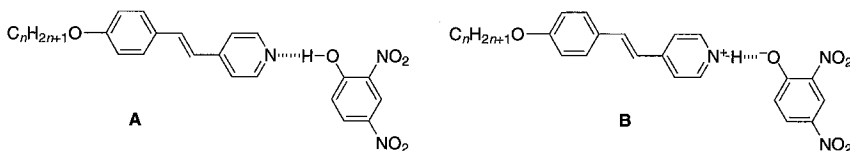


FIG. 57. Diagram to illustrate the change from neutral (A) to ionic (B) hydrogen bond.

1:1 complex which is formed. Curiously, however, the mesophases of the 4-nitrophenols were more stable than those of the 3-cyanophenols.

However, the most stable mesophases were shown by complexes using 2,4-dinitrophenol, and further studies of these systems gave more information about the hydrogen bond as a function of temperature. Thus, it was possible to perform variable-temperature electronic spectroscopy (70) on one of these complexes (based on decyloxystilbazole). It was found that on heating into and through the S<sub>A</sub> phase, the covalent hydrogen bond (with the hydrogen closest to the oxygen) changed to an ionic hydrogen bond (with the hydrogen closest to the nitrogen, Fig. 57). This was readily seen in spectra (Fig. 58), which indicated isosbestic

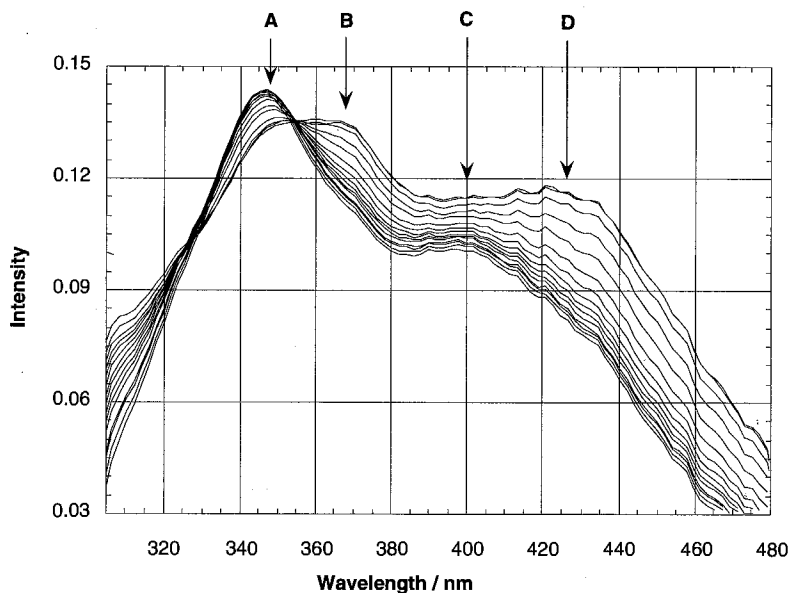


FIG. 58. Variable-temperature electronic spectra of the complex between decyloxystilbazole and 2,4-dinitrophenol. A and C indicate the absorption maxima for the stilbazole and stilbazolium moieties, respectively, while B and D indicate the absorption maxima for the phenol and phenate moieties, respectively. Reprinted with permission from *J. Mater. Chem.* 1997, 7, 883. Copyright 1997 Royal Society of Chemistry.

conversion from a neutral stilbazole species with an absorption at 348 nm to a protonated species with an absorption at 400 nm. There was a similar change in the phenol absorption from 368 to 426 nm.

A final point to note concerns the relative populations of the two states. As stilbazole and stilbazolium have similar extinction coefficients ( $30,600$  and  $33,000 \text{ dm}^3 \text{ cm mol}^{-1}$ , respectively), it can be argued that a near 50% population is obtained from about  $114^\circ\text{C}$  (data were obtained between  $90$  and  $126^\circ\text{C}$ ), the clearing point being at  $117^\circ\text{C}$ . However, a further increase in temperature above the clearing point sees a relative decrease in the population of the ionic hydrogen-bonded state. To account for this deviation from a normal thermal population of the ionic excited state, it was proposed that the environment of the smectic A phase, where there is a lamellar microphase separation of alkyl chains from the aryl cores, provides an additional stabilization of the ionic hydrogen-bonded state, as here the hydrogen bond is predominantly surrounded by polarizable (aryl groups) and polarized (nitro groups) functionalities. This supports an important general conclusion for hydrogen-bonded mesogens: Significant dissociation from the hydrogen-bonded complexes does not occur until the isotropic state is reached. Moreover, isotropization is not driven by a breakdown of the hydrogen-bonded complex; indeed, the mesophase may act to stabilize the hydrogen bond.

Finally, we note the surprising results obtained in generating hydrogen-bonded complexes based on 4-nitro- and 4-cyano-stilbazoles.

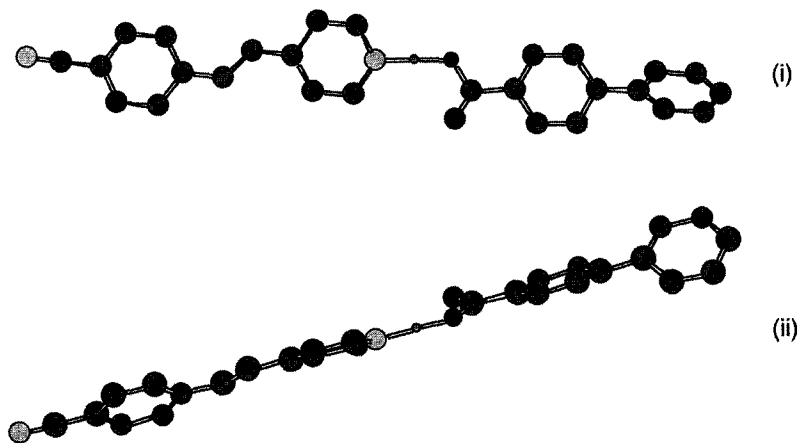


FIG. 59. Two views of the molecular structure of the complex formed between 4-cyanostilbazole and biphenyl-4-carboxylic acid.

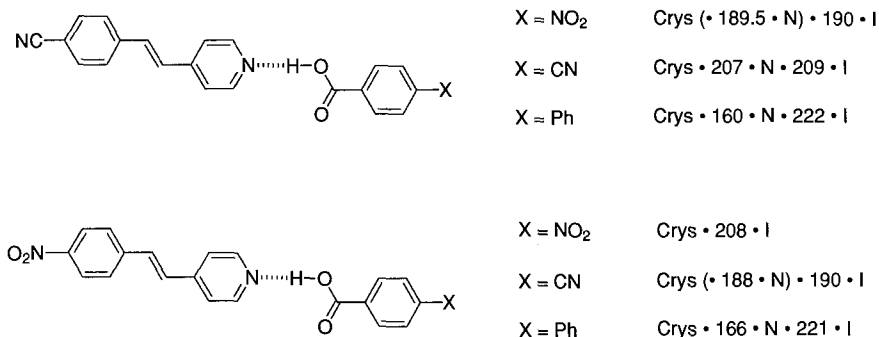


FIG. 60. Mesomorphism of hydrogen-bonded complexes of components bearing no flexible chains.

Complexes of these stilbazoles were prepared with some rather simple benzoic acids, such as 4-nitrobenzoic acid, 4-cyanobenzoic acid, and biphenyl-4-carboxylic acid (Fig. 59) (71). Here, none of the components is liquid crystalline; indeed none possesses a flexible chain. Thus one would expect that complexes between them would do nothing but melt. How wrong? The data (Fig. 60) reveal that five of the complexes exhibit a nematic phase! Remarkably, some these materials have clearing points around 220°C, indicating that the hydrogen bonds are stable to these temperatures. Whoever said hydrogen bonds are not strong?

#### IX. Concluding Remarks

The stilbazole moiety has shown itself to be quite versatile, capable of generating interesting materials chemistry both on its own and on complexation with a variety of metal centers. In studying it, we have been rewarded with an wide-ranging and rather remarkable collection of interesting observations. As this review is not an exhaustive or comprehensive treatment of work carried out, readers requiring the full story or more detail of particular aspects are encouraged to consult the original literature. In particular, we hope to have shown that the metal complex chemistry possible with this ligand, combined with the scope for structural variation offered by both the complexes themselves and the ligand, allows aspects of the materials chemistry to be controlled. After all, the ultimate goal is to change a small aspect of the molecular structure, thereby effecting a more significant influence on the bulk properties, *and* to understand why it worked!

## ACKNOWLEDGMENTS

It is my very great pleasure to acknowledge and thank those who have worked with me on these fascinating systems over the years. The initial ideas for the stilbazoles themselves came from Peter Maitlis (Sheffield), and it was early work with him and David Dunmur (Sheffield) that got this whole thing going. The nonlinear optical studies were carried out by Anna Thornton, Lap-Tak Cheng (DuPont), and Marguerite Barzoukas (Strasbourg). Anna also contributed to the L-B studies in collaboration with Tim Richardson and his group in Sheffield. The liquid-crystal studies were initiated by Elena Lalinde, then carried on by Peter Styring, Sarah Hudson, Ronan Le Lagadec, John Stacey, Sue Hunt, Bob Orr, Daniel Price, Joanne Luckhurst, Bertrand Donnio, Kim Willis, and Carsten Roll in collaboration with Takashi Kato in Tokyo, Michèle Veber, and Anne-Marie Levelut in Orsay and with Benoît Heinrich and Daniel Guillon in Strasbourg. Early parts of the LC work were also done in conjunction with Jose-Luis Serrano and Luis Oro (Zaragoza). All of the single-crystal X-ray structures were carried out by Harry Adams and Neil Bailey in Sheffield. Finally, I thank Dr. Loc Nguyen for his critical and perceptive reading of the manuscript.

## REFERENCES

1. Bruce, D. W.; Lalinde, E.; Styring, P.; Dunmur, D. A.; Maitlis, P. M. *J. Chem. Soc., Chem. Commun.* **1986**, 581. Adams, H.; Bailey, N. A.; Bruce, D. W.; Dunmur, D. A.; Lalinde, E.; Marcos, M.; Ridgway, C.; Smith A. J.; Styring, P.; Maitlis, P. M. *Liq. Cryst.* **1987**, *2*, 381.
2. Bruce, D. W.; Dunmur, D. A.; Lalinde, E.; Maitlis, P. M. Styring, P. *Liq. Cryst.* **1988**, *3*, 385.
3. Donnio, B.; Bruce, D. W.; Heinrich, B.; Guillon, D.; Delacroix, H.; Gulik-Krzywicki, T. *Chem. Mater.* **1997**, *9*, 2951.
4. Donnio, B.; Adams, H. A.; Bruce, D. W. Unpublished work.
5. Adams, H.; Bailey, N. A.; Bruce, D. W.; Hudson, S. A.; Marsden, J. R. *Liq. Cryst.* **1994**, *16*, 643.
6. Adams, H.; Bailey, N. A.; Bruce, D. W.; Hempstead, P. D.; Woodcock, K. J. Unpublished.
7. Bruce, D. W.; Dunmur, D. A.; Esteruelas, M. A.; Hunt, S. E.; Le Lagadec, R.; Maitlis, P. M.; Marsden, J. R.; Sola, E.; Stacey, J. M. *J. Mater. Chem.* **1991**, *1*, 251.
8. Bruce, D. W.; Donnio, B.; Maggs A. A.; Marsden, J. R. *Inorg. Chim. Acta* **1991**, *188*, 41.
9. Salt, N. J. S. PhD Thesis, University of Sheffield, 1989.
10. Roll, C. P.; Donnio, B.; Weigand, W.; Bruce, D. W. *Chem. Commun.* **2000**, 709.
11. Chemla, D. S.; Zyss, J., Eds. "Nonlinear Optical Properties of Organic Molecules and Crystals"; Academic Press: New York, 1987, Vols. 1 and 2.
12. Ashwell, G. J. *Adv. Mater.* **1996**, *8*, 248.
13. Meredith, G. R. "Nonlinear Optical Properties of Organic and Polymeric Materials"; ACS Symp. Ser. 233; Williams, D. J., Ed.; American Chemical Society: Washington, DC, 1983, p. 30.
14. Marder, S. R.; Perry, J. W.; Schaefer, W. P. *Science* **1989**, *245*, 626.
15. Woodcock, K. J.; Cross, G. H.; Bruce, D. W. Unpublished results.
16. Bruce, D. W.; Denning, R. G.; Grayson, M. G.; Le Lagadec, R.; Lai, K. K.; Pickup, B. T.; Thornton, A. *Adv. Mater. Opt. Electron.* **1994**, *4*, 293.
17. Bruce, D. W.; Thornton, A. *Mol. Cryst., Liq. Cryst.* **1993**, *231*, 253.

18. Hieber, W.; Frey, V. *Chem. Ber.* **1966**, *99*, 2607.
19. Lesley, M. J. G.; Woodward, A.; Taylor, N. J.; Marder, T. B.; Cazenobe, I.; Ledoux, I.; Zyss, J.; Thornton, A.; Bruce, D. W.; Kakkar, A. K. *Chem. Mater.* **1998**, *10*, 1355.
20. Petty, M. R. "Langmuir-Blodgett Films"; Cambridge University Press: Cambridge, 1996.
21. Richardson, T.; TopaÇli, A.; Abd Majid, W. H.; Greenwood, M. B.; Bruce, D. W.; Thornton, A.; Marsden, J. R. *Adv. Mater. Opt. Electron.* **1994**, *4*, 243.
22. TopaÇli, A.; Richardson, T.; Abd Majid, W. H.; Thornton, A.; Bruce, D. W.; Marsden, J. R. *Int. J. Elec.* **1994**, *77*, 951.
23. Capan, R.; Batty, S. V.; Richardson, T.; Lacey, D.; Holder, S. J.; Abd. Majid, W. H. *Thin Solid Films*, **1996**, 284-5, 915, McCartney, C. M.; Richardson, T.; Pavier, M. A.; Davis, F.; Stirling, C. J. M. *Thin Solid Films*, **1998**, 327-29, 431, McCartney, C. M.; Richardson, T.; Greenwood, M. B.; Cowlam, N.; Davis, F.; Stirling, C. J. M. *Supramol. Sci.* **1997**, *4*, 385.
24. Bruce, D. W. *Acc. Chem. Res.* **2000**, *33*, 831.
25. Kaszynski, P. *Collect. Czech. Chem. Commun.* **1999**, *64*, 986.
26. *LiqCryst*, LCI Publisher: Hamburg.
27. Leadbetter, A. J. In "Thermotropic Liquid Crystals"; Gray, G. W. Ed.; Wiley: Chichester, 1987, Chapter 1.
28. Spegt, P.; Skoulios, A. C. R. *Hebd. Séan. Acad. Sci.* **1960**, *251*, 2199.
29. Chandrasekhar, S.; Sadashiva, B. K.; Suresh, K. A. *Pramana*, **1977**, *9*, 471.
30. Malthête, J.; Nguyen, H.-T.; Destrade, C. *Liq. Cryst.* **1993**, *13*, 171. Nguyen, H.-T.; Destrade, C.; Malthête, J. *Adv. Mater.* **1997**, *9*, 375.
31. Guillon, D.; Heinrich, B.; Ribeiro, A. C.; Cruz, C.; Nguyen, H. T. *Mol. Cryst., Liq. Cryst.* **1998**, *317*, 51.
32. Diele, S.; Göring, P. In "Handbook of Liquid Crystals"; Demus, D.; Goodby, J.; Gray, G. W.; Spiess, H.-W.; Vill, V.; Eds.; Wiley-VCH: Weinheim, 1998, Vol. 2B, Chapter XIII.
33. Gray, G. W.; Jones, B.; Marson, J. *J. Chem. Soc.* **1957**, 393.
34. Etherington, G.; Leadbetter, A. J.; Wang, X. J.; Gray, G. W.; Tajbakhsh, A. *Liq. Cryst.* **1986**, *1*, 209.
35. Demus, D.; Gloza, A.; Hartung, H.; Hauser, A.; Rapthel, I.; Wiegeleben, A. *Cryst. Res. Tech.* **1981**, *16*, 1445.
36. Luzzati, V.; Spegt, P. A. *Nature* **1967**, *215*, 701.
37. Charvolin, J.; Sadoc, J. F. *J. Phys.* **1988**, *49*, 521.
38. Gray, G. W.; Goodby, J. W. "Smectic Liquid Crystals"; Leonard Hill: Glasgow, 1984.
39. Bruce, D. W. In "Inorganic Materials," 2nd ed.; Bruce, D. W., O'Hare, D., Eds.; Wiley: Chichester, 1996, Chapter 8. Donnio, B., Bruce, D. W. In "Structure and Bonding"; Mingos, D. M. P. Ed., Springer-Verlag: Berlin, 1999, 95, Chapter 5, Collinson S. R.; Bruce, D. W. In "Transition Metals in Supramolecular Chemistry"; Sauvage, J.-P., Ed.; Wiley: Chichester, 1999, Chapter 7; Serrano, J.-L., Ed. "Metallomesogens"; Wiley-VCH: Weinheim, 1996.
40. Bruce, D. W.; Dunmur, D. A.; Hunt, S. E.; Maitlis, P. M.; Orr, R. *J. Mater. Chem.* **1991**, *1*, 857. Marshall, K. L.; Jacobs, S. D. *Mol. Cryst., Liq. Cryst.* **1988**, *159*, 181.
41. Bertram, C.; Bruce, D. W.; Dunmur, D. A.; Hunt, S. E.; Maitlis, P. M.; McCann, M. *J. Chem. Soc., Chem. Commun.* **1991**, 69.
42. Bruce, D. W.; Dunmur, D. A.; Manterfield, M. R.; Maitlis, P. M.; Orr, R. *J. Mater. Chem.* **1991**, *1*, 255.
43. Esteruelas, M. A.; Sola, E.; Oro, L. A.; Ros, M. B.; Serrano, J.-L. *J. Chem. Soc., Chem. Commun.* **1989**, 55.
44. Esteruelas, M. A.; Sola, E.; Oro, L. A.; Ros, M. B.; Marcos, M.; Serrano, J.-L. *J. Organomet. Chem.* **1990**, *387*, 103.

45. Bruce, D. W.; Davis, S. C.; Dunmur, D. A.; Hudson, S. A.; Maitlis, P. M.; Styring, P. *Mol. Cryst., Liq. Cryst.* **1992**, 215, 1.
46. Rourke, J. P.; Fanizzi, F. P.; Salt, N. J. S.; Bruce, D. W.; Dunmur, D. A.; Maitlis, P. M. *J. Chem. Soc., Chem. Commun.* **1990**, 229.
47. Rourke, J. P.; Fanizzi, F. P.; Bruce, D. W.; Dunmur, D. A.; Maitlis, P. M. *J. Chem. Soc., Dalton Trans.* **1992**, 3009.
48. Bruce, D. W.; Dunmur, D. A.; Hudson, S. A.; Lalinde, E.; Maitlis, P. M.; McDonald, M. P.; Orr, R.; Styring, P.; Cherodian, A.; Richardson, R. M.; Feijoo, J. L.; Ungar, G. *Mol. Cryst., Liq. Cryst.* **1991**, 206, 79. Bruce, D. W.; Dunmur, D. A.; Lalinde, E.; Maitlis, P. M.; Styring, P. *Nature (London)* **1986**, 323, 791.
49. Marcos, M.; Ros, M. B.; Serrano, J.-L.; Esteruelas, M. A.; Sola, E.; Oro, L. A.; Barberá, J. *Chem. Mater.* **1990**, 2, 748.
50. Donnio, B.; Bruce, D. W.; Delacroix, H.; Gulik-Krzywicki, T. *Liq. Cryst.* **1997**, 23, 147.
51. Bruce, D. W.; Dunmur, D. A.; Maitlis, P. M.; Styring, P.; Esteruelas, M. A.; Oro, L. A.; Ros, M. B.; Serrano, J. L.; Sola, E. *Chem. Mater.* **1989**, 1, 479.
52. Demus, D. *Mol. Cryst., Liq. Cryst.* **1988**, 165, 45.
53. Styring, P. PhD Thesis, University of Sheffield, 1989.
54. Bruce, D. W.; Dunmur, D. A.; Hudson, S. A.; Maitlis, P. M.; Styring, P. *Adv. Mater. Opt. Electron.* **1992**, 1, 37.
55. Adams, H.; Bailey, N. A.; Bruce, D. W.; Davis, S. C.; Dunmur, D. A.; Hudson, S. A.; Thorpe, S. J. *J. Mater. Chem.* **1992**, 2, 395.
56. Bruce, D. W.; Hudson, S. A. *J. Mater. Chem.* **1994**, 4, 479.
57. Donnio, B.; Bruce, D. W. *J. Mater. Chem.* **1998**, 8, 1993.
58. Donnio, B.; Bruce, D. W. *New J. Chem.* **1999**, 23, 275.
59. Donnio, B.; Bruce, D. W. *J. Chem. Soc., Dalton Trans.* **1997**, 2745.
60. Donnio, B.; Heinrich, B.; Guillon, D. Work in progress, January 2001.
61. Aakeroy, C. B.; Seddon, K. R. *Chem. Soc. Rev.* **1993**, 22, 397.
62. Kato, T. In "Handbook of Liquid Crystals"; Demus, D., Goodby, J., Gray, G. W., Spiess, H.-W., Vill, V., Eds.; Wiley-VCH: Weinheim, Vol. 2B, Chapter XVII, 1998. Paleos, C.; Tsiourvas, D. *Angew. Chem., Int. Ed. Engl.* **1995**, 34, 1696.
63. Kato, T.; Fréchet, J. M. J. *J. Am. Chem. Soc.* **1989**, 111, 8533.
64. Kato, T.; Adachi, H.; Fréchet, J. M. J.; Fujishima, A. *Chem. Lett.* **1992**, 265.
65. Willis, K.; Luckhurst, J. E.; Price, D. J.; Fréchet, J. M. J.; Kato, T.; Ungar, G.; Bruce, D. W. *Liq. Cryst.* **1996**, 21, 585.
66. Luckhurst, J. E.; Price, D. J.; Bruce, D. W. Unpublished work.
67. Bruce, D. W.; Price, D. J. *Adv. Mater. Opt. Electron.* **1994**, 4, 273.
68. Willis, K.; Price, D. J.; Adams, H.; Ungar, G.; Bruce, D. W. *J. Mater. Chem.* **1995**, 5, 2195.
69. Price, D. J.; Willis, K.; Richardson, T.; Ungar, G.; Bruce, D. W. *J. Mater. Chem.* **1997**, 7, 883.
70. Price, D. J.; Richardson, T.; Bruce, D. W. *J. Chem. Soc., Chem. Commun.* **1995**, 1911.
71. Price, D. J.; Adams, H.; Bruce, D. W. *Mol. Cryst., Liq. Cryst.* **1996**, 289, 127.

## TETRA- AND TRINUCLEAR PLATINUM(II) CLUSTER COMPLEXES

TADASHI YAMAGUCHI and TASUKU ITO

Department of Chemistry, Graduate School of Science, Tohoku University,  
Sendai 980-8578, Japan

- I. Introduction
- II. Tetranuclear Platinum(II) Cluster Complexes
  - A. Regioselective Ligand Exchange Reaction in  $[\text{Pt}_4(\text{CH}_3\text{COO})_8]$
  - B.  $\text{Pt}_4$  Clusters and Their Structures
  - C. EHMO Study
  - D.  $^1\text{H}$  NMR of Tetraplatinum Clusters
  - E.  $^{195}\text{Pt}$  NMR of Tetraplatinum Clusters
  - F.  $\text{Pt}_4$  Cluster Core Rotation and *Chelate, Bridge* Mutual Isomerization
  - G. Pyridine Ring Rotation
  - H. Catalytic Activity of  $\text{Pt}_4$  Clusters toward the Hydration of Acetonitrile
- III. Trinuclear Platinum(II) Cluster Complexes
  - A. Synthesis—Cluster Core Transformation
  - B. Structures of Triangular Cluster Complexes
  - C. Mechanism of the Cluster Core Transformation Reaction from Square-Planar to Triangular Type
  - D. EHMO Study
  - E. Solution Behavior
  - F.  $^{195}\text{Pt}$  NMR Spectra of  $\text{Pt}_3$  Clusters
- IV. Concluding Remarks
- References

### I. Introduction

Platinum cluster complexes with Pt–Pt bond(s) having various oxidation states are well known, and many exist in low-valent oxidation state, such as a series of  $[\text{Pt}_3(\text{CO})_6]_n^{2-}$  and phosphine or isocyanide clusters (1–9). A platinum ion with an odd  $d$  electron tends to form a dimeric complex having a Pt–Pt single bond involving the unpaired electrons. Monovalent platinum forms dimeric cluster complexes with a  $d^9$ – $d^9$  configuration (10–14) and tervalent platinum forms  $d^7$ – $d^7$

dinuclear complexes (15–19). Mixed-valent Pt(II)/Pt(III) complexes, such as platinum blue, are also well known (20–23). On the other hand, divalent platinum complexes are usually square-planar monomeric compounds, and platinum(II) complexes with a Pt–Pt bond have been limited to octaacetatotetraplatinum(II),  $[\text{Pt}_4^{\text{II}}(\text{CH}_3\text{COO})_8]$  (1), and its derivatives.

The complex  $[\text{Pt}_4^{\text{II}}(\text{CH}_3\text{COO})_8]$  (1), which is a tetramer of platinum(II) acetate, was first found by Skapski and co-workers in a study aiming at the isolation of pure platinum(II) acetate (24–26). They revealed that pure “platinum acetate” obtained using the silver acetate method (27) has an unusual tetrameric structure (Fig. 1). The structure is totally different from the trimeric structure known for palladium(II) acetate,  $[\text{Pd}_3(\text{CH}_3\text{COO})_6]$  (28).

In  $[\text{Pt}_4(\text{CH}_3\text{COO})_8]$  (1), four platinum atoms form a square-planar cluster core with short Pt–Pt bonds of 2.492–2.501 Å, and adjacent platinum atoms are bridged by eight acetate ligands. Four acetates are approximately coplanar with the  $\text{Pt}_4$  cluster core (hereinafter called in-plane acetate), while the other four are arranged alternately above and below the plane of the cluster core (out-of-plane acetate). The coordination geometry around the platinum atoms is octahedral if the Pt–Pt bonds are included. The Pt–O distances ( $\sim 2.15$  Å) for the in-plane acetate are slightly longer than those ( $\sim 2.00$  Å) for the out-of-plane acetate, which is a normal  $\text{Pt}^{\text{II}}$ –O distance. The difference in the

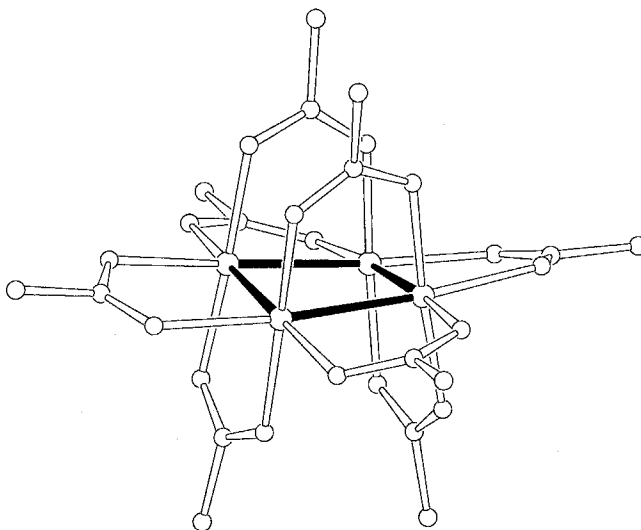


FIG. 1. Structure of  $[\text{Pt}_4(\text{CH}_3\text{COO})_8]$  (1).

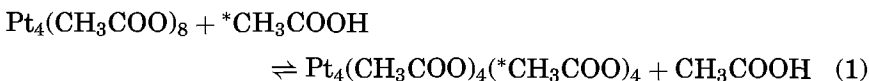
Pt—O(in-plane) and the Pt—O(out-of-plane) distances is ascribed to a *trans* influence from the Pt—Pt bonds.

Skapski *et al.* reported the structure of **1** in 1976, but the chemistry was not been studied in detail until the regioselective lability of the coordinated acetates was reported by our research group in 1989 (29). Since then, many derivatives of **1**, including trinuclear Pt(II) clusters, have been synthesized and their chemistries have been investigated. In this article, the chemistry of Pt<sup>II</sup><sub>4</sub> clusters are reviewed along with Pt<sup>II</sup><sub>3</sub> clusters, which are derived from the cluster core transformation of **1**.

## II. Tetranuclear Platinum(II) Cluster Complexes

### A. REGIOSELECTIVE LIGAND EXCHANGE REACTION IN [Pt<sub>4</sub>(CH<sub>3</sub>COO)<sub>8</sub>]

In the early stage of our studies on the chemistry of platinum(II) cluster complexes, it was found that [Pt<sub>4</sub>(CH<sub>3</sub>COO)<sub>8</sub>] (**1**) undergoes a remarkable regioselective ligand exchange reaction and that the exchange rate is remarkably fast (29). <sup>1</sup>H NMR studies showed that, in the reaction of **1** with CD<sub>3</sub>COOD [Eq. (1)], the in-plane acetate ligands were replaced by deuterated acetates immediately, whereas the out-of-plane acetates remained intact for a month at ambient temperature.



The exchange rate of the in-plane acetate ligands by CD<sub>3</sub>COO<sup>−</sup> was too rapid to follow the time course of the <sup>1</sup>H NMR signal, but not so fast that it could not be followed by dynamic NMR technique. The kinetics of the exchange reaction of Eq. (1) was successfully studied by means of the <sup>1</sup>H NMR saturation transfer method. From kinetic experiments under various conditions, the rate law for Eq. (1) was found to be expressed by Eq. (2).

$$R = 4 [\text{complex}](k_0 + k_1[\text{CH}_3\text{COOH}]) \quad (2)$$

The rate constants at 25°C were 0.36 s<sup>−1</sup> and 4.4 M<sup>−1</sup>s<sup>−1</sup> for *k*<sub>0</sub> and *k*<sub>1</sub>, respectively (29). Activation parameters for the exchange reaction were Δ*H*<sup>‡</sup><sub>1</sub> = 66.7 ± 2.4 kJ mol<sup>−1</sup> and Δ*S*<sup>‡</sup><sub>1</sub> = −14.2 ± 8.3 J mol<sup>−1</sup> K<sup>−1</sup> for *k*<sub>1</sub>, and Δ*H*<sup>‡</sup><sub>0</sub> = 35.5 ± 1.3 kJ mol<sup>−1</sup> and Δ*S*<sup>‡</sup><sub>0</sub> = −132.9 ± 4.4 J mol<sup>−1</sup> K<sup>−1</sup> for *k*<sub>0</sub>, respectively (30).

The significantly large second-order rate constant  $k_1$ , as compared with those commonly observed for substitution reactions of monomeric platinum(II) complexes, shows that the in-plane coordination sites are extremely labilized. On the other hand, the out-of-plane acetate ligands are completely inert to exchange. The remarkable regioselectivity and the striking lability of the in-plane sites in the ligand exchange reaction of  $[\text{Pt}_4(\text{CH}_3\text{COO})_8]$  are closely related to the structure of the  $\text{Pt}_4$  cluster core and arise from a strong *trans* effect from the Pt–Pt bonds. In contrast, Gerbelevu *et al.* reported that all of the trifluoroacetate ligands in  $[\text{Pt}_4(\text{CF}_3\text{COO})_8]$  are replaced by pivalate (31). The lability of the out-of-plane trifluoroacetate ligands may be due to low basicity of trifluoroacetate.

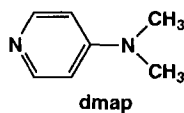
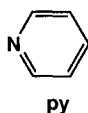
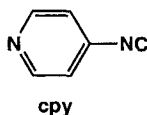
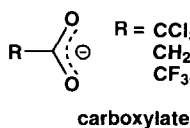
The rate law Eq. (2) suggests that there are two reaction pathways: the first-order reaction associated with  $k_0$  and the second-order reaction associated with  $k_1$ . The first-order reaction path involves a solvent-assisted mechanism, which is consistent with large negative  $\Delta S^\ddagger_0$ . Because the second pathway is second-order and has a small negative  $\Delta S^\ddagger_1$ , an  $\text{I}_a$  mechanism is probably active. The relatively small  $\Delta H^\ddagger_1$  value most likely reflects a weakened Pt–O bond owing to the *trans* influence of the Pt–Pt bond.

## B. $\text{Pt}_4$ CLUSTERS AND THEIR STRUCTURES

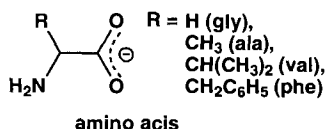
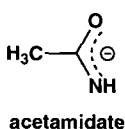
Most of the  $\text{Pt}_4$  clusters thus far known are prepared by ligand substitution of  $[\text{Pt}_4(\text{CH}_3\text{COO})_8]$  (**1**) (*vide infra*). Cluster **1** can be prepared either by reacting of  $\text{Pt}^{\text{IV}}\text{Cl}_4$  with  $\text{CH}_3\text{COOAg}$  in  $\text{CH}_3\text{COOH}$  (27) or by reacting  $\text{K}_2[\text{Pt}^{\text{II}}\text{Cl}_4]$  with  $\text{CH}_3\text{COOAg}$  in  $\text{CH}_3\text{COOH}$  (30). Other direct methods for making the  $\text{Pt}_4$  cluster core are also known. The complex  $[\text{Pt}_4(\text{CF}_3\text{COO})_8]$  (**2**) (31) was prepared by reduction of  $\text{K}_2[\text{Pt}^{\text{IV}}(\text{OH})_6]$  with  $\text{HCOOH}$  in  $\text{CF}_3\text{COOH}$ , and  $[\text{Pt}_4(\text{CH}_3\text{COO})_4(\text{H}_2\text{O})_8]^{4+}$  (**4**) (32) was synthesized by refluxing a  $\text{CH}_3\text{COOH}$  solution containing  $\text{K}_2[\text{Pt}^{\text{III}}_2(\text{SO}_4)_4(\text{H}_2\text{O})_2]$ .

As described in the previous section, the in-plane acetate ligands in **1** are labile, whereas the out-of-plane acetate ligands are inert to substitution. Using inherent lability, many in-plane substituted derivatives have been prepared by reacting **1** with various ligands, including monodentate ( $\text{L}^{\text{mono}}$ ), bidentate ( $\text{L}^{\text{bi}}$ ), tetradentate ( $\text{L}^{\text{tetra}}$ ), or hexadentate ( $\text{L}^{\text{hexa}}$ ) ligand. Ligands used in the substitution are shown in Fig. 2 with their abbreviated notations, and schematic representations of their coordination modes are shown in Fig. 3.

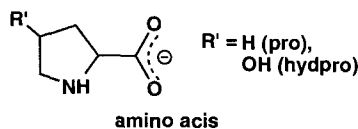
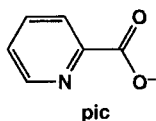
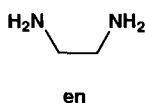
In general, syntheses of  $\text{Pt}_4$  derivatives by substitution of **1** are very simple and easy. Desired compounds can be obtained just by mixing **1**

• *Monodentate*• *Bidentate*

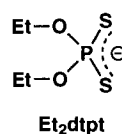
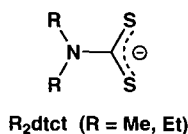
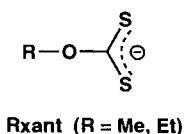
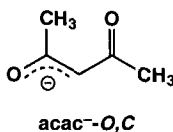
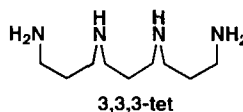
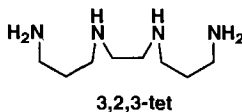
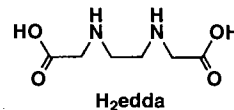
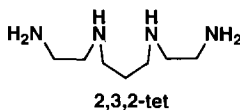
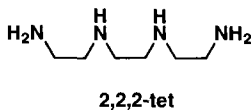
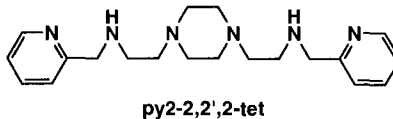
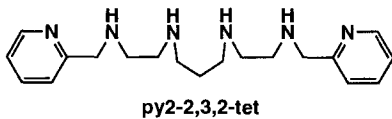
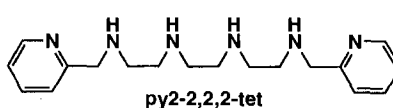
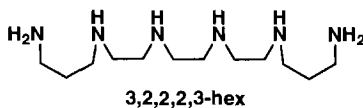
R = CCl<sub>3</sub>, CHCl<sub>2</sub>,  
CH<sub>2</sub>Cl, CBr<sub>3</sub>,  
CF<sub>3</sub>, C<sub>6</sub>H<sub>5</sub>



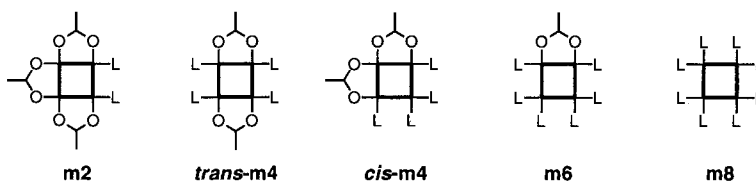
R = H (gly),  
CH<sub>3</sub> (ala),  
CH(CH<sub>3</sub>)<sub>2</sub> (val),  
CH<sub>2</sub>C<sub>6</sub>H<sub>5</sub> (phe)



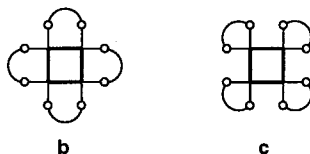
R' = H (pro),  
OH (hydrop)

• *Tetradentate*• *Hexadentate*Fig. 2. Ligands for Pt<sub>4</sub> clusters.

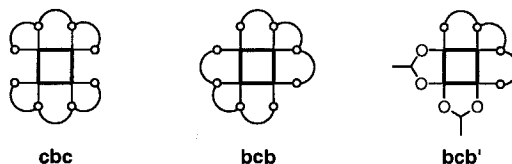
• *Monodentate*



• *Bidentate*



• *Tetradentate*



• *Hexadentate*

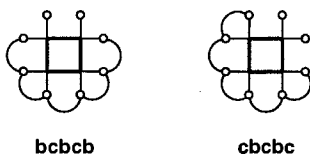


FIG. 3. Schematic structures of substituted clusters. Out-of-plane acetates are omitted for clarity (m, monodentate; b, bridge; c, chelate).

and L in  $\text{CH}_3\text{CN}$  or  $\text{CH}_2\text{Cl}_2$ , and the crude products can be purified by recrystallization or column chromatography. Some typical examples are given in Figs. 4–12.

### 1. $\text{Pt}_4$ Clusters with Monodentate Ligands

Clusters  $[\text{Pt}_4(\text{CH}_3\text{COO})_{8-n}(\text{L}^{\text{mono}})_{2n}]^{n+}$  ( $n = 2, 4$ ), where  $\text{L}^{\text{mono}}$  is pyridine (py), 4-dimethylaminopyridine (dmap), or 4-cyanopyridine (cpy), have been isolated (33). These clusters were obtained from the reaction of **1** with  $\text{L}^{\text{mono}}$  in a polar solvent such as  $\text{CH}_3\text{CN}$ . When a non-polar solvent was used, the substitution of the in-plane acetates by  $\text{L}^{\text{mono}}$  did not proceed smoothly, and some  $\text{Pt}_4$  species with monodentate

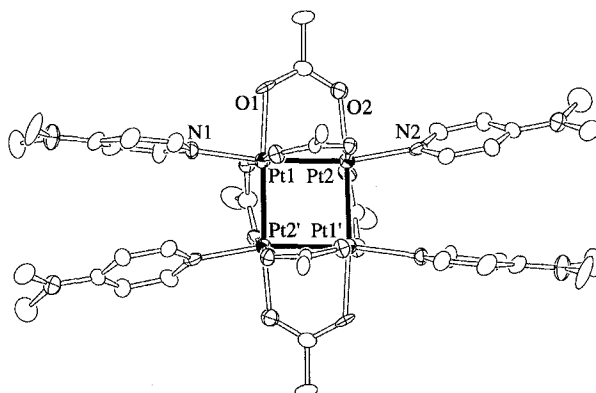


FIG. 4. An ORTEP drawing of  $[\text{Pt}_4(\text{CH}_3\text{COO})_6(\text{dmap})_4](\text{ClO}_4)_2$ .

acetate(s) and  $\text{L}^{\text{mono}}(\text{s})$  were often identified by  $^1\text{H}$  NMR. For the tetrasubstituted derivative ( $n=2$ ), there are two possible isomers, *cis*- and *trans*- $[\text{Pt}_4(\text{CH}_3\text{COO})_6(\text{L}^{\text{mono}})_4]^{2+}$  (Fig. 3). However, only the *trans* isomer was obtained for each  $\text{L}^{\text{mono}}$  when the cluster was made from **1**. This is due to the *trans* effect involving  $\text{L}^{\text{mono}}$  through the Pt–Pt bond, possibly owing to a higher thermodynamic stability of

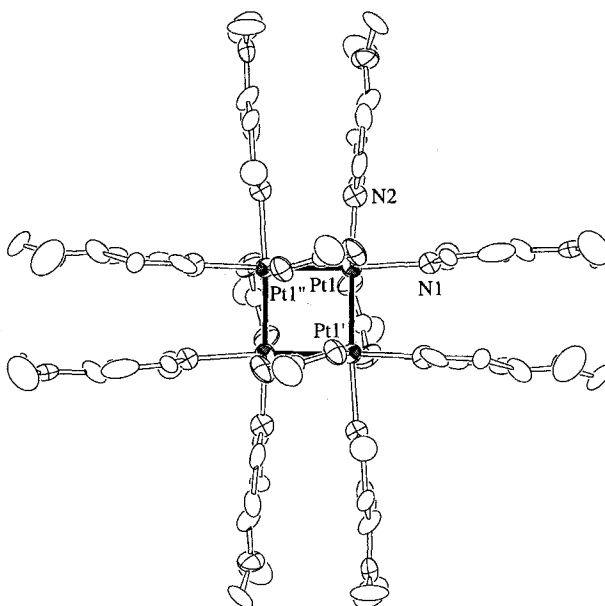


FIG. 5. An ORTEP drawing of  $[\text{Pt}_4(\text{CH}_3\text{COO})_4(\text{dmap})_8](\text{ClO}_4)_4$ .

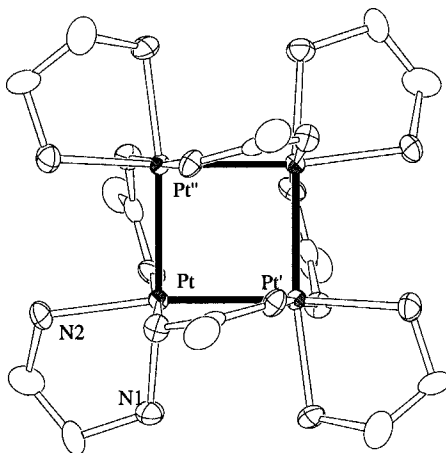


FIG. 6. An ORTEP drawing of  $[\text{Pt}_4(\text{CH}_3\text{COO})_4(\text{en})_4](\text{ClO}_4)_4$ .

the *trans* isomer. The *cis* isomer can be generated by a comproportionation reaction between 1 and  $[\text{Pt}_4(\text{CH}_3\text{COO})_4(\text{L}^{\text{mono}})_8]^{4+}$  in solution as a minor component of an equilibrium mixture. The clusters with  $n = 1$  and 3 can also be prepared in solution by a comproportionation reaction.

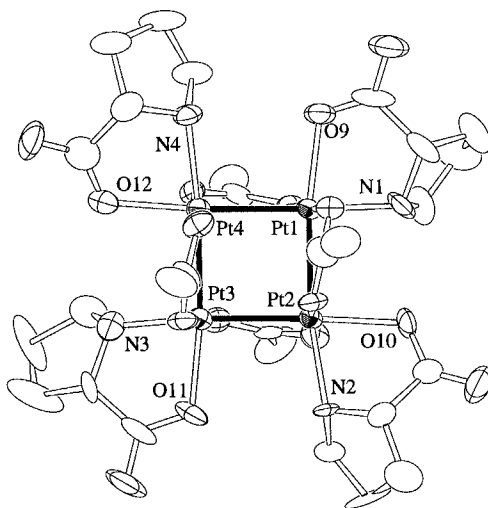


FIG. 7. An ORTEP drawing of  $[\text{Pt}_4(\text{CH}_3\text{COO})_4(\text{pro})_4]$ .

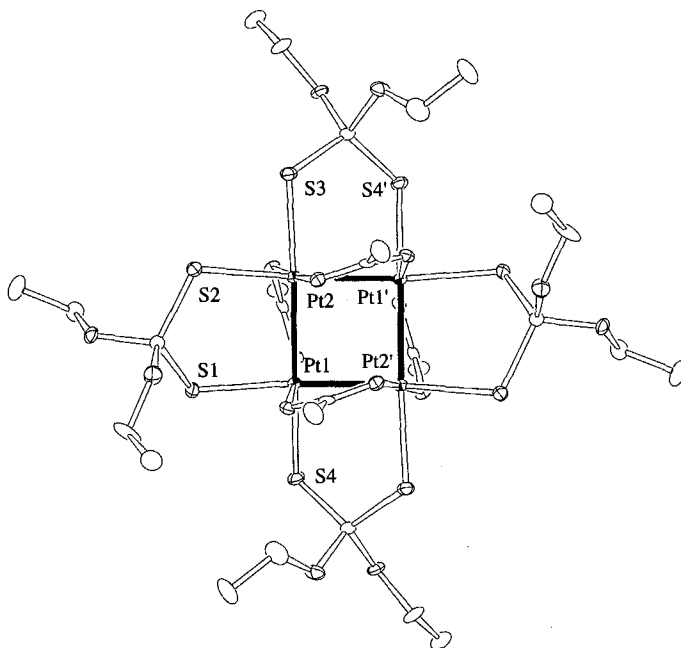


FIG. 8. An ORTEP drawing of *bridge*-[Pt<sub>4</sub>(CH<sub>3</sub>COO)<sub>4</sub>(Et<sub>2</sub>dtp)<sub>4</sub>].

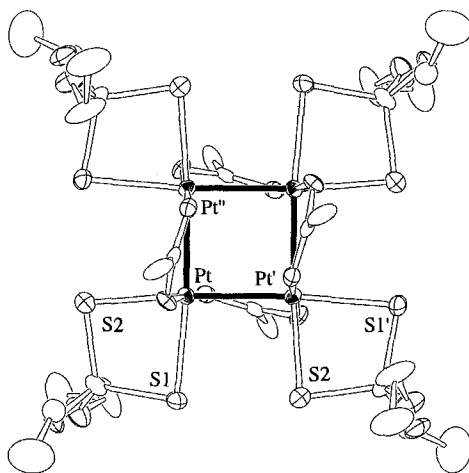


FIG. 9. An ORTEP drawing of *chelate*-[Pt<sub>4</sub>(CH<sub>3</sub>COO)<sub>4</sub>(Et<sub>2</sub>dtp)<sub>4</sub>].

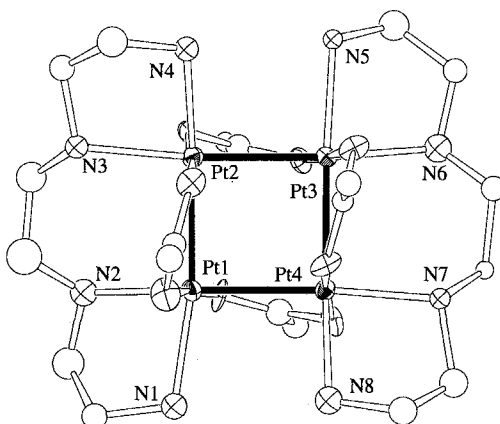


FIG. 10. An ORTEP drawing of  $[\text{Pt}_4(\text{CH}_3\text{COO})_4(2,2,2\text{-tet})_2](\text{ClO}_4)_4$ .

## 2. $\text{Pt}_4$ Clusters with Bidentate Ligands

There are two modes of coordination for a bidentate ligand at the in-plane site of the  $\text{Pt}_4$  cluster core: bridging and chelating (Fig. 3). Carboxylates (29), acetamidate (34), and acetylacetonate-*O,C* ligands (35) assume exclusively a bridging mode. In these ligands, the two donor atoms are separated by a single atom (hereinafter designated as three-atom bidentate ligand). On the other hand, a bidentate ligand that has

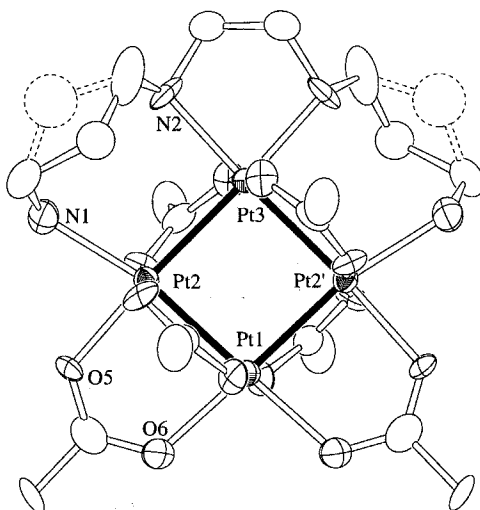


FIG. 11. An ORTEP drawing of  $[\text{Pt}_4(\text{CH}_3\text{COO})_6(3,2,3\text{-tet})](\text{ClO}_4)_2$ .

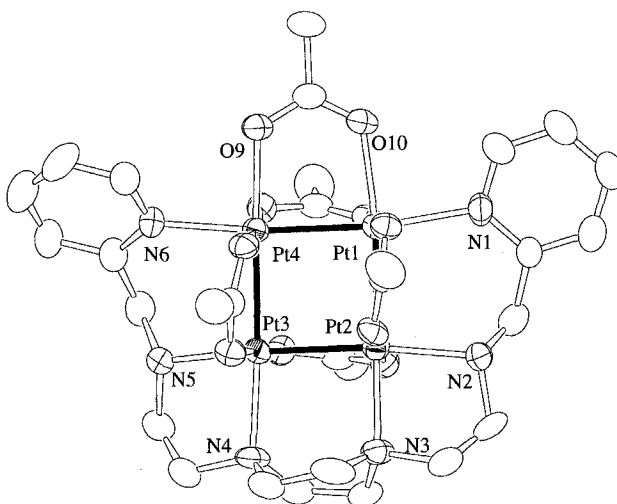


FIG. 12. An ORTEP drawing of  $[\text{Pt}_4(\text{CH}_3\text{COO})_5(\text{py}_2\text{-}2,2',2''\text{-tet})](\text{ClO}_4)_3$ .

two atoms between donor atoms (four-atom bidentate ligand) such as ethylenediamine (en) adopts a chelating mode (36). A side of the square-planar  $\text{Pt}_4$  cluster core is doubly bridged when a bridging-type bidentate ligand is used, whereas it is singly bridged when a chelating ligand is used.

$\alpha$ -Amino acid and picolinic acid have two sets of bidentate sites with either an (O,O) or (O,N) donor atom set. In  $\text{Pt}_4$  clusters having these bidentate ligands,  $[\text{Pt}_4(\text{CH}_3\text{COO})_4(\text{L}^{\text{bi}})_4]$  ( $\text{L}^{\text{bi}}$  = glycine, L-alanine, L-proline, L-hydroxyproline, L-phenylalanine, L-valine, or picolinic acid),  $\text{L}^{\text{bi}}$  always assumes a chelating mode through the (O,N) donor atom set, both in the solid and in the solution state (30–38). There are several possible isomers of  $[\text{Pt}_4(\text{CH}_3\text{COO})_4(\text{L}^{\text{bi}})_4]$  with respect to the arrangement of N and O atoms when all  $\text{L}^{\text{bi}}$  are chelating. Interestingly, only one isomer, in which N and O atoms are arranged alternately around the  $\text{Pt}_4$  cluster core, has been isolated irrespective of the kind of  $\text{L}^{\text{bi}}$ . There is no evidence for the existence of isomers, even in the glycinate complex  $[\text{Pt}_4(\text{CH}_3\text{COO})_4(\text{gly})_4]$  (17) where there is no steric interaction (38).

When the bite distance of a bidentate ligand is intermediate, its coordination mode to the  $\text{Pt}_4$  cluster core becomes subtle. Dithio ligands, dialkyldithiocarbamate and dialkyldithiophosphate, have relatively long bite distances despite being three-atom bidentate ligands. These ligands have been found to assume both bridging and chelating modes

in  $[\text{Pt}_4(\text{CH}_3\text{COO})_4(\text{L}^{\text{bi}})_4]$ , and both isomers have been isolated (39–40). On the other hand, ethylxantogenate (Etxant), a similar dithio ligand that has slightly shorter bite distance, gives only a bridged isomer of  $[\text{Pt}_4(\text{CH}_3\text{COO})_4(\text{Etxant})_4]$ . Diethyldithiophosphate ligand ( $\text{Et}_2\text{dtp}$ ) has a longer bite distance owing to the long P–S distance, and the bridged and chelated isomers of  $[\text{Pt}_4(\text{CH}_3\text{COO})_4(\text{Et}_2\text{dtp})_4]$  have been isolated. Interestingly, each cluster isomerizes to give an equilibrium mixture (Section II,F). Diethyldithiocarbamate ligand ( $\text{Et}_2\text{dtc}$ ) also affords the bridged and chelated isomers of  $[\text{Pt}_4(\text{CH}_3\text{COO})_4(\text{Et}_2\text{dtc})_4]$ .

### 3. $\text{Pt}_4$ Clusters with Tetra- and Hexadentate Ligands

$\text{Pt}_4$  cluster derivatives with multidentate linear polyamine ligands have been synthesized and structurally characterized. X-Ray structure analyses show that a part of a linear polyamine ligand that consists of a three-atom ligand tends to take the bridging coordination mode, whereas a portion of a four-atom ligand assumes the chelating mode. With tetradentate ligands ( $\text{L}^{\text{tetra}}$ ), such as 2,2,2-tet, 2,3,2-tet, or edda, two ligands occupy all of the in-plane sites in a chelate–bridge–chelate fashion (Fig. 3) to give  $[\text{Pt}_4(\text{CH}_3\text{COO})_4(\text{L}^{\text{tetra}})_2]^{n+}$  (41).

On the other hand, when the tetradentate ligand ( $\text{L}^{\text{tetra}'}$ ) is 3,2,3-tet or 3,3,3-tet, only one tetradentate ligand coordinates in a bridge–chelate–bridge fashion to give  $[\text{Pt}_4(\text{CH}_3\text{COO})_4(\text{L}^{\text{tetra}'})_2(\text{CH}_3\text{COO})_2]^{2+}$  (41). The corresponding bis complex  $[\text{Pt}_4(\text{CH}_3\text{COO})_4(\text{L}^{\text{tetra}'})_2]^{4+}$  was not obtained, owing to steric repulsion. The clusters containing a hexadentate polyamine ligand ( $\text{L}^{\text{hexa}}$ ),  $[\text{Pt}_4(\text{CH}_3\text{COO})_4(\text{L}^{\text{hexa}})(\text{CH}_3\text{COO})_2]^{2+}$  have also been synthesized, and the ligand  $\text{L}^{\text{hexa}}$  takes a bridge–chelate–bridge–chelate–bridge mode (42).

### 4. X-Ray Structures of $\text{Pt}_4$ Clusters

Table I summarizes Pt–Pt and Pt–donor atom distances for all of the  $\text{Pt}_4$  clusters thus far structurally characterized.

The square-planar cluster cores in the substituted derivatives are essentially the same as that of **1**. The four out-of-plane acetate ligands in the parent octaacetato complex **1** (up–down/up–down with respect to the cluster plane) also remained unaltered in the substituted clusters.

In some cases, a clear elongation of the Pt–Pt bond distance [2.492(1)–2.501(1) Å] is observed compared to those in **1**. The lengthening comes from the following factors:

(i) A strong *trans* influence. The Pt–Pt bond distance in  $[\text{Pt}_4(\text{CH}_3\text{COO})_4(\mu\text{-acac-OC}^3)_4]$  (**14**) is 2.595(1) Å. This compound has the carbon-bonded acetylacetonate ligands within the  $\text{Pt}_4$  cluster plane.

TABLE I  
BOND DISTANCES AND ANGLES FOR Pt<sub>4</sub> CLUSTERS

Complex	Ref.	Type <sup>a</sup>	Pt—Pt	Pt—O (out-of-plane)	Pt—X (in-plane)
[Pt <sub>4</sub> (CH <sub>3</sub> COO) <sub>8</sub> ] (1) (tetragonal)	25	b	2.492(1)–2.498(1)	1.97(1)–2.02(1)	2.13(1)–2.19(1): (O)
[Pt <sub>4</sub> (CF <sub>3</sub> COO) <sub>8</sub> ] (2) (monoclinic)	26	b	2.493(1)–2.501(1)	2.00(1)–2.02(1)	2.14(1)–2.18(1): (O)
[Pt <sub>4</sub> (CH <sub>3</sub> COO) <sub>4</sub> (CCl <sub>3</sub> COO) <sub>4</sub> ] (5)	31	b	2.503–2.513	1.994–2.025	2.139–2.175: (O)
[Pt <sub>4</sub> (CH <sub>3</sub> COO) <sub>4</sub> (acac) <sub>4</sub> ] (14)	29	b	2.492(1)	2.004(7), 2.008(7)	2.154(9), 2.158(8): (O)
[Pt <sub>4</sub> (CH <sub>3</sub> COO) <sub>4</sub> (en) <sub>4</sub> ] <sup>4+</sup> (15)	35	b	2.578(1), 2.595(1)	2.01(2)–2.04(1)	2.48(2), 2.57(2): (O)
[Pt <sub>4</sub> (CH <sub>3</sub> COO) <sub>4</sub> (pic) <sub>4</sub> ] (16)	36	c	2.557(1)	2.01(1), 2.02(1)	2.18(2), 2.21(1): (N)
[Pt <sub>4</sub> (CH <sub>3</sub> COO) <sub>4</sub> (gly) <sub>4</sub> ] (17)	36	c	2.546(1)–2.555(1)	1.99(2)–2.03(1)	2.11(1)–2.17(1): (O)
[Pt <sub>4</sub> (CH <sub>3</sub> COO) <sub>4</sub> (pro) <sub>4</sub> ] (18)	38	c	2.530(1)–2.538(1)	1.987(7)–2.010(6)	2.195(7)–2.207(8): (O)
[Pt <sub>4</sub> (CH <sub>3</sub> COO) <sub>4</sub> (Et <sub>2</sub> am) <sub>4</sub> ] (23)	37	c	2.531(1)–2.537(1)	1.96(1)–2.04(1)	2.18(1)–2.21(1): (O)
<i>chelate</i> -[Pt <sub>4</sub> (CH <sub>3</sub> COO) <sub>4</sub> (Et <sub>2</sub> dtc) <sub>4</sub> ] (25)	40	b	2.572(1)–2.578(1)	1.99(1)–2.04(1)	2.402(4)–2.475(4): (S)
<i>bridge</i> -[Pt <sub>4</sub> (CH <sub>3</sub> COO) <sub>4</sub> (Et <sub>2</sub> dtc) <sub>4</sub> ] (26)	40	b	2.578(1)	2.025(6), 2.039(7)	2.444(3), 2.486(3): (S)
<i>chelate</i> -[Pt <sub>4</sub> (CH <sub>3</sub> COO) <sub>4</sub> (Et <sub>2</sub> dtc) <sub>4</sub> ] (29)	39	c	2.568(2)	1.97(2), 1.98(1)	2.445(7), 2.446(7): (S)
<i>bridge</i> -[Pt <sub>4</sub> (CH <sub>3</sub> COO) <sub>4</sub> (Et <sub>2</sub> dtc) <sub>4</sub> ] (30)	39	b	2.573(1)	1.99(2), 2.04(2)	2.482(7), 2.494(7): (S)
[Pt <sub>4</sub> (CH <sub>3</sub> COO) <sub>4</sub> (2,2-tet) <sub>2</sub> ] <sup>4+</sup> (31)	41	cbc	2.583(1), 2.584(1)	1.994(6)–2.033(6)	2.461(3)–2.500(3): (S)
[Pt <sub>4</sub> (CH <sub>3</sub> COO) <sub>4</sub> (2,3-tet) <sub>2</sub> ] <sup>4+</sup> (32)	41	cbc	2.543(2)–2.565(2)	2.00(1)–2.03(1)	2.16(2)–2.26(2): (N)
[Pt <sub>4</sub> (CH <sub>3</sub> COO) <sub>4</sub> (3,2-tet) <sub>2</sub> ] <sup>4+</sup> (33)	41	cbc	2.564(1)–2.569(1)	2.006(7)–2.023(8)	2.18(1)–2.27(1): (N)
[Pt <sub>4</sub> (CH <sub>3</sub> COO) <sub>4</sub> (3,2-tet) <sub>2</sub> ] <sup>2+</sup> (35)	38	cbc	2.494(2), 2.579(2)	1.99(2), 2.03(1)	2.16(2), 2.19(2): (O)
[Pt <sub>4</sub> (CH <sub>3</sub> COO) <sub>4</sub> (py <sub>2</sub> -2,2'-2-tet)] <sup>+</sup> (36)	42	bcbcb	2.524(1)–2.544(1)	1.99(1)–2.03(1)	2.11(1), 2.14(1): (O)
[Pt <sub>4</sub> (CH <sub>3</sub> COO) <sub>4</sub> (dmap) <sub>4</sub> ] <sup>2+</sup> (43)	33		2.527(1)–2.542(1)	1.999(7)–2.018(7)	2.176(7)–2.193(7): (O)
[Pt <sub>4</sub> (CH <sub>3</sub> COO) <sub>4</sub> (py) <sub>4</sub> ] <sup>2+</sup> (44)	32		2.530(1), 2.545(1)	1.99(1)–2.02(1)	2.12(1), 2.19(1): (O)
[Pt <sub>4</sub> (CH <sub>3</sub> COO) <sub>4</sub> (dmap) <sub>4</sub> ] <sup>4+</sup> (50)	33		2.522(5), 2.525(3)	2.04(2)–2.06(3)	2.05(3), 2.08(3): (O)
			2.577(2)	2.02(2), 2.03(2)	2.20(3), 2.30(3): (N)

<sup>a</sup>b, bridge; c, chelate. See Fig. 3.

The donor carbon atoms exert a very strong *trans* influence, causing an elongation of the Pt–Pt bond.

(ii) A steric effect. For example, in the case of  $[\text{Pt}_4(\text{CH}_3\text{COO})_4(\text{dmap})_8]^{4+}$  (**44**) [2.577(2) Å], the steric effects among the dmap ligands are the origin.

(iii) The effect of a single bridge over the Pt–Pt bond. For example, the  $\text{Pt}_4$  cluster core in **1** is maintained with the eight acetate double bridges, whereas in  $[\text{Pt}_4(\text{CH}_3\text{COO})_4(\text{en})_4]^{2+}$  (**15**) the en ligands take the chelate coordination mode and each Pt–Pt bond has only one bridge and is slightly longer [2.557(1) Å].

As mentioned earlier, the out-of-plane Pt–O distances [1.97(1)–2.02(1) Å] in  $[\text{Pt}_4(\text{CH}_3\text{COO})_8]$  (**1**) are slightly longer (by  $\sim 0.15$  Å) than the in-plane Pt–O distances [2.13(1)–2.19(1) Å]. This elongation is a result of a *trans* influence from the Pt–Pt bond. In substituted derivatives, the Pt–O(out-of-plane) distances are irrespective of in-plane ligands, within a limited range from 1.96(1) to 2.04(1) Å, these being typical of Pt(II)–O distances (43). On the other hand, the in-plane Pt–donor atom distances in the substituted derivatives cover a wide range. In general, the in-plane Pt–donor atom distances are longer by  $\sim 0.15$  Å than those in mononuclear platinum complexes (43) owing to the *trans* influence of Pt–Pt bond as in **1**. In addition, a *trans* influence of the donor atom through the Pt–Pt bond has been also found for some cases. The most typical example is  $[\text{Pt}_4(\text{CH}_3\text{COO})_4(\text{acac-}O, C^3)_4]$  (**14**), which has exceptionally long in-plane Pt–O distances [2.48(2), 2.57(2) Å]. The elongation can be ascribed not only to a *trans* influence from the Pt–Pt bond but also to a *trans* influence from the donor carbon atom of the acac-*O*, *C*<sup>3</sup> ligand through the Pt–Pt bond.

The cluster core,  $\text{Pt}_4(\text{CH}_3\text{COO})_4$ , has  $D_{2d}$  symmetry if the  $\text{Pt}_4$  core is strictly square-planar. But the core structures found in X-ray analysis of  $\text{Pt}_4$  clusters are distorted, more or less, toward the tetrahedral in most cases, giving  $S_4$  symmetry. The Pt atoms deviate from the  $\text{Pt}_4$  best plane by 0.2–0.3 Å. Steric repulsion between two parallel out-of-plane acetates seems to be responsible for the twisting of the cluster core.

It is of interest that each Pt in  $[\text{Pt}_4(\text{CH}_3\text{COO})_4(\text{en})_4]^{4+}$  (**15**) is in a chiral environment (Fig. 13). However, the compound is optically inactive as a whole, because chelate ring configurations around the four Pt atoms are of *meso*( $\Delta\Delta\Delta\Delta$ ) form. Optically active  $\text{Pt}_4$  clusters  $[\text{Pt}_4(\text{CH}_3\text{COO})_4(\text{L-aa})_4]$  have been prepared by introducing optically active  $\alpha$ -amino acid (aa) at the in-plane sites (L-aa = L-alanine, L-proline, L-hydroxyproline, L-phenylalanine, L-valine) (37, 38). As described in the previous section, these  $\alpha$ -amino acids take the chelating coordination mode in  $\text{Pt}_4$  clusters. Therefore, as far as the chelate ring

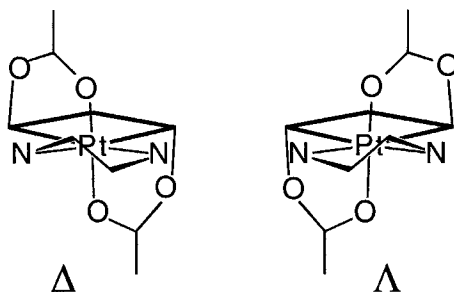


Fig. 13. Two chiral sites in  $[\text{Pt}_4(\text{CH}_3\text{COO})_4(\text{en})_4]^{4+}$ .

configuration of the four  $\alpha$ -amino acids is concerned,  $[\text{Pt}_4(\text{CH}_3\text{COO})_4(\text{L-aa})_4]$  is of *meso*( $\Delta\Delta\Delta\Delta$ ) form, but it has two diastereotopic Pt centers (see Section II,E,2,b).

### C. EHMO STUDY

In order to investigate electronic structures of the  $\text{Pt}_4$  cluster complexes, extended Hückel molecular orbital (EHMO) calculations were carried out for a model system,  $[\text{Pt}_4(\text{HCOO})_8]$  with  $D_{2d}$  symmetry, and its quarterly fragment with  $C_{2v}$  symmetry (29). The MO studies reasonably justify the presence of Pt–Pt bonds in the cluster core and the regioselective substitution reactivities.

Figure 14 shows the MO correlation diagram between  $[\text{Pt}_4(\text{HCOO})_8]$  and the fragment, where only levels near the HOMO–LUMO level associated with Pt  $d_\sigma$  orbitals are depicted. For clarity, levels associated with Pt  $d_\pi$  orbitals are omitted in Fig. 14, because low-lying  $d_\pi$  orbitals in the fragment are fully occupied; therefore, bonding and antibonding effects due to MOs derived from the  $d_\pi$  orbitals are compensated and have no net contribution to stability of the whole  $[\text{Pt}_4(\text{HCOO})_8]$  molecule or the formation of Pt–Pt bonds in the cluster core.

The fragment has two  $d_\sigma$  orbitals ( $d_{z^2}$ , and  $d_{x^2-y^2}$ ) and two  $d$  electrons; therefore, the MOs for  $[\text{Pt}_4(\text{HCOO})_8]$  derived from the fragment orbitals consist of eight levels and eight  $d_\sigma$  electrons are put into the MO levels. The  $d_{x^2-y^2}$  orbitals of the four fragments make one bonding ( $b_2$ ), one antibonding ( $a_2$ ), and one degenerate nonbonding ( $e$ ) molecular orbital. In the same way, the  $d_{z^2}$  orbitals of the fragments make one bonding ( $a_1$ ), one antibonding ( $b_1$ ), and one degenerated ( $e$ ) nonbonding molecular orbital. The resulting two nonbonding MOs with  $e$  symmetry mix with each other to give two degenerate sets of MOs with bonding and antibonding character.

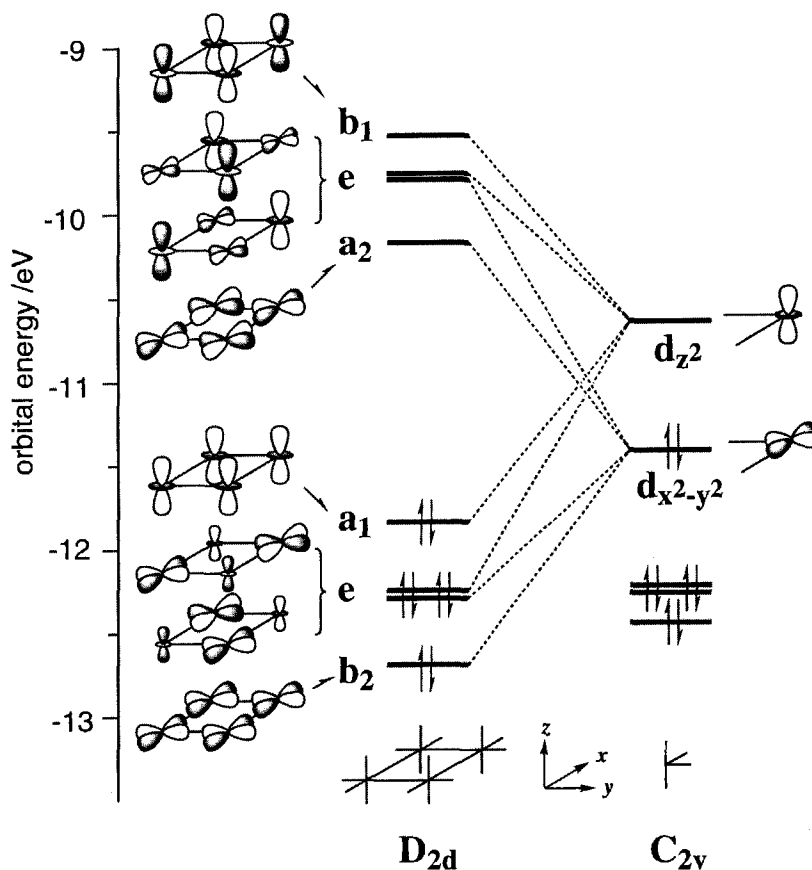


FIG. 14. EHMO diagram for a  $\text{Pt}_4$  model cluster,  $[\text{Pt}_4(\text{HCOO})_8]$ .

Eight  $d_\sigma$  electrons occupy four low-lying bonding MOs, indicating the existence of the four Pt–Pt single bonds in the molecule. The formation of the Pt–Pt bond is also supported by the calculated value of 0.325 for the overlap population between adjacent platinum atoms.

The remarkable regioselective reactivity found in substitution reactions of  $[\text{Pt}_4(\text{CH}_3\text{COO})_8]$  can be understood by examining metal–ligand interactions in the MO diagram in Fig. 14. All four occupied MOs are of antibonding type with respect to the metal–donor atom interaction, and therefore the occupation of these MOs should weaken the Pt–O bonds. The lower three orbitals ( $b_2$  and  $e$ ) are predominantly of  $d_{x^2-y^2}$  character and are antibonding for in-plane ligands. Only the highest level ( $a_1$ ) has  $d_{z^2}$  character and is antibonding with respect to the

out-of-plane ligands. As a whole, the in-plane Pt–O bonds have stronger antibonding character than the out-of-plane bonds. The overlap population for the out-of-plane Pt–O bond was found to be 0.304, whereas that for the in-plane Pt–O bond was 0.189. These values show that the out-of-plane ligands are more tightly bound to each metal ion than the in-plane ligands, leading to the striking regioselectivity.

#### D. $^1\text{H}$ NMR OF TETRAPLATINUM CLUSTERS

The  $^1\text{H}$  NMR of **1** shows two acetate methyl signals due to the in-plane and out-of-plane acetate methyls. The peak at low field is assigned to the in-plane acetate methyl protons from the fact that the peak undergoes exchange with free acetate (Section II,A) and disappears in in-plane substituted clusters. Table II summarizes in-plane and out-of-plane acetate chemical shifts for a series of tetraplatinum clusters. When the chemical shifts are compared among the tetrasubstituted clusters without aromatic ligands (the first nine compounds in Table II), the chemical shift of the out-of-plane acetate lowers as the basicity of the in-plane ligand decreases. This may be a result of the so-called electronic *cis* effect in coordination chemistry (44): The weaker the in-plane Pt–O bond is, the stronger the out-of-plane Pt–O bond is.

For the clusters containing aromatic in-plane ligands, the chemical shifts of acetate methyl protons are largely influenced by ring current effects. The chemical shifts of the acetate methyl protons in the series of  $[\text{Pt}_4(\text{CH}_3\text{COO})_{8-n}(\text{L})_{2n}]^{n+}$  ( $\text{L} = \text{dmap}, \text{py}, \text{cpy}$ ) clusters systematically change as a function of the number of pyridyl ligands ( $n$ ) (Fig. 15) (33). With an increase in  $n$ , the chemical shift of the out-of-plane acetate increases, and that of the in-plane acetate decreases slightly. Because the pyridyl ligands are coordinated perpendicularly to the  $\text{Pt}_4$  cluster plane, the in-plane and out-of-plane acetates are in the shielding and deshielding region, respectively, and the ring current effects increase with an increase in  $n$ . The chemical shift of the out-of-plane acetate also depends on the basicity of  $\text{L}$ . It shifts to lower field as the  $\text{p}K_{\text{a}}$  of  $\text{L}$  becomes smaller. Thus, the out-of-plane acetate signal for  $[\text{Pt}_4(\text{CH}_3\text{COO})_4(\text{cpy})_8]^{4+}$  occurs at the lowest field, 3.28 ppm, among the present series of clusters.

#### E. $^{195}\text{Pt}$ NMR OF TETRAPLATINUM CLUSTERS

$^{195}\text{Pt}$  NMR spectroscopy is a powerful tool for the study of platinum cluster complexes with Pt–Pt bond(s). The  $^{195}\text{Pt}$  nucleus has an  $I = \frac{1}{2}$  nuclear spin with a natural abundance of 33.8% while all other Pt nuclei

TABLE II

<sup>1</sup>H NMR CHEMICAL SHIFTS FOR Pt<sub>4</sub> CLUSTERS

Complex	Ref.	Solvent	Out-of-plane	In-plane
Pt <sub>4</sub> (CH <sub>3</sub> COO) <sub>4</sub> (acac) <sub>4</sub> ( <b>14</b> )	35	CDCl <sub>3</sub>	1.89	
Pt <sub>4</sub> (CH <sub>3</sub> COO) <sub>4</sub> (CH <sub>3</sub> CONH) <sub>4</sub> ( <b>11</b> )	49	CDCl <sub>3</sub>	1.92	
Pt <sub>4</sub> (CH <sub>3</sub> COO) <sub>4</sub> (C <sub>6</sub> H <sub>5</sub> COO) <sub>4</sub> ( <b>10</b> )	30	CDCl <sub>3</sub>	1.97	
Pt <sub>4</sub> (CH <sub>3</sub> COO) <sub>8</sub> ( <b>1</b> )	29	CDCl <sub>3</sub>	2.01	2.45
Pt <sub>4</sub> (CH <sub>3</sub> COO) <sub>4</sub> (CH <sub>2</sub> ClCOO) <sub>4</sub> ( <b>8</b> )	30	CD <sub>3</sub> CN	2.05	
Pt <sub>4</sub> (CH <sub>3</sub> COO) <sub>4</sub> (CHCl <sub>2</sub> COO) <sub>4</sub> ( <b>9</b> )	30	CD <sub>3</sub> CN	2.09	
Pt <sub>4</sub> (CH <sub>3</sub> COO) <sub>4</sub> (CF <sub>3</sub> COO) <sub>4</sub> ( <b>7</b> )	30	CD <sub>3</sub> CN	2.13	
Pt <sub>4</sub> (CH <sub>3</sub> COO) <sub>4</sub> (CCl <sub>3</sub> COO) <sub>4</sub> ( <b>5</b> )	30	CD <sub>2</sub> Cl <sub>2</sub>	2.13	
Pt <sub>4</sub> (CH <sub>3</sub> COO) <sub>4</sub> (CBr <sub>3</sub> COO) <sub>4</sub> ( <b>6</b> )	30	CD <sub>3</sub> CN	2.17	
[Pt <sub>4</sub> (CH <sub>3</sub> COO) <sub>4</sub> (en) <sub>4</sub> ] <sup>4+</sup> ( <b>15</b> )	36	CD <sub>3</sub> OD	1.98	
[Pt <sub>4</sub> (CH <sub>3</sub> COO) <sub>4</sub> (pic) <sub>4</sub> ] ( <b>16</b> )	36	CDCl <sub>3</sub>	1.68	
[Pt <sub>4</sub> (CH <sub>3</sub> COO) <sub>4</sub> (l-pro) <sub>4</sub> ] ( <b>18</b> )	37	CDCl <sub>3</sub>	1.90, 1.98	
[Pt <sub>4</sub> (CH <sub>3</sub> COO) <sub>4</sub> (edda) <sub>2</sub> ] ( <b>35</b> )	41	D <sub>2</sub> O	2.08, 2.12	
[Pt <sub>4</sub> (CH <sub>3</sub> COO) <sub>6</sub> (3,2,3-tet)] <sup>2+</sup> ( <b>33</b> )	41	CD <sub>3</sub> CN	1.98, 2.01	2.34
[Pt <sub>4</sub> (CH <sub>3</sub> COO) <sub>6</sub> (3,3,3-tet)] <sup>2+</sup> ( <b>34</b> )	41	CD <sub>3</sub> OD	1.99, 2.02	2.34
[Pt <sub>4</sub> (CH <sub>3</sub> COO) <sub>5</sub> (py <sub>2</sub> -2,2',2-tet)] <sup>+</sup> ( <b>36</b> )	42	D <sub>2</sub> O	2.00, 2.03, 2.46	2.56
[Pt <sub>4</sub> (CH <sub>3</sub> COO) <sub>4</sub> (Et <sub>3</sub> ant) <sub>4</sub> ] ( <b>23</b> )	40	CDCl <sub>3</sub>	1.80	
[Pt <sub>4</sub> (CH <sub>3</sub> COO) <sub>4</sub> (Mexant) <sub>4</sub> ] ( <b>24</b> )	40	CDCl <sub>3</sub>	1.82	
chelate-[Pt <sub>4</sub> (CH <sub>3</sub> COO) <sub>4</sub> (Et <sub>2</sub> dtc) <sub>4</sub> ] ( <b>25</b> )	40	CDCl <sub>3</sub>	1.90	
bridge-[Pt <sub>4</sub> (CH <sub>3</sub> COO) <sub>4</sub> (Et <sub>2</sub> dtc) <sub>4</sub> ] ( <b>26</b> )	40	CDCl <sub>3</sub>	1.74	
chelate-[Pt <sub>4</sub> (CH <sub>3</sub> COO) <sub>4</sub> (Me <sub>2</sub> dtc) <sub>4</sub> ] ( <b>27</b> )	40	CDCl <sub>3</sub>	1.90	
bridge-[Pt <sub>4</sub> (CH <sub>3</sub> COO) <sub>4</sub> (Me <sub>2</sub> dtc) <sub>4</sub> ] ( <b>28</b> )	40	CDCl <sub>3</sub>	1.75	
chelate-[Pt <sub>4</sub> (CH <sub>3</sub> COO) <sub>4</sub> (Et <sub>2</sub> dtp) <sub>4</sub> ] ( <b>29</b> )	39	CDCl <sub>3</sub>	1.78	
bridge-[Pt <sub>4</sub> (CH <sub>3</sub> COO) <sub>4</sub> (Et <sub>2</sub> dtp) <sub>4</sub> ] ( <b>30</b> )	39	CDCl <sub>3</sub>	1.85	
[Pt <sub>4</sub> (CH <sub>3</sub> COO) <sub>7</sub> (dmap) <sub>2</sub> ] <sup>+</sup> ( <b>40</b> )	33	CD <sub>3</sub> CN	2.01, 2.09, 2.20	2.22, 2.38
[Pt <sub>4</sub> (CH <sub>3</sub> COO) <sub>7</sub> (py) <sub>2</sub> ] <sup>+</sup> ( <b>41</b> )	33	CD <sub>3</sub> CN	2.07, 2.15, 2.26	2.23, 2.41
[Pt <sub>4</sub> (CH <sub>3</sub> COO) <sub>7</sub> (cpy) <sub>2</sub> ] <sup>+</sup> ( <b>42</b> )	33	CD <sub>3</sub> CN	2.09, 2.16, 2.26	2.23, 2.42
trans-[Pt <sub>4</sub> (CH <sub>3</sub> COO) <sub>6</sub> (dmap) <sub>4</sub> ] <sup>2+</sup> ( <b>43</b> )	33	CD <sub>3</sub> CN	2.22, 2.27	2.08
trans-[Pt <sub>4</sub> (CH <sub>3</sub> COO) <sub>6</sub> (py) <sub>4</sub> ] <sup>2+</sup> ( <b>44</b> )	33	CD <sub>3</sub> CN	2.35, 2.39	2.11
trans-[Pt <sub>4</sub> (CH <sub>3</sub> COO) <sub>6</sub> (cpy) <sub>4</sub> ] <sup>2+</sup> ( <b>45</b> )	33	CD <sub>3</sub> CN	2.38, 2.41	2.11
cis-[Pt <sub>4</sub> (CH <sub>3</sub> COO) <sub>6</sub> (dmap) <sub>4</sub> ] <sup>2+</sup> ( <b>46</b> )	33	CD <sub>3</sub> CN	2.17, 2.23	2.35
[Pt <sub>4</sub> (CH <sub>3</sub> COO) <sub>5</sub> (dmap) <sub>6</sub> ] <sup>3+</sup> ( <b>47</b> )	33	CD <sub>3</sub> CN	2.34, 2.49, 2.59	2.04
[Pt <sub>4</sub> (CH <sub>3</sub> COO) <sub>5</sub> (py) <sub>6</sub> ] <sup>3+</sup> ( <b>48</b> )	33	CD <sub>3</sub> CN	2.54, 2.70, 2.84	2.08
[Pt <sub>4</sub> (CH <sub>3</sub> COO) <sub>5</sub> (cpy) <sub>6</sub> ] <sup>3+</sup> ( <b>49</b> )	33	CD <sub>3</sub> CN	2.58, 2.74, 2.89	2.07
[Pt <sub>4</sub> (CH <sub>3</sub> COO) <sub>4</sub> (dmap) <sub>8</sub> ] <sup>4+</sup> ( <b>50</b> )	33	CD <sub>3</sub> CN	2.76	
[Pt <sub>4</sub> (CH <sub>3</sub> COO) <sub>4</sub> (py) <sub>8</sub> ] <sup>4+</sup> ( <b>51</b> )	33	CD <sub>3</sub> CN	3.07	
[Pt <sub>4</sub> (CH <sub>3</sub> COO) <sub>4</sub> (cpy) <sub>8</sub> ] <sup>4+</sup> ( <b>52</b> )	33	CD <sub>3</sub> CN	3.28	

have no nuclear spin. Chemical shifts are spread over a wide range from -5000 to 10,000 ppm (vs. K<sub>2</sub>Pt<sup>II</sup>Cl<sub>4</sub>) depending on the Pt oxidation state, donor or acceptor characteristics of the coordinating ligand, and the nature of the metal-ligand interaction (45-47). The coupling constant  $J_{\text{Pt-Pt}}$  provides some information about Pt-Pt bond, and analysis of a

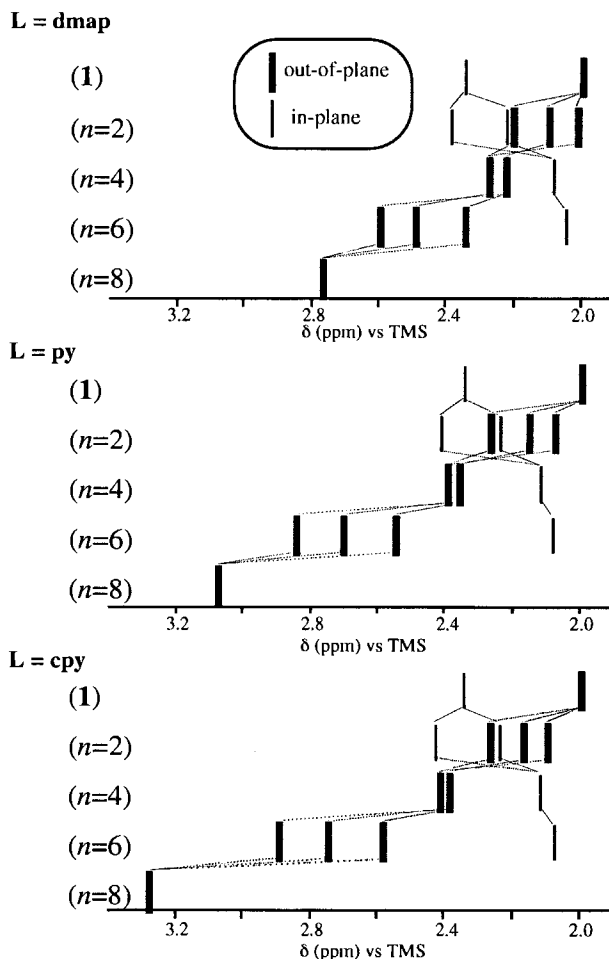


FIG. 15.  $^1\text{H}$  NMR chemical shifts of pyridine derivative clusters,  $[\text{Pt}_4(\text{CH}_3\text{COO})_{8-n}(\text{L})_{2n}]^{n+}$ .

coupling pattern affords a clue to the geometry and connection scheme of the cluster.

### 1. Symmetric Tetraplatinum Clusters

A symmetric  $\text{Pt}_4$  cluster in which all platinum atoms are chemically equivalent shows only one  $^{195}\text{Pt}$  NMR singlet peak. Table III summarizes the  $^{195}\text{Pt}$  NMR chemical shifts of symmetric  $\text{Pt}_4$  clusters.

The chemical shifts range from 200 to 1200 ppm depending mainly on the kind and number of coordinating atoms. Clusters with O-donor

TABLE III

<sup>195</sup>Pt NMR CHEMICAL SHIFTS FOR SYMMETRIC Pt<sub>4</sub> CLUSTERS

Complex	Ref.	Solvent	δ (ppm vs. K <sub>2</sub> [PtCl <sub>4</sub> ])
[Pt <sub>4</sub> (CH <sub>3</sub> COO) <sub>8</sub> ] (1)	30	CDCl <sub>3</sub>	1040
[Pt <sub>4</sub> (CH <sub>3</sub> COO) <sub>4</sub> (C <sub>6</sub> H <sub>5</sub> COO) <sub>4</sub> ] (10)	30	CDCl <sub>3</sub>	1060
[Pt <sub>4</sub> (CH <sub>3</sub> COO) <sub>4</sub> (CCl <sub>3</sub> COO) <sub>4</sub> ] (5)	30	CD <sub>3</sub> CN	1036
[Pt <sub>4</sub> (CH <sub>3</sub> COO) <sub>4</sub> (CH <sub>3</sub> CONH) <sub>4</sub> ] (11)	30	CDCl <sub>3</sub>	955
[Pt <sub>4</sub> (CH <sub>3</sub> COO) <sub>4</sub> (acac) <sub>4</sub> ] (14)	36	CDCl <sub>3</sub>	194
[Pt <sub>4</sub> (CH <sub>3</sub> COO) <sub>4</sub> (en) <sub>4</sub> ] <sup>4+</sup> (15)	36	CD <sub>3</sub> OD	802
[Pt <sub>4</sub> (CH <sub>3</sub> COO) <sub>4</sub> (pic) <sub>4</sub> ] (16)	36	CDCl <sub>3</sub>	1170
[Pt <sub>4</sub> (CH <sub>3</sub> COO) <sub>4</sub> (gly) <sub>4</sub> ] (17)	38	D <sub>2</sub> O	885
[Pt <sub>4</sub> (CH <sub>3</sub> COO) <sub>4</sub> (Etxant) <sub>4</sub> ] (23)	40	CDCl <sub>3</sub>	634
<i>chelate</i> -[Pt <sub>4</sub> (CH <sub>3</sub> COO) <sub>4</sub> (Et <sub>2</sub> dtc) <sub>4</sub> ] (26)	40	CDCl <sub>3</sub>	365
<i>bridge</i> -[Pt <sub>4</sub> (CH <sub>3</sub> COO) <sub>4</sub> (Et <sub>2</sub> dtc) <sub>4</sub> ] (27)	40	CDCl <sub>3</sub>	686
<i>chelate</i> -[Pt <sub>4</sub> (CH <sub>3</sub> COO) <sub>4</sub> (Et <sub>2</sub> dtp) <sub>4</sub> ] (29)	39	CDCl <sub>3</sub>	693
<i>bridge</i> -[Pt <sub>4</sub> (CH <sub>3</sub> COO) <sub>4</sub> (Et <sub>2</sub> dtp) <sub>4</sub> ] (30)	39	CDCl <sub>3</sub>	329
[Pt <sub>4</sub> (CH <sub>3</sub> COO) <sub>4</sub> (2,2,2-tet) <sub>2</sub> ] <sup>4+</sup> (31)	41	CD <sub>3</sub> OD	783
[Pt <sub>4</sub> (CH <sub>3</sub> COO) <sub>4</sub> (2,3,2-tet) <sub>2</sub> ] <sup>4+</sup> (32)	41	CD <sub>3</sub> OD	824
<i>trans</i> -[Pt <sub>4</sub> (CH <sub>3</sub> COO) <sub>6</sub> (damp) <sub>4</sub> ] <sup>2+</sup> (43)	33	CD <sub>3</sub> CN	1156
[Pt <sub>4</sub> (CH <sub>3</sub> COO) <sub>4</sub> (dmap) <sub>8</sub> ] <sup>4+</sup> (50)	33	CD <sub>3</sub> CN	989
<i>trans</i> -[Pt <sub>4</sub> (CH <sub>3</sub> COO) <sub>6</sub> (py) <sub>4</sub> ] <sup>2+</sup> (44)	33	CD <sub>3</sub> CN	1114
[Pt <sub>4</sub> (CH <sub>3</sub> COO) <sub>4</sub> (py) <sub>8</sub> ] <sup>4+</sup> (51)	33	CD <sub>3</sub> CN	920
<i>trans</i> -[Pt <sub>4</sub> (CH <sub>3</sub> COO) <sub>6</sub> (cpy) <sub>4</sub> ] <sup>2+</sup> (45)	33	CD <sub>3</sub> CN	1087

ligands at the in-plane sites, which have an O<sub>4</sub> donor atom set about each platinum atom, have chemical shifts around 1050 ppm; those with N-donating ligands (O<sub>2</sub>N<sub>2</sub>) are around 900 ppm; those with S-donating ligands (O<sub>2</sub>S<sub>2</sub>) are around 300 and around 700 ppm, depending on whether the ligand is chelating or bridging; and that with C-donating ligand (O<sub>3</sub>C) is at the highest field (194 ppm). The trend in chemical shifts as a function of the coordinating atom is consistent with the general trend for mononuclear platinum complexes. For clusters with an O<sub>3</sub>N environment, the chemical shift has a wide range (800–1150 ppm). It appears that the <sup>195</sup>Pt NMR chemical shift of Pt<sub>4</sub> clusters depends not only on the coordinating ligands but also on the coordinating ligand on the adjacent platinum (see Section II,E,c).

## 2. Unsymmetric Tetraplatinum Clusters

<sup>195</sup>Pt NMR spectra of Pt<sub>4</sub> clusters having nonequivalent platinum nuclei are complicated because of the presence of many isotopomers and large Pt–Pt coupling constants. In constrast to symmetric Pt<sub>4</sub> clusters, satellite peaks due to Pt–Pt coupling appear, and a second-order

pattern is observed when a coupling constant is large relative to the chemical shift difference. Because of the presence of isotopomers,  $^{195}\text{Pt}$  NMR spectra for such species are the result of the summation of the resonances for the isotopomers. Although an analysis of the spectrum is not easy in general, useful information such as spectral assignments, order of arrangement of the nuclei, or coupling constants could be derived. Note that when the term "isotopomer" is used in this article, platinum isotopes other than  $^{195}\text{Pt}$  are regarded as a single species, as they have no nuclear spin.

*a.*  $[\text{Pt}_4(\text{CH}_3\text{COO})_{8-n}(\text{CH}_3\text{CONH})_n]$  ( $n = 1, 3$ ) (34) When one of the in-plane acetates is replaced by an unsymmetric bidentate ligand such as acetamidate, the four platinum nuclei are chemically nonequivalent (Fig. 16). As an example, the  $^{195}\text{Pt}$  NMR spectrum of  $[\text{Pt}_4(\text{CH}_3\text{COO})_7(\text{CH}_3\text{CONH})]$  (**13**) is shown in Fig. 17. The spectrum can be assigned in the following way. There are sixteen possible isotopomers for this cluster, which are classified into six types, (a)–(f); these are shown in Fig. 18, together with their natural abundances. Isotopomer (a) shows no  $^{195}\text{Pt}$  NMR resonance, and isotopomers of types (e) and (f) show very complicated spectra with very weak signal intensities. The spectrum was analyzed by taking into account only the resonances due to isotopomers of types (b), (c), and (d), which show relatively strong signals. Each of the four isotopomers of type (b) shows a singlet peak (hereinafter called the main peak). Four isotopomers of type (c) show four AB-type signals because of large coupling constants ( $^1J_{\text{Pt-Pt}}$ ). Each  $^{195}\text{Pt}$  nucleus within type (d) shows a doublet as a satellite of its main peak, since the coupling constants ( $^2J_{\text{Pt-Pt}}$ ) should be relatively small. Such spectral patterns are seen in the  $^{195}\text{Pt}$  NMR spectrum of **13**, which consists of four main singlets accompanied by doublet

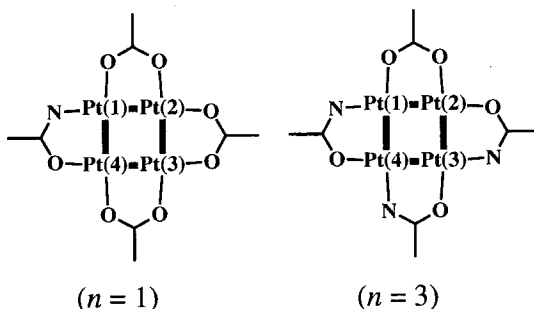


FIG. 16. The structures of  $[\text{Pt}_4(\text{CH}_3\text{COO})_{8-n}(\text{CH}_3\text{CONH})_n]$  [ $n = 1$  (**13**),  $n = 3$  (**12**)]. Only the cluster core and the ligands in the cluster plane are shown, along with the numbering.

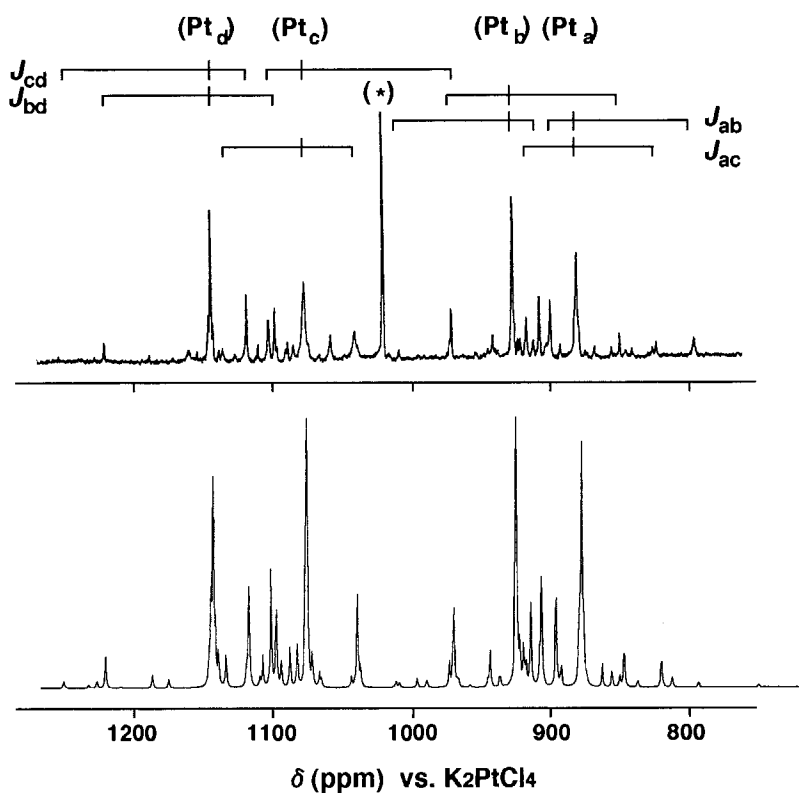


FIG. 17.  $^{195}\text{Pt}$  NMR spectra of  $[\text{Pt}_4(\text{CH}_3\text{COO})_7(\text{CH}_3\text{CONH})]$  (**13**) in  $\text{CD}_3\text{CN}$ . (a) Observed spectrum. The asterisked peak at 1047 ppm is due to **1**. (b) Calculated spectrum.

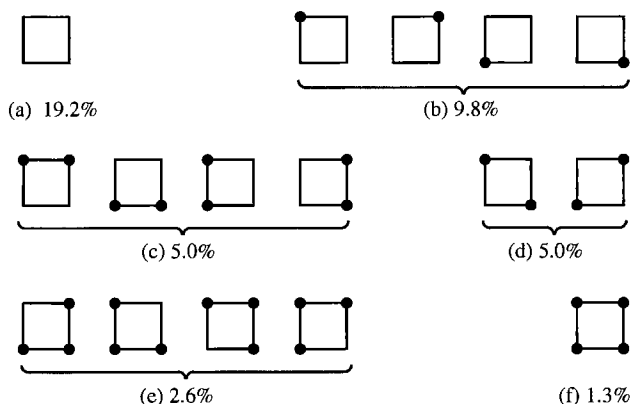


FIG. 18. Sixteen possible isotopomers and their classification into six types (a–f) for a tetranuclear cluster complex with nonequivalent  $^{195}\text{Pt}$  nuclei. A square denotes the tetranuclear cluster core and a filled circle shows the position of a  $^{195}\text{Pt}$  nucleus. The percentages are the natural abundance of the isotopomer.

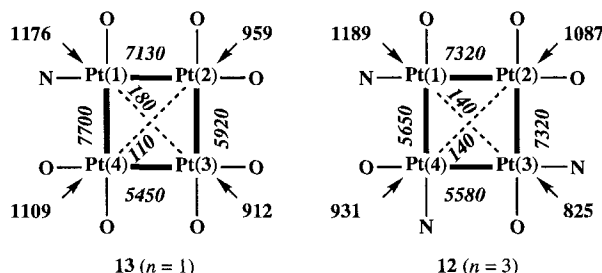


FIG. 19.  $^{195}\text{Pt}$  NMR chemical shifts and coupling constants for  $[\text{Pt}_4(\text{CH}_3\text{COO})_{8-n}(\text{CH}_3\text{CONH})_n]$  [ $n = 1$  (**13**),  $n = 3$  (**12**)].

satellites and four AB patterns, in addition to many very weak peaks. Four coupling constants obtained from the four AB-type patterns provide information regarding the connectivity of the four nuclei. Taking into account peak broadening due to the coupling with the quadrupolar  $^{14}\text{N}$  nucleus which is bound directly to the platinum nucleus (or bound to an adjacent  $^{195}\text{Pt}$  nucleus at *trans* position), a whole assignment of the spectrum was made (Fig. 17b). Similarly, the  $^{195}\text{Pt}$  NMR spectrum of  $[\text{Pt}_4(\text{CH}_3\text{COO})_5(\text{CH}_3\text{CONH})_3]$  (**12**) was successfully analyzed. Both results are summarized in Fig. 19 and Table IV.

TABLE IV

$^{195}\text{Pt}$  NMR CHEMICAL SHIFTS FOR UNSYMMETRIC  $\text{Pt}_4$  CLUSTERS

Complex	Ref.	Solvent	$\delta$ (ppm vs. $\text{K}_2[\text{PtCl}_4]$ )	$^1J_{\text{Pt-Pt}}$ (Hz)
$[\text{Pt}_4(\text{CH}_3\text{COO})_7(\text{CH}_3\text{CONH})]$ ( <b>13</b> )	34	$\text{CD}_3\text{CN}$	912, 959, 1109, 1176	5450, 5920, 7130, 7700
$[\text{Pt}_4(\text{CH}_3\text{COO})_5(\text{CH}_3\text{CONH})_3]$ ( <b>12</b> )	34	$\text{CD}_3\text{CN}$	825, 931, 1087, 1189	5580, 5650, 7320, 7320
$[\text{Pt}_4(\text{CH}_3\text{COO})_4(\text{L-ala})_4]$ ( <b>19</b> )	38	$\text{D}_2\text{O}$	852, 840	— <sup>a</sup>
$[\text{Pt}_4(\text{CH}_3\text{COO})_4(\text{L-val})_4]$ ( <b>20</b> )	38	$\text{D}_2\text{O}$	847, 833	— <sup>a</sup>
$[\text{Pt}_4(\text{CH}_3\text{COO})_4(\text{L-hydropro})_4]$ ( <b>21</b> )	38	$\text{D}_2\text{O}$	879, 798	6270, 6490
$[\text{Pt}_4(\text{CH}_3\text{COO})_4(\text{L-pro})_4]$ ( <b>18</b> )	37	$\text{CDCl}_3$	923, 789	5920, 6100
$[\text{Pt}_4(\text{CH}_3\text{COO})_7(\text{dmap})_2]^+$ ( <b>40</b> )	33	$\text{CD}_3\text{CN}$	1113, 1117	— <sup>a</sup>
$[\text{Pt}_4(\text{CH}_3\text{COO})_5(\text{dmap})_6]^{3+}$ ( <b>47</b> )	33	$\text{CD}_3\text{CN}$	1056, 1081	6900
$[\text{Pt}_4(\text{CH}_3\text{COO})_7(\text{py})_2]^+$ ( <b>41</b> )	33	$\text{CD}_3\text{CN}$	1009, 1194	6440
$[\text{Pt}_4(\text{CH}_3\text{COO})_5(\text{py})_6]^{3+}$ ( <b>48</b> )	33	$\text{CD}_3\text{CN}$	920, 1112	6750
$[\text{Pt}_4(\text{CH}_3\text{COO})_7(\text{cpy})_2]^+$ ( <b>42</b> )	33	$\text{CD}_3\text{CN}$	933, 1248	6790
$[\text{Pt}_4(\text{CH}_3\text{COO})_5(\text{cpy})_2]^{3+}$ ( <b>49</b> )	33	$\text{CD}_3\text{CN}$	840, 1154	— <sup>a</sup>
$[\text{Pt}_4(\text{CH}_3\text{COO})_6(3,2,3\text{-tet})]^{2+}$ ( <b>33</b> )	41	$\text{CD}_3\text{CN}$	710, 965, 1215	6120, 7070

<sup>a</sup> Not determined.

The chemical shifts for **13** and **12** vary over a rather wide range, as compared with those of **1** and  $[\text{Pt}_4(\text{CH}_3\text{COO})_4(\text{CH}_3\text{CONH})_4]$  (**11**) (Table III). It seems, however, that the average chemical shift for  $[\text{Pt}_4(\text{CH}_3\text{COO})_{8-n}(\text{CH}_3\text{CONH})_n]$  decreases as the value of  $n$  increases.

*b.*  $[\text{Pt}_4(\text{CH}_3\text{COO})_8(\text{L-amino acid})_4]$  (37–38) This type of cluster has two diastereotopic platinum centers because the arrangement of the out-of-plane acetates on a platinum atom makes the platinum center chiral while adjacent platinum atoms in the  $\text{Pt}_4$  cluster core have the opposite chiralities (Fig. 13). There are nine isotopomers in a cluster of this type, and they show A,  $A_2$ , B,  $B_2$ , AB, AB', AA'B, ABB', and AA'BB' spectra. Figure 20 shows the  $^{195}\text{Pt}$  NMR spectrum of  $[\text{Pt}_4(\text{CH}_3\text{COO})_4(\text{L-pro})_4]$  (**18**), which consists of two intense peaks and two AB quartet peaks, with many minor peaks. The spectrum has been completely analyzed in a similar way to the acetamidato clusters, and there is good agreement between the observed and calculated spectrum (Fig. 20). The chemical shift difference between the two diastereotopic Pt centers is fairly large (133.5 ppm), in spite of the fact that the two types of platinum have the same donor atom set.

*c.*  $[\text{Pt}_4(\text{CH}_3\text{COO})_{8-n}\text{L}_{2n}]$  ( $\text{L} = \text{pyridine derivative}$ ;  $n = 1, 3$ ) (33) Di- and hexasubstituted clusters,  $[\text{Pt}_4(\text{CH}_3\text{COO})_7\text{L}_2]^+$  (40–42) and

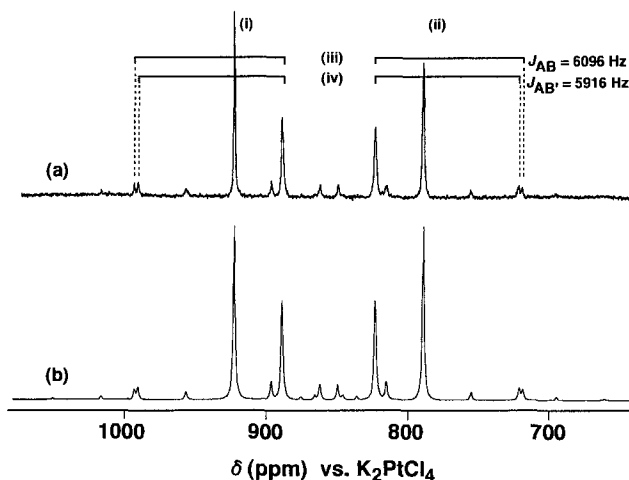


FIG. 20.  $^{195}\text{Pt}$  NMR spectrum of  $[\text{Pt}_4(\text{CH}_3\text{COO})_4(\text{L-pro})_4]$  (**18**) in  $\text{CDCl}_3$ . (a) Observed spectrum. (b) Simulated spectrum. Roman numerals show assignments of the isotopomers: (i) A and  $A_2$ , (ii) B and  $B_2$ , (iii) AB, (iv) AB'. Other weak peaks are due to the remaining isotopomers having more than two  $^{195}\text{Pt}$  nuclei.

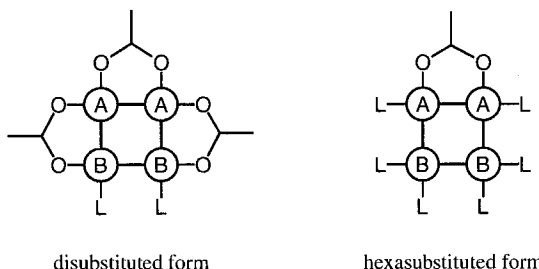


FIG. 21. A and B sites in di- and hexasubstituted clusters. Out-of-plane acetates are omitted for clarity.

$[\text{Pt}_4(\text{CH}_3\text{COO})_5\text{L}_6]^{3+}$  (**47–49**) ( $\text{L} = \text{dmap}, \text{py}, \text{cpy}$ ), have two chemically different platinum atoms within a cluster (Fig. 21). The arrangement of the four Pt atoms in **40–42** and **47–49** is of an AA'BB' type; therefore, there are nine isotopomers ( $\text{A}, \text{A}_2, \text{B}, \text{B}_2, \text{AB}, \text{AB}', \text{AA'B}, \text{ABB}'$ , and  $\text{AA'BB}'$ ). Note that an arrangement of AA'BB' nuclei in these complexes is different from that of  $\alpha$ -amino acid clusters. Figure 22 shows the  $^{195}\text{Pt}$  NMR spectrum of  $[\text{Pt}_4(\text{CH}_3\text{COO})_7\text{L}_2]^+$  (**41**), from which chemical shifts and coupling constants,  $J_{\text{AB}}$ , were obtained. The  $^{195}\text{Pt}$  NMR parameters for **40**, **42**, and **47–49**, obtained in a similar way, are given in Table IV.

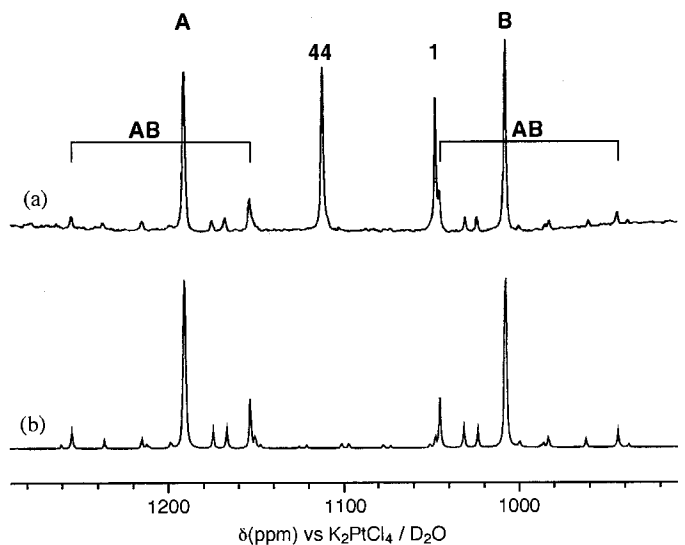


FIG. 22.  $^{195}\text{Pt}$  NMR spectrum of  $[\text{Pt}_4(\text{CH}_3\text{COO})_7(\text{py})_2]^+$  (**41**): (a) Observed spectrum of an equilibrated solution of **1** and **44**, which still contains a small amount of **1** and **44**. (b) Simulated spectrum.

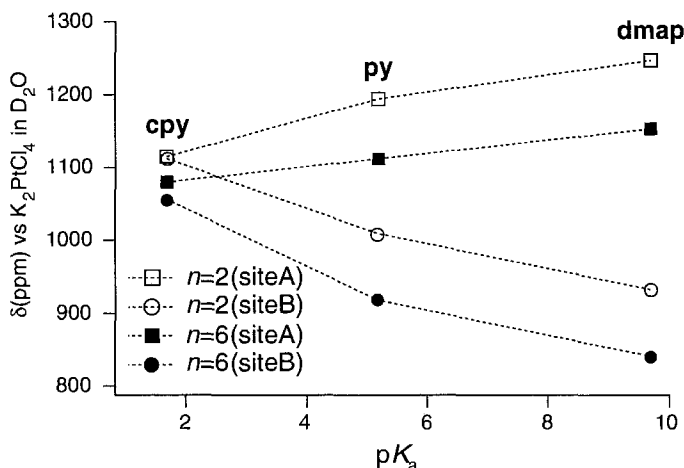


FIG. 23. Plots of  $^{195}\text{Pt}$  NMR chemical shifts of  $[\text{Pt}_4(\text{CH}_3\text{COO})_{8-n}(\text{L})_{2n}]^{n+}$  ( $\text{L} = \text{dmap}, \text{py}, \text{cpy}$ ;  $n = 1, 3$ ) versus  $\text{p}K_a$  of the coordinated ligand. See Fig. 21 for site A and B.

Figure 23 shows an effect of the  $\text{p}K_a$  of  $\text{L}$  on the  $^{195}\text{Pt}$  chemical shift for the series of clusters  $[\text{Pt}_4(\text{CH}_3\text{COO})_7\text{L}_2]^+$  and  $[\text{Pt}_4(\text{CH}_3\text{COO})_5\text{L}_6]^{3+}$  ( $\text{L} = \text{dmap}, \text{py}, \text{cpy}$ ). For all the clusters in each series, the higher field signal is assigned to site B (the Pt nuclei with more L), and the lower field peak to site A (Fig. 21). In both series 40–42 and 47–49, the signal due to site A shifts to a lower field and the site B signal shifts to a higher field as the basicity of L becomes lower. It is evident that L affects the chemical shift not only of Pt bound directly to L ( $\text{Pt}^{\text{direct}}$ ) but also of Pt *trans* to the Pt–L bond ( $\text{Pt}^{\text{remote}}$ ). It is related to the “direct and remote effect” on  $^{195}\text{Pt}$  NMR chemical shifts of  $\text{Pt}^{\text{III}}$  dimers with a Pt–Pt bond reported by Appleton *et al.* (48).

The substitution number ( $n$ ) also has an effect on the  $^{195}\text{Pt}$  chemical shifts for  $[\text{Pt}_4(\text{CH}_3\text{COO})_{8-n}(\text{L})_{2n}]^{n+}$ . For clusters with  $n = 2$  and 6, averaged chemical shifts between sites A and B (Fig. 21) are used. Irrespective of L, the chemical shift decreases significantly on going from  $n = 4$  to 8 while it increases slightly on going from  $n = 0$  to 4. The observed trend for the  $n = 4$ –8 series is ascribed to the stereochemical consequence of the pyridyl ligands. The lengthening of Pt–N distances found in  $[\text{Pt}_4(\text{CH}_3\text{COO})_4(\text{dmap})_8]^{4+}$  as compared with those in  $[\text{Pt}_4(\text{CH}_3\text{COO})_6(\text{dmap})_4]^{2+}$  corresponds to a decrease in  $\text{p}K_a$  of the coordinated dmap ligand in the former.

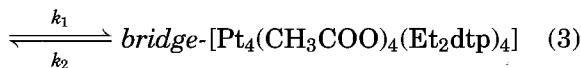
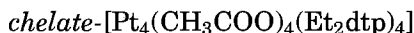
*d. Coupling Constant* It is known that there is no correlation between the  $^1J_{\text{Pt-Pt}}$  and Pt–Pt distance, and  $^1J_{\text{Pt-Pt}}$  is sensitive to

minor differences in the electronic structure of a complex, especially *s* character in the metal-metal bond (45). For platinum complexes with Pt-Pt bonds, the  $^1J_{\text{Pt-Pt}}$  coupling constants are  $\sim 1500$  Hz for low-valent triplatinum complexes, 8000–9000 Hz for  $\text{Pt}^{\text{I}}\text{-Pt}^{\text{I}}$  dimers, and 1000–12000 Hz for  $\text{Pt}^{\text{III}}\text{-Pt}^{\text{III}}$  dimers, depending on the kind of bridging and axial ligands (45–48). However, it is thought that a Pt-Pt bond exists between platinum atoms when  $^1J_{\text{Pt-Pt}}$  is more than 1000 Hz, possibly  $>5000$  Hz. Table IV summarizes the  $^1J_{\text{Pt-Pt}}$  coupling constants for unsymmetric  $\text{Pt}_4$  clusters. The coupling constants (5450–7700 Hz) are significantly large, suggesting the presence of Pt-Pt bonds. The coupling constants between platinums with different environments ( $\text{O}_4$  and  $\text{O}_3\text{N}$ ) are larger than those between platinums with the same environment [ $\text{O}_4$  and  $\text{O}_4$ , or  $\text{O}_3\text{N}$  and  $\text{O}_3\text{N}$ , as in **12** and **13** (Fig. 19)]. The  $^2J_{\text{Pt-Pt}}$  coupling constants between two  $^{195}\text{Pt}$  nuclei at opposite corners of the cluster core were determined to be 110–180 Hz for **12** and **13** (Fig. 19). The small value of  $^2J_{\text{Pt-Pt}}$  relative to  $^1J_{\text{Pt-Pt}}$  is ascribed to the right angle between the two Pt-Pt bonds as well as to an increase in the number of bonds between the two platinums.

#### F. $\text{Pt}_4$ CLUSTER CORE ROTATION AND *Chelate,Bridge* MUTUAL ISOMERIZATION

If the square-planar cluster core can rotate in  $\text{Pt}_4$  cluster compounds, leaving the peripheral ligand structure unchanged, the rotational motion may be expressed as “molecular bearing.” Experimental evidence strongly suggests that the  $\text{Pt}_4$  cluster core rotation occurs through mutual isomerization of the bridged and the chelated forms of  $[\text{Pt}_4(\text{CH}_3\text{COO})_4(\text{Et}_2\text{dtp})_4]$  (39).

Both *chelate*- $[\text{Pt}_4(\text{CH}_3\text{COO})_4(\text{Et}_2\text{dtp})_4]$  (**29**) and *bridge*- $[\text{Pt}_4(\text{CH}_3\text{COO})_4(\text{Et}_2\text{dtp})_4]$  (**30**) isomerize slowly in  $\text{CDCl}_3$  solution to give an equilibrium mixture [Eq. (3)].



The isomerization, followed by  $^1\text{H}$  NMR, has rate constants of  $k_1 = 1.2 \times 10^{-4} \text{ s}^{-1}$  and  $k_2 = 1.5 \times 10^{-4} \text{ s}^{-1}$  at  $40^\circ\text{C}$  in  $\text{CDCl}_3$ . The isomerizations also proceeded in acetonitrile with similar reaction rates ( $k_1 = 1.4 \times 10^{-4} \text{ s}^{-1}$  and  $k_2 = 3.4 \times 10^{-4} \text{ s}^{-1}$  at  $40^\circ\text{C}$ ).

In spite of similar rate constants, a striking difference in activation entropies was found between the reactions in chloroform and

acetonitrile:  $\Delta S_1^\ddagger = -9 \pm 9 \text{ J mol}^{-1} \text{ K}^{-1}$  in  $\text{CDCl}_3$ , whereas it is  $-47 \pm 11 \text{ J mol}^{-1} \text{ K}^{-1}$  in  $\text{CD}_3\text{CN}$ . This suggests that the mechanism of the isomerization is different in these solvents. The very small  $|\Delta S_1^\ddagger|$  in  $\text{CDCl}_3$  is consistent with mechanism (c) in Fig. 24, where the isomerization proceeds without Pt–S bond cleavage; that is, the reaction proceeds through an intermediate in which three sulfur atoms from two  $\text{Et}_2\text{dtp}$  ligands are coordinated simultaneously to each platinum. On the other hand, the relatively large negative value of  $\Delta S_1^\ddagger$  for the reaction in  $\text{CD}_3\text{CN}$  shows that the isomerization proceeds by a solvent-assisted mechanism (b).

The  $\text{Pt}_4$  cluster core is surrounded by eight S atoms circularly in a single plane, and the  $\text{S}_8$  ring is close to a regular octagon, as shown by X-ray structures of **29** and **30**. Simultaneous coordination of three S atoms from two  $\text{Et}_2\text{dtp}$  ligands to each Pt, giving three approximately equivalent Pt–S bonds, is possible only when eight S atoms form a regular octagon. The latter is consistent with mechanism (c) in Fig. 24. The highly symmetric arrangement of S atoms facilitates cluster core rotation, leading to the transformation from the bridging mode of  $\text{Et}_2\text{dtp}$  to the chelating mode, or vice versa.

In contrast, neither *chelate*- nor *bridge*- $[\text{Pt}_4(\text{CH}_3\text{COO})_4(\text{Et}_2\text{dtp})_4]$  undergoes isomerization. The reason appears to be the irregular  $\text{S}_8$  arrangement around the  $\text{Pt}_4$  core in these compounds. Intra- and

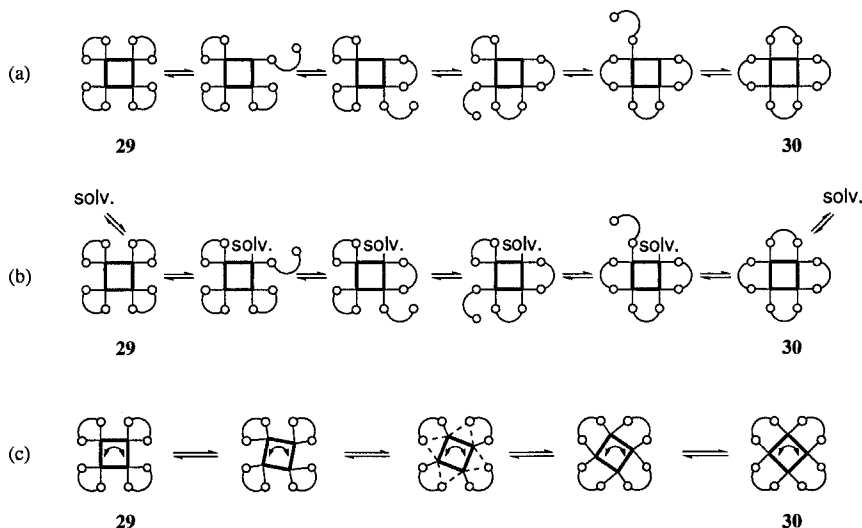


FIG. 24. Three mechanisms for the bridge/chelate isomerization of  $[\text{Pt}_4(\text{CH}_3\text{COO})_4(\text{Et}_2\text{dtp})_4]$ . The square with thick lines denotes the  $\text{Pt}_4$  cluster core, and out-of-plane acetates are omitted for clarity.  $\circ\circ$  represents  $\text{Et}_2\text{dtp}$  ligand.

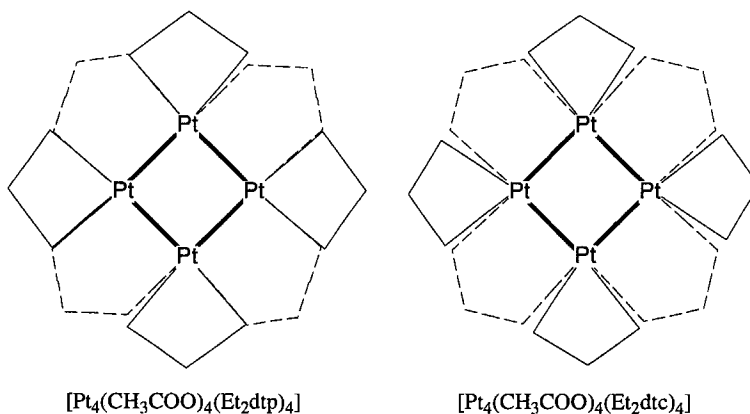


FIG. 25. Comparison of the locations of the eight S atoms in bridge and chelate isomers for (a) [Pt<sub>4</sub>(CH<sub>3</sub>COO)<sub>4</sub>(Et<sub>2</sub>dtp)<sub>4</sub>] and (b) [Pt<sub>4</sub>(CH<sub>3</sub>COO)<sub>4</sub>(Et<sub>2</sub>dtc)<sub>4</sub>]. Only the Pt<sub>4</sub> core and S—P—S (or S—C—S) moiety of dithio ligand are shown: broken line (---), bridge isomer; solid line (—), chelate isomer.

interligand S...S distances are 2.904(4) and 3.424(4) Å in the chelated form, and 3.01(1) and 3.26(1) Å in the bridged form, respectively. The arrangement of eight S atoms around the Pt<sub>4</sub> core in these compounds deviates greatly from the regular octagon. This is illustrated in Fig. 25, which compares the regular and irregular S<sub>8</sub> rings of [Pt<sub>4</sub>(CH<sub>3</sub>COO)<sub>4</sub>(Et<sub>2</sub>dtp)<sub>4</sub>] and [Pt<sub>4</sub>(CH<sub>3</sub>COO)<sub>4</sub>(Et<sub>2</sub>dtc)<sub>4</sub>].

#### G. PYRIDINE RING ROTATION

In Pt<sub>4</sub> clusters with pyridine derivatives such as **40–52**, two pyridine ligands occupy two neighboring sites on a side of the square-planar Pt<sub>4</sub> core. Under the circumstances, a strong steric interaction operates between the pair of pyridine ligands. In fact, it was confirmed by temperature-dependent <sup>1</sup>H NMR spectroscopy that the rotation of dmap about the Pt—N bond in [Pt<sub>4</sub>(CH<sub>3</sub>COO)<sub>4</sub>(dmap)<sub>8</sub>]<sup>4+</sup> (**50**) is restricted (33). The rate constant for the rotation was  $k = 4.5 \text{ s}^{-1}$  at 20°C. On the other hand, the dmap ring in [Pt<sub>4</sub>(CH<sub>3</sub>COO)<sub>6</sub>(dmap)<sub>4</sub>]<sup>2+</sup> (**43**) rotates freely at room temperature ( $k > 10^5 \text{ s}^{-1}$ ) although the rotation is slightly restricted at lower temperature ( $k \approx 3 \times 10^4 \text{ s}^{-1}$  at -30°C). The ease or difficulty with which the dmap ligand undergoes rotation in **50** and **43** can be explained by their X-ray structures. The two adjacent dmap rings in **50** are nearly parallel to each other, whereas those in **43** are splayed away from each other. This difference in orientation occurs to avoid a small N—Pt—N angle. Therefore, the distance between adjacent pyridine nitrogens of dmap in **50** is very

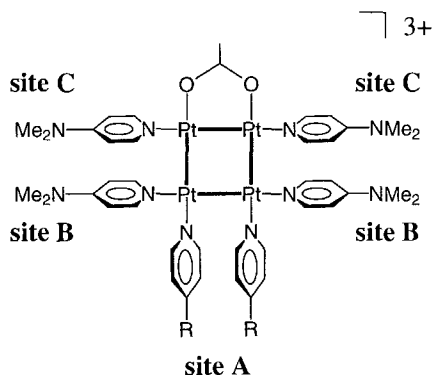


FIG. 26. Three chemical environments of the dmap ligand in  $[\text{Pt}_4(\text{CH}_3\text{COO})_5(\text{dmap})_6]^{3+}$  (**47**). Out-of-plane acetates are omitted for clarity.

short  $[\text{N} \cdots \text{N}2'] = 2.98(4)$  Å]. The short contact between two adjacent dmap rings leads to unprecedented restricted rotation of the dmap rings. On the other hand, mutually adjacent dmap rings splay out in **43** (see Fig. 4), making the rotation easier.

Site-dependent restricted rotation of the coordinated dmap rings is observed in  $[\text{Pt}_4(\text{CH}_3\text{COO})_5(\text{dmap})_6]^{3+}$  (**47**). There are three chemical environments for the coordinated dmap ligands in **47** (A, B, and C in Fig. 26). The relative arrangements of the dmap ligands suggest that sites A and B should have an environment similar to the dmap ligands in **50**, and rotation at site A should be slightly slower than at site B. Moreover, site C should be similar to **43**, and rotation at site C should be much faster than at sites A and B. In fact, three coalescence patterns are observed in temperature-dependent  $^1\text{H}$  NMR spectra of **47**. The  $^1\text{H}$  NMR spectra due to the  $\beta$  ring proton of dmap in **47**, along with its dynamic NMR simulation for sites A and B, are shown in Fig. 27, and an analysis for coalescence of two sets of doublet of doublets gave rate constants of 2.0 and  $12\text{ s}^{-1}$  at  $20^\circ\text{C}$  for sites A and B, respectively. The slightly broadened doublet due to a site-C proton shows that a relatively facile rotation occurs.

#### H. CATALYTIC ACTIVITY OF $\text{Pt}_4$ CLUSTERS TOWARD THE HYDRATION OF ACETONITRILE

Significant lability at the in-plane sites of the  $\text{Pt}_4$  clusters suggests possible catalytic activities. In fact, some of the  $\text{Pt}_4$  clusters catalyze

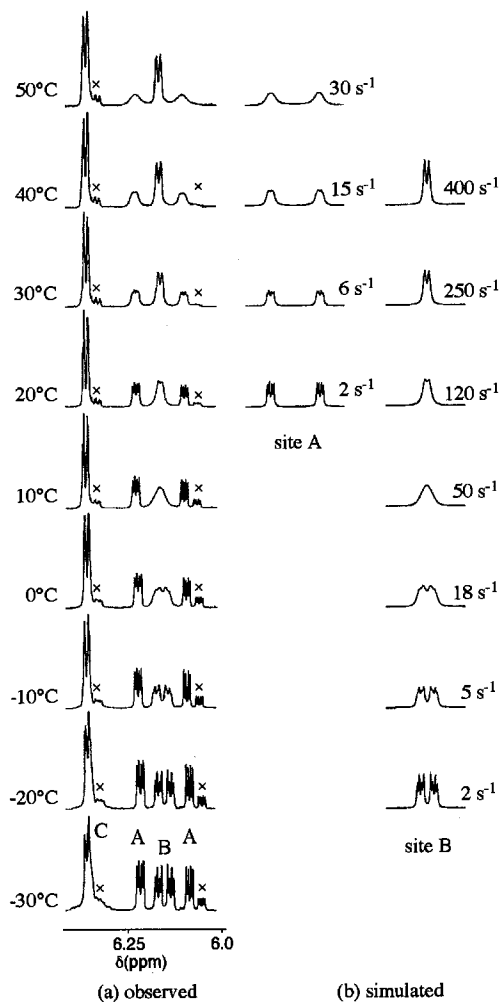


FIG. 27. Dynamic  $^1\text{H}$  NMR spectra for  $[\text{Pt}_4(\text{CH}_3\text{COO})_5(\text{dmap})_6]^{3+}$  (47).

the hydrolysis of acetonitrile to give acetamide [Eq. (4)] (49).



For example, when refluxing of acetonitrile/water (1:1) solution of **1** affords acetamide, the amount of acetamide increases linearly with time at the beginning of the reaction (at least for the initial 1 h), and then

the efficiency decreases gradually. The turnover number ( $N$ ), defined by Eq. (5),

$$N = \frac{\text{acetamide/mol}}{(\text{catalyst/mol})(\text{time/h})} \quad (5)$$

was estimated from the initial linear portion of the time course to be  $104 \text{ h}^{-1}$  at  $80^\circ\text{C}$  for  $20 \text{ cm}^{-3}$  of an aqueous–acetonitrile (1 : 1) solution containing 10 mg of **1**. Various factors that affect the catalytic activities, which include catalyst concentration, water content in solution, acidity, and so on, have been investigated in detail (49).

Nitriles coordinated to platinum are often easily hydrolyzed to corresponding amides (50–53). It is likely that the in-plane acetate ligands in **1** are substituted by acetonitrile. Coordinated acetonitrile is then attacked either directly by a free water molecule or by water coordinated at the neighboring platinum within the cluster. The resulting acetamidate ion would dissociate easily owing to the high lability of the in-plane sites. Similar  $\text{Pt}_4$  clusters,  $[\text{Pt}_4(\text{CH}_3\text{COO})_4(\text{CH}_3\text{CONH})_4]$  and  $[\text{Pt}_4(\text{CH}_3\text{COO})_4(\text{CF}_3\text{COO})_4]$ , also act as catalysts for the hydrolysis of acetonitrile, but their catalytic activities were lower than that of **1** ( $N = 48.4$  and  $62.7 \text{ h}^{-1}$ , respectively). The present  $\text{Pt}_4$  cluster complexes are good catalysts compared to the catalysts thus far reported for this reaction, although not the best.

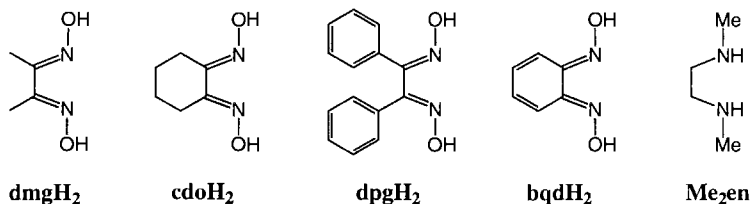
The correlation between rate of in-plane acetate ligand exchange [Eq. (1)] and catalytic activity for hydration of acetonitrile [Eq. (4)] has been studied for a series of  $\text{Pt}_4$  cluster complexes (42). The results show that there is a positive correlation. In general, as the exchange rate increases, the catalytic activity also increases. The correlation was not simply linear, however. Other factors, such as steric effects or electrostatic effects, also affect the catalytic activity.

It is evident from all the experimental results that the catalytic activity is closely associated with remarkable lability and regioselective reactivity of the in-plane coordination sites in the  $\text{Pt}_4$  clusters owing to a *trans* effect from the Pt–Pt bonds (see Section II,A–C).

### III. Trinuclear Platinum(II) Cluster Complexes

#### A. SYNTHESIS—CLUSTER CORE TRANSFORMATION

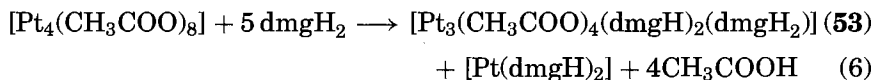
During reactivity studies involving  $[\text{Pt}_4(\text{CH}_3\text{COO})_8]$  (**1**), it was found that **1** undergoes a cluster core transformation from a square-planar

FIG. 28. Ligands (oxime and diamine) for Pt<sub>3</sub> clusters.

core to a triangular-type core upon reaction with certain dioxime or diamine ligands, affording new Pt(II) cluster complexes having a triangular core (54–55). Some of the resulting Pt<sub>3</sub> complexes undergo in-plane ligand substitution to afford new derivatives. Figure 28 shows the dioxime and diamine ligands coordinated to the Pt<sub>3</sub> clusters, together with their abbreviated notations.

### 1. Cluster Core Transformation Method

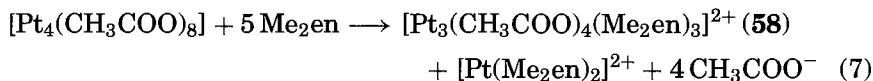
When **1** is allowed to react with an excess of dimethylglyoxime (dmgh<sub>2</sub>), the triangular cluster [Pt<sub>3</sub>(CH<sub>3</sub>COO)<sub>4</sub>(dmH)<sub>2</sub>(dmgh<sub>2</sub>)] (**53**) is obtained [Eq. (6)].



Other dioximes such as cdoH<sub>2</sub>, dpgh<sub>2</sub>, bqdh<sub>2</sub>, and dagH<sub>2</sub> undergo a similar reaction with **1** to afford [Pt<sub>3</sub>(CH<sub>3</sub>COO)<sub>4</sub>(dioxH)<sub>2</sub>(dioxH<sub>2</sub>)] [dioxH<sub>2</sub> = cdoH<sub>2</sub> (**54**), dpgh<sub>2</sub> (**55**), bqdh<sub>2</sub> (**56**), dagH<sub>2</sub> (**57**)].

Reaction conditions depend on the nature of dioxime ligand. For example, when dmgh<sub>2</sub> is used, the reaction must be refluxed for several hours, whereas with bqdh<sub>2</sub> the reaction occurs rapidly at room temperature. The required reaction conditions are harder, in the order dmgh<sub>2</sub> > dagH<sub>2</sub> ≈ cdoH<sub>2</sub> ≈ dpgh<sub>2</sub> > bqdh<sub>2</sub>. It appears that the trend corresponds to the rigidity of dioxime ligand.

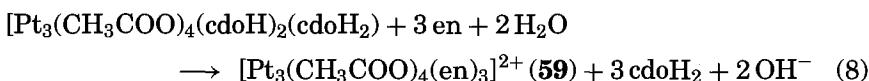
The same type of cluster core transformation occurs when the bulky bidentate chelate ligand *N,N'*-dimethylethylenediamine (Me<sub>2</sub>en) is used [Eq. (7)].



Attempts to use more bulky ligands such as tetramethylethylenediamine ( $\text{Me}_4\text{en}$ ) or ethylenediamine ( $\text{en}$ ) were unsuccessful.  $\text{Me}_4\text{en}$  did not react with **1** at all, probably for steric reasons. On the other hand, reaction of **1** with ethylenediamine afforded exclusively  $[\text{Pt}_4(\text{CH}_3\text{COO})_4(\text{en})_4]^{4+}$  (see Section II,B). These facts suggest that the stereochemistry of the entering ligand affects the cluster core transformation.

## 2. Ligand Substitution Method

Another route to new trinuclear platinum(II) clusters is in-plane ligand substitution involving trinuclear cluster complexes made through the cluster core transformation. Reaction of  $[\text{Pt}_3(\text{CH}_3\text{COO})_4(\text{cdoH})_2(\text{cdoH}_2)]$  (**54**) or  $[\text{Pt}_3(\text{CH}_3\text{COO})_4(\text{Me}_2\text{en})_3]^{2+}$  (**58**) with ethylenediamine gave  $[\text{Pt}_3(\text{CH}_3\text{COO})_4(\text{en})_3]^{2+}$  (**59**) in moderate yield [Eq. (8)].



Similarly, the reaction of  $[\text{Pt}_3(\text{CH}_3\text{COO})_4(\text{cdoH})_2(\text{cdoH}_2)]$  (**54**) with excess dimethylethylenediamine ( $\text{Me}_2\text{en}$ ) gave  $[\text{Pt}_3(\text{CH}_3\text{COO})_4(\text{Me}_2\text{en})_3]^{2+}$  (**58**). Note that **58** can be also obtained from the cluster core transformation [Eq. (7)], but **59** can be prepared only by the substitution.

## B. STRUCTURES OF TRIANGULAR CLUSTER COMPLEXES

Four complexes with a triangular  $\text{Pt}_3^{\text{II}}$  cluster core (**53**, **54**, **57**, **58**) have been structurally characterized. The core structures of these compounds are very similar to one another, each having an isosceles triangle arrangement. The structure of  $[\text{Pt}_3(\text{CH}_3\text{COO})_4(\text{dmgH}_2)(\text{dmgH})_2]$  is described here. An ORTEP drawing is shown in Fig. 29.

Three platinum atoms make an isosceles triangle, in which the unique edge  $[\text{Pt}(1)\text{--Pt}(3) = 2.605(1) \text{ \AA}]$  is somewhat longer than the similar sides  $[\text{Pt}(1)\text{--Pt}(2) = 2.522(1) \text{ \AA}, \text{Pt}(2)\text{--Pt}(3) = 2.516(1) \text{ \AA}]$ . The Pt–Pt distances are consistent with the presence of metal–metal single bonds. The latter distances are somewhat shorter than those in the  $\text{Pt}_4$  clusters with N-donor ligands at the in-plane site, whereas the unique edge is slightly longer than the Pt–Pt bonds in the  $\text{Pt}_4$  clusters (see Section II,B).

Each platinum atom has distorted octahedral coordination geometry if platinum–platinum bonds are included. Each platinum atom is coordinated by a chelating dimethylglyoximate ligand at the in-plane

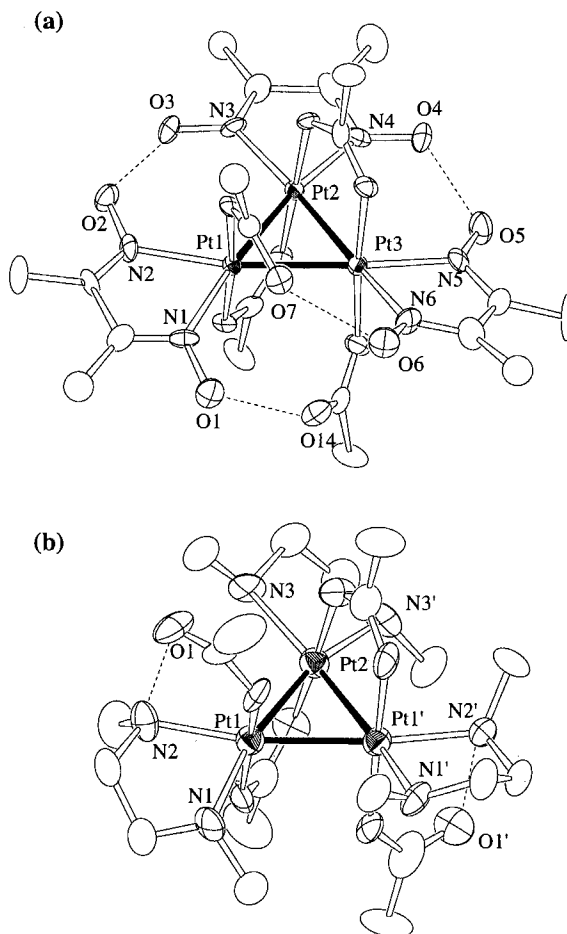


FIG. 29. ORTEP drawings of (a)  $[\text{Pt}_3(\text{CH}_3\text{COO})_4(\text{dmgh})_2(\text{dmgh}_2)]$  (53) and (b)  $[\text{Pt}_3(\text{CH}_3\text{COO})_4(\text{Me}_2\text{en})_3]^{2+}$  (58).

site. The three dimethylglyoximate ligands interact together by two hydrogen bonds between adjacent dimethylglyoximate ligands [ $\text{O}(2) \cdots \text{O}(3) = 2.49(2) \text{ \AA}$  and  $\text{O}(4) \cdots \text{O}(5) = 2.45(2) \text{ \AA}$ ]. The out-of-plane coordination sites are occupied by four acetates. Two of these bridge two platinum atoms on the similar sides [between  $\text{Pt}(1)$  and  $\text{Pt}(2)$  and between  $\text{Pt}(2)$  and  $\text{Pt}(3)$ ] and are located above and below the cluster plane. The other two acetates are coordinated to the remaining sites,  $\text{Pt}(1)$  and  $\text{Pt}(3)$ , in a monodentate fashion. The out-of-plane acetates with respect to the  $\text{Pt}_3$  plane coordinate in alternating up-down fashion

similar to that in **1**. No acetate directly bridges the longer edge [between Pt(1) and Pt(3)], but two hydrogen bonds exist between dimethylglyoximate and monodentate acetate [ $\text{O}(1) \cdots \text{O}(14) = 2.66(2) \text{ \AA}$  and  $\text{O}(6) \cdots \text{O}(7) = 2.55(2) \text{ \AA}$ ]. A pseudo- $C_2$  axis passes through Pt(2) and the midpoint of Pt(1) and Pt(3).

Pt–O distances between the platinum atoms and the out-of-plane ligands are 1.98(2)–2.02(2)  $\text{\AA}$ , which are within a normal range for Pt–O distances. Pt–N distances range from 2.09(2) to 2.17(2)  $\text{\AA}$  and are somewhat longer than those in a mononuclear platinum dioximate complex ( $\sim 2.00 \text{ \AA}$ ) (56). The elongation arises from a *trans* influence from the Pt–Pt bonds, which was observed in  $\text{Pt}_4$  clusters (see Section II,B).

All the structurally characterized  $\text{Pt}_3$  clusters have two structural features in common: (1) Entering ligands, dioxime or  $\text{Me}_2\text{en}$ , which cause the core transformation, always occupy coordination sites within the plane of the resulting  $\text{Pt}_3$  cluster; (2) the  $\text{Pt}_3$  clusters have four acetates that occupy the out-of-plane sites. We believe these originate from the regioselective substitution reactivity of **1**.

### C. MECHANISM OF THE CLUSTER CORE TRANSFORMATION REACTION FROM SQUARE-PLANAR TO TRIANGULAR TYPE

Figure 30 shows a proposed mechanism for the cluster core transformation. The first step of the core transformation is substitution of the in-plane acetates of **1** by the entering ligands, which coordinate to Pt in

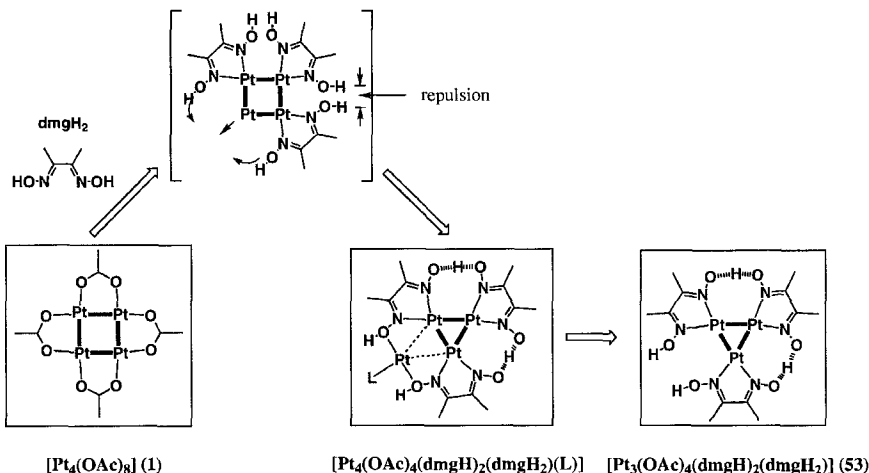


FIG. 30. Cluster core transformation mechanism from the tetranuclear cluster to the trinuclear cluster. Out-of-plane ligands are omitted for clarity.

a chelating mode rather than a bridging mode owing to stereochemical demand. As shown in Fig. 30, coordination of three entering ligands to the  $\text{Pt}_4$  cluster core promotes release of one Pt atom from the square-planar cluster core because of steric hindrance between the entering ligands. The released Pt atom is finally removed completely by excess free ligand in a reaction mixture. The four out-of-plane acetates in the starting compound **1**, which are substitutionally inert, remain at the axial sites of the resulting  $\text{Pt}_3$  cluster, two of them being unidentate.

A powdery product that is regarded as a reaction intermediate was isolated from the reaction of **1** with  $\text{dmgH}_2$  under mild conditions. In fact, this product can be converted to  $[\text{Pt}_3(\text{CH}_3\text{COO})_4(\text{dmgH})_2(\text{dmgH}_2)]$  (**53**) in the presence of an excess of free  $\text{dmgH}_2$  ligand. An X-ray structure of a single crystal obtained from the powdery product is shown in Fig. 31. The compound was a dimer of a trinuclear Pt(II) complexes bridged by  $\text{dmgH}_2$ ,  $[\{\text{Pt}_4(\text{CH}_3\text{COO})_4(\text{dmgH})_2(\text{dmgH}_2)\}_2(\mu\text{-dmgH}_2)]$  (**60**). The structure of **60** shows that one Pt atom has been partially removed from the tetranuclear cluster core of **1**, which supports the proposed mechanism.

#### D. EHMO STUDY

EHMO calculations were performed for a model system,  $[\text{Pt}^{\text{II}}_3(\text{HCOO})_4(\text{glyoxH})_2(\text{glyoxH}_2)]$  ( $\text{glyoxH}_2 = \text{glyoxime}$ ), in a way similar to the  $\text{Pt}_4$  cluster complex. The results reveal the presence of Pt–Pt bonds in the cluster core and regioselective substitution reactivity.

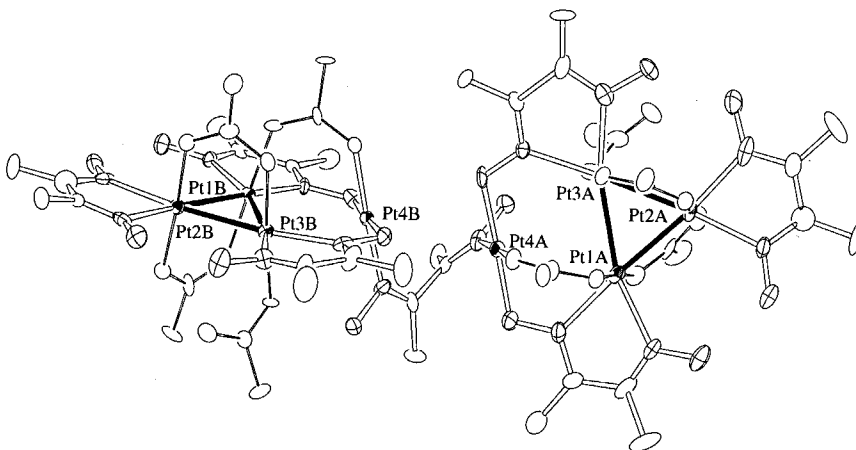


FIG. 31. An ORTEP drawing of  $[\{\text{Pt}_4(\text{CH}_3\text{COO})_4(\text{dmgH})_2(\text{dmgH}_2)\}_2(\mu\text{-dmgH}_2)]$  (**60**).

Figure 32 shows the calculated energy levels associated with the Pt 5d orbitals for the model cluster and its 1/3 fragment, and their correlation.

The relatively large HOMO–LUMO gap (1.67 eV) suggests the stability of the triangular cluster core. Molecular orbitals derived from the  $d_\pi$  ( $d_{xy}$ ,  $d_{xz}$ ,  $d_{yz}$ ) orbitals of the fragment are not considered in the following discussion for the same reason as that mentioned for the  $\text{Pt}_4$  cluster (Section II,C). Molecular orbitals derived from the  $d_\sigma$  orbitals ( $d_{x^2-y^2}$  and  $d_{z^2}$ ) of the fragment are shown as thick lines in the diagram. Three  $d_{z^2}$  orbitals of the fragments make three molecular orbitals, one bonding and two antibonding orbitals, the latter being nearly degenerate. Three  $d_{x^2-y^2}$  orbitals of the fragments also form one antibonding and

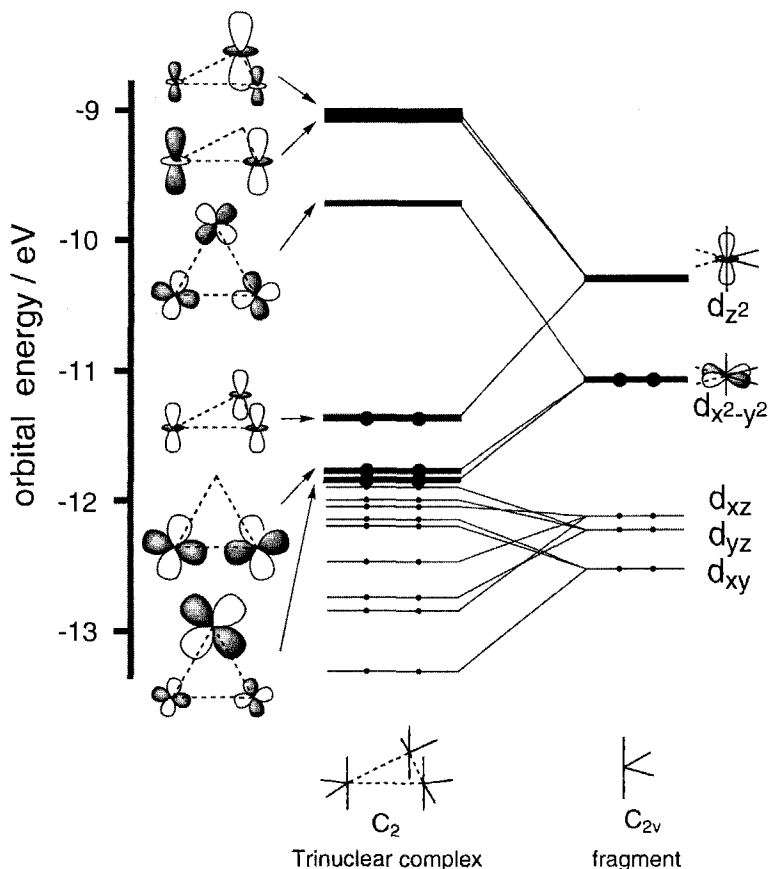


FIG. 32. EHMO diagram for a model trinuclear cluster,  $[\text{Pt}_3(\text{HCOO})_4(\text{glyoximH})_2(\text{glyoximH}_2)]$ , and its 1/3 fragment.

two closely separated bonding orbitals. Each fragment has two  $d_\sigma$  electrons and the cluster has six  $d_\sigma$  electrons. These six electrons occupy the three low-lying bonding orbitals, giving rise to three Pt–Pt single bonds between neighboring Pt atoms in the triangular framework. Moreover, the reduced overlap populations between adjacent platinum atoms are 0.355 and 0.332, suggesting the existence of metal–metal bonds between the platinum atoms.

The calculated MO scheme for the Pt<sub>3</sub> cluster also shows the regioselective reactivity. The coordination sites in the cluster plane are labile, whereas the out-of-plane sites are inert to substitution. A similar explanation concerning the acetate lability for the Pt<sub>4</sub> clusters is also proposed for the Pt<sub>3</sub> clusters (Section II,C).

## E. SOLUTION BEHAVIOR

### 1. Species in Solution

<sup>1</sup>H and <sup>13</sup>C NMR spectra of all of the dioximato clusters **53–56** in CDCl<sub>3</sub> show that each compound has C<sub>2</sub> symmetry; that is, the cluster core is an isosceles triangle. This is consistent with X-ray structures found for **53** and **54** and shows that the solid-state structure is maintained in solution. On the other hand, the Pt<sub>3</sub> cluster complexes **58** and **59** with diamine ligands show complicated <sup>1</sup>H and <sup>195</sup>Pt NMR spectra in D<sub>2</sub>O. When an excess of free diamine ligand was added to the solution, however, <sup>1</sup>H and <sup>195</sup>Pt NMR spectra typical of trinuclear platinum(II) cluster were obtained. This indicates that diamine ligands partially dissociate to give an equilibrium mixture in aqueous solution.

### 2. In-Plane Substitution Reactivity

As described in Section II,A, the tetranuclear cluster **1** shows remarkably regioselective ligand substitution, that regioselectivity being ascribed to a strong *trans* effect from the Pt–Pt bonds in the Pt<sub>4</sub> cluster core. Such regioselective substitution reactivity is also expected for the trinuclear cluster complexes, which have analogous Pt–Pt bonds. In fact, some Pt<sub>3</sub> complexes undergo in-plane ligand substitution, while the out-of-plane acetate ligands are inert to substitution. The regioselectivity is again ascribed to a strong *trans* effect from the Pt–Pt bonds. However, the reactivity of the Pt<sub>3</sub> clusters having dioxime ligands was much lower than that of the Pt<sub>4</sub> clusters, and severe conditions are required in most cases for in-plane ligand substitution. The reason is the presence of strong intramolecular hydrogen bonds among the in-plane dioxime ligands (Section III,B). However, when an incoming ligand has a stronger coordinating ability

to Pt, substitution goes smoothly, even though intramolecular hydrogen bonds are present in the starting compound. For example, reaction of  $[\text{Pt}_3(\text{CH}_3\text{COO})_4(\text{cdoH})_2(\text{cdoH}_2)]$  (**54**) with excess diamine ( $\text{Me}_2\text{en}$  or  $\text{en}$ ) at ambient temperature gave a fully substituted cluster  $[\text{Pt}_3(\text{CH}_3\text{COO})_4(\text{Me}_2\text{en})_3]^{2+}$  (**58**) or  $[\text{Pt}_3(\text{CH}_3\text{COO})_4(\text{en})_3]^{2+}$  (**59**). The  $^{195}\text{Pt}$  NMR spectrum of  $[\text{Pt}_3(\text{CH}_3\text{COO})_4(\text{Me}_2\text{en})_3]^{2+}$  (**58**) in  $\text{D}_2\text{O}$  in the presence of excess of ethylenediamine was exactly the same as that of  $[\text{Pt}_3(\text{CH}_3\text{COO})_4(\text{en})_3]^{2+}$  (**59**), providing further evidence for facile in-plane ligand substitution in solution.

#### F. $^{195}\text{Pt}$ NMR SPECTRA OF $\text{Pt}_3$ CLUSTERS

Because the  $\text{Pt}_3$  triangle of the triplatinum cluster is an isosceles triangle—that is, two kinds of Pt exist in the cluster core—the cluster shows a complicated  $^{195}\text{Pt}$  NMR spectrum similar to that of the unsymmetric  $\text{Pt}_4$  cluster (Section II,D). The spectrum consists of a summation of the spectra of five isotopomers (A,  $\text{A}_2$ , B, AB, and  $\text{A}_2\text{B}$ ) and involves two main singlets with an intensity ratio of 3 : 1 and an AB pattern in addition to weak signals. Figure 33 shows the observed and simulated

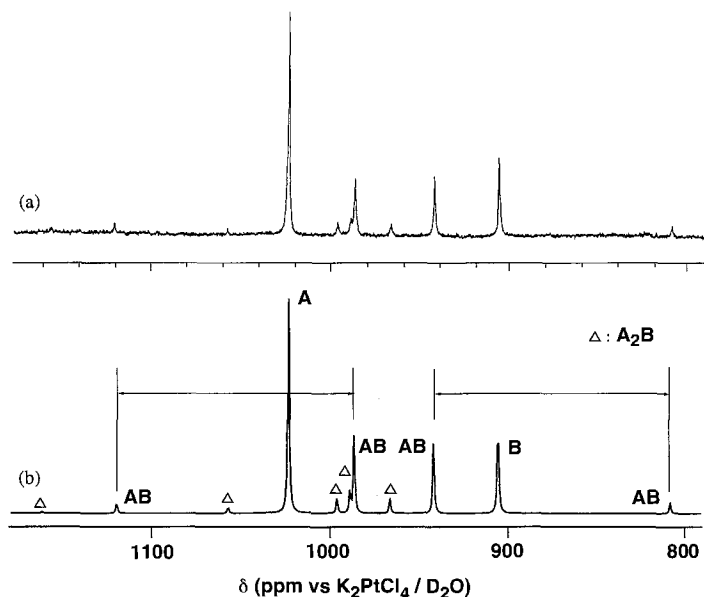


FIG. 33.  $^{195}\text{Pt}$  NMR of  $[\text{Pt}_3(\text{CH}_3\text{COO})_4(\text{bqdH})_2(\text{bqdH}_2)]$  in  $\text{CDCl}_3$ . (a) Observed spectrum. (b) Simulated spectrum.

TABLE V

<sup>195</sup>Pt NMR CHEMICAL SHIFTS AND COUPLING CONSTANTS FOR Pt<sub>3</sub> CLUSTERS

Compound	Solvent	$\delta_A^a$	$\delta_B^b$	$J_{\text{Pt-Pt}}/\text{Hz}$
[Pt <sub>3</sub> (CH <sub>3</sub> COO) <sub>4</sub> (dmgH <sub>2</sub> )(dmgH) <sub>2</sub> ] ( <b>53</b> )	CDCl <sub>3</sub>	1035.1	1038.7	— <sup>c</sup>
[Pt <sub>3</sub> (CH <sub>3</sub> COO) <sub>4</sub> (cdoH <sub>2</sub> )(cdoH) <sub>2</sub> ] ( <b>54</b> )	CDCl <sub>3</sub>	1047.8	1020.0	7670
[Pt <sub>3</sub> (CH <sub>3</sub> COO) <sub>4</sub> (dpgH <sub>2</sub> )(dpgH) <sub>2</sub> ] ( <b>55</b> )	CDCl <sub>3</sub>	974.6	995.4	7890
[Pt <sub>3</sub> (CH <sub>3</sub> COO) <sub>4</sub> (bqdH <sub>2</sub> )(bqdH) <sub>2</sub> ] ( <b>56</b> )	CDCl <sub>3</sub>	1023.4	905.7	7750
[Pt <sub>3</sub> (CH <sub>3</sub> COO) <sub>4</sub> (Me <sub>2</sub> en) <sub>3</sub> ] <sup>2+</sup> ( <b>58</b> )	D <sub>2</sub> O	1189.2	916.4	8060
[Pt <sub>3</sub> (CH <sub>3</sub> COO) <sub>4</sub> (en) <sub>3</sub> ] <sup>2+</sup> ( <b>59</b> )	D <sub>2</sub> O	1058.8	834.1	7570

<sup>a</sup> Pt at the unique apex of the Pt<sub>3</sub> isosceles triangle.<sup>b</sup> Pt atoms at both the ends of long edge of the Pt<sub>3</sub> isosceles triangle.<sup>c</sup> Not determined.

spectra for [Pt<sub>3</sub>(CH<sub>3</sub>COO)<sub>4</sub>(cdoH)<sub>2</sub>(cdoH<sub>2</sub>)] (**54**). Chemical shifts and coupling constants of Pt<sub>3</sub> clusters are summarized in Table V.

The <sup>195</sup>Pt NMR chemical shifts of dioximato clusters are around 1000 ppm (vs. K<sub>2</sub>PtCl<sub>4</sub>/D<sub>2</sub>O) and similar to those for Pt<sub>4</sub> clusters with oxygen or nitrogen donors at the in-plane positions. Although the coordination environments around the two kinds of platinum in the Pt<sub>3</sub> isosceles triangle are almost the same, the two sites show different chemical shifts. The differences for the dmg, cdo, dpg, and bq d clusters are 3.6, 28.0, 20.8, and 117.7 ppm, respectively; and the trend is similar to the order of rigidity of the ligands, which might cause a distortion of the cluster core structure. On the other hand, chemical shift differences between the two sites in diamine clusters are significantly larger than those in dioximato clusters (272.9 ppm for **58** and 224.7 ppm for **59**). This is because the diamine ligands at the two equivalent Pt sites are involved in intracluster hydrogen bonding between an NH group of the diamines and a carboxylate oxygen of the monodentate acetates, whereas the other diamine ligand does not participate in hydrogen bonding. The coupling constants ( $J_{\text{AB}}$ ) of the present trinuclear clusters (Table V) are very large (~8000 Hz). The values are similar to those of the Pt<sub>4</sub> clusters (Section II,D), again suggesting the presence of Pt–Pt bonds.

#### IV. Concluding Remarks

Most of the platinum(II) clusters are limited to tetranuclear and trinuclear platinum(II) clusters, although some Pt→M complexes having metal–metal dative bonds are known (57–61). In this article, we

reviewed the chemistry of  $\text{Pt}^{\text{II}}_4$ , and  $\text{Pt}^{\text{II}}_3$  clusters. Both clusters are taken as being constructed from a  $C_{2v}$ -type  $\text{PtL}_4$  fragment with two available singly occupied orbitals (isolobal with " $\text{CH}_2$ "). From this point of view, other new platinum(II) clusters, such as a cyclic pentanuclear cluster or a zigzag chain cluster, could be synthesized.

The  $\text{Pt}_4$  clusters have rich chemistry arising from the lability of the in-plane sites owing to a *trans* influence (effect) from the Pt–Pt bond. The site-selective lability gives many derivatives of  $\text{Pt}_4$  clusters and brings catalytic activity to the  $\text{Pt}_4$  cluster. The  $\text{Pt}_4$  clusters could be model compounds for metal surfaces as they have two adjacent reaction centers. Furthermore, each Pt in a  $\text{Pt}_4$  cluster is in the chiral environment, although  $\text{Pt}_4$  clusters are optically inactive as a whole. It is possible that an effective chiral catalyst may be obtained by choosing an appropriate ligand system. The catalytic activity of  $\text{Pt}_3$  clusters has not been investigated yet. They might be more active than  $\text{Pt}_4$  clusters, since the in-plane ligands in diamine  $\text{Pt}_3$  clusters dissociate easily in solution whereas those in diamine  $\text{Pt}_4$  cluster remain intact in solution.

#### ACKNOWLEDGMENTS

We are grateful to Professor Y. Sasaki of Hokkaido University, Japan, for collaboration in our earlier work on this subject, and also acknowledge to Dr. Brian Breedlove for helpful discussion. Financial support by Grants-in-Aid for Scientific Research (No. 12640531 and Priority Areas No. 10149102, Metal-Assembled Complexes) from the Ministry of Education, Science, Sports, and Culture, Japan, is gratefully acknowledged.

#### REFERENCES

1. Calabrese, J. C.; Dahl, L. F.; Chini, P.; Longoni, G.; Martinengo, S. *J. Am. Chem. Soc.* **1974**, *96*, 2614–2616.
2. Teo, B. K.; Disalvo, F. J.; Waszczak, J. V.; Longoni, G.; Ceriotti, A. *Inorg. Chem.* **1986**, *25*, 2262–2265.
3. Bender, R.; Braunstein, P.; Tiripicchio, A.; Camellini, M. T. *Angew. Chem., Int. Ed. Engl.* **1985**, *24*, 861–862.
4. Ferguson, G.; Lloyd, B. R.; Puddephatt, R. J. *Organometallics* **1986**, *5*, 334–348.
5. Yamamoto, Y.; Yamazaki, H.; Sakurai, T. *J. Am. Chem. Soc.* **1982**, *104*, 2329–2330.
6. Albinati, A.; Moor, A.; Pregosin, P. S.; Venanzi, L. M. *J. Am. Chem. Soc.* **1982**, *104*, 7672–7673.
7. Ramachandran, R.; Yang, D. S.; Payne, N. C.; Puddephatt, R. J. *Inorg. Chem.* **1992**, *31*, 4236–4240.
8. Zhang, T.; Drouin, M.; Harvey, P. D. *Inorg. Chem.* **1999**, *38*, 957–963.

9. Green, M.; Howard, J. A. K.; Murray, M.; Spencer, J. L.; Stone, F. G. A. *J. Chem. Soc., Dalton Trans.* **1977**, 1509–1514.
10. Yamamoto, Y.; Yamazaki, H. *Organometallics* **1993**, *12*, 933.
11. Tanase, T.; Ukaji, H.; Takahata, H.; Toda, H.; Igoshi, T.; Yamamoto, Y. *Organometallics* **1998**, *17*, 196–209.
12. Puddephatt, R. J. *Chem. Soc. Rev.* **1983**, *12*, 99–127.
13. Krevor, J. V.; Simonis, U.; Karson, A.; Castro, C.; Aliakbar, M. *Inorg. Chem.* **1992**, *31*, 312–317.
14. Xu, Q.; Heaton, B. T.; Jacob, C.; Mogi, K.; Ichihashi, Y.; Souma, Y.; Kanamori, K.; Eguchi, T. *J. Am. Chem. Soc.* **2000**, *122*, 6862–6870.
15. Woollins, J. D.; Kelly, P. F. *Coord. Chem. Rev.* **1985**, *65*, 115–140.
16. Cotton, F. A.; Walton, R. A. *Struct. Bonding* (Berlin) **1985**, *62*, 1–49.
17. Umakoshi, K.; Sasaka, Y. *Adv. Inorg. Chem.* **1993**, *40*, 187–239.
18. Cotton, F. A.; Falvello, L. R.; Han, S. *Inorg. Chem.* **1982**, *21*, 1709–1710.
19. Appleton, T. G.; Byriel, K. A.; Hall, J. R.; Kennard, C. H. L.; Mathieson, M. T. *J. Am. Chem. Soc.* **1992**, *114*, 7305–7307.
20. O'Halloran, T. V.; Mascharak, P. K.; Williams, I. D.; Roberts, M. M.; Lippard, S. J. *Inorg. Chem.* **1987**, *26*, 1261–1270.
21. Matsumoto, Y.; Sakai, K. *Adv. Inorg. Chem.* **2000**, *49*, 375–427.
22. Sakai, K.; Tanaka, Y.; Tsuchiya, Y.; Hirata, K.; Tsubomura, T.; Iijima, S.; Bhattacharjee, A. *J. Am. Chem. Soc.* **1998**, *120*, 8366–8379.
23. Sakai, K.; Takeshita, M.; Tanaka, Y.; Ue, T.; Yanagisawa, M.; Kosaya, K.; Tsubomura, T.; Ato, M.; Nakano, T. *J. Am. Chem. Soc.* **1998**, *120*, 11353–11363.
24. Carrondo, M. A. A. F. de C. T.; Skapski, A. C. *J. Chem. Soc., Chem. Commun.* **1976**, 410–411.
25. Carrondo, M. A. A. F. de C. T.; Skapski, A. C. *Acta Crystallogr., Sect. B* **1978**, *B34*, 1857–1862.
26. Carrondo, M. A. A. F. de C. T.; Skapski, A. C. *Acta Crystallogr., Sect. B* **1978**, *B34*, 3576–3578.
27. I. C. I. Ltd. Br. Patent 1970, 1,214,552.
28. Skapski, A. C.; Smart, M. L. *J. Chem. Soc., Chem. Commun.* **1970**, 658–659.
29. Yamaguchi, T.; Sasaki, Y.; Nagasawa, A.; Ito, T.; Koga, N.; Morokuma, K. *Inorg. Chem.* **1989**, *28*, 4311–4312.
30. Yamaguchi, T. Dr. Thesis, Tohoku University, 1989.
31. Gerbeleu, N. V.; Timko, G. A.; Indrichan, K. M.; Batsanov, A. S.; Manole, O. S.; Struchkov, Y. T. *Russ. J. Coord. Chem.* **1994**, *20*, 799–805.
32. Zhilyaev, A. N.; Katser, S. B.; Kuznetsova, G. N.; Fomina, T. A. *Russ. J. Inorg. Chem.* **1998**, *43*, 1137–1140.
33. Yamaguchi, T.; Shibata, A.; Ito, T. *Chem. Eur. J.* Submitted.
34. Yamaguchi, T.; Abe, K.; Ito, T. *Inorg. Chem.* **1994**, *33*, 2689–2691.
35. Yamaguchi, T.; Sasaki, Y.; Ito, T. *J. Am. Chem. Soc.*, **1990**, *112*, 4038–4040.
36. Yamaguchi, T.; Ueno, T.; Ito, T. *Inorg. Chem.* **1993**, *32*, 4996–4997.
37. Yamaguchi, T.; Shibata, A.; Ito, T. *J. Chem. Soc., Dalton Trans.* **1996**, 4031–4032.
38. Shibata, A. Dr. Thesis, Tohoku University, 1996.
39. Yamaguchi, T.; Saito, H.; Maki, T.; Ito, T. *J. Am. Chem. Soc.* **1999**, *121*, 10738–10742.
40. Yamaguchi, T.; Saito, H.; Ito, T. Unpublished result.
41. Yamaguchi, T.; Ueno, T.; Shibata, A.; Ito, T. Unpublished result.
42. Shibata, A.; Yamaguchi, T.; Ito, T. *Inorg. Chim. Acta* **1997**, *265*, 197–204.
43. Orpen, A. G.; Brammer, L.; Allen, F. H.; Kennard, O.; Watson, D. G.; Taylor, R. *J. Chem. Soc., Dalton Trans.* **1989**, S1–S83.

44. Martin, L. Y.; Sperati, C. R.; Buch, D. H. *J. Am. Chem. Soc.* **1977**, *99*, 2968.
45. Pregosin, P. S. *Coord. Chem. Rev.* **1982**, *44*, 247.
46. Mason, J. "Multinuclear NMR"; Plenum Press: New York, 1987.
47. Pregosin, P. S. In "Transition Metal Nuclear Magnetic Resonance"; Elsevier: Amsterdam, 1991, p. 216.
48. Appleton, T. G.; Hall, J. R.; Neale, D. W. *Inorg. Chim. Acta* **1985**, *104*, 19–31.
49. Yamaguchi, T.; Adachi, H.; Sasaki, Y.; Ito, T. *Bull. Chem. Soc. Jpn.* **1994**, *67*, 3116–3118.
50. Cini, R.; Fanizzi, F. P.; Intini, F. P.; Maresca, L.; Natile, G. *J. Am. Chem. Soc.* **1993**, *115*, 5123.
51. Umakoshi, K.; Murata, K.; Yamashita, S.; Isobe, K. *Inorg. Chim. Acta* **1991**, *190*, 195.
52. Rochon, F. D.; Kong, P. C.; Melanson, R. *Inorg. Chem.* **1990**, *29*, 1352.
53. Rochon, F. D.; Kong, P. C.; Melanson, R. *Inorg. Chem.* **1990**, *29*, 2708.
54. Yamaguchi, T.; Nishimura, N.; Ito, T. *J. Am. Chem. Soc.* **1993**, *115*, 1612–1613.
55. Yamaguchi, T.; Nishimura, N.; Shirakura, K.; Ito, T. *Bull. Chem. Soc. Jpn.* **2000**, *73*, 775–784.
56. Frasson, E.; Panattoni, C.; Zannetti, R. *Acta Crystallogr.* **1959**, *12*, 1027.
57. Frew, A. A.; Manojlovic-Muir, L.; Muir, K. W. *J. Chem. Soc., Chem. Commun.* **1980**, 624.
58. Mealli, C.; Pichierri, F.; Randaccio, L.; Zangrando, E.; Krumm, M.; Holtenrich, D.; Lippert, B. *Inorg. Chem.* **1995**, *34*, 3418.
59. Falvello, R. L.; Forniés, J.; Martín, A.; Navarro, R.; Sicilia, V.; Villarroja, P. *Inorg. Chem.* **1997**, *36*, 6166.
60. Yamaguchi, T.; Yamazaki, F.; Ito, T. *J. Am. Chem. Soc.* **1999**, *121*, 7405–7406.
61. Yamaguchi, T.; Yamazaki, F.; Ito, T. *J. Am. Chem. Soc.* **2001**, *123*, 743–744.

## COMPLEXES OF SQUARIC ACID AND ITS MONOSUBSTITUTED DERIVATIVES

LINCOLN A. HALL\* and DAVID J. WILLIAMS†

\*Department of Chemistry, The University of the West Indies, St. Augustine,  
Trinidad and Tobago, West Indies

†Chemical Crystallography Laboratory, Department of Chemistry, Imperial College of Science,  
Technology and Medicine, London, SW7 2AY, United Kingdom

- I. Introduction
  - A. Spectroscopy of the Squarate Ion
  - B. Coordination Modes of the Squarate Ion
- II. Squaric Acid Compounds
  - A. Salts of Squaric Acid
  - B. Squarate Complexes
  - C. Magnetochemistry and Other Electron-Transfer Phenomena
  - D. Cubic Structures
  - E. Squarate Complexes of Heavier Transition Metals and Lanthanides
  - F. The Squarate Ion as a Linking Group
  - G. Spectroscopy of Squarate Complexes
  - H. Luminescence Studies
  - I. Electrochemistry
- III. Complexes of Monosubstituted Squarate Derivatives
  - A. Complexing Properties of Monosubstituted Squarate Ligands
  - B. Substituents with Lone Pairs
  - C. Substituents without Lone Pairs
  - D. Effects of Substituent on Structure
  - E. Squarate and Monosubstituted Squarate Complexes with  $\pi$  Interactions
  - F. Complexes of Heavier Transition Metals
  - G. Electrochemical Studies
  - H. Luminescence Studies
- IV. Hydrogen Bonding and Other Weak Interactions in Complexes of Squaric Acid and Its Monosubstituted Derivatives
- References

## I. Introduction

After the first synthesis of squaric acid in 1959 (1), the focus of attention shifted rapidly to the preparation of several of its derivatives and to the exploitation of its potential as a reactant in synthetic organic chemistry, its usefulness apparently being predicated on the variety of functional groups it possesses (2–8). However, it was not until four years after its synthesis that its potential as a ligand was explored. Since then, the complexing properties of squaric acid (3,4-dihydroxycyclobut-3-ene-1,2-dione) have been extensively investigated (9–82). The compound is an extremely stable dibasic acid with a decomposition point of  $\sim 293^{\circ}\text{C}$  (1). The name “squaric acid” is actually a misnomer for the compound, since Wang *et al.* showed, by X-ray crystallography (83), that the non-ionized compound is in reality asymmetric (Fig. 1). The squarate dianion, one of a series of monocyclic aromatic anions  $\text{C}_n\text{O}_n^{2-}$ , is square and resonance-stabilized owing to the delocalization of the negative charge over the  $\text{C}_4$  ring and the four appended oxygen atoms (83, 84). This delocalization is evidenced by the near equivalence of the respective C–C and C–O bond lengths in the squarate ion in metal squarate salts (22, 85–90), except where hydrogen bonding causes a distortion

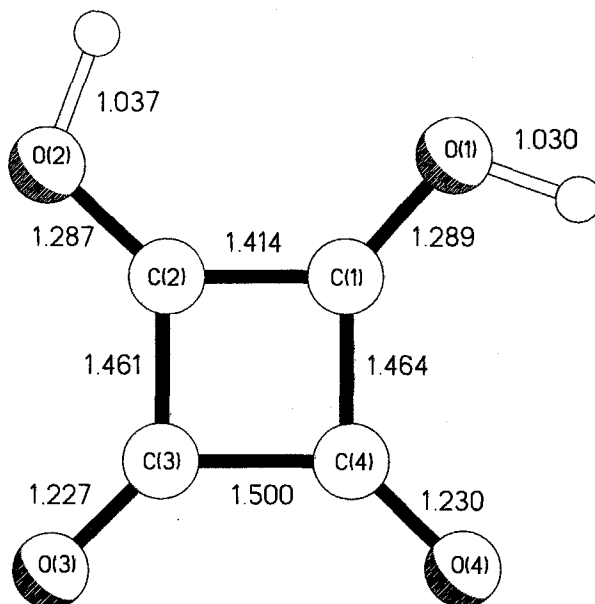


FIG. 1. The asymmetric pattern of bonding in squaric acid as seen in the neutron study by Semmingsen *et al.* (94); the esds are 0.001 Å.

resulting in a lowering of the symmetry from  $D_{4h}$  (90). A similar pattern is observed for oxalic acid *vis à vis* the oxalate ion; the former has  $C_{2h}$  symmetry (C—C bond length of 1.54 Å and C—O bond lengths of 1.21 and 1.29 Å, respectively) whereas the latter approaches  $D_{2h}$  symmetry (C—C bond length of  $\sim 1.55$  Å and C—O bond lengths that range between 1.24 and 1.26 Å). The stability of the anion is responsible for squaric acid being an unusually strong organic acid. Acid dissociation constants  $K_1$  and  $K_2$  can be defined, with  $pK_1$  quoted as  $1.2 \pm 0.2$ , and  $pK_2$  as 2.2, 3.0, and  $3.48 \pm 0.02$ . The range of  $pK_2$  values is similar to that for sulfuric acid (10, 91–93). Squaric acid is a white crystalline solid and its crystal structure has been the subject of several investigations, including X-ray and neutron diffraction analyses on both the pure compound and its deuterated form (83, 94–97). The effects of pressure on its structure have also been determined (98, 99). Neutron diffraction studies showed the existence of two types of intermolecular hydrogen bonding; this hydrogen bonding is extensive in the solid state and results in the formation (Fig. 2) of infinite planar sheets (83, 94). It is also responsible for the compound's low solubility in water and the lower alcohols.

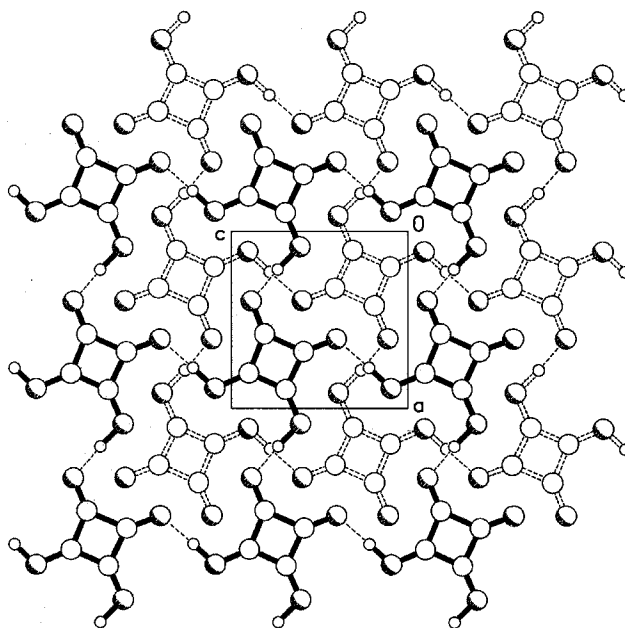


FIG. 2. Projection down the crystallographic  $b$  direction showing the offset stacking of hydrogen bonded sheets in the solid-state structure of squaric acid.

## A. SPECTROSCOPY OF THE SQUARATE ION

A detailed analysis of both the infrared and Raman spectra of squaric acid in the solid state has been carried out by Baglin and Rose (100) while Ito and West (101) have performed similar analyses on the squarate ion and its aqueous solution. The major absorptions associated with the non-ionized molecule are the C=O and C=C stretches at approximately  $1500\text{ cm}^{-1}$  and  $1640\text{ cm}^{-1}$ , respectively; the O—H stretching vibrations occur between  $2235$  and  $2275\text{ cm}^{-1}$  (Table I). However, for the symmetric  $\text{C}_4\text{O}_4^{2-}$  the C=O and C=C stretches occur at *ca.*  $1530$  and  $1090\text{ cm}^{-1}$ , respectively. The ultraviolet spectra recorded by Ireland and Walton (10) on aqueous solutions of squaric acid at different ionic strengths showed absorptions between  $220$  and  $300\text{ nm}$ , which were assumed to be due to electronic transitions from the highest energy bonding orbitals to the lowest energy antibonding orbitals in the squarate anion (84).

## B. COORDINATION MODES OF THE SQUARATE ION

Its exceptional versatility as a ligand is attributable to the fact that all four of its oxygen atoms are available as potential coordination sites. It has also been shown to adopt a range of different coordination modes, and sometimes combinations thereof, in its metal complexes; examples of monodentate, bismonodentate, bidentate, trismonodentate, and tetrakismonodentate coordination modes have been reported. In the complex  $[\text{Cu}(2,2'\text{-bipyrimidine})(\text{C}_4\text{O}_4)(\text{H}_2\text{O})_3] \cdot 2\text{H}_2\text{O}$  reported by Castro *et al.* (66), it coordinates monodentately (Fig. 3), while in  $\text{SrC}_4\text{O}_4 \cdot 3\text{H}_2\text{O}$  (35),  $[\text{Ce}(\text{H}_2\text{O})_2]_2(\text{C}_4\text{O}_4)_3$  (57), and  $\text{Pb}(\text{C}_4\text{O}_4)(\text{H}_2\text{O})_4$  (76) it is chelated (Fig. 4). It is interesting to note, however, that wherever there is chelation, the structures are polymeric, there being no structurally characterized examples of simple mononuclear, mono-, bis-, or trischelates. When the ligand coordination is bismonodentate, it is often achieved by bridging, either  $\mu$ -1,2 or  $\mu$ -1,3, although far more examples of the latter appear in the literature. The polymeric chain squarates  $\text{M}(\text{C}_4\text{O}_4) \cdot 4\text{H}_2\text{O}$  ( $\text{M} = \text{Mn}, \text{Fe}, \text{Co}, \text{Ni}$  and  $\text{Zn}$ ) (30) and  $\text{CuC}_4\text{O}_4 \cdot 2\text{H}_2\text{O}$  (33) are all examples of complexes in which the squarate ion exhibits  $\mu$ -1,3 bridging (Fig. 5), while in  $[\text{Cu}_2(\text{SalNEt}_2)_2(\text{H}_2\text{O})(\text{C}_4\text{O}_4)] \cdot \text{H}_2\text{O}$  [ $\text{SalNEt}_2 = N$ -(2-(diethylamino)ethyl)salicylideaminate] (64) and  $[\{\text{Ni}(\text{C}_4\text{O}_4)(\text{C}_{10}\text{H}_8\text{N}_2)(\text{H}_2\text{O})_2 \cdot 2\text{H}_2\text{O}\}_n]$  (41) it bridges adjacent metal atoms  $\mu$ -1,2 (Fig. 6). In  $[\text{Cu}(\text{H}_2\text{O})_2(\text{C}_4\text{O}_4)]_n$  (33) the squarate ion is coordinated in a trismonodentate fashion (Fig. 7). Bouayad *et al.* (102),

TABLE I

CHARACTERISTIC IR STRETCHING FREQUENCIES ( $\text{cm}^{-1}$ ) FOR SQUARIC ACID  
AND METAL SQUARATE COMPLEXES

	IR stretching frequencies ( $\text{cm}^{-1}$ )	Reference
Squaric acid	1822, 1643, 1513, 1380, 1360, 1318, 1245, 1166, 1070, 1056	100
Complex		
$\text{Ni}(\text{C}_4\text{O}_4)(\text{C}_3\text{N}_2\text{H}_4)_2(\text{H}_2\text{O})_2$	3250, 3050, 1480, 1100	19
$[\{\text{Ni}(\text{C}_4\text{O}_4)(\text{C}_{10}\text{H}_8\text{N}_2)(\text{H}_2\text{O})_2 \cdot 2\text{H}_2\text{O}\}_n]$	3140, 2920, 1550–1450	41
$[\text{Cu}(\text{C}_4\text{O}_4)(\text{imidazole})_2] \cdot 2\text{H}_2\text{O}$	1500	44
$[\text{Cu}_2(\text{bipy})_2(\text{C}_4\text{O}_4)(\text{H}_2\text{O})_4](\text{C}_4\text{O}_4\text{H})_2 \cdot 4\text{H}_2\text{O}$	1500	44
$[\text{Cu}_2(\text{bipy})_2(\text{C}_4\text{O}_4)(\text{H}_2\text{O})_2\text{Br}_2]$	1500	44
$[\text{Cu}_2(\text{bipy})_2(\text{OH})_2](\text{C}_4\text{O}_4) \cdot 4\text{H}_2\text{O}$	1500	50
$[\text{Fe}_2(\text{salen})_2(\text{CH}_3\text{OH})_2(\text{C}_4\text{O}_4)]$	1780, 1480	54
$[\text{Cu}(\text{bpy})(\text{H}_2\text{O})(\text{C}_4\text{O}_4)] \cdot \text{H}_2\text{O}$	1780, 1620, 1520, 1490, 1450	56
$[\text{Cu}_2(\text{bpy})_2(\text{H}_2\text{O})_2(\text{C}_4\text{O}_4)](\text{NO}_3)_2$	1730, 1610, 1525, 1480	56
$[\text{Cu}(\text{phen})(\text{H}_2\text{O})_2(\text{C}_4\text{O}_4)] \cdot 2\text{H}_2\text{O}$	1715, 1580, 1500	56
$[\text{Cu}(\text{terpy})(\text{H}_2\text{O})(\text{C}_4\text{O}_4)] \cdot \text{H}_2\text{O}$	1710, 1600, 1530	56
$[\text{Cu}_2(\text{terpy})_2(\text{H}_2\text{O})_2(\text{C}_4\text{O}_4)](\text{ClO}_4)_2$	1705, 1610, 1530, 1780	56
$[\text{Cu}_2(\text{pmdien})_2(\text{H}_2\text{O})_2(\text{C}_4\text{O}_4)](\text{NO}_3)_2$	1740, 1600, 1535, 1500	56
$[\text{Cu}(\text{mpym})(\text{H}_2\text{O})(\text{C}_4\text{O}_4)] \cdot 2\text{H}_2\text{O}$	3480, 1465	58
$[\text{Cu}_2(\text{bpca})_2(\text{H}_2\text{O})_2(\text{C}_4\text{O}_4)]$	1780, 1510–1570	59
$[\text{Cu}_2(\text{SalNEt}_2)_2(\text{H}_2\text{O})(\text{C}_4\text{O}_4)] \cdot \text{H}_2\text{O}$	1777, 1743, 1640, 1542, 1510, 1478, 1440	64
$[(n-\text{C}_4\text{H}_9)_4\text{N}][\text{V}_2\text{O}_3(\text{C}_4\text{O}_4)_2(\text{H}_2\text{O})_3] \cdot 3\text{H}_2\text{O}$	1787, 1665, 1522, 1374, 1060, 970, 879, 800, 736,	65
$[(\text{C}_4\text{H}_9)_4\text{N}]_4[\text{V}_4\text{O}_6(\text{C}_4\text{O}_4)_5(\text{H}_2\text{O})_4] \cdot 6\text{H}_2\text{O}$	1793, 1639, 1613, 1502, 1375, 988, 878, 800, 746,	65
$(\text{NH}_4)[\text{V}_2\text{O}_2(\text{OH})(\text{C}_4\text{O}_4)_2(\text{H}_2\text{O})_3] \cdot \text{H}_2\text{O}$	1793, 1624, 1518, 1092, 985, 744, 531	65
$[\text{Cu}(\text{bipym})(\text{C}_4\text{O}_4)(\text{H}_2\text{O})_3] \cdot 2\text{H}_2\text{O}$	1790, 1490	66
$[\text{Cu}_2(\text{bipym})(\text{C}_4\text{O}_4)_2(\text{H}_2\text{O})_6]$	1790, 1490	66
$[\text{Zn}(\text{C}_4\text{O}_4)(\text{H}_2\text{O})_2(\text{dmsO})_2]$	1593, 1560, 1518, 1400, 1322, 1100, 1025, 956, 707, 611, 510, 399, 351	69
$[\text{Ni}_2(\text{C}_4\text{O}_4)(\text{tren})_2(\text{H}_2\text{O})_2][\text{ClO}_4]_2$	1730, 1670, 1610, 1520	72
$[\text{Ni}_2(\text{TPPZ})(\text{H}_2\text{O})_6(\text{C}_4\text{O}_4)_2 \cdot 5\text{H}_2\text{O}]$	1631, 1597, 1473, 1303	74
$[\text{Cu}_2(\text{dpp})(\text{C}_4\text{O}_4)_2(\text{H}_2\text{O})_6]$	1490	78
$[\text{Fe}_2(\text{bpym})(\text{C}_4\text{O}_4)_2(\text{H}_2\text{O})_6] \cdot 2\text{H}_2\text{O}$	1510, 1796, 1790	79
$[\text{Cu}_2(\text{phen})_4(\text{C}_4\text{O}_4)](\text{CF}_3\text{SO}_3)_2 \cdot 3\text{H}_2\text{O}$	1770, 1705, 1640, 1520	80
$[\text{Cu}_2(\text{bipy})_4(\text{C}_4\text{O}_4)](\text{CF}_3\text{SO}_3)_2 \cdot 6\text{H}_2\text{O}$	1700, 1640, 1550	80
$[\text{Cu}_4(\text{tren})_4(\text{C}_4\text{O}_4)](\text{ClO}_4)_6$	1505	103

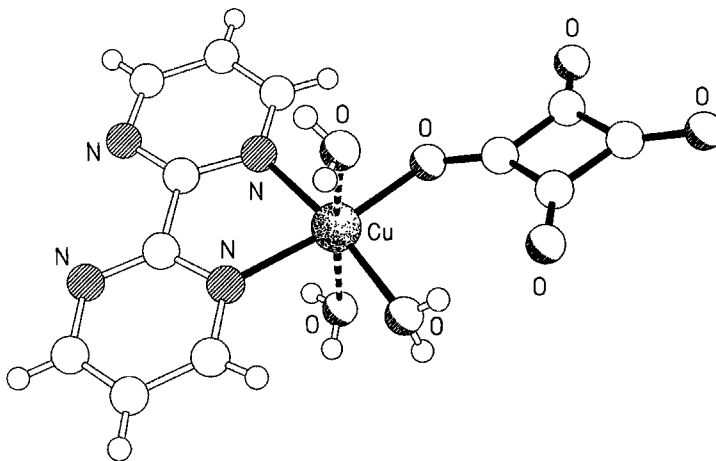


FIG. 3. The monodentate coordination of the squarate ligand to Cu(II) in the structure of  $[\text{Cu}(2,2'\text{-bipyrimidine})(\text{C}_4\text{O}_4)(\text{H}_2\text{O})_3] \cdot 2\text{H}_2\text{O}$  reported by Castro *et al.* (66).

Trombe *et al.* (57), and Castro *et al.* (103) reported the tetrakismonodentate coordination mode for the squarate ion in  $[\text{Ba}(\text{C}_4\text{O}_4)_{0.5}(\text{H}_2\text{O})_2]_2$ ,  $[\text{Cu}(\text{C}_4\text{O}_4)_2(\text{H}_2\text{O})_2]$ ,  $[\text{Ce}(\text{H}_2\text{O})_2]_4(\text{C}_4\text{O}_4)_6 \cdot 3\text{H}_2\text{O}$ , and  $[\text{Cu}_4(\text{tren})_4(\text{C}_4\text{O}_4)_4](\text{ClO}_4)_6$  [tren = tris(2-aminoethyl)amine], respectively (Fig. 8). (Note: A list of ligand names and their abbreviations is given in Table II.)

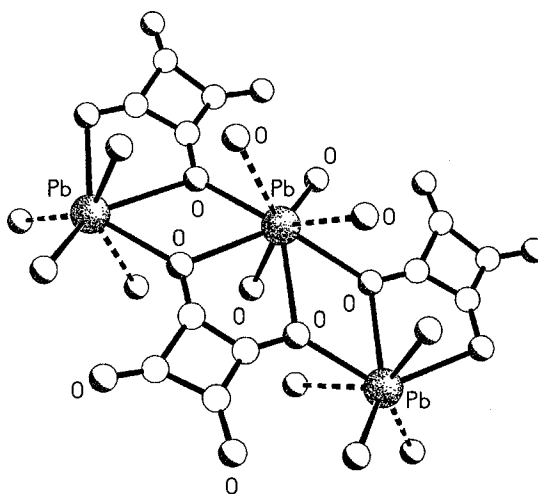


FIG. 4. Example of chelation by the squarate ligand to Pb(II) in the polymeric structure  $[\text{Pb}(\text{C}_4\text{O}_4)(\text{H}_2\text{O})_4]_n$  (76).

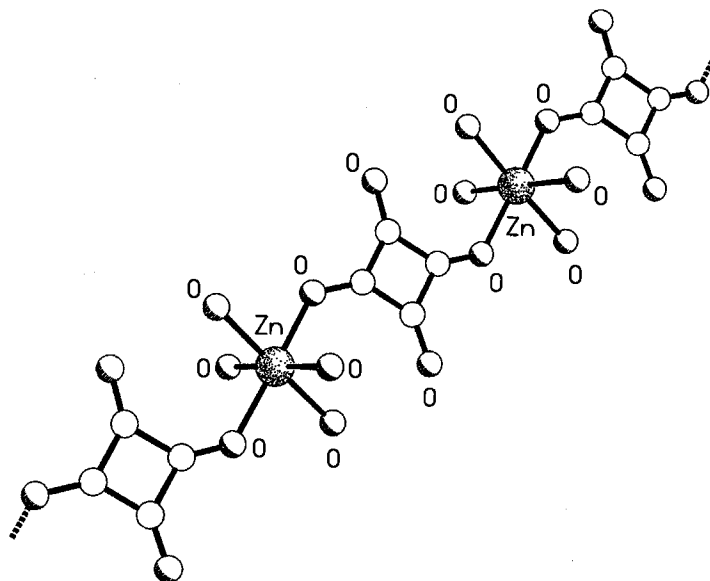


FIG. 5. The bismonodentate coordination and  $\mu$ -1,3-bridging modes of the squarate ligand to Zn(II) in the polymeric structure  $[\text{Zn}(\text{C}_4\text{O}_4)(\text{H}_2\text{O})_4]_n$  (30).

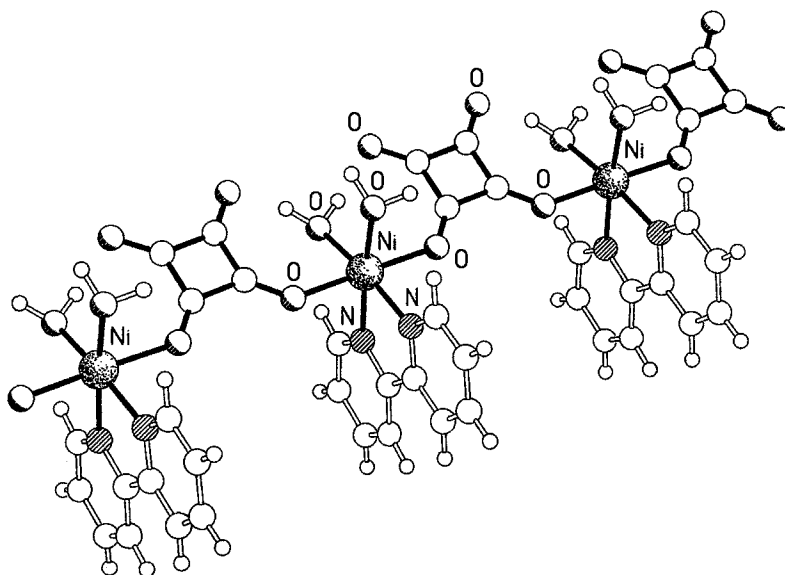


FIG. 6. The  $\mu$ -1,2-bridging mode of the squarate ligand to Ni(II) in the polymeric structure  $[\text{Ni}(\text{C}_4\text{O}_4)(\text{C}_{10}\text{H}_8\text{N}_2)(\text{H}_2\text{O})_2]_n$  (41).

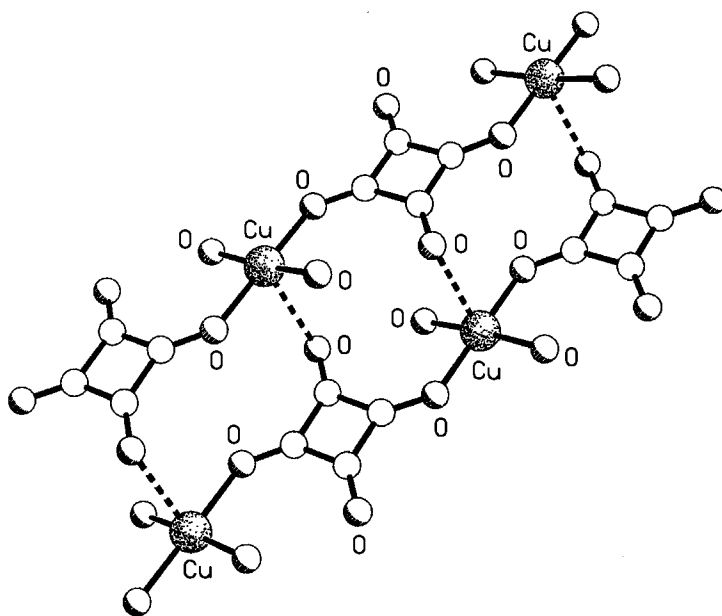


FIG. 7. The trismonodentate coordination of the squarate ion to Cu(II) in the polymeric structure  $[\text{Cu}(\text{C}_4\text{O}_4)(\text{H}_2\text{O})_2]_n$  (33).

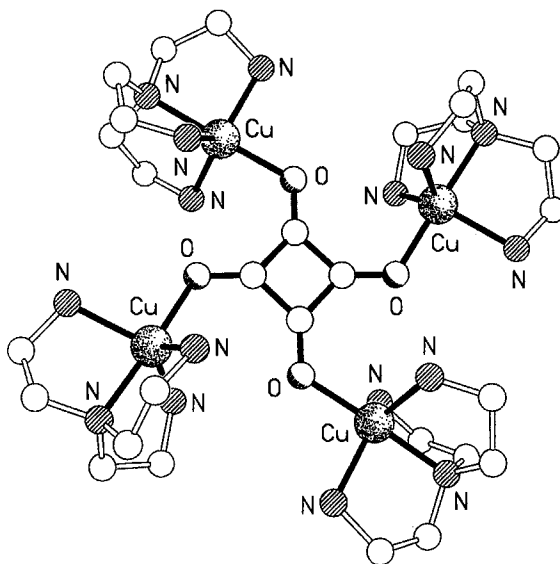


FIG. 8. The tetrakismonodentate coordination of the squarate ion to Cu(II) in the structure of  $[\text{Cu}_4(\text{tren})_4(\text{C}_4\text{O}_4)](\text{ClO}_4)_6$  [tren = tris(2-aminoethyl)amine] (103).

TABLE II

## LIGAND NAMES AND ABBREVIATIONS

---

bipy	= 2,2'-bipyridyl
bipym or bpym	= 2,2'-bipyrimidine
bpca	= bis(2-pyridylcarbonyl)amide anion
cyclen	= 1,4,7,10-tetraazacyclodecane
dmsO	= dimethylsulfoxide
dpp	= 2,3-bis(2-pyridyl)pyrazine
mpym	= 4-methoxy-2-(5-methoxy-3-methyl-1 <i>H</i> -pyrazol-1-yl)-6-methylpyrimidine
phen	= 1,10-phenanthroline
pmdien	= 1,1,4,7,7-pentamethyldiethylenetriamine
salen or SalNet <sub>2</sub>	= <i>N,N'</i> -ethylenebis(salicylideneamine)
terpy	= 2,2':6',2''-terpyridine
TPPZ	= 2,3,5,6-tetra(2-pyridyl)pyrazine
tren	= tris(2-aminoethyl)amine

---

Examples of the squarate ion exhibiting different combinations of mixed coordination modes occur in the tetranuclear complex  $[(C_4H_9)_4N]_4[V_4O_6(C_4O_4)_5(H_2O)_4] \cdot 6H_2O$  (65) synthesized by Khan *et al.* where the squarate ion adopts both  $\mu$ -1,2- and  $\mu$ -1,3-bridging roles (Fig. 9), while in  $[Eu(H_2O)_4]_2(C_4O_4)_3$  synthesized by Petit *et al.* (55),

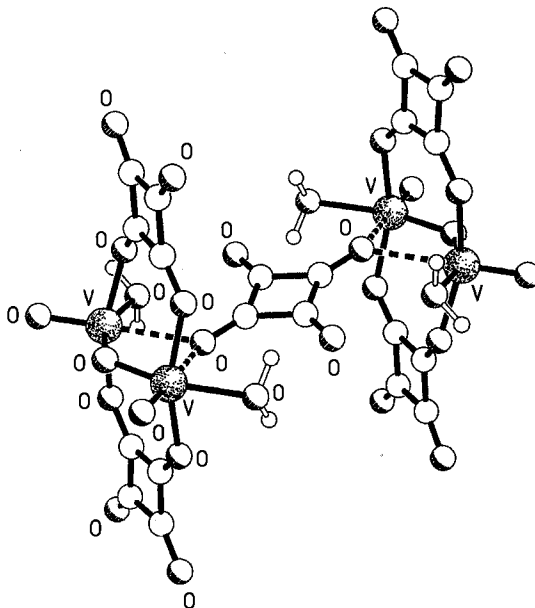


FIG. 9. The  $\mu$ -1,2- and  $\mu$ -1,3-bridging roles adopted by the squarate ion in the tetranuclear V(IV)/V(V) complex  $[(C_4H_9)_4N]_4[V_4O_6(C_4O_4)_5(H_2O)_4] \cdot 6H_2O$  (65).

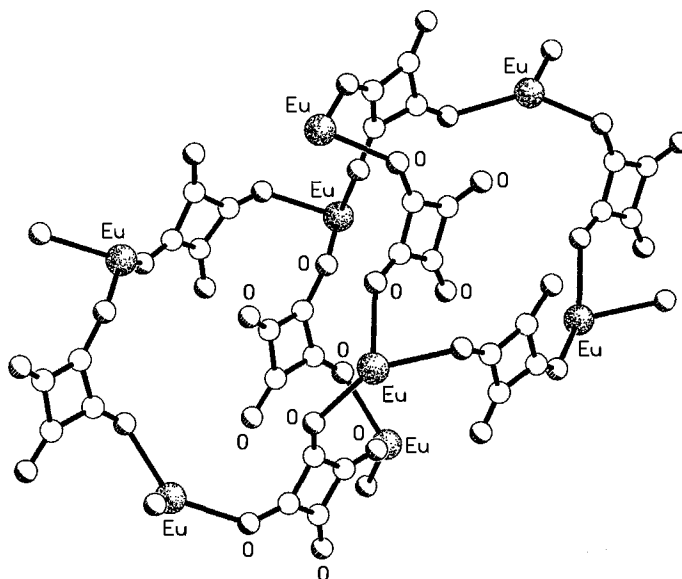


FIG. 10. The adoption of both bimonodentate and trismonodentate coordination roles by the squarate ion in the polymeric structure of the Eu(III) complex  $\{[\text{Eu}(\text{H}_2\text{O})_4]_2(\text{C}_4\text{O}_4)_3\}_n$  (55); the coordinated water molecules have been omitted for clarity.

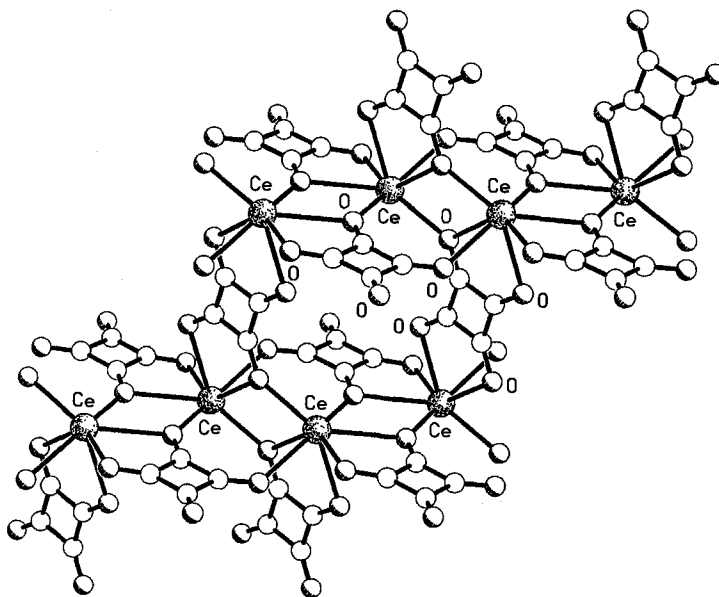


FIG. 11. The adoption of both mono- and bis-chelating coordination modes by the squarate ion to Ce(III) in the polymeric structure  $\{[\text{Ce}(\text{H}_2\text{O})_2]_2(\text{C}_4\text{O}_4)_3\}_n$  (57).

it adopts both bismonodentate and trismonodentate coordination roles (Fig. 10). By contrast, in the cerium(III) squarate  $[\text{Ce}(\text{H}_2\text{O})_2]_2(\text{C}_4\text{O}_4)_3$  prepared by Trombe *et al.* (57), the squarate ligand exhibits both mono- and bischelating coordination (Fig. 11).

## II. Squaric Acid Compounds

### A. SALTS OF SQUARIC ACID

Several salts of squaric acid have been synthesized. The significant resonance stabilization of the squarate anion confers on it the potential to form salts, especially in polar solvents and in the presence of stable cations. Peters *et al.* prepared a series of salts,  $\text{M}_2\text{C}_4\text{O}_4 \cdot x\text{H}_2\text{O}$  ( $\text{M} = \text{NH}_4$ , Na, Rb, Cs) (86). Other examples are  $\text{Cr}(\text{C}_4\text{O}_4)_{3/2} \cdot 7\text{H}_2\text{O}$  (22),  $\text{K}_2\text{C}_4\text{O}_4 \cdot \text{H}_2\text{O}$  (85),  $\text{PtBr}_2(\text{C}_2\text{H}_5\text{N}_2)_2[\text{C}_4\text{O}_4] \cdot 2\text{H}_2\text{O}$  (87),  $[\text{Ni}(\text{C}_2\text{H}_6\text{N}_4\text{O}_2)_2][\text{C}_4\text{O}_4]$  and  $[\text{Ni}(\text{C}_2\text{H}_5\text{N}_4\text{O}_2)(\text{C}_2\text{H}_6\text{N}_4\text{O}_2)]_2[\text{C}_4\text{O}_4]$  (88), and  $[\text{Pt}(\text{NH}_3)_4\text{Cl}_2]\text{C}_4\text{O}_4$  (90). In the majority of these salts the squarate ion is stated to have  $D_{4h}$  symmetry, which would be consistent with the complete delocalization of its  $\pi$  electrons (22, 85–88). Unfortunately, in most of these examples the experimental errors are so large that the assumption of the equivalence in the bond lengths should be treated with caution (Table III). However, in the structure of  $[\text{Ni}(\text{C}_2\text{H}_6\text{N}_4\text{O}_2)_2][\text{C}_4\text{O}_4]$ , the estimated standard deviations (esds) are small and the four C–C bond lengths in the squarate ion are, within statistical significance, the same, although the C=O distances differ (Fig. 12, Table III). In the report on the structure of  $[\text{Pt}(\text{NH}_3)_4\text{Cl}_2]\text{C}_4\text{O}_4$ , it is claimed that the squarate anion is distorted owing to hydrogen bonding with the ammine groups coordinated to the platinum atom (90), although the differences in bond lengths are not statistically significant (Table III).

### B. SQUARATE COMPLEXES

By far the major focus of research into squaric acid chemistry has, however, been on its complexing properties with a variety of metals, including main-group, transition, and lanthanide elements (9–82); a uranium complex has also been reported (25). A multitude of such complexes, exhibiting a significant structural diversity, which is largely a consequence of its versatility with respect to its coordination modes, have been synthesized. Included in this wide variety of structural types (9–82) are monomers, dimers, trimers, tetramers, linear chain polymers, single- and double-tiered sheets, and a range of cage compounds.

TABLE III

C<sub>4</sub> RING C—C AND C—O BOND LENGTHS (Å) IN SQUARATE SALTS

Salt	Bond lengths		Reference
	C—C	C—O	
Cr(C <sub>4</sub> O <sub>4</sub> ) <sub>3/2</sub> · 7H <sub>2</sub> O	1.447(4)	1.262(5)	22
	1.469(4)	1.253(5)	
	1.459(4)	1.255(5)	
	1.458(4)	1.256(5)	
[Ni(cyclen)(H <sub>2</sub> O) <sub>2</sub> ] <sub>2</sub> (C <sub>4</sub> O <sub>4</sub> )(ClO <sub>4</sub> ) <sub>2</sub>	1.467(6)	1.26(1)	49, 89
	1.42(2)	1.23(1)	
	1.49(1)	1.28(1)	
	1.452(6)	1.24(1)	
K <sub>2</sub> C <sub>4</sub> O <sub>4</sub> · H <sub>2</sub> O	1.469(8)	1.260(7)	85
	1.444(8)	1.258(7)	
[PtBr <sub>2</sub> (C <sub>2</sub> H <sub>8</sub> N <sub>2</sub> ) <sub>2</sub> ][C <sub>4</sub> O <sub>4</sub> ] · 2H <sub>2</sub> O	1.44(3)	1.30(3)	87
	1.45(3)	1.24(3)	
[Ni(C <sub>2</sub> H <sub>6</sub> N <sub>4</sub> O <sub>2</sub> ) <sub>2</sub> ][C <sub>4</sub> O <sub>4</sub> ]	1.464(2)	1.243(2)	88
		1.259(2)	
[Ni(C <sub>2</sub> H <sub>5</sub> N <sub>4</sub> O <sub>2</sub> )(C <sub>2</sub> H <sub>6</sub> N <sub>4</sub> O <sub>2</sub> ) <sub>2</sub> ] <sub>2</sub> [C <sub>4</sub> O <sub>4</sub> ]	1.43(4)	1.29(3)	88
	1.47(4)	1.28(3)	
[Pt(NH <sub>3</sub> ) <sub>4</sub> Cl <sub>2</sub> ][C <sub>4</sub> O <sub>4</sub> ]	1.46(3)	1.26(3)	90
	1.54(2)	1.26(2)	
	1.45(3)	1.24(3)	
	1.40(2)	1.27(2)	

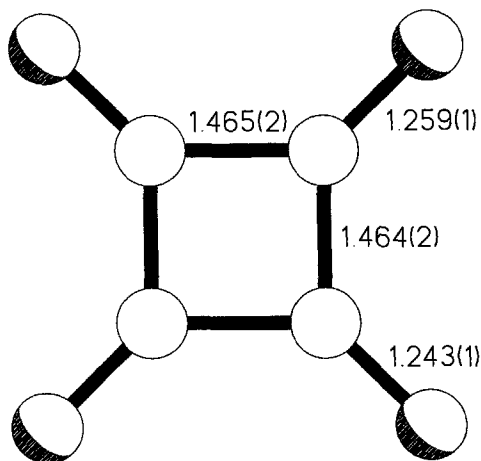


FIG. 12. The  $D_{4h}$  symmetric pattern of bonding in the C<sub>4</sub> ring in the Ni(II) salt [C<sub>4</sub>O<sub>4</sub>]<sup>2-</sup> [Ni(C<sub>2</sub>H<sub>6</sub>N<sub>4</sub>O<sub>2</sub>)<sub>2</sub>]<sup>2+</sup> (88); the crystallographic symmetry is  $C_i$ .

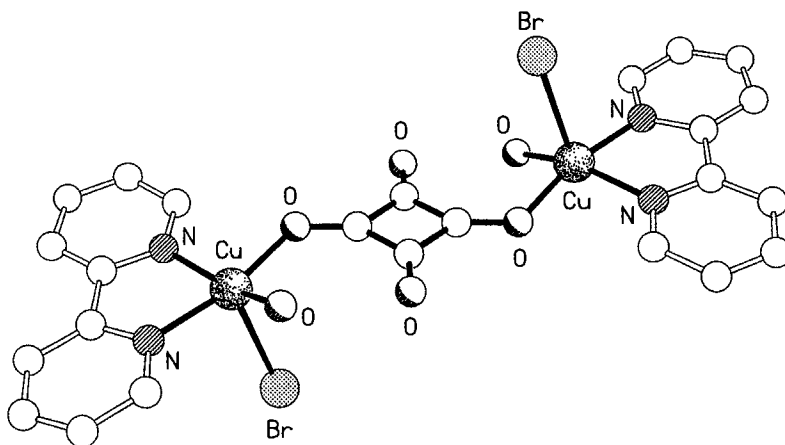


FIG. 13. The simple  $\mu$ -1,3-bridging by the squarate ion of a pair of transition metal complexes in the structure of  $[(\mu_2\text{-squarato-}O,O')\text{-bis(aqua-bromo-(2,2'\text{-bipyridyl-}N,N'))\text{-copper(II)}]]$  (44).

Hydrogen bonding plays a role in the formation of several of these networks, as described by Lee *et al.* (71). The formation of short chains is preponderant where mixed ligand systems were used in synthesis (27, 41, 43–46, 48, 49, 54, 56, 59, 63–66, 72, 74, 78–80, 103). In all these examples, however, the structure contains only one or two squarate ligands having either a single squarate ligand bridge between a pair of metal complexes (Fig. 13) or a pair of terminal ligands on either side of the complex (Fig. 14).

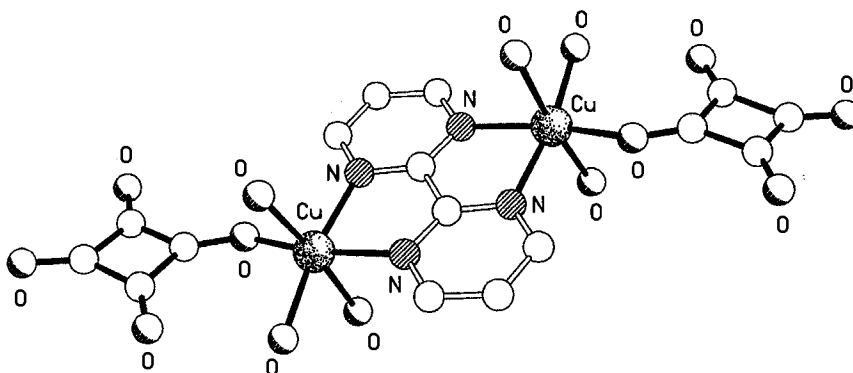


FIG. 14. The monodentate coordination of a pair of terminal squarate ligands on either side of a metal complex in the structure of  $[(\mu_2\text{-2,2'\text{-bipyrimidine})\text{bis(triaqua-(3,4-dihydroxycyclobut-3-ene-1,2-dione))copper(II)}]]$  (66).

First-row transition metal complexes were some of the earliest inorganic squaric acid compounds to be synthesized. While the majority of workers, using aqueous and alcoholic solutions, carried out their syntheses in the presence of moisture and oxygen, Hall *et al.* used dried solvents and anaerobic conditions for their preparations (26, 29, 37, 38, 47, 53). They claimed, on the basis of solid-state UV/vis spectroscopy and IR spectroscopy [and, additionally, EXAFS spectrometry in the case of the copper(II) complex] (26, 29, 37, 38, 47, 53), to have synthesized five-coordinate iron(II), cobalt(II), and nickel(II) complexes as well as a square planar copper(II) squarate complex with bidentate squarate groups. Other earlier workers also proposed, again solely on the basis of spectroscopic evidence (9, 12, 20, 104, 105), structures with bidentate squarate groups for several first-row transition metal complexes. It was subsequently indicated, however, by bite-parameter calculations, that the squarate ligand should not be able to coordinate bidentately with such small metal cations (56). Indeed, it was later shown by single-crystal X-ray structural analysis that the complexes  $[M(C_4O_4) \cdot 4H_2O]$  [ $M = Mn(II), Fe(II), Co(II), Ni(II), Zn(II)$ ] and  $CuC_4O_4 \cdot 4H_2O$ , which were originally assumed to have bidentate squarate groups, are in fact chain squarates in which the ligand is coordinated monodentately to two neighboring metal centers, which it bridges  $\mu$ -1,3 (see Fig. 5). It should be noted, however, that the analogous thiosquarate ligand is able to form chelates with first-row transition metals (106–109) even though its bite parameter is smaller than that of squaric acid because of the enhanced pliability of the metal-sulfur bonds (Fig. 15). Examples such as  $SrC_4O_4 \cdot 3H_2O$  (35),  $[Ce(H_2O)_2]_2(C_4O_4)_3$  (57), and  $Pb(C_4O_4)(H_2O)_4$  (76), in which the squarate ligand is chelated, all contain metals with sufficiently large ionic radii.

### C. MAGNETOCHEMISTRY AND OTHER ELECTRON-TRANSFER PHENOMENA

The squarate ion was assumed to have the potential for mediating magnetic interactions between metal centers because it appeared to provide a suitable conduit through which electron transfer would be possible. This potential was considered to be especially important in light of the fact that the analogous oxalate ion does not function efficiently in a similar capacity. Thus, magnetochemical analyses were performed by several investigators in order to explore this potential. Some researchers focused their attention on the linear chain squarates in which the ligand bridged  $\mu$ -1,3 in order to ascertain their suitability as precursors for molecular magnets (61), while others concentrated on different structural types. No significant antiferromagnetic

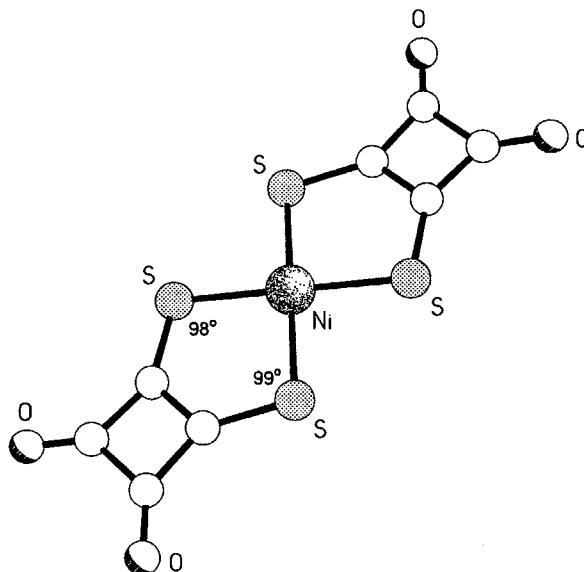


FIG. 15. The reduced valence angles at sulfur that, in conjunction with the longer C—S and M—S distances, permit the chelation of a pair of thiosquarate ligands by a first-row transition metal in the structure of the Ni(II) complex  $K_2[Ni(S_2C_4O_4)_2] \cdot 2H_2O$  (107).

interactions were observed in the one-dimensional polymer  $NiC_4O_4(C_3N_2H_4)_2(H_2O)_2$  reported by van Ooijen *et al.* (19), nor in a series of chromium(III) squarato-bridged complexes synthesized by Bang *et al.* (43). Other examples of complexes in which antiferromagnetic coupling through bridging squarate groups was essentially insignificant include  $Fe(C_4O_4)(C_4H_4N_2) \cdot 4.5H_2O$  (20),  $[Cu(mpym)(H_2O)(C_4O_4)] \cdot 2H_2O$  [mpym = 4-methoxy-2-(5-methoxy-3-methyl-1H-pyrazoyl-1-yl)-6-methylpyrimidine] (58), and  $[Ni_2(C_4O_4)(tren)_2(H_2O)_2][ClO_4]_2$  [tren = tris(2-aminoethyl)amine] (72). However, it was shown subsequently by molecular orbital calculations that the poor overlap between the squarate ligand orbitals and the metal orbitals due to the disparity in energy militated against any significant electron transfer between adjacent metal centers (64). In the complex  $[Cu_2(SalNet_2)_2(H_2O)(C_4O_4)] \cdot H_2O$ , where the ligand bridges  $\mu$ -1,2, the squarate ring geometry changes from square to trapezoidal with an accompanying lowering of its symmetry from  $D_{4h}$  to  $C_{2v}$  (64) (Table IV). The significant antiferromagnetic interactions observed in this and related complexes were attributed to enhanced overlap of the now more energetically compatible metal and ligand orbitals. However, none of

TABLE IV

C<sub>4</sub> RING C—C AND C—O BOND LENGTHS (Å) IN METAL SQUARATE COMPLEXES

Complex	Bond lengths		Mode ( $\mu$ -1,2, $\mu$ -1,3)	Reference
	C—C	C—O		
Ni(C <sub>4</sub> O <sub>4</sub> )(C <sub>3</sub> N <sub>2</sub> H <sub>4</sub> ) <sub>2</sub> (H <sub>2</sub> O) <sub>2</sub>	1.463(2)	1.250(2)	$\mu$ -1,3	19
	1.470(2)	1.252(2)		
[Ni(C <sub>4</sub> O <sub>4</sub> )(C <sub>10</sub> H <sub>8</sub> N <sub>2</sub> )(H <sub>2</sub> O) <sub>2</sub> · 2H <sub>2</sub> O] <sub>n</sub>	1.465(6)	1.249(5)	$\mu$ -1,2	41
	1.448(6)	1.259(5)		
	1.454(6)	1.255(5)		
	1.471(6)	1.258(5)		
[Cu(C <sub>4</sub> O <sub>4</sub> )(imidazole) <sub>2</sub> ] · 2H <sub>2</sub> O	1.55(1)	1.24(1)	$\mu$ -1,3	44
	1.49(1)	1.23(1)		
[Cu <sub>2</sub> (bipy) <sub>2</sub> (OH) <sub>2</sub> ](C <sub>4</sub> O <sub>4</sub> ) · 4H <sub>2</sub> O	1.471(3)	1.252(3)	$\mu$ -1,3	50
	1.460(4)	1.248(4)		
[Fe <sub>2</sub> (salen) <sub>2</sub> (CH <sub>3</sub> OH) <sub>2</sub> (C <sub>4</sub> O <sub>4</sub> )]	1.439(7)	1.290(3)	$\mu$ -1,3	54
	1.476(7)	1.260(6)		
[Cu <sub>2</sub> (bpy)(H <sub>2</sub> O)(C <sub>4</sub> O <sub>4</sub> )] · H <sub>2</sub> O	1.446(5)	1.267(5)	1,2,3 tris mono	56
	1.468(5)	1.240(4)		
	1.491(5)	1.252(5)		
	1.465(5)			
[Cu <sub>2</sub> (bpy) <sub>2</sub> (H <sub>2</sub> O) <sub>2</sub> (C <sub>4</sub> O <sub>4</sub> )](NO <sub>3</sub> ) <sub>2</sub>	1.456(4)	1.248(3)	$\mu$ -1,3	56
	1.465(4)	1.247(3)		
[Cu(phen)(H <sub>2</sub> O) <sub>2</sub> (C <sub>4</sub> O <sub>4</sub> )] · 2H <sub>2</sub> O	1.460(4)	1.257(3)	mono, terminal	56
	1.482(4)	1.252(4)		
	1.484(4)	1.245(3)		
	1.456(4)	1.257(4)		
[Cu(terpy)(H <sub>2</sub> O)(C <sub>4</sub> O <sub>4</sub> )] · H <sub>2</sub> O	1.448(7)	1.257(6)	$\mu$ -1,2	56
	1.445(8)	1.276(6)		
	1.462(8)	1.246(7)		
	1.458(7)	1.257(6)		
[Cu <sub>2</sub> (terpy) <sub>2</sub> (H <sub>2</sub> O) <sub>2</sub> (C <sub>4</sub> O <sub>4</sub> )](ClO <sub>4</sub> ) <sub>2</sub>	1.461(7)	1.255(6)	$\mu$ -1,3	56
	1.486(6)	1.230(6)		
[Cu <sub>2</sub> (pmdien) <sub>2</sub> (H <sub>2</sub> O) <sub>2</sub> (C <sub>4</sub> O <sub>4</sub> )](NO <sub>3</sub> ) <sub>2</sub>	1.446(6)	1.265(5)	$\mu$ -1,3	56
	1.476(6)	1.250(5)		
[Cu(mpy) <sub>2</sub> (H <sub>2</sub> O)(C <sub>4</sub> O <sub>4</sub> )] · 2H <sub>2</sub> O	1.438(6)	1.266(5)	$\mu$ -1,3	58
	1.462(6)	1.244(6)		
	1.469(6)	1.258(5)		
	1.464(6)	1.245(6)		
[Cu <sub>2</sub> (bpca) <sub>2</sub> (H <sub>2</sub> O) <sub>2</sub> (C <sub>4</sub> O <sub>4</sub> )]	1.467(4)	1.268(3)	$\mu$ -1,3	59
	1.449(4)	1.245(4)		
[Cu <sub>2</sub> (SalNEt <sub>2</sub> ) <sub>2</sub> (H <sub>2</sub> O)(C <sub>4</sub> O <sub>4</sub> )] · H <sub>2</sub> O	1.428(4)	1.264(4)	$\mu$ -1,2	64
	1.451(5)	1.281(4)		
	1.489(5)	1.237(4)		
	1.470(4)	1.230(4)		
(NH <sub>4</sub> )[V <sub>2</sub> O <sub>2</sub> (OH)(C <sub>4</sub> O <sub>4</sub> ) <sub>2</sub> (H <sub>2</sub> O) <sub>3</sub> ] · H <sub>2</sub> O	1.43(3)	1.25(3)	$\mu$ -1,2	65
	1.51(4)	1.20(3)		
	1.46(3)	1.30(3)		
	1.35(4)	1.27(3)		

(continued)

TABLE IV (continued)

Complex	Bond Lengths		Mode	Reference
	C—C	C—O	( $\mu$ -1,2, $\mu$ -1,3)	
$[(n\text{-C}_4\text{H}_9)_4\text{N}][\text{V}_2\text{O}_3(\text{C}_4\text{O}_4)_2(\text{H}_2\text{O})_3] \cdot 3\text{H}_2\text{O}$	1.466(13)	1.247(11)	$\mu$ -1,2	65
	1.466(10)	1.240(9)		
	1.463(13)	1.276(10)		
	1.419(10)	1.272(9)		
$[\text{Cu}(\text{bipym})(\text{C}_4\text{O}_4)(\text{H}_2\text{O})_3] \cdot 2\text{H}_2\text{O}$	1.445(3)	1.260(3)	mono, terminal	66
	1.467(3)	1.265(2)		
	1.457(3)	1.241(2)		
	1.475(3)	1.244(3)		
$[\text{Cu}_2(\text{bipym})(\text{C}_4\text{O}_4)(\text{H}_2\text{O})_6]$	1.458(3)	1.240(2)	mono, terminal	66
	1.492(3)	1.269(3)		
	1.430(3)	1.260(2)		
	1.468(3)	1.241(3)		
$\text{Ni}_2(\text{C}_4\text{O}_4)(\text{tren})_2(\text{H}_2\text{O})_2[\text{ClO}_4]_2$	1.456(3)	1.245(3)	$\mu$ -1,2	72
	1.469(3)	1.262(3)		
	1.450(3)	1.257(3)		
	1.457(3)	1.254(3)		
$[\text{Cu}_2(\text{dpp})(\text{C}_4\text{O}_4)_2(\text{H}_2\text{O})_6]$	1.447(4)	1.259(3)	mono, terminal	78
	1.453(4)	1.247(4)		
	1.489(4)	1.242(4)		
	1.470(4)	1.249(4)		
$[\text{Fe}_2(\text{bpym})(\text{C}_4\text{O}_4)_2(\text{H}_2\text{O})_6] \cdot 2\text{H}_2\text{O}$	1.453(4)	1.254(4)	mono, terminal	79
	1.463(4)	1.252(4)		
	1.475(4)	1.248(4)		
	1.479(4)	1.256(3)		
$[\text{Cu}_2(\text{phen})_4(\text{C}_4\text{O}_4)](\text{CF}_3\text{SO}_3)_2 \cdot 3\text{H}_2\text{O}$	1.409(14)	1.285(11)	$\mu$ -1,2	80
	1.49(2)	1.275(11)		
	1.462(15)	1.224(12)		
	1.51(2)	1.229(13)		
$[\text{Cu}_2(\text{bipy})_4(\text{C}_4\text{O}_4)](\text{CF}_3\text{SO}_3)_2 \cdot 6\text{H}_2\text{O}$	1.460(5)	1.254(4)	$\mu$ -1,3	80
	1.468(4)	1.239(4)		
$[\text{Cu}_4(\text{tren})_4(\text{C}_4\text{O}_4)](\text{ClO}_4)_6$	1.44(1)	1.27(1)	$\mu$ -1,2,3,4	103
	1.46(1)	1.27(1)		

these complexes is polymeric and all contain ligand groups in addition to squarate. Mixed ligand systems have also been utilized by several workers as a means of controlling polymerization in their syntheses of squarate complexes, which were used for a variety of magnetochemical analyses. For example, Castro *et al.* used the tetradentate ligand tris(2-aminoethyl)amine (tren) as a blocking group in the synthesis of  $[\text{Ni}_2(\text{C}_4\text{O}_4)(\text{tren})_2(\text{H}_2\text{O})_2][\text{ClO}_4]_2$  (72). Bis(2-pyridylmethyl)amine (43),  $[\text{N},\text{N}'\text{-ethylenebis(salicylideneaminato)}]$  (salen) (54), 2,2'-bipyridyl (50),

and [2,3,5,6-tetra(2-pyridyl)pyrazine] (TPPZ) (74) are some other examples of ligands similarly used as peripheral groups.

The squarate ion is also assumed to have the potential for providing a pathway for electron conduction when it bridges metal atoms in polymeric complexes (61). Some workers have used partial oxidation to enhance the possibility that compounds will exhibit conductivity. For example, Toftlund (110) showed that the partially oxidized platinum salt  $K_2[Pt(C_4O_4)_2] \cdot 2H_2O$  has the properties of a one-dimensional conductor, while Wroblewski and Brown (18) reported that some mixed-valence iron squarate complexes display semiconductivity.

Attempts were made by Bouayad *et al.* at synthesizing heterobimetallic complexes using the squarate ion as potential precursors for high- $T_c$  superconductors (102). To this end La/Cu, Gd/Cu, and Ba/Cu complexes were synthesized with a view to achieving this objective (62, 102). They also contemplated the possibility of synthesizing heterobimetallic complexes with the potential to function as molecular ferromagnets (102). However, in the complex they studied,  $\{[Gd_2Cu(C_4O_4)_4(H_2O)_{12}] \cdot 2H_2O\}$

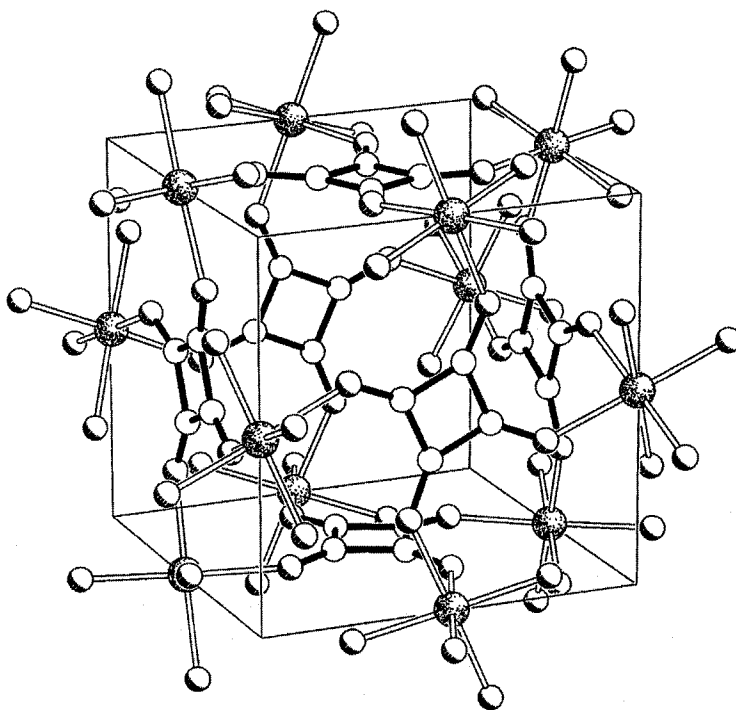


FIG. 16. Part of the "cubic" network structure formed by the Ni(II) complex  $[Ni(C_4O_4)(H_2O)_2]_3 \cdot CH_3COOH \cdot H_2O$  (31), showing the staggered relationship between the  $C_4$  rings on opposite faces.

(62), no significant spin coupling between the copper and gadolinium centers was observed. This they attributed to the poor overlap between the copper and gadolinium orbitals due to the Cu-squarate-Gd geometry and the inherent "innerness" of *f* orbitals in lanthanide metals. Insignificant metal-metal orbital overlap also militated against the complexes showing potential as superconductors.

#### D. CUBIC STRUCTURES

Weiss *et al.* synthesized a number of first-row transition metal squarates with "cubic cages." In the complexes  $(MC_4O_4 \cdot 2H_2O)_3 \cdot CH_3COOH \cdot H_2O$  [ $M = Zn(II), Ni(II)$ ] (31), which crystallize in the  $Pn3n$  space group, the squarate moieties on opposite cube faces are staggered (Fig. 16). In the related Fe(II) complex  $Fe(C_4O_4)(H_2O)_2$  (71), which crystallizes in the space group  $R\bar{3}$ , opposite faces are eclipsed (Fig. 17), as is the case in complexes [ $M = Zn(II), Mn(II)$ ] (32) that crystallize in

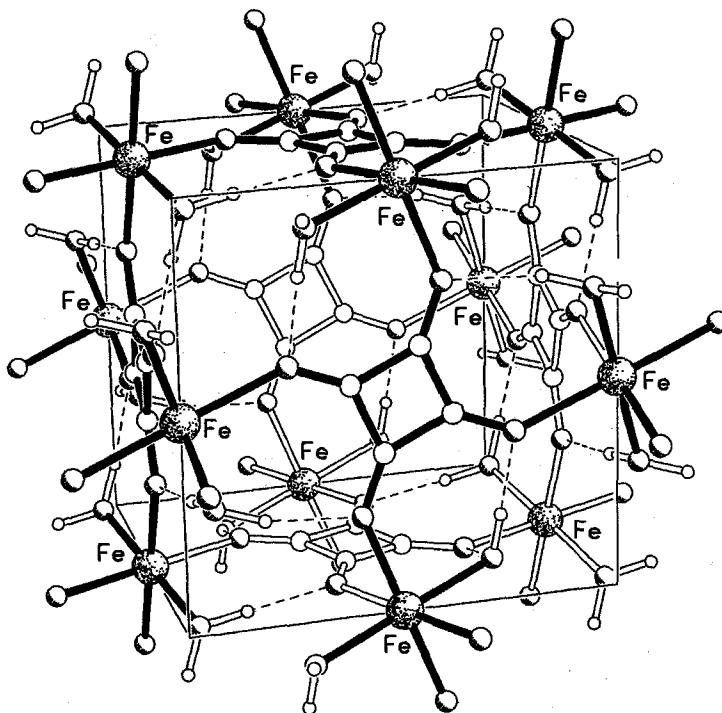


FIG. 17. Part of the "cubic" network structure formed by the Fe(II) complex  $[Fe(C_4O_4)(H_2O)_2]$  (71), showing the eclipsed relationship between the  $C_4$  rings on opposite faces and the stabilization of the network by intramolecular hydrogen bonds.

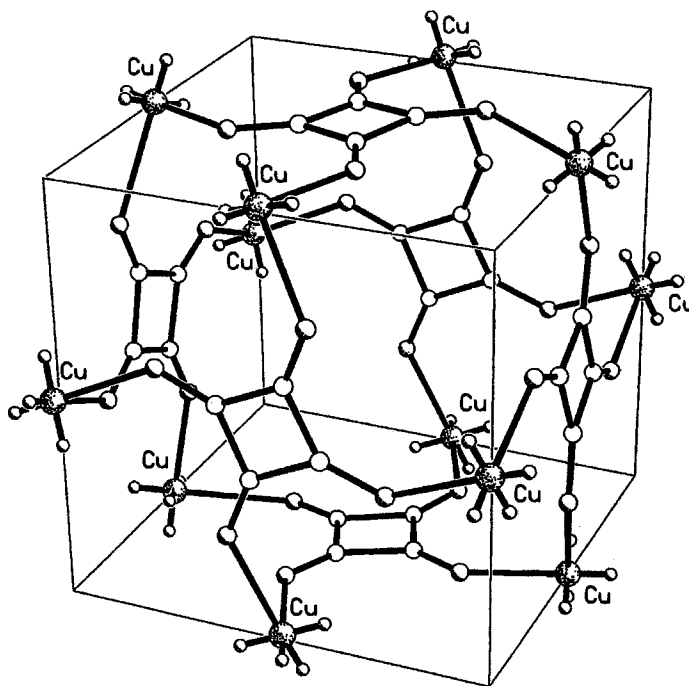


FIG. 18. Part of the "cubic" network structure formed by the Cu(II) complex  $[\text{Cu}(\text{C}_4\text{O}_4)(\text{H}_2\text{O})_2] \cdot 0.5\text{H}_2\text{O}$  (*111*) showing the presence of both eclipsed and staggered relationships between the  $\text{C}_4$  rings on opposite faces; the lengths of the bonds linking to the oxygen atoms in adjacent "cubes" have been shortened for illustrative purposes.

the space group  $P\bar{1}$ . In the copper complex  $[\text{Cu}(\text{C}_4\text{O}_4)(\text{H}_2\text{O})_2] \cdot 0.5\text{H}_2\text{O}$  unexpectedly produced by the hydrolysis of the methoxy group during the attempted preparation of a copper(II) methoxysquarate (*111*), a mixture of eclipsed and staggered geometries is observed, the complex crystallizing in the space group  $P4/n$  (Fig. 18). These examples, we believe, represent the only reported three-dimensional "cubic" complexes of the squarate ligand.

#### E. SQUARATE COMPLEXES OF HEAVIER TRANSITION METALS AND LANTHANIDES

Although there are several examples of lanthanide complexes with the squarate ion (42, 55, 57), only a few squarate complexes of second- and third-row transition metals have been reported. The platinum and

molybdenum complexes synthesized by Bernardinelli *et al.* and Hilbers *et al.*, respectively, make up the majority of complexes of the second- and third-row transition metal squarates described in the literature (28, 70, 90). Other examples of complexes of the heavier transition metals include the two dinuclear palladium complexes reported by Crispini *et al.* (82) and the rhodium(I) complexes prepared by Dhillon *et al.* (73).

The lanthanide metals, with their larger coordination numbers, invariably have the ligand coordinated in either a trismonodentate or a tetrakismonodentate fashion (42, 55, 57) (see Figs. 10 and 11). Thus, the ligand apparently tends toward the maximization of its coordinating capacity where circumstances allow, giving rise in many cases to the formation of sheet or cage structures. Limited chain formation was observed in the platinum, palladium, and rhodium complexes described, while the molybdenum complexes described by Hilbers *et al.* consist of dinuclear and tetranuclear units.

#### F. THE SQUARATE ION AS A LINKING GROUP

There are several examples of the utilization of the proven linking ability of the squarate ligand in the assembly of three-dimensional structures. For example, Yaghi *et al.* used manganese(II) and zinc(II) squarates in their study of the development and understanding of structural control in solid-state materials (69). Lin and Lii used the squarate ion as a bridging ligand in the self-assembly of inorganic polymers (112). Chen *et al.* explored the suitability of the squarate ion as an alternative to  $\text{MoO}_4^{2-}$  in the design of useful polymetalate structures (45, 46), while Muller *et al.* employed it in their study on the control of linkages in the design of engineering materials (113). Hydrothermal synthesis was the technique of choice in several studies designed to produce materials with desirable structural properties. Gutschke *et al.* used the squarate ion in the preparation of a microporous cobalt squarate (75); Lin and Lii (112), to synthesize polymeric vanadium complexes, and Trombe *et al.*, to assemble dehydrated cerium phases (57). Yaghi *et al.* (68) used silica gel as a crystallization medium for obtaining crystals of  $\text{Cu}(1,4\text{-C}_4\text{H}_4\text{N}_2)(\text{C}_4\text{O}_4)(\text{H}_2\text{O})_4$  in their research on the synthesis of three-dimensional solids.

The squarate ligand has also been used by Zou *et al.* (114, 115) as an oxygen-ligating leaving group in studies on antitumor activity. Its ability to function as a bridging ligand has also been exploited in the synthesis of gadolinium(III) complexes for use in biochemical applications (116, 117).

### G. SPECTROSCOPY OF SQUARATE COMPLEXES

Infrared and UV/vis data have been used by several authors to identify the C=C, C=O, and M-O stretches in the complexes synthesized (15, 18-21, 37, 38, 41, 44, 50, 54, 56, 58, 59, 64-66, 69, 74, 78, 80, 82, 103). Except in the initial research on first-row transition metal complexes of squaric acid, where these data were used in proposing structures, IR and UV/vis analysis have been used as supporting evidence for the particular coordination mode of the ligand (19, 21, 22, 45, 52, 59, 65). Infrared spectroscopy has also been utilized in the study of mixed oxalate/squarate complexes (118), although not to the same extent as in complexes of the oxalate ion. For example, Scott *et al.* studied the IR properties of Co(III) oxalate complexes with the ligand in a variety of chelating/bridging situations (119).

The O-H stretching vibrations between 3400 and 3600  $\text{cm}^{-1}$ , which broaden and shift to lower frequencies when hydrogen bonding occurs, were rarely mentioned in reports on metal squarate complexes (19, 41, 58) (Table I). However, the other characteristic peaks of the squarate ion, especially those observed *ca.* 1500, 1600, and 1750  $\text{cm}^{-1}$ , which correspond to C=C/C=O, C=C, and C=O stretching, respectively, were always included in IR spectral data of these complexes (15, 18-21, 37, 38, 41, 44, 50, 54, 56, 58, 59, 64-66, 69, 74, 78, 80, 82, 103) (Table I). Some authors used the differences between the C-O and C-C stretching frequencies in the IR spectra of the metal complexes and the squarate ion to assess changes in the extent of delocalization on complexation (44, 54, 59). In several examples, metal-oxygen and metal-halogen stretches in the far-infrared region were also reported (19, 20, 37, 53). The UV/vis spectra have almost invariably been used to ascertain the coordination polyhedron adopted by the metal in the squarate complexes (19, 37, 38, 41, 53).

### H. LUMINESCENCE STUDIES

The luminescence characteristics of europium(III) squarate at room temperature and 4 K, respectively, have been reported by Donega *et al.*, Legendziewicz, and Ribeiro *et al.* (120-122) and indicated a temperature dependence subsequently investigated by Alleyne *et al.* (123). The temperature-dependent, strong and multidimensional europium-europium electronic interactions observed from the luminescence decay dynamics of europium(III) squarate led Alleyne *et al.* to postulate that the energy transport process in the complex was in the dynamic regime (123). Huskowska *et al.* (124) also conducted luminescence studies on neodymium squarate,  $[\text{Nd}_2(\text{C}_4\text{O}_4)_3(\text{H}_2\text{O})_{11}] \cdot 2\text{H}_2\text{O}$ ,

which indicated the presence of neodymium atoms in two different coordination polyhedra in the complex; this was confirmed by single-crystal X-ray structural analysis.

## I. ELECTROCHEMISTRY

Electrochemical studies on squaric acid under different conditions were conducted by Sazou and Kokkinidis, Farnia *et al.*, and Rodes *et al.* (125–128). Sazou and Kokkinidis proposed a mechanism for the two-step oxidation of squaric acid on Pt surfaces which involved the initial formation of the squarate monoanion followed by further oxidation to a radical ion (125). Farnia *et al.* proposed two one-electron processes involving the sequential formation of the squarate monoanion and dianion, respectively, based on the results of their study using Pt electrodes and dimethylformamide (126). Rodes *et al.* reported the dissociative adsorption of squaric acid on Pt electrodes of differing basal orientations in acidic solutions (127, 128).

## III. Complexes of Monosubstituted Squarate Derivatives

Several complexes have been synthesized using ligands in which one of the two hydroxy groups in the squaric acid molecule is replaced by another functional group (76, 111, 123, 129–137). These monosubstituted squarate ligands are all acidic owing to the ionization of the unsubstituted OH group. At least two resonance forms of each ligand can be drawn because of the potential for electron density migration from the hydroxyl oxygen onto the C<sub>4</sub> ring. In monosubstituted squarate ligands whose substituent is attached to the C<sub>4</sub> ring by an atom containing lone pairs, additional resonance forms can be drawn. It was assumed that all the monosubstituted squarate ligands used in metal complex syntheses were resonance-stabilized and that the lower symmetry of these ligands compared to that of the squarate ion was responsible for the latter being more stable.

When monosubstituted squarate ligands (which are resonance-stabilized) are reacted with stable cationic species in sufficiently polar solvents, they form salts instead of coordination compounds, a result similar to that observed in some instances with squaric acid. For example, the salt  $[\text{Mn}(\text{H}_2\text{O})_6][\text{HC}_4\text{O}_3\text{NH}_2]_2 \cdot 2\text{H}_2\text{O}$  is produced in aqueous solution on reacting manganese(II) nitrate with 1-amino-2-methoxycyclobut-3-ene-1,2-dione (130). In this example, the stabilization of the aminosquarate ligand is enhanced by the migration of the nitrogen lone pair of electrons onto the C<sub>4</sub> cycle, the process

being facilitated by the coplanarity of the amino substituent with the  $C_4$  ring (130). Nickel(II) diphenylaminosquarate contains the stable hexaaquanickel(II) ion in association with the resonance-stabilized diphenylaminosquarate anion (134), while the complex tetraamineplatinum(II) ion is associated with the phenylsquarate anion in tetraamineplatinum(II) phenylsquarate (137) (Fig. 19). With the exception of the case of the aminosquarate ion, there is, as expected, a disparity in the C—C bond lengths on the  $C_4$  cycles of the anions of the monosubstituted squarate ligands (Table V).

While, as described earlier in this review, the complexing properties of squaric acid have been extensively investigated, it is only quite recently that any attention has been paid to those of the monosubstituted squarate ligands. Hall *et al.* and Alleyne *et al.*, among others, have reported on several complexes of monosubstituted ligands (76, 111, 123, 129, 131–137). Lead(II) aminosquarate and the lead(II) complexes of a few 1-(dialkylamino) squarate ligands were the first such complexes to be fully characterized (76, 129). The linear arrangement of the lead atoms and the  $\mu$ -1,2-bridging coordination mode adopted by the ligands in these complexes prompted investigations into the complexing properties of several other monosubstituted squarate ligands with transition and lanthanide metals. Monosubstituted squarate ligands

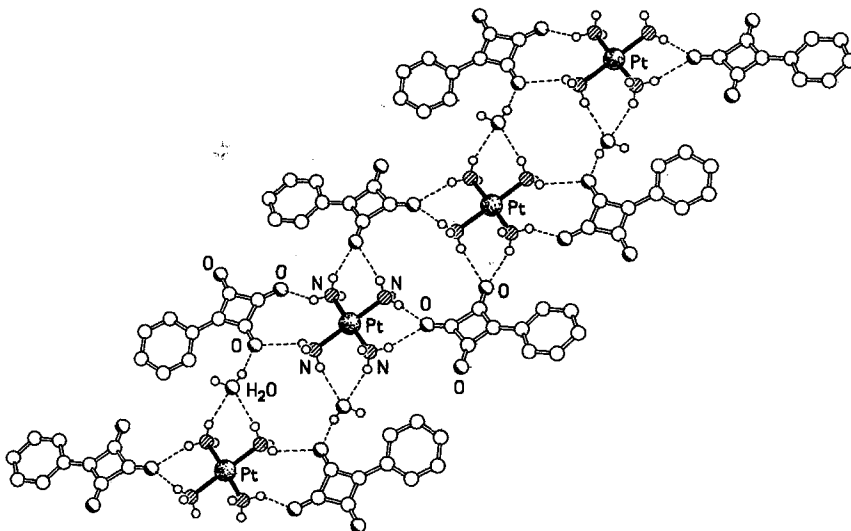


FIG. 19. Part of one of the hydrogen-bonded tapes present in the structure of the salt tetraamineplatinum(II) bisphenylsquarate hydrate (137).

TABLE V

C<sub>4</sub> RING C—C AND C—O BOND LENGTHS (Å) IN SALTS OF MONOSUBSTITUTED  
SQUARATE LIGANDS

Salt	Bond lengths		Reference
	C—C	C—O	
[Mn(H <sub>2</sub> O) <sub>6</sub> ][HC <sub>4</sub> O <sub>3</sub> NH <sub>2</sub> ] <sub>2</sub> · 2H <sub>2</sub> O	1.445(4)	1.248(4)	130
	1.466(4)	1.253(4)	
[Ni(H <sub>2</sub> O) <sub>6</sub> ][(C <sub>6</sub> H <sub>5</sub> ) <sub>2</sub> NC <sub>4</sub> O <sub>3</sub> ] <sub>2</sub> · 2H <sub>2</sub> O	1.471(2)	1.257(2)	134
	1.501(2)	1.236(2)	
	1.460(2)	1.232(2)	
	1.437(2)		
[Pt(NH <sub>3</sub> ) <sub>4</sub> ][C <sub>6</sub> H <sub>5</sub> C <sub>4</sub> O <sub>3</sub> ] <sub>2</sub> · 2H <sub>2</sub> O	1.514(8)	1.247(8)	137
	1.511(8)	1.222(7)	
	1.461(8)	1.215(8)	
	1.427(8)		

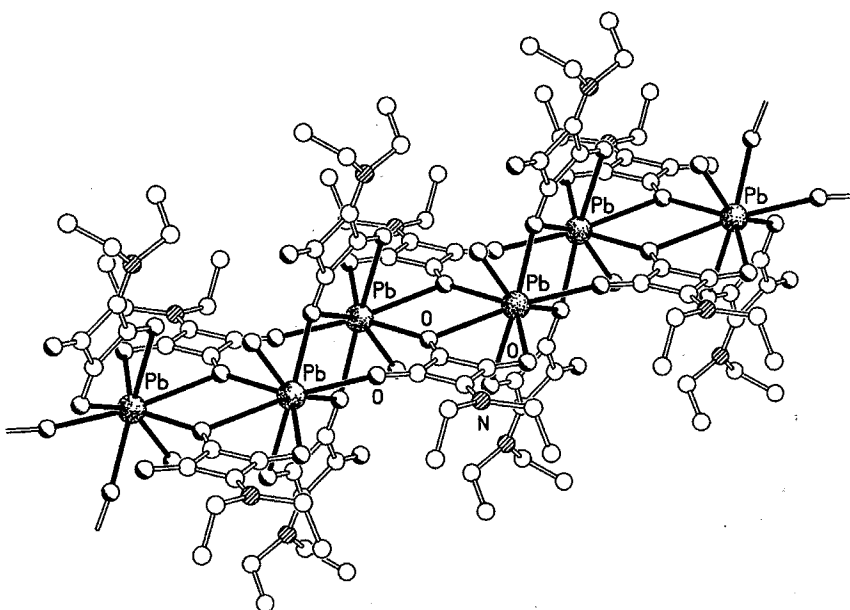


FIG. 20. Part of one of the polymer chains in the structure of lead(II) diethylaminosquarate  $\text{Pb}[(\text{C}_2\text{H}_5)_2\text{NC}_4\text{O}_3]_2(\text{H}_2\text{O})$  (76) showing the chelating and bridging roles of the aminosquarate ligand and the linear arrangement of the pairs of lead atoms.

containing substituents of varying sizes and electron-donating abilities were studied in order to determine the effects of steric and electronic factors on the structural and other characteristics of the complexes produced.

#### A. COMPLEXING PROPERTIES OF MONOSUBSTITUTED SQUARATE LIGANDS

The reduction in the number of potential coordination sites from four to three on monosubstitution of squaric acid restricts the variety of possible coordination modes possible for these ligands. In the majority of the complexes prepared by Hall *et al.*, the monosubstituted squarate ligands adopt a  $\mu$ -1,3 role, although in a few instances the ligands coordinate monodentately, adopting a pendant role (111, 123, 132–137). Expectedly, as a consequence of bite-parameter considerations, chelation is observed only in the case of the large lead(II) ion (76). In

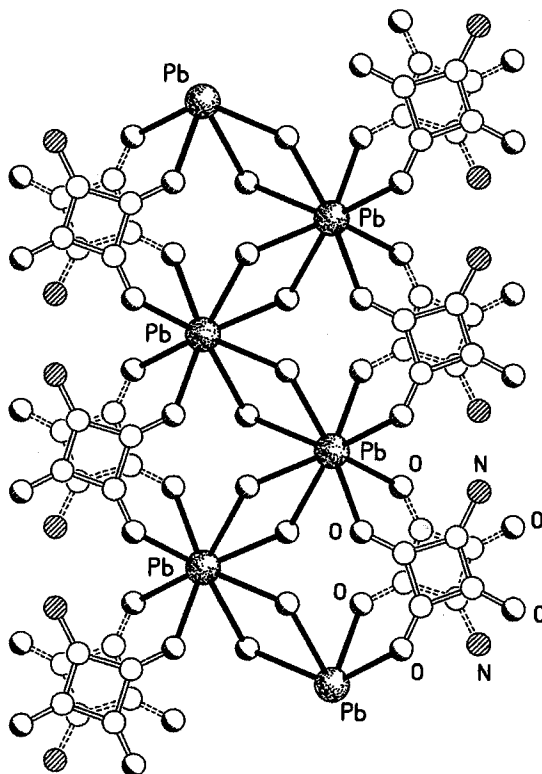


FIG. 21. Part of one of the polymer chains in the structure of lead(II) aminosquarate (129).

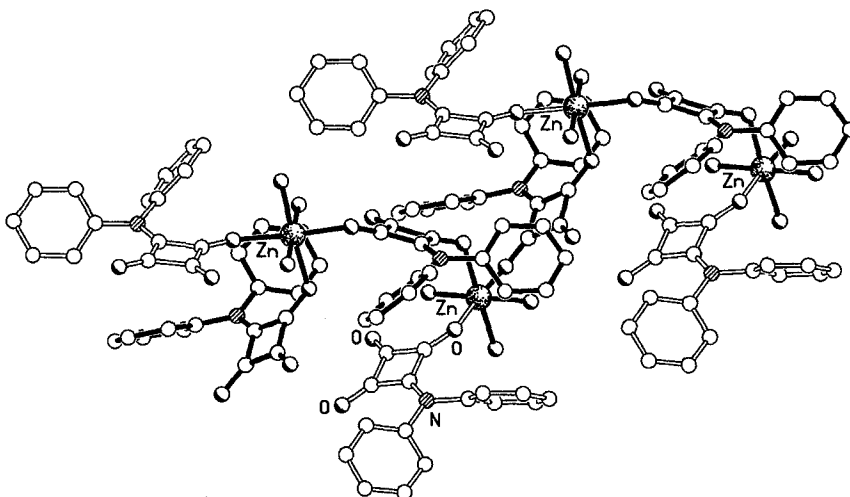


FIG. 22. Part of one of the polymer chains in the structure of zinc(II) diphenylaminosquarate (134) where the ligand bridges (filled bonds) as well as adopts a pendant coordination mode (open bonds).

lead(II) dimethylaminosquarate and diethylaminosquarate (76), in addition to the ligands exhibiting a chelating mode, one of the ligand oxygen atoms in each case is binucleating and bridges two neighboring lead atoms (Fig. 20). However, in lead(II) aminosquarate (129) the ligand groups complex in a bimonodentate fashion and serve only to bridge juxtaposed lead atoms  $\mu$ -1,2 (Fig. 21). In some phenylsquarate complexes and in cobalt(II) and zinc(II) diphenylaminosquarate (123, 134, 136, 137), the ligand both bridges and adopts a pendant coordination mode (Fig. 22).

Hall *et al.* deduced that transition metal and lanthanide complexes with structural features similar to that of the lead(II) dialkylaminosquarates should possess the potential to show desirable electronic properties such as semiconductivity, superconductivity, and molecular magnetism. In particular, multiple bond localization, a property exhibited by the squarate ion when it adopts the  $\mu$ -1,2-bridging mode owing to distortion of the  $C_4$  cycle and the consequent lowering of the  $D_{4h}$  symmetry, is observed in all the complexes of monosubstituted squarate ligands. It was suggested that the multiple bond localization exhibited by the ligands in complexes of the monosubstituted squarate ligands was to be expected because such ligands all have lower than  $D_{4h}$  symmetry by virtue of the monosubstitution of the parent squaric acid. It was also believed that this property conferred on such ligands versatility with respect to varying their orbital energies by changing

the substituent—a property lacking in the unsubstituted squarate ligand. Additionally, they surmised that monosubstituted squarate ligands would be superior to the squarate ligand with respect to synthesizing semiconductors and molecular magnets. This conclusion prompted several attempts at the syntheses of complexes with such ligands.

## B. SUBSTITUENTS WITH LONE PAIRS

The syntheses of metal complexes with monosubstituted squarate ligands containing 1-(dialkylamino), diphenylamino, and methoxy substituents have been reported (76, 111, 129, 133, 134). However, all attempts to synthesize first-row transition metal and lanthanide complexes of the 1-(dialkylamino) squarate ligands proved futile because of the metal-mediated hydrolysis of the dialkylamino substituents, which results in the formation of metal complexes of the parent unsubstituted squarate ligand (130). Alleyne *et al.* suggested that this hydrolysis could be used as a convenient synthetic tool in the preparation of X-ray-quality crystals of metal squarates, which proved difficult to prepare using the unsubstituted squaric acid (131). (This difficulty often arises because of the limited solubility of several metal squarates, which prevents the formation of X-ray-quality crystals). A similar hydrolysis of the substituent in 1-(diphenylamino) squarate did not occur because the sterically hindered carbon containing the bulky diphenylamino substituent is inaccessible to nucleophilic attack by water. Thus, several metal diphenylaminosquarate complexes were prepared. Among these were monomers, dimers, and polymers containing the ligand in different coordination roles (133, 134). For instance, in the lanthanum complex  $\text{La}[(\text{C}_6\text{H}_5)_2\text{NC}_4\text{O}_3]_3(\text{H}_2\text{O})_6 \cdot 5\text{H}_2\text{O}$ , all three diphenylaminosquarate ligands coordinated monodentately, the substituent being oriented *cis* to the ligating oxygen in one and *trans* in the other two (133) (Fig. 23). However, in the isomorphous europium, gadolinium, and terbium series of dimers, the ligands adopt both monodentate and bidentate coordination modes (Fig. 24). In all the polymeric first-row transition metal diphenylaminosquarates, the ligand bridges  $\mu$ -1,3 (134).

The methoxysquarate ligand produced only monomeric species on complexation with first-row transition metals (111) (Fig. 25). Hosein *et al.* suggested that chain propagation is prevented owing to the steric hindrance of the methoxy oxygen atom by the adjacent methyl group, with its  $sp^3$  hybridized carbon (111). The two methoxy ligands in these monomers are oriented *cis*, the methoxy substituent also being oriented *cis* with respect to the ligating oxygen atom.

In the 1-(dialkylamino) squarate and methoxysquarate ligands (111, 133, 134), bond lengths obtained from the X-ray data provided

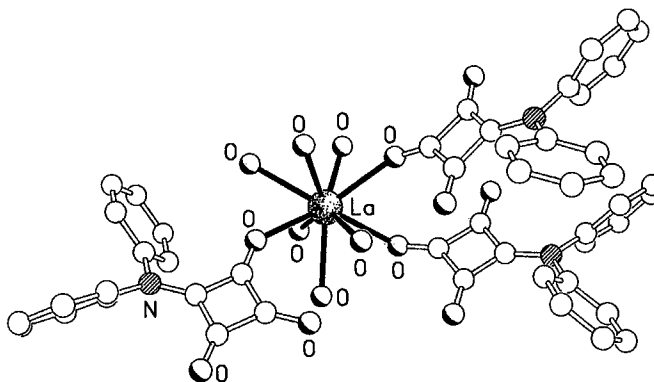


FIG. 23. The monomeric lanthanum(III) diphenylaminosquarate complex  $\text{La}[(\text{C}_6\text{H}_5)_2\text{NC}_4\text{O}_3]_3(\text{H}_2\text{O})_6 \cdot 5\text{H}_2\text{O}$  (133) showing the three diphenylaminosquarate ligands to be coordinated monodentately; in one, the substituent is oriented *cis* to the ligating oxygen, whereas in the other two it is *trans*.

substantial evidence for migration of the nitrogen and oxygen lone pairs from the dialkylamino and methoxy substituents, respectively, onto the  $\text{C}_4$  ring. For example, in the 1-(dimethylamino)squarate ligand, the  $\text{C}-\text{N}$  bond by which the substituent is attached to the  $\text{C}_4$  ring is significantly shorter than those between the nitrogen atom and its attached methyl

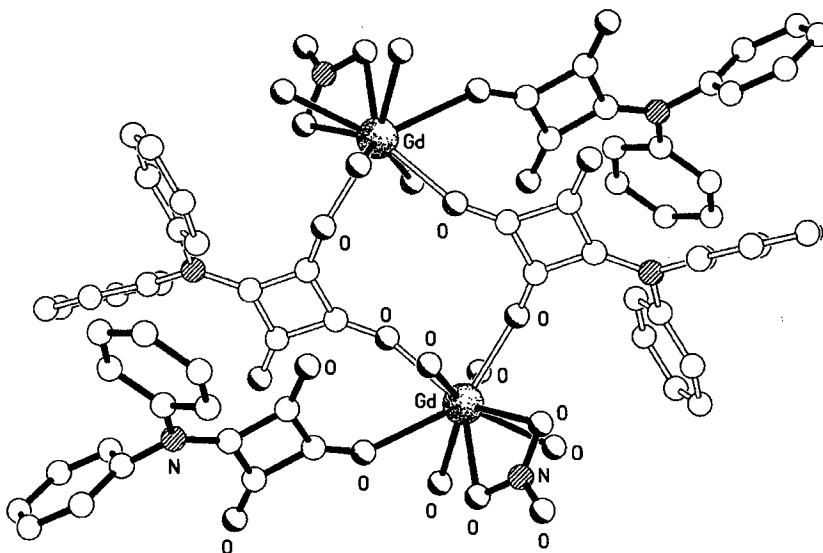


FIG. 24. The dimeric gadolinium(III) diphenylaminosquarate complex  $[\text{Gd}(\mu-(\text{C}_6\text{H}_5)_2\text{NC}_4\text{O}_3)(\text{C}_6\text{H}_5)_2\text{NC}_4\text{O}_3](\text{NO}_3)(\text{H}_2\text{O})_4 \cdot 4\text{H}_2\text{O}$  (133), showing the bidentate bridging and monodentate pendant roles of the ligand.

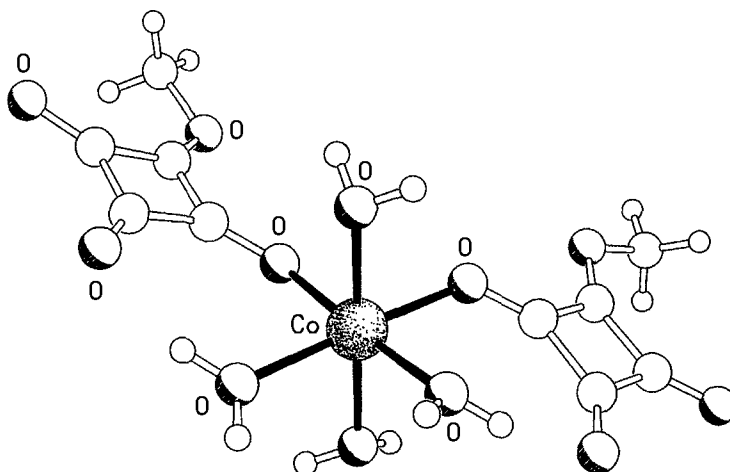


FIG. 25. The  $C_2$  symmetric monomeric cobalt(II) methoxysquarate complex  $\text{Co}(\text{CH}_3\text{OC}_4\text{O}_3)_2(\text{H}_2\text{O})_4$  (111).

groups. Similarly, in the series of monomeric first-row transition metal methoxysquarates, the C—O bond linking the methoxy group to the  $\text{C}_4$  ring is significantly shorter than the methyl to oxygen C—O bond. It was concluded that the electron migration is, in each case, facilitated by the coplanarity of the substituents with the ring, which renders the ligands susceptible to hydrolysis owing to sensitization of the substituent-containing carbon atom to nucleophilic attack. This effect, they surmised, was analogous to the observed hydrolysis during the attempted syntheses of first-row transition metal and lanthanide complexes with 1-(dialkylamino)squarate ligands. Substituent hydrolysis was also responsible for the formation of the cubic form of copper squarate (see Fig. 18) instead of the desired copper methoxysquarate when copper(II) ions were reacted with the methoxysquarate ligand (111). Surprisingly, however, no hydrolysis occurred in the synthesis of the isomorphous manganese, cobalt, and nickel complexes. It was deduced that in the case of copper the compatibility of the energies of the ligand and metal orbitals was probably responsible for hydrolysis occurring.

Hall *et al.* also observed that the extent of delocalization on the monosubstituted squarate ligand ring, and hence its dimensions, was dependent on electron migration from the substituent (111, 123, 130, 132–137) (Table VI). For example, for the methoxysquarate ligand in its metal complexes  $\Delta(\text{C—C}) = 0.05 \text{ \AA}$ , whereas in the analogous diphenylaminosquarate complexes the value is  $\sim 0.02 \text{ \AA}$  (Table VI). This difference was attributed to the smaller size of the oxygen atom relative to

TABLE VI  
C<sub>4</sub> RING C—C BOND LENGTHS (Å) IN COMPLEXES OF MONOSUBSTITUTED  
SQUARATE LIGANDS

Complex	Bond lengths		Mode ( $\mu$ -1,3; pendant)	Reference
	C—C	C—O		
Mn(CH <sub>3</sub> OC <sub>4</sub> O <sub>3</sub> ) <sub>2</sub> (H <sub>2</sub> O) <sub>4</sub>	1.427(4)	1.242(4)	pendant	111
	1.435(4)	1.307(4)		
	1.489(5)	1.245(4)		
	1.487(4)	1.220(5)		
Pb(C <sub>4</sub> O <sub>3</sub> HNH <sub>2</sub> ) <sub>2</sub> (H <sub>2</sub> O) <sub>2</sub>	1.465(15)	1.249(13)	$\mu$ -1,2	129
	1.448(15)	1.275(13)		
	1.410(17)	1.267(15)		
	1.457(16)			
Co(CH <sub>3</sub> C <sub>4</sub> O <sub>3</sub> ) <sub>2</sub> (NO <sub>3</sub> )(H <sub>2</sub> O) <sub>4</sub> · 2H <sub>2</sub> O	1.506(8)	1.242(7)	$\mu$ -1,3	132
	1.428(8)	1.218(10)		
	1.479(12)			
	1.510(2)	1.249(2)		
Ni(CH <sub>3</sub> C <sub>4</sub> O <sub>3</sub> ) <sub>2</sub> (NO <sub>3</sub> )(H <sub>2</sub> O) <sub>4</sub> · 2H <sub>2</sub> O	1.421(2)	1.215(2)	$\mu$ -1,3	132
	1.480(3)			
	1.506(2)	1.216(2)		
	1.512(2)	1.238(2)		
Mn(CH <sub>3</sub> C <sub>4</sub> O <sub>3</sub> ) <sub>2</sub> · 4H <sub>2</sub> O	1.425(2)	1.244(2)	pendant	132
	1.424(2)			
	1.522(12)	1.234(11)		
	1.506(12)	1.213(11)		
{Eu( $\mu$ -C <sub>6</sub> H <sub>5</sub> C <sub>4</sub> O <sub>3</sub> ) <sub>2</sub> (C <sub>6</sub> H <sub>5</sub> C <sub>4</sub> O <sub>3</sub> )- (CH <sub>3</sub> OH) <sub>2</sub> (H <sub>2</sub> O) <sub>2</sub> · (CH <sub>3</sub> OH)} <sub>n</sub>	1.437(12)	1.239(11)	pendant	123
	1.435(12)			
	1.503(13)	1.220(12)		
	1.515(12)	1.223(11)		
{Cu[ $\mu$ -(C <sub>6</sub> H <sub>5</sub> ) <sub>2</sub> NC <sub>4</sub> O <sub>3</sub> ] <sub>2</sub> (H <sub>2</sub> O) <sub>2</sub> }] <sub>n</sub>	1.444(13)	1.260(12)	bridging	
	1.418(12)			
	1.481(3)	1.259(2)		
	1.493(3)	1.228(3)		
{Co[ $\mu$ -(C <sub>6</sub> H <sub>5</sub> ) <sub>2</sub> NC <sub>4</sub> O <sub>3</sub> ]- [(C <sub>6</sub> H <sub>5</sub> ) <sub>2</sub> NC <sub>4</sub> O <sub>3</sub> ](H <sub>2</sub> O) <sub>3</sub> }] <sub>n</sub>	1.455(3)	1.229(3)	$\mu$ -1,3	134
	1.434(3)			
	1.471(5)	1.263(4)		
	1.481(5)	1.228(4)		
{Co[ $\mu$ -(C <sub>6</sub> H <sub>5</sub> ) <sub>2</sub> NC <sub>4</sub> O <sub>3</sub> ]- [(C <sub>6</sub> H <sub>5</sub> ) <sub>2</sub> NC <sub>4</sub> O <sub>3</sub> ](H <sub>2</sub> O) <sub>3</sub> }] <sub>n</sub>	1.453(5)	1.240(4)	$\mu$ -1,3	134
	1.451(4)			
	1.490(5)	1.248(4)		
	1.494(5)	1.228(4)		
[Mn( $\mu$ -C <sub>6</sub> H <sub>5</sub> C <sub>4</sub> O <sub>3</sub> )- (C <sub>6</sub> H <sub>5</sub> C <sub>4</sub> O <sub>3</sub> )(H <sub>2</sub> O) <sub>3</sub> ] <sub>n</sub>	1.446(5)	1.250(4)	pendant	136
	1.443(5)			
	1.519(4)	1.246(3)		
	1.505(3)	1.213(3)		
[Zn(C <sub>6</sub> H <sub>5</sub> C <sub>4</sub> O <sub>3</sub> ) <sub>2</sub> (H <sub>2</sub> O) <sub>4</sub> ]	1.423(3)	1.244(3)	$\mu$ -1,3	136
	1.426(3)			
	1.506(3)	1.241(3)		
	1.514(3)	1.215(3)		
[Zn(C <sub>6</sub> H <sub>5</sub> C <sub>4</sub> O <sub>3</sub> ) <sub>2</sub> (H <sub>2</sub> O) <sub>4</sub> ]	1.433(3)	1.241(3)	pendant	136
	1.434(3)			
	1.501(3)	1.240(3)		
	1.513(3)	1.216(3)		
	1.437(3)	1.235(3)		
	1.432(3)			

the nitrogen atom and the consequent greater difficulty for lone-pair migration. It was also proposed that when the extent of this electron migration is sufficiently great, the ligand exerts a *cis*-directing effect, since the resulting enhanced electron flow into the *trans* metal-oxygen bond prevents any nucleophilic attack along this direction.

### C. SUBSTITUENTS WITHOUT LONE PAIRS

The syntheses of a number of complexes of the methylsquarate and phenylsquarate ligands have been reported. X-Ray crystallographic analysis of these complexes showed that the extent of electron delocalization on the C<sub>4</sub> ligand rings was significantly less than that observed in those containing the diphenylaminosquarate and methoxysquarate ligands. This difference was attributed to the fact that the atom by which either the methyl or the phenyl substituents are attached to their respective C<sub>4</sub> rings did not have available lone-pair electrons for migration into these rings. The C<sub>4</sub> ring dimensions in both the methylsquarate and phenylsquarate complexes did not differ significantly (Table VI) despite the fact that the short C<sub>phenyl</sub>-C<sub>4</sub> bond length in the phenylsquarate ligand suggested conjugation between the two adjacent  $\pi$  systems. Thus, they concluded that the C<sub>4</sub> ring geometry and the extent of electron delocalization in these coordinated monosubstituted ligands are dependent solely on the extent of electron migration from the substituent. The identity of the metals to which these ligands were coordinated did not appear to have any significant effect in this regard.

### D. EFFECTS OF SUBSTITUENT ON STRUCTURE

Hall *et al.* deduced that both the steric demands and the *cis*-directing effect of the substituent appear to play a significant part in determining the structure of the metal complexes of monosubstituted squarate ligands. They used a series of first-row transition metal and lanthanide complexes of both the diphenylaminosquarate and methylsquarate ligands to illustrate the effect of the steric bulk of the substituent on structure (132-135). They observed that the number of diphenylaminosquarate groups coordinated to the central metal ion in a series of first-row transition metal complexes paralleled the decrease in the size of the metal ion as the period was traversed from manganese to zinc. In the case of the copper complex, the expected Jahn-Teller distortion reduced the steric effects of the substituent and allowed the coordination of the same number of diphenylaminosquarate ligands as

the larger manganese ion. However, the expected increased number of monosubstituted squarate ligands that should have coordinated to the lanthanide metals, which are significantly larger than the first-row transition metals, was not observed. This observation, they concluded, was due to the decreased  $O_{\text{ligand}}-M-O_{\text{ligand}}$  angles associated with the higher coordination numbers shown by the lanthanides and the resulting increased steric hindrance. As a consequence, no polymers were produced in a series of lanthanide complexes of the diphenylaminosquarate ligand. However, with the less sterically demanding methyl substituent several polymeric lanthanide methylsquarates were produced (135), including the first reported three-dimensional complex (135) of a mono-substituted squarate ligand,  $\{Eu[\mu-(CH_3C_4O_3)_3] \cdot (H_2O)_2\}_n$  (Fig. 26).

The structures of the complexes of monosubstituted squarate ligands are also dependent on the orientation of the substituent with respect to the ligating oxygen atom. For example, in the monomeric species  $M(CH_3C_4O_3)_2(H_2O)_4$  ( $M = Mn, Co, Cu, Zn$ ) (132), the methyl substituent is oriented *trans* to the ligating oxygen atom on both methylsquarate

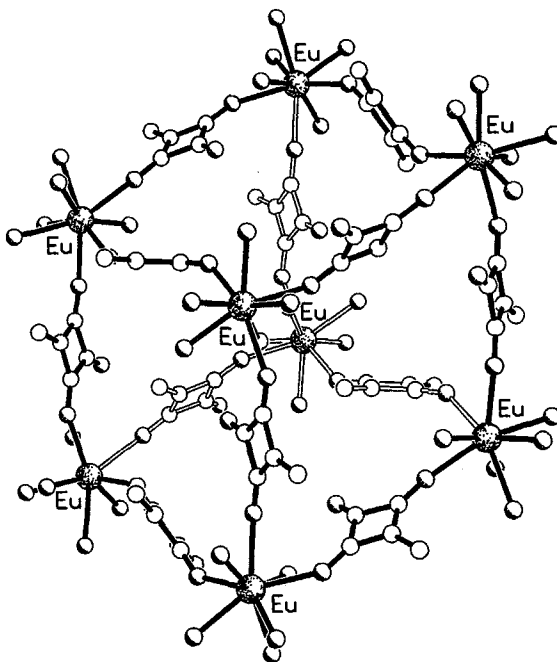


FIG. 26. Part of the rhomboidally distorted "cubic" three-dimensional network complex of the methylsquarate ligand in the Eu(III) complex  $\{Eu[\mu-(CH_3C_4O_3)_3] \cdot (H_2O)_2\}_n$  (135).

ligands coordinated to the metal ion (see Fig. 25). This geometry precludes any viable mechanism for chain propagation, hence polymerization is not observed. It was therefore suggested that the *cis*-directing effect of the methoxy substituent acts as an inhibitor to polymerization.

#### E. SQUARATE AND MONOSUBSTITUTED SQUARATE COMPLEXES WITH $\pi$ INTERACTIONS

Mention of the existence  $\pi$ - $\pi$  interactions in complexes of squaric acid is infrequent. One example is provided by the  $\pi$ -stacked layers in the organometallic salts of the cobaltocenium ion  $[\text{Co}(\eta^5\text{-C}_5\text{H}_5)_2]^+$  (77, 138). Weiss *et al.* assumed the existence of  $\pi$ - $\pi$  interactions in the polymeric complexes  $\text{M}(\text{C}_4\text{O}_4) \cdot 4\text{H}_2\text{O}$ , noting that the distance between the planes of the squarate ligands in neighboring chains was  $3.335 \pm 0.013 \text{ \AA}$  (30). Macintyre and Werkema also reported  $\pi$ - $\pi$  interactions in  $\text{K}_2\text{C}_4\text{O}_4 \cdot \text{H}_2\text{O}$  (85). The incidence of such interactions in complexes of the monosubstituted ligands is significantly greater. In several such complexes (123, 133, 134, 136, 137), where the ligands contain substituents with phenyl groups, the  $\pi$  orbitals in both the  $\text{C}_4$  cycles and the phenyl groups were shown to participate in  $\pi$ - $\pi$  interactions when the orientations of the participating moieties allowed. Furthermore, the tertiary structures and other physical properties of the complexes in which these interactions occurred are apparently influenced by these interactions. This is particularly true for metal complexes of the phenylsquarate ligand. For example, in europium(III) phenylsquarate, the  $\pi$ - $\pi$  interactions are partly responsible for holding the polymer chains together, with the resultant formation of sheets (123) (Fig. 27). In addition to sheet formation, in the complexes  $\text{M(III) phenylsquarate}$  ( $\text{M} = \text{Gd, Tb}$ ) and manganese(II) phenylsquarate,  $\pi$ -stacking was assumed to be at least partly responsible for the formation of bilayers bounded by hydrophobic layers of phenylsquarate groups (136, 137). However,  $\pi$ - $\pi$  interactions have also been observed in methylsquarate and diphenylaminosquarate complexes. In the polymeric cobalt(II) and nickel(II) methylsquarates the  $\pi$ - $\pi$  interaction occurs between the methylsquarate rings and the nitrate ions with a mean interplanar separation of  $\sim 3.3 \text{ \AA}$  (132) (Fig. 28). In the Ln diphenylaminosquarate dimers  $\{\text{Ln}[\mu\text{-(C}_6\text{H}_5)_2\text{NC}_4\text{O}_3][(\text{C}_6\text{H}_5)_2\text{NC}_4\text{O}_3][\text{NO}_3][\text{H}_2\text{O}]_4\}_2 \cdot 4\text{H}_2\text{O}$  ( $\text{Ln} = \text{Eu, Gd, Tb}$ ), the  $\pi$ - $\pi$  interaction occurs between the  $\text{C}_4$  rings of  $\mu$ -1,2-bridging and neighboring pendant diphenylaminosquarate groups (133). The centroid  $\cdots$  centroid separation in the europium analog was shown to be temperature-dependent and assumed to be responsible for excimer formation at lower temperatures.

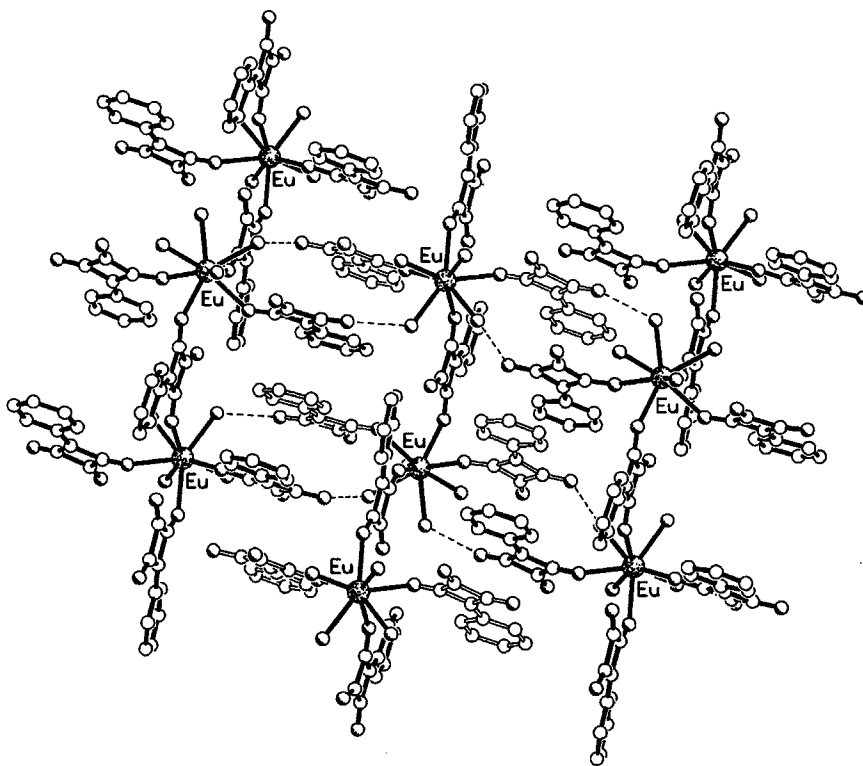


FIG. 27. Part of one of the sheets formed by  $\pi$ - $\pi$  stacking and hydrogen bonding of adjacent polymer chains in the structure of europium(III) phenylsquarate (123). The interplanar spacings between the pairs of phenylsquarate rings are in the range 3.35–3.51 Å and the hydrogen-bonding O...O distances are 2.62 and 2.64 Å.

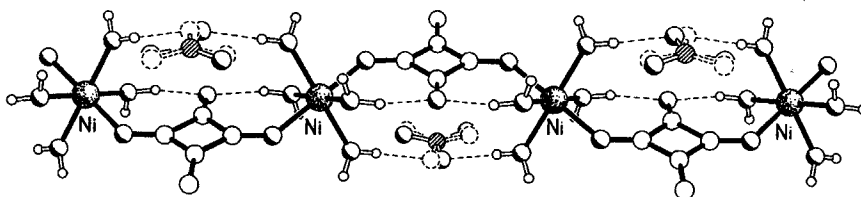


FIG. 28.  $\pi$ - $\pi$  Stacking interactions between the methylsquarate rings and the nitrate ions in the polymeric nickel(II) methylsquarate structure (132); the mean interplanar separation is 3.25 Å.

A weak electrostatic interaction was observed between nearly orthogonal C=O groups in gadolinium and terbium methylsquarates (135).

#### F. COMPLEXES OF HEAVIER TRANSITION METALS

Williams *et al.* attempted the preparation of polymeric complexes of ruthenium(II) and platinum(II) with the phenylsquarate ligand (137). However, they only managed to synthesize the monomer  $\text{Ru}(\text{dmsO})_3\text{Cl}(\text{H}_2\text{O})(\text{C}_6\text{H}_5\text{C}_4\text{O}_3) \cdot \text{H}_2\text{O}$  (Fig. 29) and the salt  $[\text{Pt}(\text{NH}_3)_4][\text{C}_6\text{H}_5\text{C}_4\text{O}_3]_2 \cdot \text{H}_2\text{O}$  using  $\text{Ru}(\text{dmsO})_4\text{Cl}_2$  and  $[\text{Pt}(\text{NH}_3)_4]\text{Cl}_2$ , respectively, as starting materials. They suggested that the medium field strength of the phenylsquarate ligand was responsible for its inability to replace more than one dmsO group from  $\text{Ru}(\text{dmsO})_4\text{Cl}_2$ , hence reducing the possibility of polymer formation. They also suggested that the salt  $[\text{Pt}(\text{NH}_3)_4][\text{C}_6\text{H}_5\text{C}_4\text{O}_3]_2 \cdot \text{H}_2\text{O}$  was produced instead of a polymer owing to the stabilities of the  $[\text{Pt}(\text{NH}_3)_4]^{2+}$  and the resonance-stabilized phenylsquarate ions in the polar medium used in synthesis.

#### G. ELECTROCHEMICAL STUDIES

Iwuoha *et al.* investigated the electrochemistry of some of the monosubstituted squarate ligands (139, 140). They found that the

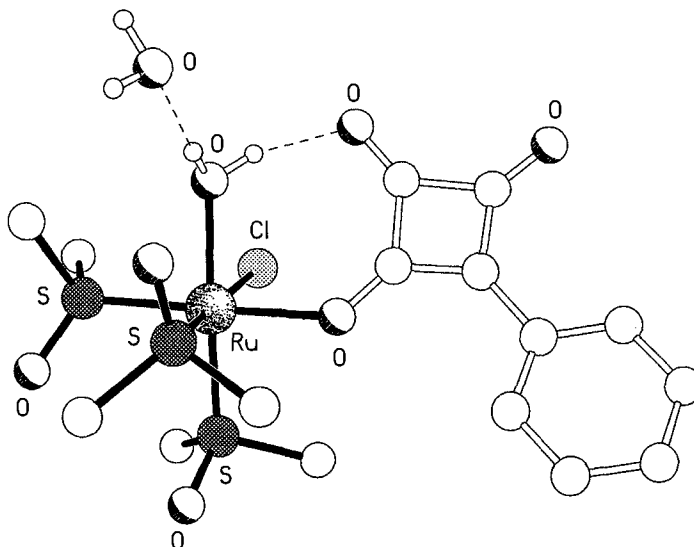


FIG. 29. The structure of the ruthenium(II) squarate monomer  $[\text{Ru}(\text{C}_6\text{H}_5\text{C}_4\text{O}_3)(\text{dmsO})_3\text{Cl}(\text{H}_2\text{O})] \cdot \text{H}_2\text{O}$  (137).

methylsquarate, phenylsquarate, and diphenylaminosquarate ligands undergo oxidation–reduction sequences similar to those of orthoquinones, the magnitudes of the oxidation and reduction potentials being dependent on the identity of the substituent (139, 140). They also proposed that, unlike squaric acid, which showed two one-electron redox processes in aqueous solutions, each methylsquarate, phenylsquarate, and diphenylaminosquarate ligand displayed a single-electron reversible process which, they assumed, occurred at the ionized hydroxyl moiety (139, 140). However, the diphenylaminosquarate ligand showed an additional one-electron redox process similar to that of the tetrahydrazone of squaric acid (140, 141).

The electrochemistry of the polymeric and isomorphous cobalt(II) and nickel(II) methylsquarates was also studied by Iwuoha *et al.* In aqueous solutions, they found evidence that both the nickel(II) methylsquarate and its cobalt analog were dissociated without any reversible redox processes occurring for the metal ions. However, the cyclic and Osteryoung square wave voltammograms, obtained using a Pt electrode for solutions of these complexes in dimethylformamide and dimethylsulfoxide, contained signals attributable to both ligand-based and metal-based redox processes (142).

#### H. LUMINESCENCE STUDIES

Luminescence studies on both europium(III) phenylsquarate and diphenylaminosquarate were carried out by Hall *et al.* in order to compare the luminescence characteristics of these complexes with that of europium(III) squarate (123). The results of these studies suggested that the interactions between the C<sub>4</sub> ring and the phenyl and diphenylamino substituents, respectively, sensitize Eu<sup>3+</sup>(<sup>5</sup>D<sub>0</sub> → <sup>7</sup>F<sub>*j*</sub>) emissions, which the unsubstituted squarate group is unable to do.

#### IV. Hydrogen Bonding and Other Weak Interactions in Complexes of Squaric Acid and Its Monosubstituted Derivatives

Hydrogen-bonding interactions in complexes of squaric acid have recently been reviewed (71); therefore, only such interactions in the complexes of monosubstituted squarates and aspects of hydrogen bonding not covered in that review will be discussed.

Most of the complexes of squaric acid and its derivatives contain hydrogen bonds that appear to have a significant influence on the tertiary structure (19, 21, 22, 28, 30, 41, 56, 62, 65, 69, 76, 82, 90, 111, 112, 121, 123, 129, 131–137). The prevalence of hydrogen bonding in these complexes is not surprising, since the metals in most instances have

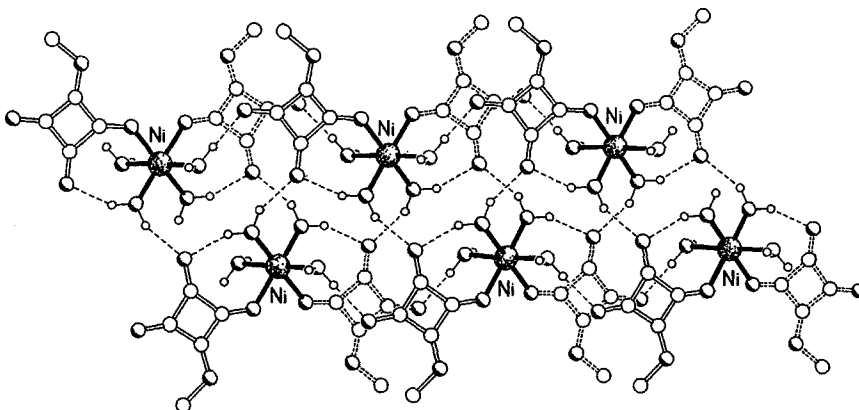


FIG. 30. The crosslinking of hydrogen-bonded chains of monomers to form tapes in the structure of nickel(II) methoxysquarate  $[\text{Ni}(\text{CH}_3\text{OC}_4\text{O}_3)_2(\text{H}_2\text{O})_4]$  (111).

aqua ligands that hydrogen-bond either intra- or intermolecularly either to themselves or to oxygen atoms on the squarate ligands. In fact, except where steric factors prevent it, the molecules tend to maximize their hydrogen-bonding potential often resulting in distortions—sometimes large—in the coordination polyhedra of the metals.

Hall *et al.* observed that in the complexes of monosubstituted squarate ligands, the ligands, invariably utilize all the hydrogen-bonding

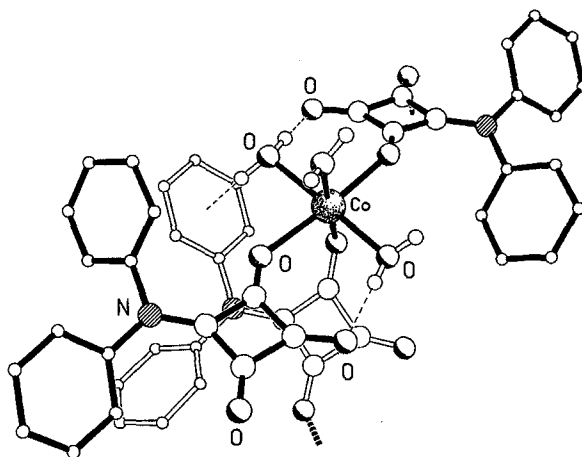


FIG. 31. Intramolecular  $\text{O}-\text{H}\cdots\text{O}$  and  $\text{O}-\text{H}\cdots\pi$  interactions in the structure of cobalt(II) diphenylaminosquarate  $\{\text{Co}[(\mu-(\text{C}_6\text{H}_5)_2\text{NC}_4\text{O}_3)][(\text{C}_6\text{H}_5)_2\text{NC}_4\text{O}_3](\text{H}_2\text{O})_3\}_n$  (134); the  $\text{H}\cdots\text{O}$  and  $\text{H}\cdots\pi$  distances are 1.77 and 2.57 Å, respectively.

contacts allowed by the conformational characteristics of the complex (76, 111, 123, 129, 132–137). Both intra- and intermolecular hydrogen bonding are prevalent in these complexes and normally involves the noncoordinated ketonic oxygen atoms on the monosubstituted squarate ligands and hydrogen atoms on neighboring aqua ligands (Fig. 30). In some instances, molecules of water of crystallization also participate in hydrogen bonding. The intermolecular hydrogen-bonding interactions in the complexes synthesized by Hall *et al.* are seen to facilitate the linking of polymer chains and the formation of discrete ribbons as well as corrugated sheets.

Weaker O—H... $\pi$  hydrogen bonds were also observed in M diphenylaminosquarate complexes (M = Mn, Co, Cu, Zn) and involve the interaction of aqua hydrogen atoms and the phenyl groups of neighboring diphenylamino substituents (134) (Fig. 31).

#### ACKNOWLEDGMENTS

L. A. H. wishes to thank the St. Augustine Campus Committee on Graduate Studies, The University of the West Indies, for financial support throughout the years, as well as Dr. B. D. Alleyne and Dr. Avril Williams-Dottin for their contributions to the research on monosubstituted squarates. D. J. W. wishes to thank the Inter American Development Bank and CARISCIENCE for financial support, and Drs. I. Baxter, S. Menzer, and A. J. P. White for their contributions to the X-ray crystal structure determinations.

#### REFERENCES

1. Cohen, S.; Lacher, J. R.; Park, J. D. *J. Am. Chem. Soc.* **1959**, *81*, 3480.
2. Smutny, E. J.; Caserio, M. C.; Roberts, J. D. *J. Am. Chem. Soc.* **1960**, *82*, 1793.
3. Blomquist, A. T.; Vierling, R. A. *Tetrahedron. Lett.* **1961**, *2*, 655.
4. Maahs, G. *Angew. Chem.* **1963**, *75*, 982.
5. Blomquist, A. T.; LaLancette, E. A. *J. Org. Chem.* **1964**, *29*, 2331.
6. Maahs, G. *Liebigs Ann. Chem.* **1965**, *686*, 55.
7. Treibs, A.; Jacob, K. *Angew. Chem.* **1965**, *77*, 680.
8. Cohen, S.; Cohen, S. G. *J. Am. Chem. Soc.* **1966**, *88*, 1533.
9. West, R.; Niu, H. Y. *J. Am. Chem. Soc.* **1963**, *85*, 2589.
10. Ireland, D. T.; Walton, H. F. *J. Phys. Chem.* **1967**, *71*, 751.
11. Doyle, G.; Tobias, R. S. *Inorg. Chem.* **1968**, *7*, 2484.
12. Ludi, A.; Schindler, P. *Angew. Chem.* **1968**, *80*, 664.
13. Tedesco, P. H.; Walton, H. F. *Inorg. Chem.* **1969**, *8*, 932.
14. Bailey, R. A.; Mills, W. N.; Tangredi, W. J. *J. Inorg. Nucl. Chem.* **1971**, *33*, 2387.
15. Gerstein, B. C.; Habenschuss, M. *J. Appl. Phys.* **1972**, *43*, 5155.
16. Duggan, D. M.; Barefield, E. K.; Hendrickson, D. N. *Inorg. Chem.* **1973**, *12*, 985.
17. Habenschuss, M.; Gerstein, B. C. *J. Chem. Phys.* **1974**, *61*, 852.

18. Wroblewski, J. T.; Brown, D. B. *Inorg. Chem.* **1978**, *17*, 2959.
19. Van Ooijen, J. A. C.; Reedijk, J.; Spek, A. L. *Inorg. Chem.* **1979**, *18*, 1184.
20. Wroblewski, J. T.; Brown, D. B. *Inorg. Chem.* **1979**, *18*, 2738.
21. Reinprecht, J. T.; Miller, J. G.; Vogel, G. C.; Haddad, M. S.; Hendrickson, D. N. *Inorg. Chem.* **1980**, *19*, 927.
22. Chesick, J. P.; Doany, F. *Acta Crystallogr.* **1981**, *B37*, 1076.
23. Simonsen, O.; Toftlund, H. *Inorg. Chem.* **1981**, *20*, 4044.
24. Doyle, G.; Eriksen, K. A.; Modrick, M.; Ansell, G. *Organometallics* **1982**, *1*, 1613.
25. Wilson, A. S. *Cryst. Struct. Commun.* **1982**, *11*, 809.
26. Headley, O. St. C.; Hall, L. A. *Polyhedron* **1985**, *4*, 1697.
27. Altman, J.; Beck, W. *Inorg. Chim. Acta* **1986**, *119*, 203.
28. Bernardinelli, G.; Castan, P.; Soules, R. *Inorg. Chim. Acta* **1986**, *120*, 205.
29. Headley, O. St. C.; Hall, L. A. *Polyhedron* **1986**, *5*, 1829.
30. Weiss, A.; Riegler, E.; Alt, I.; Böhme, H.; Robl, C. *Z. Naturforsch.* **1986**, *41b*, 18.
31. Weiss, A.; Riegler, E.; Robl, C. *Z. Naturforsch.* **1986**, *41b*, 1329.
32. Weiss, A.; Riegler, E.; Robl, C. *Z. Naturforsch.* **1986**, *41b*, 1333.
33. Robl, C.; Weiss, A. *Z. Naturforsch.* **1986**, *41b*, 1341.
34. Robl, C.; Weiss, A. *Z. Naturforsch.* **1986**, *41b*, 1485.
35. Robl, C.; Weiss, A. *Z. Naturforsch.* **1986**, *41b*, 1490.
36. Robl, C.; Weiss, A. *Z. Anorg. Allg. Chem.* **1987**, *546*, 161.
37. Maharaj, D. I.; Hall, L. A. *Inorg. Chim. Acta* **1988**, *145*, 235.
38. Maharaj, D. I.; Hall, L. A. *Polyhedron* **1988**, *7*, 2155.
39. Robl, C.; Kuhs, W. F. *J. Solid State Chem.* **1988**, *73*, 172.
40. Robl, C.; Kuhs, W. F. *J. Solid State Chem.* **1988**, *75*, 15.
41. Soules, R.; Dahan, F.; Laurent, J.-P.; Castan, P. *J. Chem. Soc., Dalton Trans.* **1988**, 587.
42. Trombe, J.-C.; Petit, J.-F.; Gleizes, A. *New. J. Chem.* **1988**, *12*, 197.
43. Bang, E.; Michelsen, K.; Nielsen, K. M.; Pedersen, E. *Acta Chem. Scand.* **1989**, *43*, 748.
44. Bernardinelli, G.; Deguenon, D.; Soules, R.; Castan, P. *Can. J. Chem.* **1989**, *67*, 1158.
45. Chen, Q.; Liu, S.; Zubieta, J. *Inorg. Chim. Acta* **1989**, *164*, 115.
46. Chen, Q.; Ma, L.; Liu, S.; Zubieta, J. *J. Am. Chem. Soc.* **1989**, *111*, 5944.
47. Hall, L. A. *Polyhedron* **1989**, *8*, 1335.
48. Soules, R.; Mosset, A.; Laurent, J.-P.; Castan, P.; Bernardinelli, G.; Delamar, M. *Inorg. Chim. Acta* **1989**, *155*, 105.
49. Bencini, A.; Bianchi, A.; Garcia-España, E.; Jeannin, Y.; Julve, M.; Marcelino, V.; Philoche-Levisalles, M. *Inorg. Chem.* **1990**, *29*, 963.
50. Castro, I.; Faus, J.; Julve, M.; Verdaguer, M.; Monge, A.; Gutierrez-Puebla, E. *Inorg. Chim. Acta* **1990**, *170*, 251.
51. Chen, Q.; Liu, S.; Zubieta, J. *Angew. Chem., Int. Ed. Engl.* **1990**, *29*, 70.
52. Chen, Q.; Liu, S.; Zubieta, J. *Inorg. Chim. Acta* **1990**, *175*, 269.
53. Hall, L. A. *P. M. Polyhedron* **1990**, *9*, 2575.
54. Lloret, F.; Julve, M.; Faus, J.; Solans, X.; Journaux, Y.; Morgenstern-Badarau, I. *Inorg. Chem.* **1990**, *29*, 2232.
55. Petit, J.-F.; Gleizes, A.; Trombe, J.-C. *Inorg. Chim. Acta* **1990**, *167*, 51.
56. Solans, X.; Aguiló, M.; Gleizes, A.; Faus, J.; Julve, M.; Verdaguer, M. *Inorg. Chem.* **1990**, *29*, 775.
57. Trombe, J.-C.; Petit, J.-F.; Gleizes, A. *Inorg. Chim. Acta* **1990**, *167*, 69.
58. Benetó, M.; Soto, L.; García-Lozano, J.; Escrivá, E.; Legros, J.-P.; Dahan, F. *J. Chem. Soc., Dalton Trans.* **1991**, 1057.

59. Castro, I.; Faus, J.; Julve, M.; Journaux, Y.; Sletten, J. *J. Chem. Soc., Dalton Trans.* **1991**, 2533.
60. Sisley, M. J.; Jordan, R. B. *Inorg. Chem.* **1991**, 30, 2190.
61. Frankenbach, G. M.; Beno, M. A.; Kini, A. M.; Williams, J. M.; Welp, U.; Thompson, J. E.; Whangbo, M.-H. *Inorg. Chim. Acta* **1992**, 192, 195.
62. Bouayad, A.; Brouca-Cabarrecq, C.; Trombe, J.-C.; Gleizes, A. *Inorg. Chim. Acta* **1992**, 195, 193.
63. Xanthopoulos, C. E.; Sigalas, M. P.; Katsoulos, G. A.; Tsipis, C. A.; Terzis, A. *Polyhedron* **1992**, 11, 2819.
64. Xanthopoulos, C. E.; Sigalas, M. P.; Katsoulos, G. A.; Tsipis, C. A.; Hadjikostas, C. C.; Terzis, A.; Mentzafos, M. *Inorg. Chem.* **1993**, 32, 3743.
65. Khan, M. I.; Chang, Y.-D.; Chen, Q.; Salta, J.; Lee, Y.-S.; O'Connor, C. J.; Zubieta, J. *Inorg. Chem.* **1994**, 33, 6340.
66. Castro, I.; Sletten, J.; Glaerum, L. K.; Cano, J.; Lloret, F.; Faus, J.; Julve, M. *J. Chem. Soc., Dalton Trans.* **1995**, 3207.
67. Shi, J.-M.; Yan, S.-P.; Liao, D.-Z.; Jaing, Z.-H.; Wang, G.-L.; Wang, R.-J.; Wang, H.-C.; Yao, X.-K. *Chinese J. Struct. Chem. (Jiegou Huaxue)*. **1995**, 14, 102.
68. Yaghi, O. M.; Li, G.; Groy, T. L. *J. Solid State Chem.* **1995**, 117, 256.
69. Yaghi, O. M.; Li, G.; Groy, T. L. *J. Chem. Soc., Dalton Trans.* **1995**, 727.
70. Hilbers, M.; Meiwald, M.; Mattes, R. Z. *Naturforsch.* **1996**, 51b, 57.
71. Lee, C.-R.; Wang, C.-C.; Wang, Y. *Acta Crystallogr.* **1996**, B52, 966.
72. Castro, I.; Calatayud, M. L.; Sletten, J.; Lloret, F.; Julve, M. *J. Chem. Soc., Dalton Trans.* **1997**, 811.
73. Dhillon, R.; Elduque, A.; Oro, L. A.; Pinillos, M. T. *Inorg. Chim. Acta* **1997**, 255, 351.
74. Graf, M.; Stoeckli-Evans, H.; Escuer, A.; Vicente, R. *Inorg. Chim. Acta* **1997**, 257, 89.
75. Gutschke, S. O. H.; Molinier, M.; Powell, A. K.; Wood, P. T. *Angew. Chem. Int. Ed. Engl.* **1997**, 36, 991.
76. Hall, L. A.; Williams, D. J.; Menzer, S.; White, A. J. P. *Inorg. Chem.* **1997**, 36, 3096.
77. Braga, D.; Grepioni, F. *Chem. Commun.* **1998**, 911.
78. Sletten, J.; Bjørsvik, O. *Acta Chem. Scand.* **1998**, 52, 770.
79. Sletten, J.; Daraghme, H.; Lloret, F.; Julve, M. *Inorg. Chim. Acta* **1998**, 279, 127.
80. Castro, I.; Calatayud, M. L.; Sletten, J.; Lloret, F.; Julve, M. *Inorg. Chim. Acta* **1999**, 287, 173.
81. Yufit, D. S.; Price, D. J.; Howard, J. A. K.; Gutschke, S. O. H.; Powell, A. K.; Wood, P. T. *Chem. Commun.* **1999**, 1561.
82. Crispini, A.; Pucci, D.; Aiello, I.; Ghedini, M. *Inorg. Chim. Acta* **2000**, 304, 219.
83. Wang, Y.; Stucky, G. D.; Williams, J. M. *J. Chem. Soc., Perkin Trans. 2*, **1974**, 35.
84. West, R.; Powell, D. L. *J. Am. Chem. Soc.* **1963**, 85, 2577.
85. Macintyre, W. M.; Werkema, M. S. *J. Chem. Phys.* **1964**, 42, 3563.
86. Peters, K.; Peters, E. M.; v. Schnering, H. G. *Acta Crystallogr.* **1978**, A34, S101.
87. Keller, H. J.; Traeger, U. *Acta Crystallogr.* **1979**, B35, 1887.
88. Endres, H.; Schendzielorz, M. *Acta Crystallogr.* **1983**, C39, 1528.
89. Marsh, R. E.; Bernal, I. *Acta Crystallogr.* **1995**, B51, 300.
90. Castan, P.; Deguenon, D.; Fabre, P.-L.; Bernardinelli, G. *Polyhedron* **1992**, 11, 901.
91. MacDonald, D. J. *J. Org. Chem.* **1968**, 33, 4559.
92. Schwartz, L. M.; Howard, L. O. *J. Phys. Chem.* **1971**, 75, 1798.
93. Schwartz, L. M.; Howard, L. O. *J. Phys. Chem.* **1970**, 74, 4374.
94. Semmingsen, D.; Hollander, F. J.; Koetzle, T. F. *J. Chem. Phys.* **1977**, 66, 4405.
95. Semmingsen, D. *Acta Chem. Scand.* **1973**, 27, 3961.

96. Semmingsen, D. *Acta Chem. Scand. Ser. A*, **1975**, 29, 470.
97. McMahon, M. I.; Nelmes, R. J.; Kuhs, W. F.; Semmingsen, D. *Z. Kristallogr.* **1991**, 195, 231.
98. Katrusiak, A.; Nelmes, R. J. *J. Phys. C: Solid State Phys.* **1986**, 19, L765.
99. Tun, Z.; Nelmes, R. J.; McIntyre, G. J. *J. Phys. C: Solid State Phys.* **1987**, 20, 5667.
100. Baglin, F. G.; Rose, C. B. *Spectrochim. Acta* **1970**, 26A, 2293.
101. Ito, M.; West, R. *J. Am. Chem. Soc.* **1963**, 85, 2580.
102. Bouayad, A.; Trombe, J.-C.; Gleizes, A. *Inorg. Chim. Acta* **1995**, 230, 1.
103. Castro, I.; Sletten, J.; Calatayud, M. L.; Julve, M.; Cano, J.; Lloret, F.; Caneschi, A. *Inorg. Chem.* **1995**, 34, 4903.
104. Condren, S. M.; McDonald, H. O. *Inorg. Chem.* **1973**, 12, 57.
105. Long, G. J. *Inorg. Chem.* **1978**, 17, 2959.
106. Coucouvanis, D.; Hollander, F. J.; West, R.; Eggerding, D. *J. Am. Chem. Soc.* **1974**, 96, 3006.
107. Coucouvanis, D.; Holah, D. G.; Hollander, F. J. *Inorg. Chem.* **1975**, 14, 2657.
108. Petit, J.-F.; Trombe, J.-C.; Gleizes, A.; Galy, J. C. R. *Seances Acad. Sci. Ser. 2*, **1987**, 304, 1117.
109. Arrizabalaga, P.; Bernardinelli, G.; Geoffroy, M. *Inorg. Chim. Acta* **1988**, 154, 35.
110. Toftlund, H. *J. Chem. Soc., Chem. Commun.* **1979**, 837.
111. Hosein, H.-A.; Jaggernauth, H.; Alleyne, B. D.; Hall, L. A.; White, A. J. P.; Williams, D. J. *Inorg. Chem.* **1999**, 38, 3716.
112. Lin, K.-J.; Lii, K.-H. *Angew. Chem., Int. Ed. Engl.* **1997**, 36, 2076.
113. Müller, A.; Rohlfing, R.; Krickemeyer, E.; Bögge, H. *Angew. Chem., Int. Ed. Engl.* **1993**, 32, 909.
114. Zou, J.; Dou, P. Y.; Wang, K. *J. Inorg. Biochem.* **1997**, 65, 145.
115. Zou, J.; Dong Yang, X.; An, F.; Wang, K. *J. Inorg. Biochem.* **1998**, 70, 227.
116. Aime, S.; Botta, M.; Crich, S. G.; Giovenzana, G.; Palmisano, G.; Sisti, M. *Bioconj. Chem.* **1999**, 10, 192.
117. Aime, S.; Botta, M.; Fasano, M.; Crich, S. G.; Terreno, E. *Coord. Chem. Rev.* **1999**, 186, 321.
118. Trombe, J.-C.; Petit, J.-F.; Gleizes, A. *Eur. J. Solid State Inorg. Chem.* **1991**, 28, 669.
119. Scott, K. L.; Weighardt, K.; Sykes, A. G. *Inorg. Chem.* **1973**, 12, 655.
120. Donegá, C. de M.; Ribeiro, S. J. L.; Gonçaves, R. R.; Blasse, G. *J. Phys. Chem. Solids* **1996**, 57, 1727.
121. Legendziewicz, J. *Acta Phys. Pol. A*, **1996**, 90, 127.
122. Ribeiro, S. J. L.; Gonçaves, R. R.; de Oliveira, L. F. C.; Santos, P. S. *J. Alloys and Compounds* **1994**, 216, 61.
123. Alleyne, B. D.; Hall, L. A.; Kahwa, I. A.; White, A. J. P.; Williams, D. J. *Inorg. Chem.* **1999**, 38, 6278.
124. Huskowska, E.; Glowiak, T.; Legendziewicz, J.; Oremek, G. *J. Alloys and Compounds* **1992**, 179, 13.
125. Sazou, D.; Kokkinidis, G. *Can. J. Chem.* **1987**, 65, 397.
126. Farnia, G.; Sandonà, G.; Marcuzzi, F. *J. Electroanal. Chem.* **1993**, 348, 339.
127. Rodes, A.; Pérez, J. M.; Orts, J. M.; Feliu, J. M.; Aldaz, A. *J. Electroanal. Chem.* **1993**, 352, 345.
128. Rodes, A.; Orts, J. M.; Pérez, J. M.; Feliu, J. M.; Aldaz, A. *J. Electroanal. Chem.* **1997**, 421, 195.
129. Narinesingh, D.; Ramcharitar, N.; Hall, L. A.; Williams, D. J. *Polyhedron* **1994**, 13, 45.

130. Hosein, H.-A.; Hall, L. A.; Lough, A. J.; Desmarais, W.; Vela, M. J.; Foxman, B. M. *Inorg. Chem.* **1998**, *37*, 4184.
131. Alleyne, B. D.; Hall, L. A.; Hosein, H.-A.; Jaggernauth, H.; White, A. J. P.; Williams, D. J. *J. Chem. Soc., Dalton Trans.* **1998**, 3845.
132. Alleyne, B. D.; Hosein, H.-A.; Jaggernauth, H.; Hall, L. A.; White, A. J. P.; Williams, D. J. *Inorg. Chem.* **1999**, *38*, 2416.
133. Alleyne, B. D.; St. Bernard, L.; Jaggernauth, H.; Hall, L. A.; Baxter, I.; White, A. J. P.; Williams, D. J. *Inorg. Chem.* **1999**, *38*, 3774.
134. Williams, A. R.; Alleyne, B. D.; Hall, L. A.; White, A. J. P.; Williams, D. J.; Thompson, L. K. *Inorg. Chem.* **2000**, *39*, 5265.
135. Alleyne, B. D.; Williams, A. R.; Hall, L. A.; White, A. J. P.; Williams, D. J. *Inorg. Chem.* **2001**, *40*, 1045.
136. Williams, A. R.; Alleyne, B. D.; Hosein, H.-A.; Jaggernauth, H.; Hall, L. A.; Foxman, B. M.; Thompson, L. K.; Agosta, C. *Inorg. Chim. Acta* **2001**, *313*, 56.
137. Williams, A. R.; Hall, L. A.; White, A. J. P.; Williams, D. J. *Inorg. Chim. Acta* **2001**, *314*, 117.
138. Braga, D.; Bazzi, C.; Maini, L.; Grepioni, F. *Cryst. Eng. Commun.* **1999**, *5*.
139. Iwuoha, E.; Williams, A. R.; Hall, L. A. *Biosensors and Bioelectronics* **2000** (submitted).
140. Iwuoha, E.; Williams-Dottin, A. R.; Hall, L. A. *Electroanal. Chem.* (submitted).
141. Seitz, G.; Imming, P. *Chem. Rev.* **1992**, *92*, 1227.
142. Iwuoha, E.; Williams-Dottin, A. R.; Hall, L. A. *Electrochim. Acta* (submitted).

# APPLICATIONS FOR POLYAZA MACROCYCLES WITH NITROGEN-ATTACHED PENDANT ARMS

KEVIN P. WAINWRIGHT

School of Chemistry Physics and Earth Sciences, The Flinders University of South Australia,  
GPO Box 2100, Adelaide, South Australia 5001, Australia

- I. Introduction
  - A. Second-Generation Pendant-Arm Macrocycles
- II. Bioinorganic Applications
  - A. Hydrolytic Enzyme Models
  - B. Synthetic Ribonucleases
  - C. Nucleobase Recognition Reagents
  - D. Oxygenase Promoters
- III. Luminescent Sensors
  - A. Complexes with Pendant Fluorophores
  - B. Lanthanide Complexes with Pendant Antennae
- IV. Contrast Reagents for Magnetic Resonance Imaging
- V. Tumor-Directed Radioisotope Carriers
- VI. Surfactants
- VII. Molecular Receptors
- References

## I. Introduction

### A. SECOND-GENERATION PENDANT-ARM MACROCYCLES

Ever since the first report in 1976 (1), the synthesis and characterization of nitrogen-attached pendant donor polyaza macrocyclic ligands and their complexes have been a major focus of curiosity-driven research (2–4). Although initiated out of curiosity over whether they could be synthesized, and about the nature of the complexes they might form, there was, nonetheless, a steadfast belief, at least in the mind of this author (5), that once the syntheses had been mastered, the complexes would contribute to our understanding of a variety of aspects of bioinorganic chemistry. The connection between the two is that pendant

donor macrocycles provide a metal ion with a set of collectively nonlabile donors capable of localizing it and a set of labile donors capable of mediating the chemistry at other coordination sites, their role being similar to the dual role performed by the set of donor groups at the metal-ion binding sites found in some metalloenzymes and metalloproteins. It is pleasing to note now that contributions to bioinorganic chemistry began to emerge about a decade ago, moreover, these contributions have not been confined to that area of science alone. Indeed, the original notion of a pendant donor as one that would bind to its parent metal ion has now broadened to embrace pendant arms, which are capable of interacting noncovalently with a substrate attached to the metal ion or with the solvent. This review focuses on the complexes of nitrogen-attached pendant-arm polyaza macrocyclic ligands that have been prepared and used, with specific application to some secondary areas of scientific investigation in mind. To distinguish these macrocycles from those produced to test synthetic techniques or purely to establish the characteristics of their coordination chemistry, I have coined the term "second-generation pendant-arm macrocycle." It serves as a tribute to all the chemists who have devoted, and continue to devote, their expertise to the development of the synthetic methodology and to an understanding of the ensuing coordination chemistry.

## II. Bioinorganic Applications

### A. HYDROLYTIC ENZYME MODELS

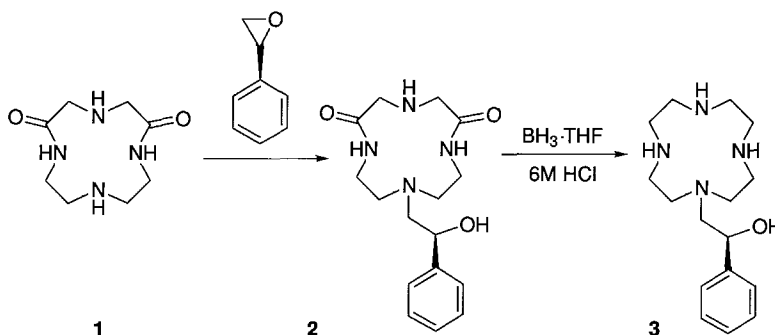
Kimura and his associates have been preeminent in exploiting the potential of Zn(II) complexes of pendant-arm polyaza macrocycles to act as models for the hydrolytic Zn(II)-containing enzymes. Collectively, their work in this area involves structurally unmodified macrocycles as well as pendant-arm macrocycles, and the reader is referred to a number of reviews (6–15) that summarize their work in its entirety. The particular object of this section is to examine how different types of pendant arm have been introduced onto a macrocyclic framework and how it has been possible to utilize their presence to elicit information of relevance to a particular group of enzymes. The enzyme groups studied using pendant-arm macrocycles have been the alkaline phosphatases and the class II aldolases.

#### 1. *Models for Alkaline Phosphatases*

Alkaline phosphatases, a highly efficient class of metalloenzymes containing two Zn(II) ions at the active site, hydrolyze phosphomonoesters

at close to the diffusion-controlled limit (16). It is now well established that the phosphomonoester substrate bridges the two Zn(II) sites and undergoes nucleophilic attack, first by the alkoxide group belonging to Ser 102, activated at one site, yielding a phosphoseryl intermediate, and then by hydroxide that emanates from a water molecule bound to the other Zn(II) site. Thus, the enzyme utilizes one Zn(II) site to activate the serine toward deprotonation and the other to deprotonate a water molecule, while both serve to enhance the electrophilicity of the phosphorus(V) center by being disposed in such a way that the phosphate can simultaneously bind to each of them through one or two of its oxo groups.

The first successful attempt to simulate some aspects of alkaline phosphatase activity by using a pendant donor macrocycle was done using the Zn(II) complex of ligand (**3**), which was formed from 2,6-dioxocyclen (cyclen = 1,4,7,10-tetraazacyclododecane) (**1**) (17) by reaction with (*S*)-styrene oxide followed by reduction of the intermediate diamide (**2**) (18).



The Zn(II) ion is held by the tetraaza assembly and further coordinated by the labile pendant alcohol, which simulates Ser 102 in the enzyme. Under these conditions, the pendant alcohol is activated toward deprotonation such that its  $\text{p}K_{\text{a}}$  drops from about 15 to 7.51 (at 298 K). Above pH 7.5, deprotonation of the pendant alcohol rather than a coordinated water molecule, was shown by NMR spectral changes associated with the protons in the pendant arm and by the crystal structure of the deprotonated Zn(II) complex (Fig. 1). Apparently,  $[\text{Zn}(\mathbf{3})]^+$  hydrolyzes phosphomonoesters too slowly for ease of investigation; however, the reaction with a phosphodiester, bis(4-nitrophenyl) phosphate, which is sufficient to clarify the proposed cooperative role of Ser 102 and Zn(II) in alkaline phosphatases, is considerably faster and was

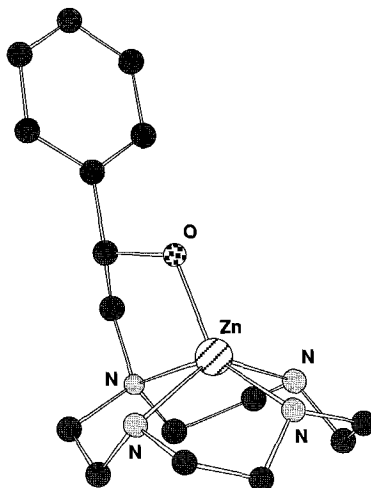
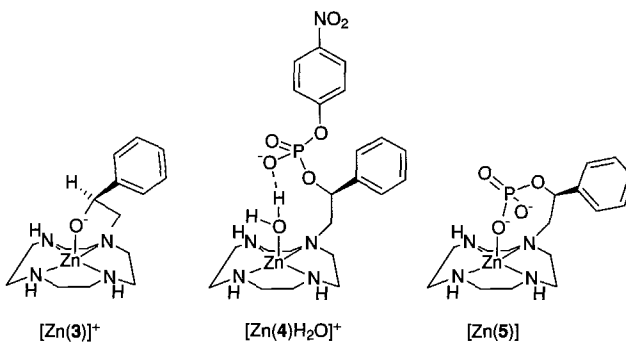
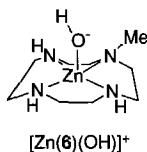


FIG. 1. Molecular structure of the Zn(II) complex of ligand **3** when isolated at pH 9.5.

thoroughly investigated. This reaction initially yields the phosphoseryl analog  $[\text{Zn}(\mathbf{4})\text{H}_2\text{O}]^+$  and then the bound monophosphoester  $[\text{Zn}(\mathbf{5})]$ .

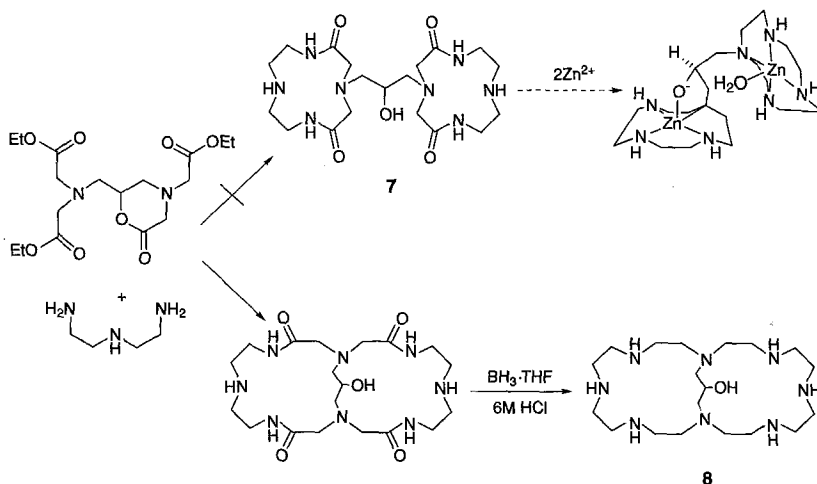


The rate of phosphorylation was found to be 125 times faster than hydrolysis of bis(4-nitrophenyl) phosphate by  $[\text{Zn}(\mathbf{6})(\text{OH})]^+$  (**19**, **20**), which lacks the pendant alcohol,

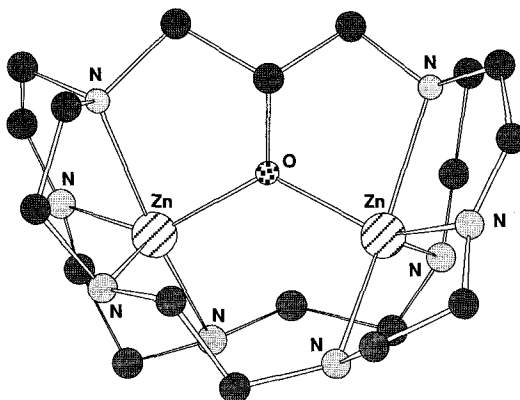


and the subsequent hydrolysis is 45,000 times faster than the rate of hydrolysis of ethyl(4-nitrophenyl) phosphate by  $[\text{Zn}(\mathbf{6})(\text{OH})]^+$ . The  $\text{p}K_{\text{a}}$  of the bound water molecule in  $[\text{Zn}(\mathbf{4})\text{H}_2\text{O}]^+$  is 9.1, which is considerably higher than is normally the case for water bound to a Zn(II) tetraaza macrocyclic complex ( $\mathbf{14}$ ), and higher than the value of 7.4 reported for water in the enzyme. This is thought to be due to competition between the water and the pendant phosphodiester anion for the coordination site, which probably does not occur in the enzyme owing to the availability of two Zn(II) sites. The monophosphoester  $[\text{Zn}(\mathbf{5})]$  was found to be inert toward further hydrolysis, and so, despite its otherwise illuminating properties,  $[\text{Zn}(\mathbf{3})]^+$  does not actually act as a catalyst.

The work described above indicated two reasons that explain why a dinuclear model is essential if one is to model alkaline phosphatase more closely: the high  $\text{p}K_{\text{a}}$  of  $[\text{Zn}(\mathbf{4})(\text{H}_2\text{O})]^+$ , and the inability of  $[\text{Zn}(\mathbf{5})]$  to sustain hydrolysis, probably because of the strong bonding of the dianionic phosphomonoester (compared to a monoanionic diester), which prevents formation of a Zn(II)-bound hydroxide at the same Zn(II) center. Kimura and co-workers addressed this need by attempting the synthesis of macrocycle  $\mathbf{7}$  in which two cyclen macrocycles are linked by a propyl group that carries the required pendant alcohol at the 2 position, according to the reaction shown in Scheme 1 ( $\mathbf{21}$ ). Instead of forming  $\mathbf{7}$ , however, this reaction produced the unexpected octaazacryptand  $\mathbf{8}$  which, although initially thought to be unpromising, reacted exclusively with the phosphomonoester dianion 4-nitrophenyl

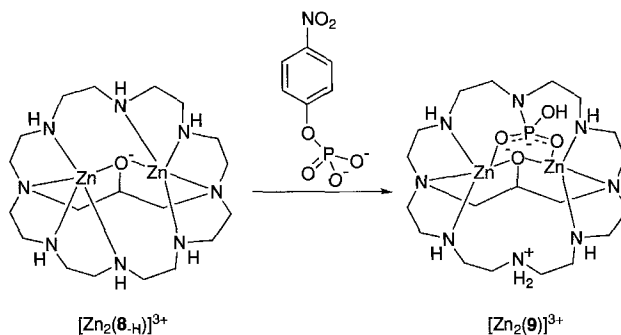


SCHEME 1 Reaction pathway used to form ligand **8**.

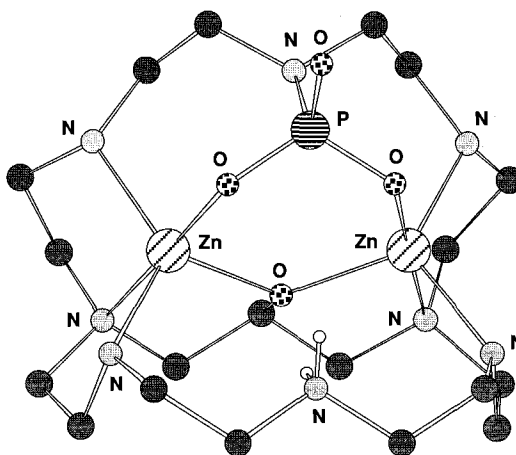
FIG. 2. Molecular structure of  $[\text{Zn}_2(\mathbf{8-H})]^{3+}$ .

phosphate, and not at all with the usually more reactive phosphodiester monoanion bis(4-nitrophenyl) phosphate or the neutral phosphotriester tris(4-nitrophenyl) phosphate. The initial complexation of Zn(II) with **8** produces only two observable species during potentiometric titration;  $[\text{Zn}_2(\mathbf{8})]^{4+}$  and  $[\text{Zn}_2(\mathbf{8-H})]^{3+}$ . The latter, having a deprotonated pendant alcohol predominates above pH 4.

The X-ray structure of  $[\text{Zn}_2(\mathbf{8-H})]^{3+}$  is shown in Fig. 2. The  $\text{pK}_a$  for the doubly coordinated pendant alcohol is below 4, in accord with corresponding measurements made on water molecules coordinated to a pair of Zn(II) ions in a cyclic octaamine (<7) (22), or in a cyclic tetraamine with four pendant amines (<5.3) (23). On reaction with 4-nitrophenyl phosphate, 4-nitrophenol is released and a complexed phosphoramidate is produced,  $[\text{Zn}_2(\mathbf{9})]^{3+}$ , resulting from attack of a secondary amine at phosphorus.



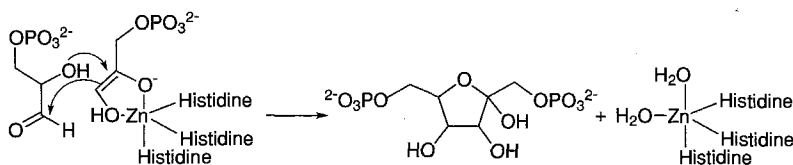
The crystal structure of  $[\text{Zn}_2(\mathbf{9})]^{3+}$  has been determined (Fig. 3), and from this it is known that the phosphoramidate bridges both Zn(II)

FIG. 3. Molecular structure of  $[\text{Zn}_2(\mathbf{9})]^{3+}$ .

ions, situated 3.65 Å apart, using two of its oxo groups. With adenosine triphosphate ( $\text{ATP}^{4-}$ ), phosphoryl transfer to  $[\text{Zn}_2(\mathbf{8}_{\text{-H}})]^{3+}$  occurs in a similar manner, yielding adenosine diphosphate ( $\text{ADP}^{3-}$ ) and  $[\text{Zn}_2(\mathbf{9})]^{3+}$ . However, the same reaction carried out with free **8** gave inorganic phosphate and  $\text{ADP}^{3-}$ . From this, it is evident that the Zn(II) ions play a significant role in stabilizing the phosphoryl-transferred intermediate  $[\text{Zn}_2(\mathbf{9})]^{3+}$ .

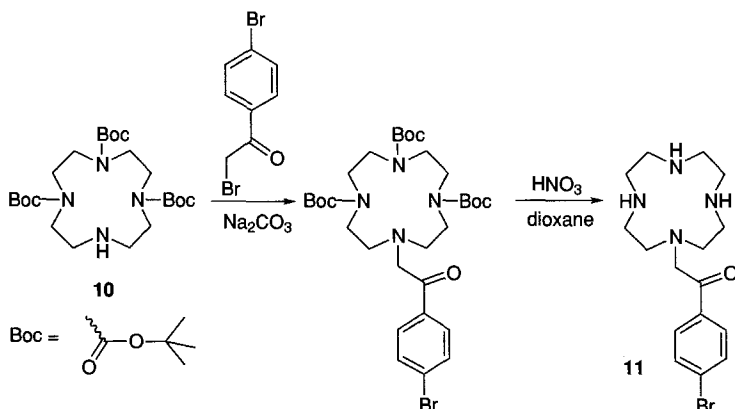
## 2. Model for Class II Aldolases

The class II aldolase enzymes contain a single Zn(II) ion that is believed to be responsible for stabilizing the enediolate form of dihydroxyacetone phosphate such that it can undergo aldol condensation with an aldol acceptor such as D-glyceraldehyde 3-phosphate, leading to the catalytic formation and decomposition of, in this case, D-fructose 1,6-bis(phosphate) (24). This is shown diagrammatically in Scheme 2. To test this hypothesis and to establish whether Zn(II) is a sufficiently strong Lewis acid to deprotonate a methylene group adjacent to a carbonyl



SCHEME 2 Proposed stabilization of the enediolate form of dihydroxyacetone phosphate by Zn(II) in the class II aldolase enzyme fructose 1,6-bis(phosphate) aldolase, and its reaction with D-glyceraldehyde 3-phosphate to form D-fructose 1,6-bisphosphate.

group (which normally has a  $pK_a$  of 18–19) to produce an enolate, the pendant donor macrocyclic ligand **11** was synthesized (25). This was achieved by the reaction of 1,4,7-tris(*tert*-butoxycarbonyl)cyclen (**10**) (26) with  $\alpha,4'$ -dibromoacetophenone in  $\text{CH}_3\text{CN}$  and subsequent deprotection with aqueous  $\text{HNO}_3$ .



The X-ray structure of the  $\text{Zn}(\text{II})$  complex of **11** was solved, establishing that the ligand binds in its keto form with the carbonyl group and one water molecule combining with the four nitrogen atoms of the macrocycle to produce the octahedral complex shown in Fig. 4.

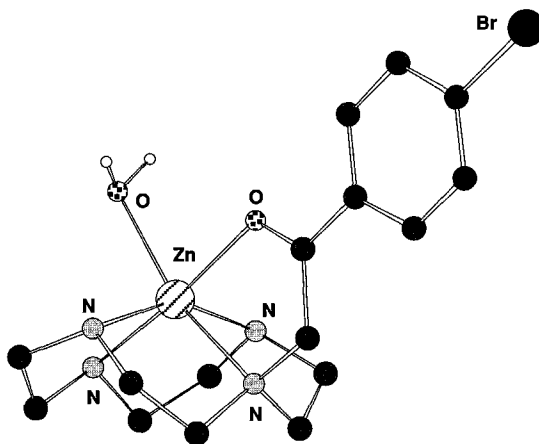
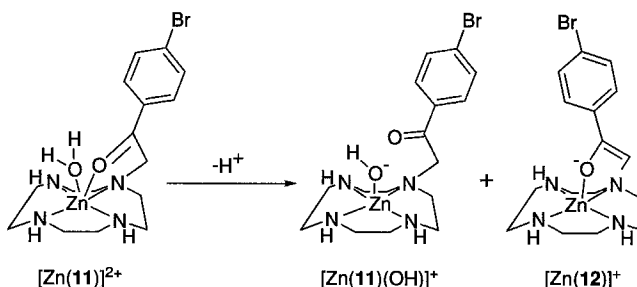


FIG. 4. Molecular structure of the  $\text{Zn}(\text{II})$  complex of ligand **11**, showing it to be in the keto form.

Potentiometric titration of free **11** in aqueous solution indicated no tendency for deprotonation of the active methylene group below pH 11. In the presence of Zn(II), however, a similar titration indicated a deprotonation corresponding to a  $pK_a$  of 8.41. With the assistance of spectroscopic data, this deprotonation was unambiguously assigned to the formation of a 3:1 equilibrium mixture of  $[Zn(11)(OH)]^+$  and the enolate complex  $[Zn(12)]^+$ .



The equilibrium moves completely towards  $[Zn(12)]^+$  when the aqueous solvent is replaced by  $CH_3CN$ , and from this it was possible to isolate  $[Zn(12)]ClO_4$ .

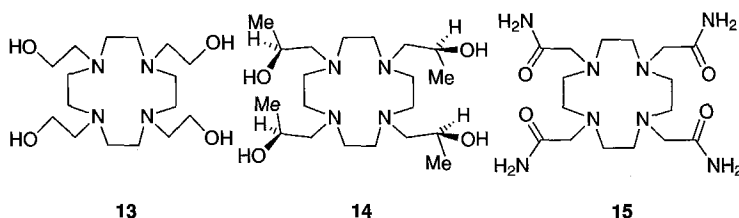
This appears to be the first example of a macrocycle with a pendant enolate, and its characterization in this system supports the suggestion that similar species occur as intermediates in the reaction pathway associated with the class II aldolases. Deprotonation of the carbonyl methylene group at near physiological pH corresponds to a change in the  $pK_a$  for this moiety of more than 10 orders of magnitude and indicates the extraordinary ability of Zn(II) in a constrained polyaza environment to polarize species that are coordinated to it. The observation of simultaneous formation of  $[Zn(11)(OH)]^+$ , coincidentally, suggested a mechanism for the retroaldol condensation in which the class II aldolases catalyze, for example, the decomposition of D-fructose 1,6-bis(phosphate) into its two aldol components. This requires deprotonation of the  $C_4$  hydroxyl group, and it has not hitherto been apparent how this is accomplished. It now seems possible that changing the hydrophilicity of the Zn(II) environment may be the means by which the direction of the enzymatic catalysis is controlled (7).

#### B. SYNTHETIC RIBONUCLEASES

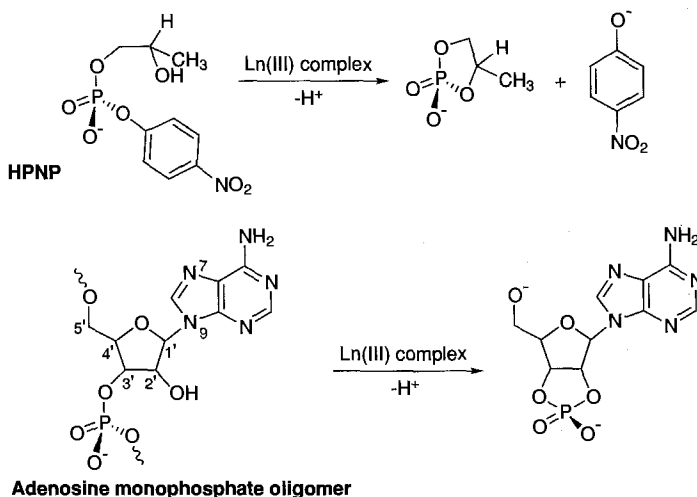
The observation that Ln(III) ions can catalyze phosphate ester transesterification, hydrolysis, and RNA cleavage (27) has prompted

extensive investigation of the possible use of Ln(III) complexes as synthetic ribonucleases. The use of macrocycles derived from cyclen with four pendant donors for this purpose is attractive, as they are known to form complexes that are inert toward dissociation (28, 29); and pendant alcohols coordinated to Ln(III), which probably occur substantially as alkoxides at physiological pH (30), can act as nucleophiles in the transesterification process.

Early investigations (30) of the rate of internal transesterification of the 4-nitrophenylphosphate ester of propylene glycol (HPNP) and also on RNA oligomers of adenosine phosphate were carried out using Ln(III) complexes of ligands **13** (31) **14** (32) and **15** (29, 33, 34).

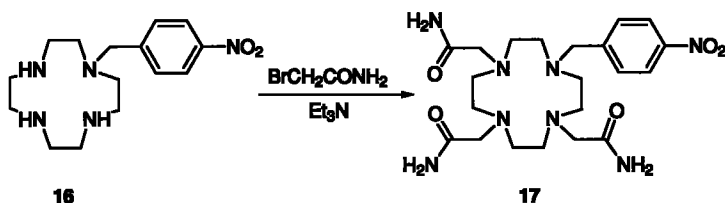


HPNP acts as a model substrate for RNA, as shown in Scheme 3. It was discovered that, for catalysis, the Ln(III) complex requires two vacant coordination sites in cases where a pendant alkoxide is not available, or one if it is. Thus, potentially nine-coordinate Ln(III) complexes of



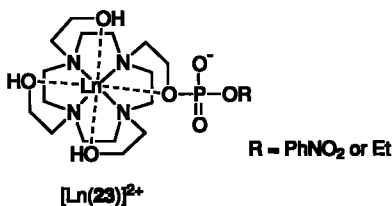
SCHEME 3 The relationship between the transesterification of HPNP and RNA cleavage.

**13** or **14** catalyze transesterification, but those of **15** do not, except when the metal ion is La(III), which is capable of ten coordination (29, 35). It appears from this that coordination of Ln(III) to the phosphate is essential for catalysis; and if alkoxide is not available, coordination of water (hydroxide at physiological pH) is also required. This theory was tested through the synthesis of the Eu(III) complex of new pendant donor macrocycle **17** (36) from **16** (37).

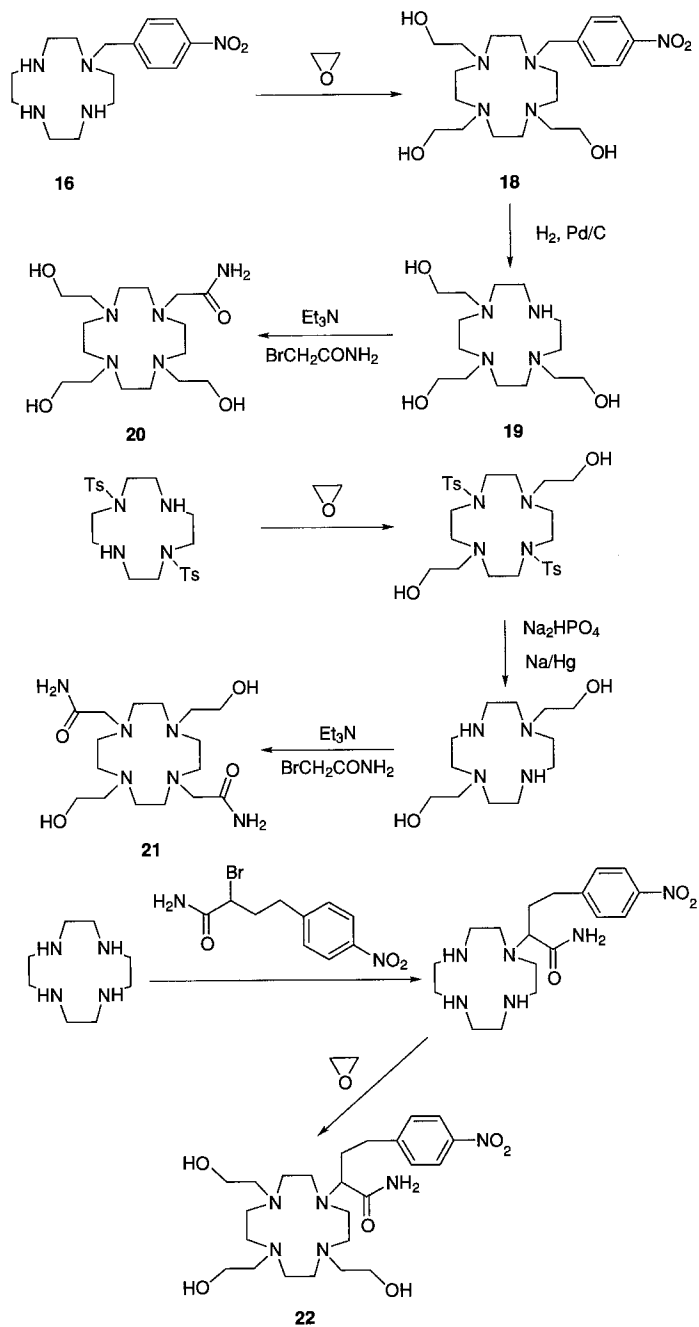


This complex appears to be a particularly useful precursor to pendant donor macrocycles in which one pendant arm is noncoordinating. In contrast to octadentate [Eu(**15**)]<sup>3+</sup>, the heptadentate complex [Eu(**17**)]<sup>3+</sup> catalyzes the internal transesterification of the RNA model substrate. Other mixed pendant donor ligands, **18**–**22**, were also synthesized to test these points (Scheme 4) (38). The heptadentate hydroxyethyl Eu(III) complexes of **18** and **19** were too dissociatively unstable to be considered for applications, but the octadentate amide-containing Eu(III) complexes of **20**–**22** were considerably more stable and were found to catalyze internal transesterification of the model RNA substrate, but at a rate about 10 times more slowly than that of [Eu(**13**)]<sup>3+</sup>.

Stoichiometric transesterification reactions in which the pendant hydroxyl group of La or [Eu(**13**)](CF<sub>3</sub>SO<sub>3</sub>)<sub>3</sub> is phosphorylated, giving [Ln(**23**)](CF<sub>3</sub>SO<sub>3</sub>)<sub>2</sub>, have been observed when bis(4-nitrophenyl) phosphate or ethyl(4-nitrophenyl) phosphate are used as the substrate (39). The reaction is 10-fold faster when the more acidic Eu(III) ion is used.



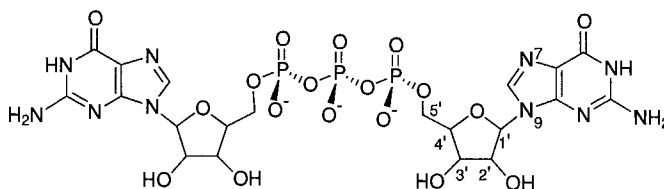
Advances in this area of work have led to the use of [Eu(**13**)]<sup>3+</sup> as a reagent able to cleave the 5' cap that forms the terminus of cellular



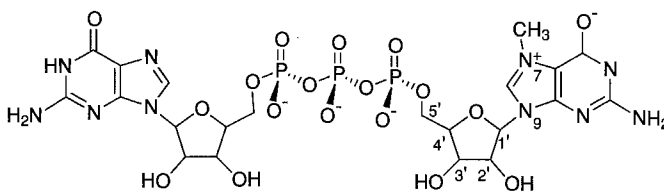
SCHEME 4

and viral RNAs synthesized by RNA polymerase II (40). This is deemed significant, as it may provide a way to inactivate the messenger RNA transcript which would then selectively inhibit gene expression at the mRNA level (41). The 5'-cap structure is an N7-methylated guanosine that is connected to the 5'-terminal nucleotide of the mRNA (transcription initiation site) via a triphosphate linkage between the 5'-hydroxyl groups of each sugar residue. Through initial experiments on a 5'-capped RNA:antisense substrate, it was demonstrated that  $[\text{Eu}(\mathbf{13})]^{3+}$  effected substantial decapitation; interestingly, however,  $[\text{Eu}(\mathbf{14})]^{3+}$  and  $[\text{Eu}(\mathbf{15})]^{3+}$  did not.

Detailed experiments on two 5'-cap model compounds, GpppG and  $m^7$  GpppG, have been used to investigate the chemistry of the  $[\text{Eu}(\mathbf{13})]^{3+}$  interaction.



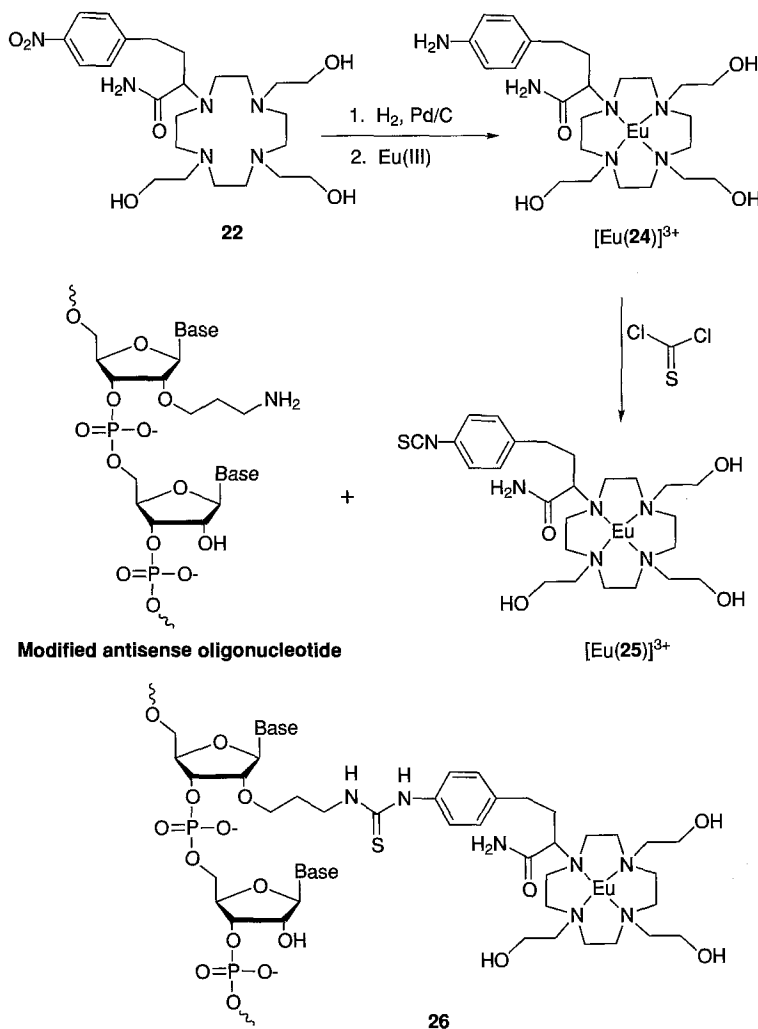
GpppG

 $m^7$ GpppG

From this, it is evident that the complex acts in a stoichiometric sense, binding via a pendant alkoxide preferentially to a phosphate adjacent to a guanosine, or in the case of  $m^7$  GpppG, to the phosphate adjacent to the nonmethylated guanosine, and so inducing cleavage. The principal macrocyclic product formed is analogous to  $[\text{Ln}(\mathbf{23})]^{2+}$  with  $R =$  guanosine. The presence of one equivalent of  $\text{Zn}(\text{II})$  [but not  $\text{Mg}(\text{II})$ ], which may aid the cleavage by polarizing the pair of phosphates not under attack by the pendant alkoxide, brings about a 15-fold rate enhancement of this reaction (42).

To extend this work so that  $[\text{Eu}(\mathbf{13})]^{3+}$  could be attached to an antisense oligonucleotide, which would target the capped end of a mRNA, it was necessary to convert the nitro group of ligand **22** to an

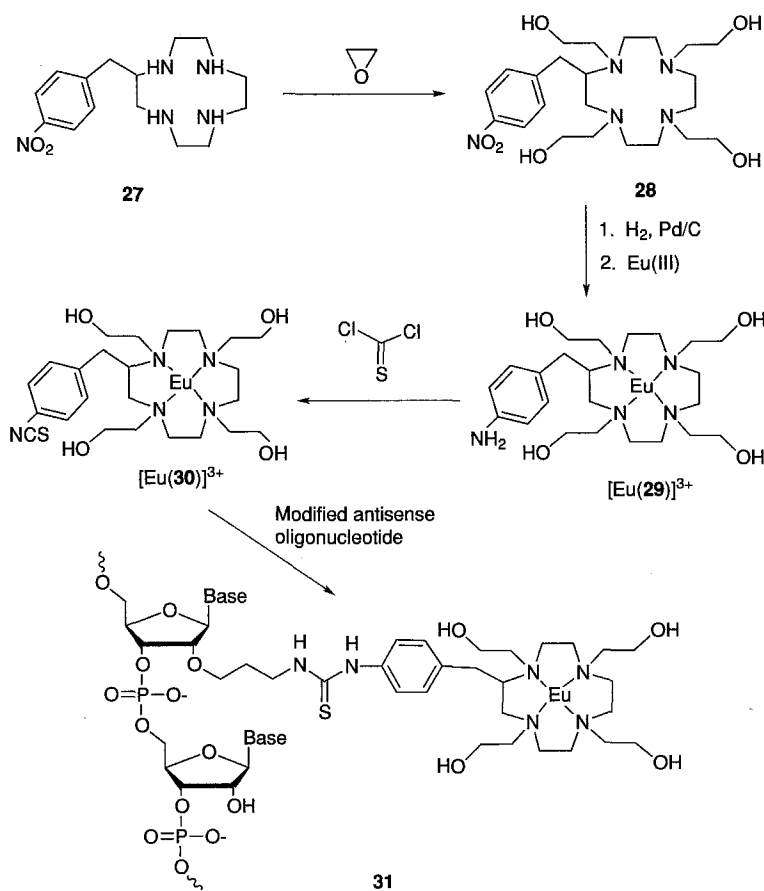
isothiocyanato group. This was done via the amine **24** and reaction of its Eu(III) complex with thiophosgene to give complex **25** (Scheme 5) (43). [Eu(**25**)]<sup>3+</sup> was reacted with a 2'-propylamine modified oligonucleotide to give the oligonucleotide-europium complex conjugate, **26** (41). By equipping the antisense oligonucleotide with the Eu(III) complex, a 3-fold higher inhibition of protein expression was achieved than in the absence of the attached Eu(III) complex (41). It is possible that this is a



SCHEME 5

result of 5'-cap cleavage, involving the same mechanism as that determined for the model compounds GpppG and m<sup>7</sup>GpppG: alternatively, it may be that the macrocyclic complex simply exerts a steric blocking effect toward one of the proteins important in translation. It was noted that the 5'-cap cleavage reaction proceeded slowly and that significant loss of Eu(III) from the complex was apparent after 24 h, ultimately limiting the extent of 5'-cap cleavage to about 25%.

Experiments directed toward sequence-specific RNA cleavage have been conducted using both **26** and the Eu(III) complex **31** derived from **27** (44) by the same sequence of reactions used to form **26** (Scheme 6). Surprisingly, in view of the results described above, where phosphate

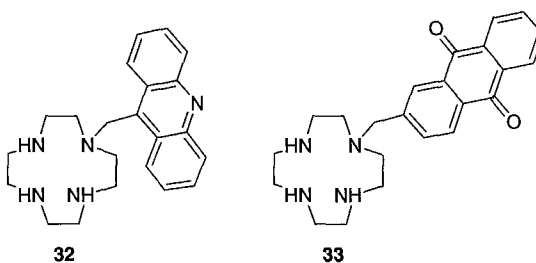


SCHEME 6

cleavage was seen to be best promoted by the Eu(III) complex having the greatest number of pendant hydroxyethyl groups, it was found that [Eu(**26**)]<sup>3+</sup> promotes a slightly greater extent of cleavage than does [Eu(**31**)]<sup>3+</sup>, although the difference is just barely beyond the bounds of experimental error. Other workers have shown that the attachment of pendant groups to the carbon framework of the macrocycle has a destabilizing effect on the Ln(III) complexes (45, 46), and this may be a contributing reason.

### C. NUCLEOBASE RECOGNITION REAGENTS

Molecular recognition of DNA and RNA components is clearly an important biochemical objective that presents a considerable challenge to the synthetic chemist. One approach to this has used pendant-arm macrocycles to build upon the earlier observation that [Zn(cyclen)]<sup>2+</sup> is able to bind deoxythymidine (dT) and uridine (U) selectively from a mixture of all nucleosides in aqueous solution at physiological pH, with binding constants of 10<sup>5.6</sup> and 10<sup>5.2</sup> M<sup>-1</sup>, respectively (47). These particular nucleosides are differentiated by the presence of the imido group (OC-NH-CO) which, upon deprotonation, coordinates to Zn(II) via the nitrogen, then hydrogen-bonds to a *trans*-related pair of cyclen NH groups via the two carbonyl oxygen atoms, either directly or with the interpolation of a water molecule (Fig. 5). It occurred to Kimura and co-workers that this binding could be enhanced by the attachment of a pendant aromatic moiety to the cyclen, which would be capable of engaging in a stabilizing  $\pi$ - $\pi$  interaction. Accordingly, ligands **32** and **33** were synthesized using excess cyclen and 9-bromomethylacridine (48) or 2-bromomethylantraquinone (49).



This appears to be the first time that pendant arms have been deliberately introduced onto a macrocycle to stabilize a host-guest interaction in a ternary complex via noncovalent interaction. The effect of the pendant acridine is to stabilize the interaction with dT and U

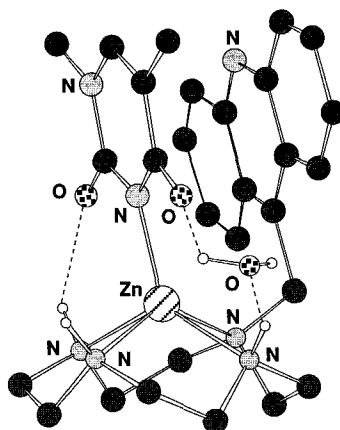
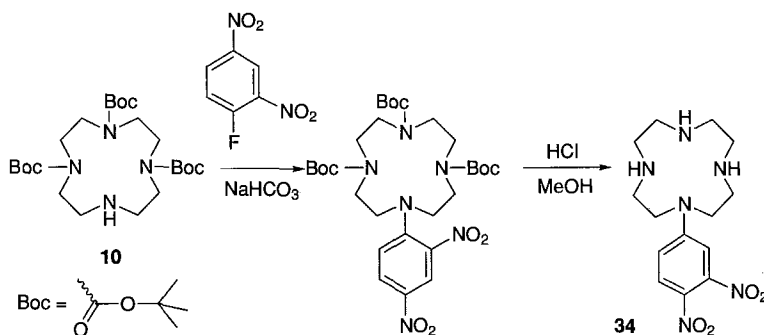


FIG. 5. The orientation of 1-methylthymine and the pendant acridine in the Zn(II) complex of **32**.

by a factor of about 40, and slightly less in the case of the pendant anthraquinone containing complex. A strengthening of the otherwise negligible binding to 2'-deoxyguanosine (dG), presumably because of a favorable acridine-purine  $\pi$ - $\pi$  interaction, was also noted. The nature of the  $\pi$ - $\pi$  interaction is clearly seen in the crystal structure of the 1-methylthymine adduct of  $[\text{Zn}(\mathbf{32})]^{2+}$ , shown in Fig. 5. A similar stability enhancement is seen using ligand **34**.

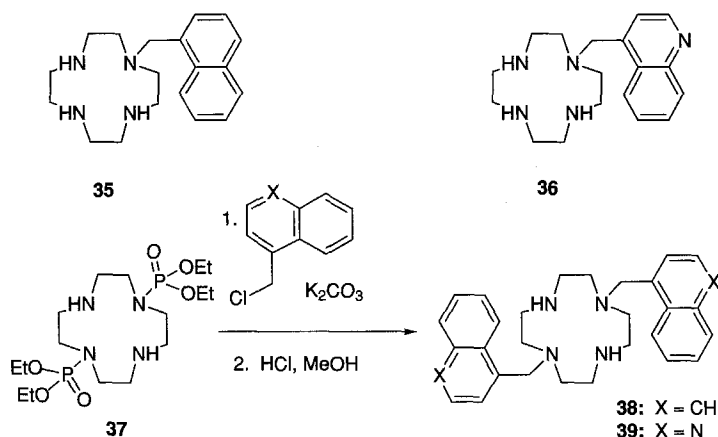


Ligand **34** acts as a tridentate ligand toward Zn(II), with the anilino nitrogen uncoordinated, but as a tetradentate ligand with Cu(II) (**50**).  $[\text{Zn}(\mathbf{34})]^{2+}$  binds dT with  $\log K = 6.9$  and the crystal structure of the 1-methylthymine adduct again shows evidence of  $\pi$ - $\pi$  interaction.

The interactions of  $[\text{Zn}(\mathbf{32})]^{2+}$  with uracil and thymine have been investigated in situations where these nucleobases occur as a part of a

single, polyU, or double-stranded polynucleotide (51, 52). It was discovered that  $[\text{Zn}(\mathbf{32})]^{2+}$  interacts with the uracil in polyU through deprotonation of the uracil at N(3) with little interference from the anionic phosphate backbone. The structures of double-stranded poly(A)·poly(U) and poly(dA)·poly(dT) were also significantly altered in the presence of  $[\text{Zn}(\mathbf{32})]^{2+}$ , indicating that the interactions with U and dT are preserved in this situation also. Experiments with the dinucleotide thymylthymidine showed that two  $[\text{Zn}(\mathbf{32})]^{2+}$  entities bind cooperatively to the thymidine bases, the binding constant for the second interaction being 20 times greater than that for the first (53). This cooperativity is not seen with  $[\text{Zn}(\text{cyclen})]^{2+}$ , highlighting the additional attributes that can be provided to these systems by the addition of an appropriate pendant arm, particularly as  $[\text{Zn}(\mathbf{32})]^{2+}$  also proved more efficient at disintegrating a thymine containing double-stranded octanucleotide than  $[\text{Zn}(\text{cyclen})]^{2+}$ .

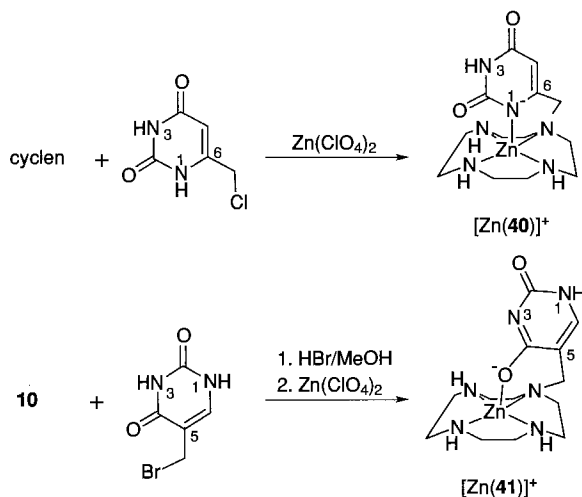
Further work on double-stranded DNA has called for the synthesis of ligands **35–39** (54–56).



Ligands **35** and **36** were prepared from precursor **10** and from unprotected cyclen, respectively, using standard methods. Ligands **38** and **39**, which have the uncommon 1,7-substitution pattern, were prepared with 4,10-protection of the cyclen residue achieved using bis(phosphoramidate) **37** (57). The Zn(II) complexes of **35**, **36**, **38**, and **39** as well as **32** selectively bind to the adenine/thymine-rich regions of double-stranded DNA via the thymine base using the fifth coordination site of the Zn(II) ion.

More detailed work has been done on uracil, to address in particular, the question of why the N(1) site is specifically selected for enzymatic

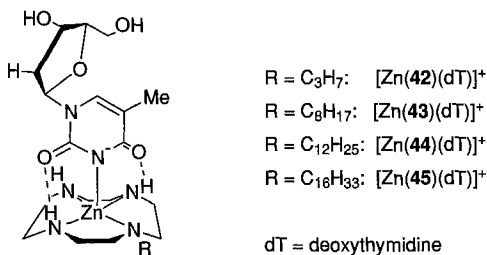
glycosylation rather than the more nucleophilic N(3) site (58). To do this, uracil was appended to cyclen through its 6 and 5 sites (ligands **40** and **41**) to investigate the ability of both Zn(II) and protonated amines in the metal free ligand to facilitate deprotonation of N(1) and to stabilize the negative charge at that site.



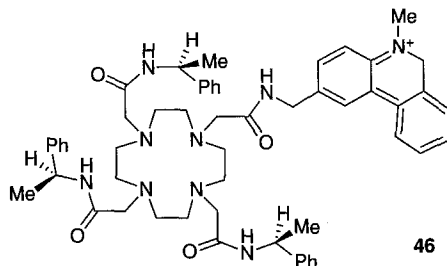
The findings from this work show that the  $pK_a$  of the N(1) site is lowered from 9.5 in free uracil to 7.1 in diprotonated (at *trans*-secondary amines) **40** and to about 3.9 in [Zn(**40**)]<sup>2+</sup>. Furthermore, tautomerization, through which proton transfer shifts the negative charge to N(3), is substantially reduced by Zn(II) complexation or by diprotonation, providing insight into how enzymatic control over this tendency may be achieved. Ligand **41** affords a less favorable geometric arrangement for positioning N(1) adjacent to the protonated amines of the diprotonated macrocycle, or to Zn(II) in the complex; accordingly, the  $pK_a$  of the uracil is reduced to 8.6 (6.0 in the complex) and the conjugate base is predominantly the C(4) enolate anion arising from N(3) deprotonation.

Enhancing the cell membrane-crossing capability of the Zn(II)-cyclen-based nucleobase recognition reagents was tackled by using pendant-arm macrocycles with a single long-chain alkyl pendant (**59**). These were derived from cyclen by reacting **10** with the appropriate alkyl bromide in the presence of Na<sub>2</sub>CO<sub>3</sub> and (*n*-Bu)<sub>4</sub>NI, followed by deprotection. Of the Zn(II) complexes of ligands **42–45**, [Zn(**45**)]<sup>2+</sup> was found to be the most efficient, raising the percentage of dT and U

extracted from basic aqueous solution (pH 9) into  $\text{CHCl}_3$ , from 0% to 22% and 13%, respectively, while not facilitating the extraction other nucleosides at all.



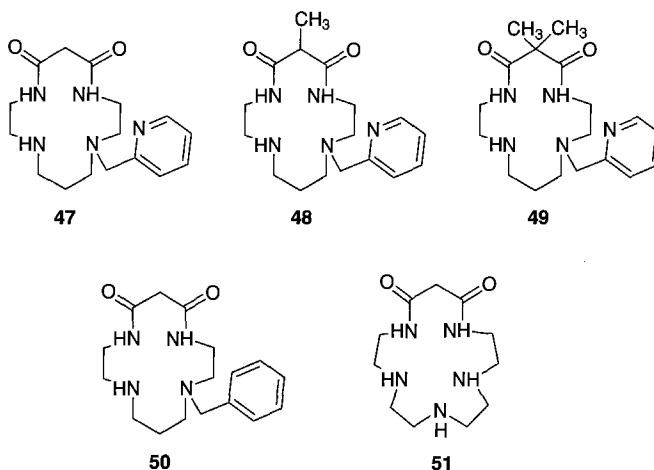
The binding of the Eu(III) complex of **46** to  $[(\text{CG})_6]_2$ ,  $[(\text{AT})_6]_2$ , and calf thymus DNA has been observed (60).



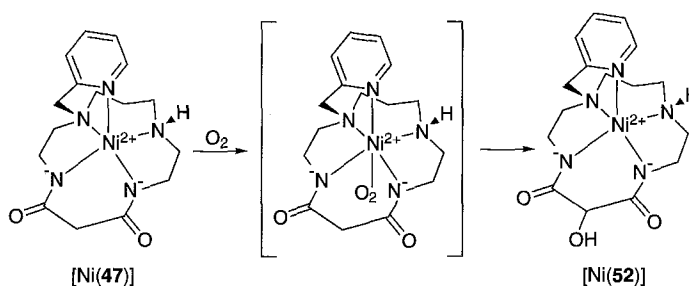
This is believed to occur by intercalation of the positively charged phenanthridinium unit, and it is noted that this occurs 50 times more effectively at the electron-rich C and G bases than at the AT sites. Ligand **46** was prepared by reaction of the acid chloride form of the pendant (61) to the molybdenum tricarbonyl complex of cyclen (62). The monosubstituted cyclen was then reacted with 3 moles of (*R*)- or (*S*)-*N*-(2-chloroethanoyl)-2-phenylethylamine (61). Quarternization was achieved by reaction of methyl iodide with the Eu(III) complex (61).

#### D. OXYGENASE PROMOTERS

A series of dioxocyclam (cyclam = 1,4,8,11-tetraazacyclotetradecane) based ligands (63–65) have been equipped with a single pyridyl moiety, forming ligands **47–49**, for the purpose of studying their potential for monooxygenase activity and its effect on DNA cleavage (66). Ligand **50** was produced as a reference compound.



These endeavors expand on an earlier observation of monooxygenase activity by the five-coordinate nickel(II) complex of dioxopentamine **51** (67) by replacing a ring nitrogen atom with a pendant nitrogen atom. It was found that  $[\text{Ni}(\mathbf{47})]$  reacts with an equimolar amount of dioxygen to produce  $[\text{Ni}(\mathbf{52})]$ . By comparison with results from **48–50**, it was shown that for this type of system to have monooxygenase activity, it is necessary for it to have a five-coordinate structure, with both amides deprotonated, apical coordination of the pyridine, and at least one C–H proton between the malonylamide groups. The formation of  $[\text{Ni}(\mathbf{52})]$



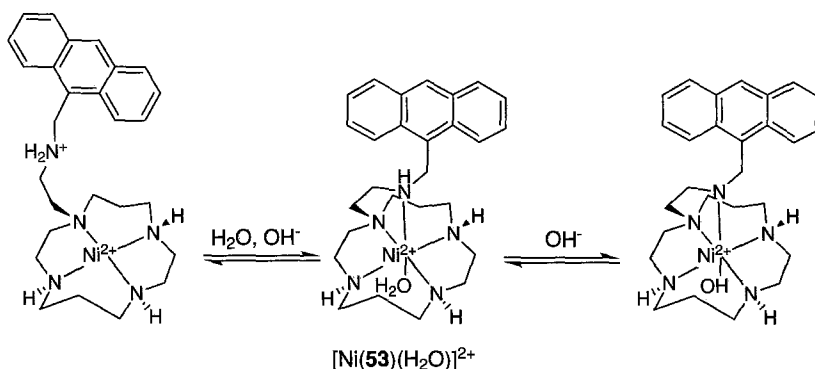
is believed to proceed through a 1:1  $\text{O}_2$  adduct. Like  $[\text{Ni}(\mathbf{51})]$ ,  $[\text{Ni}(\mathbf{47})]$  and, to a lesser extent,  $[\text{Ni}(\mathbf{48})]$  have the ability to activate oxygen to cleave plasmid DNA, but can perform this at pH 7.9, rather than 9.5; therefore, they may be more practical DNA cleavage reagents under physiological conditions.

## III. Luminescent Sensors

Chemical sensors generally consist of two components separated by a spacing linkage: a recognition unit that selectively interacts with the analyte, and a signaling unit that indicates the occurrence of a recognition event. One of the easiest and most sensitive signaling mechanisms that can be utilized in practical devices is a change in the fluorescence or luminescence of the sensor. In sensors where a metal ion is involved, macrocyclic ligands provide a convenient way of positioning the metal ion in a kinetically inert species. A fluorophore can then be attached as a pendant group to the macrocycle, with or without the capability for binding to the metal ion, in accordance with the demands of the individual sensor. Alternatively, changes in the luminescence of a lanthanide ion [Ln(III), usually Eu(III) or Tb(III), which luminesce in the visible region] can be used as indicators of changes in the concentration of the analyte. Again, pendant donor macrocycles, especially those providing eight coordination, are useful, since they produce an inert environment for the Ln(III) ion. The weak absorbance bands in Ln(III) spectra require that for adequate luminescence an antenna chromophore be attached to the molecule. In favorable cases, this absorbs strongly at a suitable wavelength and transfers the excitation energy to the Ln(III) ion, raising it to an excited state from which it can radiatively decay. The attachment can conveniently be done by allowing the antenna to form a part of one or more of the pendant donors.

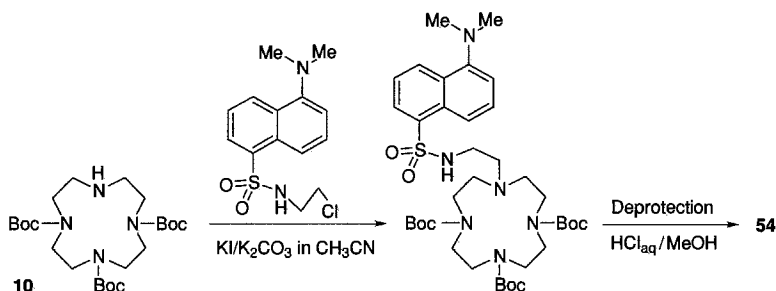
## A. COMPLEXES WITH PENDANT FLUOROPHORES

A pH-sensing system has been designed by attaching an anthracene moiety (the fluorophore), through a methylene group, to an ethylamine linkage that is pendant to one of the secondary amino groups in



cyclam (68). Depending on the pH, the Ni(II) complex of this ligand, **53**, may be square-planar, with the pendant amine protonated; octahedral, with the pendant amine coordinated and a water molecule *trans* to it, or octahedral, with the pendant amine coordinated and a hydroxyl ion *trans* to it. The complex shows its maximum fluorescence below pH 2; but this reversibly reduces by about 40% between pH 2 and pH 5, as the aquo species forms, then again between pH 7 and pH 10, effectively to nothing as the hydroxo species forms.

The observation that Zn(II) incorporation into apocarbonic anhydrase in the presence of dansylamide raises the fluorescence of the dansylamide (69) has led to the adoption of the dansyl group as a pendant accessory to cyclen to generate a Zn(II)-sensitive fluorophore **54** (70–72).



The Lewis acidity of the incoming Zn(II) ion deprotonates the sulfonamide group in aqueous solution at physiological pH, giving a single species which has been characterized by X-ray crystallography as that shown in Fig. 6. The fluorescence of the free ligand is enhanced by a

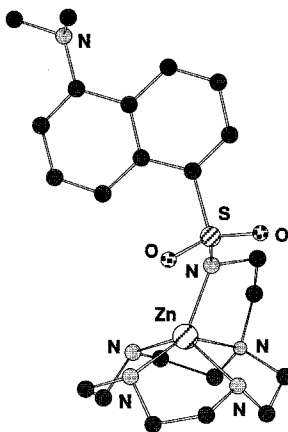
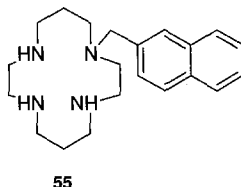


FIG. 6. Molecular structure of the Zn(II) sensor formed from ligand **54**.

factor of 4.9 upon Zn(II) incorporation and the emission wavelength is blue-shifted by 27 nm. The only other metal ion having a comparable effect on the fluorescence is Cd(II), and the only biologically significant interfering metal is Cu(II), which has a higher formation constant with **54**<sub>-H</sub> than Zn(II) and quenches the fluorescence.

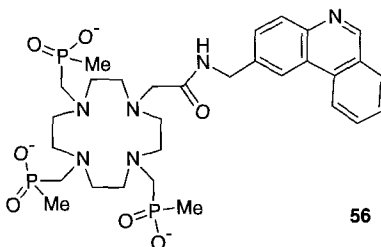
Temperature sensing has been suggested using the Ni(II) complex of ligand **55** (73).



In this case, increasing the temperature between about 27 and 65°C gradually switches the complex from a blue octahedral form, where two solvent molecules are coordinated in a *trans* relationship, to a yellow square-planar form. As this occurs, the fluorescence from the pendant naphthalene moiety increases by a factor of about 2.5 and is easily discernible in a micromolar solution of the complex.

#### B. LANTHANIDE COMPLEXES WITH PENDANT ANTENNAE

Luminescent sensors for pH, pO<sub>2</sub>, halide, and hydroxide concentrations have been developed using the Eu(III) and Tb(III) complexes of ligands **46** and **56** in their N-methylated, nonmethylated, or protonated forms (61, 74).

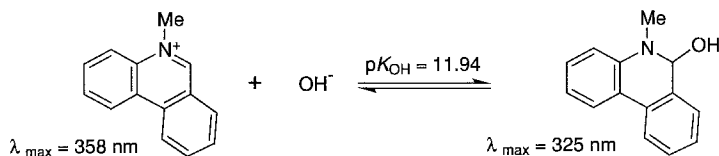


Ligands **56** and **46** were made by the same procedure except that in **56** *N*-(2-chloroethanoyl)-2-phenylethylamine was replaced by a combination of paraformaldehyde and MeP(OEt)<sub>2</sub> and the resulting triphosphinate ester was subjected to base hydrolysis.

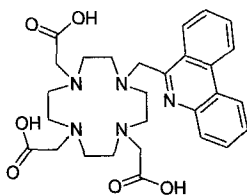
The principle behind the sensors is that the level of Ln(III)-based delayed luminescence, arising from the intramolecular energy transfer

that flows from the UV excitation of the antenna chromophore (the pendant phenanthridine), can be perturbed by the prevailing concentration of the analyte, each of which interacts with the chromophore in a different way. Protonation at the phenanthridine nitrogen in non-methylated **46** and **56** increases the intensity of the UV absorption by a factor of about 2, and shifts the longest absorption wavelength from about 350 nm to about 370 nm. For this reason, and because protonation diminishes the quenching of the intermediate singlet excited state by charge transfer to Eu(III), excitation at 370 nm of the Eu(III) complexes of nonmethylated **46** and **56** produces a sigmoidally increasing fluorescence as the pH is reduced from 7 to 2. With the corresponding Tb(III) complexes, excitation at the isosbestic wavelength (for the protonated and neutral phenanthridine) induces pH-dependent luminescence in the opposite direction, with the neutral form of the complex quite strongly emissive. This luminescence, however, is dependent on the level of dissolved oxygen. Thus, the Tb(III) complexes of non-methylated **46** and **56** can act as combined pH and O<sub>2</sub> sensors, or, if N-methylated, as O<sub>2</sub> sensors alone (61, 75). N-Methylated **46** and **56** undergo reversible hydroxide ion addition, as shown in Scheme 7. Since this results in the loss of the absorption band at 358 nm from **46**, Eu(III) luminescence, induced by excitation at 360 nm, is correspondingly reduced as the pH changes from 10 to 13. N-Methylphenanthridinium fluorescence is quenched by charge transfer from halide ions to the singlet excited state of the cation. Thus, the intensity of Eu(III) luminescence of complexes of **46** and **56** is sensitive to the presence of chloride ions at physiological concentration levels and may be used to determine their concentration. Interference from other biologically significant anions, such as citrate, lactate, bicarbonate, or hydrogen phosphate, is minimal.

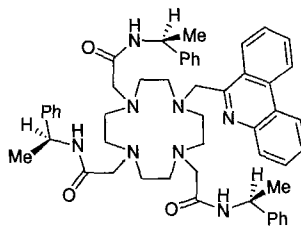
To assess the effect of distance between the antenna chromophore and the Eu(III) center on luminescence sensitization, a series of four additional Eu(III) complexes, of ligands **57–60**, each having the pendant phenanthridyl group at a different distance from the Eu(III) center, have been synthesized for comparison with [Eu(**46**)]<sup>4+</sup> (76).



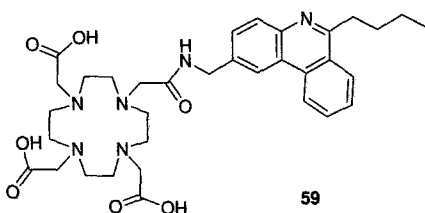
SCHEME 7 Reaction with OH<sup>−</sup> that allows [Eu(**46**)]<sup>4+</sup> to operate as an OH<sup>−</sup> sensor.



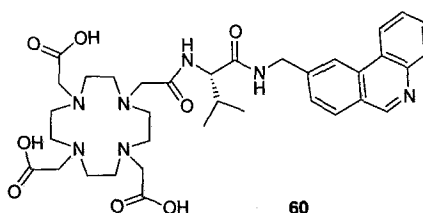
57



58



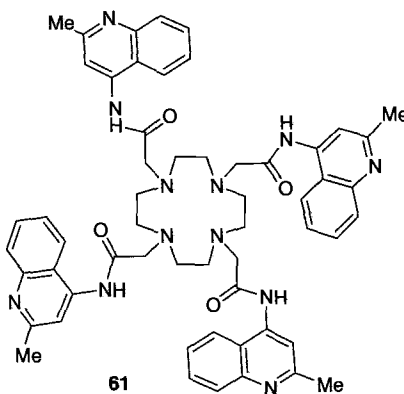
59



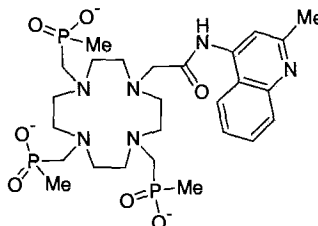
60

The finding was that the Eu(III) ion and the chromophore distance for 50% attenuation of the sensitisation is about 5.5 Å.

Wide-range pH sensors have also been made using the Eu(III) complexes of ligands **61** and **62**, which are prepared from the appropriate  $\alpha$ -haloamide of 2-methylquinoline reacting either with cyclen or with the molybdenum tricarbonyl complex of cyclen (**62**) followed by phosphinoxymethylation and base hydrolysis (**77**).



61

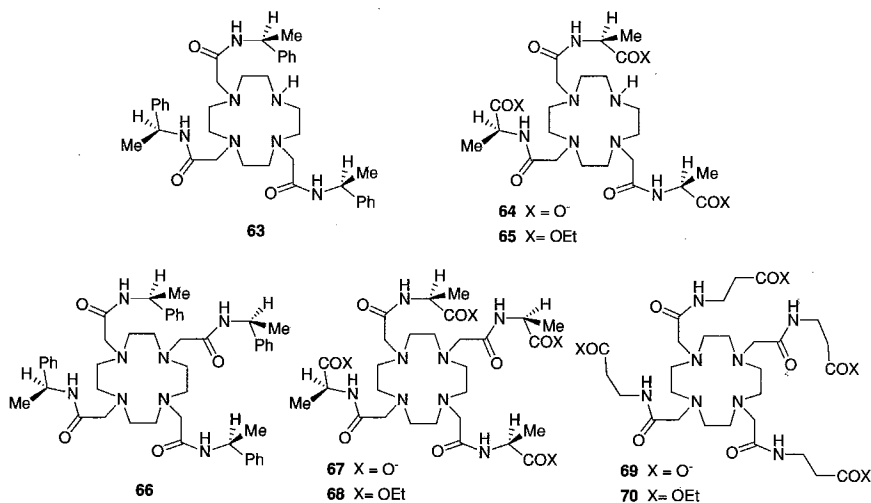


62

The delayed Eu(III) emission is switched on in acidic solution and behaves similarly to Eu(III) with **46** and **56**, providing pH sensing in the range pH 2.5–6.5 in the case of [Eu(**61**)]<sup>3+</sup>, and over a narrower range

(4.5–6.5) for [Eu(**62**)], which has only a single quinolyl nitrogen atom available for protonation. In the acidic range, the fluorescence emission from the ligand in either complex shows no significant change; rather, it undergoes a marked reduction between pH 8 and 11 as the aryl amide proton is removed, providing pH sensing in a region complementary to that accessed by observing the Eu(III) emission. The luminescence of [Tb(**62**)] shows enhancement only in acidic conditions in the absence of oxygen (which quenches the triplet state of the antenna chromophore). This complex has been proposed as a molecular logic gate corresponding to a two-input INHIBIT function (78): A response, luminescence enhancement, is observed as a result of just two chemical inputs—the presence of protons and the absence of oxygen.

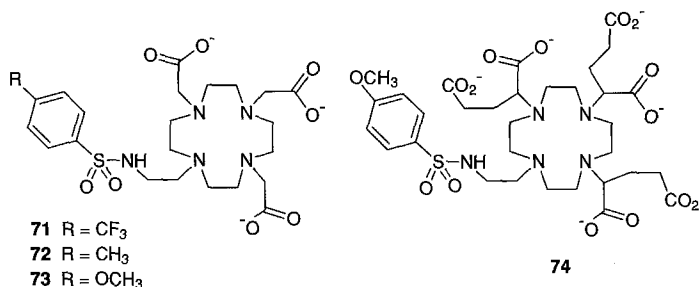
Selective sensitivity to bicarbonate concentration of Ln(III) luminescence, or the NMR relaxivity behavior of Gd(III) complexes (see Section IV), has been discovered using the heptadentate ligands **63** and **64** (79, 80). These allow for the coordination of two water molecules in the Ln(III) complexes, both of which undergo simultaneous replacement by a chelating bicarbonate ion. This induces a sudden drop in the NMR relaxivity and a sudden increase in luminescence. Other anions do not appear to replace both water molecules simultaneously, and so the effect with them is not as marked. Ligands **65**–**70** were also prepared during the course of this work.



Formation of **63** was achieved with three equivalents of (*R*)-*N*-(2-chloroethanoyl)-2-phenylethylamine using cyclen that was *p*-methoxytosylated at one amino site. Deprotection was achieved reductively

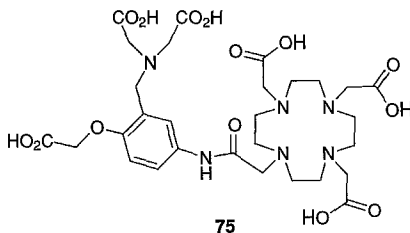
using Na with liquid ammonia in an EtOH-THF mixture. Ligand **64** was formed without protection of a cyclen amino site by alkylation under mild conditions with (*S*)-ethyl-*N*-2-chloroethanoylalanate followed by hydrolysis of the Ln(III) complexed triester.

Another instance of eliminating two water molecules coordinated to Ln(III) and thereby inducing a marked luminescence increase has been found using the pendant *p*-substituted benzene sulfonamides **71–74** (81).



In the Ln(III) complex, the sulfonamide nitrogen atom is uncoordinated while protonated; but on deprotonation, which commences above pH 5–6 depending on the *p*-substituent, it coordinates, displacing two water molecules and initiating an increase in luminescence which maximizes when deprotonation is complete at about pH 7.5. Within this pH range the level of luminescence can be used to measure pH to  $\pm 0.1$  units. Interference from bicarbonate is obviated by using **74**, which generates tri- or tetraanionic complexes. The various arylsulfonamides were introduced onto the cyclen ring by ring opening of the appropriate arylsulfonylaziridine with tris(*t*-butoxycarbonylmethyl)cyclen, followed by trifluoroacetic acid deprotection.

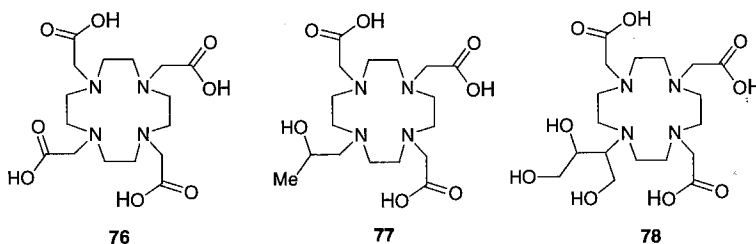
Selective signaling of Zn(II) ions by modulation of the Tb(III) luminescence in a macrocyclic complex carrying a combined antenna chromophore and pendant ligand designed specifically for Zn(II) has been noted using ligand **75** (82).



This ligand is formed by reaction of the chloromethyl form of the pendant group with tris(*t*-butoxycarbonylmethyl)cyclen followed by hydrolysis of the resulting triester.

#### IV. Contrast Reagents for Magnetic Resonance Imaging

Magnetic resonance imaging (MRI) is now a widely used clinical  $^1\text{H}$  NMR technique that provides images of tissues and organs based on their water distribution. The intensity of the water resonance increases in the presence of a deliberately injected paramagnetic contrast reagent because of the relaxation-time reduction that occurs for the protons in its vicinity. This provides contrast in the image received from water-containing areas to which the paramagnetic reagent distributes, compared to those where it does not. Gd(III) complexes are favored for this application because of the high magnetic susceptibility and long electron-spin relaxation time of the Gd(III) ion; however, at the dose levels used in MRI work, free Gd(III) is too toxic to be used and must be injected as a kinetically stable, water-soluble complex. To induce a reasonably high relaxivity, the kinetically stable complex must facilitate exchange of water molecules between the aqueous environment and, ideally, the primary coordination sphere of the complex. This necessitates that at least one coordination site on the generally nine-coordinate Gd(III) ion not be occupied by the ligand donor atoms. Eight-coordinate pendant donor macrocyclic ligands are able to strike a satisfactory balance, producing Gd(III) complexes with sufficient stability and sufficient relaxivity. Three that have been approved for clinical use to date, as their Gd(III) complexes, are **76–78**.



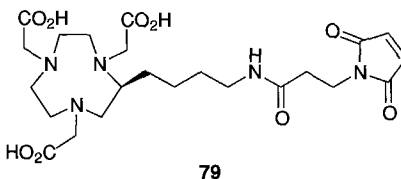
These are marketed as Dotarem, ProHance, and Gadovist, respectively. Dozens of other Ln(III) complexes of cyclen-based ligands, too numerous to detail here, have also been investigated, either as potential MRI reagents or to shed light on the factors important in optimizing the

relaxivity. Several excellent reviews on the subject summarize recent work and predict its future directions (83–86).

#### V. Tumor-Directed Radioisotope Carriers

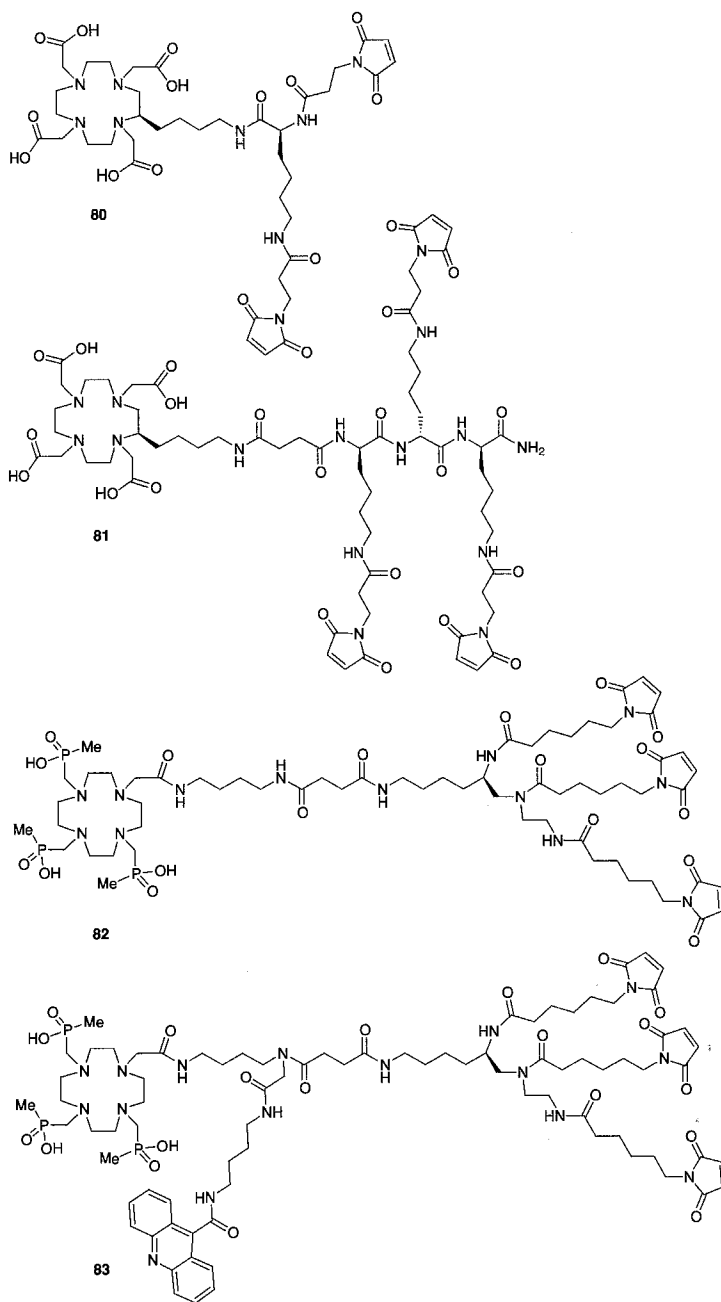
Directing radioisotopes to tumor sites has become an achievable aim following the isolation of monoclonal antibodies that target the antigens produced by tumors. Gamma-emitting indium-111 and gallium-67 are particularly suitable isotopes for imaging purposes and beta-emitting yttrium-90 is used for therapeutic work. Thus, the challenge for the inorganic chemist is to attach the desired radioisotope to the antibody. As with magnetic resonance imaging, it is essential to lock the radioisotope ion into a kinetically stable complex to eliminate toxic effects that may arise from its binding within the body, and, if possible, to use the nature of the complex to direct the radioisotope to a particular bodily organ and the tumor therein (87).

In pursuit of the imaging objective,  $^{111}\text{In(III)}$  has been incorporated into ligand **79**, which involves the macrocycle 1,4,7-triazacyclononane with three pendant acetate moieties (88).



This produces a neutral six-coordinate species with the requisite inertness and good tumor uptake (89). Attachment of this species to the appropriate antibody is accomplished by means of the carbon-attached pendant group which terminates in a maleimide moiety. This can be induced to couple with a thiol that exists as a part of a favorably positioned cysteine residue in the antibody or has been introduced by reacting an exposed lysine residue in the antibody with 2-iminothiolane (Traut's reagent).

Incorporation of  $^{90}\text{Y(III)}$  into a kinetically stable complex suitable for attachment to an antibody calls for an octadentate ligand, and so pendant-arm cyclen derivatives are appropriate. In particular, two or three antigen-binding fragments of an antibody (Fabs) have been attached to the di- or trimaleimide ligands **80–82** (Scheme 8) (90, 91)

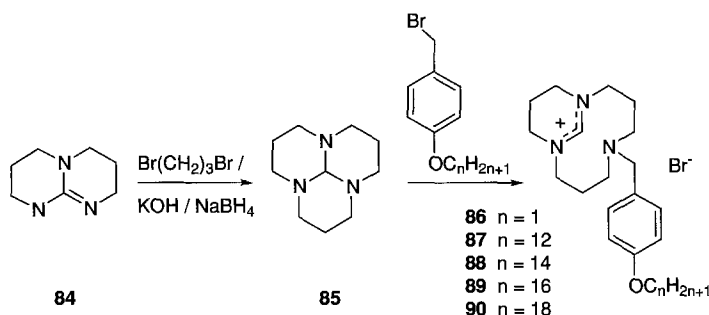


SCHEME 8

derived from cyclen tetraacetate (DOTA) or cyclen tris(methylphosphinate). Multiple antigen-binding fragments crosslinked by the macrocycle are favored over a single Fab attachment, as this leads to faster blood clearance and a greater concentration of the radioisotope at the tumor site. In a further development, intended to direct the  $^{90}\text{Y}(\text{III})$  as closely as possible to the chromosomal DNA of tumor stem cells (the target), ligand **83** (Scheme 8) has been produced (92). Ligand **83** has all the attributes of **82**, but in addition carries a pendant 9-substituted acridine, which is a known DNA intercalator.

## VI. Surfactants

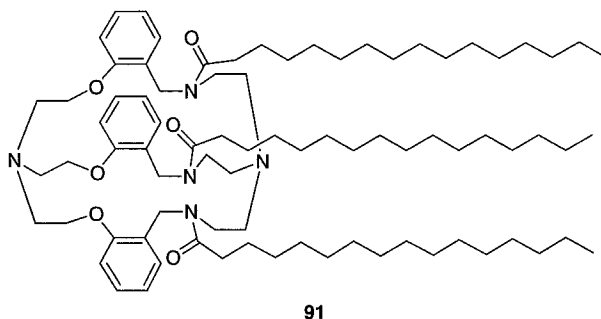
Pendant donor macrocycles have been investigated as a basis for producing cationic surfactants. The potential ligands **86–90** can easily be produced in an elegant two-step synthesis starting from **84** (93, 94).



Ligands **87–90** have been found to have critical micelle concentrations (cmcs) below  $10^{-4} \text{ mol dm}^{-3}$ , about an order of magnitude less than that normally found for cationic surfactants, owing to the hydrophobic nature of the head group and the dispersed nature of the charge. At higher concentrations, and with increasing temperature, lyotropic hexagonal, cubic, and lamellar phases are successively formed, allowing the surfactant molecules to be organized in a predetermined manner. Corresponding compounds derived from the nine-membered triaza macrocyclic orthoamide analogous to **85** have been prepared, but are unstable in water (94).

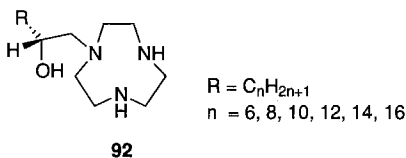
Metallosurfactants, where the cationic head group is a polyaza macrocycle or cavitand containing a strongly coordinated metal ion and the hydrophobic tail is a pendant arm attached to a nitrogen atom of the

head group, have also been investigated. Compound **91** has been formed by treating the parent cryptand (**95**) with palmitoyl chloride in the presence of base (**96**).

**91**

Both **91** and its Cu(II) complex form unilamellar vesicles of about 400 nm diameter that are indefinitely stable in water.

A series of metallosurfactants based on structure **92** has also been prepared by reacting a large excess (20 equivalents) of 1,4,7-triazacyclononane with the appropriate 1,2-epoxyalkane, in either the racemic or an optically active form (**97**).

**92**

The crystal structure of the racemic Ni(II) complex of one of these has been solved, and the alkyl chain ( $C_{10}H_{21}$ ) was found to lie in the fully extended conformation, as shown in Fig. 7. The cations pack into a lamellar structure that is formed from an antiparallel arrangement,

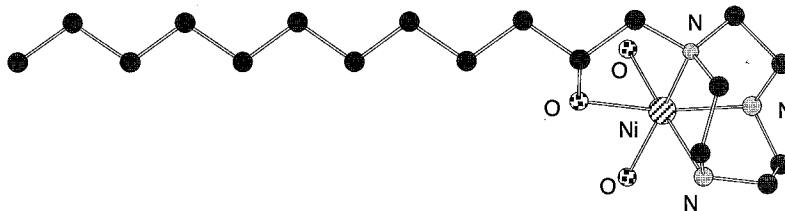


FIG. 7. The solid-state structure of a single cation of the surfactant  $[Ni(\mathbf{92})(H_2O)_2]Cl_2$ , where  $R = C_{10}H_{21}$ .

where alternating layers within the structure have opposite chirality. Both the Ni(II) and Cu(II) complexes form micelles with cmcs in the millimolar region. In the case of the structurally characterized surfactant cation shown in Fig. 7, small-angle neutron scattering experiments show that the micelle consists of about 50 cations and has a radius of about 34 Å.

## VII. Molecular Receptors

Four-armed pendant donor macrocycles derived from cyclen invariably coordinate to a metal ion in such a way that all four pendant arms project in the same direction. If, in addition to carrying a donor group, these arms also have a phenyl or polycyclic aromatic group attached to them, the possibility arises of using the coordination of the ligand to a metal ion as a way of assembling a molecular receptor with a substantial hydrophobic cavity that arises from the juxtaposition of the aromatic groups. On rare occasions, the inclusion of a small molecule has been observed adventitiously in situations where the macrocyclic complex was prepared for another purpose (98). An example is shown in Fig. 8, where an acetonitrile molecule has been captured within the confines of a cavity formed from four quinolyl groups which have juxtaposed as a consequence of the coordination of the remainder of the ligand to sodium(I). The three hydrogen atoms of the acetonitrile molecule are

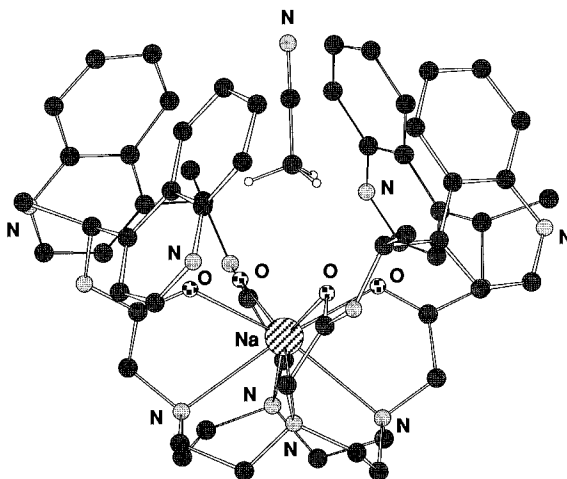
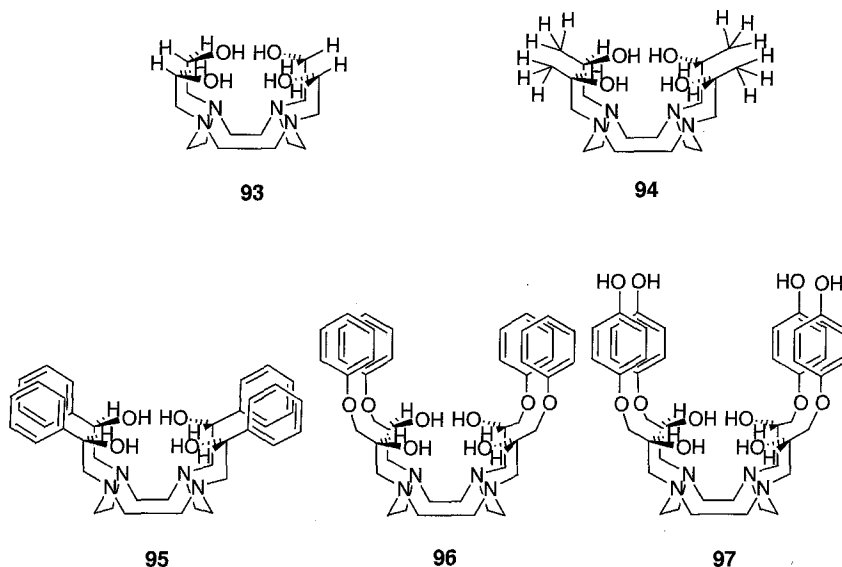


Fig. 8. Inclusion of acetonitrile within the cavity of the sodium(I) complex of a cyclen-based ligand carrying four pendant quinolyl groups.

located at distances of 3.082, 3.067, and 3.344 Å from the centers of C=C bonds in the aromatic rings, suggesting that C-H/ $\pi$  interactions (99) are responsible for its retention in the cavity.

More deliberate attempts to set up molecular receptors based on cyclen with four pendant donor arms, which assemble into an appropriate conformation in the presence of an eight-coordinate metal ion, have been described recently (100). The objective of this work has been to initiate a means by which the well established phenomenon seen in biology, whereby a protein (the ligand), a metal ion, and a substrate (the guest) come together in the assembly and subsequent functioning of a metalloenzyme, could be simulated. Hydroxyethyl ligands **93–97**, which are all formed by the reaction of the appropriate epoxide with cyclen, have been investigated for this purpose.



In cases where the epoxide is chiral, an optically pure form is used to ensure that the resulting ligand is homochiral. These ligands assemble into a cone conformation upon complexation with a cavity that varies from being negligible in **93** and **94** (101, 102), to saucer-shaped in **95** (103, 104), to quite deep in **96** and **97** (100, 105). The dimensions and shape of the cavity can be varied according to the ionic radius of the metal ion that is incorporated (103, 104). With Cd(II), the cavity that is created with ligand **96** is an effective receptor site for aromatic anions such as *p*-toluenesulfonate (100), *p*-nitrophenolate (100, 105–107), (*L*)-phenylalaninate (106), and *p*-aminobenzoate (106), all of

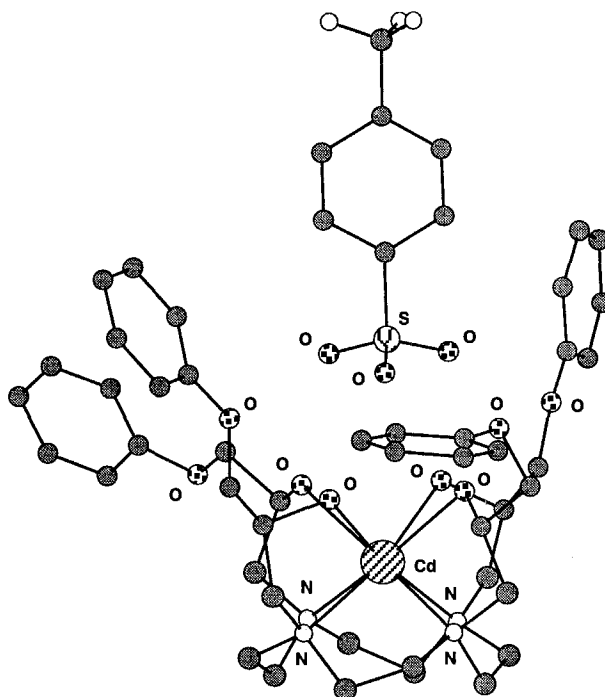


FIG. 9. Inclusion of *p*-toluenesulfonate within the structure of  $[\text{Cd}(\mathbf{96})]^{2+}$ .

which have been observed through X-ray diffraction studies to bind within the cavity in the solid state. Some of these structures are shown in Fig. 9–11. It is evident from the structures that the anions bind to the cavity predominantly through the agency of two or more hydrogen bonds formed from the oxoanion to the pendant hydroxyl groups. There is no evidence for  $\pi$ – $\pi$  interaction between the aromatic groups comprising the walls of the cavity, or between the guest and any of these; however, in the case of the bis(*p*-nitrophenolate), shown in Fig. 10, the two guests are situated in a face-to-face arrangement with a separation of 3.23 Å indicative of an inter-guest  $\pi$ – $\pi$  interaction. In all cases, the distance between the anionic center and Cd(II) is greater than 3.9 Å, indicating that direct electrostatic interaction between the ions is not a major contributor to the stabilization of the anion within the cavity.

NMR and conductivity studies indicate that these structures are substantially preserved in DMSO and methanol solutions. Binding constants for the host–guest interactions determined in DMSO solution are shown in Table I as  $\log (K/M^{-1})$  values (106). It can be seen from a comparison of these that the depth of the cavity does not

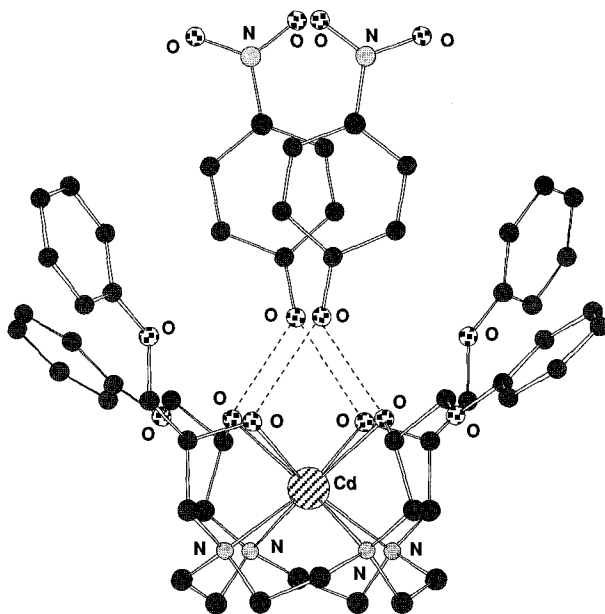


FIG. 10. The double inclusion of *p*-nitrophenolate within the cavity of  $[\text{Cd}(\mathbf{96})]^{2+}$ .

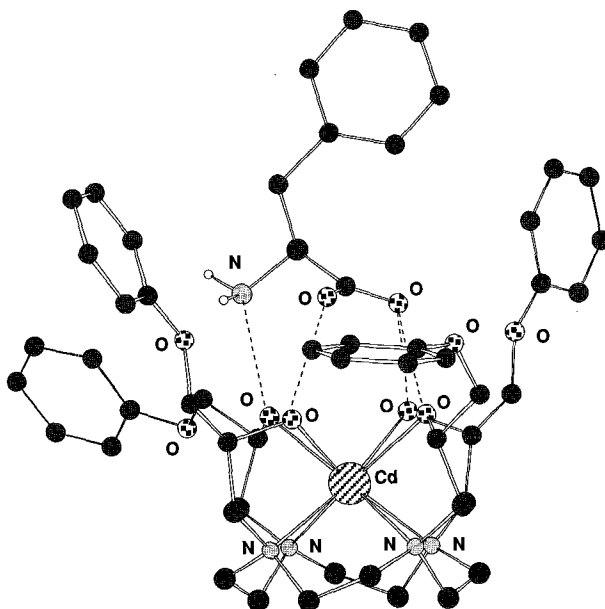


FIG. 11. The inclusion of the amino acid anion (*L*)-phenylalaninate within the structure of  $[\text{Cd}(\mathbf{96})]^{2+}$ .

TABLE I

BINDING CONSTANTS [ $\log (K/M^{-1})$ ] FOR GUEST ANIONS WITH RECEPTOR COMPLEXES OF **93**, **95**, AND **96**  
DETERMINED BY  $^1\text{H}$  NMR TITRATION IN  $\text{DMSO-d}_6$  AT 298 K

Receptor	Metal ion	Guest					
		<i>p</i> -Nitrophenolate	<i>p</i> -Nitrobenzoate	Phenoxyacetate	Acetate	( <i>D</i> )-Histidinate	( <i>L</i> )-Histidinate
<b>93</b>	Cd(II)	3.2	3.9		3.6		
<b>95</b>	Cd(II)	4.0	4.9	3.7	3.6		
<b>95</b>	Pb(II)	3.4		3.1			
<b>96</b>	Cd(II)	4.2	4.5	>5	3.3	4.2	4.2

always make a substantial difference to the binding constant, providing it is formed from aromatic moieties, that aromatic guests are favored when this is the case, and that Cd(II) forms a better receptor cavity than Pb(II) for the guests in question. This last point presumably relates to the greater ionic radius of Pb(II), which increases the distances between the hydroxyl hydrogen bond donors, hence they are less favorably positioned for the guest anion to bridge than are those in the Cd(II) complex.

These receptors are inherently chiral because the spiraling of the pendant arms in either a  $\Delta$  or  $\Lambda$  conformation, and also because of the stereogenic center in each arm at the point of attachment of the hydroxyl group in **94–97**; however, no thermodynamic or kinetic chiral discrimination between enantiomeric guests has yet been observed. For example, the binding constants for the (*D*) and (*L*) enantiomers of histidinate with  $[\text{Cd}(\mathbf{96})]^{2+}$  are the same within experimental error, despite the fact that there are significant differences in the  $^1\text{H}$  NMR spectra of the diastereomeric host–guest complexes, indicative of a different binding environment for each enantiomeric form of the guest (106).

#### ACKNOWLEDGMENTS

It is a pleasure to acknowledge the individual contributions made by my students and academic colleagues to this area of chemistry. Their names are recorded in the collection of references. We are grateful to the Australian Research Council and to Flinders University for supporting our work financially, and to Dr. Ashley Stephens for preparing the figures used in this review.

#### REFERENCES

1. Stetter, H.; Frank, W. *Angew. Chem., Int. Ed. Engl.* **1976**, *15*, 686.
2. Kaden, T. A. *Top. Curr. Chem.* **1984**, *121*, 154.

3. Bernhardt, P. V.; Lawrance, G. A. *Coord. Chem. Rev.* **1990**, *104*, 297.
4. Wainwright, K. P. *Coord. Chem. Rev.* **1997**, *166*, 35.
5. Wainwright, K. P. *J. Chem. Soc., Dalton Trans.* **1980**, 2117.
6. Kimura, E.; Kikuta, E. *Prog. Reaction Kinetics* **2000**, *25*, 1.
7. Kimura, E.; Kikuta, E. *J. Biol. Inorg. Chem.* **2000**, *5*, 139.
8. Kimura, E.; Koike, T. In "Bioinorganic Catalysis"; Reedijk, J., Bouwman, E., Eds.; Marcel Dekker: New York, **1999**, 33–54.
9. Kimura, E.; Koike, T. *Chem. Commun.* **1998**, 1495.
10. Kimura, E.; Koike, T.; Shionoya, M. *Struct. Bonding* **1997**, *89*, 1.
11. Kimura, E.; Koike, T. *Adv. Inorg. Chem.* **1996**, *44*, 229.
12. Kimura, E.; Koike, T. In "Comprehensive Supramolecular Chemistry"; Atwood, J. L., Davies, J. E. D., MacNicol, D. D., Vögtle, F., Lehn, J.-M., Eds., Pergamon: Oxford, 1996; Vol. 10, p. 429.
13. Kimura, E.; Shionoya, M. In "Transition Metals in Supramolecular Chemistry"; Fabrizzi, L., Poggi, A., Eds.; Kluwer: Amsterdam, 1994; pp. 245–249.
14. Kimura, E. *Prog. Inorg. Chem.* **1994**, *41*, 443.
15. Kimura, E.; Koike, T. *Comments Inorg. Chem.* **1991**, *11*, 285.
16. Holtz, K. M.; Kantrowitz, E. R. *FEBS Lett.* **1999**, *462*, 7.
17. Kimura, E.; Kuramoto, Y.; Koike, T.; Fujioka, H.; Kodama, M. *J. Org. Chem.* **1990**, *55*, 42.
18. Kimura, E.; Kodama, Y.; Koike, T.; Shiro, M. *J. Am. Chem. Soc.* **1995**, *117*, 8304.
19. Rohovec, J.; Vojtisek, P.; Hermann, P.; Ludvík, J.; Lukes, I. *J. Chem. Soc., Dalton Trans.* **2000**, 141.
20. Buckingham, D. A.; Clark, C. R.; Rogers, A. J.; Simpson, J. *Inorg. Chem.* **1995**, *34*, 3646.
21. Koike, T.; Inoue, M.; Kimura, E.; Shiro, M. *J. Am. Chem. Soc.* **1996**, *118*, 3091.
22. Bencini, A.; Bianchi, A.; Dapporto, P.; Garcia-España, E.; Micheloni, M.; Paoletti, P. *Inorg. Chem.* **1989**, *28*, 1188.
23. Tan, L. H.; Taylor, M. R.; Wainwright, K. P.; Duckworth, P. A. *J. Chem. Soc., Dalton Trans.* **1993**, 2921.
24. Fessner, W.; Schneider, A.; Held, H.; Sinerius, G.; Walter, C.; Hixon, M.; Schloss, J. V. *Angew. Chem., Int. Ed. Engl.* **1996**, *35*, 2219.
25. Kimura, E.; Gotoh, T.; Koike, T.; Shiro, M. *J. Am. Chem. Soc.* **1999**, *121*, 1267.
26. Kimura, E.; Aoki, S.; Koike, T.; Shiro, M. *J. Am. Chem. Soc.* **1997**, *119*, 3068.
27. Breslow, R.; Huang, D.-L. *Proc. Natl. Acad. Sci. U.S.A.* **1991**, *88*, 4080.
28. Morrow, J. R.; Chin, K. A. O. *Inorg. Chem.* **1993**, *32*, 3357.
29. Amin, S.; Morrow, J. R.; Lake, C. H.; Churchill, M. R. *Angew. Chem., Int. Ed. Engl.* **1994**, *33*, 773.
30. Morrow, J. R.; Chin, K. A. O. *Inorg. Chem.* **1994**, *32*, 5036.
31. Bugen, S.; Dale, J.; Krane, J. *Acta Chem. Scand. B*, **1984**, *38*, 773.
32. Chin, K. O. A.; Morrow, J. R.; Lake, C. H.; Churchill, M. R. *Inorg. Chem.* **1994**, *33*, 656.
33. Carlton, L.; Hancock, R. D.; Maumela, H.; Wainwright, K. P. *J. Chem. Soc., Chem. Commun.* **1994**, 1007.
34. Maumela, H.; Hancock, R. D.; Carlton, L.; Reibenspies, J. H.; Wainwright, K. P. *J. Am. Chem. Soc.* **1995**, *117*, 6698.
35. Amin, S.; Voss, D. A., Jr.; Horrocks, W. D., Jr.; Lake, C. H.; Churchill, M. R.; Morrow, J. R. *Inorg. Chem.* **1995**, *34*, 3294.
36. Amin, S.; Voss, D. A. Jr.; Horrocks, W. D. Jr.; Morrow, J. R. *Inorg. Chem.* **1996**, *35*, 7466.
37. Kruper, W. J., Jr.; Rudolf, P. R.; Langhoff, C. A. *J. Org. Chem.* **1993**, *58*, 3869.

38. Chappell, L. L.; Voss, D. A., Jr.; Horrocks, W. D., Jr.; Morrow, J. R. *Inorg. Chem.* **1998**, *37*, 3989.
39. Morrow, J. R.; Aures, K.; Epstein, D. *J. Chem. Soc., Chem. Commun.* **1995**, 2431.
40. Baker, B. F.; Khalili, H.; Wei, N.; Morrow, J. R. *J. Am. Chem. Soc.* **1997**, *38*, 8749.
41. Baker, B. F.; Lot, S. S.; Kringel, J.; Cheng-Flournoy, S.; Villiet, P.; Sasmor, H. M.; Siwkowski, A. M.; Chappell, L. L.; Morrow, J. R. *Nucleic Acids Res.* **1999**, *27*, 1547.
42. Epstein, D. M.; Chappell, L. L.; Khalili, H.; Supkowski, R. M.; Horrocks, W. D., Jr.; Morrow, J. R. *Inorg. Chem.* **2000**, *39*, 2130.
43. Huang, L.; Chappell, L. L.; Iranzo, O.; Baker, B. F.; Morrow, J. R. *J. Biol. Inorg. Chem.* **2000**, *5*, 85.
44. McMurtry, T. J.; Brechbiel, M.; Kumar, K.; Gansow, O. A. *Bioconj. Chem.* **1992**, *3*, 108.
45. Edlin, C. D.; Faulkner, S.; Parker, D.; Wilkinson, M. P.; Woods, M.; Lin, J.; Lasri, E.; Neth, F.; Port, M. *New J. Chem.* **1998**, 1359.
46. Edlin, C. D.; Faulkner, S.; Parker, D.; Wilkinson, M. P. *J. Chem. Soc. Chem. Commun.* **1996**, 1249.
47. Shionoya, M.; Kimura, E.; Shiro, M. *J. Am. Chem. Soc.* **1993**, *115*, 6730.
48. Shionoya, M.; Ikeda, T.; Kimura, E.; Shiro, M. *J. Am. Chem. Soc.* **1994**, *116*, 3848.
49. Tucker, J. H. R.; Koike, T.; Shionoya, M.; Kimura, E. *Bull. Chem. Soc. Jpn.* **1995**, *68*, 2465.
50. Koike, T.; Gotoh, T.; Aoki, S.; Kimura, E.; Shiro, M. *Inorg. Chim. Acta*, **1998**, *270*, 424.
51. Kimura, E.; Ikeda, T.; Shionoya, M. *J. Biol. Inorg. Chem.* **1998**, *3*, 259.
52. Kimura, E.; Ikeda, T.; Aoki, S.; Shionoya, M. *Pure Appl. Chem.* **1997**, *69*, 2187.
53. Kimura, E.; Kitamura, H.; Ohtani, K.; Koike, T. *J. Am. Chem. Soc.* **2000**, *122*, 4668.
54. Kikuta, E.; Murata, M.; Katsube, N.; Koike, T.; Kimura, E. *J. Am. Chem. Soc.* **1999**, *121*, 5426.
55. Kikuta, E.; Katsube, N.; Kimura, E. *J. Biol. Inorg. Chem.* **1999**, *4*, 431.
56. Kikuta, E.; Koike, T.; Kimura, E. *J. Inorg. Biochem.* **2000**, *79*, 253.
57. Dumont, A.; Jacques, V.; Qixiu, P.; Desreux, J. F. *Tetrahedron Lett.* **1994**, *35*, 3707.
58. Kimura, E.; Kitamura, H.; Koike, T.; Shiro, M. *J. Am. Chem. Soc.* **1997**, *119*, 10909.
59. Aoki, S.; Honda, Y.; Kimura, E. *J. Am. Chem. Soc.* **1998**, *120*, 10018.
60. Govenlock, L. J.; Mathieu, C. E.; Maupin, C. L.; Parker, D.; Riehl, J. P.; Silgardi, G.; Williams, J. A. G. *J. Chem. Soc., Chem. Commun.* **1999**, 1699.
61. Parker, D.; Senanayake, K.; Williams, J. A. G. *J. Chem. Soc., Perkin Trans. 2*, **1998**, 2129.
62. Yaouanc, J. J.; Bris, N. L.; Gall, G. L.; Clement, J. C.; Hanel, H.; des Abbayes, H. *J. Chem. Soc., Chem. Commun.* **1991**, 206.
63. Tabushi, I.; Taniguchi, Y.; Kato, H. *Tetrahedron Lett.* **1977**, 1049.
64. Kimura, E.; Korenari, S.; Shionoya, M.; Shiro, M. *J. Chem. Soc., Chem. Commun.* **1988**, 1166.
65. Kimura, E.; Kurogi, Y.; Wada, S.; Shionoya, M. *J. Chem. Soc., Chem. Commun.* **1989**, 781.
66. Kimura, E.; Sasada, M.; Shionoya, M.; Koike, T.; Kurosaki, H.; Shiro, M. *J. Biol. Inorg. Chem.* **1997**, *2*, 74.
67. Kimura, E.; Machida, R. *J. Chem. Soc., Chem. Commun.* **1984**, 499.
68. Fabbriizzi, L.; Licchelli, M.; Pallavicini, P.; Parodi, L. *Angew. Chem., Int. Engl. Ed.* **1998**, *37*, 800.
69. Thompson, R. B.; Jones, E. R. *Anal. Chem.* **1993**, *65*, 730.

70. Koike, T.; Watanabe, T.; Aoki, S.; Kimura, E.; Shiro, M. *J. Am. Chem. Soc.* **1996**, *118*, 12696.
71. Kimura, E. S. *Afr. J. Chem.* **1997**, *50*, 240.
72. Kimura, E.; Koike, T. *Chem. Soc. Rev.* **1998**, *27*, 179.
73. Engeser, M.; Fabbrizzi, L.; Licchelli, M.; Sacchi, D. *J. Chem. Soc., Chem. Commun.* **1999**, 1191.
74. Parker, D.; Senanayake, K.; Williams, J. A. G. *J. Chem. Soc., Chem. Commun.* **1997**, 1777.
75. Parker, D.; Williams, J. A. G. *J. Chem. Soc., Chem. Commun.* **1998**, 245.
76. Clarkson, I. M.; Beeby, A.; Bruce, J. I.; Govenlock, L. J.; Lowe, M. P.; Mathieu, C. E.; Parker, D.; Senanayake, K. *New J. Chem.* **2000**, **2000**, 24, 377.
77. Gunnlaugsson, T.; Parker, D. *J. Chem. Soc., Chem. Commun.* **1998**, 511.
78. Gunnlaugsson, T.; Mac, Dónail, D. A.; Parker, D. *J. Chem. Soc., Chem. Commun.* **2000**, 93.
79. Dickins, R. S.; Gunnlaugsson, T.; Parker, D.; Peacock, R. D. *J. Chem. Soc., Chem. Commun.* **1998**, 1643.
80. Aime, S.; Barge, A.; Botta, M.; Howard, J. A. K.; Katakya, R.; Lowe, M. P.; Moloney, J. M.; Parker, D.; de Sousa, A. S. *J. Chem. Soc., Chem. Commun.* **1999**, 1047.
81. Lowe, M. P.; Parker, D. *J. Chem. Soc., Chem. Commun.* **2000**, 707.
82. Reany, O.; Gunnlaugsson, T.; Parker, D. *J. Chem. Soc., Chem. Commun.* **2000**, 473.
83. Caravan, P.; Ellison, J. J.; McMurry, T. J.; Lauffer, R. B. *Chem. Rev.* **1999**, *99*, 2293.
84. Comblin, V.; Gilsoul, D.; Hermann, M.; Humblet, V.; Jacques, V.; Mesbahi, M.; Sauvage, C.; Desreux, J. F. *Coord. Chem. Rev.* **1999**, *185–186*, 451.
85. Aime, S.; Botta, M.; Fasano, M.; Terreno, E. *Chem. Soc. Rev.* **1998**, *27*, 19.
86. Parker, D.; Williams, J. A. G. *J. Chem. Soc., Dalton Trans.* **1996**, 3613.
87. Parker, D. In "Comprehensive Supramolecular Chemistry"; Atwood, J. L., Davies, J. E. D., MacNicol, D. D., Vögtle, F., Lehn, J.-M., Eds.; Pergamon: Oxford, 1996; Vol. 10, p. 497.
88. Parker, D. *Chem. Brit.* **1990**, 942.
89. Turner, A.; King, D. J.; Farnsworth, A. P. H.; Rhind, S. K.; Pedley, R. B.; Boden, J.; Boden, R.; Millican, T. A.; Millar, K.; Boyce, B.; Beeley, N. R. A.; Eaton, M. A. W.; Parker, D. *Br. J. Cancer* **1994**, *70*, 35.
90. King, D. J.; Turner, A.; Farnsworth, A. P. H.; Adair, J. R.; Owens, R. J.; Pedley, R. B.; Baldock, D.; Proudfoot, K. A.; Lawson, A. D. G.; Beeley, N. R. A.; Millar, K.; Millican, A. T.; Boyce, B. A.; Antoniow, P.; Mountain, A.; Begent, R. H. J.; Schochat, D.; Yarranton, G. T. *Cancer Res.* **1994**, *54*, 6176.
91. Norman, T. J.; Parker, D.; Royle, L.; Harrison, A.; Antoniow, P.; King, D. J. *J. Chem. Soc., Chem. Commun.* **1995**, 1877.
92. Norman, T. J.; Parker, D.; Smith, F. C.; King, D. J. *J. Chem. Soc., Chem. Commun.* **1995**, 1879.
93. Kim, D. H.; Wilson, M.; Heseltine, J. *Synth. Commun.* **1994**, *24*, 3109.
94. Pidwell, A. D.; Collinson, S. R.; Coles, S. J.; Hursthouse, M. B.; Schröder, M.; Bruce, D. W. *J. Chem. Soc., Chem. Commun.* **2000**, 955.
95. Ragunathan, K. G.; Bharadwaj, P. K. *Tetrahedron Lett.* **1992**, 7581.
96. Ghosh, P.; Khan, T. K.; Bharadwaj, P. K. *J. Chem. Soc., Chem. Commun.* **1996**, 189.
97. Fallis, I. A.; Griffiths, P. C.; Griffiths, P. M.; Hibb, D. E.; Hursthouse, M. B.; Winnington, A. L. *J. Chem. Soc., Chem. Commun.* **1998**, 665.
98. Govenlock, L. J.; Howard, J. A. K.; Moloney, J. M.; Parker, D.; Peacock, R. D.; Sili-gardi, G. *J. Chem. Soc., Perkin Trans. 2*, **1999**, 2415.

99. Nishio, M.; Hirota, M.; Umezawa, Y. "The CH/ $\pi$  Interaction"; New York: Wiley-VCH, 1998.
100. Smith, C. B.; Wallwork, K. S.; Weeks, J. M.; Buntine, M. A.; Lincoln, S. F.; Taylor, M. R.; Wainwright, K. P. *Inorg. Chem.* **1999**, *38*, 4986.
101. Dhillon, R. S.; Madbak, S. E.; Ciccone, F. G.; Buntine, M. A.; Lincoln, S. F.; Wainwright, K. P. *J. Am. Chem. Soc.* **1997**, *119*, 6126.
102. Dhillon, R. S.; Madbak, S. E.; Ciccone, F. G.; Buntine, M. A.; Lincoln, S. F.; Wainwright, K. P. *J. Am. Chem. Soc.* **1998**, *120*, 11212.
103. Whitbread, S. L.; Valente, P.; Buntine, M. A.; Clements, P.; Lincoln, S. F.; Wainwright, K. P. *J. Am. Chem. Soc.* **1998**, *120*, 2862.
104. Whitbread, S. L.; Valente, P.; Buntine, M. A.; Clements, P.; Lincoln, S. F.; Wainwright, K. P. *J. Am. Chem. Soc.* **1998**, *120*, 11212.
105. Smith, C. B.; Lincoln, S. F.; Wainwright, K. P. *Inorg. Chim. Acta* **2001**, *317*, 21.
106. Smith, C. B.; Stephens, A. K. W.; Wallwork, K. S.; Lincoln, S. F.; Taylor, M. R.; Wainwright, K. P. *Inorg. Chem.*, submitted.
107. Davies, P. J.; Lincoln, S. F.; Smith, C. B.; Taylor, M. R.; Wainwright, K. P.; Wallwork, K. S. *Acta Crystallogr.* **2000**, *C56*, 28.

## PERFLUORINATED CYCLIC PHOSPHAZENES

ANIL J. ELIAS\* and JEAN'NE M. SHREEVE†

\*Department of Chemistry, Indian Institute of Technology, Kanpur, 208016, India; and

†Department of Chemistry, University of Idaho, Moscow, Idaho, 83844-2343

- I. Introduction
- II. Synthesis of Perfluorinated Cyclic Phosphazenes
- III. Physical and Spectral Properties of Perfluoro Cyclic Phosphazenes
- IV. Structures of Perfluorinated Cyclic Phosphazenes
- V. Reactions of Cyclic Trimeric Fluorophosphazenes
  - A. With Monofunctional Reagents
  - B. With Difunctional Reagents
- VI. Reactions of Cyclic Tetrameric and Higher Fluorophosphazenes
- VII. Conclusions
- References

### I. Introduction

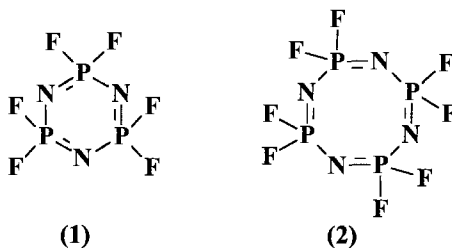
Among inorganic heterocycles, perhalogenated cyclic phosphazenes occupy a very prominent place as the precursors for polyphosphazenes whose properties can be tuned by changing the substituents on the phosphorus sites (1). The heterocycles, as such, provide a robust framework for building a variety of novel molecules that have high thermal stability and flame retardancy, and have also been used recently to prepare a variety of dendrimers (2). The most widely studied among these are the perchlorinated cyclophosphazenes. Their syntheses, reactions, properties, and application potential have been well documented (1, 3–7).

Surprisingly, although perfluorinated cyclic phosphazenes have been known for a long time and their reactivity well explored by various research groups, with the exception of a brief summary (8), no attempts have been made to consolidate this interesting chemistry. Compared to chlorophosphazenes, the fluoro analogs are more stable, more highly volatile, and less reactive. Another notable difference is the lower basicity of the ring nitrogen atoms, this arises from the high electronegativity

of the fluorine atoms attached to the phosphorus centers and facilitates a much cleaner reaction with organometallic compounds such as organolithium and Grignard reagents (9). A wide variety of reactions carried out on perfluorinated cyclic phosphazenes have shown that the reactivity of the P—F bonds of these heterocycles differs distinctly from that of the P—Cl bonds of chlorophosphazenes. This review consolidates the properties and reaction chemistry of perfluorinated cyclophosphazenes, with an emphasis on comparing their reactivity with that of the perchlorinated analogs.

## II. Synthesis of Perfluorinated Cyclic Phosphazenes

In contrast to chloro- and bromophosphazenes, for which a variety of synthetic methods have been reported, the only effective way of making fluorophosphazenes has been by fluorinating chlorophosphazenes to per- or polyfluorinated derivatives using a variety of fluorinating reagents. The fluorinating agents that have been successfully utilized are  $\text{PbF}_2$  (10–12),  $\text{KSO}_2\text{F}$  (13–19),  $\text{AgF}$  (10, 11, 20),  $\text{AgF}_2$  (3),  $\text{SbF}_3$  (18, 21–23),  $\text{NaF}$  (3, 17, 24–26),  $\text{KF/18-crown-6}$  (27), and  $\text{Et}_3\text{N}\cdot\text{HF}$  (28). Among these, the most effective method for making  $\text{N}_3\text{P}_3\text{F}_6$  (**1**) and  $\text{N}_4\text{P}_4\text{F}_8$  (**2**) involves the use of  $\text{NaF}$  in a polar solvent such as acetonitrile or nitrobenzene (25). The larger rings, such as  $(\text{NPF}_2)_{5-12}$ , are prepared from the mixture of the corresponding perchloro compounds by using potassium fluorosulfite,  $\text{KSO}_2\text{F}$  (19). The individual compounds are separated by distillation and purified by gas-liquid chromatography. Cyclic fluorophosphazenes up to  $(\text{NPF}_2)_{40}$  have been detected chromatographically.



Fluorination of chlorophosphazenes, especially the trimeric phosphazene, has been the subject of studies primarily to understand the

mechanism and regiospecificity involved in metathetical reactions. Reactions of three fluorinating reagents have been studied in detail: namely, NaF, KSO<sub>2</sub>F, and SbF<sub>3</sub> with catalytic amounts of SbCl<sub>5</sub>. Fluorination reactions of (NPCl<sub>2</sub>)<sub>3-5</sub> with anionic reagents, NaF (for trimer) and KSO<sub>2</sub>F (for tetramer and pentamer), all follow a geminal pathway (17, 29). At the trisubstitution stage for the tetramer, 2,2,4- rather than 2,2,6-substitution is favored, while for the pentamer equal amounts of both the isomers are formed. Approximate kinetic studies indicate that the rate of fluorination of a P(F)(Cl) center is greater than that of a PCl<sub>2</sub> center by a factor of 9 for the trimer, 7 for the pentamer, and 100 for the tetramer. In contrast to these systems, fluorination using an SbF<sub>3</sub>/SbCl<sub>5</sub> mixture results in the formation of nongeminal derivatives (30). This difference is also observed in the fluorination of dimethylamino-substituted trimeric chlorophosphazenes. Reaction of N<sub>3</sub>P<sub>3</sub>Cl<sub>5</sub>NMe<sub>2</sub> with NaF or KSO<sub>2</sub>F results in the fluorination of the PCl<sub>2</sub> groups first, with the chlorine atom geminal to the dimethylamino group being the most difficult one to react (31). The reverse is observed when SbF<sub>3</sub>/SbCl<sub>5</sub> is used as the fluorinating agent. A similar pattern of behavior is observed in the partial fluorination of 2,4-N<sub>3</sub>P<sub>3</sub>Cl<sub>4</sub>(NMe<sub>2</sub>)<sub>2</sub> to give 2,4-N<sub>3</sub>P<sub>3</sub>Cl<sub>2</sub>F<sub>2</sub>(NMe<sub>2</sub>)<sub>2</sub>, where KSO<sub>2</sub>F effects substitution at the PCl<sub>2</sub> centers and SbF<sub>3</sub> at the P(NMe<sub>2</sub>)Cl sites (18).

The geminal pathway followed in fluorination reactions using fluoride salts, such as NaF, and the rate of acceleration on going from a reaction at a PCl<sub>2</sub> center to the one at a P(F)Cl center have been explained using an electrostatic argument. The presence of the highly electronegative fluorine atom increases the positive charge on the phosphorus atom, thus favoring nucleophilic attack. In tetrameric compounds, a PF<sub>2</sub> center competes effectively for lone-pair electron density on an adjacent nitrogen atom relative to an adjacent PCl<sub>2</sub> group; this increases the positive charge on the PCl<sub>2</sub> center and favors fluorination at that center, resulting in 2,2,4-regioisomer formation. The nongeminal pathway followed by the antimony reagents was thought to result from the coordination of the antimony compound, a Lewis acid, to the most basic nitrogen atom in the ring (18).

The electron-withdrawing ability of the fluorine atom can draw electron density from an adjacent nitrogen atom, making a distant nitrogen more basic. A second effect is the shortening of the P—Cl bond in a P(F)Cl vs. a PCl<sub>2</sub> center (32). Thus, an incoming Lewis acid will interact with the phosphazene at a site that is distant from the P(F)Cl site.

## III. Physical and Spectral Properties of Perfluoro Cyclic Phosphazenes

In general, perfluorinated cyclic phosphazenes are low-melting solids or liquids at room temperature. In Table I are listed some of the important physical and spectral properties of the homologous series of cyclic fluorophosphazenes  $(\text{PNF}_2)_n$  ( $n = 3-11$ ) (19). The boiling points of the cyclic fluorophosphazenes are similar to those of saturated aliphatic fluorocarbons of comparable molecular weight. The hexameric phosphonitrilic fluoride ( $M = 498$ ) boils  $21.9^\circ$  higher than perfluorononane ( $M = 488$ ), while the decameric phosphonitrilic fluoride ( $M = 830$ ) boils only  $1.2^\circ$  below perfluorohexadecane ( $M = 834$ ). The entropies of vaporization of the phosphonitrilic fluorides are high and tend to increase with molecular weight. Unlike fluorocarbons, the cyclic phosphonitrilic fluorides are flexible molecules. The infrared spectra show no evidence of the multiple peak characteristics of configurational isomerism observed in the hydrocarbon series. Barriers to internal motion in the fluorides are therefore small. Further evidence that the molecules can fold in on themselves economically is obtained from the molar volumes  $V_m = (43.753n + 8.19)$  ml, within an average deviation of 0.27 ml. This constant term, which is a measure of the volume made unavailable by ring closure, is 13.3 ml for the parallel series of cyclic dimethyl siloxanes and approximately 20 ml for cycloparaffins (19). Based on this argument, the fluorides are the most flexible of the three series. Molecular flexibility is further demonstrated directly by viscosities. The viscosity of the pentameric fluoride at  $25^\circ\text{C}$  is 1.37 cp, while for decamethyl pentasiloxane, the corresponding value is 3.824 cp (19).

Also found in Table I are the P-N stretching frequencies obtained from the infrared spectra of the cyclic phosphazenes. These values fall in the range  $1297-1408\text{ cm}^{-1}$ . For the chlorophosphazenes,  $(\text{NPCl}_2)_n$  ( $n = 3-6$ ), this frequency is observed in the range  $1218-1354\text{ cm}^{-1}$  (3).

TABLE I

PHYSICAL, THERMODYNAMIC, AND SPECTRAL PROPERTIES OF  $(\text{PNF}_2)_n$ 

$n$ in $(\text{PNF}_2)_n$	3	4	5	6	7	8	9	10	11
mp ( $^\circ\text{C}$ )	27.1	30.4	-50	-45.5	-61.0	-16.9	< -78	-51	< -78
bp ( $^\circ\text{C}$ )	51.0	89.7	120.1	147.2	170.7	192.8	214.4	230.8	246.7
$\Delta H$ , vap. (kcal/mol)	7.65	8.91	9.80	—	11.6	12.0	12.7	13.5	14.6
$\Delta S$ , vap. (e.u)	23.6	24.6	24.9	—	26.2	25.8	26.1	26.9	28.0
$\nu_{\text{P-N}}$ ( $\text{cm}^{-1}$ )	1297	1419	1439	1408	1400	1386	1375	1363	1357

Vibrational Raman spectra of  $(\text{NPF}_2)_3$ , both as such and as a function of applied pressure, were measured and used to confirm mode assignments (33). UV-absorption spectral studies carried out on trimeric and tetrameric fluorophosphazenes show absorption maxima at 149.4 and 147.5  $\text{m}\mu$ , respectively. No bands attributable to  $p\pi-d\pi$ -electron delocalization were found, indicating that the rings are not aromatic (34, 35). This evidence helps to reject the model of a highly delocalized  $\pi$ -electron system and supports the localized three-center  $\pi$ -electron model proposed by Dewar. The ionization potentials of the phosphonitrilic fluorides  $(\text{NPF}_2)_n$  ( $n = 3-8$ ) have been measured by photoelectron spectroscopy. The six-membered heterocycle has a first ionization potential larger than that of the eight-membered ring. The first ionization potentials alternate as the size of the ring increases beyond eight atoms (36, 37). Ionization energies for a few alkenyl and alkynyl fluorophosphazenes have also been determined recently (38).

Details of NMR spectra of substituted fluorophosphazenes have been well documented (39). The  $^{19}\text{F}$  NMR spectra of  $\text{N}_3\text{P}_3\text{F}_6$  and  $\text{N}_4\text{P}_4\text{F}_8$  clearly indicate a doublet of multiplets with a  $^1J_{\text{P}-\text{F}}$  coupling constant in the range of 868–901 Hz. The  $^{31}\text{P}$  NMR spectra also show a triplet of multiplets with similar P–F coupling constants. In Table II are the fluorine NMR spectral data for the perfluorinated cyclophosphazenes with ring size varying from six to eighteen atoms. All of the  $\text{PF}_2$  groups are equivalent and the chemical shifts decrease with increasing ring size, while the  $^1J_{\text{P}-\text{F}}$  coupling constants follow a reverse order.

In contrast, the phosphorus chemical shifts of  $(\text{NPF}_2)_n$  ( $n = 3-6$ ) are 13.9, –17.7, –21.9, and –22.2 ppm, respectively, indicating a significant change from trimeric to the higher analogs. Mass spectral fragmentation patterns of the cyclic phosphonitrilic fluorides have also been investigated systematically by Paddock and Brion (41). The larger fluorinated rings tend to break down, possibly through transannular interaction, into cyclic fragments, when these are otherwise known to be stable.

TABLE II

$\delta(\text{F})$  AND  $^1J_{\text{P}-\text{F}}$  OF PERFLUORINATED CYCLIC PHOSPHAZENES  $(\text{NPF}_2)_n$ <sup>a</sup>

<i>n</i>	3	4	5	6	7	8	9
$\delta(\text{F})$	–71.90	–71.85	–69.05	–68.60	–68.00	–68.00	–67.95
$^1J_{\text{P}-\text{F}}$ (Hz)	868	836	874	885	901	903	901

<sup>a</sup>Reference (40).

## IV. Structures of Perfluorinated Cyclic Phosphazenes

Structures of cyclic fluorophosphazenes, especially those of the smaller rings, received increased attention largely because these data were utilized to support theoretical studies in which participation of phosphorus *d* orbitals and contraction of *d* orbitals for effective overlap for  $\pi$  bonding were discussed (42–45). The gas-phase structure of  $\text{N}_3\text{P}_3\text{F}_6$ , reported in 1971, supported a planar ring (46). Although single-crystal X-ray studies were carried out as early as 1960, the refinement was grossly inaccurate, with *R* values of  $\sim 32\%$  (47). Quite recently, the structure was redetermined at  $20^\circ\text{C}$  with better reliability, reconfirming the planar structure (Fig.1) (48). In contrast, the structure of  $\text{N}_4\text{P}_4\text{F}_8$  was found to be more complex. The crystal structure, first determined in 1961, suggested a planar eight-membered ring (49). However, infrared and Raman spectral calculations indicated a nonplanar structure with a symmetry of  $C_{2h}$  or lower (3, 50). It is also of interest that many theoretical studies have made use of the planar description of the structure of  $\text{N}_4\text{P}_4\text{F}_8$  (43–45, 51). Recently, however, the structure was redetermined and analyzed in detail using high- and low-temperature X-ray diffraction, gas electron diffraction, neutron diffraction, and differential

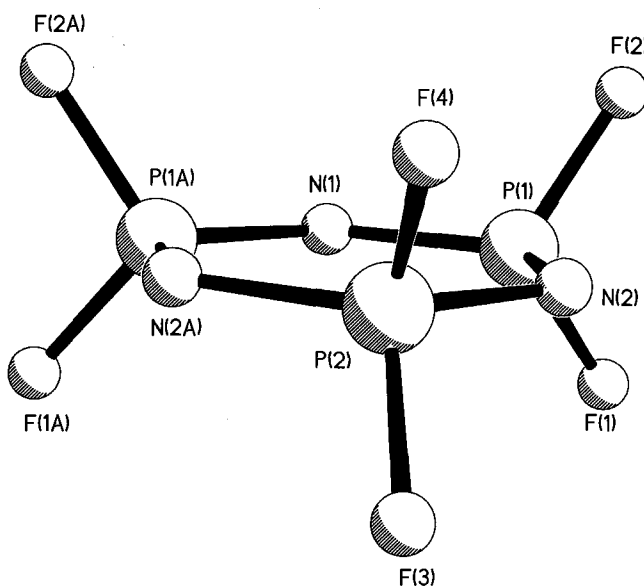


FIG. 1. Crystal structure of  $\text{N}_3\text{P}_3\text{F}_6$ . Reproduced with permission from Ref. (48). Copyright 2000, American Chemical Society.

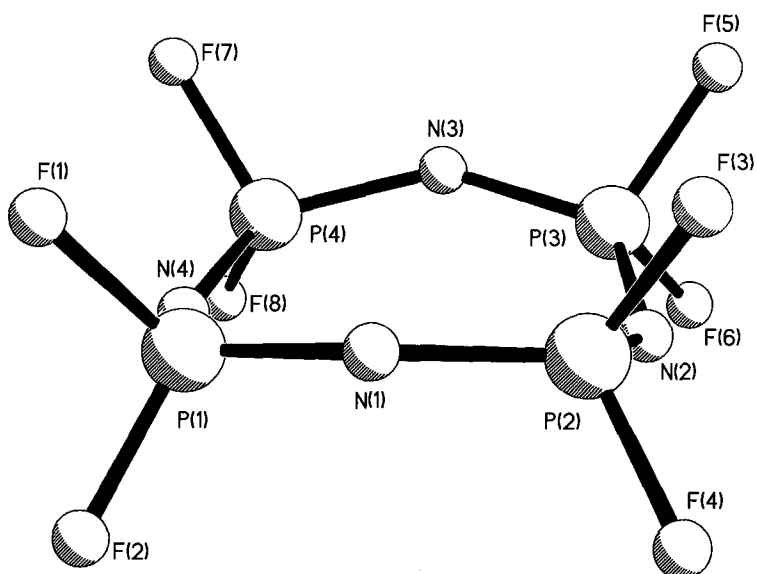


FIG. 2. Crystal structure of  $N_4P_4F_8$  (low temperature).

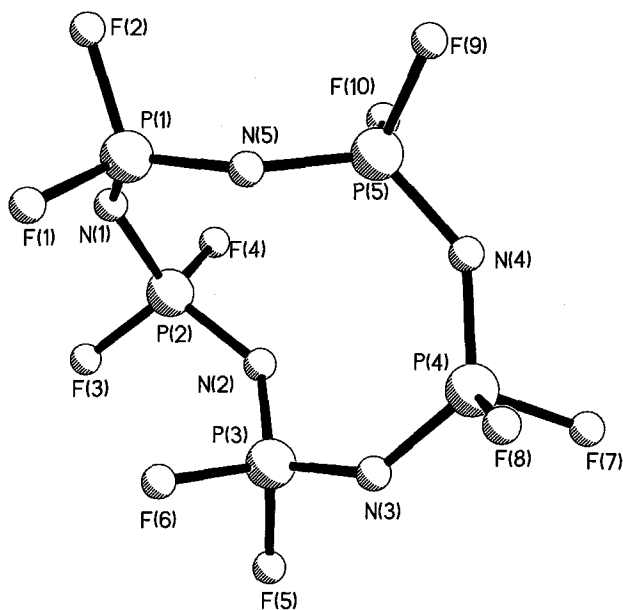


FIG. 3. Crystal structure of  $N_5P_5F_{10}$ . Reproduced with permission from Ref. (53). Copyright 1978, Royal Society of Chemistry.

scanning calorimetric techniques (52). All of these studies support a nonplanar structure at low temperatures (Fig. 2) with a phase transition above  $-74^{\circ}\text{C}$ . The high-temperature phase has a quasiplanar eight-membered P—N skeleton. The puckering of the ring resembles that of the saddle (K form) of  $\text{N}_4\text{P}_4\text{Cl}_8$  (3). The unit cell of the low-temperature phase is derived from that of the high-temperature phase by doubling the  $c$  axis and removing one-half of the symmetry elements. The low-temperature structure determination of  $\text{N}_5\text{P}_5\text{F}_{10}$  shows two different puckered ring orientations, one of which is shown in Fig. 3 (53). The P—N bond distances of  $\text{N}_3\text{P}_3\text{F}_6$  are in the range 1.564–1.576 Å, while those for  $\text{N}_4\text{P}_4\text{F}_8$  (LT) and  $\text{N}_5\text{P}_5\text{F}_{10}$  (LT) are in the range 1.538–1.548 Å and 1.530–1.561 Å, respectively.

## V. Reactions of Cyclic Trimeric Fluorophosphazenes

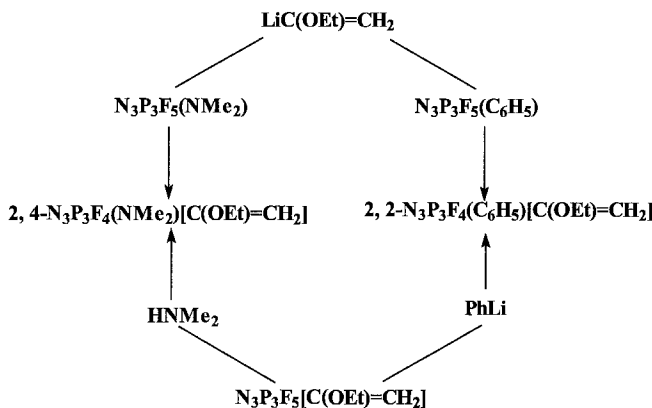
### A. WITH MONOFUNCTIONAL REAGENTS

Reactions of a variety of monofunctional nucleophiles have been carried out with trimeric perfluorinated phosphazenes. The majority of these reactions are with organometallic reagents. The popularity of these reagents probably stems from the fact that in fluorinated phosphazenes, unlike chlorinated phosphazenes, the lower basicity of the ring nitrogen atoms aids in a clean reaction with organometallic reagents. Reactions of chlorinated phosphazenes with organolithium and Grignard reagents have, in many cases, resulted in a complex mixture of products, which has been ascribed to the higher basicity of the ring nitrogen atoms (9). Interesting reactivity differences were also observed in the reactions of amines with chloro- and fluoro-phosphazenes.

The aminolysis of fluorophosphazenes has been less intensively studied than that of chlorophosphazenes and bromophosphazenes. Reactions of  $\text{N}_3\text{P}_3\text{F}_6$  with amines are slow to proceed to higher degrees of substitution (54). Kinetic studies indicate that the first F substitution for  $\text{N}_3\text{P}_3\text{F}_6$  by  $\text{Me}_2\text{NH}$  is approximately 20 times slower than the first Cl substitution in  $\text{N}_3\text{P}_3\text{Cl}_6$  (55). On comparing the activation parameters of  $\text{N}_3\text{P}_3\text{Cl}_6$  with those of  $\text{N}_3\text{P}_3\text{F}_6$  in their reaction with dimethylamine, it is observed that the enthalpy of activation is much higher for the perfluorinated compound (56). The reduced P—N bond distances of the perfluorinated trimer have also been suspected as the cause of the reduction in the acceptor ability of the phosphorus atom in this compound.

Desilylation, destannylation, and delithiation of trimethylsilyl, trimethylstannyl, and lithiated primary and secondary amines have been reported with  $N_3P_3F_6$ , the result being only partial substitution (54, 57, 58). Similar results were observed in the reactions of silylated phosphinimines with  $N_3P_3F_6$  (59–61). In contrast to the reaction of dimethylamine with  $N_3P_3F_6$ , which yields only a nongeminal disubstituted product, reaction of lithium dimethylamide with  $N_3P_3F_6$  results in the formation of a mixture of tri- and tetrasubstituted products (54). Allcock and Evans have tried to explain this observation based on the relative reactivities of  $[NP(F)NRR']_{3,4}$  and  $[NP(Cl)NRR']_{3,4}$  ( $R = H$  or  $Me$ ) and on the relative nucleophilicities of the reagents employed. Electrons supplied by one amino residue attached to a phosphorus atom can deactivate the second P–F bond at that site. The combined influences of the low nucleophilicity of the free amine and the poor leaving ability of the fluoride ion would make this effect more pronounced. The higher reactivity of sodium alkoxides and aryloxides as well as lithium dimethylamide has been attributed to their higher nucleophilicities. The nongeminal substitution observed with amines has been utilized to generate partially chlorinated and brominated fluorophosphazenes, as the amino group can be cleaved with HCl or HBr (57, 62).

At the disubstitution stage of  $N_3P_3F_6$ , the geminal pathway is the one that is usually taken by organometallic reagents. The mode of substitution is also governed not only by the nature of the group already present on the fluorophosphazene ring but also by the steric bulkiness of the incoming group. As the steric demands of the substituent or the incoming group increase, formation of nongeminal species is found to be favored. Within the nongeminal species, steric considerations favor the *trans* isomer. Evidence for this type of reaction behavior is observed from the regio- and stereospecific formation of *tert*-butyl fluorophosphazenes (63) and the nongeminal preference in the reactions of aryllithium reagents (64–67). An interesting variation is observed in the reactions of phenyl magnesium bromide and phenyllithium reagents. The former gives geminal products while the latter gives nongeminal products. This is attributed to the fact that under the reaction conditions, the Grignard reagent is monomeric (68) while the phenyllithium reagent is dimeric and more sterically demanding (69), leading to a nongeminal substitution. The substituent control is demonstrated by the fact that a common reagent,  $LiC(OEt)=CH_2$ , follows different pathways in reactions with  $N_3P_3F_5NMe_2$  and  $N_3P_3F_5Ph$  (70) (Scheme 1). While geminal substitution is preferred in the phenyl compound, nongeminal substitution is the preferred pathway for  $N_3P_3F_5NMe_2$ .



SCHEME 1

In contrast to  $\text{N}_3\text{P}_3\text{Cl}_6$ ,  $\text{N}_3\text{P}_3\text{F}_6$  does not undergo Friedel–Crafts reactions. However, partially substituted derivatives of  $\text{N}_3\text{P}_3\text{F}_6$  can be made to undergo arylation at the  $\text{P(R)F}$  site by Friedel–Crafts reaction. The reactions of the aryl derivatives  $\text{N}_3\text{P}_3\text{F}_5\text{C}_6\text{H}_4\text{-}p\text{-X}$  [ $\text{X} = \text{H}$  (71),  $\text{NMe}_2$  (67),  $\text{Cl}$ ,  $\text{F}$ ,  $\text{OMe}$ ,  $\text{Me}$  (72)] and  $2,4\text{-N}_3\text{P}_3\text{F}_4(\text{C}_6\text{H}_4\text{-}p\text{-X})_2$  [ $\text{X} = \text{H}$  (71),  $\text{NMe}_2$  (67)] have been studied in detail. Nonarylated monosubstituted fluorophosphazenes also undergo phenylation exclusively at the  $\text{P(R)F}$  positions (73).

Reactions of saturated aliphatic monolithiated reagents  $c\text{-C}_6\text{H}_{11}\text{Li}$  (74),  $\text{MeLi}$  (75),  $n\text{-BuLi}$ ,  $t\text{-BuLi}$  (63), and  $\text{Me}_3\text{SiCH}_2\text{Li}$  (76) with  $\text{N}_3\text{P}_3\text{F}_6$  have been reported. With  $\text{MeLi}$  and  $n\text{-BuLi}$ , low yields of the disubstituted geminal derivatives are obtained. However, with  $t\text{-BuLi}$ , good yields of the *trans*- $\text{N}_3\text{P}_3\text{F}_{6-n}(\text{t-C}_4\text{H}_9)_n$  ( $n = 2, 3$ ) are obtained (63). The reaction of  $\text{Me}_3\text{SiCH}_2\text{Li}$  proceeds with complete substitution and replacement of all  $\text{P-F}$  bonds (76). On treatment of  $(\text{NPR}_2)_3$  ( $\text{R} = \text{CH}_2\text{SiMe}_3$ ) with  $\text{Bu}_4\text{N}^+\text{F}^-$ , followed by addition of a proton source, formation of  $(\text{NPMe}_2)_3$  in 60% yield is observed (76). The hexakistrifluoromethyl derivative,  $[(\text{CF}_3)_2\text{PN}]_3$ , was prepared in good yield by the reaction of  $\text{CF}_3\text{SiMe}_3$  with  $\text{N}_3\text{P}_3\text{F}_6$  in the presence of  $\text{CsF}$  as catalyst (48).

A variety of alkynyl derivatives, including trimethylsilyl acetylene and terminal acetylene derivatives, have also been prepared by delithiation reactions with  $\text{N}_3\text{P}_3\text{F}_6$  (77, 79). The terminal silyl group of the trimethylsilyl acetylene derivatives has been substituted by  $\text{H}$  using  $\text{KF}$  and  $\text{EtOH}$ . The alkynyl groups of some of these substituted phosphazenes have been found to react with  $\text{Co}_2(\text{CO})_8$ , forming  $\text{Co}_2(\text{CO})_6$  complexes (77).

Reactions of  $N_3P_3F_6$  with a variety of lithium enolates have been studied in detail. With the lithium enolate of acetaldehyde,  $LiOCH=CH_2$ , the reaction was slow to go beyond the trisubstitution stage, and the F atom in  $N_3P_3F(OCH=CH_2)_5$  was not replaced, even under forcing conditions (80). A modified procedure with improved yields of  $N_3P_3F_5(OCH=CH_2)$  was reported recently (81). In contrast, the reaction of  $N_3P_3F_6$  with  $CF_3CH_2OSiMe_3$  in the presence of CsF leads to the complete substitution of all the P–F bonds (82). Fluorophosphazenes with alkenyl groups directly bound to the ring, as well as with an aryl spacer group, were prepared by Allen and co-workers (64, 70, 83, 84). Polymerization of the monosubstituted fluorophosphazene  $N_3P_3F_5(C(Me)=CH_2)$  with styrene yielded a copolymer with phosphazene as a pendant group; this copolymer exhibited fire-retardant properties (84). Reactions of the methoxide ion with  $N_3P_3F_5(N=PPh_3)$  indicate that the fluorine atom on the phosphinimino-substituted phosphorus is the most difficult one to replace (85).

Whereas chlorophosphazenes are found to undergo ring degradation and ring opening under a variety of conditions, very few reactions have been reported in which  $N_3P_3F_6$  behaves similarly. The trimer ring opens with polymerization to yield the perfluorophosphazene at 350°C (86, 87). Dimethylsulfoxide (DMSO) has also been reported to degrade both chloro- and fluorophosphazenes, leading to partially or fully hydroxylated phosphazenes or phosphazanes. DMSO is converted to  $XCH_2SMe$  ( $X = Cl$  or  $F$ ) (88). Strong nucleophiles, such as diethylamine, have also been reported to cleave the phosphazene ring skeleton (62). Mews and co-workers have reported a fluoride ion-induced ring opening of  $N_3P_3F_6$  (89, 90). Reaction of TASF with  $N_3P_3F_6$  yields  $(TAS^+)_2(P_3N_3F_5NPF_2NPF_2NPF_5)^{2-}$ , a fluorocyclophosphazene with a phosphazane dianion side chain (Fig. 4). Reaction of monolithiated ferrocene with  $N_3P_3F_6$  results in the formation of a ferrocene-substituted fluorophosphazene (Fig. 5) (91). On thermal ring-opening polymerization, this was found to yield a polyfluorophosphazene with pendant ferrocenyl moieties (92).

## B. WITH DIFUNCTIONAL REAGENTS

One of the interesting properties of cyclophosphazenes is the possibility of obtaining an array of structural isomers at the multisubstitution stage in the reactions with monofunctional reagents. The products possible with a difunctional reagent are also unique for these heterocycles, involving, in principle, five different types of products: spiro (A), ansa (B), dangling (C), bridging (D), and polymeric (E)

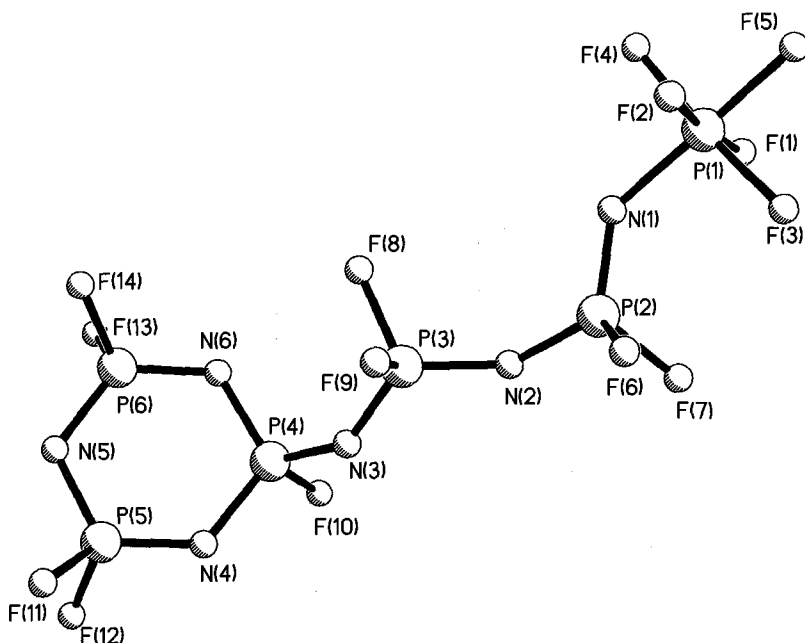


FIG. 4. Molecular structure of  $[\text{P}_3\text{N}_3\text{F}_5\text{NPF}_2\text{NPF}_2\text{NPF}_5]^{2-}$  (cations omitted). Reproduced with permission from Ref. (88). Copyright 1995, Royal Society of Chemistry.

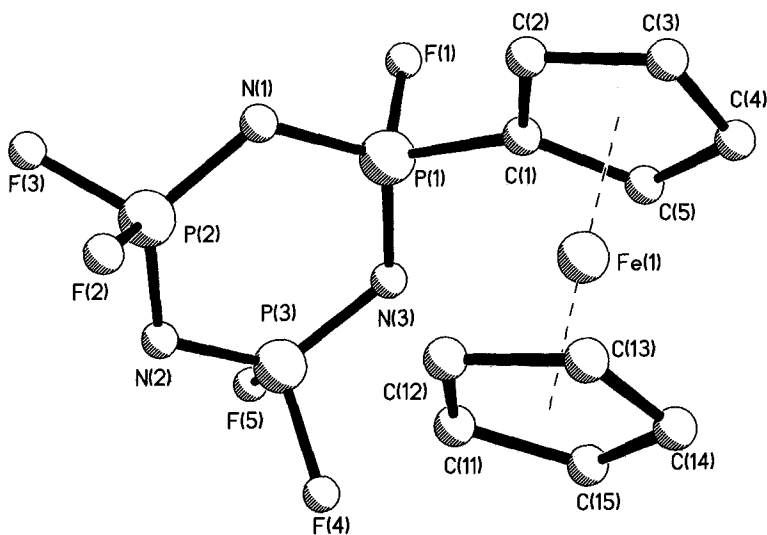
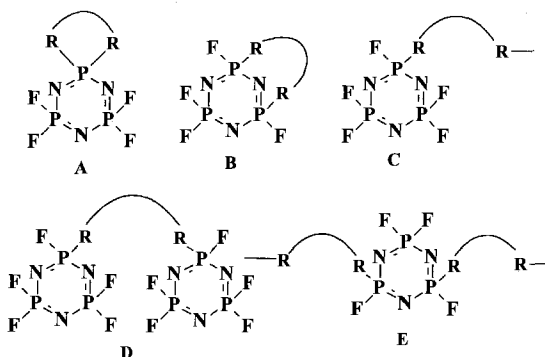


FIG. 5. Crystal structure of  $\text{N}_3\text{P}_3\text{F}_5(\text{C}_5\text{H}_4\text{FeC}_5\text{H}_5)$ . Reproduced with permission from Ref. (90). Copyright 1982, Royal Society of Chemistry.

(Scheme 2). However, the actual possibility is controlled by a variety of factors, such as chain length, the nature of the reacting group, and the mode of activation of the reacting group. Reactions of difunctional reagents with chlorophosphazenes have been well documented (93).

The first reactions of difunctional reagents with  $N_3P_3F_6$  were reported by Chivers and Hedgeland (94). In their study, equimolar reactions of *N,N*-dimethylethylenediamine and 1,2,2,3-tetramethyl-1,3-diaza-2-silacyclopropane yielded monospirocyclic compounds, which were characterized by spectral and analytical methods. This study clearly indicated the difference between di- and monofunctional amines, where nongeminal substituted products were the favored products. Similar reactions carried out by Kumara Swamy and Krishnamurthy with 1,2-diaminoethane and 1,3-diaminopropane also afforded monospirocyclic products in 10–20% yields (95). Reactions of disilylated ethylenediamine were used in the preparation of mono-, di-, and trispirocyclic derivatives of  $N_3P_3F_6$ . Energetic nitramine-containing compounds were synthesized from these by nitration of the reactive N–H groups using  $NO_2BF_4$  (96, 97).

Allcock and co-workers have carried out extensive reactions using dilithiated metallocenes, including ferrocene, ruthenocene, and dibenzylchromium (98–100). Reactions of these compounds with  $N_3P_3F_6$  were found to result in the exclusive formation of ansa-substituted fluorophosphazenes. The crystal structures of these ansa compounds indicate that the phosphazene ring is distorted, and the nitrogen atom flanked by the bridging phosphorus sites was seen to be displaced 0.56–0.66 Å from the plane defined by the five remaining ring atoms. On heating, some of these ansa derivatives undergo strain-induced

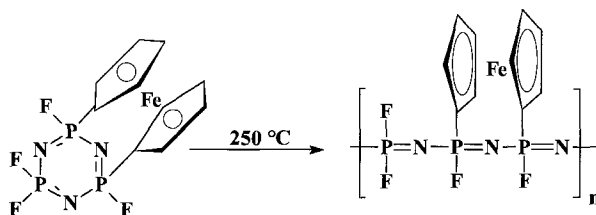


SCHEME 2

ring-opening polymerization, leading to ferrocene-substituted polyphosphazenes (92) (Scheme 3). The interesting feature of these reactions is the fact that a halogen atom is not required on the heterocycle for ring-opening polymerization to occur. In a few cases, on heating, instead of polymerization, the molecule was found to undergo ring expansion that led to twelve-membered heterocycles while retaining the vicinal binding of the ferrocene. A unique example of a three-membered spirocyclic compound having P–Fe bonds was prepared by first making a geminally disubstituted derivative with  $\text{NaFe}(\text{CO})_2\text{Cp}$  which, on photolysis, was decarbonylated to yield the spirocycle. This was characterized structurally. The same approach with similar ruthenium reagents resulted in products having Ru–P and Fe–Ru bonds (101–103).

Desilylation reactions of silylated diols, thioalcohols, and dithiols with  $\text{N}_3\text{P}_3\text{F}_6$ , in the presence of a catalyst such as CsF, were first reported by Shreeve *et al.* (82, 104). These reactions, which proceed with the liberation of  $\text{Me}_3\text{SiF}$ , illustrate a good method for making bridged derivatives of  $\text{N}_3\text{P}_3\text{F}_6$ . In addition, these reactions yield spirocyclic derivatives and, in some cases, dangling products as well. Aromatic disiloxanes are very facile reagents for the formation of spirocyclic products with  $\text{N}_3\text{P}_3\text{F}_6$ . Mono and dispiro derivatives are readily obtained with disilylated 1,2-catechol and related disiloxanes (Fig. 6). The interesting transformation of a bridged fluorophosphazene to a spirocyclic derivative has also been observed to occur in THF at elevated temperatures in the presence of CsF as catalyst (82).

Herberhold *et al.* reported interesting differences in the reactions of 1,1'-ferrocenediol, dithiol, and diselenol with  $\text{N}_3\text{P}_3\text{F}_6$  (105). While the diol in the presence of  $\text{Et}_3\text{N}$  gave ansa-substituted products, dithiol and diselenol only resulted in spirocyclic compounds. The same results were observed with trimeric chlorophosphazenes. In 2000, the first examples of exo and endo isomers of ansa-substituted fluorophosphazenes were reported by Elias and co-workers (106). A reaction of the dilithiated diol  $\text{RCH}_2\text{P}(\text{S})(\text{CH}_2\text{OLi})_2$  ( $\text{R} = \text{Fc}$ ,  $\text{Ph}$ ) with  $\text{N}_3\text{P}_3\text{F}_6$  resulted in the formation



SCHEME 3

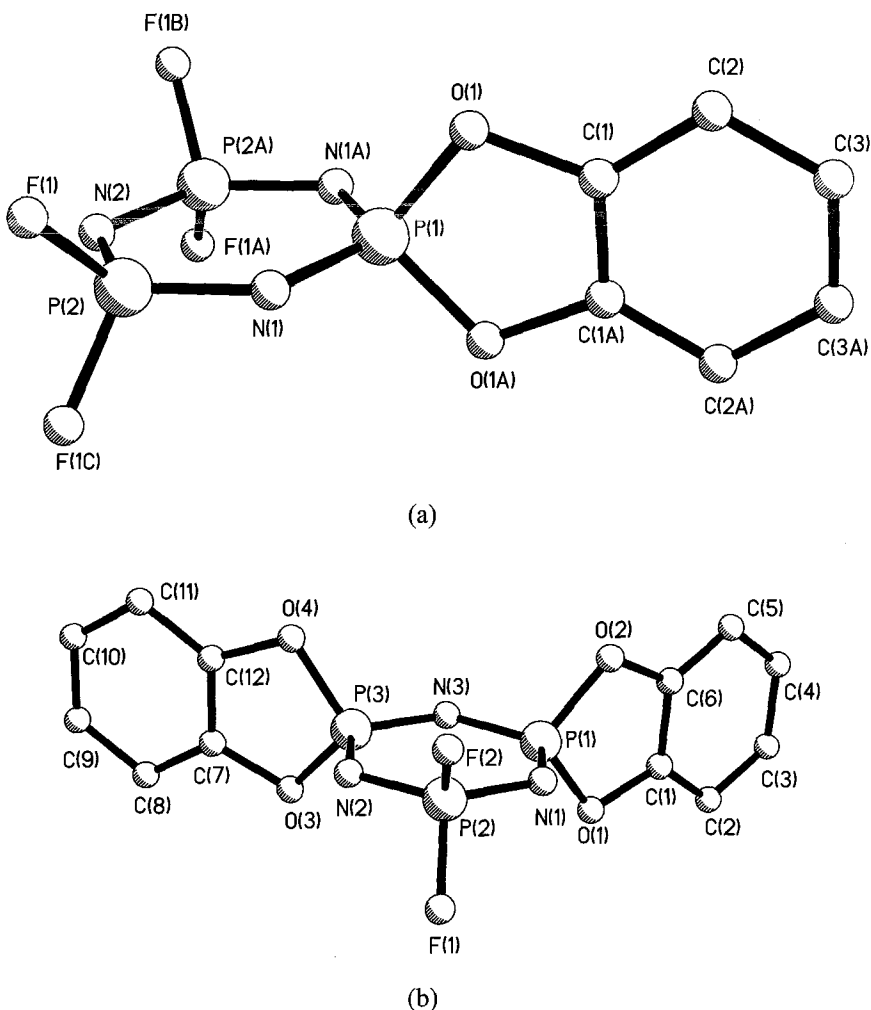
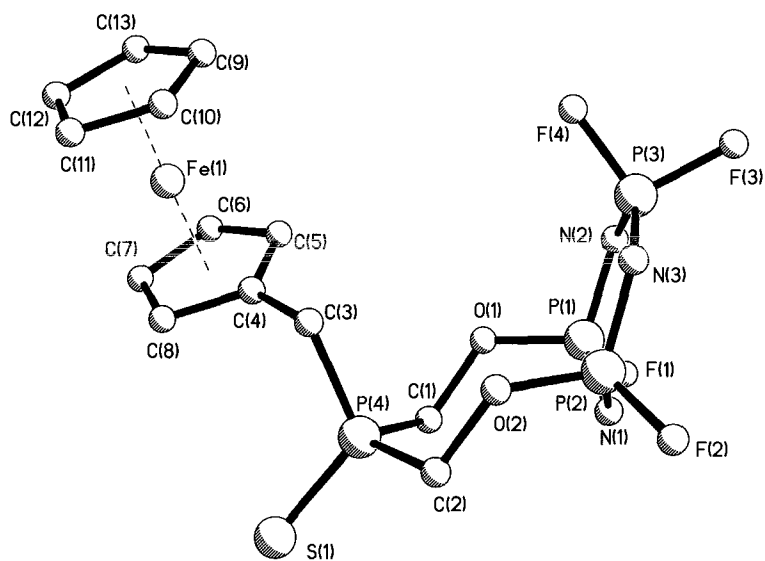
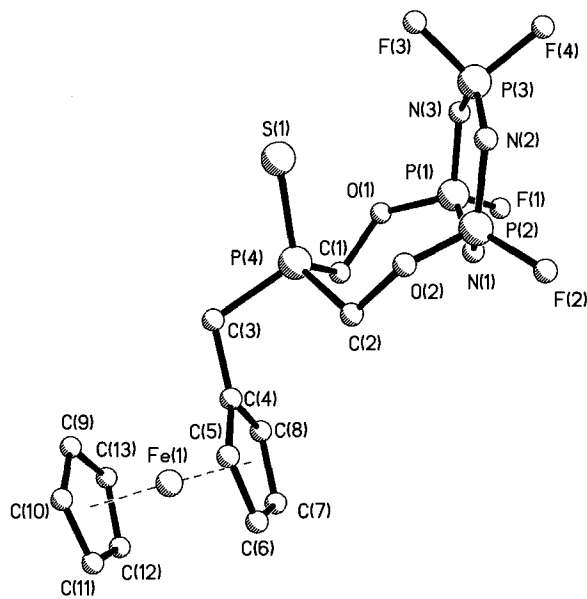


FIG. 6. Molecular structures of monospiro  $N_3P_3F_4$  (1,2- $C_6H_4O_2$ ) (a) and dispiro  $N_3P_3F_2$  (1,2- $C_6H_4O_2$ )<sub>2</sub> (b). Reproduced with permission from Ref. (104). Copyright 1996, American Chemical Society.

of two structural isomers, *endo*- $RCH_2P(S)(CH_2O)_2[P(F)N]_2(F_2PN)$  and *exo*- $RCH_2P(S)(CH_2O)_2[P(F)N]_2(F_2PN)$  ( $R = Fc, Ph$ ) (Fig. 7). More interesting was the fact that, on stirring with catalytic amounts of  $CsF$  in THF, these ansa compounds transformed to spirocyclic isomers (Scheme 4). This transformation was followed by time-dependent  $^{31}P$  NMR spectroscopy.

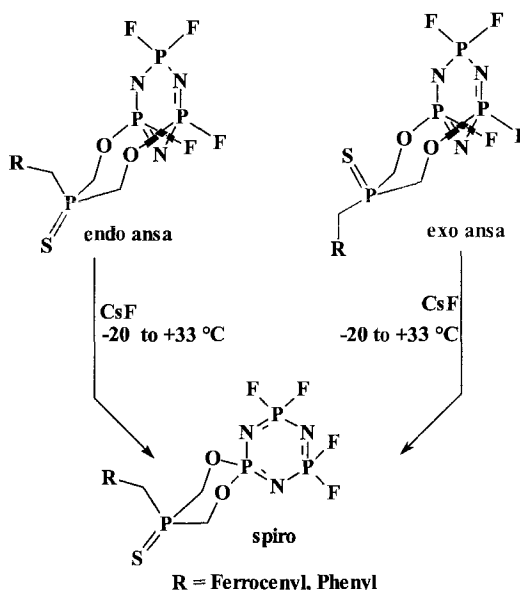


(a)



(b)

FIG. 7. Crystal structures of *endo*- $\text{FcCH}_2\text{P}(\text{S})(\text{CH}_2\text{O})_2[\text{P}(\text{F})\text{N}]_2(\text{F}_2\text{PN})$  (a) and *exo*- $\text{FcCH}_2\text{P}(\text{S})(\text{CH}_2\text{O})_2[\text{P}(\text{F})\text{N}]_2(\text{F}_2\text{PN})$  (b). Reproduced with permission from Ref. (106). Copyright 2000, American Chemical Society.

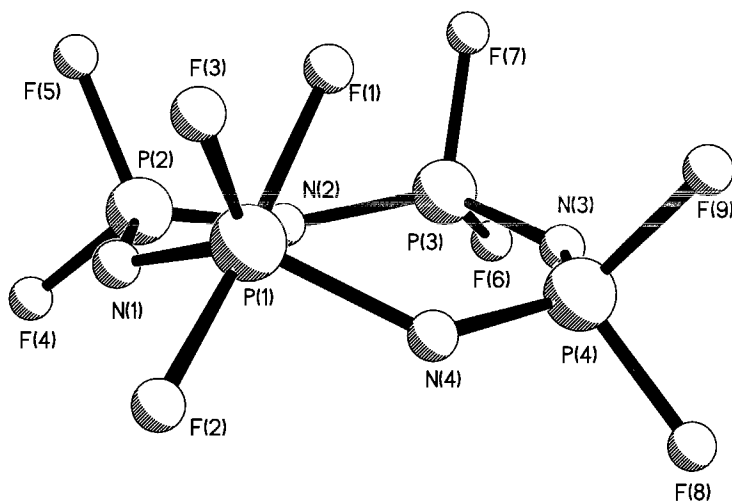


SCHEME 4

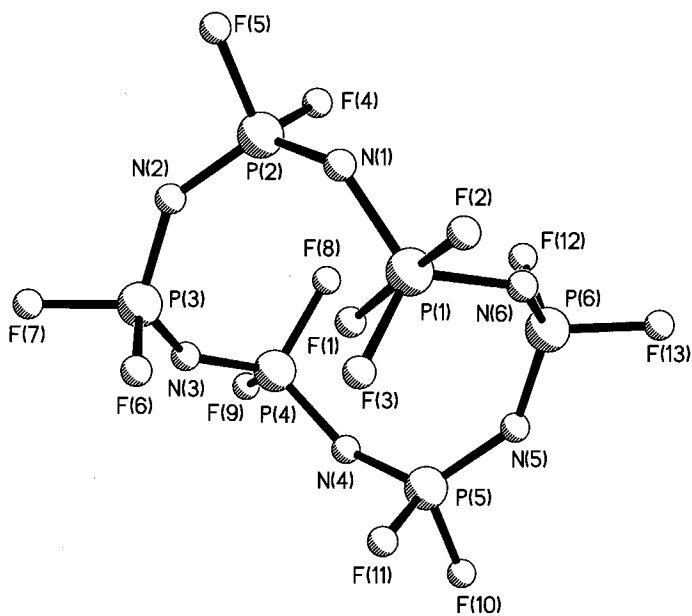
## VI. Reactions of Cyclic Tetrameric and Higher Fluorophosphazenes

Compared to trimeric fluorophosphazenes, very few detailed studies have explored the reaction chemistry of tetrameric and higher fluorophosphazenes. Among these, unique reactions that specifically gave stable phosphazenate anions were reported by Mews *et al.*, who described  $N_4P_4F_8$  and  $N_6P_6F_{12}$  with TASF (107). These were characterized structurally (Fig. 8). This observation was in contrast to similar reactions with  $N_3P_3F_6$  which result in the cleavage of the  $N_3P_3$  ring to give a six-membered heterocycle with a phosphazane dianion side chain, thus supporting the greater flexibility of the larger ring systems.

Reactions of monolithiated 1-methylpyrrole (108) and ferrocene as well as MeLi (75, 108) were carried out with  $N_4P_4F_8$ . The reaction of MeLi was studied in detail and found to result in methyl, dimethyl, trimethyl, and tetramethyl as well as octamethyl derivatives. The tetramethyl derivative exhibited an interesting orientation pattern, *viz.*, geminal substitution followed by a reaction at an antipodal site. Methylation of  $(NPF_2)_3$  with methyllithium cannot be carried beyond *gem*- $N_3P_3F_4Me_2$  because skeletal cleavage and elimination of alkyl halide interfere. However, the reaction of  $(NPF_2)_4$  with methyllithium produced  $(NPM_2)_4$  in 70% yield. Reactions of methylamine, dimethylamine, and *n*-butylamine with  $N_4P_4F_8$  proceeded with replacement of



(a)



(b)

FIG. 8. Crystal structure of  $\text{N}_4\text{P}_4\text{F}_9^-$  (a) and  $\text{N}_6\text{P}_6\text{F}_{13}^-$  (b) anions (cations omitted). Reproduced with permission from Ref. (107). Copyright 1995, VCH Verlag GmbH.

one fluorine atom per phosphorus under conditions that lead to total replacement of chlorine atoms in  $N_4P_4Cl_8$  (54). Mass and NMR spectral identification of the products indicated formation of nongeminally tri- and tetrasubstituted products. In contrast, reactions of sodium trifluoroethoxide and sodium phenoxide with  $N_4P_4F_8$  resulted in the replacement of all the fluorine atoms. The rationale for the different behavior of amines is discussed in Section V.

Reactions of dilithioferrocene and dilithioruthenocene with  $N_4P_4F_8$  were found to yield a mixture of 1,3- and 1,5-ansa-substituted derivatives. Separation of the ferrocenyl derivatives was achieved by liquid chromatography, but only the 1,5-isomer was obtained in the pure form from the ruthenocene reaction (98, 99). The 1,5-transannular substituted compound of ruthenocene, when further reacted with 1 mol of 1,1'-dilithiated ruthenocene yielded a bis-1,5-diansa-substituted compound.

Chivers and Hedgeland prepared the first spirocyclic amino derivative of  $N_4P_4F_8$  by the reaction of *N,N'*-dimethylethylenediamine (94). Examples of monospirocyclic derivatives of diols were first reported from the reaction of  $(CF_2)_n(CF_2CH_2OSiMe_3)_2$  ( $n = 0, 1$ ) with  $N_4P_4F_8$  in the presence of CsF as catalyst (110). The crystal structure of the compound  $[(CF_2CH_2O)_2PN](F_2PN)_3$  (Fig. 9) shows that the  $P_4N_4$  ring is nonplanar with a geometry similar to that of the parent fluorophosphazene. A bridged derivative was also formed in this reaction. Quite

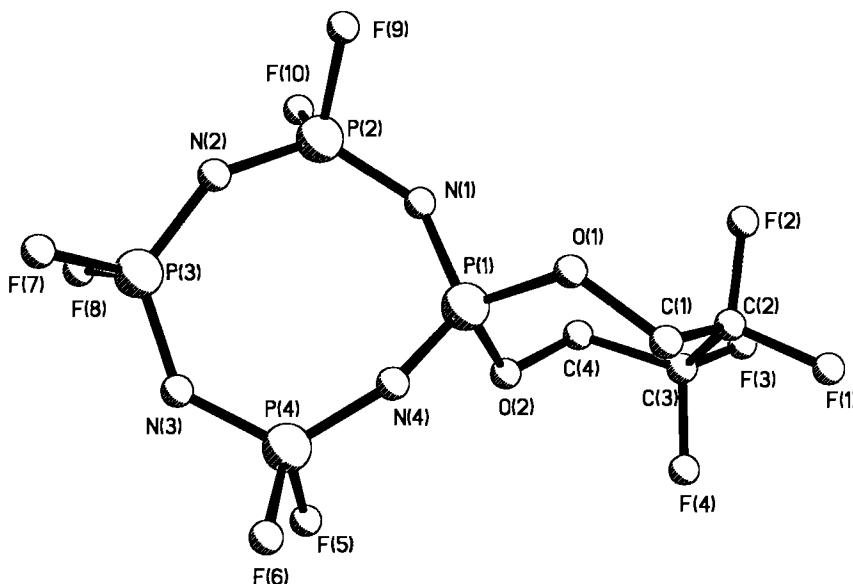


Fig. 9. Crystal structure of *spiro*- $[(CF_2CH_2O)_2PN][(F_2PN)_3]$ .

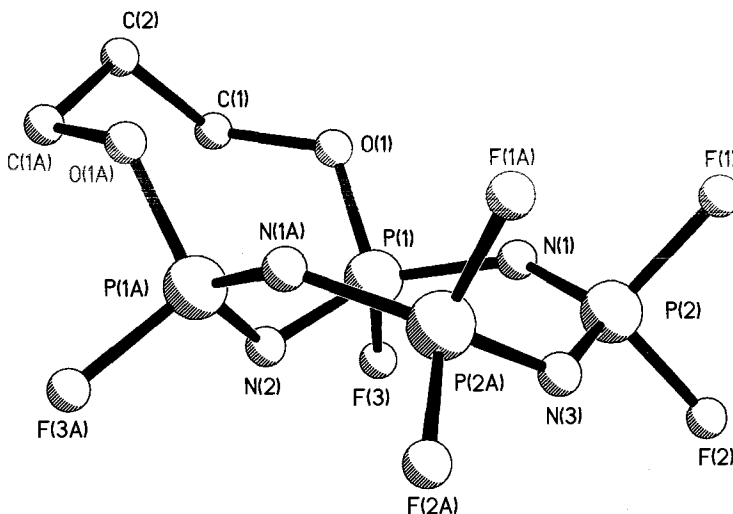


FIG. 10. Crystal structure of 1,3-ansa-[CH<sub>2</sub>(CH<sub>2</sub>O)<sub>2</sub>P(F)N]<sub>2</sub>[(F<sub>2</sub>PN)<sub>2</sub>].

interestingly, a reaction of dilithiated propanediol gave the 1,3-ansa-substituted derivative CH<sub>2</sub>(CH<sub>2</sub>O)<sub>2</sub>[P(F)N]<sub>2</sub>(F<sub>2</sub>PN)<sub>2</sub> as the major product, along with the monospirocyclic compound as the minor product. The overall geometry of the phosphazene ring of the 1,3-ansa-substituted compound was similar to that of the ring structure of monospirocyclic tetrameric fluorophosphazene (Fig. 10). The P—N—P angle between the two phosphorus centers forming the ansa bridge was smaller than the rest of the P—N—P angles of the ring framework. In spite of the flexibility associated with the eight-membered ring, on treating with CsF in THF at room temperature, the 1,3-ansa-substituted compound was found to transform to the spirocyclic compound (Scheme 5), thus providing further evidence for the higher thermodynamic stability of the spirocyclic phosphazenes relative to the ansa derivatives. In contrast, the dilithiated 1,3-propanedithiol was found to yield only the spirocyclic compound as the product.



SCHEME 5

Although perfluorinated cyclic phosphazenes have been detected chromatographically to  $(\text{NPF}_2)_{40}$ , reactions have been performed on rings only up to  $(\text{NPF}_2)_{12}$ . Fluorophosphazenes,  $(\text{NPF}_2)_6$  to  $(\text{NPF}_2)_{12}$ , were reacted with methylmagnesium bromide to yield the permethylated products  $(\text{NPMe}_2)_{9-12}$ , which were also structurally characterized (111, 112).

## VII. Conclusions

In spite of the ease of preparation, separation, and purification of cyclic perfluorinated phosphazenes, very little has been done to explore their reaction chemistry, especially that of the larger ring compounds. The perfluorinated heterocycles are more stable and less reactive than the corresponding chloro and bromo compounds. With the availability of high-field and high-resolution NMR,  $^{19}\text{F}$  NMR spectral studies on these heterocycles have become more comprehensible and useful in understanding the reactions of the cyclic fluorophosphazenes compared to the chloro and bromo compounds. The preparation of bridged and ansa compounds with fluorinated phosphazenes is more straightforward, and the product yields are high. Also, reactions with organometallic reagents are less complex and better understood. Reactions of amines, although not fully explored, provide interesting differences compared to the chloro analogs. The relatively higher stability of spiro relative to ansa and bridged cyclophosphazenes has been determined experimentally by studies of the corresponding interconversions of the fluorinated phosphazenes.

## ACKNOWLEDGMENTS

A.J.E. thanks CSIR India and DST India for financial support in the form of research grants. The authors are grateful to British Nuclear Fuels plc, and the National Science Foundation (CHE-9720635) for generous support of the work accomplished at the University of Idaho and during the preparation of this review.

## REFERENCES

1. Mark, J. E.; Allcock, H. R.; West, R. "Inorganic Polymers"; Prentice Hall: Englewood Cliffs, NJ, 1992.
2. Schneider, R.; Köllner, C.; Weber, I.; Togni, A. *Chem. Commun.* **1999**, 2415.
3. Allcock, H. R. "Phosphorus Nitrogen Compounds"; Academic Press: New York, 1972.

4. Allen, C. W. *Chem. Rev.* **1991**, *91*, 119.
5. Krishnamurthy, S. S.; Sau, A. C.; Woods, M. *Adv. Inorg. Chem. Radiochem.* **1978**, *21*, 41.
6. Allen, C. W. *Coord. Chem. Rev.* **1994**, *130*, 137.
7. Chandrasekhar, V.; Thomas, K. R. *J. Struct. Bonding* **1993**, *81*, 41.
8. Allen, C.W. *Gov. Rep. Announce. Index (U.S.)* **1981**, *81*, 89; *Chem. Abstr.* **1981**, *94*, 192179a.
9. Chandrasekhar, V.; Thomas, K. R. *J. Appl. Organomet. Chem.* **1993**, *67*, 1.
10. Schmitz-Dumont, O.; Kùlkens, H. Z. *Anorg. Allg. Chem.* **1938**, *238*, 189.
11. Schmitz-Dumont, O.; Braschos, A. Z. *Anorg. Allg. Chem.* **1939**, *243*, 113.
12. Schmitz-Dumont, O.; Walther, M. Z. *Anorg. Allg. Chem.* **1959**, *298*, 193.
13. Seel, F.; Langer, J. *Angew. Chem.* **1956**, *68*, 461.
14. Seel, F.; Langer, J. Z. *Anorg. Allg. Chem.* **1958**, *295*, 316.
15. Chapman, A. C.; Paine, D. H.; Searle, H. T.; Smith, D. R.; White, R. F. M. *J. Chem. Soc.* **1961**, 1798.
16. Allen, G.; Barnard, M.; Emsley, J.; Paddock, N. L.; White, R. F. M. *Chem. Ind.* **1963**, 952.
17. Emsley, J.; Paddock, N. L. *J. Chem. Soc. A*, **1968**, 2590.
18. Green, B.; Sowerby, D. B. *J. Chem. Soc., Chem. Commun.* **1969**, 628; *J. Chem. Soc. A*, **1970**, 987.
19. Chapman, A. C.; Paddock, N. L.; Paine, D. H.; Searle, H. T.; Smith, D. R. *J. Chem. Soc.* **1960**, 3608.
20. Rätz, R.; Grundman, C. *J. Inorg. Nucl. Chem.* **1960**, *16*, 60.
21. Green, B.; Sowerby, D. B. *Inorg. Nucl. Chem. Lett.* **1969**, *5*, 989.
22. Paddock, N. L.; Patmore, D. J. *J. Chem. Soc., Dalton Trans.* **1976**, 1029.
23. Bamgboye, T. T.; Sowerby, D. B. *J. Inorg. Nucl. Chem.* **1981**, *43*, 2253.
24. Moeller, T.; John, K.; Tsang, F. *Chem. Ind.* **1961**, 347.
25. Schmutzler, R. *Inorg. Synth.* **1967**, *9*, 75.
26. Moeller, T.; Tsang, F. *Inorg. Synth.* **1967**, *9*, 78.
27. Walsh, E. J.; Derby, E.; Smegal, J. *Inorg. Chim. Acta* **1976**, *16*, L9.
28. Loewe, C.; Riesel, L. Z. *Anorg. Allg. Chem.* **1995**, *21*, 901.
29. Paddock, N. L.; Serregi, J.; Can, J. *Chem.* **1974**, *52*, 2546.
30. Henne, A. L. *Org. React.* **1944**, *2*, 49.
31. Green, B. *J. Chem. Soc., Dalton Trans.* **1974**, 1113.
32. Clare, P.; King, T. J.; Sowerby, D. B. *J. Chem. Soc., Dalton Trans.* **1974**, 2071.
33. Exarhos, G. J.; Hess, N. J. *Microbeam. Anal.* **1988**, *23*, 161.
34. Lakatos, B.; Hesz, A.; Vetessy, Z.; Horvath, G. *Acta Chim. Sci. Hung.* **1969**, *60*, 309.
35. Lakatos, B.; Hesz, A.; Vetessy, Z.; Horvath, G. *Magy. Kem. Foly.* **1968**, *74*, 468.
36. Branton, G. R.; Brion, C. E.; Frost, D. C.; Mitchell, K. A. R.; Paddock, N. L. *J. Chem. Soc. A*, **1970**, 151.
37. Allen, C. W.; Green, J. *Inorg. Chem.* **1980**, *19*, 1719.
38. Allen, C. W.; Worley, S. D. *Inorg. Chem.* **1999**, *38*, 5187.
39. Krishnamurthy, S. S.; Woods, M. *Ann. Rep. NMR Spectrosc.* **1987**, *19*, 175.
40. Chivers, T.; Paddock, N. L. *Inorg. Chem.* **1972**, *11*, 848.
41. Brion, C. E.; Paddock, N. L. *J. Chem. Soc. A*, **1968**, *2*, 392.
42. Haddon, R. C. *Chem Phys. Lett.* **1985**, *120*, 372.
43. Ferris, K. M.; Friedman, P.; Friedrich, D. M. *Int. J. Quantum Chem., Quantum Chem. Symp.* **1988**, *22*, 207.
44. Faucher, J. P.; Labarre, J. F. *Phosphorus* **1974**, *3*, 265.

45. Faucher, J. P.; Devanneaux, J.; Leibovici, C.; Labarre, J. F. *J. Mol. Struct.* **1971**, *10*, 439.
46. Davis, M. I.; Paul, J. W. *J. Mol. Struct.* **1971**, *9*, 478.
47. Jagodzinski, H.; Oppermann, I. Z. *Kristallogr.* **1960**, *113*, 241.
48. Singh, R. P.; Vij, A.; Kirchmeier, R. L.; Shreeve, J. M. *Inorg. Chem.* **2000**, *39*, 375.
49. McGeachin, H. M.; Tromans, F. R. *J. Chem. Soc.* **1961**, 4777.
50. Becher, H. J.; Seel, F. Z. *Anorg. Allg. Chem.* **1960**, *305*, 148.
51. Breza, M. *Polyhedron*, **2000**, *19*, 389.
52. Elias, A. J.; Twamley, B.; Haist, R.; Oberhammer, H.; Henkel, G.; Krebs, B.; Lork, E.; Mews, R.; Shreeve, J. M. Unpublished results.
53. Hartsuiker, J. G.; Wagner, A. J. *J. Chem. Soc., Dalton. Trans.* **1978**, 1425.
54. Evans, T.; Allcock, H. R. *Inorg. Chem.* **1979**, *18*, 2342.
55. Katti, K. V.; Krishnamurthy, S. S. *J. Chem. Soc., Dalton Trans.* **1985**, 285.
56. Goldschmidt, J. M. E.; Licht, E. *J. Chem. Soc. A*, **1971**, 2429.
57. Chivers, T.; Oakley, R. T.; Paddock, N. L. *J. Chem. Soc. A*, **1970**, 2324.
58. Roesky, H. W.; Harmut, W. *Chem. Ber.* **1973**, *106*, 280.
59. Dahmann, D.; Rose, H.; Walz, W. Z. *Naturforsch. B, Anorg. Chem. Org. Chem.* **1980**, *35B*, 964.
60. Dahmann, D.; Rose, H.; Shaw, R. A. Z. *Naturforsch. B, Anorg. Chem. Org. Chem.* **1977**, *32B*, 236.
61. DuPlessis, J. A. K.; Rose, H.; Shaw, R. A. Z. *Naturforsch. B, Anorg. Chem. Org. Chem.* **1976**, *31B*, 997.
62. Glemser, O.; Niecke, E.; Roesky, H. W. *Chem Commun.* **1969**, 282.
63. Ramachandran, K.; Allen, C. W. *J. Am. Chem. Soc.* **1982**, *104*, 2396.
64. Shaw, J. C.; Allen, C. W. *Inorg. Chem.* **1986**, *25*, 4632.
65. Allen, C. W.; Moeller, T. *Inorg. Chem.* **1968**, *7*, 2177.
66. Allen, C. W.; White, A. J. *Inorg. Chem.* **1974**, *13*, 1220.
67. Allen, C. W.; Toch, P. L. *Inorg. Chem.* **1981**, *20*, 8.
68. Walker, F. W.; Ashby, E. C. *J. Am. Chem. Soc.* **1969**, *91*, 3845.
69. Seebach, D.; Hässrg, R.; Gabriel, J. *Helv. Chim. Acta* **1983**, *66*, 308.
70. Allen, C. W.; Bright, R. P. *Inorg. Chem.* **1983**, *22*, 1291.
71. Allen, C. W.; Tsang, F. Y.; Moeller, T. *Inorg. Chem.* **1968**, *7*, 2177.
72. Allen, C. W.; Brunst, G. E.; Perlman, M. E. *Inorg. Chim. Acta* **1980**, *41*, 265.
73. Allen, C. W.; Bedell, S.; Pennington, W. T.; Cordes, A. W. *Inorg. Chem.* **1985**, *24*, 1653.
74. Blumentrit, J.; Moeller, T. *Inorg Nucl. Chem. Lett.* **1978**, *14*, 263.
75. Paddock, N. L.; Ranganathan, T. N.; Todd, S. M. *Can. J. Chem.* **1971**, *49*, 164.
76. Allcock, H. R.; Coggio, W. D.; Parvez, M.; Turner, M. L. *Organometallics* **1991**, *10*, 677.
77. Chivers, T. *Inorg Nucl. Chem. Lett.* **1971**, *7*, 827.
78. Allen, C. W.; Bahadur, M. *Phosphorus, Sulfur, Silicon Relat. Elem.* **1993**, *76*, 463.
79. Allen, C. W.; Desorcie, J. L.; Ramachandran, K. *J. Chem. Soc., Dalton Trans.* **1984**, 2843.
80. Allen, C. W.; Bright, R. P. *Inorg. Chim. Acta.* **1985**, *99*, 107.
81. Allen, C. W.; Brown, D. E.; Worley, S. D. *Inorg. Chem.* **2000**, *39*, 810.
82. Elias, A. J.; Kirchmeier, R. L.; Shreeve, J. M. *Inorg. Chem.* **1994**, *33*, 2727.
83. Allen, C. W.; Randall, R. P.; Ramachandran, K. *ACS Symp. Ser.* **1981**, *171*, 321.
84. Allen, C. W.; Dupont, J. G. *Ind. Eng. Chem. Prod. Res. Dev.* **1979**, *18*, 80.
85. Kumara Swamy, K. C.; Krishnamurthy, S. S. *Inorg. Chem.* **1986**, *25*, 920.
86. Seel, F.; Langer, J. *Angew. Chem.* **1956**, *68*, 461.

87. Allcock, H. R.; Kugel, R. L.; Konopski, G. F.; Strohm, E. G. *Chem Commun.* **1970**, 985.
88. Walsh, E. J.; Kaluzene, S.; Jubach, T. *J. Inorg. Nucl. Chem.* **1976**, *38*, 397.
89. Lork, E.; Watson, P. G.; Mews, R. *J. Chem. Soc., Chem Commun.* **1995**, 1717.
90. Lork, E.; Chen, S.-J.; Knitter, G.; Mews, R. *Phosphorus, Sulfur, Silicon Relat. Elem.* **1994**, *93*, 309.
91. Suzuki, P. R.; Whittle, R. R.; Allcock, H. R. *J. Chem. Soc., Chem. Commun.* **1982**, 960.
92. Allcock, H. R.; Lavin, K. D.; Riding, G. H. *Macromolecules* **1985**, *18*, 1340.
93. Chandrasekhar, V.; Muralidhara, M. G. R.; Selvaraj, I. I. *Heterocycles* **1990**, *31*, 2231.
94. Chivers, T.; Hedgeland, R. *Can J. Chem.* **1972**, *50*, 1017.
95. Kumara Swamy, K. C.; Krishnamurthy, S. S. *Indian J. Chem., Sect. A*, **1984**, *23A*, 717.
96. Forohar, F. D.; Paritosh, R.; Axenrod, T.; Bedford, C. D.; Gilardi, R.; George, G. *Phosphorus, Sulfur, Silicon Relat. Elem.* **1995**, *101*, 161.
97. Paritosh, D. R.; Forohar, F.; Chaykovsky, M.; Bedford, C. U.S. Patent 5352829 1993; *CA* **1993**, *121*, 35869.
98. Allcock, H. R.; Desorcie, J. L.; Riding, G. H. *Polyhedron* **1987**, *6*, 119.
99. Allcock, H. R.; Lavin, K. D.; Riding, G. H.; Suszko, P. R.; Whittle, R. R. *J. Am. Chem. Soc.* **1984**, *106*, 2337.
100. Riding, G. F.; Parvez, M.; Allcock, H. R. *Organometallics* **1986**, *5*, 2153.
101. Allcock, H. R.; Wagner, L. J.; Levin, M. L. *J. Am. Chem. Soc.* **1983**, *195*, 1321.
102. Allcock, H. R.; Greigiger, P. P.; Wagner, L. J. *Inorg. Chem.* **1981**, *20*, 716.
103. Greigiger, P. P.; Allcock, H. R. *J. Am. Chem. Soc.* **1979**, *101*, 2492.
104. Vij, A.; Geib, S. J.; Kirchmeier, R. L.; Shreeve, J. M. *Inorg. Chem.* **1996**, *35*, 2915.
105. Herberhold, M.; Hofmann, A.; Milius, W. Z. *Anorg. Allg. Chem.* **1997**, *623*, 545.
106. Muralidharan, K.; Reddy, N. D.; Elias, A. J. *Inorg. Chem.* **2000**, *39*, 3988.
107. Lork, E.; Boehler, D.; Mews, R. *Angew. Chem., Int. Ed. Engl.* **1995**, *34*, 2696.
108. Sharma, R. D.; Rettig, S. J.; Paddock, N. L.; Trotter, J. *Can. J. Chem.* **1982**, *60*, 535.
109. Ranganathan, T. N.; Todd, S. M.; Paddock, N. L. *Inorg. Chem.* **1973**, *12*, 316.
110. Elias, A. J.; Twamley, B.; Shreeve, J. M. *Inorg. Chem.* **2001**, *40*, 2120.
111. Searle, H. T.; Dyson, J.; Ranganathan, T. N.; Paddock, N. L. *J. Chem. Soc., Dalton Trans.* **1975**, 203.
112. Oakley, R. T.; Rettig, S. J.; Paddock, N. L.; Trotter, J. *J. Am. Chem. Soc.* **1985**, *107*, 6923.

# SUBJECT INDEX

## A

- Ab initio* calculations, transition metal–noble gas complexes, 142–143
- Acetonitrile hydration, 234–236
- Acetylene derivatives, fluorophosphazenes, 344
- Aldolases, hydrolytic enzyme models, 299–301
- Aliphatic monolithiated reagents, 344
- Alkaline phosphatase, hydrolytic enzyme models, 294–299
- Alkoxide vanadium cages, 16
- 4-Alkoxybenzaldehyde, 152
- Alkoxystilbazoles
  - background, 151–152
  - with 4-cyanophenol, 196
  - liquid-crystalline metal complexes
    - early studies, 181
    - mesomorphic complexes, 182–183
    - monoalkoxystilbazoles, 185–190
    - poly(alkoxy)stilbazole complexes, 191–192
    - structures, 183–185
  - with 4-nitrophenol, 196–197
- Amines
  - with fluorophosphazenes, 343
  - ligands in octanuclear iron cages, 53–54
  - lithiated amines, 343
  - secondary amines, 24–25
  - trimethylsilyl amines, 343
  - trimethylstannyl amines, 343
- Aminoalkoxide ligands, hexanuclear copper cages, 81
- Aminolysis, fluorophosphazenes, 342
- Antennae, pendant, lanthanide complexes, 316–321
- Apocarbonic anhydrase, Zn(II) incorporation, 315

- Argon compounds
  - Fourier-transform microwave spectroscopy, 134
  - from low-temperature matrix isolation spectroscopy, 115
  - M(CO)<sub>5</sub> interactions, 142
- Azathioprine, in octanuclear copper cages, 92

## B

- BDE, *see* Bond dissociation energy
- Benzoic acid, with stilbazole, 195–196
- N*-Benzyl derivatives, stilbazoles, 162
- Beryllium, Ar–Be compounds, 115
- Bicarbonate, Ln(III) luminescence sensitivity, 319
- Bidentate ligands, Pt<sub>4</sub> clusters, 214–216
- Biphen, in decanuclear manganese cages, 39–41
- 2,2'-Biphenoxide, *see* Biphen
- Biphenyl-4-carboxylic acid, stilbazole complexes, 201
- 2,6-Bis(aminomethyl)-4-methylphenol monohydrochloride, 85
- 1,3-Bis(dimethylamino)-2-propanolato, 81
- Bis(pyridine) ligand, in hexanuclear iron cages, 51
- Bond dissociation energy
  - Au–Xe bond, 113–114
  - in [AuXe<sub>4</sub><sup>2+</sup>][Sb<sub>2</sub>F<sub>11</sub>]<sub>2</sub>, 145–146
  - transition metal–noble gas complexes, 141–146
  - W–Xe, 132–133
- Bp\*Rh(CO)<sub>2</sub>, *see* Dihydridobis(3,5-dimethylpyrazolyl)borate Rh(CO)<sub>2</sub>
- 4-*tert*-Butyl-2,6-diformylphenol, 85–86

## C

- Cadmium(II) complexes, molecular receptors, 328–330
- Calamitic mesogens, 170–172
- Carbamate ligands, in hexanuclear manganese cages, 26–29
- Carbon monoxide, substitution kinetics, 140
- Carboxylates
- bridged hexanuclear iron cages, 48–49
  - as bridging ligand, 6–7
  - chromium cages, 22–23
  - copper, for hexanuclear copper cages, 80–81
- Cell membranes, and nucleobase recognition reagents, 311–312
- Chlorophosphazenes, fluorination, 336–337
- Chromium cages, heptanuclear cages, 25
- Chromium compounds
- ab initio* calculations, 143
  - bonding to Xe, 130–131
  - gas-phase studies, 130
  - in liquefied noble gas solution, 125
  - matrix-isolation studies, 119–120
  - noble gas interaction, 142
  - polynuclear chemistry, 17–25
  - TRIR spectroscopy, 135–136
- Clearing point, liquid crystals, 179
- Cluster core transformation, triplatinum clusters, 237–238, 240–241
- Cobalt cages
- decanuclear cages, 68–70
  - heptanuclear cages, 64–65
  - hexanuclear cages, 62–64
  - largest cages, 72
  - nonanuclear cage, 67–68
  - octanuclear cages, 65–67
  - tridecanuclear cages, 71–72
  - undecanuclear paramagnetic cage, 70–71
- Columnar phases, discotic mesogen phases, 174
- Contrast reagents, for MRI, 321–322
- Coordination mode, squarate ion, 252–259
- Copper cages
- dodecanuclear cages, 92–95
  - heptanuclear cages, 87–88
  - hexanuclear cages, 80–87
  - homometallic cages, 90–91
  - nonanuclear cages, 92
  - octanuclear cages, 88–92
  - tetradecanuclear cages, 95–96
- Copper carboxylates, for hexanuclear copper cages, 80–81
- Copper(I)-3,5-dimethylpyrazole, in octanuclear copper cages, 90
- Copper(II) pivalate, hexanuclear copper cages, 81
- Copper triangles, 82
- Coupling constants, tetraplatinum clusters, 230–231
- Crystallization, solvent choice, in serendipitous assembly, 8
- Cubanes, as cages family, 98–101
- Cubic cages, squarates, 267–268
- Cubic phases, liquid crystals, 177–178
- Cyanide bridges, in single-molecule magnets, 5
- 4-Cyanobenzoic acid, stilbazole complexes, 201
- Cyanobiphenyl, with alkoxy stilbazoles, 152
- 4-Cyanophenol, with alkoxy stilbazoles, 196
- 4-Cyanostilbazoles, hydrogen-bonded complexes, 200–201
- Cyclic phosphazenes, perfluorinated, 336–337
- Cyclic tetrameric fluorophosphazenes, 351–355
- Cyclic trimeric fluorophosphazenes
- with difunctional reagents, 345–350
  - with monofunctional reagents, 341–345
- Cyclohexasiloxanolate ligands, in hexanuclear manganese cages, 29
- Cyclopentadienyl-ring substituents, in half-sandwich complexes, 139–140

## D

- Dansylamide, fluorescence, 315
- Decanuclear cobalt cages, 68–70
- Decanuclear iron cages, 55–56
- Decanuclear manganese cages
- with 2,2'-biphenoxide as ligand, 39–40
  - with decametallate core, 39
  - first synthesis, 38–39

- $\text{Mn}_{11}$ , 41–42  
 from tetranuclear cages, 41  
 Decanuclear nickel cages, 76–77  
 Decanuclear vanadium cages, 13–14  
 Decyloxystilbazole, with  
   2,4-dinitrophenol, 199–200  
 Delithiation, with fluorophosphazenes,  
   343–344  
 Density functional calculations, transition  
   metal–noble gas complexes, 142–143  
 Desilylation, with fluorophosphazenes,  
   343, 348  
 Destannylation, with fluorophosphazenes,  
   343  
 3,4-Dialkoxystilbazoles  
   Pd complexes, 192–193  
   silver dodecylsulfate, 191–192  
 1,3-Diamino-2-hydroxypropane, for  
   hexanuclear copper cages, 86  
 1,5-Diamino-3-hydroxypropane, for  
   hexanuclear copper cages, 85–86  
 Dibenzoyl methane derivatives, in  
   hexanuclear manganese cages, 29  
 6-(Diethylamino)-hydroxo-4-sulfanyl-  
   1,3,5-triazine, hexanuclear cobalt  
   cages, 63  
 Differential scanning calorimetry, liquid  
   crystals, 181  
 2,6-Diformyl-4-methylphenol, for  
   hexanuclear copper cages, 85  
 Difunctional reagents, with cyclic trimeric  
   fluorophosphazenes, 345–350  
 Dihydridobis(3,5-  
   dimethylpyrazolyl)borate  
    $\text{Rh}(\text{CO})_2$ , 129  
 $\beta$ -Diketones, 82  
 Dilithiated metallocenes, with  
   fluorophosphazenes, 347–348  
 Dilithioferrocene, 353  
 Dilithioruthenocene, 353  
 $N,N'$ -Dimethylethylenediamine,  
   353–354  
 Dimine ligands, hexanuclear copper  
   cages, 83–84  
 2,4-Dinitrophenol, with alkoxystilbazoles,  
   199–200  
 Dioxocyclam, pendant-arm macrocycles,  
   312  
 Dioxopentamine,  $\text{Ni}(\text{II})$  complex,  
   monooxygenase activity, 313  
 Diphenylaminosquarate, luminescence  
   studies, 285  
 Di-2-pyridyl ketone, for heptanuclear  
   copper cages, 87–88  
 Discotic mesogens, phases, 172–175  
 $d^8$ -metal center, matrix-isolation  
   spectroscopy, 122–123  
 DNA, nucleobase recognition reagents,  
   308–312  
 Dodecanuclear copper cages, 87–88,  
   92–95  
 Dodecanuclear iron cages, mixed-valenet  
   cage, 58–59  
 Dodecanuclear manganese cages  
   as SMMs, 2–3  
   synthesis, 42–44  
 Dodecanuclear nickel cages, 76–77  
 Dodecanuclear vanadium cages, 14–15  
 Dodecylsulfate salts,  
   monoalkoxystilbazoles, 186–187, 190  
 DOS, *see* Dodecylsulfate salts  
 DSC, *see* Differential scanning  
   calorimetry

## E

- EFFF, *see* Energy-factored force field  
 EHMO calculations, *see* Extended Hückel  
   molecular orbital calculations  
 Electrochemistry  
   monosubstituted squarate ligands,  
     284–285  
   squaric acid, 271  
 Electron paramagnetic resonance,  
    $\text{KrMn}(\text{CO})_5$  and  $[\text{KrFe}(\text{CO})_5]^+$ , 123  
 Electron transfer, in squaric acid  
   compounds, 262–267  
 Enantiotropic, liquid crystals, 179  
 Energy barrier, single-molecule  
   magnets, 3  
 Energy-factored force field, metal carbonyl  
   analyses, 117–118  
 1,2-Epoxyalkane, in metallosurfactant  
   preparation, 325  
 Europium(III) complexes  
   pH sensors, 318  
   synthetic ribonucleases, 303–308  
 Europium(III) phenylsquarate, 285  
 Europium(III) squarate, 270–271

Extended Hückel molecular orbital calculations  
tetranuclear platinum(II) cluster complexes, 219–221  
trinuclear platinum(II) cluster complexes, 241–243

## F

Ferrocene, with  $\text{N}_4\text{P}_4\text{F}_8$ , 351–353  
1,1'-Ferrocenediol, with fluorophosphazenes, 348–349  
1,1'-Ferrocenediselenol, with fluorophosphazenes, 348–349  
1,1'-Ferrocenedithiol, with fluorophosphazenes, 348–349  
Films, *see* Langmuir–Blodgett films  
Fluorescence, dansylamide, 315  
Fluoride salts, chlorophosphazene fluorination, 337  
Fluorination, chlorophosphazenes, 336–337  
Fluorophores, pendant, complexes, 314–316  
Fluorophosphazenes  
cyclic tetrameric fluorophosphazenes, 351–355  
cyclic trimeric fluorophosphazenes with difunctional reagents, 345–350  
with monofunctional reagents, 341–345  
Fourier-transform microwave spectroscopy, supersonic jets, 134

## G

Gadolinium(III) complexes, in magnetic resonance imaging, 321  
Gas-phase studies, transition metal–noble gas complexes, 130–134  
Gold complexes  
Au–Xe, 113–114, 145–146  
cation, theoretical studies, 145  
stilbazole complexes, 183–185  
Group 7, half-sandwich complexes, 139–140  
Group 8, mesomorphic complexes, 182–183

Group 10, mesomorphic stilbazole complexes  
monoalkoxystilbazoles, 185–190  
poly(alkoxy)stilbazole complexes, 191–194  
structures, 183–185  
Group 11, mesomorphic stilbazole complexes  
monoalkoxystilbazoles, 185–190  
poly(alkoxy)stilbazole complexes, 191–194  
structures, 183–185

## H

Half-sandwich complexes, group VII, 139–140  
Heptadecanuclear iron cages  
cocrystallization with nonadecanuclear cage, 60–61  
from  $[\text{Fe}_2\text{OCl}_6]^{2-}$  and  $\text{Na}(\text{chp})$ , 60  
mixed-valent cage, 59  
Heptanuclear chromium cages, 25  
Heptanuclear cobalt cages, 64–65  
Heptanuclear copper cages, 87–88  
Heptanuclear iron cages, 52  
Heptanuclear manganese cages  
first synthesis, 30–31  
metallocrowns, 32–33  
mixed-valent cage, 33  
Mn(II) cage, 31  
with twisted trigonal prism, 33–34  
Heptanuclear nickel cages, 74  
Heptanuclear vanadium cages, 11–12  
N-Heterocycles, in hexanuclear iron cages, 49–50  
Heterometallic alkoxides, 36–37  
Hexacatenar mesogens, 177  
Hexadecanuclear manganese cages, 46  
Hexadecanuclear vanadium cages, 15  
Hexadentate ligands, tetraplatinum clusters, 216  
Hexanuclear cobalt cages, 62–64  
Hexanuclear copper cages  
from dimeric copper carboxylates, 80–81  
with dimine ligands, 83–84  
from phenoxyacetate, 80  
related metal cages, 82–83  
various preparations, 84–87

- Hexanuclear iron cages  
 with bis(pyridine) ligand, 51  
 carboxylate-bridged triangles, 48–49  
 with *N*-(2-hydroxypropyl)iminodiacetic acid, 51–52  
 with polydentate ligands, 49–50  
 synthesis, 51  
 with triethanolamine ligands, 51
- Hexanuclear manganese cages  
 with carbamate ligands, 26–29  
 with cyclohexasiloxanolate ligands, 29  
 with dibenzoyl methane derivatives, 29  
 first cage, 25–26  
 high-spin cage, 26  
 with pentadentate Schiff-base ligand, 29
- Hexanuclear nickel cages, 72–74
- Hexanuclear vanadium cages, 10–11
- Higher fluorophosphazene reactions, 351–355
- High-nuclearity iron cages, 50–51
- High-resolution infrared spectroscopy,  $\text{Cr}(\text{CO})_5$ , 120
- Homometallic copper cages, 90–91
- Host–guest interaction, pendant-arm macrocycles, 309
- HPNP, *see* 4-Nitrophenylphosphate ester
- Hydration, acetonitrile, 234–236
- Hydridotris(3,5-dimethylpyrazolyl)borate  $\text{Rh}(\text{CO})_2$ , TRIR spectroscopy, 129
- Hydrogen bonding  
 monosubstituted squaric acid, 285–287  
 squaric acid complexes, 285–287  
 stilbazole mesogens, 194–201
- Hydrolytic enzyme models  
 for alkaline phosphatases, 294–299  
 for class II aldolases, 299–301
- 2-Hydroxy-1,3-propanediylbis(acetylacetonimine), 91–92
- N*-(2-Hydroxypropyl)iminodiacetic acid, 51–52
- I**
- 2-(4-Imidazolyl)-ethylimino-6-methylpyridine, 84–85
- Infinite periodic minimal surface model, 178
- Infrared spectroscopy  
 $\text{Cr}(\text{CO})_5$ , 120  
 perfluoro cyclic phosphazenes, 338  
 squarate complexes, 270  
 time-resolved, *see* Time-resolved infrared spectroscopy
- In phase, single-molecule magnets, 3
- Interconnecting rod model, 178
- Iron cages  
 decanuclear cage, 55–56  
 dodecanuclear cage, 58–59  
 heptadecanuclear cage, 59–61  
 heptanuclear cage, 52  
 hexanuclear cages, 48–52  
 high-nuclearity cage, 50–51  
 nonadecanuclear cages, 60–61  
 nonanuclear cage, 55  
 octadecanuclear wheel, 61–62  
 octahedral cages, 50  
 octanuclear cages, 52–55  
 undecanuclear cage, 57–58
- Iron complexes, photolysis, 117–118
- Isomerization, tetraplatinum clusters, 231–233
- K**
- Krypton  
 associated chemistry, 116  
 bonding to  $\text{M}(\text{CO})_5$ , 130–131  
 liquefied solution, 125–126  
 $\text{M}(\text{CO})_5$  interactions, 142
- L**
- Langmuir–Blodgett films  
 basic concepts, 165–166  
 metal stilbazole complexes, 167–169
- Lanthanide complexes  
 bicarbonate concentration, 319  
 with pendant antennae, 316–321  
 squarate complexes, 268–269  
 synthetic ribonucleases, 301–303
- L-B films, *see* Langmuir–Blodgett films
- Ligand substitution, triplatinum clusters, 238

- Linking groups, squarate ion as, 269
- Liquefied noble gas studies, transition metal–noble gas complexes, 123–130
- Liquid crystals
- alkoxystilbazole complexes
    - early studies, 181
    - mesomorphic complexes, 182–183
    - mesomorphic stilbazole complexes
      - monoalkoxystilbazoles, 185–190
      - poly(alkoxy)stilbazole complexes, 191–194
    - structures, 183–185
  - basic concepts, 169–170
  - calamitic mesogen phases, 170–172
  - cubic phase, 177–178
  - discotic mesogen phases, 172–175
  - mesophases, 178–181
  - metals into, 181
  - polycatenar mesogens, 175–177
  - thermotropic, hydrogen bonding, 195
- Lithiated amines, with fluorophosphazenes, 343
- Lithium enolates, with fluorophosphazenes, 345
- Lone pairs
- squarate substituents with, 275–280
  - squarate substituents without, 280
- Low-temperature matrix isolation spectroscopy, Ar compounds, 115
- Luminescence
- diphenylaminosquarate, 285
  - europium(III) phenylsquarate, 285
  - europium(III) squarate, 270–271
- Luminescent sensors
- lanthanide complexes with pendant antennae, 316–321
  - pendant fluorophore complexes, 314–316
- M**
- Macrocycles, pendant-arm, *see* Pendant-arm macrocycles
- Magnetic properties
- chromium, 17–25
  - iron cages, 53
  - single-molecule
    - polynuclear cages, 4–5
    - properties, 2–4
  - vanadium, 9–17
- Magnetic protein, decanuclear manganese cages, 41
- Magnetic resonance imaging, contrast reagents, 321–322
- Magnetochemistry, squaric acid compounds, 262–267
- Manganese cages
- decanuclear cages, 38–42
  - dodecanuclear Mn(II) cage, 42–44
  - heptanuclear Mn cages, 30–33
  - hexadecanuclear cages, 46
  - hexanuclear Mn cages, 25–30
  - nonanuclear cage, 37–38
  - octadecanuclear cage, 46–47
  - octanuclear manganese cages, 34–37
  - picolinate-bridged cages, 34–35
  - tetranuclear cage, 37
  - tridecanuclear cage, 45–46
- Mass spectrometry, transition metal–noble gas interactions, 133
- Matrix-isolation studies, transition metal–noble gas complexes, 117–123
- Melting point, liquid crystals, 179
- o*-Mercaptophenolate ligands, heptanuclear cobalt cages, 65
- Mesogens
- calamitic mesogens, 170–172
  - discotic mesogens, 172–175
  - hexacatenar mesogens, 177
  - metallomesogens, 181
  - polycatenar mesogens, 175–177
  - tetracatenar mesogens, 175–177
  - thermotropic mesogens, 177
- Mesomorphic complexes, group 8 metals, 182–183
- Mesomorphic stilbazole complexes
- monoalkoxystilbazoles, 185–190
  - poly(alkoxy)stilbazole complexes, 191–194
  - structures, 183–185
- Mesophases
- calamitic mesogens, 171–172
  - discotic mesogen phases, 172–173
  - liquid crystals
    - characterization, 180–181
    - transitions, 178–180
- Metal cages
- cubanes, 98–101
  - trigonal prisms, 101

- wheels and metallocrowns, 96–98
  - Metal carbonyls, EFFF studies, 117–118
  - Metal complexes
    - cyanobiphenyls, alkoxystilbazoles, 152
    - liquid-crystalline, alkoxystilbazoles, 181
    - stilbazoles, 154–158, 163
  - Metallocenes, dilithiated, with
    - fluorophosphazenes, 347–348
  - Metallocrowns
    - as cage family, 96–98
    - hexanuclear cobalt cages, 62–64
    - hexanuclear copper cages, 87
    - hexanuclear iron cages, 51
    - synthesis, 32–33
  - Metallocyanates, single-molecule
    - magnets, 5
  - Metallomesogens, 181
  - Metallodetergents, pendant-arm
    - macrocycles, 324–325
  - Metals
    - into liquid crystals, 181
    - 3d
      - chromium, 17–25
      - iron, 47–62
      - overview, 8–9
      - vanadium, 9–17
  - Metal stilbazole complexes,
    - Langmuir–Blodgett films, 167–169
  - Metal wheels, as cage family, 96–98
  - N-Methyldiethanolamine, in hexanuclear
    - iron cages, 51
  - Methyl lithium, with  $N_4P_4F_8$ , 351–353
  - 1-Methylpyrrole, with  $N_4P_4F_8$ ,
    - 351–353
  - Methylsquarate complexes, 280
  - Models
    - hydrolytic enzyme, 294–301
    - liquid crystal cubic phase, 178
    - RNA substrate, 302–303
  - Molecular receptors, pendant-arm
    - macrocycles, 326–330
  - Molybdenum compounds
    - ab initio* calculations, 143
    - bonding to Xe, 130–131
    - noble gas interaction, 142
    - TRIR spectroscopy, 135–136
  - Monoalkoxystilbazoles complexes,
    - 185–190
  - Monodentate ligands,  $Pt_4$  clusters,
    - 210–213
  - Monooxygenase, activity of
    - dioxopentamine Ni(II) complex, 313
  - Monosubstituted squarate complexes
    - derivatives, 271–273, 285–287
    - ligands
      - complexing properties, 273–274
      - electrochemical studies, 284–285
      - substituent effects, 280–282
      - substituents with lone pairs, 275–280
      - substituents without lone pairs, 280
    - $\pi$  interactions, 282–284
  - Monotropic, liquid crystals, 179
  - MRI, *see* Magnetic resonance imaging
- N**
- Nematic phase
    - calamitic mesogens, 171–172
    - discotic mesogen, 172–173
  - Nickel cages
    - decanuclear cages, 76–77
    - dodecanuclear cages, 76–77
    - heptanuclear cages, 74
    - hexanuclear cages, 72–74
    - largest cages, 78–80
    - nonanuclear cages, 75–76
    - octanuclear cage, 75
    - undecanuclear cages, 76–77
  - Nickel complexes, dioxopentamine,
    - monooxygenase activity, 313
  - 4-Nitrobenzoic acid, stilbazole complexes,
    - 201
  - 3-Nitrophenol, with 4-octyloxystilbazole,
    - 198–199
  - 4-Nitrophenol, with alkoxystilbazoles,
    - 196–197
  - 4-Nitrophenylphosphate ester, propylene
    - glycol, as RNA substrate model,
      - 302–303
  - 4-Nitrostilbazoles, hydrogen-bonded
    - complexes, 200–201
  - NLO, *see* Nonlinear optics
  - Noble gases
    - liquefied, 123–130
    - properties, 114
    - transition metal complexes,
      - see* Transition metal–noble gas
        - complexes
  - Nonadecanuclear iron cages, 60–61

- Nonanuclear cobalt cages, 67–68  
 Nonanuclear copper cages, 92  
 Nonanuclear iron cages, 55  
 Nonanuclear manganese cages, 37–38  
 Nonanuclear nickel cages, 75–76  
 Nonanuclear vanadium cages, 13, 16–17  
 Nonlinear optics  
   basic concepts, 159–160  
   stilbazole derivatives, 161–165  
 $N_3P_3F_6$   
   with difunctional reagents, 345–350  
   with monofunctional reagents, 341–345  
 $N_4P_4F_8$   
   reactions, 351–353  
   spirocyclic amino derivative, 353–354  
 Nuclear magnetic resonance  
   fluorophosphazenes, 339  
   Pt<sub>3</sub> clusters, 244–245  
   symmetric tetraplatinum clusters, 223–224  
   tetraplatinum clusters, 221–223  
   unsymmetric tetraplatinum clusters, 224–231  
 Nucleobase recognition reagents, 308–312
- O**
- Octadecanuclear iron wheel, 61–62  
 Octadecanuclear manganese cages, 46–47  
 Octadecanuclear vanadium cages, 16  
 Octahedral iron cages, 50  
 Octanuclear chromium wheel, 18–21  
 Octanuclear cobalt cages, 65–67  
 Octanuclear copper cages  
   with azathioprine, 92  
   from copper(I)-3,5-dimethylpyrazole, 90  
   homometallic cages, 90–91  
   from 2-hydroxy-1,3-propanediylbis(acetylacetoneimine), 91–92  
   from 6,6'-oxybis[1,4-bis(2'-pyridylamino)phthalazine], 91  
   pyridonate ligands, 90  
   from uridine, 90  
   various preparations, 88–90  
 Octanuclear iron cages  
   formation FeCl<sub>3</sub> and Na(O<sub>2</sub>CR), 54–55  
   with iron-oxo core, 54  
   synthesis, 52–53  
   tripodal iron ligands, 53–54  
 Octanuclear manganese cages  
   and heterometallic alkoxides, 36–37  
   homovalent cage, 35–36  
   picolinate-bridged cage, 34–35  
   with polydentate ligands, 36  
   synthesis, 34  
 Octanuclear nickel cages, 75  
 Octanuclear vanadium cages, 12  
 4-Octyloxystilbazole, with 3-nitrophenol, 198–199  
 Octylsulfate, monoalkoxystilbazoles, 188  
 Oligomerization, chromium cages, 24  
 Organometallic reagents, with cyclic trimeric fluorophosphazenes, 341–342  
 OS, *see* Octylsulfate  
 Out of phase, single-molecule magnets, 3  
 Oxime ligands, hexanuclear copper cages, 81–82  
 Oxo-centered manganese triangles, in serendipitous assembly, 7  
 6,6'-Oxybis[1,4-bis(2'-pyridylamino)phthalazine], 91  
 Oxygenase promoters, pendant-arm macrocycles, 312–313
- P**
- Palladium complexes  
   monoalkoxystilbazoles, 185  
   stilbazoles, 157–158, 183–185  
   3,4,5-trialkoxystilbazoles, 192–194  
 Palmitoyl chloride, in surfactant preparation, 325  
 Pauli repulsion, transition metal–noble gas complexes, 144  
 Pendant antennae, lanthanide complexes, 316–321  
 Pendant-arm macrocycles  
   carrier reagents for MRI, 321–322  
   hydrolytic enzyme models  
     for alkaline phosphatase, 294–299  
     for class II aldolases, 299–301  
   lanthanide complexes, with pendant antennae, 316–321  
   luminescent sensors, pendant fluorophores, 314–316

- molecular receptors, 326–330
  - nucleobase recognition reagents, 308–312
  - oxygenase promoters, 312–313
  - second-generation, 293–294
  - surfactants, 324–326
  - synthetic ribonucleases, 301–308
  - tumor-directed radioisotope carriers, 322–324
  - Pendant fluorophores, complexes, 314–316
  - Pentadentate Schiff-base ligand, in hexanuclear manganese cages, 29
  - Perfluorinated cyclic phosphazenes
    - physical and spectral properties, 338–339
    - structures and synthesis, 336–337, 340–341
  - Phenylarsonate ligands, in dodecanuclear vanadium cages, 14
  - Phenylsquarate complexes
    - heavier transition metals, 284
    - synthesis, 280
  - Phosphazenes
    - chlorophosphazenes, 336–337
    - cyclic phosphazenes, 336–337
    - cyclic tetrameric fluorophosphazenes, 351–355
    - cyclic trimeric fluorophosphazenes, 341–350
    - fluorophosphazenes, 341–355
    - perfluorinated cyclic phosphazenes, 336–341
  - Photolysis
    - $(\epsilon^2\text{-}(\text{C}_2\text{F}_5)_2\text{PCH}_2\text{CH}_2\text{P}(\text{C}_2\text{F}_5)_2)$   
 $\text{Cr}(\text{CO})_4$ , 122
    - $\text{Fe}(\text{CO})_5$ , 117–118
  - pH sensors
    - $\text{Eu}(\text{III})$  complexes, 318
    - pendant fluorophores, 314–316
  - Picolinate-bridged manganese cages, 34–35
  - 4-Picoline, in stilbazole synthesis, 152
  - $\pi$  interactions
    - monosubstituted squarate complexes, 282–284
    - squarate complexes, 282–284
  - Platinum complexes
    - EHMO study, 241–243
    - monoalkoxystilbazoles, 185
    - $\text{Pt}_4(\text{CH}_3\text{COO})_8$ , 207–208
    - $\text{Pt}_3$  clusters, *see* Triplatinum clusters
    - $\text{Pt}_4$  clusters, *see* Tetraplatinum clusters
    - $^{195}\text{Pt}$  NMR, 225–230
    - stilbazoles, 157, 183–185
    - 3,4,5-trialkoxystilbazoles, 192–194
  - Poly(alkoxy)stilbazoles complexes, 191–194
  - Polycatenar mesogens, stilbazoles, 175–177
  - Polydentate ligands
    - in hexanuclear iron cages, 49–50
    - in octanuclear manganese cages, 36
  - Polynuclear cages, synthetic strategies, 4–5
  - Polyoxovanadate cages, in polynuclear vanadium chemistry, 9
  - Pyridine ring rotation,  $\text{Pt}_4$  clusters, 233–234
  - Pyridonate ligands
    - as bridging ligands, 6–7
    - in octanuclear copper cages, 90
- R**
- Radon, associated chemistry, 117
  - Rhodium–xenon, liquefied noble gas studies, 129
  - Ribonucleases, synthetic, 301–308
  - RNA
    - nucleobase recognition reagents, 308–312
    - substrate model, 302–303
- S**
- Secondary amines, for chromium cages, 24–25
  - Sensors
    - luminescent sensors, 314–321
    - pH sensors, 314–316, 318
    - temperature, 316
  - Serendipitous assembly, as synthetic approach, 6–8
  - $\sigma$  complexes, matrix-isolation studies, 121
  - Silver dodecylsulfate salts
    - 3,4-dialkoxystilbazole complexes, 191–192

- Silver dodecylsulfate salts (*cont.*)  
  poly(alkoxy)stilbazole complexes,  
    191–192
- Silver(I) stilbazole complexes  
  monoalkoxystilbazoles, 185–190  
  structure, 183–185
- Silylated diols, with fluorophosphazenes,  
  348
- Silylated dithiols, with  
  fluorophosphazenes, 348
- Silylated thiols, with fluorophosphazenes,  
  348
- Single-molecule magnets  
  dodecanuclear manganese cages, 44  
  iron cages, 53  
  polynuclear cages, 4–5  
  properties, 2–4
- Smectic phase, calamitic mesogens,  
  171–172
- SMM, *see* Single-molecule magnets
- Solution, trinuclear platinum(II) cluster  
  complexes species, 243
- Spectroscopy  
  for Ar compounds, 115  
  Cr(CO)<sub>5</sub>, 120  
  KrMn(CO)<sub>5</sub> and [KrFe(CO)<sub>5</sub>]<sup>+</sup>, 123  
  perfluoro cyclic phosphazenes, 338–339  
  squarate complexes, 270  
  squarate ion, 252  
  supersonic jets, 134  
  time-resolved infrared,  
    *see* Time-resolved infrared  
    spectroscopy
- Squarates  
  coordination modes, 252–259  
  cubic structures, 267–268  
  heavier transition metals, 268–269  
  lanthanides, 268–269  
  as linking group, 269  
  monosubstituted, *see* Monosubstituted  
    squarate complexes  
  with  $\pi$  interactions, 282–284  
  spectroscopy, 252, 270  
  various compounds, 259–262
- Squaric acids  
  electrochemistry, 271  
  electron-transfer phenomena, 262–267  
  hydrogen bonding complexes, 285–287  
  magnetochemistry, 262–267  
  salts, 259
- Stilbazoles  
  hydrogen-bonded compounds, 194–201  
  Langmuir–Blodgett films  
    basic concepts, 165–166  
    metal complexes, 167–169  
  liquid crystals  
    basic concepts, 169–170  
    calamitic mesogen phases, 170–172  
    cubic phase, 177–178  
    discotic mesogen phases, 172–175  
    mesophases, 178–181  
    metals into, 181  
    polycatenar mesogens, 175–177  
  metal complexes, 154–158  
  nonlinear optics  
    basic concepts, 159–160  
    properties, 161–165  
  synthesis and characterization,  
    152–154
- Supercritical-fluid studies, transition  
  metal–noble gas complexes, 134–141
- Supersonic jets, Fourier-transform  
  microwave spectroscopy, 134
- Surface curvature, tetracatenar  
  mesogens, 176
- Surfactants, pendant-arm macrocycles,  
  324–326
- Symmetric tetraplatinum clusters, <sup>195</sup>Pt  
  NMR, 223–224
- Synthetic ribonucleases, 301–308

**T**

- Temperature sensors, pendant  
  fluorophores, 316
- Terminal acetylene derivatives, with  
  fluorophosphazenes, 344
- Tetracatenar mesogens, stilbazoles,  
  175–177
- Tetradecanuclear copper cages, 95–96
- Tetradentate ligands, Pt<sub>4</sub> clusters, 216
- 1,1,6,6-Tetrakis(imidazol-2-yl)-  
  2,5-diazaheptane, 85
- N,N,N',N'*-Tetramethylethane-  
  1,2-diamine, 83–84
- Tetranuclear manganese cages, 37
- Tetranuclear vanadium cages, 9
- Tetraplatinum clusters  
  in acetonitrile hydration, 234–236

- bidentate ligands, 214–216  
core rotation, 231–233  
EHMO study, 219–221  
with hexadentate ligands, 216  
 $^1\text{H}$  NMR, 221–223  
with monodentate ligands, 210–213  
 $^{195}\text{Pt}$  NMR, 221–223  
pyridine ring rotation, 233–234  
regioselective ligand exchange reaction, 207–208  
structures, 208–210  
symmetric clusters, 223–224  
with tetradentate ligands, 216  
unsymmetric clusters, 224–231  
X-ray structures, 216–219  
Thermotropic liquid crystals, hydrogen bonding, 195  
Thermotropic mesogens, cubic phase, 177  
Thymine, nucleobase recognition reagents, 309–310  
Time-resolved infrared spectroscopy  
   $\text{Bp}^*\text{Rh}(\text{CO})_2$ , 129  
   $\text{CpMn}(\text{CO})$  and  $\text{CpMn}(\text{CO})_2$ , 133  
  in liquefied noble gas studies, 127–128  
   $\text{Tp}^*\text{Rh}(\text{CO})_2$ , 129  
   $\text{W}(\text{CO})_5\text{Xe}$ , 131  
 $\text{Tp}^*\text{Rh}(\text{CO})_2$ , *see* Hydridotris(3,5-dimethylpyrazolyl)borate  
   $\text{Rh}(\text{CO})_2$   
Transesterification,  
  4-nitrophenylphosphate ester of propylene glycol, 302–303  
Transition metal–noble gas complexes  
  Ar–Be compounds, 115  
  BDEs, 141–146  
  bonding, 146–147  
  first stable complex, 113–114  
  gas-phase studies, 130–134  
  Kr compounds, 116  
  liquefied noble gas studies, 123–130  
  matrix–isolation studies, 117–123  
  Rn compounds, 117  
  supercritical-fluid studies, 134–141  
  Xe compounds, 116–117  
Transition metals  
  phenylsquarate complexes, 284  
  squarate complexes, 268–269  
3,4,5-Trialkoxystilbazoles  
  Pt and Pd complexes, 192–194  
  silver complexes, 192  
Triangular cluster complexes, 238–240  
  1,4,7-Triazacyclononane, 325  
Tridecanuclear cobalt cages, 71–72  
Tridecanuclear manganese cages, 45–46  
Triethanolamine, in hexanuclear iron cages, 51  
Trigonal prisms, as cage family, 101  
Trimethylsilyl acetylene derivatives, with fluorophosphazenes, 344  
Trimethylsilyl amines, with fluorophosphazenes, 343  
Trimethylstannyl amines, with fluorophosphazenes, 343  
Trinuclear platinum(II) cluster complexes  
  cluster core transformation, 240–241  
  EHMO study, 241–243  
  in-plane substitution reactivity, 243–244  
   $\text{Pt}_3$  clusters,  $^{195}\text{Pt}$  NMR, 244–245  
  species in solution, 243  
  synthesis, 236–238  
  triangular cluster complexes, structures, 238–240  
Triplatinum clusters,  $^{195}\text{Pt}$  NMR, 244–245  
TRIR spectroscopy, *see* Time-resolved infrared spectroscopy  
Tumor-directed radioisotope carriers, pendant-arm macrocycles, 322–324  
Tungsten compounds  
  *ab initio* calculations, 143  
  bonding to Xe and Kr, 130–131  
  TRIR spectroscopy, 131, 135–136  
  W–Xe, BDE, 132–133
- U**
- Ultraviolet photochemistry,  $\text{HMn}(\text{CO})_5$  and  $\text{CH}_3\text{Mn}(\text{CO})_5$ , 122  
Ultraviolet–visible spectroscopy, squarate complexes, 270  
Undecanuclear iron cages, 57–58  
Undecanuclear nickel cages, 76–77  
Undecanuclear paramagnetic cobalt cages, 70–71  
Unsymmetric tetraplatinum clusters, 224–231  
Uracil, nucleobase recognition reagents, 309–310  
Uridine, in octanuclear copper cages, 90

**V**

- Vanadium cages  
  alkoxide cages, 16  
  decanuclear cage, 13–14  
  dodecanuclear cages, 14–15  
  heptanuclear cages, 11–12  
  hexadecanuclear cages, 15  
  hexanuclear cages, 10–11  
  nonanuclear cages, 13, 16–17  
  octadecanuclear cages, 16  
  octanuclear cage, 12  
  polyoxovanadate cages, 9  
  tetranuclear cage, 9  
Vibrational Raman spectroscopy,  
  perfluoro cyclic phosphazenes, 339

**W**

- Wheels, as cage family, 96–98

**X**

- Xenon compounds  
  associated chemistry, 116–117  
  liquefied solution, 125–126  
  M(CO)<sub>5</sub> interactions, 130–131, 142  
  Xe–Au bond, BDE, 113–114  
  Xe–Rh, liquefied noble gas studies, 129  
  Xe–W, BDE, 132–133  
X-ray studies  
  hydrolytic enzyme models, 298  
  liquid crystals, 181  
  Pt<sub>4</sub> clusters, 216–219  
  stilbazole ligands, 154

**Z**

- Zinc complexes  
  apocarbonic anhydrase, 315  
  synthetic ribonucleases, 309–310

## CONTENTS OF PREVIOUS VOLUMES

### VOLUME 39

Synthetic Approach to the Structure and  
Function of Copper Proteins  
*Nobumasa Kitajima*

Transition Metal and Organic  
Redox-Active Macrocycles Designed  
to Electrochemically Recognize  
Charged and Neutral Guest Species  
*Paul D. Beer*

Structure of Complexes in Solution  
Derived from X-Ray Diffraction  
Measurements  
*Georg Johansson*

High-Valent Complexes of Ruthenium  
and Osmium  
*Chi-Ming Che and Vivian  
Wing-Wah Yam*

Heteronuclear Gold Cluster Compounds  
*D. Michael P. Mingos and  
Michael J. Watson*

Molecular Aspects on the Dissolution and  
Nucleation of Ionic Crystals in Water  
*Hitoshi Ohtaki*

INDEX

### VOLUME 40

Bioinorganic Chemistry of  
Pterin-Containing Molybdenum and  
Tungsten Enzymes  
*John H. Enemark and Charles G. Young*

Structure and Function of Nitrogenase  
*Douglas C. Rees, Michael K. Chan, and  
Jongsun Kim*

Blue Copper Oxidases  
*A. Messerschmidt*

Quadruply Bridged Dinuclear Complexes  
of Platinum, Palladium, and Nickel  
*Keisuke Umakoshi and Yoichi Sasaki*

Octacyano and Oxo- and  
Nitridotetracyano Complexes of  
Second and Third Series Early  
Transition Metals  
*Johann G. Leipoldt, Stephen S. Basson,  
and Andreas Roodt*

Macrocyclic Complexes as Models for  
Nonporphine Metalloproteins  
*Vickie McKee*

Complexes of Sterically Hindered  
Thiolate Ligands  
*J. R. Dilworth and J. Hu*

INDEX

### VOLUME 41

The Coordination Chemistry of  
Technetium  
*John Baldas*

Chemistry of Pentafluorosulfanyl  
Compounds  
*R. D. Verma, Robert L. Kirchmeier, and  
Jean'ne M. Shreeve*

The Hunting of the Gallium Hydrides  
*Anthony J. Downs and Colin R. Pulham*

The Structures of the Group 15  
Element(III) Halides and  
Halogenoanions  
*George A. Fisher and  
Nicholas C. Norman*

Intervalence Charge Transfer and  
Electron Exchange Studies of  
Dinuclear Ruthenium Complexes  
*Robert J. Crutchley*

Recent Synthetic, Structural,  
Spectroscopic, and Theoretical  
Studies on Molecular Phosphorus  
Oxides and Oxide Sulfides  
*J. Clade, F. Frick, and M. Jansen*

Structure and Reactivity of Transferrins  
*E. N. Baker*

## INDEX

## VOLUME 42

Substitution Reactions of Solvated Metal Ions  
*Stephens F. Lincoln and  
André E. Merbach*

Lewis Acid–Base Behavior in Aqueous Solution: Some Implications for Metal Ions in Biology  
*Robert D. Hancock and  
Arthur E. Martell*

The Synthesis and Structure of Organosilanols  
*Paul D. Lickiss*

Studies of the Soluble Methane Monooxygenase Protein System: Structure, Component Interactions, and Hydroxylation Mechanism  
*Katherine E. Liu and  
Stephen J. Lippard*

Alkyl, Hydride, and Hydroxide Derivatives in the *s*- and *p*-Block Elements Supported by Poly(pyrazolyl)borato Ligand: Models for Carbonic Anhydrase, Receptors for Anions, and the Study of Controlled Crystallographic Disorder  
*Gerard Parkin*

## INDEX

## VOLUME 43

Advances in Thallium Aqueous Solution Chemistry  
*Julius Glaser*

Catalytic Structure–Function Relationships in Heme Peroxidases  
*Ann M. English and  
George Tsapraillis*

Electron-, Energy-, and Atom-Transfer

Reactions between Metal Complexes and DNA

*H. Holden Thorp*

Magnetism of Heterobimetallics: Toward Molecular-Based Magnets

*Olivier Kahn*

The Magnetochemistry of Homo- and Hetero-Tetranuclear First-Row *d*-Block Complexes

*Keith S. Murray*

Diiron–Oxygen Proteins

*K. Kristoffer Andersson and Astrid  
Gräslund*

Carbon Dioxide Fixation Catalyzed by Metals Complexes

*Koji Tanaka*

## INDEX

## VOLUME 44

Organometallic Complexes of Fullerenes

*Adam H. H. Stephens and  
Malcolm L. H. Green*

Group 6 Metal Chalcogenide Cluster Complexes and Their Relationships to Solid-State Cluster Compounds  
*Taro Saito*

Macrocyclic Chemistry of Nickel

*Myunghyun Paik Suh*

Arsenic and Marine Organisms

*Kevin A. Francesconi and  
John S. Edmonds*

The Biochemical Action of Arsonic Acids Especially as Phosphate Analogues

*Henry B. F. Dixon*

Intrinsic Properties of Zinc(II) Ion Pertinent of Zinc Enzymes

*Eiichi Kimura and Tohru Koike*

Activation of Dioxygen by Cobalt Group Metal Complexes

*Claudio Bianchini and Robert  
W. Zoellner*

Recent Developments in Chromium  
Chemistry  
*Donald A. House*

INDEX

VOLUME 45

Syntheses, Structures, and Reactions of  
Binary and Tertiary Thiomolybdate  
Complexes Containing the (O)Mo(S<sub>x</sub>)  
and (S)Mo(S<sub>x</sub>) Functional Groups  
(*x* = 1, 2, 4)  
*Dimitri Coucouvanis*

The Transition Metal Ion Chemistry of  
Linked Macrocyclic Ligands  
*Leonard F. Lindoy*

Structure and Properties of Copper–Zinc  
Superoxide Dismutases  
*Ivano Bertini, Stefano Mangani, and  
Maria Silvia Viezzoli*

DNA and RNA Cleavage by Metal  
Complexes  
*Genevieve Pratviel, Jean Bernadou, and  
Bernard Meunier*

Structure–Function Correlations in High  
Potential Iron Problems  
*J. A. Cowan and Siu Man Lui*

The Methylamine Dehydrogenase  
Electron Transfer Chain  
*C. Dennison, G. W. Canters, S. de Vries,  
E. Vijgenboom, and R. J. van Spanning*

INDEX

VOLUME 46

The Octahedral M<sub>6</sub>Y<sub>6</sub> and M<sub>6</sub>Y<sub>12</sub> Clusters  
of Group 4 and 5 Transition Metals  
*Nicholas Prokopuk and D. F. Shriver*

Recent Advances in Noble–Gas Chemistry  
*John H. Holloway and Eric G. Hope*

Coming to Grips with Reactive  
Intermediates  
*Anthony J. Downs and Timothy  
M. Greene*

Toward the Construction of Functional  
Solid-State Supramolecular Metal  
Complexes Containing Copper(I) and  
Silver(I)  
*Megumu Munakata, Liang Ping Wu,  
and Takayoshi Kuroda-Sowa*

Manganese Redox Enzymes and Model  
Systems: Properties, Structures, and  
Reactivity  
*Neil A. Law, M. Tyler Caudle, and  
Vincent L. Pecoraro*

Calcium-Binding Proteins  
*Bryan E. Finn and Torbjörn Drakenberg*

Leghemoglobin: Properties and Reactions  
*Michael J. Davies, Christel Mathieu,  
and Alain Puppò*

INDEX

VOLUME 47

Biological and Synthetic [Fe<sub>3</sub>S<sub>4</sub>] Clusters  
*Michael K. Johnson, Randall E.  
Duderstadt, and Evert C. Duin*

The Structures of Rieske and Rieske-Type  
Proteins  
*Thomas A. Link*

Structure, Function, and Biosynthesis of  
the Metallosulfur Clusters in  
Nitrogenases  
*Barry E. Smith*

The Search for a “Prismane” Fe–S Protein  
*Alexander F. Arendsen and Peter F.  
Lindley*

NMR Spectra of Iron–Sulfur Proteins  
*Ivano Bertini, Claudio Luchinat, and  
Antonio Rosato*

Nickel–Iron–Sulfur Active Sites:  
Hydrogenase and CO Dehydrogenase  
*Juan C. Fontecilla-Camps and  
Stephen W. Ragsdale*

FeS Centers Involved in Photosynthetic  
Light Reactions  
*Barbara Schoepp, Myriam Brugna,  
Evelyne Lebrun, and Wolfgang Nitschke*

Simple and Complex Iron–Sulfur  
Proteins in Sulfate Reducing  
Bacteria

*Isabel Moura, Alice S. Pereira,  
Pedro Tavares, and  
José J. G. Moura*

Application of EPR Spectroscopy to the  
Structural and Functional Study of  
Iron–Sulfur Proteins

*Bruno Guigliarelli and  
Patrick Bertrand*

INDEX

VOLUME 48

Cumulative Index for Volumes 1–47

VOLUME 49

Inorganic and Bioinorganic Reaction  
Mechanisms: Application of  
High-Pressure Techniques

*Rudi van Eldik, Carlos Dücker-Benfer,  
and Florian Thaler*

Substitution Studies of Second- and  
Third-Row Transition Metal Oxo  
Complexes

*Andreas Roodt, Amira Abou-Hamdan,  
Hendrik P. Engelbrecht, and  
Andre E. Merbach*

Protonation, Oligomerization, and  
Condensation Reactions of  
Vanadate(V), Molybdate(VI), and  
Tungstate(VI)

*J. J. Cruywagen*

Medicinal Inorganic Chemistry

*Zijian Guo and Peter J. Sadler*

The Cobalt(III)-Promoted Synthesis of  
Small Peptides

*Rebecca J. Browne, David A.  
Buckingham, Charles R. Clark, and  
Paul A. Sutton*

Structures and Reactivities of  
Platinum-Blues and the Related

Amidate-Bridged Platinum<sup>III</sup>  
Compounds

*Kazuko Matsumoto and Ken Sakai*

INDEX

VOLUME 50

The Reactions of Stable Nucleophilic  
Carbenes with Main Group  
Compounds

*Claire J. Carmalt and Alan H. Cowley*

Group 1 Complexes of P- and As-Donor  
Ligands

*Keith Izod*

Aqueous Solution Chemistry of Beryllium

*Lucia Alderighi, Peter Gans,  
Stefano Midollini, and Alberto Vacca*

Group 2 Element Precursors for the  
Chemical Vapor Deposition of  
Electronic Materials

*Jason S. Matthews and  
William S. Rees Jr.*

Molecular, Complex Ionic, and Solid-State  
PON Compounds

*Roger Marchand, Wolfgang Schnick,  
and Norbert Stock*

Molecular Clusters of Dimetalated  
Primary Phosphanes and Arsanes

*Matthias Driess*

Coordination Complexes of Bismuth(III)  
Involving Organic Ligands with  
Pnictogen or Chalcogen Donors

*Glen G. Briand and Neil Burford*

Phanes Bridged by Group 14 Heavy  
Elements

*Hideki Sakurai*

INDEX

VOLUME 51

Clinical Reactivity of the Active Site of  
Myoglobin

*Emma Lloyd Raven and  
A. Grant Mauk*

Enzymology and Structure of Catalases  
*Peter Nicholls, Ignacio Fita, and  
Peter C. Loewen*

Horseradish Peroxidase  
*Nigel C. Veitch and Andrew T. Smith*

Structure and Enzymology of Diheme  
Enzymes: Cytochrome *cd*<sub>1</sub> Nitrate  
and Cytochrome *c* Peroxidase  
*Vilmos Fülöp, Nicholas J. Watmough,  
and Stuart J. Ferguson*

Binding and Transport of Iron-Porphyrins  
by Hemopexin  
*William T. Morgan and Ann Smith*

Structures of Gas-Generating Heme  
Enzymes: Nitric Oxide Synthase and  
Heme Oxygenase

*Thomas L. Poulos, Huiying Li,  
C. S. Raman, and David J. Schuller*

The Nitric Oxide-Releasing Heme  
Proteins from the Saliva of the  
Blood-Sucking Insect  
*Rhodnius prolixus*  
*F. Ann Walker and William  
R. Montfort*

Heme Oxygenase Structure  
and Mechanism  
*Paul R. Ortiz de Montellano and  
Angela Wilks*

*De Novo* Design and Synthesis  
of Heme Proteins  
*Brian R. Gibney and P. Leslie Dutton*

INDEX